



HAL
open science

The early nitrogen biogeochemical cycle: insights into the temporality and routes of Earth's oxygenation

Alice Pellerin Pellerin-Lefebvre

► To cite this version:

Alice Pellerin Pellerin-Lefebvre. The early nitrogen biogeochemical cycle: insights into the temporality and routes of Earth's oxygenation. Earth and Planetary Astrophysics [astro-ph.EP]. Université Bourgogne Franche-Comté, 2024. English. NNT: 2024UBFCK020 . tel-04707965

HAL Id: tel-04707965

<https://theses.hal.science/tel-04707965v1>

Submitted on 24 Sep 2024

HAL is a multi-disciplinary open access archive for the deposit and dissemination of scientific research documents, whether they are published or not. The documents may come from teaching and research institutions in France or abroad, or from public or private research centers.

L'archive ouverte pluridisciplinaire **HAL**, est destinée au dépôt et à la diffusion de documents scientifiques de niveau recherche, publiés ou non, émanant des établissements d'enseignement et de recherche français ou étrangers, des laboratoires publics ou privés.



BIOGÉOSCIENCES

Thèse de doctorat

Université de Bourgogne Franche-Comté

Spécialité : **Géochimie isotopique**

Préparée au laboratoire Biogéosciences, UMR CNRS 6282, Université de Bourgogne

École Doctorale Environnement Santé, UFR SVTE

Par

Alice PELLERIN

The early nitrogen biogeochemical cycle : insights into the temporality and routes of Earth's oxygenation

Le cycle biogéochimique précoce de l'azote : un éclairage sur la temporalité et les modalités d'oxygénation de la Terre

Composition du Jury:

Eva E. STUËKEN	Reader, University of St Andrews	rapportrice
Kevin LEPOT	Maître de conférences, HDR, Université de Lille	rappporteur
Emmanuelle VENNIN	Professeure des universités, Université de Bourgogne	examinatrice, présidente du jury
Daniele L. PINTI	Professeur, Université du Québec à Montréal	examineur
Pierre CARTIGNY	Directeur de recherche CNRS, Université Paris Cité	examineur
Christophe THOMAZO	Maître de conférences, HDR, Université de Bourgogne	directeur de thèse
Magali ADER	Professeure des universités, Université Paris Cité	co-directrice de thèse
Pascal PHILIPPOT	Directeur de recherche CNRS, Université de Montpellier	invité

ABSTRACT

Nitrogen is an essential nutrient for all living organisms, its availability strongly influencing biological productivity. Additionally, the nitrogen isotopic composition of organic matter is controlled by both metabolic activity and redox speciation, given that key biologically-mediated pathways of the oceanic nitrogen cycle are redox-dependent. As such, the nitrogen isotopic signature preserved in sedimentary rocks ($\delta^{15}\text{N}_{\text{sed}}$) has become a standard tool for uncovering redox changes in the oceans associated with the evolution of the biosphere. In particular, this work explores the transition from an anoxic world to oxygenated oceans using secular variations in the Precambrian $\delta^{15}\text{N}_{\text{sed}}$ signature. It aims at precisising the timing, modalities and driving factors of oceanic oxygenation leading to the Great Oxidation Event (GOE). First, using an updated $\delta^{15}\text{N}_{\text{sed}}$ database spanning the Precambrian, this thesis pinpoints grey areas in our current understanding of the reliability of the $\delta^{15}\text{N}_{\text{sed}}$ proxy as a paleoecological and paleoenvironmental archive and in the assumptions that underpin nitrogen cycle reconstructions. It targets three sites spanning from 3.4 to 2.5 Ga, and representative of different lithologies and depositional environments. Besides improving the temporal resolution of the Archean $\delta^{15}\text{N}$ record, they enhance our understanding of the N-biogeochemical cycle dynamics in three key contexts. The 3.4 Ga Buck Reef Chert sedimentary deposit (Kaalvaal Craton, South Africa) is one of the first records of how the N cycle operated in anoxic and ferruginous conditions representative of many Paleoproterozoic depositional environments. The $\delta^{15}\text{N}$ signature for this deposit suggests an early rise of N redox cycling using iron oxides as an electron acceptor, suggesting a coupling between the Fe and N cycles before the rise of oxygen. The 2.7 Ga Serra Sul Formation (Amazonian Craton, Brazil) records a new occurrence of positive $\delta^{15}\text{N}$ values in the 2.8-2.6 Ga time interval. This unique feature of the Neoproterozoic record highlights the onset of ammonium oxidation locally, reflecting oxygen production through oxygenic photosynthesis more than 200 Ma before the GOE. It marks the earliest steps of the major biogeochemical reorganization that led to surface waters and subsequent atmospheric oxygenation. Finally, the 2.5 Ga Malmani Subgroup (Kaalvaal Craton, South Africa) shows that stromatolitic carbonates, although potential niches for early aerobic systems, might be more representative of local N cycle processes than of the global oxygenation of the water column. As a whole, this study confirms that N isotopes are a powerful tool to record both large scale redox changes and local biological processes. Yet, it identifies some shortcomings in current interpretations of the $\delta^{15}\text{N}$ signature, such that positive $\delta^{15}\text{N}$ values do not necessarily indicate the presence of an oxygen-sustained nitrate reservoir, or the importance

of multi-parameter studies of the $\delta^{15}\text{N}$ signal. It proposes a framework including lithology, metamorphism, and organic carbon isotopes to guide future analyses of sedimentary $\delta^{15}\text{N}$ records.

RÉSUMÉ

L'azote est un nutriment essentiel pour tous les organismes vivants, sa disponibilité influant fortement sur la productivité primaire biologique. En outre, la composition isotopique de l'azote de la matière organique est contrôlée à la fois par l'activité métabolique et par la spéciation redox, les voies métaboliques majeures du cycle de l'azote océanique étant dépendants de l'état redox de la colonne d'eau. Ainsi, la signature isotopique en azote préservée dans les roches sédimentaires ($\delta^{15}\text{N}_{\text{sed}}$) est un outil largement utilisé pour identifier les changements redox des océans en lien avec l'évolution de la biosphère. Ce travail explore en particulier la transition d'un océan anoxique à un océan oxygéné, en utilisant les variations séculaires du $\delta^{15}\text{N}_{\text{sed}}$ au cours du Précambrien. Il vise à préciser la temporalité, les modalités et les moteurs de l'oxygénation des océans ayant conduit au Grand Événement d'Oxygénation (GEO). Tout d'abord, la construction d'une base de données de $\delta^{15}\text{N}_{\text{sed}}$ au Précambrien a permis de mettre en évidence les incertitudes dans notre compréhension actuelle de la fiabilité du $\delta^{15}\text{N}_{\text{sed}}$ en tant qu'archive paléocéologique et paléoenvironnementale, et dans les hypothèses qui sous-tendent les reconstructions du cycle de l'azote. Cette thèse cible trois sites d'étude âgés de 3,4 à 2,5 Ga, représentatifs de différentes lithologies et environnements de dépôt. Tout en enrichissant la résolution temporelle de l'enregistrement du $\delta^{15}\text{N}_{\text{sed}}$ Archéen, ils améliorent notre compréhension de la dynamique du cycle biogéochimique de l'azote dans trois de ses contextes clés. Le dépôt sédimentaire du Buck Reef Chert (3,4 Ga, craton du Kaapvaal, Afrique du Sud) est l'un des premiers enregistrements de la dynamique du cycle de l'azote dans des conditions anoxiques et ferrugineuses, représentatives de nombreux environnements de dépôt Paléoarchéens. Le $\delta^{15}\text{N}_{\text{sed}}$ de cette formation suggère des changements redox précoces du cycle de l'azote, en utilisant les oxydes de fer comme accepteurs d'électrons, ce qui suggère un couplage entre les cycles du fer et de l'azote avant l'augmentation des teneurs en oxygène dans les océans. La formation de Serra Sul (2,7 Ga, craton amazonien, Brésil) enregistre une nouvelle occurrence de valeurs extrêmes du $\delta^{15}\text{N}_{\text{sed}}$ dans l'intervalle de temps 2.8-2.6 Ga. Cette caractéristique unique de l'enregistrement Néoarchéen met en évidence une oxydation locale d'ammonium, qui reflète la production d'oxygène par photosynthèse oxygénique plus de 200 Ma avant le GEO. Cet événement marque la première étape de la plus grande réorganisation biogéochimique de l'histoire de la Terre, ayant permis l'oxygénation des océans et de l'atmosphère. Enfin, les roches du Malmani Subgroup (2,5 Ga, craton du Kaapvaal, Afrique du Sud) montrent que les carbonates stromatolitiques, bien que constituant des niches préférentielles pour les premiers écosystèmes aérobies, sont plus représentatifs de processus

locaux du cycle de l'azote que de l'oxygénation globale de la colonne d'eau. Dans l'ensemble, cette étude confirme que les isotopes de l'azote constituent un outil puissant pour enregistrer à la fois les changements redox à l'échelle des océans et les processus biologiques locaux. Néanmoins, elle identifie des lacunes dans les interprétations actuelles de la signature isotopique en azote, comme le fait que les valeurs de $\delta^{15}\text{N}_{\text{sed}}$ positives n'indiquent pas nécessairement la présence d'un réservoir de nitrates soutenu par des conditions oxydatives, ou l'importance d'études multi-paramétriques du $\delta^{15}\text{N}_{\text{sed}}$. Elle propose un cadre incluant la lithologie, le métamorphisme et les isotopes du carbone organique pour guider les analyses futures des enregistrements en $\delta^{15}\text{N}_{\text{sed}}$.

“If you want to have good ideas you must have many ideas.

Most of them will be wrong, and what you have to learn

is which ones to throw away.”

Linus Pauling

REMERCIEMENTS

Bien plus qu'une aventure scientifique, une thèse est une aventure humaine, et si ces 3 années (et un peu plus car affinités) m'ont vue grandir, c'est grâce à toutes les personnes qui m'ont donné de leur temps et de leur énergie.

Merci, en particulier,

Aux membres du jury, pour avoir accepté de lire et d'évaluer mon travail. Il est loin d'être parfait, mais j'y ai mis du cœur et du jus de cerveau, et je repars avec au moins autant de questions que de réponses.

A l'ensemble du laboratoire Biogéosciences et de l'équipe GIS de l'IPGP, où j'ai toujours été très bien accueillie.

A Christophe et Magali, qui m'ont fait rêver, grandir, et réfléchir. Si j'ai aimé cette thèse, c'est surtout parce que j'ai aimé travailler avec vous. Vous m'avez toujours laissé beaucoup de liberté tout en étant disponibles quand j'avais besoin d'aide.

Merci Magali de m'avoir accueillie chez toi pendant toutes ces semaines de manips, de m'avoir appris les « trucs et astuces » de ta ligne d'azote, d'avoir partagé une fraction de tes réflexions sur la géochimie et la recherche en général, dans le RER ou en visio. Merci pour ton enthousiasme pendant ma rédaction, qui m'a reboostée puissance mille quand j'étais dans le dur.

Christophe, je te dois énormément et ces quelques mots seront bien insuffisants pour décrire la reconnaissance que j'ai pour toi. Je pense sans prétention avoir eu le meilleur directeur de la Terre ;-). Il y a les choses évidences : tu es le superman des relectures et corrections, et le rapporteur d'opportunités (« Tu veux pas aller faire une conf dans le Gers ? »). Notre seul point de discord majeur durant ces cinq années ensemble restant le style vestimentaire pour lequel on ne s'est jamais compris (« doudoune sans manches » vs. « chemise colorée style rideau »), on peut dire que notre association a été un succès. Merci pour ta bienveillance, ton positivisme, ton éternel enthousiasme scientifique, ta confiance en moi et en mes projets, à l'opposé de l'éducation que j'ai reçue. J'espère que tu as déteint sur moi, au moins un petit peu. Tes « *morning morning* » et le son de ton rire dans le couloir avant d'arriver à la bibliothèque me manquent déjà.

Aux héros analytiques qui mont épaulée techniquement : Ludo, Anne-Lise, Ivan, Rémi, Virginia, Gérard, Pierre A., Pierre C. & Thomas.

Aux collaborateurs avec lesquels j'ai eu la chance de travailler de près ou de loin: Johanna, Julien, Thomas, Virgil, Marie-No, Nicolas, Axel, Lizzie, Emmanuelle, Vincent, Pascal, Camille, Eric, Pierre Ca., Karim, Neha.

A Jean-François Deconinck et Pierre Cartigny, qui ont accepté de faire partie de mon Comité de Suivi de Thèse et m'ont donné de précieux conseils.

A ce lieu emblématique, à mi-chemin entre un dépôt, une île aux trésors, un musée et un bureau, qu'on nomme « la bibliothèque ». Cet endroit ne serait pas aussi magique sans les meilleurs ~~bureaux~~ bibliothécaires de l'univers entier (sans exagération aucune). Jérôme (alias « vous cherchez Jérôme ? »), gardien des lieux, merci pour tes recommandations houblonnées, visites des collections, fournitures de bureau (belette, tapis de souris ammonite, fleuret en plastique), et soutien moral. Erwan, discret entre deux bateaux/avions vers l'autre bout du monde. Robin & Ophélie, mes co-bureaux d'amour, j'ai eu de la chance de vous avoir pendant ces 3 ans. Merci pour votre patience, votre soutien et nos bonnes tranches de rigolades. Ophélie, merci pour tes chasses aux œufs entre les rayonnages et les mnm's partagés des vendredi aprem. Robin, d'Hawaï à Lyon en passant par Dijon, spéciale dédicace à nos discussions, couvrant un large spectre allant de l'effondrement des chimioclines aux mérites des différents goûts de Pim's. Le comique de répétition du téléphone banane à 15h et tes chansons fredonnées plein pot n'auront pas eu raison de notre complicité ;-).

A toute la team de doctorants & post-doctorants qui a accompagné une partie de ces années, et sans qui tout aurait été bien vide : Chris, Pierre, Louis, Alexandrine, Sarah, Agathe, Camille, Morgane, Marlisa, Esteban, Julien, Clément, Tessie, Myriam, Batistin, Pauline, Justine, Yann, Quentin, Gaëtan, Maïwenn, Luc, William, Nathan, Erwan, Mathilde, Charlène, Thomas, Alexandre... j'espère que je n'oublie personne. Les tea-times sur le toit, grands sauveurs de mes fins d'après-midi. Le flan, aux abricots s'il vous plaît. Le pic de cholestérol des 28 galettes dinosaures du mois de janvier. La brigade du style, toujours au rendez-vous.

Et merci du fond du cœur :

A tous mes copains sportifs festifs, j'ai trouvé une famille de cœur grâce à vous : Caro, Pio, Julie, Steph, Vincent, Coline, Ben, Alain, Benjamin, Jérôme, Ségo, la team de swimrunners, et tout ceux que j'oublie. A Lise, Flo, Simon-Pierre, Samuel, Mathieu, Aurore & Ben, Alex, Justine, Christian, MAB, Lolo. J'ai de la chance d'avoir des amis comme vous. A Manu, mon soutien et coéquipier pendant ces 3 années. Merci d'avoir toujours trouvé matière à me faire rire, de la bouillabaisse montpelliéraine aux bouchées à la reine. Jamais je n'aurais cru que le centre de la Terre ressemblerait autant à une soirée disco des années 80.

A ma famille, mes parents, et surtout mon frangin et ma frangine, toujours là pour moi. Je ne rirai jamais autant qu'avec vous, vous êtes les meilleurs. A Lilian, mon meilleur training partner, même s'il paraît que peu en sont restés à ce stade. Merci pour tes grands bras, tu boucheras mes artères avec du morbier et du comté mais ça en aura valu la peine.

TABLE OF CONTENTS

GENERAL INTRODUCTION	1
CHAPTER 1. THE MODERN OCEANIC BIOGEOCHEMICAL NITROGEN CYCLE	5
Introduction	6
1.1. Nitrogen stable isotopes - $\delta^{15}\text{N}$	9
1.2. N-assimilation pathways.....	12
1.2.1. Biological N_2 fixation (BNF)	12
1.2.2. Ammonification.....	15
1.2.3. Ammonium uptake	16
1.2.4. Nitrate uptake	17
1.3. Energy-yielding pathways	17
1.3.1. Nitrification	17
1.3.2. Denitrification	18
1.3.3. Anaerobic ammonium oxidation (anammox).....	20
1.3.4. Minor energy-yielding pathways of the modern N cycle.....	21
1.3.4.1. Feammox.....	21
1.3.4.2. Dissimilatory nitrate reduction to ammonium (DNRA)	21
1.3.4.3. Ammonium oxidation by methanotrophic bacteria.....	22
1.4. First-order controls on the modern oceanic N budget and the average oceanic $\delta^{15}\text{N}$	22
References.....	27
CHAPTER 2. A FRAMEWORK OF NITROGEN ISOTOPES INTERPRETATION IN PRECAMBRIAN SEDIMENTARY ROCKS	35
2.1. Preservation of the nitrogen isotope signature of primary producers through water-column transfers and post-depositional history	36
2.1.1. Primary producers' isotopic signature transfer to the sediment	37
2.1.2. Effect of diagenesis on sedimentary N concentration and isotope composition.....	39
2.1.3. Metamorphic and metasomatic alteration of the $\delta^{15}\text{N}$ signature	41
2.2. Nitrogen sources to the Archean Earth's surficial reservoirs and their isotope composition	43

2.2.1. Stability of the nitrogen atmospheric isotope composition through time	43
2.2.2. Organic hazes and aerosols production on the prebiotic Earth	43
2.2.3. Hydrothermalism.....	44
2.2.4. Biological and alternative fixed nitrogen sources	44
2.3. The evolution of biological and abiotic pathways of the early nitrogen cycle	45
2.3.1. Biological N ₂ fixation and the evolution of nitrogenase enzymes	45
2.3.2. The emergence of oxidative pathways of the N cycle: nitrogen as a proxy of paleoredox conditions	47
2.3.2.1. Dominantly oxic oceans.....	48
2.3.2.2. Redox-stratified oceans.....	48
2.3.2.3. Fully anoxic oceans.....	50
2.3.3. Ammonia degassing, an abiotic process that could have impacted the Archean N cycle and associated isotopic signature of sedimentary archive	52
2.4. The size of the dissolved nitrogen reservoir: insights into nutrient availability during the Archean	54
2.5. Conclusion: strengths and limits of using the $\delta^{15}\text{N}$ proxy in deep time	56
References.....	58
CHAPTER 3. SECULAR EVOLUTION IN PRECAMBRIAN $\delta^{15}\text{N}$ SIGNATURES	72
3.1. Introduction - Main features of the Precambrian sedimentary $\delta^{15}\text{N}$ record	73
3.2. Methods - Building an updated Precambrian $\delta^{15}\text{N}$ database	78
3.3. Results	79
3.4. Discussion - Secular evolution of the $\delta^{15}\text{N}$ signature through the Precambrian	82
3.4.1. Potential biases that may impact our interpretation of the $\delta^{15}\text{N}$ secular evolution through the Precambrian.....	82
3.4.2. First-order secular variations of the $\delta^{15}\text{N}$ signature through the Precambrian	84
3.4.3. Identifying analytical biases, secondary alteration and paleoenvironmental changes	85
3.5. Conclusions	87
References.....	129
Supplementary Information.....	133

CHAPTER 4. GEOLOGICAL CONTEXT OF THE STUDIED SAMPLES	140
4.1. Selection criteria for investigating grey areas of the Archean biogeochemical nitrogen cycle.	141
4.2. The Buck Reef Chert Formation (3.4 Ga, South Africa).....	144
4.2.1. Regional context.....	144
4.2.2. Stratigraphic framework of the Buck Reef Chert.....	147
4.2.3. Petrographic features and sedimentary facies	150
4.2.4. Paleoenvironment and chemical conditions.....	153
4.3. The Serra Sul Formation (2.7 Ga, Brazil).....	156
4.3.1. Regional context.....	156
4.3.2. Stratigraphic framework and geochronological constraints.....	157
4.3.3. Petrographic features and sedimentary facies	161
4.3.4. Paleoenvironments of the Serra Sul Formation.....	167
4.4. The Malmani Subgroup (2.5 Ga, South Africa)	168
4.4.1. Regional context.....	168
4.4.2. Stratigraphic framework of the studied samples	170
4.4.3. Petrographic features and sedimentary facies	173
4.4.4. Paleoenvironments and chemical conditions	176
CHAPTER 5. ANALYTICAL TECHNIQUES	184
5.1. Introduction	186
5.2. Sampling.....	187
5.3. Petrographic observations.....	187
5.4. Mineralogy.....	188
5.4.1. X-Ray Diffraction (XRD)	188
5.4.2. Raman spectroscopy.....	188
5.5. Elemental analyses.....	189
5.5.1. Major, minor and trace element concentrations	189
5.5.2. Electron Probe Micro-Analyses (EPMA)	189
5.5.3. Scanning Electron Microscopy (SEM)	190
5.5.4. Micro X-Ray Fluorescence (μ XRF).....	190

5.6. Carbon and nitrogen geochemical analyses.....	191
5.6.1. Sample preparation and chemical treatment	191
5.6.1.1. Decarbonated samples	191
5.6.1.2. Kerogen extracts	193
5.6.2. Carbon analyses : concentrations and isotope compositions	193
5.6.2.1. General principles of EA-IRMS	193
5.6.2.2. Total Organic Carbon (TOC) content and $\delta^{13}\text{C}_{\text{org}}$	194
5.6.2.3. Inorganic carbon content and $\delta^{13}\text{C}_{\text{carb}}$	194
5.6.3. Nitrogen analyses: concentrations and isotope compositions	195
5.6.3.1. Reliable N isotope measurements of small N quantities	195
5.6.3.2. Sealed tube combustion	196
5.6.3.2.1. Preparation of the sealed tubes	196
5.6.3.2.2. Reagents.....	197
5.6.3.2.3. Quantity of powder.....	197
5.6.3.2.4. Degassing under vacuum and sealing.....	197
5.6.3.2.5. Combustion.....	198
5.6.3.3. Extraction and purification on the vacuum line.....	198
5.6.3.4. Isotopic analysis by dual-inlet IRMS.....	199
5.6.3.6. Correction of $\delta^{15}\text{N}$ values of the blank contribution	200
References.....	201

CHAPTER 6. THE 3.4 GA BUCK REEF CHERT, A WINDOW INTO THE PALEOARCHEAN N CYCLE IN ANOXIC & FERRUGINOUS CONDITIONS..... 211

6.1. Article published in <i>Geobiology</i>	215
6.2. Methods	228
6.3. Supplementary Information	230
References.....	234

CHAPTER 7. NEOARCHEAN OXYGEN-BASED NITROGEN CYCLE EN ROUTE TO THE GREAT OXIDATION EVENT..... 236

Abstract..... 239

7.1. Nitrogen isotopes record water column oxidation..... 239

7.2. Extreme positive $\delta^{15}\text{N}$ values unique to the Neoproterozoic sedimentary record 240

7.3. Defining a Nitrogen Isotope Event (NIE)..... 243

7.4. A transitional state in the evolution of the N-biogeochemical cycle 246

7.5. From the NIE to the GOE..... 248

7.6. Methods 250

7.7. Supplementary Information..... 252

 7.7.1. Geological context of the Serra Sul and Tumbiana Formations..... 256

 7.7.2. Studied drill-cores 257

 7.7.3. Preservation of the primary N isotope signature 261

References..... 262

CHAPTER 8. ARE STROMATOLITIC CARBONATES IDEAL CANDIDATES TO STUDY THE ARCHEAN N-BIOGEOCHEMICAL CYCLE? INSIGHTS FROM THE 2.5 GA MALMANI SUBGROUP, SOUTH AFRICA..... 270

Abstract..... 273

8.1. Introduction 273

8.2. Geological context..... 277

8.3. Methods 283

8.4. Results 286

8.5. Discussion..... 294

 8.5.1. A primary nitrogen isotope signature despite potential organic carbon resetting 294

 8.5.2. Oxidative pathways of the N-biogeochemical cycle are not recorded in the Malmani carbonates..... 300

 8.5.3. A record of ammonium assimilation inside the microbial mats 301

8.6. Conclusions 302

References..... 306

GENERAL CONCLUSIONS AND PERSPECTIVES	311
APPENDIX. OTHER CONTRIBUTIONS	320
A.1. Co-author of Tau et al., 2024 (<i>Precambrian Research</i>).....	321
A.2. Book Chapter “Interactions géosphère-biosphère”, Chapter 6 “L’importance du vivant dans les cycles du carbone et de l’azote ”	338
A.3. Conference abstracts	364
A.3.1. Goldschmidt (2021, online).....	364
A.3.2. M-FED Microbialites: Formation, Evolution, Diagenesis (2021, Paris, France).....	366
A.3.3. Goldschmidt (2022, Honolulu, U.S.A.).....	368
A.3.4. GES12: Geochemistry of the Earth’s Surface (2022, Zürich, Switzerland).....	370
A.3.5. Goldschmidt (2023, Lyon, France).....	372
A.3.6. M-FED Microbialites: Formation, Evolution, Diagenesis (2023, Leysin, Switzerland) ..	374
A.3.7. RESMO: Matière organique, environnement et société (2024, France)	376
A.4. Reviewing activities.....	379

GENERAL INTRODUCTION

An ubiquitous element of all geological reservoirs, including Earth's core, mantle and crust, nitrogen (N) is also the main component of the atmosphere in the form of gaseous N₂. Most importantly, as an integral part of amino acids and nucleic acids, the building blocks of proteins and DNA, respectively, nitrogen is an essential nutrient for all known forms of life. Along with that of phosphorus and iron, the availability of nitrogen controls biological activity on the modern Earth. Indeed, marine biomass contains on average 16 atoms of nitrogen for every 106 atoms of carbon (Redfield ratio). Furthermore, nitrogen can exist in a number of redox states depending on the amount of O₂ in the environment. The evolution of N biogeochemistry is thus tightly linked to that of Earth's ecosystems and surficial environments. **Reconstructing the evolution of the nitrogen biogeochemical cycle through time can therefore help to refine our understanding of the joint evolution of life and environments over Earth's history, especially during the Precambrian, when oceanic and atmospheric oxygen content started increasing.**

Because physical, chemical and biological processes discriminate between the two stable nitrogen isotopes, leading to measurable difference in ¹⁵N/¹⁴N ratios of sedimentary organic matter, nitrogen isotopes hold the potential to record past metabolic activity. In paleoenvironmental studies, the δ¹⁵N proxy has already provided some insights into the Precambrian evolution of the marine nitrogen cycle and into its links to the history of Earth's oxygenation (Fig. 0.1). Today, the secular evolution of nitrogen isotope composition through Earth's history is classically interpreted as recording a three-step evolution of the marine biogeochemical cycle of nitrogen, starting with an ammonium-dominated "reduced" N cycle in oceans devoid of oxygen, followed by a rise of oceanic oxidants during the Neoproterozoic, leading to the progressive stabilization of a nitrate reservoir and oxygenated surface oceans similar to the modern world (Fig. 0.1).

The aim of this thesis is to narrow down some of the remaining uncertainties related to the precise timing, modalities and driving factors of this evolution by addressing the following questions: *Over which space and time scales do redox changes occur? Are they sudden or progressive? Are they synchronous over sedimentary basins? Is it possible to distinguish between local and global changes? When do biological innovations lead to environmental changes?* Some other more "practical" concerns also need to be further explored and refined,

such as the preservation potential of primary $\delta^{15}\text{N}$ signatures through post-depositional processes, the potential of various types of rocks to record oceanic redox changes, possibly overlapping fractionations between anoxic vs. oxygen-dependent metabolisms, and biotic or abiotic reactions.

This work begins with two introductory chapters. The first chapter is a condensed review of the dynamics of the modern oceanic biogeochemical nitrogen cycle and of its impact on the N isotope signature ($\delta^{15}\text{N}$) and N speciation in the ocean. The second attempts to describe how the knowledge gained from studying N speciation and transfers through biologically-mediated pathways in the modern ocean can help build a framework of nitrogen isotope interpretations in sedimentary rocks, especially beyond the Phanerozoic. These two chapters should provide the basis of why and how the $\delta^{15}\text{N}$ proxy (reliably?) traces the past N-biogeochemical cycle in an attempt to reconstruct major biological and redox evolutionary trends throughout Earth history.

Chapter 3 provides an updated Precambrian $\delta^{15}\text{N}$ database, that serves as a starting point to discuss how secular variations in Precambrian $\delta^{15}\text{N}$ signatures and redox changes may interrelate. In addition to providing a compilation of data, this chapter pinpoints grey areas in our current understanding of the reliability of sedimentary $\delta^{15}\text{N}$ as a palaeoecological and paleoenvironmental archive and in the assumptions that underpin Precambrian nitrogen cycling reconstructions. It raises questions that I then attempt to address in my PhD work.

Chapter 4 briefly introduces the three study sites selected for this PhD work, in terms of regional geological context, stratigraphic framework, petrographic features, sedimentary facies, and paleoenvironment: the ca. 3.4 Ga Buck Reef Chert sedimentary sequence (Kromberg Formation, Kaapvaal Craton, South Africa), the ca. 2.7 Ga Serra Sul Formation (Carajás Basin, Amazonian Craton, Brazil), and the ca. 2.5 Ga Malmani Subgroup (Transvaal Supergroup, Kaapvaal Craton, South Africa).

Chapter 5 describes the analytical techniques used for the isotopic analysis of small nitrogen and carbon quantities, as well as for all complementary indicators used in this study, which include petrographic observations, mineralogy, and elemental analyses. Measuring the $\delta^{15}\text{N}$ of the trace amounts of N present in the studied samples was a challenge. I used sealed-tube off-line extraction on one of the last vacuum lines in the world, and pushed its sensitivity to a limit

never attained so far. In this chapter, the protocol used and its validation are thus more detailed than for the other methods, which are more conventional.

Chapter 6, 7 and 8 each focus on a studied set of samples from one of the three study sites, starting with the Paleoproterozoic Buck Reef Chert sedimentary deposit (Kaapvaal Craton, South Africa), to the Neoproterozoic Serra Sul Formation (Amazonian Craton, Brazil), and finally the Malmani Subgroup (Kaapvaal Craton, South Africa), deposited just before the Archean-Proterozoic transition. These three chapters are in the form of research articles: the first one is published, the second one is in review and the last one in preparation.

A general conclusion goes over the main findings of each chapter, integrating them into some key takeaways regarding the evolution of the N-biogeochemical cycle through the Archean and associated redox interpretations. It provides updated perspectives as to the strengths and limits of using the $\delta^{15}\text{N}$ proxy in deep time, and potential orientations for future studies.

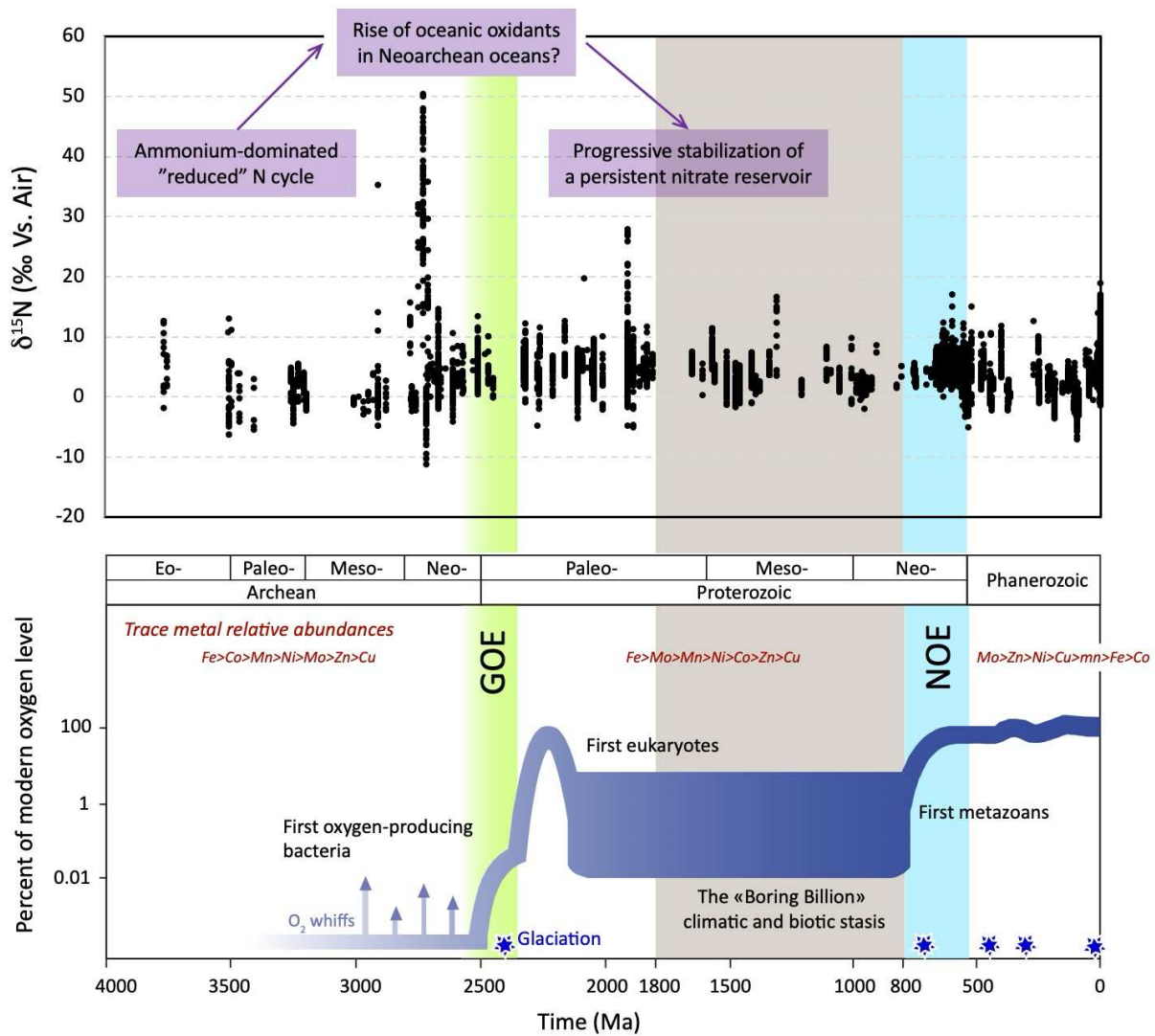


Fig. 0.1. Timeline of major biogeochemical and climatic events through Earth history (bottom), and coeval sedimentary $\delta^{15}\text{N}$ secular variations with associated N-biogeochemical cycle current interpretations (top, after Ader et al., 2016). Atmospheric oxygen levels are from Lyons et al. (2014) and trace metal relative abundances from Rucker & Kaçar (2023). GOE stands for Great Oxidation Event. NOE stands for Neoproterozoic Oxygenation Event. The $\delta^{15}\text{N}$ database compiled from the literature is available in Chapter 3.

CHAPTER 1. THE MODERN OCEANIC BIOGEOCHEMICAL NITROGEN CYCLE

Introduction.....	6
1.1. Nitrogen stable isotopes - $\delta^{15}\text{N}$	9
1.2. N-assimilation pathways.....	12
1.2.1. Biological N_2 fixation (BNF).....	12
1.2.2. Ammonification	15
1.2.3. Ammonium uptake.....	16
1.2.4. Nitrate uptake.....	17
1.3. Energy-yielding pathways.....	17
1.3.1. Nitrification.....	17
1.3.2. Denitrification.....	18
1.3.3. Anaerobic ammonium oxidation (anammox)	20
1.3.4. Minor energy-yielding pathways of the modern N cycle	21
1.3.4.1. Feammox.....	21
1.3.4.2. Dissimilatory nitrate reduction to ammonium (DNRA).....	21
1.3.4.3. Ammonium oxidation by methanotrophic bacteria.....	22
1.4. First-order controls on the modern oceanic N budget and the average oceanic $\delta^{15}\text{N}$..	22
References.....	27

CHAPTER 1. THE MODERN OCEANIC BIOGEOCHEMICAL NITROGEN CYCLE

Introduction

Being an integral part of amino acids and nucleic acids, the elementary units of proteins and DNA, respectively, nitrogen is one of the essential nutrients for the biosphere. It is a central component of marine biomass, which contains on average 16 atoms of nitrogen for every 106 atoms of carbon (Redfield ratio, Redfield, 1934). Along with that of phosphorus and iron, the availability of nitrogen exerts a strong control on biological productivity (Ustick et al., 2021), especially through the availability of its “fixed” bioavailable forms (i.e., non-N₂), in particular ammonium (NH₄⁺), nitrite (NO₂⁻) and nitrate (NO₃⁻), that can be readily uptaken by primary producers.

On the modern Earth, the atmosphere is the main surface nitrogen reservoir, where N is present mostly as gaseous dinitrogen N₂ (Ward, 2012). According to Henry’s law, atmospheric N₂ partial pressure is at equilibrium with dissolved N₂ in the upper water column. Therefore, dissolved N₂ is the most abundant N species in seawater, accounting for about half of dissolved oceanic nitrogen (Sharp, 1983; Ward, 2012). A peculiarity of N compared to other nutrients is that it is the only major nutrient for which biological processes almost exclusively control the oceanic inventory, meaning that its sources and sinks are mostly internal to the ocean and biologically-mediated (Fig. 1.1). In the modern ocean, nitrogen is present as dissolved dinitrogen (N₂) and bioavailable molecules (Fig. 1.1): ammonium (NH₄⁺), nitrite (NO₂⁻), nitrate (NO₃⁻) and dissolved and particulate nitrogen forms (DON and PON for *dissolved organic nitrogen* and *particulate organic nitrogen*, respectively). All these forms are interconnected through biogeochemical processes. Indeed, transfers between these different oceanic nitrogen “reservoirs” (N₂, NH₄⁺, NO₃⁻ and dissolved and particulate organic nitrogen DON and PON) are mainly controlled by biological processes involving redox reactions. As it occurs in oxidation states ranging from -3 (NH₄⁺) to +5 (NO₃⁻) (Fig. 1.2), nitrogen is a redox-active component and thus a potential source of metabolic energy through electrochemical activity (Schoepp-Cothenet et al., 2013). Organisms produce and obtain energy through redox reactions that convert nitrogen among its stable states, controlling the distribution of N in the ocean. Therefore, the redox state of the different parts of a given oceanic or lacustrine basin plays a major role in how nitrogen is cycled through the water column.

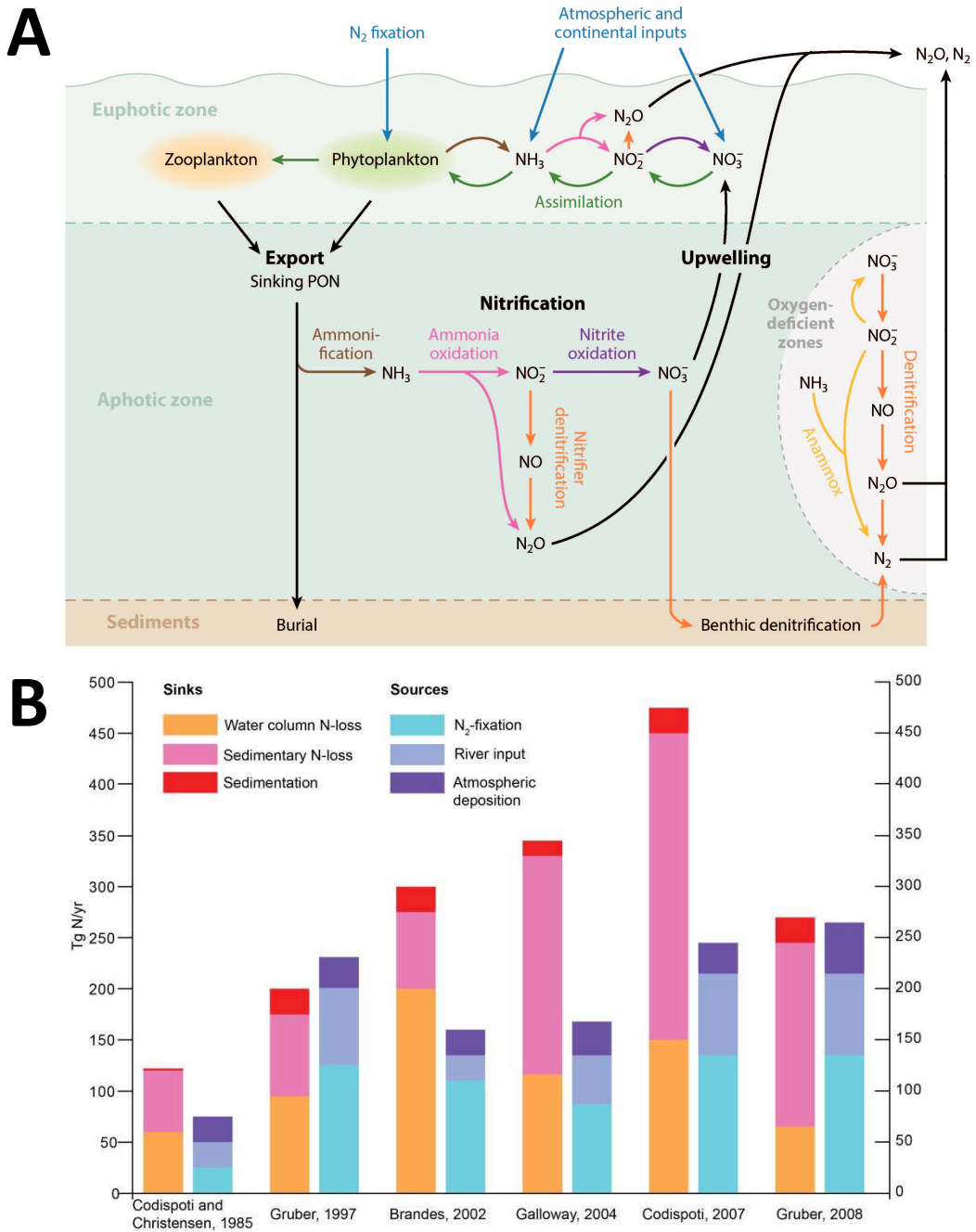


Fig. 1.1. Overview of the marine N cycle ((A), Casciotti, 2016) and budget estimations of its sources and sinks ((B), Ryabenko, 2013). N inputs (N₂ fixation, atmospheric and continental inputs) are shown in blue in (A) and in blue and purple in (B). N losses (denitrification and anammox) are shown in orange and yellow in (A), respectively, and in orange to red in (B). Internal processes of the N cycle (A) are shown in green (assimilation and grazing), brown (ammonification), pink (ammonia oxidation), and purple (nitrite oxidation). Physical processes (A) are shown in black.

Understanding the driving factors controlling biological pathways and conversions of the modern biogeochemical nitrogen cycle and constraining the rates of these processes is essential before applying this proxy in deep time. This chapter aims to providing a general picture of the N-biological cycle dynamics in the modern ocean using stable isotopes, through a concise description of the different pathways it involves. Assimilation pathways have been separated from energy-yielding pathways. This will allow the reader to understand the first-order controls on the oceanic N budget and the average oceanic nitrogen isotope signature, and how that knowledge can be transferred to ancient sediments.

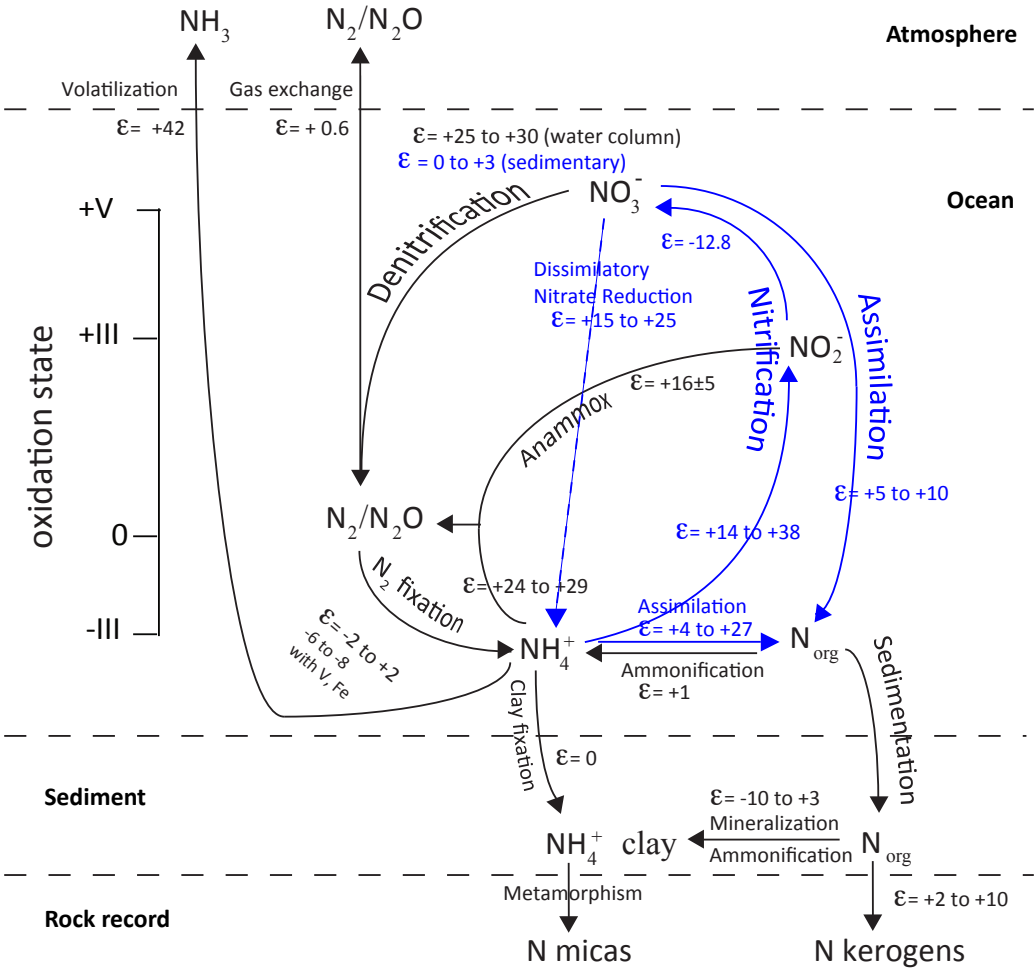


Fig. 1.2. Simplified model of the biogeochemical N cycle in modern oceans (modified from Thomazo et al., 2011). Isotopic fractionations are noted as $\epsilon = \delta^{15}\text{N}_{\text{reactant}} - \delta^{15}\text{N}_{\text{product}}$, where $\delta^{15}\text{N} = [(\frac{^{15}\text{N}}{^{14}\text{N}})_{\text{sample}} / (\frac{^{15}\text{N}}{^{14}\text{N}})_{\text{standard}} - 1] \cdot 1000$, and the standard is atmospheric air (Mariotti, 1982). Analyses of N_2 contained in fluid inclusions dating back to 3.5 Ga suggest that the composition of air has not changed by more than 2‰ (Nishizawa et al., 2007; Marty et al., 2013).

1.1. Nitrogen stable isotopes - $\delta^{15}\text{N}$

Nitrogen has two stable isotopes, atoms that share the same number of protons but a different number of neutrons: $^{14}_7\text{N}$ (hereafter noted ^{14}N , the most abundant, 99.63% of the N found in nature) and $^{15}_7\text{N}$ (hereafter noted ^{15}N , accounting for 0.37%). Physical, chemical and biological processes discriminate between the two isotopes, leading to slight but measurable differences in the ratio of ^{15}N to ^{14}N among the different forms of nitrogen that can be found in Earth's environments (Sigman et al., 2009). Therefore, N isotope measurements can be used to trace oceanic processes.

These N isotope ratios are expressed in delta notation, where $\delta^{15}\text{N}$ is expressed in permil versus air, as $\delta^{15}\text{N} = \left[\frac{(^{15}\text{N}/^{14}\text{N})_{\text{sample}}}{(^{15}\text{N}/^{14}\text{N})_{\text{standard}}} - 1 \right] \cdot 1000$. Atmospheric N_2 being the N isotope reference, its $\delta^{15}\text{N}$ is 0‰. The $\delta^{15}\text{N}$ values of different N-containing molecules vary as a result of isotopic fractionation during chemical, physical and biological processes.

“Isotopic fractionation” refers to the isotope ratio differences between a substrate and a product, caused when reactions discriminate between the two N isotopes. Two types of isotopic fractionations are customarily distinguished: equilibrium fractionation and kinetic fractionation. Equilibrium fractionation is governed by the laws of thermodynamics. Isotopes are separated between two or more substances in chemical equilibrium but there is no net reaction. This equilibrium fractionation is strongest at low temperatures. Kinetic fractionation is characterized by an incomplete and unidirectional reaction, where no isotopic equilibrium is attained.

Nitrogen isotope variations in the ocean mostly result from kinetic fractionation associated with the biochemical conversions from one N species to another. This enzymatic fractionation results from small but significant differences in the rates of reactions containing heavy and light isotopes. If the reaction rate can be characterized by a first-order dependence on the substrate concentration, then the fractionation factor, α , can be defined as $^1k/^h k$, where 1k is the first-order rate constant for the reaction of the light-isotope-containing molecule and $^h k$ is the first-order rate constant for the reaction of the heavy-isotope-containing molecule. The fractionation factor can be expressed in permil notation as an isotope effect, ϵ , defined as $(\alpha - 1) \cdot 1000$.

Oceanic N isotope data are frequently interpreted using two simple models, “Rayleigh” and “steady-state”. Both models include the degree of consumption of the reactant N pool (f), the

$\delta^{15}\text{N}$ of the reactant N pool ($\delta^{15}\text{N}_{\text{initial}}$) and the kinetic isotope effect (ϵ). In the Rayleigh model, the reaction is unidirectional with a constant kinetic isotope effect, and the reactant N pool is neither lost nor replenished from the system during the reaction. The isotopic variation of the reactant N pool ($\delta^{15}\text{N}_{\text{reactant}}$; equation 1), the instantaneously generated product N ($\delta^{15}\text{N}_{\text{instantaneous}}$; equation 2), and the accumulated product N pool ($\delta^{15}\text{N}_{\text{product}}$; equation 3) can be described using the following equations (Fig. 1.3-1.4):

$$(1) \quad \delta^{15}\text{N}_{\text{reactant}} = \delta^{15}\text{N}_{\text{initial}} - \epsilon \{\ln(f)\}$$

$$(2) \quad \delta^{15}\text{N}_{\text{instantaneous}} = \delta^{15}\text{N}_{\text{reactant}} - \epsilon$$

$$(3) \quad \delta^{15}\text{N}_{\text{product}} = \delta^{15}\text{N}_{\text{initial}} + \epsilon \{f/(1-f)\} \ln(f)$$

Where f is the fraction of the reactant remaining, $\delta^{15}\text{N}_{\text{initial}}$ is the $\delta^{15}\text{N}$ of the initial reactant N pool, and ϵ is the kinetic isotope effect of the reaction. At a very low degree of reactant consumption, (i.e. when f is close to 1), the $\delta^{15}\text{N}$ values of the instantaneous and accumulated products are similar and approximately equal to the $\delta^{15}\text{N}$ of the reactant supply minus the kinetic isotope effect. Conversely, when the degree of reactant consumption is high (i.e. when f is close to 0), the $\delta^{15}\text{N}$ of the reactant is extremely shifted (Fig. 1.3-1.4). Alternatively, in the steady-state model, the reactant N is continuously supplied and only partially consumed. The isotopic variation of the reactant N pool ($\delta^{15}\text{N}_{\text{reactant}}$; equation 4), and the product N pool ($\delta^{15}\text{N}_{\text{product}}$; equation 5) can be described using the following equations (Fig. 1.3-1.4):

$$(4) \quad \delta^{15}\text{N}_{\text{reactant}} = \delta^{15}\text{N}_{\text{initial}} - \epsilon (1-f)$$

$$(5) \quad \delta^{15}\text{N}_{\text{product}} = \delta^{15}\text{N}_{\text{initial}} - \epsilon (f)$$

In the case of nearly complete consumption (i.e. when f is close to 0), the reactant stands as an intermediate: its $\delta^{15}\text{N}$ is equal to the $\delta^{15}\text{N}$ of the initial reactant supply plus the kinetic isotope effect of the consuming process (Fig. 1.3-1.4). Both the Rayleigh and the steady-state models describe processes governing the marine N cycle. For instance, the Rayleigh model has been used to describe phytoplanktonic nitrate uptake (Sigman and Fripiat, 2019) while the steady-state model is more appropriate to describe the consumption of nitrate during sedimentary denitrification.

Isotopic fractionation results in predictable differences between the isotope ratio of the substrate and the product of a reaction. The product of an enzymatic reaction is generally depleted in the

heavy isotope compared with the substrate because the molecules containing the light isotope react preferentially. For example, during the assimilation of NO_3^- by phytoplanktonic organisms, NO_3^- in the photic zone is progressively enriched in ^{15}N as its pool is consumed (Fig. 1.2, 1.4; Casciotti et al., 2002; Granger et al., 2004, 2010). Conversely, during NO_2^- oxidation to NO_3^- (the second step of nitrification, Casciotti, 2009), ^{15}N -containing NO_2^- is preferentially oxidized to NO_3^- , leaving the residual NO_2^- progressively depleted in ^{15}N (Fig. 1.2, 1.4). Two factors determine the $\delta^{15}\text{N}$ of a given N species: the $\delta^{15}\text{N}$ of the nutrient source and the isotope fractionation factor during the uptake and assimilation of the nutrient, or the oxidation/reduction of the substrate (Mariotti et al., 1981).

With sources and sinks internal to the ocean, and the oceanic fixed N being supplied by N_2 fixation and removed by denitrification and anammox, N isotopes are useful to trace both the N input/output budgets, and the cycling of fixed N in the ocean.

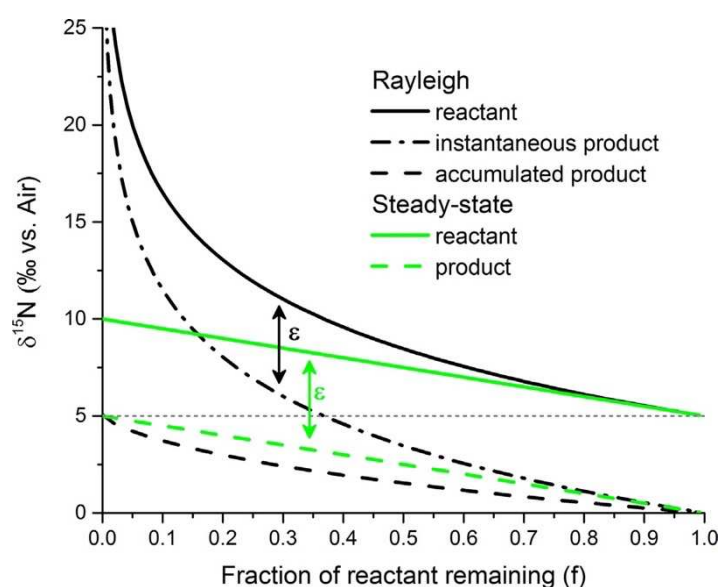


Fig. 1.3. Simple models of N isotope changes associated with the consumption of a substrate (Sigman & Fripiat, 2019). The $\delta^{15}\text{N}$ of the reactant (solid lines) and the product (dashed lines) for a single unidirectional reaction are given for two different models of reactant supply and consumption: the Rayleigh model (black lines) applies for a closed pool of reactant while the steady-state model (green lines) applies when the reactant is supplied continuously. For both models, the same isotopic parameters are used: an isotope effect (ϵ) of 5‰ and a $\delta^{15}\text{N}$ of 5‰ for the initial reactant supply. The grey dotted horizontal line indicates the $\delta^{15}\text{N}$ of the initial reactant supply.

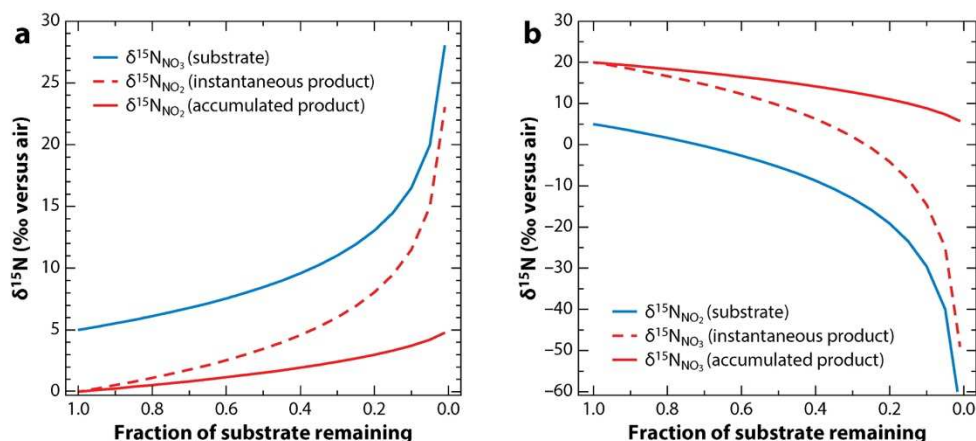
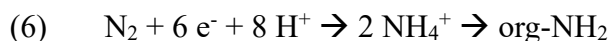


Fig. 1.4. Rayleigh fractionation in a closed system for (a) assimilatory NO_3^- reduction to NO_2^- with an isotope effect of 5‰ and (b) NO_2^- oxidation to NO_3^- with an isotope effect of -15‰ (Casciotti, 2016). In each case, the substrate is shown as a solid blue line, the accumulated product as a solid red line, and the instantaneous product as a dashed red line.

1.2. N-assimilation pathways

1.2.1. Biological N_2 fixation (BNF)

Today, atmospheric N_2 makes up the largest surface reservoir of N (Johnson and Goldblatt, 2015). The biogeochemical nitrogen cycle thus primarily relies on the biological conversion of atmospheric N_2 to ammonium (NH_4^+), followed by the production of organic N compounds (R-NH_2). Despite nitrogen being abundant as N_2 , it is not readily available for most organisms, as N_2 can only be assimilated by diazotrophs, prokaryotes who possess the nitrogenase enzyme, making them capable of biological N_2 fixation (BNF), a metabolism also known as diazotrophy (Raymond et al., 2004). This endergonic reduction of N_2 to NH_4^+ follows reaction (6), needing 16 molecules of ATP to break every single $\text{N}\equiv\text{N}$ bond.



N_2 fixation is the major input and the exclusive biological source of new fixed N to the ocean (Raymond et al., 2004) (Fig. 1.1), controlling what can subsequently be cycled through the water column (Sigman et al., 2009).

The capacity for nitrogen fixation relies entirely on the nitrogenase enzyme, a complex of highly conserved proteins, for which the *nif* genes code (Karl et al., 2002). Three varieties of

nitrogenases can be distinguished by the metal cofactors associated to their active site: the classical nitrogenase is the Mo-Fe nitrogenase, also called Nif. Alternatively, Mo can be replaced by either Fe or V, resulting in the Anf (Fe-Fe) and Vnf (Fe-V) alternative nitrogenases (Joerger et al., 1988; Miller and Eady, 1988). These alternative nitrogenases have only been found in a limited subset of diazotrophs, and are expressed only when Mo concentrations become limiting. Alternative nitrogenases may have predated the classical Mo-Fe nitrogenase, and may still be present in several lineages of prokaryotes (Anbar and Knoll, 2002). Phylogenetic analyses of nitrogenase sequences reveal that diazotrophs include a taxonomically diverse range of prokaryotic organisms, including the archaeal and bacterial domains, while eukaryotes are unable to fix N₂ (Dos Santos et al., 2012). This ca. 15% of prokaryotes capable of N₂ fixation (Dos Santos et al., 2012) displays a large range of ecological and physiological characteristics, with both phototrophs and chemotrophs, autotrophs and heterotrophs (Karl et al., 2002). Initially thought to occur essentially in subtropical oligotrophic surface waters (Capone et al., 1997; Mahaffey et al., 2005), diazotrophs have then been found in oxygen minimum zones (Bonnet et al., 2013; Fernandez et al., 2011; Hamersley et al., 2011), mesotrophic and/or eutrophic surface waters (Dekaezemacker et al., 2013; Raimbault and Garcia, 2008), sediments (Fulweiler et al., 2007) and even hydrothermal vent fluids (Mehta and Baross, 2006). Nitrogen fixation is not restricted to the photic zone but widespread throughout the water column. In the modern ocean, the highest N₂ fixation rates are measured in oligotrophic surface waters, coastal upwelling systems and oxygen minimum zones (OMZs), where the fixed N supply becomes limiting (Fernandez et al., 2011; Karl et al., 1997).

A number of factors can control N₂ fixation rates in a given oceanic environment, such as oceanic chemistry and the availability of other nutrients, in particular metal cofactors for the nitrogenase enzyme. First, the synthesis and activity of the nitrogenase enzyme is strongly inhibited by oxygen (Gallon, 1992). Thus, in addition to the high rates of nitrogenase replacement, diazotrophs have developed efficient O₂ removal and O₂ protection mechanisms such as spatial compartmentalization in heterocystous cells or temporal separation with fixation during the night (Bergman et al., 2013; Berman-Frank et al., 2003). In addition, phosphorus availability is one of the main factors limiting N₂ fixation (Karl et al., 1997). Another control on N₂ fixation is exerted by iron (Dekaezemacker et al., 2013; Howard and Rees, 1996) and molybdenum (Cole et al., 1993) availability, which are critical metallic cofactors for the nitrogenase enzyme. Sulfate concentrations can also indirectly impact N₂ fixation through molybdenum inhibition: indeed, the uptake of molybdate competes with phosphate as they use

the same transporters (Stal et al., 1999). Decreases in sulfate concentrations have been found to stimulate N₂ fixation in the Baltic Sea (Stal et al., 1999).

Because biological N₂ fixation is energetically costly (16 ATP for the hydrolysis of every N≡N bond) and diazotrophs can grow on fixed N compounds, they are unlikely to fix nitrogen when ammonium and/or nitrate is available in the proximal environment. Nitrogenase synthesis is induced by the depletion of fixed N substrates and repressed when bioavailable N is abundant (Karl et al., 2002), creating a negative feedback between the amount of bioavailable N in the surface ocean and biological N₂ fixation. Regions with fixed N deficiencies provide an ideal ecological niche for the proliferation of N₂ fixers (Raimbault and Garcia, 2008). N₂-fixing organisms are particularly active in oceanic regions with low N/P ratios (Sachs and Repeta, 1999), in turn increasing the N/P ratio of dissolved and particulate organic matter and depleting these regions of phosphorus.

Organic matter produced through N₂ fixation has a δ¹⁵N ranging from -2 to 0‰ (Fig. 1.2, 1.5) (Hoering and Ford, 1960; Macko et al., 1987; Minagawa and Wada, 1986; Montoya et al., 2002; Wada and Hattori, 1976). Cyanobacterial cultures of more than 20 species, including *Trichodesmium*, the main open-ocean N₂-fixating genus, yield a δ¹⁵N of -2.2‰ to +0.5‰ compared to N₂, with an average of -1.5‰ (Bauersachs et al., 2009). An average δ¹⁵N of -1‰ is usually proposed to account for the fixed N oceanic input from biological N₂ fixation (Sigman et al., 2009). While fractionations imparted by biological N₂ fixation with classical Mo-based nitrogenase range from -2‰ to +2‰ (Fig. 1.2, 1.5), alternative nitrogenases using Fe or V as cofactors produce fixed nitrogen with significantly lower δ¹⁵N values (-6 to -7‰), and can impart negative fractionations as large as -8‰ (Zhang et al., 2014) (Fig. 1.2).

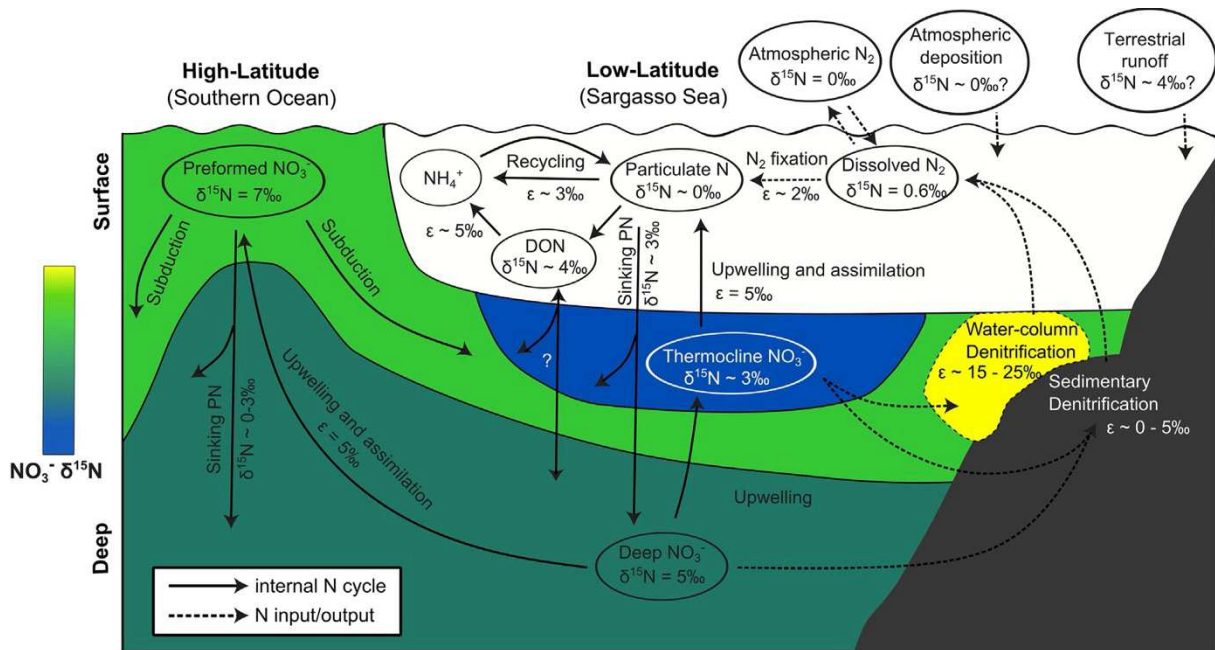


Fig. 1.5. Processes affecting N isotopes in the ocean (Sigman & Fripiat, 2019). The inputs and outputs (dashed arrows) control the ocean's fixed N inventory, while internal cycling pathways (solid arrows) control the $\delta^{15}\text{N}$ of fixed N species, the majority being in the form of nitrate. Color indicates the $\delta^{15}\text{N}$ of nitrate, from nitrate with low $\delta^{15}\text{N}$ values in blue to nitrate with high $\delta^{15}\text{N}$ values in yellow. The low-latitude surface has been left blank because nitrate is almost completely consumed. Preformed NO_3^- is the portion of nitrate that originates from surface waters rather than from *in situ* organic matter respiration.

1.2.2. Ammonification

Ammonification, i.e. the degradation of organic nitrogen to ammonium, is the main remineralization pathway of the N biological cycle, as it returns the organic N to its mineral form. This mineralization of organic matter derived from diazotrophs, in the water column or in sediments (Sigman et al., 2009), provides most bioavailable nitrogen to the biosphere as ammonium (NH_4^+) (Fig. 1.1). Ammonium release during organic matter remineralization imparts a small isotope fractionation, between -2 and -1‰ (Fig. 1.2; Möbius, 2013). In the sediment, aerobic microbial organic matter degradation causes a joint decrease in organic nitrogen content with increasing $\delta^{15}\text{N}_{\text{org}}$ (Freudenthal et al., 2001), while inorganic nitrogen, mostly as fixed ammonium, is depleted in ^{15}N (Fig. 1.2). However, the isotope effect becomes negligible the more remineralization is efficient, which is typically the case in oligotrophic environments (Möbius, 2013). Therefore, the $\delta^{15}\text{N}_{\text{bulk}}$ variability during early diagenetic processes is less than 1‰, thus can be considered negligible when interpreting $\delta^{15}\text{N}$ variations

of more than a few permil. This is confirmed by the small enrichments reported in sediments over sinking particles (Robinson et al., 2012). Some field studies suggest that both bacteria and zooplankton preferentially degrade low $\delta^{15}\text{N}$ organic N, leaving residual organic matter enriched in ^{15}N . However, given organic matter heterogeneity, it is difficult to estimate the isotope effect associated with organic matter degradation. The analysis of sinking organic particles has shown that their $\delta^{15}\text{N}$ reflected that of phytoplankton, itself reflecting the $\delta^{15}\text{N}$ of the nutrient sustaining primary productivity (Nakanishi and Minagawa, 2003). The preservation of the nitrogen isotope signature of primary producers through water-column transfers and post-depositional history is discussed in further detail in Chapter 2, paragraph 2.1.

Bioavailable N released from organic matter mineralization can subsequently be (i) uptaken by the biomass, (ii) aerobically oxidized to nitrite (NO_2^-) and nitrate (NO_3^-) during nitrification, or (iii) preserved in the sediment as organic N or as ammonium substituting for potassium in phyllosilicates (Fig 1.1-1.2).

1.2.3. Ammonium uptake

Both autotrophs and heterotrophs use ammonium for growth. Ammonium is assimilated into organic matter, first into amino acids, which are themselves incorporated into proteins and nucleotides. Proteins make up the main nitrogen reservoir of the biomass. Ammonium is the preferred inorganic nitrogen source for many, if not most, marine organisms (Ward, 2012). Indeed, it can be readily uptaken using little metabolic energy, given that it has the same oxidation state as amino acids.

All known phytoplankton species preferentially consume ^{14}N relative to ^{15}N , therefore ammonium uptake enriches residual ammonium in ^{15}N (Fig. 1.2). This fractionation depends on the ammonium concentrations: indeed, culture and field studies suggest an isotope effect of ca. 20‰ under high ammonium concentrations, decreasing to ca. 0 to 4‰ when ammonium concentrations decrease (Hoch et al., 1992). However, ammonium released during organic matter mineralization is rapidly and quantitatively assimilated into the biomass. Hence, even if organisms preferentially incorporate ^{14}N , ammonium uptake fractionation is rarely expressed in the water column and in the sedimentary record (Fig. 1.2). In specific cases tied to strong water column redoxcline, i.e. in stratified basins, $\delta^{15}\text{N}$ measurements of ammonium during its consumption by bacteria show isotopic enrichments near the oxycline, between 5 and 15‰ for the Black Sea and between 20 and 30‰ in the Norwegian Framvaren Fjord (Velinsky et al.,

1991). The magnitude of the isotope fractionation appears to be mainly related to ambient ammonium concentrations: $\delta^{15}\text{N}_{\text{NH}_4}$ increases towards the chemocline, as the NH_4^+ concentration decreases (Velinsky et al., 1991).

1.2.4. Nitrate uptake

In the modern ocean, nitrate is also a major source of fixed N for phytoplankton growth. Its consumption varies spatially, from complete assimilation in stable stratified waters to partial assimilation in upwelling regions (Fig. 1.1, 1.5).

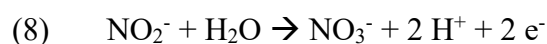
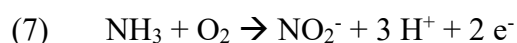
All known phytoplankton species preferentially consume ^{14}N relative to ^{15}N , therefore nitrate uptake, similarly to ammonium uptake, enriches residual nitrate in ^{15}N (Fig. 1.2, 1.5). Although the intrinsic isotope effect of the nitrate reductase enzyme, responsible for nitrate assimilation, is very close to 0‰ (Granger et al., 2004; Mariotti et al., 1982; Wada and Hattori, 1978), most field-based estimates of the isotope effect of nitrate assimilation range from 5 to 10‰ (Fig. 1.2) (Altabet et al., 1999; Goering et al., 1990; Sigman et al., 1999).

1.3. Energy-yielding pathways

1.3.1. Nitrification

In oxygenated surface waters, ammonium can be successively nitrified to nitrite (NO_2^-) and nitrate (NO_3^-) (Fig. 1.1), which are then either assimilated by photosynthetic organisms or biologically reduced through denitrification or anaerobic ammonium oxidation (anammox) (Fig. 1.1) in dysoxic and anoxic conditions (Dalsgaard and Thamdrup, 2002; Sigman et al., 2009).

Nitrification is the biological source of nitrate in the modern ocean, providing nitrogen to many heterotrophic organisms. For nitrifying bacteria, ammonium can be used as a source of reducing power to fix CO_2 instead of simply serving as a nitrogen source for building biomass. Nitrification occurs in two steps (Fig. 1.1), performed by two different groups of organisms: the oxidation of ammonium to nitrite (reaction 7) is carried out by ammonium-oxidizing bacteria and archaea (AOB and AOA) through the ammonia monooxygenase enzyme, and the subsequent oxidation of nitrite to nitrate (reaction 8) is performed by nitrite-oxidizing bacteria using the nitrite oxidoreductase enzyme.



Oxygen is used as an electron acceptor for the oxidation of NO_2^- to NO_3^- . Therefore, nitrification is generally considered to be an oxygen requiring process (Stenstrom and Poduska, 1980), although alternative electron acceptors including Fe(III), Mn(IV) and iodate (IO_3^-) could be used instead of O_2 . Recent work has shown that nitrification can operate even under nanomolar levels of O_2 (Bristow et al., 2016).

Microbial ammonium oxidation to nitrite, the first step of nitrification, enriches residual ammonium in ^{15}N and depletes residual nitrate in ^{15}N with a kinetic isotope effect of 14 to 38‰ (Fig. 1.2; Casciotti et al., 2003; Delwiche and Steyn, 1970; Mariotti et al., 1981; Yoshida, 1988). Microbial nitrite oxidation to nitrate, the second step of nitrification, has an inverse kinetic isotope effect of 13‰ (Fig. 1.2), meaning that it is residual nitrite progressively becomes depleted in ^{15}N (Casciotti, 2009). However, except in rare cases of seasonal variations in lacustrine settings (Hadas et al., 2009), nitrification goes to completion (i.e. nitrate, Fig. 1.2) and its fractionation is not expressed.

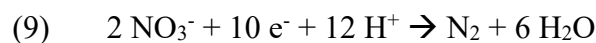
Nitrification is a crucial pathway of the biogeochemical N cycle, as it is the step that controls the oxidation state of bioavailable nitrogen (Fig. 1.2). Nitrite is simultaneously a reactant, a product and an intermediate in oxidative and anoxic pathways of the nitrogen cycle (Fig. 1.2), namely ammonium oxidation, denitrification and anammox. As such, its concentrations in the water column are generally low, except at the bottom of the photic zone where it accumulates, which is called the primary nitrite maximum (PNM) and in oxygen-deficient zones, where we find the secondary nitrite maximum (SNM). Nitrification also produces the main fixed N specie used by marine organisms, nitrate, that can subsequently be used for either assimilation or energy production.

1.3.2. Denitrification

Denitrification, the bacterial reduction of nitrate to N_2 , is the major mechanism of fixed N loss from the modern ocean (Fig. 1.1, 1.5). It occurs under low O_2 concentrations ($<5\mu\text{mol/kg}$, Dalsgaard et al., 2012) both in oxygen minimum zones (OMZs) in the water column, and in sediments (Fig. 1.1, 1.5). Nitrogen oxides are respired instead of O_2 in these anoxic settings.

Thus, denitrification is an alternative for anaerobic microorganisms to generate energy for growth (catabolism).

A wide range of bacteria can use the nitrate formed by nitrification as a respiratory substrate, meaning that they respire oxygen when it is present, but switch to an anaerobic nitrate respiration when oxygen becomes scarce. Denitrification sequentially reduces nitrate (NO_3^-) to N_2 (reaction 9) through oxidized intermediates: nitrite (NO_2^-), nitric oxide (NO), nitrous oxide (N_2O) and dinitrogen (N_2), using each intermediate as a respiratory substrate. Most denitrifiers are heterotrophs and consume organic matter, consequently the rates of denitrification inside OMZs are heterogenous and depend on the organic matter supplied from primary producers in surface waters (Babbin et al., 2014; Lipschultz et al., 1990). Therefore, denitrification and N_2 fixation rates are tightly coupled.



Water-column denitrification in OMZs strongly enriches the residual nitrate pool in ^{15}N (Fig. 1.6), with a mean isotope effect that can range from 15 to 30‰ (Fig. 1.6; Sigman and Fripiat, 2019), but that is generally considered of 30‰ (Fig. 1.2) (Mariotti et al., 1981). Conversely, its isotope effect in sediments is usually considered negligible (Fig. 1.2, 1.6) (Brandes and Devol, 1997; Lehmann et al., 2003), although some studies might suggest otherwise (a fractionation of 19‰ was measured by Dähnke and Thamdrup (2013) in surface sediments from the coastal Baltic Sea).

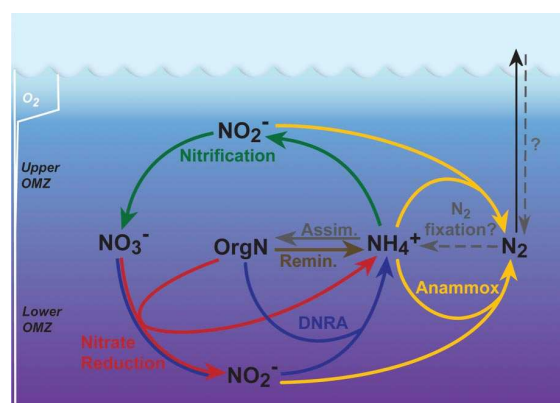


Fig. 1.6. A revised nitrogen cycle in the Peruvian OMZ (Lam et al., 2009). Anammox (yellow) has been found to be the predominant pathway for nitrogen loss and was coupled directly to nitrate reduction (red) and aerobic ammonia oxidation (the first step of nitrification, green) for sources of NO_2^- . The NH_4^+ required by anammox originated from DNRA (blue) and remineralization of organic matter via nitrate reduction and probably from microaerobic respiration.

Denitrification and anammox release N_2O or N_2 , which are subsequently lost to the atmosphere, making them the major oceanic sinks of fixed nitrogen (Dalsgaard et al., 2012). Denitrification allows the return of N_2 to the atmosphere, compensating for N_2 fixated by diazotrophs. The balance between N_2 fixation and denitrification/anammox, which is considered to be at steady state, therefore determines the total fixed N inventory of the ocean (Codispoti, 1995).

1.3.3. Anaerobic ammonium oxidation (anammox)

Anaerobic ammonium oxidation, usually referred to as “anammox” (Mulder et al., 1995), is the other mechanism of fixed N loss operating alongside denitrification (Fig. 1.6). Similarly to denitrification, this microbially-mediated reaction (Van de Graaf et al., 1995), that has only been documented for the bacterial phylum *Planctomycetes* (Strous et al., 1999, 2006) occurs in sediments or in OMZs in the water column. Anammox uses nitrite to oxidize ammonium to N_2 following reaction (10) (Kartal et al., 2011). Studies from the Eastern Tropical South Pacific OMZ show that nitrite comes from nitrate reduction and aerobic ammonia oxidation while ammonium comes from DNRA, remineralization via nitrate reduction and microaerobic respiration (Fig. 1.6; Kalvelage et al., 2013; Lam et al., 2009). The anammox metabolism thus depends on the NH_4^+ that is supplied from organic matter degradation in the water column or in the sediment, and is thought to be tightly coupled to denitrification.



The N isotope effect for NO_2^- oxidation by anammox ranges from 24 to 29‰ (Fig. 1.2; Brunner et al., 2013). However, it should be noted that this net isotopic effect depends on the source of nitrite and ammonium, and the degree to which these substrates are consumed (Sigman and Fripiat, 2019). Indeed, while nitrite comes from nitrate reduction by denitrifiers and ammonium comes from remineralization processes, nitrite and ammonium are usually completely consumed within the suboxic zones. Therefore, anammox only has a very small net isotopic effect and simply acts as a loss mechanism for nitrite and ammonium.

Initially considered as a minor pathway of the marine nitrogen cycle, studies from both OMZs and continental shelf sediments have revealed that anammox can be the prevalent pathway for nitrogen loss instead of denitrification (Fig. 1.6; Dalsgaard et al., 2003; Kalvelage et al., 2013; Lam et al., 2009; Thamdrup and Dalsgaard, 2002), accounting for up to 67% of the total N_2 produced in sediments (Thamdrup and Dalsgaard, 2002) and for up to 58% of the total N_2

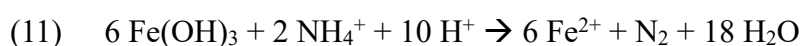
produced in OMZs (Dalsgaard et al., 2003). Average estimates suggest that in the global ocean, anammox may be responsible for 30-50% of N₂ production (Devol, 2003), but that denitrification and anammox are likely heterogeneously distributed spatially (Ward, 2013).

1.3.4. Minor energy-yielding pathways of the modern N cycle

Alongside denitrification and anammox, other biologically-mediated pathways may significantly fuel nitrogen loss in marine or freshwater environments. These reactions and their interplay with other biogeochemical cycles, such as S, Fe or C, might complexify our understanding of the N-biogeochemical cycle.

1.3.4.1. Feammox

Most metabolic pathways oxidizing NH₄⁺ need free O₂, and even classic anaerobic ammonium oxidation (anammox) requires the presence of nitrite, which cannot be produced without O₂ (Grotzinger and Kasting, 1993). However, in anoxic and ferruginous conditions, NH₄⁺ can be oxidized to N₂ in the presence of iron oxides through the Feammox reaction (11) (Sawayama, 2006):



This metabolic reaction has only recently been described in modern environments, namely in iron-rich conditions in wetland soils and marine sediments (Rios-Del Toro et al., 2018; Yang et al., 2012). It is thermodynamically favored when Fe²⁺ concentrations are below 100 μM and NH₄⁺ concentrations are above 1 μM, for pH between 6 and 8 (Stüeken et al., 2016; Xiong et al., 2022). Ammonium and iron concentrations measured in modern anoxic and ferruginous lacustrine environments (Petrash et al., 2021; Xiong et al., 2022) fall into this range and thus it is possible that this reaction is more widely distributed than initially thought.

1.3.4.2. Dissimilatory nitrate reduction to ammonium (DNRA)

During dissimilatory nitrate reduction to ammonium (DNRA), nitrate is reduced comparably to classic denitrification, but the end product is ammonium instead of N₂. DNRA has been observed both in sediments (Sørensen, 1978) and in the water column of some OMZs (Lam et al., 2009). Studies have shown that anammox bacteria could be mediating water-column

DNRA, providing most if not all of the ammonium needed for anammox (Fig. 1.6; Kartal et al., 2007).

The importance of DNRA relative to denitrification is difficult to estimate, as they can both enrich residual nitrate in ^{15}N with a fractionation on the order of 30‰ (Fig. 1.2; McCready et al., 1983). The presence of ^{15}N -depleted ammonium alongside ^{15}N -enriched nitrate could indicate that DNRA is active. DNRA might play a significant role in coastal settings, where it can account for about 30% of nitrate reduction (Giblin et al., 2013).

An important aspect that distinguishes DNRA from denitrification is that it conserves N within the ecosystem, as ammonium is released in the water column while denitrification generates N_2 that is ultimately lost to the atmosphere. This may have important implications for the overall N budget between reservoirs and the steady state hypothesis (Giblin et al., 2013).

1.3.4.3. Ammonium oxidation by methanotrophic bacteria

Alongside the oxidation of NH_3 by ammonium oxidizing bacteria (AOB), the oxidation of NH_4^+ to N_2O by methane oxidizing bacteria (methanotrophs) can be considered as a particular type of nitrification (Mandernack et al., 2000, 2009). This reaction has been identified in soils and freshwater sediments (Mandernack et al., 2000; Megraw and Knowles, 1989; Roy and Knowles, 1994; Yoshinari, 1985). Laboratory incubation experiments with cultures of methanotrophic bacteria have measured a large N isotope fractionation ranging from -48 to -55‰ between NH_4^+ and N_2O (Mandernack et al., 2009). Therefore, although it depends on the $\delta^{15}\text{N}$ variability of available nitrogen sources (e.g. NH_4^+ , NO_2^- and NO_3^-), NH_4^+ oxidation via methanotrophic nitrifying bacteria yields lower $\delta^{15}\text{N}_{\text{N}_2\text{O}}$ values than denitrification and enriches residual NH_4^+ in ^{15}N . Ammonium oxidation by methanotrophic bacteria might have played a significant role in past environments, where methane concentrations were more elevated than on the modern Earth (Thomazo et al., 2009, 2011).

1.4. First-order controls on the modern oceanic N budget and the average oceanic $\delta^{15}\text{N}$

In the modern oxygenated ocean, nitrate accounts for most of the fixed N (Ryabenko, 2013). The $\delta^{15}\text{N}$ of nitrate varies regionally between 2 and 20‰ (Fig. 1.7; Sigman and Fripiat, 2019), depending on the relative rates of N_2 fixation, nitrification, nitrate assimilation and denitrification (Fig. 1.8). However, across all oceanic basins, below 2 km depth, the $\delta^{15}\text{N}$ of

nitrate is relatively constant around +5‰ (Fig. 1.7). This stability results from the fact that organic N is often quantitatively consumed, its $\delta^{15}\text{N}$ converging on that of the nitrate supply, and because remineralization does not greatly affect the $\delta^{15}\text{N}$ of nitrate.

Nitrate $\delta^{15}\text{N}$ is minimal in the upper part of the water column from low-latitude oligotrophic regions (Fig. 1.7). In such regions, enhanced N_2 fixation is followed by the oxidation of newly fixed N that has a $\delta^{15}\text{N}$ near -1 to 0‰, and N_2 fixation overtakes denitrification. Conversely, nitrate with $\delta^{15}\text{N}$ values higher than +5‰ are observed in oxygen-deficient zones where denitrification is active or in surface waters where nitrate is partially assimilated by phytoplankton (Fig. 1.7). Inside the water column, nitrate $\delta^{15}\text{N}$ is maximal in oxygen-deficient denitrifying regions, where the $\delta^{15}\text{N}$ of nitrate can reach up to 15‰ (Fawcett et al., 2011).

The $\delta^{15}\text{N}$ of mean deep ocean nitrate is controlled by the (i) the balance between N_2 fixation and denitrification (Fig. 1.8-1.9) (Granger et al., 2011), and (ii) the balance between sedimentary and water column denitrification (Fig. 1.8-1.9). When the ocean N budget is at a steady state, the $\delta^{15}\text{N}$ of fixed N inputs by N_2 fixation (around -1‰) equals the $\delta^{15}\text{N}$ of fixed N outputs by sedimentary and water column denitrification (Fig. 1.9). If water column denitrification was responsible for all fixed N losses, with its isotope effect of 20‰, the mean $\delta^{15}\text{N}$ of oceanic nitrate would be of 19‰. The fact that the mean $\delta^{15}\text{N}$ of oceanic nitrate is around 5‰ indicates that sedimentary denitrification, with its minimal isotope effect, accounts for a significant proportion of total denitrification (Fig. 1.9). It also points to the fact that water column denitrification might not be homogenous throughout the ocean. Studies estimate that in the modern ocean, water column denitrification is responsible for 30% of fixed N losses, leaving sedimentary denitrification responsible for the remaining 70% (Sigman and Fripiat, 2019).

Miyake and Wada (1967) found that $\delta^{15}\text{N}_{\text{NO}_3}$ values averaged 5-6‰ in deep waters and increased in regions of NO_3^- removal, to 7.5‰ in and around the OMZ (Fig. 1.7). As denitrification imparts a large nitrogen isotope fractionation of $\approx 30\%$ (Sigman et al., 2009), modern and by extension Phanerozoic sedimentary $\delta^{15}\text{N}$ values around +5‰ result from the balance between N_2 fixation inputs and denitrification/anammox outputs.

However, some important issues remain regarding the use of N isotopes to investigate N cycle processes in the ocean. For instance, when pathways with similar N isotope signatures (such as denitrification and anammox) occur simultaneously, they are impossible to single out. In

addition, sedimentary $\delta^{15}\text{N}$ averages seasonal variability by displaying a mean isotope signal, which can conceal N cycle processes occurring in the ocean over short timescales.

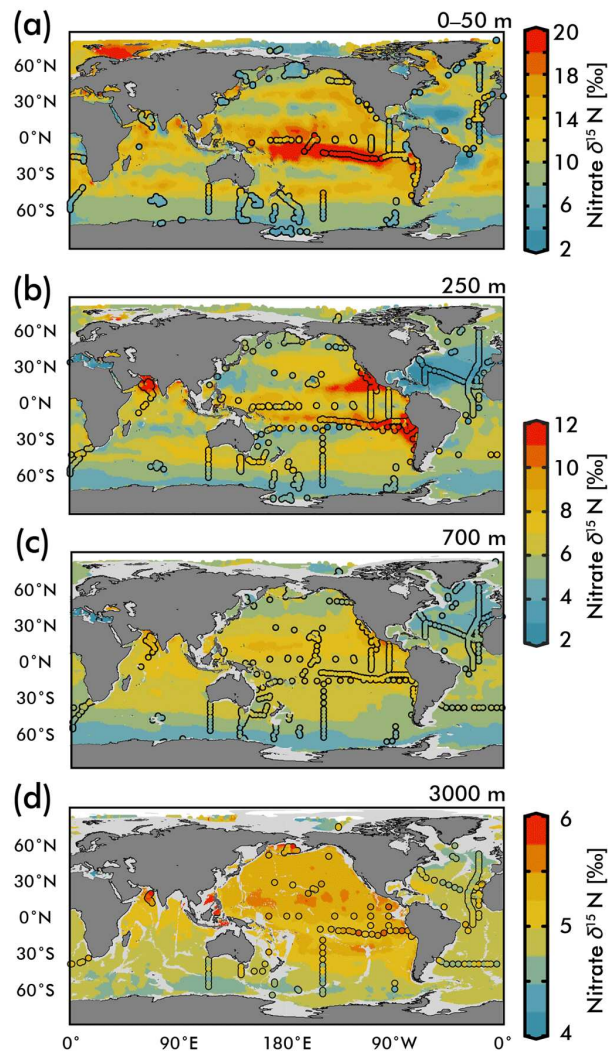


Fig. 1.7. Spatial distribution of nitrate $\delta^{15}\text{N}$ (Rafter et al., 2019) at depths of 0-50 m (a), 250 m (b), 700 m (c), and 3000 m (d), modelled from observations (circles).

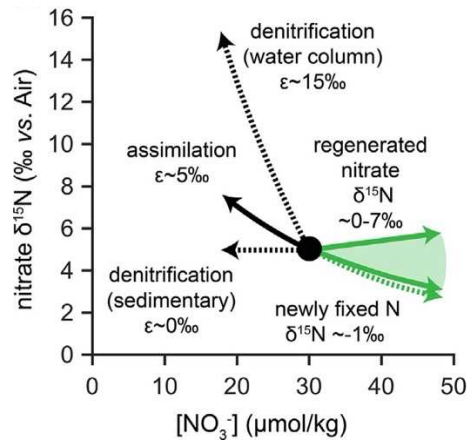


Fig. 1.8. The effect of different marine N cycle processes on nitrate concentration ($[\text{NO}_3^-]$) and $\delta^{15}\text{N}$ (Sigman & Fripiat, 2019). Dashed arrows denote processes that add or remove fixed N from the ocean, while solid arrows denote components of the oceanic fixed N internal cycling. Regenerated nitrate corresponds to nitrate regenerated from organic N in the ocean interior, its isotope signature depending on the $\delta^{15}\text{N}$ of the organic N that is remineralized.

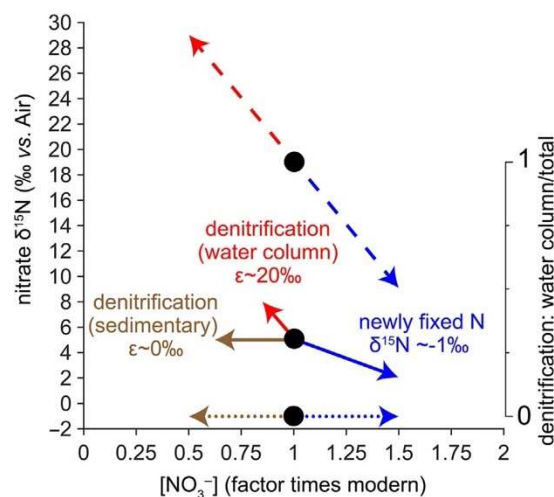


Fig. 1.9. Sensitivity of the $\delta^{15}\text{N}$ of global mean ocean nitrate to the relative importance of sedimentary vs. water column denitrification (Sigman & Fripiat, 2019). For all three cases displayed, N_2 fixation and denitrification fluxes are considered equivalent. Absolute lengths of the vectors are arbitrary. For the $\delta^{15}\text{N}$ to oceanic nitrate to be stable, the net isotopic impacts of the vertical components must be equal. The mean $\delta^{15}\text{N}$ of oceanic nitrate, i.e. the vertical position of black circles, depends on the relative proportions of water column vs. sedimentary denitrification. Sedimentary denitrification removes nitrate with a $\delta^{15}\text{N}$ similar to that of mean ocean nitrate, therefore its isotopic impact is balanced when the $\delta^{15}\text{N}$ of global ocean nitrate is the same as that of N_2 fixation (dotted arrows). Conversely, when water column denitrification is responsible for all ocean N loss, removing nitrate with its large isotope effect, the isotopic impacts of N_2 fixation and denitrification are balanced when nitrate $\delta^{15}\text{N}$ is high (dashed

arrows). The observed ocean nitrate $\delta^{15}\text{N}$ of about 5‰ (solid arrows) implies a partitioning between water column and sedimentary denitrification in which sedimentary denitrification is responsible for more N loss.

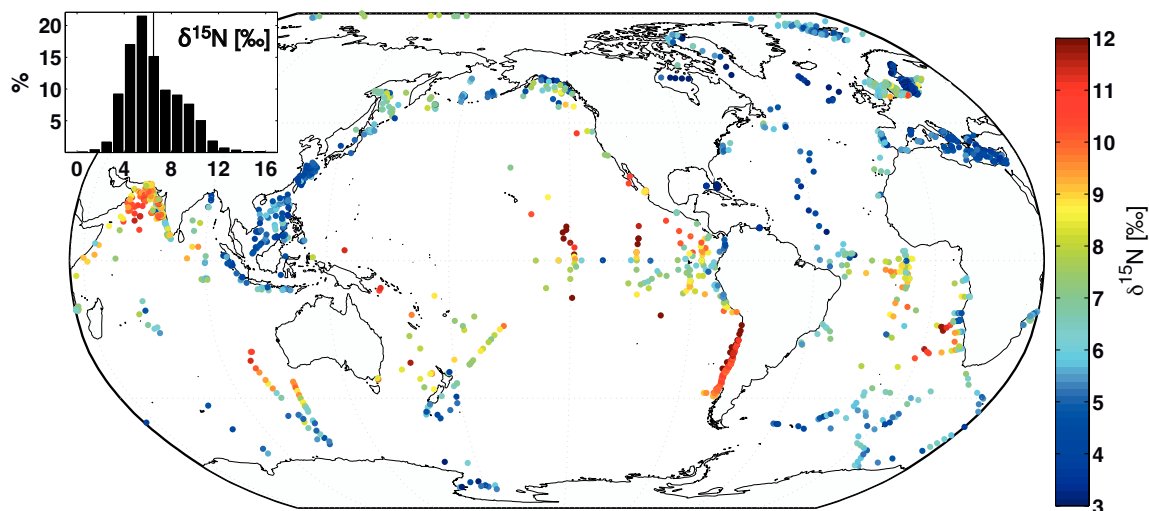


Fig. 1.10. Spatial distribution of surface sediment $\delta^{15}\text{N}$ (Tesdal et al., 2012). Inset: histogram of surface $\delta^{15}\text{N}$ in 1 ka bins, the vertical line indicating the mean of 6.7‰.

References

- Altabet, M.A., Pilskaln, C., Thunell, R., Pride, C., Sigman, D., Chavez, F., Francois, R., 1999. The nitrogen isotope biogeochemistry of sinking particles from the margin of the Eastern North Pacific. *Deep Sea Research Part I: Oceanographic Research Papers* 46, 655–679. [https://doi.org/10.1016/S0967-0637\(98\)00084-3](https://doi.org/10.1016/S0967-0637(98)00084-3)
- Anbar, A.D., Knoll, A.H., 2002. Proterozoic ocean chemistry and evolution: A bioinorganic bridge? *Science* 297, 1137–1142. <https://doi.org/10.1126/science.1069651>
- Babbin, A.R., Keil, R.G., Devol, A.H., Ward, B.B., 2014. Organic Matter Stoichiometry, Flux, and Oxygen Control Nitrogen Loss in the Ocean. *Science* 344, 406–408. <https://doi.org/10.1126/science.1248364>
- Bauersachs, T., Schouten, S., Compaoré, J., Wollenzien, U., Stal, L.J., Sinninghe Damstée, J.S., 2009. Nitrogen isotopic fractionation associated with growth on dinitrogen gas and nitrate by cyanobacteria. *Limnology and Oceanography* 54, 1403–1411. <https://doi.org/10.4319/lo.2009.54.4.1403>
- Bergman, B., Sandh, G., Lin, S., Larsson, J., Carpenter, E.J., 2013. Trichodesmium— a widespread marine cyanobacterium with unusual nitrogen fixation properties. *FEMS Microbiology Reviews* 37, 286–302. <https://doi.org/10.1111/j.1574-6976.2012.00352.x>
- Berman-Frank, I., Lundgren, P., Falkowski, P., 2003. Nitrogen fixation and photosynthetic oxygen evolution in cyanobacteria. *Research in Microbiology* 154, 157–164. [https://doi.org/10.1016/S0923-2508\(03\)00029-9](https://doi.org/10.1016/S0923-2508(03)00029-9)
- Bonnet, S., Dekaezemacker, J., Turk-Kubo, K.A., Moutin, T., Hamersley, R.M., Grosso, O., Zehr, J.P., Capone, D.G., 2013. Aphotic N₂ Fixation in the Eastern Tropical South Pacific Ocean. *PLOS ONE* 8, e81265. <https://doi.org/10.1371/journal.pone.0081265>
- Brandes, J.A., Devol, A.H., 1997. Isotopic fractionation of oxygen and nitrogen in coastal marine sediments. *Geochimica et Cosmochimica Acta* 61, 1793–1801. [https://doi.org/10.1016/S0016-7037\(97\)00041-0](https://doi.org/10.1016/S0016-7037(97)00041-0)
- Bristow, L.A., Dalsgaard, T., Tiano, L., Mills, D.B., Bertagnolli, A.D., Wright, J.J., Hallam, S.J., Ulloa, O., Canfield, D.E., Revsbech, N.P., Thamdrup, B., 2016. Ammonium and nitrite oxidation at nanomolar oxygen concentrations in oxygen minimum zone waters. *Proceedings of the National Academy of Sciences* 113, 10601–10606. <https://doi.org/10.1073/pnas.1600359113>
- Brunner, B., Contreras, S., Lehmann, M.F., Matantseva, O., Rollog, M., Kalvelage, T., Klockgether, G., Lavik, G., Jetten, M.S.M., Kartal, B., Kuypers, M.M.M., 2013. Nitrogen isotope effects induced by anammox bacteria. *PNAS* 110, 18994–18999. <https://doi.org/10.1073/pnas.1310488110>
- Capone, D.G., Zehr, J.P., Paerl, H.W., Bergman, B., Carpenter, E.J., 1997. Trichodesmium, a Globally Significant Marine Cyanobacterium. *Science* 276, 1221–1229. <https://doi.org/10.1126/science.276.5316.1221>
- Casciotti, K.L., 2009. Inverse kinetic isotope fractionation during bacterial nitrite oxidation.

- Geochimica et Cosmochimica Acta 73, 2061–2076. <https://doi.org/10.1016/j.gca.2008.12.022>
- Casciotti, K.L., Sigman, D.M., Hastings, M.G., Böhlke, J.K., Hilkert, A., 2002. Measurement of the Oxygen Isotopic Composition of Nitrate in Seawater and Freshwater Using the Denitrifier Method. *Anal. Chem.* 74, 4905–4912. <https://doi.org/10.1021/ac020113w>
- Casciotti, K.L., Sigman, D.M., Ward, B.B., 2003. Linking Diversity and Stable Isotope Fractionation in Ammonia-Oxidizing Bacteria. *Geomicrobiology Journal* 20, 335–353. <https://doi.org/10.1080/01490450303895>
- Codispoti, L.A., 1995. Is the ocean losing nitrate? *Nature* 376, 724–724. <https://doi.org/10.1038/376724a0>
- Cole, J.J., Lane, J.M., Marino, R., Howarth, R.W., 1993. Molybdenum assimilation by cyanobacteria and phytoplankton in freshwater and salt water. *Limnology and Oceanography* 38, 25–35. <https://doi.org/10.4319/lo.1993.38.1.0025>
- Dähnke, K., Thamdrup, B., 2013. Nitrogen isotope dynamics and fractionation during sedimentary denitrification in Boknis Eck, Baltic Sea. *Biogeosciences* 10, 3079–3088. <https://doi.org/10.5194/bg-10-3079-2013>
- Dalsgaard, T., Canfield, D.E., Petersen, J., Thamdrup, B., Acuña-González, J., 2003. N₂ production by the anammox reaction in the anoxic water column of Golfo Dulce, Costa Rica. *Nature* 422, 606–608. <https://doi.org/10.1038/nature01526>
- Dalsgaard, T., Thamdrup, B., 2002. Factors Controlling Anaerobic Ammonium Oxidation with Nitrite in Marine Sediments. *Applied and Environmental Microbiology*. <https://doi.org/10.1128/AEM.68.8.3802-3808.2002>
- Dalsgaard, T., Thamdrup, B., Farías, L., Revsbech, N.P., 2012. Anammox and denitrification in the oxygen minimum zone of the eastern South Pacific. *Limnology and Oceanography* 57, 1331–1346. <https://doi.org/10.4319/lo.2012.57.5.1331>
- Dekaezemacker, J., Bonnet, S., Grosso, O., Moutin, T., Bressac, M., Capone, D. g., 2013. Evidence of active dinitrogen fixation in surface waters of the eastern tropical South Pacific during El Niño and La Niña events and evaluation of its potential nutrient controls. *Global Biogeochemical Cycles* 27, 768–779. <https://doi.org/10.1002/gbc.20063>
- Delwiche, C.C., Steyn, P.L., 1970. Nitrogen isotope fractionation in soils and microbial reactions. *Environ. Sci. Technol.* 4, 929–935. <https://doi.org/10.1021/es60046a004>
- Devol, A.H., 2003. Solution to a marine mystery. *Nature* 422, 575–576. <https://doi.org/10.1038/422575a>
- Dos Santos, P.C., Fang, Z., Mason, S.W., Setubal, J.C., Dixon, R., 2012. Distribution of nitrogen fixation and nitrogenase-like sequences amongst microbial genomes. *BMC Genomics* 13, 162. <https://doi.org/10.1186/1471-2164-13-162>
- Fawcett, S.E., Lomas, M.W., Casey, J.R., Ward, B.B., Sigman, D.M., 2011. Assimilation of upwelled nitrate by small eukaryotes in the Sargasso Sea. *Nature Geosci* 4, 717–722. <https://doi.org/10.1038/ngeo1265>

- Fernandez, C., Farías, L., Ulloa, O., 2011. Nitrogen Fixation in Denitrified Marine Waters. *PLOS ONE* 6, e20539. <https://doi.org/10.1371/journal.pone.0020539>
- Freudenthal, T., Wagner, T., Wenzhöfer, F., Zabel, M., Wefer, G., 2001. Early diagenesis of organic matter from sediments of the eastern subtropical Atlantic: evidence from stable nitrogen and carbon isotopes. *Geochimica et Cosmochimica Acta* 65, 1795–1808. [https://doi.org/10.1016/S0016-7037\(01\)00554-3](https://doi.org/10.1016/S0016-7037(01)00554-3)
- Fulweiler, R.W., Nixon, S.W., Buckley, B.A., Granger, S.L., 2007. Reversal of the net dinitrogen gas flux in coastal marine sediments. *Nature* 448, 180–182. <https://doi.org/10.1038/nature05963>
- Gallon, J.R., 1992. Reconciling the incompatible: N₂ fixation And O₂. *New Phytologist* 122, 571–609. <https://doi.org/10.1111/j.1469-8137.1992.tb00087.x>
- Giblin, A.E., Tobias, C.R., Song, B., Weston, N., Banta, G.T., H.Rivera-Monroy, V., 2013. The Importance of Dissimilatory Nitrate Reduction to Ammonium (DNRA) in the Nitrogen Cycle of Coastal Ecosystems. *Oceanography* 26, 124–131.
- Goering, J., Alexander, V., Haubensack, N., 1990. Seasonal variability of stable carbon and nitrogen isotope ratios of organisms in a North Pacific Bay. *Estuarine, Coastal and Shelf Science* 30, 239–260. [https://doi.org/10.1016/0272-7714\(90\)90050-2](https://doi.org/10.1016/0272-7714(90)90050-2)
- Granger, J., Prokopenko, M.G., Sigman, D.M., Mordy, C.W., Morse, Z.M., Morales, L.V., Sambrotto, R.N., Plessen, B., 2011. Coupled nitrification-denitrification in sediment of the eastern Bering Sea shelf leads to ¹⁵N enrichment of fixed N in shelf waters. *Journal of Geophysical Research (Oceans)* 116, C11006. <https://doi.org/10.1029/2010JC006751>
- Granger, J., Sigman, D.M., Needoba, J.A., Harrison, P.J., 2004. Coupled nitrogen and oxygen isotope fractionation of nitrate during assimilation by cultures of marine phytoplankton. *Limnology and Oceanography* 49, 1763–1773. <https://doi.org/10.4319/lo.2004.49.5.1763>
- Granger, J., Sigman, D.M., Rohde, M.M., Maldonado, M.T., Tortell, P.D., 2010. N and O isotope effects during nitrate assimilation by unicellular prokaryotic and eukaryotic plankton cultures. *Geochimica et Cosmochimica Acta* 74, 1030–1040. <https://doi.org/10.1016/j.gca.2009.10.044>
- Grotzinger, J.P., Kasting, J.F., 1993. New Constraints on Precambrian Ocean Composition. *The Journal of Geology* 101, 235–243. <https://doi.org/10.1086/648218>
- Hadas, O., Altabet, M.A., Agnihotri, R., 2009. Seasonally varying nitrogen isotope biogeochemistry of particulate organic matter in Lake Kinneret, Israel. *Limnology and Oceanography* 54, 75–85. <https://doi.org/10.4319/lo.2009.54.1.0075>
- Hamersley, M.R., Turk, K.A., Leinweber, A., Gruber, N., Zehr, J.P., Gunderson, T., Capone, D.G., 2011. Nitrogen fixation within the water column associated with two hypoxic basins in the Southern California Bight. *Aquatic Microbial Ecology* 63, 193–205. <https://doi.org/10.3354/ame01494>
- Hoch, M.P., Fogel, M.L., Kirchman, D.L., 1992. Isotope fractionation associated with ammonium uptake by a marine bacterium. *Limnology and Oceanography* 37, 1447–1459. <https://doi.org/10.4319/lo.1992.37.7.1447>

- Hoering, T.C., Ford, H.T., 1960. The isotope effect in the fixation of nitrogen by *Azotobacter*. *Journal of the American Chemical Society* 82, 376–378.
- Howard, J.B., Rees, D.C., 1996. Structural Basis of Biological Nitrogen Fixation. *Chem. Rev.* 96, 2965–2982. <https://doi.org/10.1021/cr9500545>
- Joerger, R.D., Bishop, P.E., Evans, H.J., 1988. Bacterial Alternative Nitrogen Fixation Systems. *CRC Critical Reviews in Microbiology* 16, 1–14. <https://doi.org/10.3109/10408418809104465>
- Johnson, B., Goldblatt, C., 2015. The nitrogen budget of Earth. *Earth-Science Reviews* 148, 150–173. <https://doi.org/10.1016/j.earscirev.2015.05.006>
- Kalvelage, T., Lavik, G., Lam, P., Contreras, S., Arteaga, L., Löscher, C.R., Oshlies, A., Paulmier, A., Stramma, L., Kuypers, M.M.M., 2013. Nitrogen cycling driven by organic matter export in the South Pacific oxygen minimum zone. *Nature Geoscience* 6, 228–234. <https://doi.org/10.1038/ngeo1739>
- Karl, D., Letelier, R., Tupas, L., Dore, J., Christian, J., Hebel, D., 1997. The role of nitrogen fixation in biogeochemical cycling in the subtropical North Pacific Ocean. *Nature* 388, 533–538. <https://doi.org/10.1038/41474>
- Karl, D., Michaels, A., Bergman, B., Capone, D., Carpenter, E., Letelier, R., Lipschultz, F., Paerl, H., Sigman, D., Stal, L., 2002. Dinitrogen fixation in the world's oceans. *Biogeochemistry* 57, 47–98. <https://doi.org/10.1023/A:1015798105851>
- Kartal, B., Kuypers, M.M.M., Lavik, G., Schalk, J., Op den Camp, H.J.M., Jetten, M.S.M., Strous, M., 2007. Anammox bacteria disguised as denitrifiers: nitrate reduction to dinitrogen gas via nitrite and ammonium. *Environmental Microbiology* 9, 635–642. <https://doi.org/10.1111/j.1462-2920.2006.01183.x>
- Kartal, B., Maalcke, W.J., de Almeida, N.M., Cirpus, I., Gloerich, J., Geerts, W., Op den Camp, H.J.M., Harhangi, H.R., Janssen-Megens, E.M., Francoijs, K.-J., Stunnenberg, H.G., Keltjens, J.T., Jetten, M.S.M., Strous, M., 2011. Molecular mechanism of anaerobic ammonium oxidation. *Nature* 479, 127–130. <https://doi.org/10.1038/nature10453>
- Lam, P., Lavik, G., Jensen, M.M., van de Vossenberg, J., Schmid, M., Woebken, D., Gutiérrez, D., Amann, R., Jetten, M.S.M., Kuypers, M.M.M., 2009. Revising the nitrogen cycle in the Peruvian oxygen minimum zone. *Proceedings of the National Academy of Sciences* 106, 4752–4757. <https://doi.org/10.1073/pnas.0812444106>
- Lehmann, M.F., Reichert, P., Bernasconi, S.M., Barbieri, A., McKenzie, J.A., 2003. Modelling nitrogen and oxygen isotope fractionation during denitrification in a lacustrine redox-transition zone. *Geochimica et Cosmochimica Acta* 67, 2529–2542. [https://doi.org/10.1016/S0016-7037\(03\)00085-1](https://doi.org/10.1016/S0016-7037(03)00085-1)
- Lipschultz, F., Wofsy, S.C., Ward, B.B., Codispoti, L.A., Friedrich, G., Elkins, J.W., 1990. Bacterial transformations of inorganic nitrogen in the oxygen-deficient waters of the Eastern Tropical South Pacific Ocean. *Deep Sea Research Part A. Oceanographic Research Papers* 37, 1513–1541. [https://doi.org/10.1016/0198-0149\(90\)90060-9](https://doi.org/10.1016/0198-0149(90)90060-9)
- Macko, S.A., Fogel, M.L., Hare, P.E., Hoering, T.C., 1987. Isotopic fractionation of nitrogen and carbon in the synthesis of amino acids by microorganisms. *Chemical Geology: Isotope*

Geoscience section 65, 79–92. [https://doi.org/10.1016/0168-9622\(87\)90064-9](https://doi.org/10.1016/0168-9622(87)90064-9)

Mahaffey, C., Michaels, A.F., Capone, D.G., 2005. The conundrum of marine N₂ fixation. *American Journal of Science* 305, 546–595. <https://doi.org/10.2475/ajs.305.6-8.546>

Mandernack, K.W., Kinney, C.A., Coleman, D., Huang, Y.-S., Freeman, K.H., Bogner, J., 2000. The biogeochemical controls of N₂O production and emission in landfill cover soils: the role of methanotrophs in the nitrogen cycle. *Environmental Microbiology* 2, 298–309. <https://doi.org/10.1046/j.1462-2920.2000.00106.x>

Mandernack, K.W., Mills, C.T., Johnson, C.A., Rahn, T., Kinney, C., 2009. The $\delta^{15}\text{N}$ and $\delta^{18}\text{O}$ values of N₂O produced during the co-oxidation of ammonia by methanotrophic bacteria. *Chemical Geology, Combined Ecological and Geologic Perspectives in Ecosystem Studies* 267, 96–107. <https://doi.org/10.1016/j.chemgeo.2009.06.008>

Mariotti, A., Germon, J.C., Hubert, P., Kaiser, P., Letolle, R., Tardieux, A., Tardieux, P., 1981. Experimental determination of nitrogen kinetic isotope fractionation: Some principles; illustration for the denitrification and nitrification processes. *Plant Soil* 62, 413–430. <https://doi.org/10.1007/BF02374138>

Mariotti, A., Mariotti, F., Champigny, M.-L., Amarger, N., Moyse, A., 1982. Nitrogen Isotope Fractionation Associated with Nitrate Reductase Activity and Uptake of NO₃⁻ by Pearl Millet. *Plant Physiol.* 69, 880–884. <https://doi.org/10.1104/pp.69.4.880>

McCready, R.G.L., Gould, W.D., Barendregt, R.W., 1983. Nitrogen isotope fractionation during the reduction of NO₃⁻ to NH₄⁺ by *Desulfovibrio* sp. *Can. J. Microbiol.* 29, 231–234. <https://doi.org/10.1139/m83-038>

Megraw, S.R., Knowles, R., 1989. Methane-dependent nitrate production by a microbial consortium enriched from a cultivated humisol. *FEMS Microbiology Ecology* 5, 359–365. <https://doi.org/10.1111/j.1574-6968.1989.tb03391.x>

Mehta, M.P., Baross, J.A., 2006. Nitrogen Fixation at 92°C by a Hydrothermal Vent Archaeon. *Science* 314, 1783–1786. <https://doi.org/10.1126/science.1134772>

Miller, R.W., Eady, R.R., 1988. Molybdenum and vanadium nitrogenases of *Azotobacter chroococcum*. Low temperature favours N₂ reduction by vanadium nitrogenase. *Biochemical Journal* 256, 429–432. <https://doi.org/10.1042/bj2560429>

Minagawa, M., Wada, E., 1986. Nitrogen isotope ratios of red tide organisms in the East China Sea: A characterization of biological nitrogen fixation. *Marine Chemistry* 19, 245–259. [https://doi.org/10.1016/0304-4203\(86\)90026-5](https://doi.org/10.1016/0304-4203(86)90026-5)

Miyake, Y., Wada, E., 1967. The abundance ratio of ¹⁵N/¹⁴N in marine environments. *Rec. Oceanogr. Works Jpn* 9, 37–53.

Möbius, J., 2013. Isotope fractionation during nitrogen remineralization (ammonification): Implications for nitrogen isotope biogeochemistry. *Geochimica et Cosmochimica Acta* 105, 422–432. <https://doi.org/10.1016/j.gca.2012.11.048>

Montoya, J.P., Carpenter, E.J., Capone, D.G., 2002. Nitrogen fixation and nitrogen isotope abundances in zooplankton of the oligotrophic North Atlantic. *Limnology and Oceanography*

47, 1617–1628. <https://doi.org/10.4319/lo.2002.47.6.1617>

Mulder, A., van de Graaf, A.A., Robertson, L.A., Kuenen, J.G., 1995. Anaerobic ammonium oxidation discovered in a denitrifying fluidized bed reactor. *FEMS Microbiology Ecology* 16, 177–183. [https://doi.org/10.1016/0168-6496\(94\)00081-7](https://doi.org/10.1016/0168-6496(94)00081-7)

Nakanishi, T., Minagawa, M., 2003. Stable carbon and nitrogen isotopic compositions of sinking particles in the northeast Japan Sea. *Geochemical Journal* 37, 261–275. <https://doi.org/10.2343/geochemj.37.261>

Petrash, D.A., Steenbergen, I.M., Valero, A., Meador, T.B., Pačes, T., Thomazo, C., 2021. Aqueous system-level processes and prokaryote assemblages in the ferruginous and sulfate-rich bottom waters of a post-mining lake. *Biogeosciences Discussions* 1–37. <https://doi.org/10.5194/bg-2021-253>

Rafter, P.A., Bagnell, A., Marconi, D., DeVries, T., 2019. Global trends in marine nitrate N isotopes from observations and a neural network-based climatology. *Biogeosciences* 16, 2617–2633. <https://doi.org/10.5194/bg-16-2617-2019>

Raimbault, P., Garcia, N., 2008. Evidence for efficient regenerated production and dinitrogen fixation in nitrogen-deficient waters of the South Pacific Ocean: impact on new and export production estimates. *Biogeosciences* 5, 323–338. <https://doi.org/10.5194/bg-5-323-2008>

Raymond, J., Siefert, J.L., Staples, C.R., Blankenship, R.E., 2004. The Natural History of Nitrogen Fixation. *Mol Biol Evol* 21, 541–554. <https://doi.org/10.1093/molbev/msh047>

Redfield, A.C., 1934. On the proportions of organic derivatives in sea water and their relation to the composition of plankton. university press of liverpool Liverpool.

Rios-Del Toro, E.E., Valenzuela, E.I., López-Lozano, N.E., Cortés-Martínez, M.G., Sánchez-Rodríguez, M.A., Calvario-Martínez, O., Sánchez-Carrillo, S., Cervantes, F.J., 2018. Anaerobic ammonium oxidation linked to sulfate and ferric iron reduction fuels nitrogen loss in marine sediments. *Biodegradation* 29, 429–442. <https://doi.org/10.1007/s10532-018-9839-8>

Robinson, R.S., Kienast, M., Albuquerque, A.L., Altabet, M., Contreras, S., Holz, R.D.P., Dubois, N., Francois, R., Galbraith, E., Hsu, T.-C., Ivanochko, T., Jaccard, S., Kao, S.-J., Kiefer, T., Kienast, S., Lehmann, M., Martinez, P., McCarthy, M., Möbius, J., Pedersen, T., Quan, T.M., Ryabenko, E., Schmittner, A., Schneider, R., Schneider-Mor, A., Shigemitsu, M., Sinclair, D., Somes, C., Studer, A., Thunell, R., Yang, J.-Y., 2012. A review of nitrogen isotopic alteration in marine sediments. *Paleoceanography* 27. <https://doi.org/10.1029/2012PA002321>

Roy, R., Knowles, R., 1994. Effects of Methane Metabolism on Nitrification and Nitrous Oxide Production in Polluted Freshwater Sediment. *Applied and Environmental Microbiology* 60, 3307–3314. <https://doi.org/10.1128/aem.60.9.3307-3314.1994>

Ryabenko, E., 2013. Stable Isotope Methods for the Study of the Nitrogen Cycle. pp. 49–88. <https://doi.org/10.5772/56105>

Sachs, J.P., Repeta, D.J., 1999. Oligotrophy and nitrogen fixation during eastern mediterranean sapropel event. *Science* 286, 2485–2488. <https://doi.org/10.1126/science.286.5449.2485>

Sawayama, S., 2006. Possibility of anoxic ferric ammonium oxidation. *Journal of Bioscience*

and Bioengineering 101, 70–72. <https://doi.org/10.1263/jbb.101.70>

Schoepp-Cothenet, B., van Lis, R., Atteia, A., Baymann, F., Capowiez, L., Ducluzeau, A.-L., Duval, S., ten Brink, F., Russell, M.J., Nitschke, W., 2013. On the universal core of bioenergetics. *Biochimica et Biophysica Acta (BBA) - Bioenergetics*, The evolutionary aspects of bioenergetic systems 1827, 79–93. <https://doi.org/10.1016/j.bbabi.2012.09.005>

Sharp, J.H., 1983. The distributions of inorganic nitrogen and dissolved and particulate organic nitrogen in the sea. *Nitrogen in the marine environment* 1–35.

Sigman, D.M., Altabet, M.A., McCorkle, D.C., Francois, R., Fischer, G., 1999. The $\delta^{15}\text{N}$ of nitrate in the southern ocean: Consumption of nitrate in surface waters. *Global Biogeochemical Cycles* 13, 1149–1166. <https://doi.org/10.1029/1999GB900038>

Sigman, D.M., Fripiat, F., 2019. Nitrogen Isotopes in the Ocean, in: *Encyclopedia of Ocean Sciences*. Elsevier, pp. 263–278. <https://doi.org/10.1016/B978-0-12-409548-9.11605-7>

Sigman, D.M., Karsh, K.L., Casciotti, K.L., 2009. Nitrogen Isotopes in the Ocean. *Encyclopedia of Ocean Sciences* 40–54. <https://doi.org/10.1016/B978-012374473-9.00632-9>

Sørensen, J., 1978. Capacity for Denitrification and Reduction of Nitrate to Ammonia in a Coastal Marine Sediment. *Appl Environ Microbiol* 35, 301–305.

Stal, L.J., Staal, M., Villbrandt, M., 1999. Nutrient control of cyanobacterial blooms in the Baltic Sea. *Aquatic Microbial Ecology* 18, 165–173. <https://doi.org/10.3354/ame018165>

Stenstrom, M.K., Poduska, R.A., 1980. The effect of dissolved oxygen concentration on nitrification. *Water Research* 14, 643–649. [https://doi.org/10.1016/0043-1354\(80\)90122-0](https://doi.org/10.1016/0043-1354(80)90122-0)

Strous, M., Fuerst, J.A., Kramer, E.H.M., Logemann, S., Muyzer, G., van de Pas-Schoonen, K.T., Webb, R., Kuenen, J.G., Jetten, M.S.M., 1999. Missing lithotroph identified as new planctomycete. *Nature* 400, 446–449. <https://doi.org/10.1038/22749>

Strous, M., Pelletier, E., Mangenot, S., Rattei, T., Lehner, A., Taylor, M.W., Horn, M., Daims, H., Bartol-Mavel, D., Wincker, P., Barbe, V., Fonknechten, N., Vallenet, D., Segurens, B., Schenowitz-Truong, C., Médigue, C., Collingro, A., Snel, B., Dutilh, B.E., Op den Camp, H.J.M., van der Drift, C., Cirpus, I., van de Pas-Schoonen, K.T., Harhangi, H.R., van Niftrik, L., Schmid, M., Keltjens, J., van de Vossenberg, J., Kartal, B., Meier, H., Frishman, D., Huynen, M.A., Mewes, H.-W., Weissenbach, J., Jetten, M.S.M., Wagner, M., Le Paslier, D., 2006. Deciphering the evolution and metabolism of an anammox bacterium from a community genome. *Nature* 440, 790–794. <https://doi.org/10.1038/nature04647>

Stüeken, E.E., Kipp, M.A., Koehler, M.C., Buick, R., 2016. The evolution of Earth's biogeochemical nitrogen cycle. *Earth-Science Reviews* 160, 220–239. <https://doi.org/10.1016/j.earscirev.2016.07.007>

Tesdal, J.E., Galbraith, E.D., Kienast, M., 2012. The marine sedimentary nitrogen isotope record. *Biogeosciences Discussions* 9.

Thamdrup, B., Dalsgaard, T., 2002. Production of N_2 through Anaerobic Ammonium Oxidation Coupled to Nitrate Reduction in Marine Sediments. *Appl. Environ. Microbiol.* 68, 1312–1318. <https://doi.org/10.1128/AEM.68.3.1312-1318.2002>

- Thomazo, C., Ader, M., Farquhar, J., Philippot, P., 2009. Methanotrophs regulated atmospheric sulfur isotope anomalies during the Mesoarchean (Tumbiana Formation, Western Australia). *Earth and Planetary Science Letters* 279, 65–75. <https://doi.org/10.1016/j.epsl.2008.12.036>
- Thomazo, C., Ader, M., Philippot, P., 2011. Extreme ^{15}N -enrichments in 2.72-Gyr-old sediments: evidence for a turning point in the nitrogen cycle. *Geobiology* 9, 107–120. <https://doi.org/10.1111/j.1472-4669.2011.00271.x>
- Ustick, L.J., Larkin, A.A., Garcia, C.A., Garcia, N.S., Brock, M.L., Lee, J.A., Wiseman, N.A., Moore, J.K., Martiny, A.C., 2021. Metagenomic analysis reveals global-scale patterns of ocean nutrient limitation. *Science* 372, 287–291. <https://doi.org/10.1126/science.abe6301>
- Van de Graaf, A.A., Mulder, A., de Bruijn, P., Jetten, M.S., Robertson, L.A., Kuenen, J.G., 1995. Anaerobic oxidation of ammonium is a biologically mediated process. *Appl Environ Microbiol* 61, 1246–1251.
- Velinsky, D.J., Fogel, M.L., Todd, J.F., Tebo, B.M., 1991. Isotopic fractionation of dissolved ammonium at the oxygen-hydrogen sulfide interface in anoxic waters. *Geophysical Research Letters* 18, 649–652. <https://doi.org/10.1029/91GL00344>
- Wada, E., Hattori, A., 1978. Nitrogen isotope effects in the assimilation of inorganic nitrogenous compounds by marine diatoms. *Geomicrobiology Journal* 1, 85–101. <https://doi.org/10.1080/01490457809377725>
- Wada, E., Hattori, A., 1976. Natural abundance of ^{15}N in particulate organic matter in the North Pacific Ocean. *Geochimica et Cosmochimica Acta* 40, 249–251. [https://doi.org/10.1016/0016-7037\(76\)90183-6](https://doi.org/10.1016/0016-7037(76)90183-6)
- Ward, B., 2012. The Global Nitrogen Cycle, in: *Fundamentals of Geobiology*. John Wiley & Sons, Ltd, pp. 36–48. <https://doi.org/10.1002/9781118280874.ch4>
- Ward, B.B., 2013. How Nitrogen Is Lost. *Science* 341, 352–353. <https://doi.org/10.1126/science.1240314>
- Xiong, Y., Du, Y., Deng, Y., Ma, T., Wang, Y., 2022. Feammox in alluvial-lacustrine aquifer system: Nitrogen/iron isotopic and biogeochemical evidences. *Water Research* 222, 118867. <https://doi.org/10.1016/j.watres.2022.118867>
- Yang, W.H., Weber, K.A., Silver, W.L., 2012. Nitrogen loss from soil through anaerobic ammonium oxidation coupled to iron reduction. *Nature Geosci* 5, 538–541. <https://doi.org/10.1038/ngeo1530>
- Yoshida, N., 1988. ^{15}N -depleted N_2O as a product of nitrification. *Nature* 335, 528–529. <https://doi.org/10.1038/335528a0>
- Yoshinari, T., 1985. Nitrite and nitrous oxide production by *Methylosinus trichosporium*. *Can. J. Microbiol.* 31, 139–144. <https://doi.org/10.1139/m85-027>
- Zhang, X., Sigman, D.M., Morel, F.M.M., Kraepiel, A.M.L., 2014. Nitrogen isotope fractionation by alternative nitrogenases and past ocean anoxia. *PNAS* 111, 4782–4787. <https://doi.org/10.1073/pnas.1402976111>

CHAPTER 2. A FRAMEWORK OF NITROGEN ISOTOPES INTERPRETATION IN PRECAMBRIAN SEDIMENTARY ROCKS

2.1. Preservation of the nitrogen isotope signature of primary producers through water-column transfers and post-depositional history	36
2.1.1. Primary producers' isotopic signature transfer to the sediment.....	37
2.1.2. Effect of diagenesis on sedimentary N concentration and isotope composition....	39
2.1.3. Metamorphic and metasomatic alteration of the $\delta^{15}\text{N}$ signature	41
2.2. Nitrogen sources to the Archean Earth's surficial reservoirs and their isotope composition.....	43
2.2.1. Stability of the nitrogen atmospheric isotope composition through time	43
2.2.2. Organic hazes and aerosols production on the prebiotic Earth.....	43
2.2.3. Hydrothermalism	44
2.2.4. Biological and alternative fixed nitrogen sources.....	44
2.3. The evolution of biological and abiotic pathways of the early nitrogen cycle	45
2.3.1. Biological N_2 fixation and the evolution of nitrogenase enzymes.....	45
2.3.2. The emergence of oxidative pathways of the N cycle: nitrogen as a proxy of paleoredox conditions	47
2.3.2.1. Dominantly oxic oceans.....	48
2.3.2.2. Redox-stratified oceans.....	48
2.3.2.3. Fully anoxic oceans.....	50
2.3.3. Ammonia degassing, an abiotic process that could have impacted the Archean N cycle and associated isotopic signature of sedimentary archive.....	52
2.4. The size of the dissolved nitrogen reservoir: insights into nutrient availability during the Archean	54
2.5. Conclusion: strengths and limits of using the $\delta^{15}\text{N}$ proxy in deep time	56
References.....	58

CHAPTER 2. A FRAMEWORK OF NITROGEN ISOTOPES INTERPRETATION IN PRECAMBRIAN SEDIMENTARY ROCKS

As we have seen with the dynamics of the modern biogeochemical nitrogen cycle, the speciation of nitrogen and the fate of nitrogen species in the ocean essentially depend on the balance between the different metabolic reactions at play, themselves tightly controlled by the availability of oxidants throughout the water column. As sediments preserve the fraction of organic and mineral nitrogen that escapes remineralization and oxidation, sedimentary $\delta^{15}\text{N}$ values have been increasingly used to trace the redox dynamics of the N cycle in past environments.

Reconstructing the Precambrian biogeochemical nitrogen cycle provides a useful tool to understand the evolution of Precambrian environments, both in terms of structure and oxidation state of the water column, in terms of the evolution of past metabolisms, and in terms of nutrient dynamics and paleoproductivity.

This chapter will explore how the nitrogen isotopic signature recorded in sedimentary rocks can act as a reliable proxy of the Precambrian N-biogeochemical cycle, and how studying the early evolution of the nitrogen cycle can trace the oxygenation of Precambrian environments before, during and after the Great Oxidation Event (GOE) during the Archean-Proterozoic transition. It will give an overview of the current framework of nitrogen isotopes interpretation in Precambrian sedimentary rocks, and point out its shortcomings and challenges.

2.1. Preservation of the nitrogen isotope signature of primary producers through water-column transfers and post-depositional history

One of the main challenges of studying the nitrogen isotope signature of Precambrian sedimentary rocks and interpreting it in terms of past nitrogen cycling is the potential alteration by post-depositional processes, namely diagenesis and metamorphism (Fig. 2.1). The effects of diagenetic and metamorphic alteration have to either be negligible or quantified so as to get back to the original isotope signature and draw conclusions about the Precambrian N cycle (Fig. 2.1).

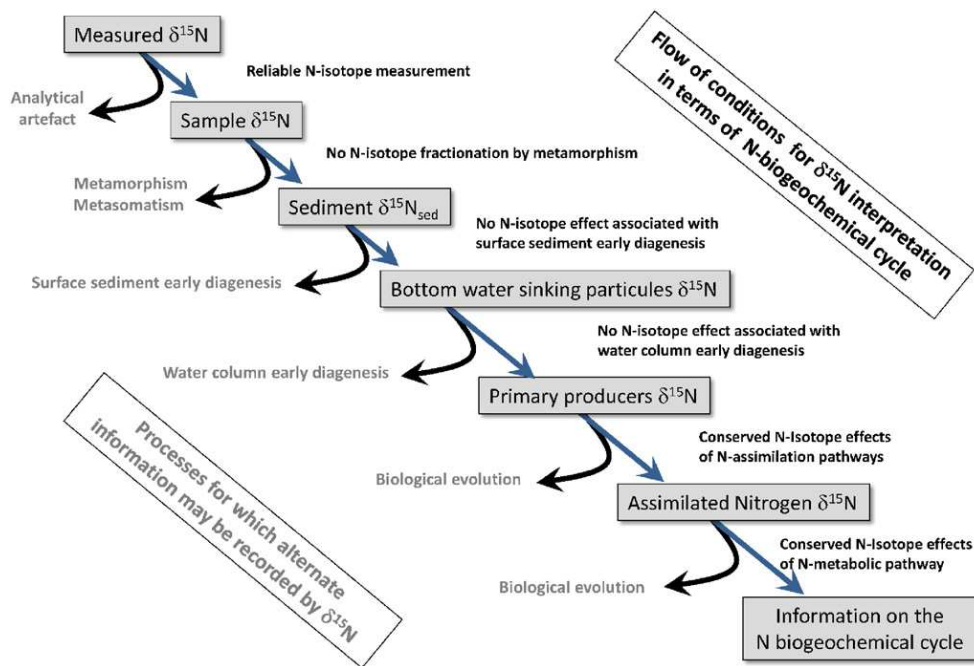


Fig. 2.1. Flow of conditions that are required to interpret the $\delta^{15}\text{N}$ data measured in sedimentary rocks in terms of N biogeochemical cycle, and processes for which alternate information may be recorded in $\delta^{15}\text{N}$ data (Ader et al., 2016).

2.1.1. Primary producers' isotopic signature transfer to the sediment

Two parameters control the $\delta^{15}\text{N}$ of primary producers: the $\delta^{15}\text{N}$ of the nitrogen sources they feed on, mostly ammonium, nitrate, dissolved organic nitrogen (DON) and N_2 , and the fractionation associated with the respective assimilation pathways (Fig. 2.2), namely ammonium assimilation, nitrate assimilation and N_2 fixation. These processes and the fractionation they impart in the modern ocean have been detailed in Chapter 1.

Nitrogen in modern surface sediments mostly consists of soluble and insoluble amino acids and sugars, and fixed or exchangeable ammonium (Kemp and Mudrochova, 1973). In those sediments, nitrogen essentially comes from sinking particulate organic matter derived from primary producers (Sigman et al., 2009). Therefore, sedimentary $\delta^{15}\text{N}$ should reflect the $\delta^{15}\text{N}$ of primary producers if biodegradation processes occurring in the water column and in surface sediments are negligible or if they can be quantified and scaled from $\delta^{15}\text{N}$ measurements (Fig. 2.1).

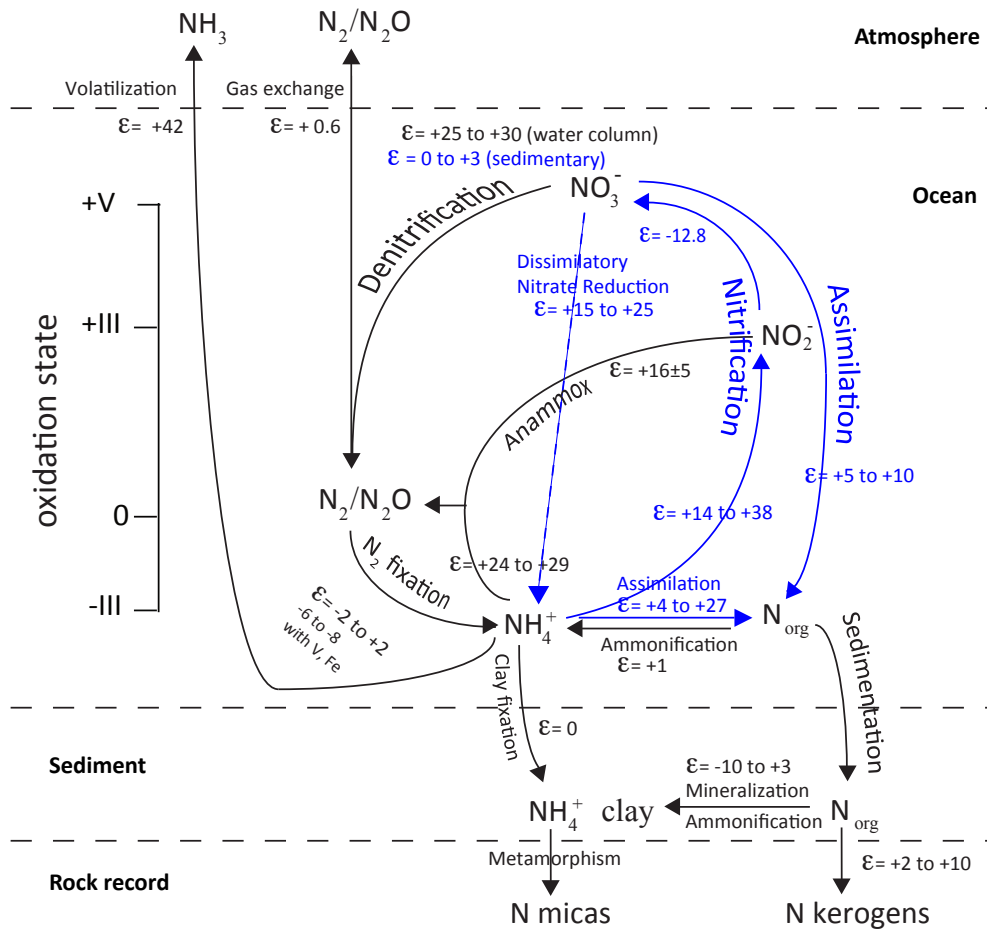


Fig. 2.2. Simplified model of the biogeochemical N cycle in modern oceans (modified from Thomazo et al., 2011). Isotopic fractionations are noted as $\epsilon = \delta^{15}\text{N}_{\text{reactant}} - \delta^{15}\text{N}_{\text{product}}$, where $\delta^{15}\text{N} = [({}^{15}\text{N}/{}^{14}\text{N})_{\text{sample}} / ({}^{15}\text{N}/{}^{14}\text{N})_{\text{standard}} - 1] \cdot 1000$, and the standard is atmospheric air (Mariotti, 1983). Analyses of N_2 contained in fluid inclusions dating back to 3.5 Ga suggest that the composition of air has not changed by more than 2‰ (Nishizawa et al., 2007; Marty et al., 2013). Pathways that typically go to completion in the modern ocean and leave no net isotopic trace in most sediments are shown in blue.

Organic matter alteration in the water column and surface sediments soon after deposition mainly depends on its O_2 exposure time (Robinson et al., 2012), which is itself controlled by the degree of water column oxygenation, the duration of particle sinking, itself depending on their size and water column depth, and the residence time at the sediment-water interface, function of the sedimentation rate. When organic matter has been highly exposed to O_2 , which is the case for most modern sediments, deposited under low sedimentation rates in deep water columns and exposed to high O_2 concentrations, its $\delta^{15}\text{N}$ is enriched by +3 to +5‰ compared to surface particulate organic matter (Altabet et al., 1999; Brummer et al., 2002; Gaye et al., 2009; Lehmann et al., 2002; Möbius et al., 2011, 2010; Nakanishi and Minagawa, 2003; Prahl

et al., 2003; Robinson et al., 2012; Sachs and Repeta, 1999). This increase likely results from isotope fractionation during ammonium release and partial oxidation (Möbius, 2013; Prokopenko et al., 2006). Conversely, sediments deposited in O₂-depleted waters, or in shallow environments with high sedimentation rates such as deltas, have similar or slightly lower (<1‰) δ¹⁵N values than surface particulate organic matter (Altabet et al., 1999; Chen et al., 2008; Emmer and Thunell, 2000; Higgins et al., 2010; Kienast et al., 2002; Lehmann et al., 2002; Möbius et al., 2010; Pride et al., 1999; Sachs and Repeta, 1999; Thunell and Kepple, 2004).

Because most Archean sedimentary rocks were deposited when O₂ concentration in the ocean was null or extremely low (<10⁻⁵ PAL, *present atmospheric level*, Holland, 2006; Lyons et al., 2014), primary producers' isotopic signature transfer to the sediment is generally assumed to occur without significant δ¹⁵N modifications (Ader et al., 2016). In addition, in modern continental shelves, the depth of the water column is generally insufficient for δ¹⁵N modifications to be preserved in sediments (Altabet et al., 1999; Altabet and Francois, 1994). Therefore, if sediments are deposited on continental shelves, δ¹⁵N modifications are unlikely, even under an oxic water column.

2.1.2. Effect of diagenesis on sedimentary N concentration and isotope composition

Sedimentary diagenesis can be subdivided into two phases: long-term early diagenesis, mainly influenced by microbial activity occurring directly in the sediment, and burial diagenesis, for which compaction and temperature increase are the main drivers.

In sediments and thermally immature sedimentary rocks, N is present either as organic N or as fixed ammonium, because NH₄⁺ can substitute for K⁺ in phyllosilicates (Freudenthal et al., 2001; Müller, 1977). Since organic matter decomposition generates a single major product, ammonium, in the absence of oxidative metabolic or diagenetic reactions, the isotopic composition of ammonium in the sediment reflects that of decomposing organic matter (Prokopenko et al., 2006).

During long-term early diagenesis, microbial remineralization of organic N generates some NH₄⁺ which can be converted into N₂, N₂O, NO₂⁻ or NO₃⁻ depending on O₂ concentrations in porewaters. A compilation of published alteration data comparing the isotopic signature of surface sediments to that of sinking particles through sediment traps (Robinson et al., 2012) has

shown that seafloor $\delta^{15}\text{N}$ increases according to the amount of time it has been exposed to oxygen. However, this alteration seems uniform through time, making sedimentary $\delta^{15}\text{N}$ measurements relevant to study changes in the biogeochemical nitrogen cycle. The isotopic analysis of porewater ammonium and organic nitrogen from anoxic sediments of the Eastern Subtropical North Pacific region and the Santa Barbara Basin shows that the $\delta^{15}\text{N}$ of ammonium essentially depends on bacterial processes occurring in the sediment (Prokopenko et al., 2006). When organic matter decomposition is the only reaction, the isotopic fractionation is minimal, as residual organic matter is depleted by -0.7‰ (Prokopenko et al., 2006). Although a significant portion of sedimentary N can be bound as NH_4^+ in phyllosilicates (up to 60%, Kemp and Mudrochova, 1973; Müller, 1977) the bulk isotope composition ($\delta^{15}\text{N}_{\text{bulk}}$) of sediments does not appear to change significantly with depth (Freudenthal et al., 2001; Kohzu et al., 2011; Prokopenko et al., 2006, 2006; Yamaguchi et al., 2010).

An exception to this in the modern world is the case of sediments deposited in OMZs, where $\delta^{15}\text{N}$ enrichments of up to $+8\text{‰}$ have been measured from 4m-depth sediments towards the sediment-water interface (Prokopenko et al., 2006). There, a biologically-mediated active transport of NO_3^- from the dysoxic to anoxic waters overlying the sediment, to the ammonium-rich top of the anoxic sedimentary column (Prokopenko et al., 2013), fuels anammox and enriches the ammonium in ^{15}N . Although this process is unlikely to have happened in anoxic oceans of the early Archean where nitrate and nitrite were absent or cryptic, it might have been relevant for Neoproterozoic or Proterozoic oxygen oases. One way to detect this ^{15}N -enriched ammonium would be to measure the isotopic signature of the organic nitrogen fraction ($\delta^{15}\text{N}_{\text{ker}}$) and comparing it to the bulk sedimentary $\delta^{15}\text{N}$ (Ader et al., 2016).

During burial diagenesis, sedimentary organic matter can be altered by thermal maturation, where the temperature increase is accompanied by the compaction of the sediment. Studies that have measured the $\delta^{15}\text{N}$ of mineral N in clay minerals show that it does not differ ($<2\text{‰}$) from the $\delta^{15}\text{N}$ preserved in the surrounding organic matter nor from the bulk sedimentary $\delta^{15}\text{N}$ (Mingram et al., 2005; Williams et al., 1995). It suggests that ammonium is released from the organic matter and fixed in clay minerals without significant isotope fractionation. Similarly, studies that have measured the C/N ratios and N isotope composition of bulk sediments or kerogens during thermal maturation have not found any significant impact, and concluded that burial diagenesis had a negligible impact on the $\delta^{15}\text{N}$ (Boudou et al., 1984; Macko and Quick, 1986; Rigby and Batts, 1986; Rivera et al., 2015; Whiticar, 1996; Williams et al., 1995).

2.1.3. Metamorphic and metasomatic alteration of the $\delta^{15}\text{N}$ signature

During prograde metamorphism, kerogen is progressively converted to graphite (Kitchen and Valley, 1995). This graphitization process is associated with thermal denitrogenation, a significant N loss compared to C, increasing the TOC/TN ratios of bulk organic matter (Boudou et al., 2008; Daniels and Altaner, 1993, 1990; Volkova and Bogdanova, 1989).

While an increase in $\delta^{15}\text{N}$, a decrease in TN and an increase in TOC/TN has often been documented during prograde metamorphism (Bebout and Fogel, 1992; Boyd and Philippot, 1998; Haendel et al., 1986; Jia, 2006), studies on coal series show that nitrogen loss from organic matter during anthracitization is not associated with significant $\delta^{15}\text{N}_{\text{ker}}$ increase (Ader et al., 1998, 2006; Boudou et al., 2008) despite TOC/TN increases from 50 to 1000 (Ader et al., 1998, 2006; Schimmelmann et al., 2009). This suggests that during thermal denitrogenation, N is released from the organic matter without fractionation, probably in the form of ammonium. This ammonium can then be lost from the system through the migration of fluids and/or be retained in the mineral lattice of clay minerals (Daniels and Altaner, 1993, 1990; Juster et al., 1987; Mingram et al., 2005; Šucha et al., 1994). When the ammonium-bearing minerals are metamorphosed and if the redox conditions in the rock allow it, ammonium can be released as ^{15}N -depleted N_2 or NH_3 , increasing the rock $\delta^{15}\text{N}$ value and decreasing its TN content (Bebout et al., 1999; Bebout and Fogel, 1992; Mingram et al., 2005; Mingram and Bräuer, 2001; Svensen et al., 2008). This release follows a Rayleigh distillation trend, the isotopic effect increasing with metamorphic grade. Maximum isotopic enrichments documented for greenschist facies metamorphism are below 2‰ (Jia, 2006; Stüeken et al., 2017), while those documented for amphibolite and upper amphibolite facies metamorphism can go up to +4‰ and +10‰, respectively (Bebout et al., 1999; Bebout and Fogel, 1992; Boyd and Philippot, 1998; Haendel et al., 1986; Jia, 2006; Mingram et al., 2005; Mingram and Bräuer, 2001; Pitcairn et al., 2005; Plessen et al., 2010; Yui et al., 2009). However, such a NH_4^+ destabilization is not systematically occurring, and it is interesting to note that some studies on highly metamorphosed rocks in the eclogite or granulite facies document minimal $\delta^{15}\text{N}$ enrichments (Busigny et al., 2003; Palya et al., 2011), which makes it difficult to correct $\delta^{15}\text{N}$ values from metamorphic effects. Generally, rocks that are metamorphosed above the greenschist facies are thus avoided in N cycle biogeochemical studies.

Secondary modification of $\delta^{15}\text{N}$ values can also occur during metasomatic ammonium addition through fluid circulation and hydrothermal recycling, which tend to decrease the TOC/TN

(Glasmacher et al., 2003; Jia and Kerrich, 2000, 1999; Sterne et al., 1982; Svensen et al., 2008) and either increase or decrease the $\delta^{15}\text{N}$ depending on the isotopic signature of recycled sediments (Stüeken et al., 2021b, 2021c).

As a significant proportion of the organic nitrogen can be transferred from the organic matter to clay minerals as ammonium, an issue that has been debated in the literature is about which phase best captures the $\delta^{15}\text{N}$ signature of the original organic matter (Stüeken et al., 2017). $\delta^{15}\text{N}$ measurements can either be made on (i) kerogen extracts, the residual organic-bound nitrogen phase (Beaumont and Robert, 1999; Godfrey and Falkowski, 2009; Kump et al., 2011; Stüeken et al., 2015), (ii) potassic minerals (K-bearing phyllosilicates and feldspars), that retain ammonium in their mineral lattice (Boyd and Philippot, 1998; Busigny et al., 2005, 2003) or (iii) bulk rocks, that include both phases. Kerogen extracts being more difficult to obtain and measure, subject to contamination during the extraction process and sensitive to metasomatic alteration (Beaumont and Robert, 1999; Godfrey et al., 2013; Kump et al., 2011; Schimmelmann and Lis, 2010; Svensen et al., 2008), bulk measurements are often preferred. Stüeken et al. (2017) found that metamorphism depletes kerogen-bound nitrogen in ^{15}N while enriching silicate-bound nitrogen in ^{15}N , with an isotopic effect of up to 3-4‰ for rocks up to the greenschist facies. They concluded that since for low-grade sedimentary rocks this phase partitioning was larger than the isotopic effect of metamorphic nitrogen loss (1-2‰), the primary biomass composition was best approximated by bulk measurements. In highly metamorphosed rocks, kerogen extracts may provide a more reliable record. When possible, the most interesting strategy remains to measure and compare both the $\delta^{15}\text{N}$ of kerogen extracts and bulk rocks.

To conclude, nitrogen isotope measurements in Precambrian sediments are usually used to determine if the depositional environment was oxic, and the effects of water column diagenesis in oxic conditions, sedimentary diagenesis, and metamorphism, all enrich sedimentary organic matter in ^{15}N like oxidative processes of the N-biogeochemical cycle do. This is why, when studying small $\delta^{15}\text{N}$ variations (<5‰) in Precambrian sediments, it is essential to estimate their contribution. This pitfall also makes quantitative interpretations of positive values from sedimentary rocks impossible: for instance, positive $\delta^{15}\text{N}$ values can be used to infer the stability of nitrate in a paleoenvironment but not to constrain the size of its reservoir through uptake estimations.

2.2. Nitrogen sources to the Archean Earth's surficial reservoirs and their isotope composition

2.2.1. Stability of the nitrogen atmospheric isotope composition through time

Reconstructing the Precambrian N biogeochemical cycle and directly interpreting sedimentary $\delta^{15}\text{N}$ values in terms of paleo biological pathways requires the nitrogen isotope composition of the atmosphere, i.e. the main N reservoir on Earth, to have remained stable since the beginning of the Archean Eon. $\delta^{15}\text{N}_{\text{N}_2}$ measurements of nitrogen trapped in 3.5 to 3.0 Ga fluid inclusions (Marty et al., 2013; Nishizawa et al., 2007) suggest that the $\delta^{15}\text{N}_{\text{N}_2}$ of the Archean atmosphere has remained similar to that of the present-day atmosphere ($\delta^{15}\text{N}_{\text{N}_2}=0\text{‰}$).

A nitrogen contribution from meteoritical impact to the early Earth's atmosphere might have occurred during the Precambrian. A ^{15}N -enriched atmospheric source derived from chondritic material with a $\delta^{15}\text{N}$ between +30 and +42‰ has been proposed to explain some unusually high Neoproterozoic $\delta^{15}\text{N}$ values (Jia and Kerrich, 2004; Kerrich et al., 2006). While it cannot be completely ruled out, it seems unlikely given that meteoritical impact to the Earth's atmosphere and ocean should be observed well before the Neoproterozoic, and should show a decrease with time. Besides, no other Precambrian dataset displays $\delta^{15}\text{N}$ values higher than +30‰.

2.2.2. Organic hazes and aerosols production on the prebiotic Earth

Nitrogen-bearing organic molecules produced in organic hazes such as in Titan's atmosphere are sometimes mentioned as an abiotic alternative to organic matter production during the Archean (Izon et al., 2015; Trainer et al., 2006). However, organic molecules (tholins) generated through experimental aerosols production setups in plasma or photochemical flow reactors are depleted in ^{15}N (by a factor ranging from 0.8‰ to -25.5‰) compared to the initial N_2 gas from which they precipitated (Kuga et al., 2014; Sebree et al., 2016). Given that the $\delta^{15}\text{N}_{\text{N}_2}$ of the Archean atmosphere has remained similar to that of the present-day atmosphere ($\delta^{15}\text{N}_{\text{N}_2}=0\text{‰}$), the range of $\delta^{15}\text{N}$ values observed throughout the Precambrian is inconsistent with a significant contribution of ^{15}N -depleted abiotic organic matter. Given the suggested rapid oscillations between hazy and haze-free states, for example during the Neoproterozoic (Izon et al., 2015; Thomazo et al., 2009; Zerkle et al., 2012), one way to spot nitrogen-bearing organic molecules

produced in organic hazes might be to look for an instability of TN contents along a sedimentary section where other parameters such as lithology are comparable.

Nevertheless, some isotopically light $\delta^{15}\text{N}$ values observed in the 3.7 Ga Isua Supracrustal Belt and falling outside the typical range of fractionation for N_2 fixation, even more so for metasedimentary rocks, have been interpreted as resulting from lightning and/or high energy photochemical reactions in the early atmosphere (Stüeken et al., 2021a).

2.2.3. Hydrothermalism

While hydrothermal activity may have been widespread on Archean oceans seafloor, and hydrothermal processes have likely influenced the availability of nutrients like dissolved iron (Kump and Seyfried, 2005; Poulton and Canfield, 2011), it seems unlikely that hydrothermalism either made a strong contribution of abiotic organic molecules during the Precambrian or that it significantly shifted its sedimentary $\delta^{15}\text{N}$ signal. Indeed, the contribution of mantle N to hydrothermal systems seems low compared to hydrothermal remobilization of previously sedimented nitrogen (Lilley et al., 1993; Stüeken et al., 2021b, 2021c). Typical mantle $\delta^{15}\text{N}$ values around -5‰ (Cartigny and Marty, 2013) are rare to absent in the Precambrian sedimentary record, with the lowest $\delta^{15}\text{N}$ values consistent with the range of fractionation displayed by Mo-based biological fixation of N_2 by diazotrophs (Nishizawa et al., 2014; Raymond et al., 2004; Zhang et al., 2014). As recent work on the modern Mid-Atlantic Ridge has shown the abiotic formation of amino acids through Friedel-Crafts reactions during the alteration of serpentinites (Ménez et al., 2018), one key undertaking for future studies will be to determine if nitrogen isotopes are fractionated during hydrothermal recycling processes, and measuring potential fractionations and fluxes.

2.2.4. Biological and alternative fixed nitrogen sources

Biological N_2 fixation by diazotrophs (Chapter 1) is the major source of fixed nitrogen to the biosphere in modern environments (e.g. Ward, 2012), exceeding by far all abiotic nitrogen sources (reviewed in Stüeken et al., 2016). Modern biological N_2 fixation rates average 10^{13} moles of N per year (Canfield et al., 2010), but Precambrian rates are unknown and could have been much smaller if the biosphere was less developed. Meanwhile, maximum estimates for all sources of abiotically fixed nitrogen in the Precambrian (reviewed in Stüeken et al., 2016), if

combined, reach similar rates, around 10^{13} moles of N per year. This total includes the contribution, in moles of N per year, from impact delivery (max. $1 \cdot 10^5$, Smirnov et al., 2008), interplanetary dust (avg. $7.1 \cdot 10^8$, Chyba and Sagan, 1992), post-impact plume (avg. $1.6 \cdot 10^{12}$, Kasting, 1990), hydrothermal reduction (max. $1.1 \cdot 10^{12}$, Brandes et al., 1998; Schoonen and Xu, 2001; Smirnov et al., 2008), photochemical reduction (max. $4.9 \cdot 10^{12}$, Henderson-Sellers and Schwartz, 1980), UV photolysis (max. $2.7 \cdot 10^{12}$, Tian et al., 2011), lightning (max. $6.7 \cdot 10^{10}$, Kasting and Walker, 1981; Navarro-González et al., 2001; Navarro-González et al., 1998), and volcanic eruptions and coronal discharge (max. $1 \cdot 10^{11}$, Mather et al., 2004; Nna-Mvondo et al., 2005). Therefore, while no single abiotic source of fixed nitrogen equals the rates of N_2 fixation, the contribution of several of these sources might be important when taken together. The isotopic signature of these sources remains to be assessed.

2.3. The evolution of biological and abiotic pathways of the early nitrogen cycle

2.3.1. Biological N_2 fixation and the evolution of nitrogenase enzymes

Phylogenetic studies of nitrogenase structural gene products can provide insights as to the evolution of biological N_2 fixation. Two competing hypotheses, based on phylogenetic analyses of nitrogenase sequences, have been put forward: some authors argue that nitrogenase was present in the Last Universal Common Ancestor (LUCA) (Leigh, 2000; Raymond et al., 2004) while others suggest that it may have derived from the ancestral methanogens (Boyd and Peters, 2013; Boyd et al., 2015). In any case, the ancestry of the nitrogenase enzyme stands out, dating it back at least to the Paleoproterozoic.

Geochemical data indicate that biological N_2 fixation must have been an important source of fixed nitrogen in the Paleoproterozoic, dating back to at least 3.2 Ga (Stüeken et al., 2015) and maybe even back to 3.4 Ga (Pellerin et al., 2023). Recent gene and species tree studies results also indicate that biological Mo-based N_2 fixation arose between 3.1 and 2.7 Ga, supporting geochemical data (Parsons et al., 2021).

While fractionations imparted by biological N_2 fixation with canonical Mo-based nitrogenase are centered around -1‰ (Bauersachs et al., 2009; Sigman et al., 2009) alternative nitrogenases using Fe or V as cofactors produce fixed nitrogen with significantly lower $\delta^{15}N$ values, on average -6 to -7‰, down to -8‰ (Zhang et al., 2014). In rocks dated between 3.8 and 3.5 Ga,

negative $\delta^{15}\text{N}$ values down to -4.5‰ have been interpreted to reflect biological N_2 fixation using these alternative V or Fe nitrogenases (Zhang et al., 2014). It suggests a coupling between the cycling of some trace elements and nitrogen, and questions whether in the Archean, where the availability of Fe should have exceeded that of Mo (e.g. Wang, 2012), biological N_2 fixation was dominated by the Fe-Fe nitrogenase. Phylogenetic and structural studies of some nitrogenase proteins suggest that the Mo-nitrogenase emerged within the methanogenic archaea, predating the appearance of Fe-Fe and Fe-V nitrogenases (Boyd et al., 2011a, 2011b; Garcia et al., 2020). Thus, those two alternative forms could have emerged in response to Mo limitation. Hence, in the ferruginous Archean oceans, Mo shortage may have triggered the evolution of the Fe-Fe nitrogenase (Zhang et al., 2014).

As mentioned in Chapter 1, the type of diazotrophic communities can also impact the fractionation imparted during biological N_2 fixation. Nishizawa et al. (2014) found that hyperthermophilic methanogens, who are likely to have been the dominant primary producers in Archean hydrothermal environments, produced more ^{15}N -depleted biomass (-4‰ relative to N_2) than what was previously reported for photosynthetic prokaryotes (Fig. 2.3).

As diazotrophy exerts a primary control on the oceanic fixed N supply and as the nitrogenase enzyme is O_2 -sensitive (Chapter 1), it has been argued that the rise of oxygen levels before the GOE could have temporarily disrupted N_2 fixation, causing a fixed N crisis in the surface ocean (Olson et al., 2016). This nutrient limitation could in turn have hindered primary productivity, potentially delaying oxygenation through a negative feedback mechanism (Olson et al., 2016).

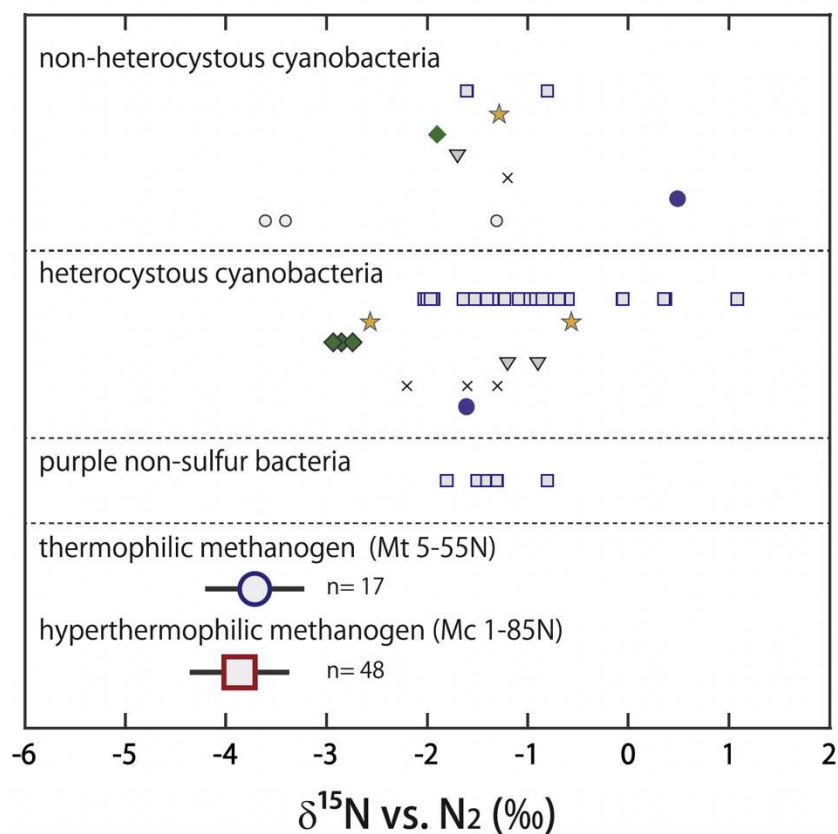


Fig. 2.3. Nitrogen isotope ratios of cellular nitrogen compounds of diazotrophs relative to the substrate N_2 (Nishizawa et al., 2014 and all references therein) for non-heterocystous and heterocystous cyanobacteria, purple non-sulfur bacteria, thermophilic and hyperthermophilic methanogens. Shapes indicate different species, detailed in Nishizawa et al. (2014).

2.3.2. The emergence of oxidative pathways of the N cycle: nitrogen as a proxy of paleoredox conditions

For nitrogen isotopes to be used as a proxy of paleoredox conditions, a set of conditions needs to be met (Fig. 2.1). Besides reliable N isotope measurements (Chapter 5), the nitrogen isotope composition of the studied sample must reflect that of the sediment at its time of deposition, meaning that the impact of post-depositional processes, namely diagenesis and metamorphism, must either be negligible or measurable (2.1.2 and 2.1.3). Then, the nitrogen isotope composition of primary producers must reflect that of the N sources consumed by phytoplanktonic organisms (2.1.1 and 2.2), and the isotope effect of N assimilation pathways must be conserved. Most importantly, the isotope composition of the extant N species must reflect the speciation of N in the ocean and the preponderance of key metabolic pathways of the N-biogeochemical cycle. Besides, the fractionation factor associated with these N

transformation pathways must have remained similar to today following the principle, and assuming the limit, of actualism.

Three main conceptual scenarios can summarize how changes in the redox state of the water column, from fully anoxic to redox stratified to oxygenated, can affect key biogeochemical reactions and fluxes of the nitrogen cycle and thus sedimentary $\delta^{15}\text{N}$ values (Fig. 2.4, Ader et al., 2016; Stüeken et al., 2016). It is obvious that intermediate or mixed states between those scenarios must have occurred in space and time across Earth history.

2.3.2.1. Dominantly oxic oceans

In a fully oxygenated ocean, similar to modern oceans (Fig. 2.4A) and probably through most of the Phanerozoic, anoxia is restricted to oxygen-deficient zones (ODZs), oxygen minimum zones (OMZs) and sediments below the sediment-water interface (Lam and Kuypers, 2011; Paulmier and Ruiz-Pino, 2009; Ulloa et al., 2012). NO_3^- losses are limited, occurring only in those oxygen-poor zones, resulting in low rates of partial denitrification in OMZs and complete denitrification in sediments. This generates small ^{15}N -enrichments in the biomass, that are reflected in a sedimentary $\delta^{15}\text{N}$ mode around 5-6‰ (Fig. 2.4A) (Tesdal et al., 2013). If the oceans had been more oxygenated than today, through the shrinking or disappearance of OMZs, NO_3^- losses would have been minimal to null and the $\delta^{15}\text{N}$ of sediments would fall around 0‰ (Algeo et al., 2014). Conversely, in a slightly more reduced oxic ocean compared to modern days (Fig. 2.4B), NO_3^- is quantitatively lost in the core of the euxinic OMZ, non-quantitative denitrification occurring on the edges. This results in slightly lower $\delta^{15}\text{N}_{\text{NO}_3}$ and hence, lower sedimentary $\delta^{15}\text{N}$ (Fig. 2.4B) (Quan and Falkowski, 2009).

2.3.2.2. Redox-stratified oceans

In redox-stratified oceans, a chemocline chemically separates oxic surface waters from anoxic deep waters. This scenario is thought to have prevailed during the time interval between the Great Oxidation Event (GOE) around 2.4 Ga or a few hundred million years before (e.g. Cheng et al., 2019; Ossa Ossa et al., 2022; Planavsky et al., 2014; Zerkle et al., 2017), marking the onset of surface ocean and atmospheric oxygenation, and the Neoproterozoic Oxidation Event (NOE), marking the oxygenation of the deep ocean (e.g. Ader et al., 2014; Kipp et al., 2018; Koehler et al., 2017; Sánchez-Baracaldo et al., 2014). This redox structure is also thought to be

representative of Phanerozoic Oceanic Anoxic Events (OAEs, Jenkyns, 2010) and of restricted oceanic basins (i.e. the Cariaco Basin, Thunell et al., 2004).

Redox stratification separates the two main fixed N species: in oxic waters above the chemocline, ammonium generated through remineralization can be nitrified to nitrate, which is the dominant fixed N species, whereas in anoxic waters below the chemocline, ammonium will be the dominant fixed N species. Nitrate diffusing downwards from oxygenated waters above the chemocline and ammonium diffusing upwards from anoxic waters below the chemocline will both be consumed within this redox-transition zone (Fig. 2.4C) and converted to N_2 or N_2O through coupled nitrification and denitrification or anammox, creating a fixed N deficit (Meckler et al., 2007; Thunell et al., 2004; Wenk et al., 2014). As long as physical stratification is maintained (Fig. 2.4C), this deficit of bioavailable nitrogen will only be compensated by N_2 fixation, if the supply of other nutrients is sufficient, driving sedimentary $\delta^{15}N$ values toward 0‰ (Fig. 2.4C) (Quan and Falkowski, 2009).

The dynamics of the N cycle in redox-stratified oceans is inferred from the study of modern analogs with stratified water masses such as the Black Sea (e.g. Fry et al., 1991; Fuchsman et al., 2008; Konovalov et al., 2008) or stratified lakes (e.g. Cadeau et al., 2021; Hadas et al., 2009). The main limitation of such analogs is that these semi-closed or closed systems are both physically stratified in addition to being redox-stratified (Fig. 2.4C), preventing water exchanges across the chemocline, whereas in Precambrian oceans the redox stratification would have been maintained in the absence of physical stratification, that is to say in the presence of upwelling and downwelling currents. Such convection movements would have allowed upwelling of ammonium from anoxic deep waters to the photic zone, where it would have been re-assimilated and/or oxidized to N_2 , N_2O or NO_3^- (Fig. 2.4D). If ^{15}N -enriched by partial oxidation, this ammonium ^{15}N -enriched signature would have been transferred to the primary producers and hence to the sediment, leading to positive sedimentary $\delta^{15}N$ values (Fig. 2.4D), contrary to physically stratified systems (Fig. 2.4C). The depth of the redox transition zone can induce regional variation of the isotope signature of the sediments. A convecting redox-stratified ocean with a deep chemocline (Fig. 2.4D) would increase the likelihood of ammonium oxidation to nitrate and subsequent ^{15}N -enrichment through denitrification (Fig. 2.4D) in addition to simply being assimilated by phytoplankton (Fig. 2.4E). This scenario has been proposed as an explanation for positive sedimentary $\delta^{15}N$ values recorded in several Paleoproterozoic basins (Godfrey et al., 2013; Papineau et al., 2009). In contrast, in a convecting redox-stratified ocean with a chemocline rising high into the photic zone (Fig. 2.4E),

only the fractionation associated with ammonium assimilation, if non-quantitative, would be recorded (Kump et al., 2005). Thus, the depth of the chemocline, as well as its dynamics (diffusion versus convection) impacts processes of the N-biogeochemical cycle and associated sedimentary $\delta^{15}\text{N}$ values (Fig. 2.4D, 2.4E).

In summary, redox stratified oceanic systems with upwelling zones can produce a large range of sedimentary $\delta^{15}\text{N}$ values. Therefore, it is interesting, when possible, to compare shallow margin to deep water sediments within the same basin.

2.3.2.3. Fully anoxic oceans

Before the spread of oxygenic photosynthesis, and throughout most of the Archean, where the low levels of O_2 produced by photosynthetic organisms were rapidly and quantitatively consumed, the oceans must have been essentially devoid of O_2 (Lyons et al., 2014). In these fully anoxic waters, bioavailable N sourced by N_2 fixation in the photic zone and subsequently ammonified during organic matter degradation, essentially in the form of ammonium, would have generated sedimentary $\delta^{15}\text{N}$ values around 0‰ (Fig. 2.4F). In upwelling regions, variable $\delta^{15}\text{N}$ values could have been produced during partial ammonium assimilation (Fig. 2.4F; Papineau et al., 2009; Yang et al., 2019). Sediments would then record both the upwelled ^{15}N -depleted organic matter fraction and the ^{15}N -enriched remaining fraction, with a $\delta^{15}\text{N}$ mode around 0‰.

Although most known metabolic pathways oxidizing ammonium directly or indirectly need O_2 , no ammonium oxidation processes should occur in fully anoxic oceans. However, it is possible that in the presence of iron oxides, Feammox (iron-driven ammonium oxidation to N_2) could have modified the $\delta^{15}\text{N}_{\text{NH}_4}$ and the resulting $\delta^{15}\text{N}$ signature of sediments (Pellerin et al., 2023; Stüeken et al., 2016).

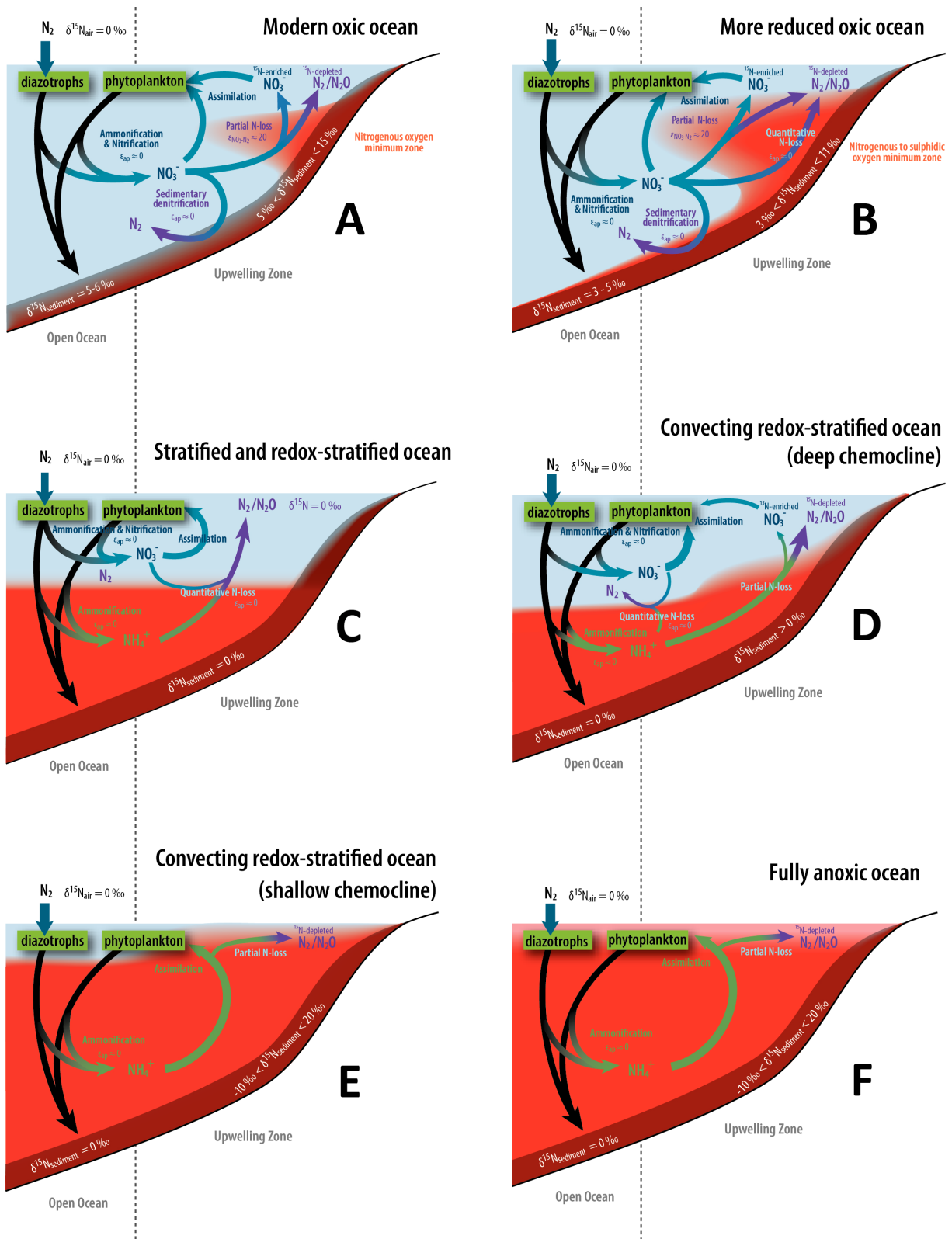


Fig. 2.4. Simplified representation of the N biogeochemical cycle for different ocean redox structures that might have occurred throughout the Precambrian, and their expected N signature in marine

sediments (Ader et al., 2016). (A) Modern oxic ocean. (B) More reduced oxic ocean. (C) Physically stratified and redox-stratified ocean. (D) Convecting redox-stratified ocean with a deep chemocline. (E) Convecting redox-stratified ocean with a shallow chemocline. (F) Fully anoxic ocean.

2.3.3. Ammonia degassing, an abiotic process that could have impacted the Archean N cycle and associated isotopic signature of sedimentary archive

Isotope fractionations of the marine N-biogeochemical cycle have probably been largely dominated by oxidative pathways starting between after 2.7 and 2.5 Ga, in particular denitrification (2.3.2. this chapter; Chapter 3) (Ader et al., 2016; Garvin et al., 2009; Godfrey and Falkowski, 2009; Kipp et al., 2018; Koehler et al., 2018; Stüeken et al., 2016; Thomazo et al., 2011; Zerkle et al., 2017). Nevertheless, an abiotic process that might have been prevalent in Archean environments and impacted the nitrogen isotope composition of Archean sedimentary rocks is ammonia degassing under alkaline conditions (Fig. 2.5). At $\text{pH} > 9.2$ (pK_a of $\text{NH}_3/\text{NH}_4^+$ in standard conditions, Fig. 2.5A), dissolved ammonium (NH_4^+) dissociates to dissolved ammonia (NH_3), with a large isotopic fractionation of 45‰ at 23°C (Li et al., 2012, this fractionation increasing with decreasing temperature), strongly enriching residual ammonium in ^{15}N (solid black line in Fig. 2.5B). Isotope fractionation higher than 20‰ have never been recorded in modern highly alkaline environments (Cadeau et al., 2021; Hadas et al., 2009; Talbot and Johannessen, 1992). However, as surface waters are systematically oxygenated, it is more difficult to degas ammonia and therefore these systems are not necessarily representative of ancient environments under an anoxic atmosphere. Variations in the intensity of distillation processes could possibly have increased this fractionation and produced sedimentary $\delta^{15}\text{N}$ values above 20‰ (Fig. 2.4). This process alone, if active, could explain positive and extremely positive $\delta^{15}\text{N}$ values of the lacustrine Precambrian sedimentary record (Stüeken et al., 2015, 2017; Thomazo et al., 2011), and potentially also the marine one (Garvin et al., 2009; Godfrey and Falkowski, 2009; Kipp et al., 2018; Koehler et al., 2018; Zerkle et al., 2017). Since its isotope fractionation also superimposes onto those of oxidative processes, such as denitrification or anammox, it is difficult to determine the relative contribution of abiotic vs. biotic oxidative processes of the N-biogeochemical cycle. One way to pinpoint ammonia degassing in past environments might be the occurrence of high TOC/TN ratios resulting from the loss of N from the system: this has been observed in the late Archean lacustrine Tumbiana Formation in Australia (Stüeken et al., 2015). However, measured N quantities in ancient sedimentary rocks have to be carefully considered, as they can be

differently impacted by post-depositional processes. Careful petrological and geochemical studies are therefore needed to determine whether the studied sediments have been deposited in highly alkaline settings (for example by looking for gypsum pseudomorphs), and how they have been impacted by diagenesis and metamorphism.

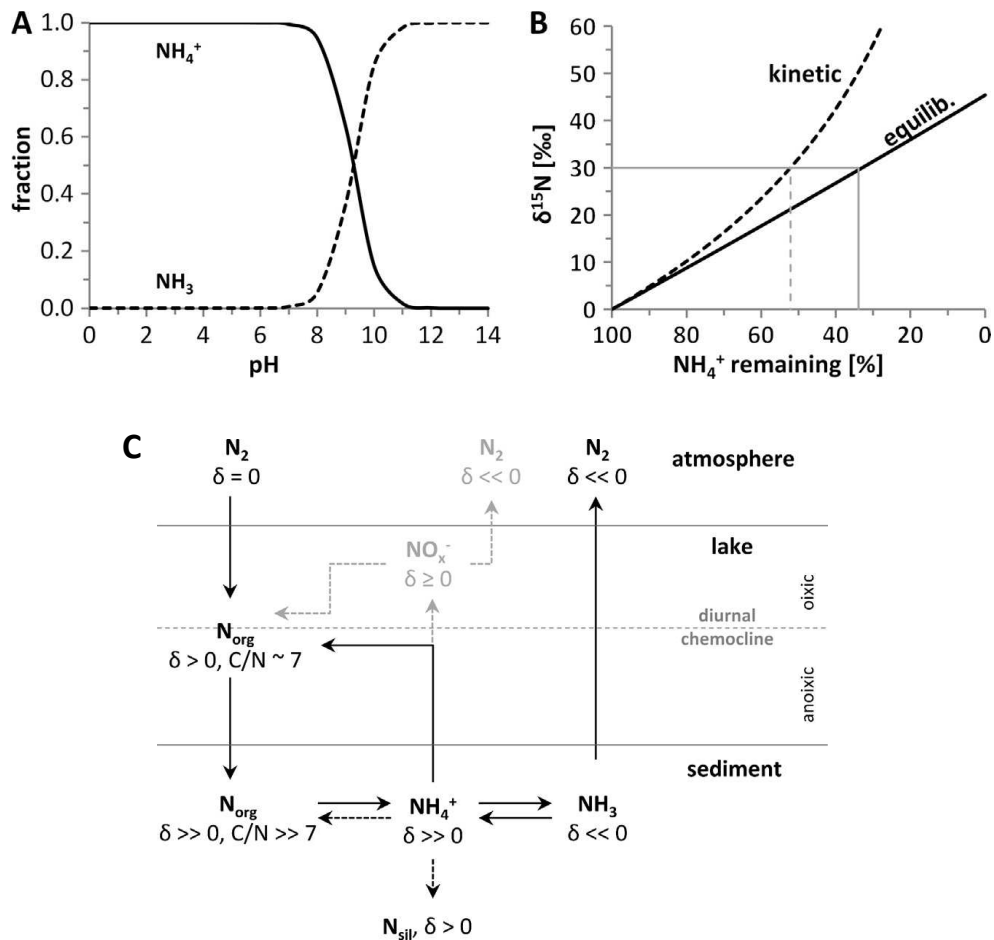


Fig. 2.5. pH effects on nitrogen isotopes (Stüeken et al., 2015). (A) Relative proportion of ammonium (NH_4^+) and ammonia (NH_3) as a function of pH at 25°C. (B) Isotope composition of the remaining NH_4^+ in solution as it is progressively converted to volatile NH_3 . (C) Hypothetical pH-dependent reactions of the early nitrogen cycle. Major fluxes are represented by solid black arrows, minor fluxes by dashed black arrows, possible minor pathways by grey dashed arrows. δ stands for $\delta^{15}\text{N}$ in permil (‰).

If ammonia degassing was an important mechanism operating on the Archean Earth, one consequence that might be relevant to consider is nutrient limitation. Indeed, by rerouting a significant portion of a major nutrient for the biosphere, ammonium, outside of the oceanic or lacustrine system, ammonia degassing might have hindered the productivity of the ecosystem. If this mechanism was prevalent on larger scales, as it might be the case in the scenario of an

early alkaline “soda ocean” (Kempe and Degens, 1985; Kempe and Kazmierczak, 2002), then it might even have impacted the evolution of the whole biosphere.

2.4. The size of the dissolved nitrogen reservoir: insights into nutrient availability during the Archean

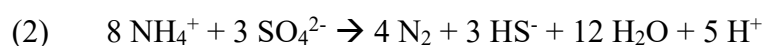
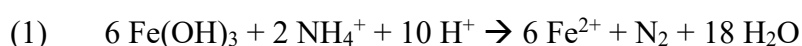
Before the emergence of biological N₂ fixation in the Paleoproterozoic (2.3.1) (Raymond et al., 2004; Stüeken et al., 2015), bioavailable nitrogen should have been restricted to abiotic inputs (2.2), in turn limiting the size of biomass in the oceans and the evolution of this biomass in terms of metabolic diversity. After the emergence of biological N₂ fixation, it is the availability of metal cofactors for the nitrogenase enzyme, in particular Fe and Mo, that could have limited the size of the fixed N reservoir. Studies show that some dissolved Mo was available in seawater during the Paleoproterozoic (McManus et al., 2002; Planavsky et al., 2014), but in concentrations 10 to 100 times lower than in the modern ocean (Anbar, 2008; Reinhard et al., 2013; Scott et al., 2008). Such low Mo concentrations could have hindered and even temporarily suppressed biological N₂ fixation (Zerkle et al., 2006). However, such limitations were likely heterogeneous in space and time, given evidence for N₂ fixation from 3.2 Ga onwards (Stüeken et al., 2015). Alongside metal cofactor limitation, other limiting nutrients, in particular phosphorus, might have put a limit to biomass production (Guilbaud et al., 2020; Hao et al., 2020; Kipp and Stüeken, 2017; Reinhard et al., 2017). Moreover, as nitrogen fixation is an energetically costly metabolism (Hoffman et al., 2014), if the photic zone had been ammonium-rich, diazotrophs would have preferentially consumed ammonium, returning to N₂ fixation only when ammonium levels had become scarce enough.

In the modern ocean, where oligotrophic surface waters show high rates of N₂ fixation, ammonium concentrations remain low, as it is rapidly uptaken, nitrified to nitrite and nitrate or oxidized through alternative oxidation mechanisms (Sigman et al., 2009). It is possible that before the GOE, the absence of available oxidant in the water column made ammonium more readily available for assimilation. Without a significant biomass under the photic zone in anoxic Archean oceans, ammonium would not have been quantitatively consumed, hence ammonium levels may have been more significant than in the Phanerozoic (Beaumont and Robert, 1999; Falkowski and Godfrey, 2008). However, if ammonification occurred in the sediment, ammonium is likely to have been trapped in clay minerals, lowering dissolved concentrations in the water column. Therefore, it is difficult to establish the extent to which TN contents in

Archean sedimentary rocks reflect different ammonium concentrations in the early oceans or different ammonium preservation in sediments. The study of secular variations in TOC/TN ratios might prove relevant to unveil this issue, but only when comparing samples of similar lithology that underwent comparable post-depositional processes, which is so far impossible given the sparse and heterogenous Precambrian $\delta^{15}\text{N}$ record.

An isotopic argument against the presence of a larger ammonium reservoir during the Precambrian is the absence of the large isotopic fractionations generated by partial ammonium assimilation. Except for the $\delta^{15}\text{N}$ excursions measured in the 2.7 Ga Tumbiana Formation in Australia (Stüeken et al., 2015; Thomazo et al., 2011) and the 1.9 Ga Aravalli Supergroup in India (Papineau et al., 2009, 2013), no extremely high $\delta^{15}\text{N}$ values that would record non-quantitative ammonium assimilation resulting from the upwelling of a large ^{15}N -enriched NH_4^+ reservoir were evidenced during the Precambrian. Likewise, a single set of negative $\delta^{15}\text{N}$ values, from the Manjeri Formation in Zimbabwe (Yang et al., 2019) has been interpreted as reflecting the uptake of the partially assimilated complementary ^{15}N -depleted reservoir.

An element that could have impacted the size of the dissolved ammonium reservoir before the GOE and the generalization of free oxygen in the water column is the occurrence of minor ammonium oxidation pathways of the N cycle, that may have been enhanced in the conditions of the Archean ocean. Namely, NH_4^+ oxidation to N_2 in the presence of iron oxides, termed Feammox (1) (Sawayama, 2006) has been shown to be thermodynamically feasible for ranges of Paleoarchean ammonium and iron contents and pH (Fig. 2.6B) (Stüeken et al., 2016). We suggest that this pathway can account for some positive $\delta^{15}\text{N}$ values in the anoxic and ferruginous Paleoarchean environment (see Chapter 6; Pellerin et al., 2023). Similarly, sulfate-driven ammonium oxidation to N_2 , termed Sulfammox (2), has been shown to be thermodynamically feasible for Neoproterozoic ammonium and sulfate concentrations, and pH conditions (Fig. 2.6A) (Stüeken et al., 2012, 2016). Such conditions might have been met close to the chemocline in Neoproterozoic water columns or in ecosystems dominated by sulfate reduction with widespread euxinia during the Proterozoic (Kendall et al., 2011; Poulton et al., 2004; Reinhard et al., 2009).



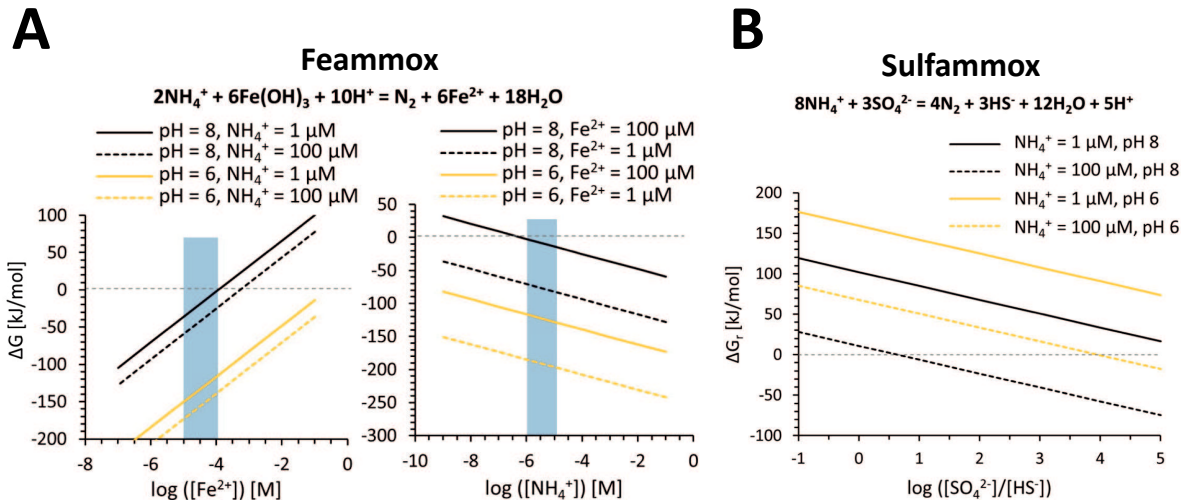


Fig. 2.6. (A) Thermodynamic feasibility of Feammox, iron-driven ammonium oxidation to N_2 (Stüeken et al., 2016). (B) Thermodynamic feasibility of Sulfammox, sulfate-driven ammonium oxidation to N_2 (Stüeken et al., 2016). The free energy of the reactions (ΔG) is a function of NH_4^+ concentrations, Fe^{2+} concentrations, and pH for Feammox (A) and a function of NH_4^+ concentrations, pH, and the ratio of SO_4^{2-} to HS^- for Sulfammox (B). Blue bars indicate the range of total N (ammonium or nitrate) levels in the modern ocean. Reactions are thermodynamically feasible if $\Delta G < 0$.

2.5. Conclusion: strengths and limits of using the $\delta^{15}\text{N}$ proxy in deep time

The nitrogen stable isotope composition recorded in sedimentary rocks ($\delta^{15}\text{N}_{\text{sed}}$) has become a standard tool for reconstructing changes in the N-biogeochemical cycle throughout Earth's history (Algeo et al., 2014), including during the Precambrian (reviewed in Ader et al., 2016; Stüeken et al., 2016). For Precambrian environment studies, $\delta^{15}\text{N}_{\text{sed}}$ measurements hold the potential to provide some insight into biological and abiotic pathways governing early environments, early life and its associated metabolisms, paleoproductivity and nutrient availability, and maybe most importantly, paleoredox conditions and ocean oxygenation.

Yet, a number of uncertainties remain regarding the applicability of this proxy (reviewed in Ader et al., 2022). First, the preservation of the nitrogen isotope signature through post-depositional processes can be variable and more studies of the effects of diagenesis,

metamorphism and fluid circulations on different N phases and lithologies need to be conducted.

Then, biological N₂ fixation is often assumed to be the sole nitrogen source from the Paleoproterozoic onwards. While it may be the major pathway supplying fixed nitrogen to the N-biogeochemical cycle, the contribution of alternative abiotic nitrogen sources is often overlooked in Precambrian studies, mostly because the isotope compositions of these sources are unknown or weakly constrained.

Another major limit resides in the overlapping of isotope fractionations associated with some of the major nitrogen cycle pathways. This prevents a given N isotope fractionation to be directly associated with a particular redox state, i.e. with the presence or absence of oxygen in the studied depositional environment. This overlapping may also prevent the determination of nitrogen speciation as ammonium or nitrate. Complementary redox indicators such as iron, sulfur, molybdenum, or selenium provide a way to alleviate this issue.

Finally, nitrogen isotope interpretations in sedimentary rocks rely almost exclusively on analogies with the modern marine nitrogen cycle, and assume an actualistic biomass. If the structure of Precambrian depositional environments were more similar to lakes and restricted basins than modern open oceans, current interpretations may not hold. Therefore, studying the dynamics of the N-biogeochemical cycle in a variety of modern systems such as stratified lakes (e.g. Cadeau et al., 2021), lagoons with strong salinity gradients (e.g. Priestley et al., 2022) or restricted basins (e.g. Konovalov et al., 2008) is essential to refine our interpretation of sedimentary $\delta^{15}\text{N}$ signals in deep time.

References

- Ader, M., Boudou, J.-P., Javoy, M., Goffe, B., Daniels, E., 1998. Isotope study on organic nitrogen of Westphalian anthracites from the Western Middle field of Pennsylvania (U.S.A.) and from the Bramsche Massif (Germany). *Organic Geochemistry, Advances in Organic Geochemistry 1997 Proceedings of the 18th International Meeting on Organic Geochemistry Part I. Petroleum Geochemistry* 29, 315–323. [https://doi.org/10.1016/S0146-6380\(98\)00072-2](https://doi.org/10.1016/S0146-6380(98)00072-2)
- Ader, M., Cartigny, P., Boudou, J.-P., Oh, J.-H., Petit, E., Javoy, M., 2006. Nitrogen isotopic evolution of carbonaceous matter during metamorphism: Methodology and preliminary results. *Chemical Geology* 232, 152–169. <https://doi.org/10.1016/j.chemgeo.2006.02.019>
- Ader, M., Sansjofre, P., Halverson, G.P., Busigny, V., Trindade, R.I.F., Kunzmann, M., Nogueira, A.C.R., 2014. Ocean redox structure across the Late Neoproterozoic Oxygenation Event: A nitrogen isotope perspective. *Earth and Planetary Science Letters* 396, 1–13. <https://doi.org/10.1016/j.epsl.2014.03.042>
- Ader, M., Stüeken, E., Sansjofre, P., Algeo, T.J., Xie, S., 2022. Editorial: Refining the Interpretation of Nitrogen Isotopes in Deep Time Systems. *Frontiers in Earth Science* 10.
- Ader, M., Thomazo, C., Sansjofre, P., Busigny, V., Papineau, D., Laffont, R., Cartigny, P., Halverson, G.P., 2016. Interpretation of the nitrogen isotopic composition of Precambrian sedimentary rocks: Assumptions and perspectives. *Chemical Geology* 429, 93–110. <https://doi.org/10.1016/j.chemgeo.2016.02.010>
- Algeo, T.J., Meyers, P.A., Robinson, R.S., Rowe, H., Jiang, G.Q., 2014. Icehouse–greenhouse variations in marine denitrification. *Biogeosciences* 11, 1273–1295. <https://doi.org/10.5194/bg-11-1273-2014>
- Altabet, M.A., Francois, R., 1994. Sedimentary nitrogen isotopic ratio as a recorder for surface ocean nitrate utilization. *Global Biogeochemical Cycles* 8, 103–116. <https://doi.org/10.1029/93GB03396>
- Altabet, M.A., Pilskaln, C., Thunell, R., Pride, C., Sigman, D., Chavez, F., Francois, R., 1999. The nitrogen isotope biogeochemistry of sinking particles from the margin of the Eastern North Pacific. *Deep Sea Research Part I: Oceanographic Research Papers* 46, 655–679. [https://doi.org/10.1016/S0967-0637\(98\)00084-3](https://doi.org/10.1016/S0967-0637(98)00084-3)
- Anbar, A.D., 2008. Elements and Evolution. *Science* 322, 1481–1483. <https://doi.org/10.1126/science.1163100>
- Bauersachs, T., Kremer, B., Schouten, S., Sinninghe Damsté, J.S., 2009. A biomarker and $\delta^{15}\text{N}$ study of thermally altered Silurian cyanobacterial mats. *Organic Geochemistry* 40, 149–157. <https://doi.org/10.1016/j.orggeochem.2008.11.008>
- Beaumont, V., Robert, F., 1999. Nitrogen isotope ratios of kerogens in Precambrian cherts: a record of the evolution of atmosphere chemistry? *Precambrian Research* 96, 63–82. [https://doi.org/10.1016/S0301-9268\(99\)00005-4](https://doi.org/10.1016/S0301-9268(99)00005-4)
- Bebout, G.E., Cooper, D.C., Bradley, A.D., Sadofsky, S.J., 1999. Nitrogen-isotope record of fluid-rock interactions in the Skiddaw Aureole and granite, English Lake District. *American*

Mineralogist 84, 1495–1505. <https://doi.org/10.2138/am-1999-1002>

Bebout, G.E., Fogel, M.L., 1992. Nitrogen-isotope compositions of metasedimentary rocks in the Catalina Schist, California: Implications for metamorphic devolatilization history. *Geochimica et Cosmochimica Acta* 56, 2839–2849. [https://doi.org/10.1016/0016-7037\(92\)90363-N](https://doi.org/10.1016/0016-7037(92)90363-N)

Boudou, J.-P., Mariotti, A., Oudin, J.-L., 1984. Unexpected enrichment of nitrogen during the diagenetic evolution of sedimentary organic matter. *Fuel* 63, 1508–1510. [https://doi.org/10.1016/0016-2361\(84\)90215-1](https://doi.org/10.1016/0016-2361(84)90215-1)

Boudou, J.-P., Schimmelmann, A., Ader, M., Mastalerz, M., Sebito, M., Gengembre, L., 2008. Organic nitrogen chemistry during low-grade metamorphism. *Geochimica et Cosmochimica Acta* 72, 1199–1221. <https://doi.org/10.1016/j.gca.2007.12.004>

Boyd, E., Peters, J., 2013. New insights into the evolutionary history of biological nitrogen fixation. *Frontiers in Microbiology* 4.

Boyd, E.S., Anbar, A.D., Miller, S., Hamilton, T.L., Lavin, M., Peters, J.W., 2011a. A late methanogen origin for molybdenum-dependent nitrogenase. *Geobiology* 9, 221–232. <https://doi.org/10.1111/j.1472-4669.2011.00278.x>

Boyd, E.S., Costas, A.M.G., Hamilton, T.L., Mus, F., Peters, J.W., 2015. Evolution of Molybdenum Nitrogenase during the Transition from Anaerobic to Aerobic Metabolism. *Journal of Bacteriology* 197, 1690–1699. <https://doi.org/10.1128/JB.02611-14>

Boyd, E.S., Hamilton, T., Peters, J., 2011b. An Alternative Path for the Evolution of Biological Nitrogen Fixation. *Frontiers in Microbiology* 2.

Boyd, S.R., Philippot, P., 1998. Precambrian ammonium biogeochemistry: a study of the Moine metasediments, Scotland. *Chemical Geology* 144, 257–268. [https://doi.org/10.1016/S0009-2541\(97\)00135-6](https://doi.org/10.1016/S0009-2541(97)00135-6)

Brandes, J.A., Boctor, N.Z., Cody, G.D., Cooper, B.A., Hazen, R.M., Yoder, H.S., 1998. Abiotic nitrogen reduction on the early Earth. *Nature* 395, 365–367. <https://doi.org/10.1038/26450>

Brummer, G.J.A., Kloosterhuis, H.T., Helder, W., 2002. Monsoon-driven export fluxes and early diagenesis of particulate nitrogen and its $\delta^{15}\text{N}$ across the Somalia margin. *Geological Society, London, Special Publications* 195, 353–370. <https://doi.org/10.1144/GSL.SP.2002.195.01.19>

Busigny, V., Ader, M., Cartigny, P., 2005. Quantification and isotopic analysis of nitrogen in rocks at the ppm level using sealed tube combustion technique: A prelude to the study of altered oceanic crust. *Chemical Geology* 223, 249–258. <https://doi.org/10.1016/j.chemgeo.2005.08.002>

Busigny, V., Cartigny, P., Philippot, P., Ader, M., Javoy, M., 2003. Massive recycling of nitrogen and other fluid-mobile elements (K, Rb, Cs, H) in a cold slab environment: evidence from HP to UHP oceanic metasediments of the Schistes Lustrés nappe (western Alps, Europe). *Earth and Planetary Science Letters* 215, 27–42. [https://doi.org/10.1016/S0012-821X\(03\)00453-9](https://doi.org/10.1016/S0012-821X(03)00453-9)

Cadeau, P., Ader, M., Jézéquel, D., Chaduteau, C., Sarazin, G., Bernard, C., Leboulanger, C., 2021. Nitrogen Isotope Discrepancy Between Primary Producers and Sediments in an Anoxic and Alkaline Lake. *Frontiers in Earth Science* 9.

Canfield, D.E., Glazer, A.N., Falkowski, P.G., 2010. The Evolution and Future of Earth's Nitrogen Cycle. *Science* 330, 192–196. <https://doi.org/10.1126/science.1186120>

Cartigny, P., Marty, B., 2013. Nitrogen Isotopes and Mantle Geodynamics: The Emergence of Life and the Atmosphere–Crust–Mantle Connection. *Elements* 9, 359–366. <https://doi.org/10.2113/gselements.9.5.359>

Chen, F., Zhang, L., Yang, Y., Zhang, D., 2008. Chemical and isotopic alteration of organic matter during early diagenesis: Evidence from the coastal area off-shore the Pearl River estuary, south China. *Journal of Marine Systems* 74, 372–380. <https://doi.org/10.1016/j.jmarsys.2008.02.004>

Cheng, C., Busigny, V., Ader, M., Thomazo, C., Chaduteau, C., Philippot, P., 2019. Nitrogen isotope evidence for stepwise oxygenation of the ocean during the Great Oxidation Event. *Geochimica et Cosmochimica Acta* 261, 224–247. <https://doi.org/10.1016/j.gca.2019.07.011>

Chyba, C., Sagan, C., 1992. Endogenous production, exogenous delivery and impact-shock synthesis of organic molecules: an inventory for the origins of life. *Nature* 355, 125–132. <https://doi.org/10.1038/355125a0>

Daniels, E.J., Altaner, S.P., 1993. Inorganic nitrogen in anthracite from eastern Pennsylvania, USA. *International Journal of Coal Geology* 22, 21–35. [https://doi.org/10.1016/0166-5162\(93\)90036-A](https://doi.org/10.1016/0166-5162(93)90036-A)

Daniels, E.J., Altaner, S.P., 1990. Clay mineral authigenesis in coal and shale from the anthracite region, Pennsylvania. *American Mineralogist* 75, 825–839.

Emmer, E., Thunell, R.C., 2000. Nitrogen isotope variations in Santa Barbara Basin sediments: Implications for denitrification in the eastern tropical North Pacific during the last 50,000 years. *Paleoceanography* 15, 377–387. <https://doi.org/10.1029/1999PA000417>

Falkowski, P.G., Godfrey, L.V., 2008. Electrons, life and the evolution of Earth's oxygen cycle. *Philosophical Transactions of the Royal Society B: Biological Sciences* 363, 2705–2716. <https://doi.org/10.1098/rstb.2008.0054>

Freudenthal, T., Wagner, T., Wenzhöfer, F., Zabel, M., Wefer, G., 2001. Early diagenesis of organic matter from sediments of the eastern subtropical Atlantic: evidence from stable nitrogen and carbon isotopes. *Geochimica et Cosmochimica Acta* 65, 1795–1808. [https://doi.org/10.1016/S0016-7037\(01\)00554-3](https://doi.org/10.1016/S0016-7037(01)00554-3)

Fry, B., Jannasch, H.W., Molyneaux, S.J., Wirsén, C.O., Muramoto, J.A., King, S., 1991. Stable isotope studies of the carbon, nitrogen and sulfur cycles in the Black Sea and the Cariaco Trench. *Deep Sea Research Part A. Oceanographic Research Papers, Black Sea Oceanography: Results from the 1988 Black Sea Expedition* 38, S1003–S1019. [https://doi.org/10.1016/S0198-0149\(10\)80021-4](https://doi.org/10.1016/S0198-0149(10)80021-4)

Fuchsman, C.A., Murray, J.W., Konovalov, S.K., 2008. Concentration and natural stable isotope profiles of nitrogen species in the Black Sea. *Marine Chemistry, Ocean*

Biogeochemistry: From GEOSECS to JGOFS and beyond - In celebration of the 65th birthday of Peter G. Brewer 111, 90–105. <https://doi.org/10.1016/j.marchem.2008.04.009>

Garcia, A.K., McShea, H., Kolaczowski, B., Kaçar, B., 2020. Reconstructing the evolutionary history of nitrogenases: Evidence for ancestral molybdenum-cofactor utilization. *Geobiology* 18, 394–411. <https://doi.org/10.1111/gbi.12381>

Garvin, J., Buick, R., Anbar, A.D., Arnold, G.L., Kaufman, A.J., 2009. Isotopic Evidence for an Aerobic Nitrogen Cycle in the Latest Archean. *Science* 323, 1045–1048. <https://doi.org/10.1126/science.1165675>

Gaye, B., Wiesner, M.G., Lahajnar, N., 2009. Nitrogen sources in the South China Sea, as discerned from stable nitrogen isotopic ratios in rivers, sinking particles, and sediments. *Marine Chemistry* 114, 72–85. <https://doi.org/10.1016/j.marchem.2009.04.003>

Glasmacher, U.A., Zentilli, M., Ryan, R., 2003. Nitrogen distribution in Lower Palaeozoic slates/phyllites of the Meguma Supergroup, Nova Scotia, Canada: implications for Au and Zn–Pb mineralisation and exploration. *Chemical Geology* 194, 297–329. [https://doi.org/10.1016/S0009-2541\(02\)00322-4](https://doi.org/10.1016/S0009-2541(02)00322-4)

Godfrey, L.V., Falkowski, P.G., 2009. The cycling and redox state of nitrogen in the Archaean ocean. *Nature Geoscience* 2, 725–729. <https://doi.org/10.1038/ngeo633>

Godfrey, L.V., Poulton, S.W., Bebout, G.E., Fralick, P.W., 2013. Stability of the nitrogen cycle during development of sulfidic water in the redox-stratified late Paleoproterozoic Ocean. *Geology* 41, 655–658. <https://doi.org/10.1130/G33930.1>

Guilbaud, R., Poulton, S.W., Thompson, J., Husband, K.F., Zhu, M., Zhou, Y., Shields, G.A., Lenton, T.M., 2020. Phosphorus-limited conditions in the early Neoproterozoic ocean maintained low levels of atmospheric oxygen. *Nat. Geosci.* 13, 296–301. <https://doi.org/10.1038/s41561-020-0548-7>

Hadas, O., Altabet, M.A., Agnihotri, R., 2009. Seasonally varying nitrogen isotope biogeochemistry of particulate organic matter in Lake Kinneret, Israel. *Limnology and Oceanography* 54, 75–85. <https://doi.org/10.4319/lo.2009.54.1.0075>

Haendel, D., Mühle, K., Nitzsche, H.-M., Stiehl, G., Wand, U., 1986. Isotopic variations of the fixed nitrogen in metamorphic rocks. *Geochimica et Cosmochimica Acta* 50, 749–758. [https://doi.org/10.1016/0016-7037\(86\)90351-0](https://doi.org/10.1016/0016-7037(86)90351-0)

Hao, J., Knoll, A.H., Huang, F., Schieber, J., Hazen, R.M., Daniel, I., 2020. Cycling phosphorus on the Archean Earth: Part II. Phosphorus limitation on primary production in Archean ecosystems. *Geochimica et Cosmochimica Acta* 280, 360–377. <https://doi.org/10.1016/j.gca.2020.04.005>

Henderson-Sellers, A., Schwartz, A.W., 1980. Chemical evolution and ammonia in the early Earth's atmosphere. *Nature* 287, 526–528. <https://doi.org/10.1038/287526a0>

Higgins, M.B., Robinson, R.S., Carter, S.J., Pearson, A., 2010. Evidence from chlorin nitrogen isotopes for alternating nutrient regimes in the Eastern Mediterranean Sea. *Earth and Planetary Science Letters* 290, 102–107. <https://doi.org/10.1016/j.epsl.2009.12.009>

- Hoffman, B.M., Lukoyanov, D., Yang, Z.-Y., Dean, D.R., Seefeldt, L.C., 2014. Mechanism of Nitrogen Fixation by Nitrogenase: The Next Stage. *Chem. Rev.* 114, 4041–4062. <https://doi.org/10.1021/cr400641x>
- Holland, H.D., 2006. The oxygenation of the atmosphere and oceans. *Philosophical Transactions of the Royal Society B: Biological Sciences* 361, 903–915. <https://doi.org/10.1098/rstb.2006.1838>
- Izon, G., Zerkle, A.L., Zhelezinskaia, I., Farquhar, J., Newton, R.J., Poulton, S.W., Eigenbrode, J.L., Claire, M.W., 2015. Multiple oscillations in Neoproterozoic atmospheric chemistry. *Earth and Planetary Science Letters* 431, 264–273. <https://doi.org/10.1016/j.epsl.2015.09.018>
- Jenkyns, H.C., 2010. Geochemistry of oceanic anoxic events. *Geochemistry, Geophysics, Geosystems* 11. <https://doi.org/10.1029/2009GC002788>
- Jia, Y., 2006. Nitrogen isotope fractionations during progressive metamorphism: A case study from the Paleozoic Cooma metasedimentary complex, southeastern Australia. *Geochimica et Cosmochimica Acta* 70, 5201–5214. <https://doi.org/10.1016/j.gca.2006.08.004>
- Jia, Y., Kerrich, R., 2004. Nitrogen 15-enriched Precambrian kerogen and hydrothermal systems. *Geochemistry, Geophysics, Geosystems* 5. <https://doi.org/10.1029/2004GC000716>
- Jia, Y., Kerrich, R., 2000. Giant quartz vein systems in accretionary orogenic belts: the evidence for a metamorphic fluid origin from $\delta^{15}\text{N}$ and $\delta^{13}\text{C}$ studies. *Earth and Planetary Science Letters* 184, 211–224. [https://doi.org/10.1016/S0012-821X\(00\)00320-4](https://doi.org/10.1016/S0012-821X(00)00320-4)
- Jia, Y., Kerrich, R., 1999. Nitrogen isotope systematics of mesothermal lode gold deposits: Metamorphic, granitic, meteoric water, or mantle origin? *Geology* 27, 1051–1054. [https://doi.org/10.1130/0091-7613\(1999\)027<1051:NISOML>2.3.CO;2](https://doi.org/10.1130/0091-7613(1999)027<1051:NISOML>2.3.CO;2)
- Juster, T.C., Brown, P.E., Bailey, S.W., 1987. NH_4 -bearing illite in very low grade metamorphic rocks associated with coal, northeastern Pennsylvania. *American Mineralogist* 72, 555–565.
- Kasting, J.F., 1990. Bolide impacts and the oxidation state of carbon in the Earth's early atmosphere. *Origins Life Evol Biosphere* 20, 199–231. <https://doi.org/10.1007/BF01808105>
- Kasting, J.F., Walker, J.C.G., 1981. Limits on oxygen concentration in the prebiological atmosphere and the rate of abiotic fixation of nitrogen. *Journal of Geophysical Research: Oceans* 86, 1147–1158. <https://doi.org/10.1029/JC086iC02p01147>
- Kemp, A.L.W., Mudrochova, A., 1973. The distribution and nature of amino acids and other nitrogen-containing compounds in Lake Ontario surface sediments. *Geochimica et Cosmochimica Acta* 37, 2191–2206. [https://doi.org/10.1016/0016-7037\(73\)90016-1](https://doi.org/10.1016/0016-7037(73)90016-1)
- Kempe, S., Degens, E.T., 1985. An early soda ocean? *Chemical Geology* 53, 95–108. [https://doi.org/10.1016/0009-2541\(85\)90023-3](https://doi.org/10.1016/0009-2541(85)90023-3)
- Kempe, S., Kazmierczak, J., 2002. Biogenesis and Early Life on Earth and Europa: Favored by an Alkaline Ocean? *Astrobiology* 2, 123–130. <https://doi.org/10.1089/153110702753621394>
- Kendall, B., Gordon, G.W., Poulton, S.W., Anbar, A.D., 2011. Molybdenum isotope constraints on the extent of late Paleoproterozoic ocean euxinia. *Earth and Planetary Science Letters* 307,

450–460. <https://doi.org/10.1016/j.epsl.2011.05.019>

Kerrich, R., Jia, Y., Manikyamba, C., Naqvi, S.M., 2006. Secular variations of N-isotopes in terrestrial reservoirs and ore deposits. *Geological Society of America Bulletin* 118, 450–460. [https://doi.org/10.1130/2006.1198\(05\)](https://doi.org/10.1130/2006.1198(05))

Kienast, S.S., Calvert, S.E., Pedersen, T.F., 2002. Nitrogen isotope and productivity variations along the northeast Pacific margin over the last 120 kyr: Surface and subsurface paleoceanography. *Paleoceanography* 17, 7-1-7–17. <https://doi.org/10.1029/2001PA000650>

Kipp, M.A., Stüeken, E.E., 2017. Biomass recycling and Earth's early phosphorus cycle. *Science Advances* 3, eaao4795. <https://doi.org/10.1126/sciadv.aao4795>

Kipp, M.A., Stüeken, E.E., Yun, M., Bekker, A., Buick, R., 2018. Pervasive aerobic nitrogen cycling in the surface ocean across the Paleoproterozoic Era. *Earth and Planetary Science Letters* 500, 117–126. <https://doi.org/10.1016/j.epsl.2018.08.007>

Kitchen, N.E., Valley, J.W., 1995. Carbon isotope thermometry in marbles of the Adirondack Mountains, New York. *Journal of Metamorphic Geology* 13, 577–594. <https://doi.org/10.1111/j.1525-1314.1995.tb00244.x>

Koehler, M.C., Buick, R., Kipp, M.A., Stüeken, E.E., Zaloumis, J., 2018. Transient surface ocean oxygenation recorded in the ~2.66 Ga Jeerinah Formation, Australia. *Proceedings of the National Academy of Sciences* 115, 7711–7716. <https://doi.org/10.1073/pnas.1720820115>

Koehler, M.C., Stüeken, E.E., Kipp, M.A., Buick, R., Knoll, A.H., 2017. Spatial and temporal trends in Precambrian nitrogen cycling: A Mesoproterozoic offshore nitrate minimum. *Geochimica et Cosmochimica Acta* 198, 315–337. <https://doi.org/10.1016/j.gca.2016.10.050>

Kohzu, A., Imai, A., Miyajima, T., Fukushima, T., Matsushige, K., Komatsu, K., Kawasaki, N., Miura, S., Sato, T., 2011. Direct evidence for nitrogen isotope discrimination during sedimentation and early diagenesis in Lake Kasumigaura, Japan. *Organic Geochemistry* 42, 173–183. <https://doi.org/10.1016/j.orggeochem.2010.10.010>

Konovalov, S.K., Fuchsman, C.A., Belokopitov, V., Murray, J.W., 2008. Modeling the distribution of nitrogen species and isotopes in the water column of the Black Sea. *Marine Chemistry, Ocean Biogeochemistry: From GEOSECS to JGOFS and beyond - In celebration of the 65th birthday of Peter G. Brewer* 111, 106–124. <https://doi.org/10.1016/j.marchem.2008.01.006>

Kuga, M., Carrasco, N., Marty, B., Marrocchi, Y., Bernard, S., Rigaudier, T., Fleury, B., Tissandier, L., 2014. Nitrogen isotopic fractionation during abiotic synthesis of organic solid particles. *Earth and Planetary Science Letters* 393, 2–13. <https://doi.org/10.1016/j.epsl.2014.02.037>

Kump, L.R., Junium, C., Arthur, M.A., Brasier, A., Fallick, A., Melezhik, V., Lepland, A., CČrne, A.E., Luo, G., 2011. Isotopic Evidence for Massive Oxidation of Organic Matter Following the Great Oxidation Event. *Science* 334, 1694–1696. <https://doi.org/10.1126/science.1213999>

Kump, L.R., Pavlov, A., Arthur, M.A., 2005. Massive release of hydrogen sulfide to the surface ocean and atmosphere during intervals of oceanic anoxia. *Geology* 33, 397–400.

<https://doi.org/10.1130/G21295.1>

Kump, L.R., Seyfried, W.E., 2005. Hydrothermal Fe fluxes during the Precambrian: Effect of low oceanic sulfate concentrations and low hydrostatic pressure on the composition of black smokers. *Earth and Planetary Science Letters* 235, 654–662. <https://doi.org/10.1016/j.epsl.2005.04.040>

Lam, P., Kuypers, M.M.M., 2011. Microbial Nitrogen Cycling Processes in Oxygen Minimum Zones. *Annual Review of Marine Science* 3.

Lehmann, M.F., Bernasconi, S.M., Barbieri, A., McKenzie, J.A., 2002. Preservation of organic matter and alteration of its carbon and nitrogen isotope composition during simulated and in situ early sedimentary diagenesis. *Geochimica et Cosmochimica Acta* 66, 3573–3584. [https://doi.org/10.1016/S0016-7037\(02\)00968-7](https://doi.org/10.1016/S0016-7037(02)00968-7)

Leigh, J.A., 2000. Nitrogen Fixation in Methanogens: The Archaeal Perspective. *Current Issues in Molecular Biology* 2, 125–131. <https://doi.org/10.21775/cimb.002.125>

Li, L., Lollar, B.S., Li, H., Wortmann, U.G., Lacrampe-Couloume, G., 2012. Ammonium stability and nitrogen isotope fractionations for NH_4^+ - $\text{NH}_3(\text{aq})$ - $\text{NH}_3(\text{gas})$ systems at 20–70°C and pH of 2–13: Applications to habitability and nitrogen cycling in low-temperature hydrothermal systems. *Geochimica et Cosmochimica Acta* 84, 280–296. <https://doi.org/10.1016/j.gca.2012.01.040>

Lilley, M.D., Butterfield, D.A., Olson, E.J., Lupton, J.E., Macko, S.A., McDuff, R.E., 1993. Anomalous CH_4 and NH_4^+ concentrations at an unsedimented mid-ocean-ridge hydrothermal system. *Nature* 364, 45–47. <https://doi.org/10.1038/364045a0>

Lyons, T.W., Reinhard, C.T., Planavsky, N.J., 2014. The rise of oxygen in Earth's early ocean and atmosphere. *Nature* 506, 307–315. <https://doi.org/10.1038/nature13068>

Macko, S.A., Quick, R.S., 1986. A geochemical study of oil migration at source rock reservoir contacts: Stable isotopes. *Organic Geochemistry* 10, 199–205. [https://doi.org/10.1016/0146-6380\(86\)90023-9](https://doi.org/10.1016/0146-6380(86)90023-9)

Mariotti, A., 1983. Atmospheric nitrogen is a reliable standard for natural ^{15}N abundance measurements. *Nature* 303, 685–687. <https://doi.org/10.1038/303685a0>

Marty, B., Zimmermann, L., Pujol, M., Burgess, R., Philippot, P., 2013. Nitrogen Isotopic Composition and Density of the Archean Atmosphere. *Science* 342, 101–104. <https://doi.org/10.1126/science.1240971>

Mather, T.A., Pyle, D.M., Allen, A.G., 2004. Volcanic source for fixed nitrogen in the early Earth's atmosphere. *Geology* 32, 905–908. <https://doi.org/10.1130/G20679.1>

McManus, J., Nägler, T.F., Siebert, C., Wheat, C.G., Hammond, D.E., 2002. Oceanic molybdenum isotope fractionation: Diagenesis and hydrothermal ridge-flank alteration. *Geochemistry, Geophysics, Geosystems* 3, 1–9. <https://doi.org/10.1029/2002GC000356>

Meckler, A.N., Haug, G.H., Sigman, D.M., Plessen, B., Peterson, L.C., Thierstein, H.R., 2007. Detailed sedimentary N isotope records from Cariaco Basin for Terminations I and V: Local and global implications. *Global Biogeochemical Cycles* 21.

<https://doi.org/10.1029/2006GB002893>

Ménez, B., Pisapia, C., Andreani, M., Jamme, F., Vanbellingen, Q.P., Brunelle, A., Richard, L., Dumas, P., Réfrégiers, M., 2018. Abiotic synthesis of amino acids in the recesses of the oceanic lithosphere. *Nature* 564, 59–63. <https://doi.org/10.1038/s41586-018-0684-z>

Mingram, B., Bräuer, K., 2001. Ammonium concentration and nitrogen isotope composition in metasedimentary rocks from different tectonometamorphic units of the European Variscan Belt. *Geochimica et Cosmochimica Acta* 65, 273–287. [https://doi.org/10.1016/S0016-7037\(00\)00517-2](https://doi.org/10.1016/S0016-7037(00)00517-2)

Mingram, B., Hoth, P., Lüders, V., Harlov, D., 2005. The significance of fixed ammonium in Palaeozoic sediments for the generation of nitrogen-rich natural gases in the North German Basin. *Int J Earth Sci (Geol Rundsch)* 94, 1010–1022. <https://doi.org/10.1007/s00531-005-0015-0>

Möbius, J., 2013. Isotope fractionation during nitrogen remineralization (ammonification): Implications for nitrogen isotope biogeochemistry. *Geochimica et Cosmochimica Acta* 105, 422–432. <https://doi.org/10.1016/j.gca.2012.11.048>

Möbius, J., Gaye, B., Lahajnar, N., Bahlmann, E., Emeis, K.-C., 2011. Influence of diagenesis on sedimentary $\delta^{15}\text{N}$ in the Arabian Sea over the last 130kyr. *Marine Geology* 284, 127–138. <https://doi.org/10.1016/j.margeo.2011.03.013>

Möbius, J., Lahajnar, N., Emeis, K.-C., 2010. Diagenetic control of nitrogen isotope ratios in Holocene sapropels and recent sediments from the Eastern Mediterranean Sea. *Biogeosciences* 7, 3901–3914. <https://doi.org/10.5194/bg-7-3901-2010>

Müller, P.J., 1977. CN ratios in Pacific deep-sea sediments: Effect of inorganic ammonium and organic nitrogen compounds sorbed by clays. *Geochimica et Cosmochimica Acta* 41, 765–776. [https://doi.org/10.1016/0016-7037\(77\)90047-3](https://doi.org/10.1016/0016-7037(77)90047-3)

Nakanishi, T., Minagawa, M., 2003. Stable carbon and nitrogen isotopic compositions of sinking particles in the northeast Japan Sea. *Geochemical Journal* 37, 261–275. <https://doi.org/10.2343/geochemj.37.261>

Navarro-González, R., McKay, C.P., Mvondo, D.N., 2001. A possible nitrogen crisis for Archaean life due to reduced nitrogen fixation by lightning. *Nature* 412, 61–64. <https://doi.org/10.1038/35083537>

Navarro-González, R., Molina, M.J., Molina, L.T., 1998. Nitrogen fixation by volcanic lightning in the early Earth. *Geophysical Research Letters* 25, 3123–3126. <https://doi.org/10.1029/98GL02423>

Nishizawa, M., Miyazaki, J., Makabe, A., Koba, K., Takai, K., 2014. Physiological and isotopic characteristics of nitrogen fixation by hyperthermophilic methanogens: Key insights into nitrogen anabolism of the microbial communities in Archean hydrothermal systems. *Geochimica et Cosmochimica Acta* 138, 117–135. <https://doi.org/10.1016/j.gca.2014.04.021>

Nishizawa, M., Sano, Y., Ueno, Y., Maruyama, S., 2007. Speciation and isotope ratios of nitrogen in fluid inclusions from seafloor hydrothermal deposits at ~ 3.5 Ga. *Earth and Planetary Science Letters* 254, 332–344. <https://doi.org/10.1016/j.epsl.2006.11.044>

Nna-Mvondo, D., Navarro-González, R., Raulin, F., Coll, P., 2005. Nitrogen Fixation By Corona Discharge On The Early Precambrian Earth. *Orig Life Evol Biosph* 35, 401–409. <https://doi.org/10.1007/s11084-005-1972-9>

Olson, S.L., Reinhard, C.T., Lyons, T.W., 2016. Cyanobacterial Diazotrophy and Earth's Delayed Oxygenation. *Frontiers in Microbiology* 7.

Ossa Ossa, F., Spangenberg, J.E., Bekker, A., König, S., Stüeken, E.E., Hofmann, A., Poulton, S.W., Yierpan, A., Varas-Reus, M.I., Eickmann, B., Andersen, M.B., Schoenberg, R., 2022. Moderate levels of oxygenation during the late stage of Earth's Great Oxidation Event. *Earth and Planetary Science Letters* 594, 117716. <https://doi.org/10.1016/j.epsl.2022.117716>

Palya, A.P., Buick, I.S., Bebout, G.E., 2011. Storage and mobility of nitrogen in the continental crust: Evidence from partially melted metasedimentary rocks, Mt. Stafford, Australia. *Chemical Geology* 281, 211–226. <https://doi.org/10.1016/j.chemgeo.2010.12.009>

Papineau, D., Purohit, R., Fogel, M.L., Shields-Zhou, G.A., 2013. High phosphate availability as a possible cause for massive cyanobacterial production of oxygen in the Paleoproterozoic atmosphere. *Earth and Planetary Science Letters* 362, 225–236. <https://doi.org/10.1016/j.epsl.2012.11.050>

Papineau, D., Purohit, R., Goldberg, T., Pi, D., Shields, G.A., Bhu, H., Steele, A., Fogel, M.L., 2009. High primary productivity and nitrogen cycling after the Paleoproterozoic phosphogenic event in the Aravalli Supergroup, India. *Precambrian Research* 171, 37–56. <https://doi.org/10.1016/j.precamres.2009.03.005>

Parsons, C., Stüeken, E.E., Rosen, C.J., Mateos, K., Anderson, R.E., 2021. Radiation of nitrogen-metabolizing enzymes across the tree of life tracks environmental transitions in Earth history. *Geobiology* 19, 18–34. <https://doi.org/10.1111/gbi.12419>

Paulmier, A., Ruiz-Pino, D., 2009. Oxygen minimum zones (OMZs) in the modern ocean. *Progress in Oceanography* 80, 113–128. <https://doi.org/10.1016/j.pocean.2008.08.001>

Pellerin, A., Thomazo, C., Ader, M., Marin-Carbonne, J., Alleon, J., Vennin, E., Hofmann, A., 2023. Iron-mediated anaerobic ammonium oxidation recorded in the early Archean ferruginous ocean. *Geobiology* 21, 277–289. <https://doi.org/10.1111/gbi.12540>

Pitcairn, I.K., Teagle, D.A.H., Kerrich, R., Craw, D., Brewer, T.S., 2005. The behavior of nitrogen and nitrogen isotopes during metamorphism and mineralization: Evidence from the Otago and Alpine Schists, New Zealand. *Earth and Planetary Science Letters* 233, 229–246. <https://doi.org/10.1016/j.epsl.2005.01.029>

Planavsky, N.J., Asael, D., Hofmann, A., Reinhard, C.T., Lalonde, S.V., Knudsen, A., Wang, X., Ossa Ossa, F., Pecoits, E., Smith, A.J.B., Beukes, N.J., Bekker, A., Johnson, T.M., Konhauser, K.O., Lyons, T.W., Rouxel, O.J., 2014. Evidence for oxygenic photosynthesis half a billion years before the Great Oxidation Event. *Nature Geosci* 7, 283–286. <https://doi.org/10.1038/ngeo2122>

Plessen, B., Harlov, D.E., Henry, D., Guidotti, C.V., 2010. Ammonium loss and nitrogen isotopic fractionation in biotite as a function of metamorphic grade in metapelites from western Maine, USA. *Geochimica et Cosmochimica Acta* 74, 4759–4771. <https://doi.org/10.1016/j.gca.2010.05.021>

- Poulton, S.W., Canfield, D.E., 2011. Ferruginous Conditions: A Dominant Feature of the Ocean through Earth's History. *Elements* 7, 107–112. <https://doi.org/10.2113/gselements.7.2.107>
- Poulton, S.W., Fralick, P.W., Canfield, D.E., 2004. The transition to a sulphidic ocean ~ 1.84 billion years ago. *Nature* 431, 173–177. <https://doi.org/10.1038/nature02912>
- Prahl, F.G., Cowie, G.L., De Lange, G.J., Sparrow, M.A., 2003. Selective organic matter preservation in “burn-down” turbidites on the Madeira Abyssal Plain. *Paleoceanography* 18. <https://doi.org/10.1029/2002PA000853>
- Pride, C., Thunell, R., Sigman, D., Keigwin, L., Altabet, M., Tappa, E., 1999. Nitrogen isotopic variations in the Gulf of California since the Last Deglaciation: Response to global climate change. *Paleoceanography* 14, 397–409. <https://doi.org/10.1029/1999PA900004>
- Priestley, S.C., Tyler, J., Liebelt, S.R., Mosley, L.M., Wong, W.W., Shao, Y., Woolston, Z., Farrell, M., Welsh, D.T., Brookes, J.D., Collins, A.S., Keneally, C., Farkaš, J., 2022. N and C Isotope Variations Along an Extreme Eutrophication and Salinity Gradient in the Coorong Lagoon, South Australia. *Frontiers in Earth Science* 9.
- Prokopenko, M.G., Hammond, D.E., Berelson, W.M., Bernhard, J.M., Stott, L., Douglas, R., 2006. Nitrogen cycling in the sediments of Santa Barbara basin and Eastern Subtropical North Pacific: Nitrogen isotopes, diagenesis and possible chemosymbiosis between two lithotrophs (*Thioploca* and *Anammox*)—“riding on a glider.” *Earth and Planetary Science Letters* 242, 186–204. <https://doi.org/10.1016/j.epsl.2005.11.044>
- Prokopenko, M.G., Hirst, M.B., De Brabandere, L., Lawrence, D.J.P., Berelson, W.M., Granger, J., Chang, B.X., Dawson, S., Crane Iii, E.J., Chong, L., Thamdrup, B., Townsend-Small, A., Sigman, D.M., 2013. Nitrogen losses in anoxic marine sediments driven by *Thioploca* –*anammox* bacterial consortia. *Nature* 500, 194–198. <https://doi.org/10.1038/nature12365>
- Quan, T.M., Falkowski, P.G., 2009. Redox control of N:P ratios in aquatic ecosystems. *Geobiology* 7, 124–139. <https://doi.org/10.1111/j.1472-4669.2008.00182.x>
- Raymond, J., Siefert, J.L., Staples, C.R., Blankenship, R.E., 2004. The Natural History of Nitrogen Fixation. *Mol Biol Evol* 21, 541–554. <https://doi.org/10.1093/molbev/msh047>
- Reinhard, C.T., Planavsky, N.J., Gill, B.C., Ozaki, K., Robbins, L.J., Lyons, T.W., Fischer, W.W., Wang, C., Cole, D.B., Konhauser, K.O., 2017. Evolution of the global phosphorus cycle. *Nature* 541, 386–389. <https://doi.org/10.1038/nature20772>
- Reinhard, C.T., Planavsky, N.J., Robbins, L.J., Partin, C.A., Gill, B.C., Lalonde, S.V., Bekker, A., Konhauser, K.O., Lyons, T.W., 2013. Proterozoic ocean redox and biogeochemical stasis. *Proceedings of the National Academy of Sciences* 110, 5357–5362. <https://doi.org/10.1073/pnas.1208622110>
- Reinhard, C.T., Raiswell, R., Scott, C., Anbar, A.D., Lyons, T.W., 2009. A Late Archean Sulfidic Sea Stimulated by Early Oxidative Weathering of the Continents. *Science* 326, 713–716. <https://doi.org/10.1126/science.1176711>
- Rigby, D., Batts, B.D., 1986. The isotopic composition of nitrogen in Australian coals and oil shales. *Chemical Geology: Isotope Geoscience section* 58, 273–282.

[https://doi.org/10.1016/0168-9622\(86\)90016-3](https://doi.org/10.1016/0168-9622(86)90016-3)

Rivera, K.T., Puckette, J., Quan, T.M., 2015. Evaluation of redox versus thermal maturity controls on $\delta^{15}\text{N}$ in organic rich shales: A case study of the Woodford Shale, Anadarko Basin, Oklahoma, USA. *Organic Geochemistry* 83–84, 127–139. <https://doi.org/10.1016/j.orggeochem.2015.03.005>

Robinson, R.S., Kienast, M., Albuquerque, A.L., Altabet, M., Contreras, S., Holz, R.D.P., Dubois, N., Francois, R., Galbraith, E., Hsu, T.-C., Ivanochko, T., Jaccard, S., Kao, S.-J., Kiefer, T., Kienast, S., Lehmann, M., Martinez, P., McCarthy, M., Möbius, J., Pedersen, T., Quan, T.M., Ryabenko, E., Schmittner, A., Schneider, R., Schneider-Mor, A., Shigemitsu, M., Sinclair, D., Somes, C., Studer, A., Thunell, R., Yang, J.-Y., 2012. A review of nitrogen isotopic alteration in marine sediments. *Paleoceanography* 27. <https://doi.org/10.1029/2012PA002321>

Sachs, J.P., Repeta, D.J., 1999. Oligotrophy and nitrogen fixation during eastern mediterranean sapropel event. *Science* 286, 2485–2488. <https://doi.org/10.1126/science.286.5449.2485>

Sánchez-Baracaldo, P., Ridgwell, A., Raven, J.A., 2014. A Neoproterozoic Transition in the Marine Nitrogen Cycle. *Current Biology* 24, 652–657. <https://doi.org/10.1016/j.cub.2014.01.041>

Sawayama, S., 2006. Possibility of anoxic ferric ammonium oxidation. *Journal of Bioscience and Bioengineering* 101, 70–72. <https://doi.org/10.1263/jbb.101.70>

Schimmelmann, A., Lis, G.P., 2010. Nitrogen isotopic exchange during maturation of organic matter. *Organic Geochemistry, Stable Isotopes in Biogeosciences (III)* 41, 63–70. <https://doi.org/10.1016/j.orggeochem.2009.01.005>

Schimmelmann, A., Mastalerz, M., Gao, L., Sauer, P.E., Topalov, K., 2009. Dike intrusions into bituminous coal, Illinois Basin: H, C, N, O isotopic responses to rapid and brief heating. *Geochimica et Cosmochimica Acta* 73, 6264–6281. <https://doi.org/10.1016/j.gca.2009.07.027>

Schoonen, M.A.A., Xu, Y., 2001. Nitrogen Reduction Under Hydrothermal Vent Conditions: Implications for the Prebiotic Synthesis of C-H-O-N Compounds. *Astrobiology* 1, 133–142. <https://doi.org/10.1089/153110701753198909>

Scott, C., Lyons, T.W., Bekker, A., Shen, Y., Poulton, S.W., Chu, X., Anbar, A.D., 2008. Tracing the stepwise oxygenation of the Proterozoic ocean. *Nature* 452, 456–459. <https://doi.org/10.1038/nature06811>

Seebree, J.A., Stern, J.C., Mandt, K.E., Domagal-Goldman, S.D., Trainer, M.G., 2016. ^{13}C and ^{15}N fractionation of CH_4/N_2 mixtures during photochemical aerosol formation: Relevance to Titan. *Icarus, Titan's Surface and Atmosphere* 270, 421–428. <https://doi.org/10.1016/j.icarus.2015.04.016>

Sigman, D.M., Karsh, K.L., Casciotti, K.L., 2009. Nitrogen Isotopes in the Ocean. *Encyclopedia of Ocean Sciences* 40–54. <https://doi.org/10.1016/B978-012374473-9.00632-9>

Smirnov, A., Hausner, D., Laffers, R., Strongin, D.R., Schoonen, M.A., 2008. Abiotic ammonium formation in the presence of Ni-Fe metals and alloys and its implications for the Hadean nitrogen cycle. *Geochemical Transactions* 9, 5. <https://doi.org/10.1186/1467-4866-9-5>

- Sterne, E.J., Reynolds, R.C., Zantop, H., 1982. Natural Ammonium Illites from Black Shales Hosting a Stratiform Base Metal Deposit, DeLong Mountains, Northern Alaska. *Clays Clay Miner.* 30, 161–166. <https://doi.org/10.1346/CCMN.1982.0300301>
- Stüeken, E.E., Boocock, T., Szilas, K., Mikhail, S., Gardiner, N.J., 2021a. Reconstructing Nitrogen Sources to Earth's Earliest Biosphere at 3.7 Ga. *Frontiers in Earth Science* 9.
- Stüeken, E.E., Boocock, T.J., Robinson, A., Mikhail, S., Johnson, B.W., 2021b. Hydrothermal recycling of sedimentary ammonium into oceanic crust and the Archean ocean at 3.24 Ga. *Geology* 49, 822–826. <https://doi.org/10.1130/G48844.1>
- Stüeken, E. E., Buick, R., Anderson, R.E., Baross, J.A., Planavsky, N.J., Lyons, T.W., 2017. Environmental niches and metabolic diversity in Neoarchean lakes. *Geobiology* 15, 767–783. <https://doi.org/10.1111/gbi.12251>
- Stüeken, E.E., Buick, R., Guy, B.M., Koehler, M.C., 2015. Isotopic evidence for biological nitrogen fixation by molybdenum-nitrogenase from 3.2 Gyr. *Nature* 520, 666–669. <https://doi.org/10.1038/nature14180>
- Stüeken, E. E., Buick, R., Schauer, A.J., 2015. Nitrogen isotope evidence for alkaline lakes on late Archean continents. *Earth and Planetary Science Letters* 411, 1–10. <https://doi.org/10.1016/j.epsl.2014.11.037>
- Stüeken, E.E., Catling, D.C., Buick, R., 2012. Contributions to late Archaean sulphur cycling by life on land. *Nature Geoscience* 5, 722–725. <https://doi.org/10.1038/ngeo1585>
- Stüeken, E.E., Gregory, D.D., Mukherjee, I., McGoldrick, P., 2021c. Sedimentary exhalative venting of bioavailable nitrogen into the early ocean. *Earth and Planetary Science Letters* 565, 116963. <https://doi.org/10.1016/j.epsl.2021.116963>
- Stüeken, E.E., Kipp, M.A., Koehler, M.C., Buick, R., 2016. The evolution of Earth's biogeochemical nitrogen cycle. *Earth-Science Reviews* 160, 220–239. <https://doi.org/10.1016/j.earscirev.2016.07.007>
- Stüeken, E.E., Zaloumis, J., Meixnerová, J., Buick, R., 2017. Differential metamorphic effects on nitrogen isotopes in kerogen extracts and bulk rocks. *Geochimica et Cosmochimica Acta* 217, 80–94. <https://doi.org/10.1016/j.gca.2017.08.019>
- Šucha, V., Kraus, I., Madejová, J., 1994. Ammonium illite from anchimetamorphic shales associated with anthracite in the Zemplinicum of the western Carpathians. *Clay Minerals* 29, 369–377. <https://doi.org/10.1180/claymin.1994.029.3.08>
- Svensen, H., Bebout, G., Kronz, A., Li, L., Planke, S., Chevallerier, L., Jamtveit, B., 2008. Nitrogen geochemistry as a tracer of fluid flow in a hydrothermal vent complex in the Karoo Basin, South Africa. *Geochimica et Cosmochimica Acta* 72, 4929–4947. <https://doi.org/10.1016/j.gca.2008.07.023>
- Talbot, M.R., Johannessen, T., 1992. A high resolution palaeoclimatic record for the last 27,500 years in tropical West Africa from the carbon and nitrogen isotopic composition of lacustrine organic matter. *Earth and Planetary Science Letters* 110, 23–37. [https://doi.org/10.1016/0012-821X\(92\)90036-U](https://doi.org/10.1016/0012-821X(92)90036-U)

- Tesdal, J.-E., Galbraith, E.D., Kienast, M., 2013. Nitrogen isotopes in bulk marine sediment: linking seafloor observations with subseafloor records. *Biogeosciences* 10, 101–118. <https://doi.org/10.5194/bg-10-101-2013>
- Thomazo, C., Ader, M., Farquhar, J., Philippot, P., 2009. Methanotrophs regulated atmospheric sulfur isotope anomalies during the Mesoarchean (Tumbiana Formation, Western Australia). *Earth and Planetary Science Letters* 279, 65–75. <https://doi.org/10.1016/j.epsl.2008.12.036>
- Thomazo, C., Ader, M., Philippot, P., 2011. Extreme ^{15}N -enrichments in 2.72-Gyr-old sediments: evidence for a turning point in the nitrogen cycle. *Geobiology* 9, 107–120. <https://doi.org/10.1111/j.1472-4669.2011.00271.x>
- Thunell, R.C., Kepple, A.B., 2004. Glacial-Holocene $\delta^{15}\text{N}$ record from the Gulf of Tehuantepec, Mexico: Implications for denitrification in the eastern equatorial Pacific and changes in atmospheric N_2O . *Global Biogeochemical Cycles* 18. <https://doi.org/10.1029/2002GB002028>
- Thunell, R.C., Sigman, D.M., Muller-Karger, F., Astor, Y., Varela, R., 2004. Nitrogen isotope dynamics of the Cariaco Basin, Venezuela. *Global Biogeochemical Cycles* 18. <https://doi.org/10.1029/2003GB002185>
- Tian, F., Kasting, J.F., Zahnle, K., 2011. Revisiting HCN formation in Earth's early atmosphere. *Earth and Planetary Science Letters* 308, 417–423. <https://doi.org/10.1016/j.epsl.2011.06.011>
- Trainer, M.G., Pavlov, A.A., DeWitt, H.L., Jimenez, J.L., McKay, C.P., Toon, O.B., Tolbert, M.A., 2006. Organic haze on Titan and the early Earth. *PNAS* 103, 18035–18042. <https://doi.org/10.1073/pnas.0608561103>
- Ulloa, O., Canfield, D.E., DeLong, E.F., Letelier, R.M., Stewart, F.J., 2012. Microbial oceanography of anoxic oxygen minimum zones. *Proceedings of the National Academy of Sciences* 109, 15996–16003. <https://doi.org/10.1073/pnas.1205009109>
- Volkova, I.B., Bogdanova, M.V., 1989. Properties of high-rank coals and dispersed organic matter of associated rocks in the Donets Basin (U.S.S.R.). *International Journal of Coal Geology* 11, 315–339. [https://doi.org/10.1016/0166-5162\(89\)90122-5](https://doi.org/10.1016/0166-5162(89)90122-5)
- Wang, D., 2012. Redox chemistry of molybdenum in natural waters and its involvement in biological evolution. *Frontiers in Microbiology* 3.
- Ward, B., 2012. The Global Nitrogen Cycle, in: *Fundamentals of Geobiology*. John Wiley & Sons, Ltd, pp. 36–48. <https://doi.org/10.1002/9781118280874.ch4>
- Wenk, C.B., Zopfi, J., Blees, J., Veronesi, M., Niemann, H., Lehmann, M.F., 2014. Community N and O isotope fractionation by sulfide-dependent denitrification and anammox in a stratified lacustrine water column. *Geochimica et Cosmochimica Acta* 125, 551–563. <https://doi.org/10.1016/j.gca.2013.10.034>
- Whiticar, M.J., 1996. Stable isotope geochemistry of coals, humic kerogens and related natural gases. *International Journal of Coal Geology* 32, 191–215. [https://doi.org/10.1016/S0166-5162\(96\)00042-0](https://doi.org/10.1016/S0166-5162(96)00042-0)

- Williams, L.B., Ferrell, R.E., Hutcheon, I., Bakel, A.J., Walsh, M.M., Krouse, H.R., 1995. Nitrogen isotope geochemistry of organic matter and minerals during diagenesis and hydrocarbon migration. *Geochimica et Cosmochimica Acta* 59, 765–779. [https://doi.org/10.1016/0016-7037\(95\)00005-K](https://doi.org/10.1016/0016-7037(95)00005-K)
- Yamaguchi, K.E., Oguri, K., Ogawa, N.O., Sakai, S., Hirano, S., Kitazato, H., Ohkouchi, N., 2010. Geochemistry of modern carbonaceous sediments overlain by a water mass showing photic zone anoxia in the saline meromictic Lake Kai-ike, southwest Japan: I. Early diagenesis of organic carbon, nitrogen, and phosphorus. *Palaeogeography, Palaeoclimatology, Palaeoecology* 294, 72–82. <https://doi.org/10.1016/j.palaeo.2009.10.024>
- Yang, J., Junium, C.K., Grassineau, N.V., Nisbet, E.G., Izon, G., Mettam, C., Martin, A., Zerkle, A.L., 2019. Ammonium availability in the Late Archaean nitrogen cycle. *Nat. Geosci.* 12, 553–557. <https://doi.org/10.1038/s41561-019-0371-1>
- Yui, T.-F., Kao, S.-J., Wu, T.-W., 2009. Nitrogen and N-isotope variation during low-grade metamorphism of the Taiwan mountain belt. *Geochemical Journal* 43, 15–27. <https://doi.org/10.2343/geochemj.1.0003>
- Zerkle, A.L., Claire, M.W., Domagal-Goldman, S.D., Farquhar, J., Poulton, S.W., 2012. A bistable organic-rich atmosphere on the Neoproterozoic Earth. *Nature Geosci* 5, 359–363. <https://doi.org/10.1038/ngeo1425>
- Zerkle, A.L., House, C.H., Cox, R.P., Canfield, D.E., 2006. Metal limitation of cyanobacterial N₂ fixation and implications for the Precambrian nitrogen cycle. *Geobiology* 4, 285–297. <https://doi.org/10.1111/j.1472-4669.2006.00082.x>
- Zerkle, A.L., Poulton, S.W., Newton, R.J., Mettam, C., Claire, M.W., Bekker, A., Junium, C.K., 2017. Onset of the aerobic nitrogen cycle during the Great Oxidation Event. *Nature* 542, 465–467. <https://doi.org/10.1038/nature20826>
- Zhang, X., Sigman, D.M., Morel, F.M.M., Kraepiel, A.M.L., 2014. Nitrogen isotope fractionation by alternative nitrogenases and past ocean anoxia. *PNAS* 111, 4782–4787. <https://doi.org/10.1073/pnas.1402976111>

CHAPTER 3. SECULAR EVOLUTION IN PRECAMBRIAN $\delta^{15}\text{N}$ SIGNATURES

3.1. Introduction - Main features of the Precambrian sedimentary $\delta^{15}\text{N}$ record	73
3.2. Methods - Building an updated Precambrian $\delta^{15}\text{N}$ database	78
3.3. Results.....	79
3.4. Discussion - Secular evolution of the $\delta^{15}\text{N}$ signature through the Precambrian	82
3.4.1. Potential biases that may impact our interpretation of the $\delta^{15}\text{N}$ secular evolution through the Precambrian.....	82
3.4.2. First-order secular variations of the $\delta^{15}\text{N}$ signature through the Precambrian	84
3.4.3. Identifying analytical biases, secondary alteration and paleoenvironmental changes	85
3.5. Conclusions.....	87
References.....	129
Supplementary Information	133

CHAPTER 3. SECULAR EVOLUTION IN PRECAMBRIAN $\delta^{15}\text{N}$ SIGNATURES

3.1. Introduction - Main features of the Precambrian sedimentary $\delta^{15}\text{N}$ record

Growing steadily with the improvements of analytical techniques for nitrogen isotope measurement, a number of Precambrian $\delta^{15}\text{N}_{\text{sed}}$ datasets have been used to report secular variations in sedimentary $\delta^{15}\text{N}$ signatures through the Archean and the Proterozoic (compiled in Ader et al., 2016; Stüeken et al., 2016; Yang et al., 2019; Zerkle et al., 2017; Supplementary Table 8.1).

The vast majority of Precambrian sedimentary $\delta^{15}\text{N}$ data falls between 0 and +8‰ (Fig. 3.1-3.2) (Ader et al., 2016; Stüeken et al., 2016), except for two episodes where highly positive $\delta^{15}\text{N}$ values are recorded in specific localities, at ca. 2.7 Ga in the Tumbiana and Kylene Formations in Australia (up to +50‰, Stüeken et al., 2015, 2017; Thomazo et al., 2011) and at ca. 1.9 Ga in the Aravalli Supergroup in India (up to +27‰, Papineau et al., 2009).

Previous compilations of Precambrian sedimentary $\delta^{15}\text{N}$ data have shown a subtle evolution of the mode of $\delta^{15}\text{N}$ distribution through time (Ader et al., 2016). The lowest $\delta^{15}\text{N}$ mode ($\approx +2\text{‰}$) was found during the 3.8-2.8 Ga time interval (Fig. 3.2). Then the $\delta^{15}\text{N}$ mode increased to $\approx +3\text{‰}$ during the 2.8-2.4 Ga time interval and to $\approx +5\text{‰}$ during the 2.2-1.8 Ga time interval (Fig. 3.2). Finally, the 680-540 Ma displays a tighter $\delta^{15}\text{N}$ distribution between -2 and +10‰ (Fig. 3.2), with a mode of $\approx +3\text{‰}$ (Fig. 3.2). Those secular trends in Precambrian N isotope data were interpreted as showing a three-step evolution of the marine N-biogeochemical cycle, from an ammonium-dominated “reduced” N cycle in pre-GOE anoxic oceans, followed by a rise of oceanic oxidants during the Neoproterozoic some time before the GOE, possibly even as early as 2.7 Ga, and later by the progressive stabilization of a persistent nitrate reservoir in oxygenated surface waters (Fig. 3.3). In light of this evolution, scenarios for the dynamics of the N-biogeochemical cycle have been explored for different stages in Earth’s history from the Mesoarchean to the beginning of the Phanerozoic (Fig. 3.3, Stüeken et al., 2016).

Large-scale Precambrian $\delta^{15}\text{N}$ studies have explored major questions regarding nitrogen isotope measurements in Precambrian rocks and Precambrian nitrogen cycling, such as which phase best captures the primary nitrogen isotope signature (e.g. Ader et al., 2016; Boocock et al., 2020; Kipp et al., 2018; Stüeken et al., 2016), the impact of the studied samples’ metamorphic grade (reviewed in Ader et al., 2016; Stüeken et al., 2016), the link with molybdenum

concentrations (Stüeken et al., 2016), potential parallel trends between $\delta^{15}\text{N}$ and $\delta^{13}\text{C}_{\text{org}}$ secular evolution (Kipp et al., 2018), or the evolution of TOC/TN ratios across the Paleoproterozoic (Kipp et al., 2018). Paired $\delta^{15}\text{N}$ - $\delta^{13}\text{C}_{\text{org}}$ have even been looked at for different depositional environments among a basin (Koehler et al., 2017).

Yet, at the scale of the whole Archean, or even the whole Precambrian Eons, the links between the nitrogen isotope signature and some key parameters, such as metamorphism, lithology, depositional environment, TOC contents, TN contents, TOC/TN ratios, or $\delta^{13}\text{C}_{\text{org}}$ values remain poorly defined. This chapter aims at both (i) validating previous hypotheses using an updated Precambrian $\delta^{15}\text{N}$ data compilation, and (ii) look for new possible trends and processes affecting secular $\delta^{15}\text{N}$ variations through the Precambrian, especially the Archean, by cross-examining key indicators, such as lithology and metamorphism. It hopes to point towards new directions for future studies using the $\delta^{15}\text{N}$ proxy in deep time, both in terms of sample selection and choice of complementary indicators to measure.

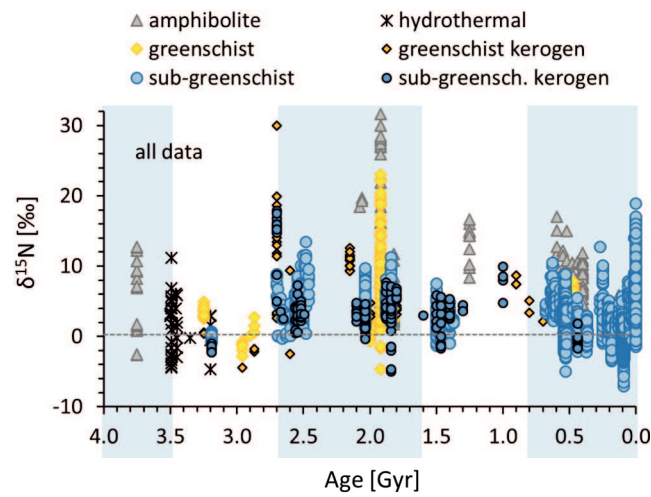
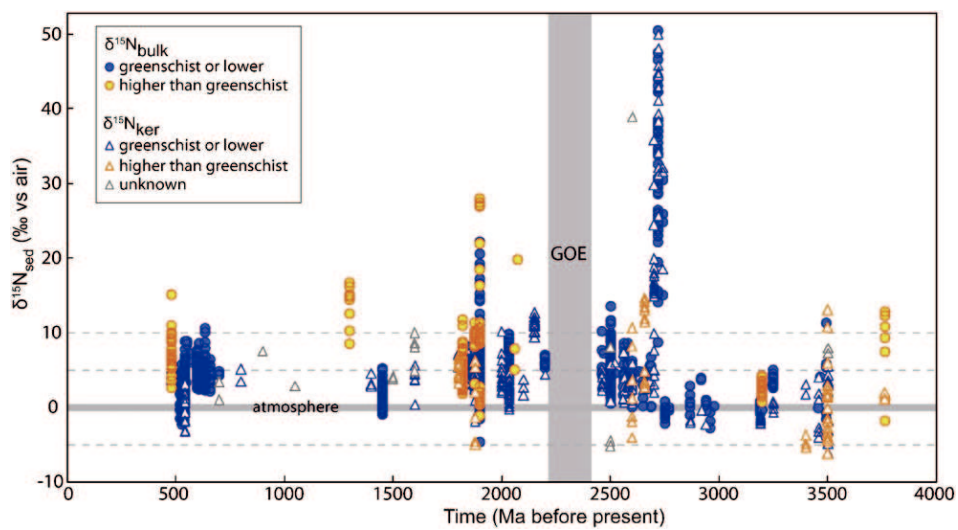
A**B**

Fig. 3.1. Compilations of sedimentary $\delta^{15}\text{N}$ data plotted versus time, separated by metamorphic grade and/or phase analyzed ((A), Stüeken et al., 2016), and ((B), Ader et al., 2016). GOE stands for Great Oxidation Event. Note that timescales are reversed between graphs A and B.

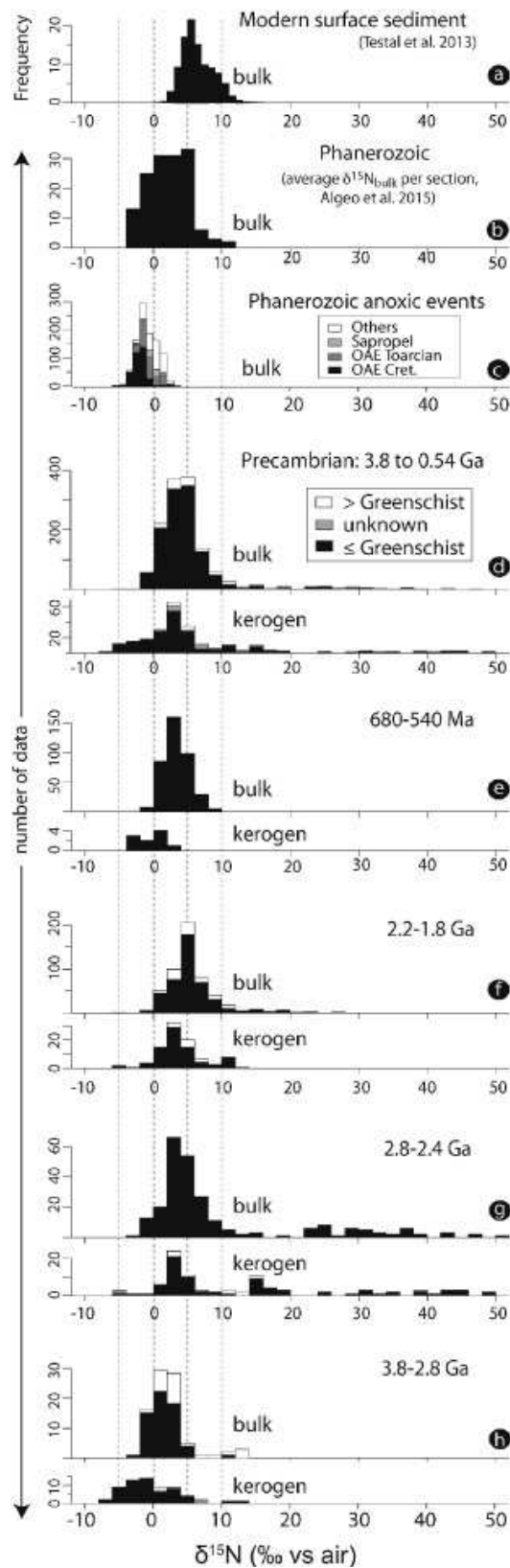


Fig. 3.2. Histograms representing the number of $\delta^{15}\text{N}_{\text{bulk}}$ and $\delta^{15}\text{N}_{\text{ker}}$ data for (d) the whole Precambrian and for the time intervals 680 to 540 Ma (e), 2.2 to 1.8 Ga (f), 2.8 to 2.4 Ga (g), and 3.8 to 2.8 Ga, compared to modern surface sediments (a), the Phanerozoic (b), and Phanerozoic anoxic events (c). From Ader et al. (2016).

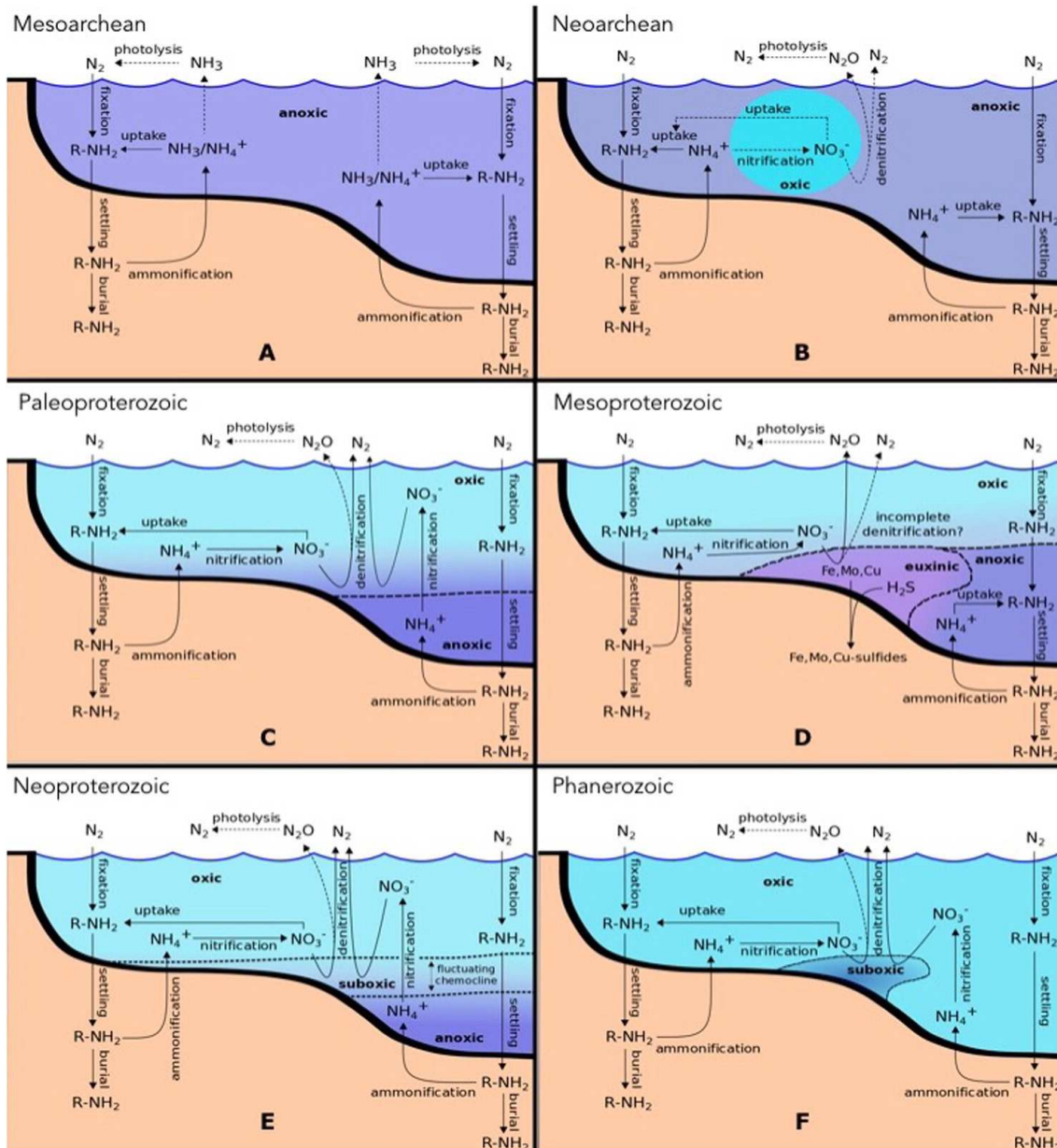


Fig. 3.3. Sketches representing the N-biogeochemical cycle dynamics occurring in the water column and surface sediments, from shallower (left) to deeper (right) paleoenvironments, for different stages in Earth's history (Stüeken et al., 2016): (A) Mesoarchean, 3.2-2.8 Ga; (B) Neoproterozoic, 2.8-2.5 Ga; (C) Paleoproterozoic, 2.5-1.8 Ga; (D) Mesoproterozoic, 1.8-0.8 Ga; (E) Neoproterozoic, 0.8-0.5 Ga; (F) Phanerozoic, from 0.5 Ga on. Minor processes are represented using dotted arrows. Sedimentary denitrification has been omitted but is considered stable throughout the Precambrian.

3.2. Methods - Building an updated Precambrian $\delta^{15}\text{N}$ database

Four existing $\delta^{15}\text{N}$ compilations (Ader et al., 2016; Stüeken et al., 2016; Yang et al., 2019; Zerkle et al., 2017) were merged into a single database. The database was then expanded with all available new data from publications between 2016 and 2022 (see list in Supplementary Information). The number of $\delta^{15}\text{N}$ data has grown since 2016, with 2705 new $\delta^{15}\text{N}$ measurements (1887 in 2016 vs. 4592 in 2022) from 35 new publications (32 in 2016 vs. 67 in 2022).

This database records, for each Precambrian (4.0 to 0.54 Ga) $\delta^{15}\text{N}$ data and when available in the literature, its source publication, its age, its location (Craton and Formation name), its stratigraphic features (sample name, core or outcrop name, stratigraphic depth or height), the analyzed phase, the method of $\delta^{15}\text{N}$ analysis, its nitrogen content (TN), its organic carbon content and isotopic signature (TOC and $\delta^{13}\text{C}_{\text{org}}$), its TOC/TN ratio, its potassium content (K), its inorganic carbon isotopic signature ($\delta^{13}\text{C}_{\text{carb}}$), its metamorphic grade, its lithology and its inferred depositional environment as described in the original publication (Supplementary Table 3.1).

Some key parameters have been selected in order to filter the studied $\delta^{15}\text{N}$ dataset: analyzed phase, lithology, metamorphism, $\delta^{13}\text{C}_{\text{org}}$, and TOC/TN. Secular trends in $\delta^{15}\text{N}$ data have been explored through the lens of these different parameters (Fig. 3.4-3.11).

In addition, principal component analyses (PCA) were run to help visualize and understand correlations between quantitative variables: $\delta^{15}\text{N}_{\text{bulk}}$, $\delta^{15}\text{N}_{\text{ker}}$, $\delta^{13}\text{C}_{\text{org}}$, TOC, TN, and TOC/TN. A PCA was first run on the whole dataset (Fig. 3.12), then on each of the three main lithologies (shales, carbonates and cherts/BIFs; Fig. 3.13), then on each of the three main categories of metamorphic grades (lower than greenschist, greenschist, higher than greenschist; Fig. 3.13). The first two dimensions of the PCA express the percentage of the total data inertia, meaning that this percentage of the variables cloud total variability is explained by the plane. The higher this percentage the better the first plane represents data variability. The variability explained by the plane is considered significant when the sum of the two first dimensions is greater than the reference value of 37.95%. Variables that are grouped together are positively correlated to each other, while variables that are negatively correlated are displayed to the opposite sides of the biplot's origin. the higher the distance between the variable and the origin, the better that variable is represented.

Boxplots (Fig. 3.14) show how the $\delta^{15}\text{N}$ distribution differs across the analyzed phase, lithology, metamorphism, TOC/TN, and $\delta^{13}\text{C}_{\text{org}}$. Then, boxplots combining lithology and metamorphism show how the $\delta^{15}\text{N}$ distribution differs across shales, carbonates and cherts/BIFs depending on their respective category of metamorphic grade (Fig. 3.15). The box in the boxplot extends from the lower quartile to the upper quartile, with the line in between showing the median of the distribution. Horizontal dashed lines, known as “whiskers”, extend to one and a half times the interquartile range, but are limited to reaching actual data points. Any value falling outside the range of the whiskers is an outlier.

Crossplots show paired $\delta^{15}\text{N}_{\text{bulk}}$ - $\delta^{15}\text{N}_{\text{ker}}$ values (Fig. 3.16), filtered according to lithology and metamorphic grade, paired $\delta^{15}\text{N}$ - $\delta^{13}\text{C}_{\text{org}}$ values (Fig. 3.17-3.25), filtered according to the analyzed phase, lithology, metamorphism, and TOC/TN, as well as paired $\delta^{15}\text{N}$ -TOC/TN values (Fig. 3.26-3.31), filtered according to analyzed phase, lithology, metamorphism, and $\delta^{13}\text{C}_{\text{org}}$.

3.3. Results

In Fig. 3.4A, all available $\delta^{15}\text{N}$ data ($n=3561$) are plotted as a function of time.

The analyzed phase (Fig. 3.4D, 3.5) represents the nitrogen fraction on which $\delta^{15}\text{N}$ measurements have been made, i.e. (i) kerogen N (Fig. 3.5C), the residual organic-bound nitrogen phase, (ii) silicate N, potassic minerals (Fig. 3.5D) that retain ammonium in their mineral lattice or (iii) bulk N (Fig. 3.5B), that includes both phases. The pros and cons of each technique are detailed in Chapter 2; in any case it is interesting to assess if the type of analyzed phase impacts data distributions and/or secular trends. Most $\delta^{15}\text{N}$ measurements on Precambrian rocks have been made on bulk N ($n=2733$, Fig. 3.5B), with less measurements made on kerogen N ($n=648$, Fig. 3.5C), and even less on silicate N ($n=180$, Fig. 3.5D).

The lithology (Fig. 3.4C and 3.6), e.g. the type of rock on which the $\delta^{15}\text{N}$ measurements have been made, has been sorted into three main categories: (i) shales ($n=2047$, Fig. 3.6B), (ii) carbonates ($n=538$, Fig. 3.6C) and (iii) cherts and BIFs (Banded Iron Formations) ($n=199$, Fig. 3.6D) (Supplementary Table 3.1). Minor types of lithologies have been left out of the lithology compilations for the sake of clarity. Note that as the aim was to look for secular trends, the distinction between the three types of lithology have been made on whole datasets based on their dominant features, rather than on individual samples (Supplementary Table 3.1).

Therefore, the compilation cannot readily be used to study the heterogeneity inside a specific Formation.

Metamorphism (Fig. 3.4B, 3.7, 3.8) has been sorted into three homogenized categories: below the greenschist facies ($n=1882$, Fig. 3.7B), inside the greenschist facies ($n=1047$, Fig. 3.7C), and above the greenschist facies ($n=238$, Fig. 3.7D). This choice has been made based on the differential effect of metamorphism on $\delta^{15}\text{N}$ values for these three coupled ranges of pressure-temperature, that are discussed in Chapter 2. Sedimentary rocks that are metamorphosed above the greenschist facies are underrepresented, mainly because they are not deemed to be reliable paleoenvironmental archives for many geochemical tracers, including nitrogen isotopes (Chapter 2).

As the $\delta^{13}\text{C}_{\text{org}}$ signal mostly reflects the primary metabolism of CO_2 -fixing autotrophic organisms (Schidlowski, 2001), $\delta^{13}\text{C}_{\text{org}}$ values have been divided into four ranges (Fig 3.4E, 3.9): $\delta^{13}\text{C}_{\text{org}} < -40\text{‰}$ ($n=395$, Fig. 3.9E), $\delta^{13}\text{C}_{\text{org}}$ from -40 to -32‰ ($n=965$, Fig. 3.9D), $\delta^{13}\text{C}_{\text{org}}$ from -32 to -28‰ ($n=820$, Fig. 3.9C), and $\delta^{13}\text{C}_{\text{org}} > -28\text{‰}$ ($n=685$, Fig. 3.9B), partly based on the range of fractionation imparted by major groups of autotrophs present during the Precambrian (methanotrophic bacteria, cultured cyanobacteria, natural cyanobacteria, and anoxygenic photosynthesizers) and the impact of metamorphic alteration as reported in Schidlowski (2001), Havig et al. (2017), and Hurley et al. (2021). The idea is to explore if and when $\delta^{15}\text{N}$ and $\delta^{13}\text{C}_{\text{org}}$ variations are coupled, and if other parameters such as the lithology or metamorphism impact this coupling.

The exploration of TOC/TN ratio variations along with $\delta^{15}\text{N}$ values (Fig 3.4F, 3.10) will show the potential effects of thermal denitrogenation and/or metasomatic ammonium addition for various lithologies and metamorphic grades. Indeed, most studies show a joint increase in TOC/TN and $\delta^{15}\text{N}$ with increasing metamorphism (Bebout and Fogel, 1992; Boyd and Philippot, 1998; Haendel et al., 1986; Jia, 2006), but others have reported constant $\delta^{15}\text{N}$ values even when TOC/TN was underwent a tenfold increase (Ader et al., 1998, 2006; Boudou et al., 2008; Schimmelmann et al., 2009). Conversely, metasomatic ammonium addition through fluid circulation and hydrothermal recycling decreases TOC/TN ratios (Glasmacher et al., 2003; Jia and Kerrich, 2000, 1999; Sterne et al., 1982; Svensen et al., 2008). TOC/TN values have been divided into four equivalent ranges: TOC/TN < 50 ($n=1631$, Fig. 3.10B), TOC/TN from 50 to 100 ($n=510$, Fig. 3.10C), TOC/TN from 100 to 150 ($n=222$, Fig. 3.10D), and TOC/TN > 150 ($n=208$, Fig. 3.10E).

New sedimentary $\delta^{15}\text{N}$ data provided through the updated $\delta^{15}\text{N}$ compilation mostly fall within the 0 to +8‰ range estimated in previous work (Ader et al., 2016; Stüeken et al., 2016). No additional extremely positive $\delta^{15}\text{N}$ values were recorded, neither at 2.7 Ga, like in the Tumbiana Formation in Australia (Stüeken et al., 2015; Thomazo et al., 2011), nor at 1.9 Ga, like in the Aravalli Supergroup in India (Papineau et al., 2009), nor at any other Precambrian time. The subtle increase of the mode of $\delta^{15}\text{N}$ distribution through time evidenced by Ader et al. (2016), from $\approx+2\text{‰}$ during the 3.8-2.8 Ga time interval to $\approx+3\text{‰}$ during the 2.8-2.4 Ga time interval and to $\approx+5\text{‰}$ during the 2.2-1.8 Ga time interval (Fig. 3.2) still stands. Sorting sedimentary $\delta^{15}\text{N}$ data according to metamorphic grade (Fig. 3.4B, 3.7, 3.8), lithology (Fig. 3.4C, 3.6), analyzed phase (Fig. 3.4D, 3.5), $\delta^{13}\text{C}_{\text{org}}$ values (Fig. 3.4E, 3.9) or TOC/TN ratios (Fig. 3.4F, 3.10) does not seem to affect $\delta^{15}\text{N}$ secular trends throughout the Precambrian. No secular trends in TOC/TN ratios were observed during the Precambrian, even when considering the degree of metamorphism (Fig. 3.11).

$\delta^{15}\text{N}_{\text{bulk}}$ and $\delta^{15}\text{N}_{\text{ker}}$ data are well correlated ($R^2=0.80$, Fig. 3.16A). The correlation is better in carbonates ($R^2=0.96$) than in shales ($R^2=0.75$) (Fig. 3.16B), and similar across all metamorphic grades ($R^2=0.80$, Fig. 3.16C). $\delta^{15}\text{N}_{\text{ker}}$ are usually isotopically lighter compared to their bulk counterparts by about 2‰, which is consistent with previously published studies (Stüeken et al., 2017). This $\approx 2\text{‰}$ offset is homogenous across all studied lithologies and metamorphic grades (Fig. 3.16).

As for PCAs, when the whole dataset is considered (Fig. 3.12), three clusters of variables can be identified: (1) $\delta^{15}\text{N}_{\text{bulk}}$, $\delta^{15}\text{N}_{\text{ker}}$ and TOC/TN, (2) TOC and TN and (3) $\delta^{13}\text{C}_{\text{org}}$. The $\delta^{15}\text{N}_{\text{bulk}}$, $\delta^{15}\text{N}_{\text{ker}}$ and TOC/TN are positively correlated to each other, similarly to TOC and TN. The $\delta^{15}\text{N}_{\text{bulk}}$, $\delta^{15}\text{N}_{\text{ker}}$ and TOC/TN are negatively correlated to $\delta^{13}\text{C}_{\text{org}}$. In PCAs for the different lithologies (Fig. 3.13), this pattern is conserved in shales and carbonates, but differs in cherts/BIFs where $\delta^{15}\text{N}_{\text{ker}}$ clusters with $\delta^{13}\text{C}_{\text{org}}$. In PCAs considering different metamorphic grades (Fig. 3.13), this pattern is only conserved in samples below greenschist. For samples inside and above the greenschist facies, clustering disappears.

Boxplots (Fig. 3.14-3.15) show that $\delta^{15}\text{N}$ distributions do not significantly differ across the analyzed phase (Fig. 3.14A), lithology (Fig. 3.14B), metamorphism (Fig. 3.14C), and $\delta^{13}\text{C}_{\text{org}}$ (Fig. 3.14E). As for TOC/TN ratios, $\delta^{15}\text{N}$ values are higher and significantly more scattered for TOC/TN above 150 (Fig. 3.14D). Boxplots combining lithology and metamorphism show that $\delta^{15}\text{N}$ distributions in shales do not significantly differ across metamorphic grades (Fig. 3.15A).

In carbonates, $\delta^{15}\text{N}$ values are lower above greenschist, with narrower distributions with higher metamorphic grade (Fig. 3.15B). It is the same in cherts/BIFs, where $\delta^{15}\text{N}$ values above greenschist are lower, but this time with a more scattered distribution than for below greenschist and greenschist facies (Fig. 3.15C).

Crossplots showing paired $\delta^{15}\text{N}$ - $\delta^{13}\text{C}_{\text{org}}$ values for all data (Fig. 3.17A) or filtered according to the analyzed phase (Fig. 3.17B, 3.18) and TOC/TN ratios (Fig. 3.17E, 3.25) do not show any particular trends. Crossplots showing paired $\delta^{15}\text{N}$ - $\delta^{13}\text{C}_{\text{org}}$ values for different homogenized metamorphic grades/ranges/facies (Fig. 3.17C, 3.20) show a similar range of $\delta^{15}\text{N}$ values but a shift towards higher $\delta^{13}\text{C}_{\text{org}}$ values with increasing metamorphism. Crossplots showing paired $\delta^{15}\text{N}$ - $\delta^{13}\text{C}_{\text{org}}$ values for different lithologies (Fig. 3.17D, 3.19) show a similar range of $\delta^{15}\text{N}$ values, a similar range of $\delta^{13}\text{C}_{\text{org}}$ values for shales and carbonates, but a more restricted range of $\delta^{13}\text{C}_{\text{org}}$ values between -20 and -40‰ for cherts/BIFs.

Crossplots showing paired $\delta^{15}\text{N}$ - $\delta^{13}\text{C}_{\text{org}}$ values for shales (Fig. 3.21B, 3.22) or cherts/BIFs (Fig. 3.21D, 3.24) filtered by metamorphic grade show similar trends to those observed across all lithologies. However, crossplots showing paired $\delta^{15}\text{N}$ - $\delta^{13}\text{C}_{\text{org}}$ values for carbonates filtered by metamorphic grade (Fig. 3.21C, 3.23) show a shift towards lower $\delta^{15}\text{N}$ values and higher $\delta^{13}\text{C}_{\text{org}}$ with increasing metamorphism.

Crossplots showing paired $\delta^{15}\text{N}$ -TOC/TN values for all data (Fig. 3.26A) or filtered according to metamorphic grade (Fig. 3.26B, 3.28), lithology (Fig. 3.26C, 3.27), and metamorphic grade for the different lithologies, ie. shales (Fig. 3.26D, 3.29), carbonates (Fig. 3.26E, 3.30), and cherts/BIFs (Fig. 3.26F, 3.31) do not show any particular trends.

3.4. Discussion - Secular evolution of the $\delta^{15}\text{N}$ signature through the Precambrian

3.4.1. Potential biases that may impact our interpretation of the $\delta^{15}\text{N}$ secular evolution through the Precambrian

A number of biases need to be taken into account when considering potential large-scale trends and conclusions drawn from time series compilation. While identifying potential biases is mostly straightforward, evaluating their contribution to secular trends is challenging. Nevertheless, these biases question what is the best way to account for the $\delta^{15}\text{N}$ evolution through the Precambrian.

First, as it was the case for previously compiled datasets, some time intervals are overrepresented in terms of number of $\delta^{15}\text{N}$ data compared to others. The temporal resolution still displays some major gaps in the $\delta^{15}\text{N}$ record, particularly between 3.4-3.2 Ga, 3.2-3.0 Ga, 2.5-2.3 Ga, 1.8-1.6 Ga, 1.3-1.1 Ga, and 1.0-0.7 Ga (Fig. 3.4). Compared with the two compilations from 2016, no major temporal gaps have been filled, but the resolution has increased homogeneously. $\delta^{15}\text{N}$ data during the pre-GOE and GOE interval remain sparse. Towards the Phanerozoic, the number of available data considerably exceeds that of previous time intervals, risking of statistically biasing the conclusions on secular trends. In addition, the Proterozoic/Phanerozoic transition is complex and would deserve a study of its own. As for the spatial resolution, most time intervals are still being represented by data stemming from a single location, a single Formation or a single craton (Supplementary Table 3.1). This generates a dataset that is highly heterogenous, with some sedimentary successions and basins overly represented compared to others, which therefore dominate the distributions. For instance, this is the case for the Kaapvaal and Pilbara cratons, that have been extensively studied compared to other cratons, such as the Indian or Amazonian cratons. Besides, sampling intervals are not homogenous in space and time, and given that sedimentation rates for most Precambrian Formations are poorly constrained, the number of data per time interval is highly variable. It might not be relevant to compare drill cores of a few meters long to ones that are several hundred meters long. Statistical biases are also introduced by the fact that measurements alongside a transect or a drill core are not independent observations. Nevertheless, most biases mentioned above are inherent to practical constraints regarding preservation through the rock record and sample availability.

Moreover, $\delta^{15}\text{N}$ measurements compiled in this dataset were performed using different analytical techniques, on samples displaying highly variable nitrogen contents, therefore the reliability for each measurement is not equivalent. Indeed, contrary to the sealed-tube combustion method (Chapter 5), the EA-IRMS method does not allow to quantify the blank contribution, and may be less reliable for samples containing less than a few hundred ppms of N (Ader et al., 2016). As for the phase on which N measurements are performed, the updated $\delta^{15}\text{N}$ compilation is consistent with previous observations that $\delta^{15}\text{N}_{\text{ker}}$ are usually isotopically lighter compared to their bulk counterparts by about 2‰, (Fig. 3.16; Stüeken et al., 2017). The fact that this $\approx 2\text{‰}$ offset is homogenous across all studied lithologies and metamorphic grades (Fig. 3.16) confirms that it likely depends on the extraction procedure and/or isotopic measurement method. The good correlation ($R^2=0.75$) between $\delta^{15}\text{N}_{\text{bulk}}$ and $\delta^{15}\text{N}_{\text{ker}}$ across all

lithologies and metamorphic grades indicates that both bulk and kerogen N isotope measurements are likely to provide reliable information. Nevertheless, it remains interesting to compare the isotopic signature of these two phases on similar samples, when possible, to refine our understanding of the factors that may lead to isotope partitioning.

The different parameters that have been selected to filter the studied $\delta^{15}\text{N}$ dataset are also a source of bias. For the sake of simplicity, lithology has been assigned for each set of sedimentary $\delta^{15}\text{N}$ data, based on the main lithology as described in the source publication. Therefore, all variability inside a given formation has been smoothed, which may bias the dataset for formations with heterogeneous lithologies. As for $\delta^{13}\text{C}_{\text{org}}$ ranges, they are dependent on paleo partial CO_2 pressures, which may have varied throughout Earth history, on conservation of the range of fractionation for different metabolisms back to the Archean, and on the assumption that the ocean DIC remained at 0‰. Similarly, TOC/TN ratios are only relevant to study thermal denitrogenation or ammonium addition if no joint C loss has occurred. It is also relevant to consider that among the different parameters that have been selected to filter the $\delta^{15}\text{N}$ dataset, the number of data for the different categories is highly variable. For instance, shales are overrepresented compared to cherts/BIFs, $\delta^{15}\text{N}$ measurements are preferentially made on low metamorphosed samples, limiting the risk of metamorphic alteration. For the reader to keep this bias in mind, the number of data has been added to most graphs.

Another major uncertainty is how to account for the depositional environment. It should be reflected at least partially in the lithology, but some are debated, such as for cherts and BIFs. Even for individual studies, the depositional environment is not always well-constrained, if not controversial.

3.4.2. First-order secular variations of the $\delta^{15}\text{N}$ signature through the Precambrian

One major takeaway from this chapter is that the updated $\delta^{15}\text{N}$ compilation shows similar first-order secular variations of the $\delta^{15}\text{N}$ signature regardless of the analyzed phase, lithology, metamorphic grade, range of $\delta^{13}\text{C}_{\text{org}}$ values or TOC/TN ratios (Fig. 3.4-3.10). First-order $\delta^{15}\text{N}$ secular variations can therefore be interpreted in terms of N-biogeochemical cycle and hence paleoenvironmental changes. Given that those secular trends in Precambrian N isotope data were interpreted as showing a three-step evolution of the marine N-biogeochemical cycle (Ader

et al., 2016; Stüeken et al., 2016), from an ammonium-dominated “reduced” N cycle in pre-GOE anoxic oceans, followed by a rise of oceanic oxidants during the Neoproterozoic some time before the GOE, possibly even as early as 2.7 Ga, and later by the progressive stabilization of a persistent nitrate reservoir in oxygenated surface waters (Fig. 3.3), the N-biogeochemical cycle dynamics that has been proposed for different stages in Earth’s history from the Mesoarchean to the beginning of the Phanerozoic (Fig. 3.3) remains both relevant and subject to unresolved questions about the mechanism and timing of the N-cycle evolution from anoxic to oxic.

3.4.3. Identifying analytical biases, secondary alteration and paleoenvironmental changes

Alongside large-scale patterns in Precambrian $\delta^{15}\text{N}$ data with time, cross-examining key indicators, such as $\delta^{15}\text{N}$, $\delta^{13}\text{C}_{\text{org}}$, TOC, TN, and TOC/TN ratios, for different lithologies and metamorphic ranges, may point towards analytical biases, secondary alteration or paleoenvironmental changes. Identifying such patterns from a database spanning all of the Precambrian is interesting, as it gives an opportunity for future studies to select preferential complementary indicators to measure and to test hypotheses made on a large dataset on specific cases.

The main analytical bias that can affect $\delta^{15}\text{N}$ measurements is the contribution of analytical blanks. Blank quantities, and therefore blank contributions for each sample measurement can be determined when using the sealed tubes combustion technique (Chapter 5), which is not possible with the EA-IRMS method used for most Precambrian $\delta^{15}\text{N}$ measurements. While this blank contribution is likely to be negligible for samples containing more than 1 μmole of N (Ader et al., 2016), it could be significant for smaller N quantities, representative of many Precambrian rocks. Any Precambrian $\delta^{15}\text{N}$ measurement for which the associated TOC/TN value is lower than 50 (Fig. 3.10B) should be considered likely to hold a significant blank contribution (Ader et al., 2016; Yamaguchi, 2002), unless the proportion of mineral N compared to organic N is important (i.e. for clay-rich samples). When possible, TN and $\delta^{15}\text{N}$ values should be individually corrected from the blank contribution, either using the reference blank value of $\delta^{15}\text{N} = -3.7\text{‰}$ measured by Busigny et al. (2005) or using $\delta^{15}\text{N}_{\text{air}} = 0\text{‰}$. Blank-corrected $\delta^{15}\text{N}$ values are usually higher than their raw counterparts. In individual studies where the blank contribution cannot be readily quantified, preventing $\delta^{15}\text{N}$ corrections, one way to spot blank

contamination might be to look for correlations between TN contents and $\delta^{15}\text{N}$ values. The shift towards lower $\delta^{15}\text{N}$ values in carbonates might result from a higher blank contribution than in shales, as shales generally have higher TN contents than carbonates (Fig. 3.21).

As for secondary alteration, post-depositional processes, i.e. diagenesis, metamorphism and metasomatism can affect the organic matter preserved in sediments, by shifting TOC, TN, TOC/TN, $\delta^{15}\text{N}$ and $\delta^{13}\text{C}_{\text{org}}$ values. During the graphitization process that accompanies prograde metamorphism, the reorganization of the aromatic structure progressively allows isotope exchange between coexisting carbonaceous matter and carbonates, leading to organic matter enrichment in ^{13}C (Wada et al., 1994). Fractionations can go from a few permil to 20‰, depending on the temperature and the lithology. Significant $\delta^{13}\text{C}_{\text{org}}$ modifications can start at 300°C with the formation of the first graphite crystals (Kitchen and Valley, 1995). Isotopic equilibrium can only be reached when all the organic matter has been graphitized, which can start at 500°C but in numerous cases is not attained below 700°C. TN, TOC/TN and $\delta^{15}\text{N}$ can either be modified by nitrogen devolatilization preferentially to carbon during graphitization, ammonium input and mobility through fluids and/or fractionation during these processes (Chapter 2). Organic N and mineral N (fixed NH_4^+ that substitutes for K^+ in some phyllosilicates) often coexist in samples, and may be affected differently by post-depositional processes (Chapter 2). While an increase in $\delta^{15}\text{N}$ and a decrease in TN is usually seen during prograde metamorphism (Bebout and Fogel, 1992; Boyd and Philippot, 1998; Haendel et al., 1986; Jia, 2006), maximum isotopic enrichments documented for greenschist facies metamorphism are below 2‰ (Jia, 2006; Stüeken et al., 2017), and those documented for amphibolite and upper amphibolite facies metamorphism can go up to +4‰ and +10‰, respectively (Bebout et al., 1999; Bebout and Fogel, 1992; Boyd and Philippot, 1998; Haendel et al., 1986; Jia, 2006; Mingram et al., 2005; Mingram and Bräuer, 2001; Pitcairn et al., 2005; Plessen et al., 2010; Yui et al., 2009). The more positive $\delta^{13}\text{C}_{\text{org}}$ values with increasing metamorphic grade observed for the whole dataset of the compilation (Fig. 3.17C, 3.20) point towards a contribution of secondary alteration of the $\delta^{13}\text{C}_{\text{org}}$ signal. This trend is similar in the shales subset (Fig. 3.21B, 3.22). In cherts/BIFs, the absence of $\delta^{13}\text{C}$ values > -20 ‰ suggests that this lithology might be more resistant to metamorphic alteration (Fig. 3.21D, 3.24). In highly carbonated rocks, which also have lower TOC contents compared to shales, the clear shift towards more positive $\delta^{13}\text{C}_{\text{org}}$ values with increasing metamorphic grade compared to shales and cherts/BIFs (Fig. 3.21C, 3.23) could point towards partial or complete isotopic reequilibration of the organic matter with the carbonates. In that case the $\delta^{13}\text{C}_{\text{org}}$ signature would

not be directly meaningful in terms of paleo primary productivity and carbon fixation pathways. The nitrogen isotope signature recorded in carbonated samples also seems to be more sensitive to metamorphism than in shales. Indeed, Precambrian carbonates above the greenschist facies consistently display an increased $\delta^{13}\text{C}$ and a decreased $\delta^{15}\text{N}$ signal, which is not the case for shales (Fig. 3.21C, 3.23). Most metamorphosed carbonates seem to be both ^{13}C -enriched and ^{15}N -depleted compared to shales and cherts/BIFs in the same metamorphic range. This might be accountable to both analytical biases (for N) and post-depositional modifications (for C). Further work needs to be conducted to assess if this trend indeed reflects a higher sensitivity of carbonates to alteration processes or if carbonates could hold the potential to record different processes of the N-biogeochemical cycle or different paleoenvironments than shales and cherts/BIFs.

In terms of depositional environment, it should be reflected by sorting $\delta^{15}\text{N}$ data according to $\delta^{13}\text{C}_{\text{org}}$ values and lithology, if none of these indicators have been altered. As most Precambrian N isotope compositions are measured in shales, which are supposed to be more representative of global oceans, it is interesting to determine whether carbonates and cherts/BIFs also provide relevant archives to trace early Earth oxygenation using N isotopes.

3.5. Conclusions

The updated Precambrian $\delta^{15}\text{N}$ database provides an opportunity to explore nitrogen isotope variations on long timescales, and hopefully pinpoint secular changes reflecting the evolution of the global N-biogeochemical cycle. It also provides an opportunity to explore potential links between the nitrogen isotope signature and key parameters such as metamorphism, lithology, depositional environment, TOC contents, TN contents, TOC/TN ratios, or $\delta^{13}\text{C}_{\text{org}}$ values. In addition to continue filling the major gaps in the Precambrian $\delta^{15}\text{N}$ records, especially before and around the Great Oxidation Event and the Archean/Proterozoic transition, future nitrogen isotope studies might benefit from improving our understanding of the joint impact of lithology and metamorphism on paired $\delta^{15}\text{N}$ - $\delta^{13}\text{C}_{\text{org}}$ signatures.

The main results yielded by this compilation, and the subsequent research questions it has allowed us to identify are:

- 1- The $\delta^{15}\text{N}$ secular variations evidenced using this compilation seem to be robust at first order. Improving the resolution of time intervals where data is scarce and where redox changes are

thought to have occurred is therefore meaningful in order to refine existing interpretations regarding the links between the evolution of the N-biogeochemical cycle through time and oceans oxygenation. This might allow us to gain some insights into the exact timing and mechanisms of N-biogeochemical cycle changes.

Three low density time periods and/or key for the evolution of the N-biogeochemical cycle have been selected for this thesis:

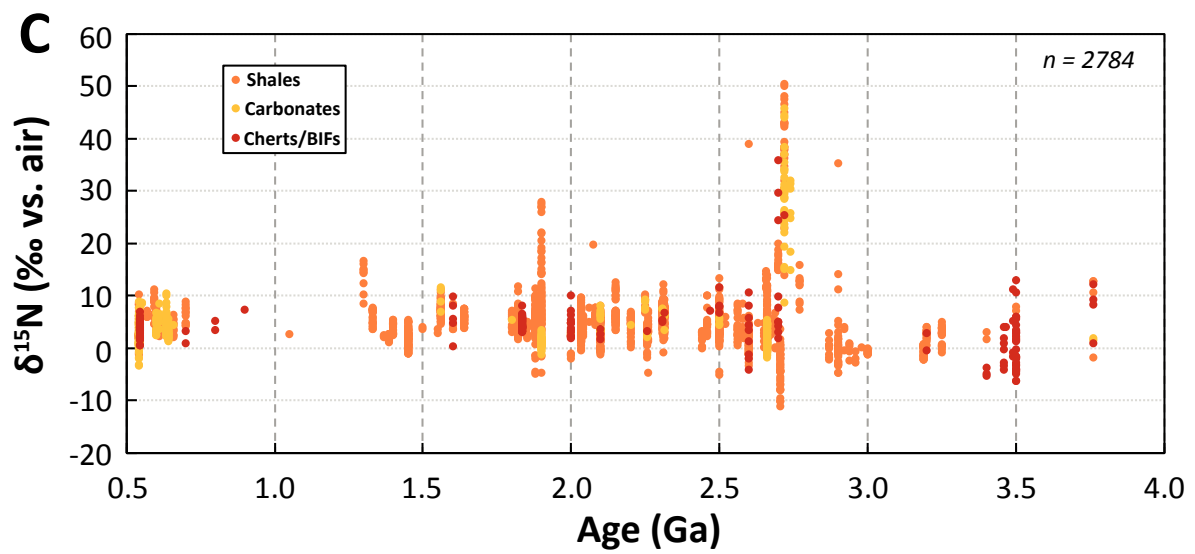
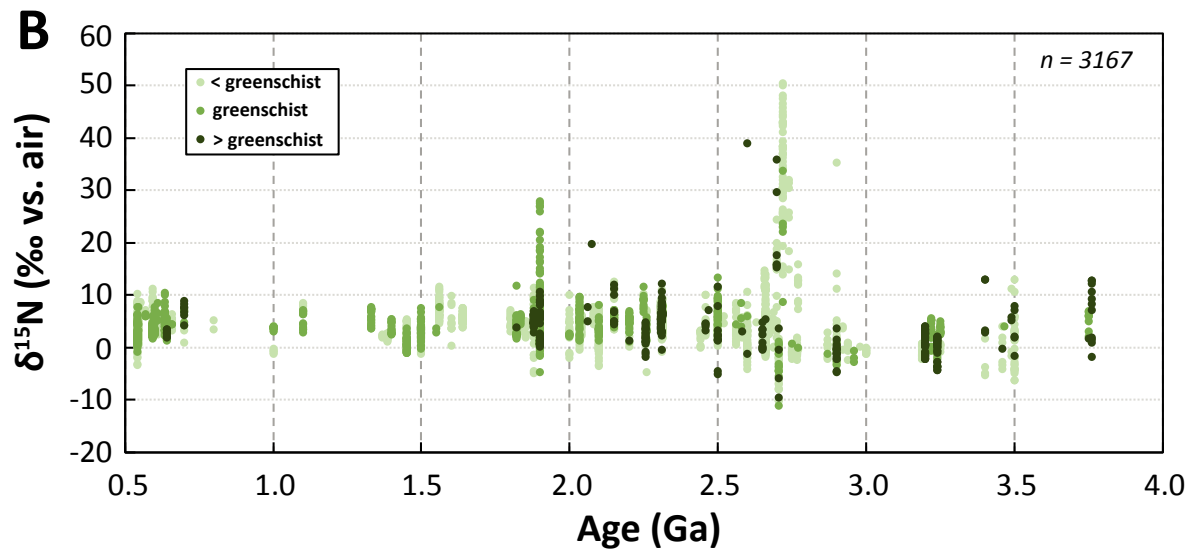
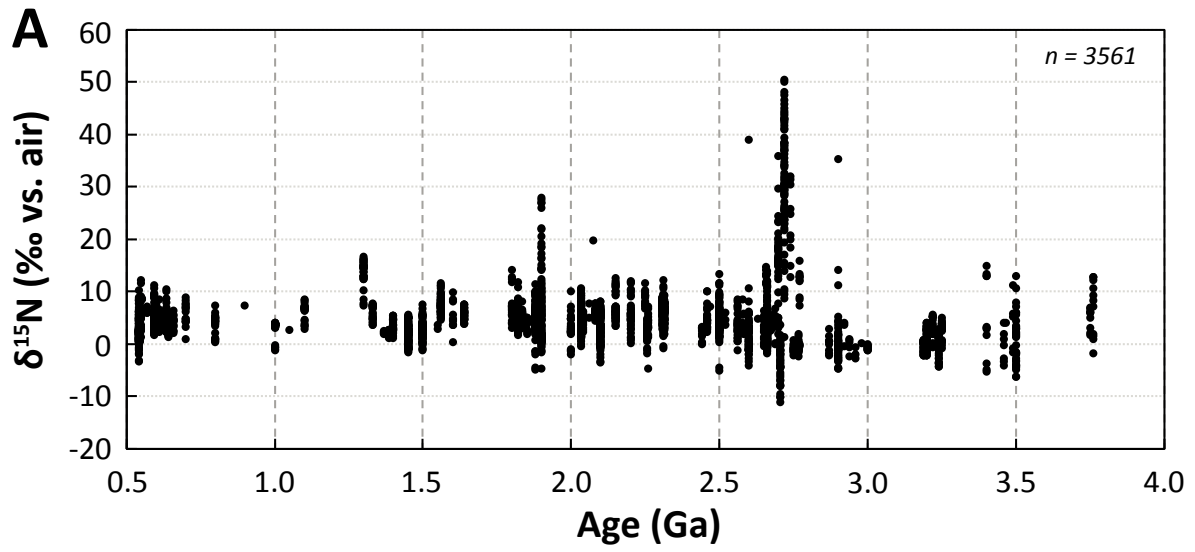
- The 3.5-3.2 Ga time interval, here we might expect low $\delta^{15}\text{N}$ signatures close to 0‰, typical of fully anoxic environments.
- The 2.8-2.6 Ga time interval, comprising the most extreme $\delta^{15}\text{N}$ values ever recorded ($\delta^{15}\text{N}$ up to +50‰), which significance in terms of global N-biogeochemical cycle remains debated, due to their occurrence in a single Formation.
- The 2.6-2.5 Ga time interval, just before or during the onset of the GOE, where redox changes are expected.

2 – The Precambrian $\delta^{15}\text{N}$ compilation suffers from sampling bias. Indeed, most $\delta^{15}\text{N}$ measurements were made on shales compared to other lithologies, such as carbonates or cherts/BIFs, because shales are supposed to be more representative of marine settings. Nevertheless, other lithologies might provide additional information regarding the evolution of the N-biogeochemical cycle through time. Likewise, very few $\delta^{15}\text{N}$ measurements were performed on highly metamorphosed rocks above the greenschist facies. While the reason lies in the better chance of preservation of the $\delta^{15}\text{N}$ signature in low metamorphosed rocks, it might be interesting to assess whether some lithologies best preserve the $\delta^{15}\text{N}$ signal with increasing metamorphic grade.

3 - The range of $\delta^{15}\text{N}$ variations for any given time interval is quite large. Thus, second order dependencies to factors such as TOC, TN, TOC/TN, $\delta^{13}\text{C}_{\text{org}}$, lithology, metamorphism, or depositional environment, might be worth exploring and remain to be better constrained. The updated compilation seems to validate previous results showing a moderate to low increase in $\delta^{15}\text{N}$ with metamorphism. It shows for the first time that carbonate rocks that underwent metamorphism higher than the greenschist facies present both heavier $\delta^{13}\text{C}_{\text{org}}$ values, compatible with the onset of isotope exchange between carbonates and organic matter, and lower $\delta^{15}\text{N}$ values, towards 0‰. Because these samples are also those presenting the lowest TN contents, it is possible that these $\delta^{15}\text{N}$ represent a blank contribution. Here, carbonate samples

from the 2.5 Ga Malmani Subgroup metamorphosed in the greenschist facies will allow to investigate this issue using a method for which the blank contribution can be quantified and corrected.

In the future, similar compilation work might be performed on other isotopic tracers such as $\delta^{34}\text{S}$, $\delta^{56}\text{Fe}$ or REEs following the same factor dependencies, and put in parallel.



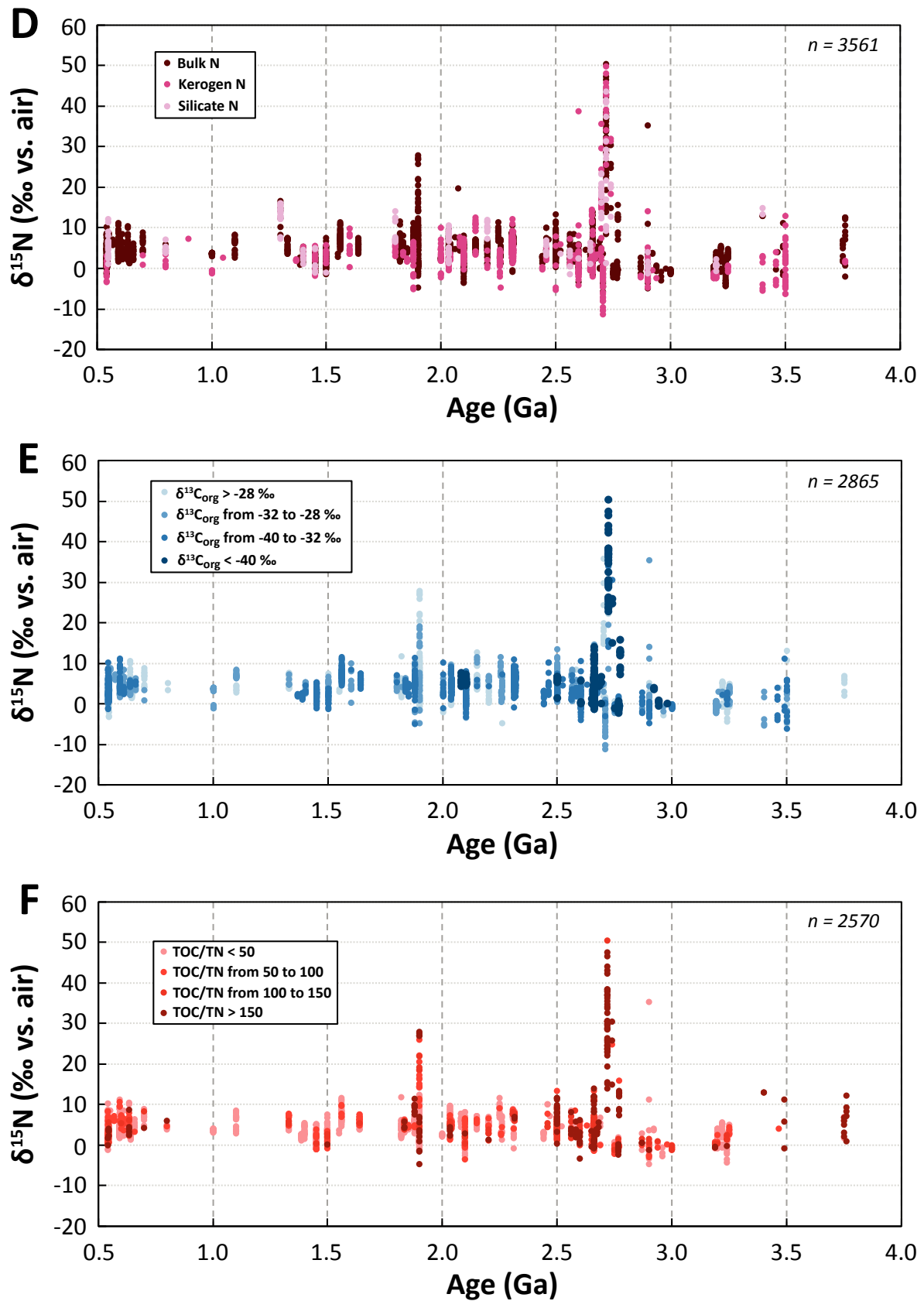


Fig. 3.4. Secular trends in $\delta^{15}\text{N}$ data through the Precambrian (4.0-0.5 Ga) for: (A) all available $\delta^{15}\text{N}$ data; (B) $\delta^{15}\text{N}$ data sorted according to metamorphic grade (lower than greenschist, greenschist, higher

than greenschist); (C) $\delta^{15}\text{N}$ data sorted according to lithology (shales, carbonates, cherts/BIFs); (D) $\delta^{15}\text{N}$ data sorted according to the analyzed phase (bulk N, kerogen N, silicate N); (E) $\delta^{15}\text{N}$ data sorted according to paired $\delta^{13}\text{C}_{\text{org}}$ values; (F) $\delta^{15}\text{N}$ data sorted according to TOC/TN ratios. n indicates the number of data points for each graph.

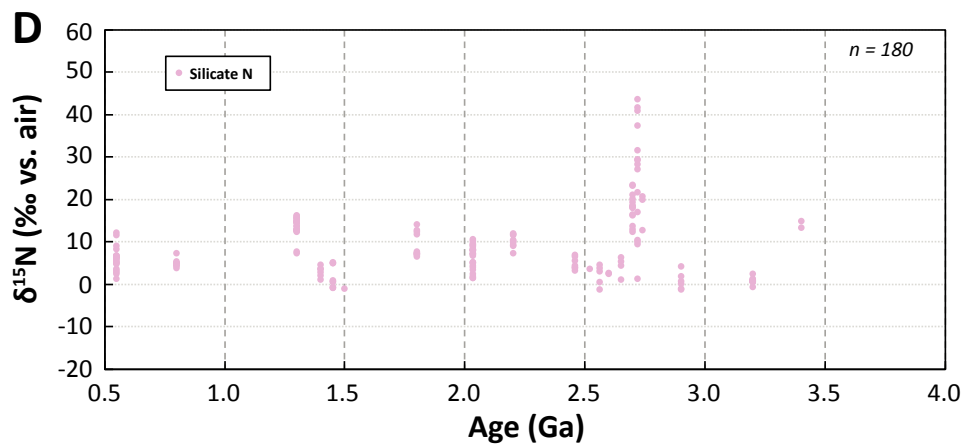
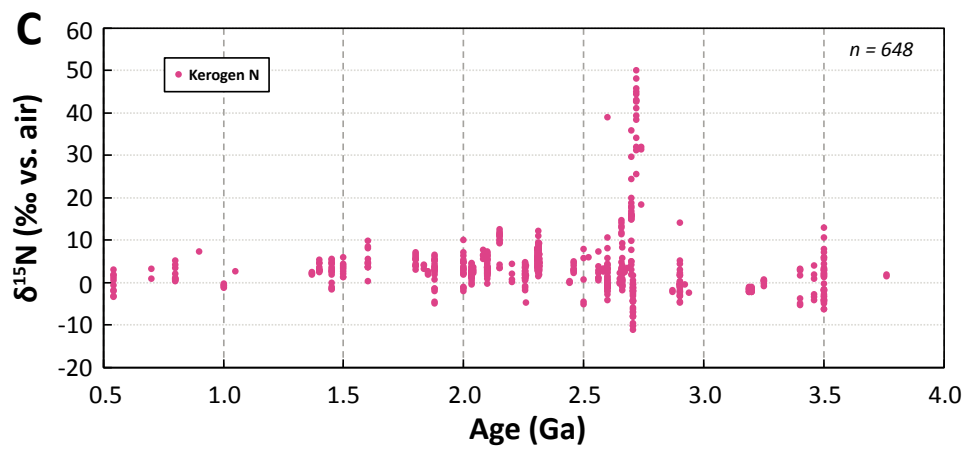
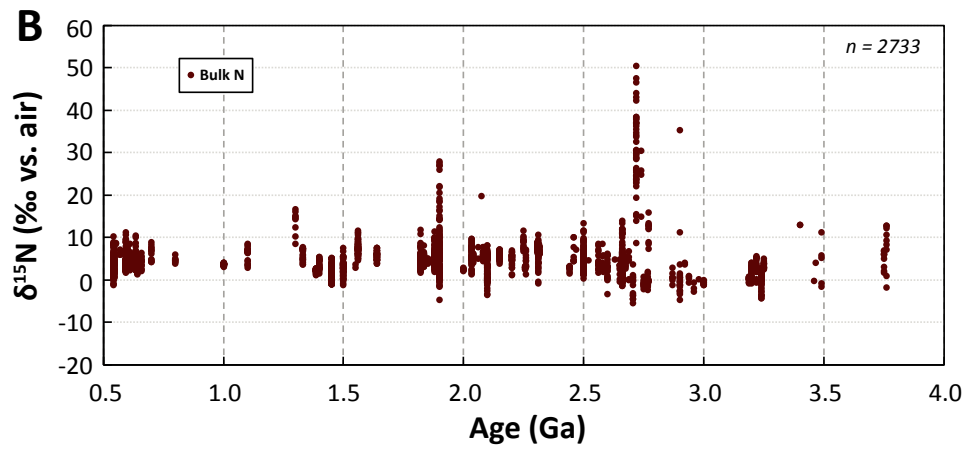
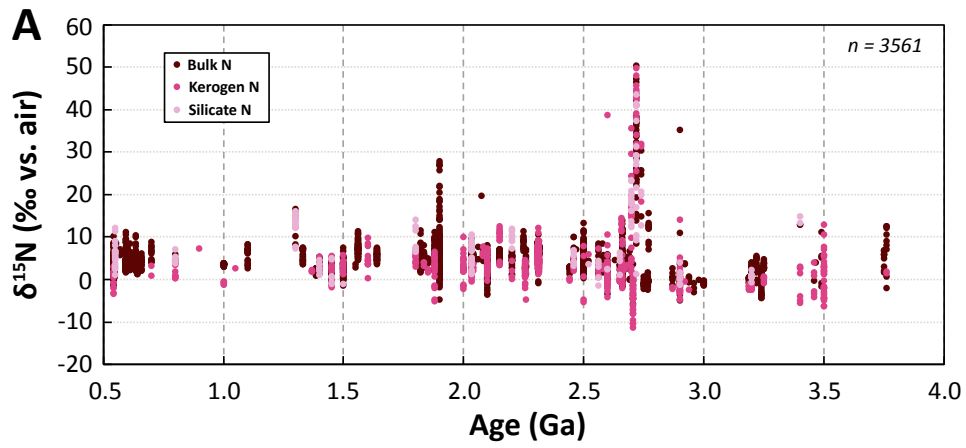


Fig. 3.5. Secular trends in $\delta^{15}\text{N}$ data through the Precambrian (4.0-0.5 Ga) for: (A) all $\delta^{15}\text{N}$ data sorted according to the analyzed phase (bulk N, kerogen N, silicate N); (B) bulk N; (C) kerogen N; (D) silicate N. n indicates the number of data points for each graph.

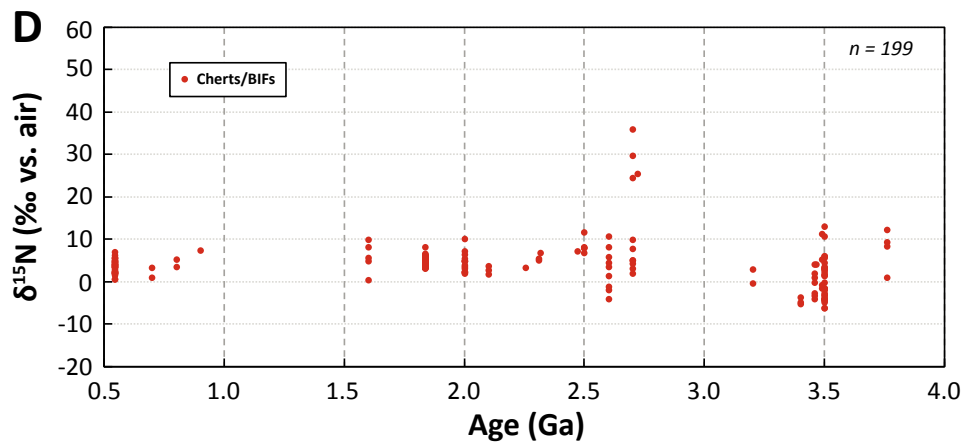
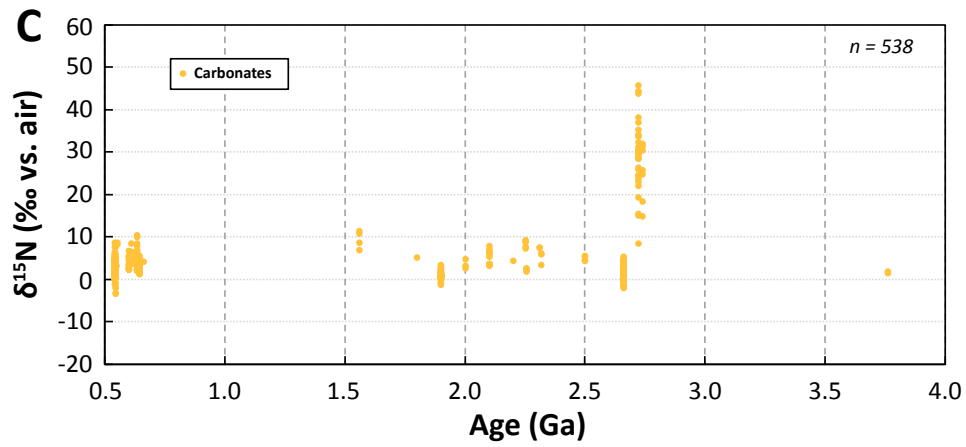
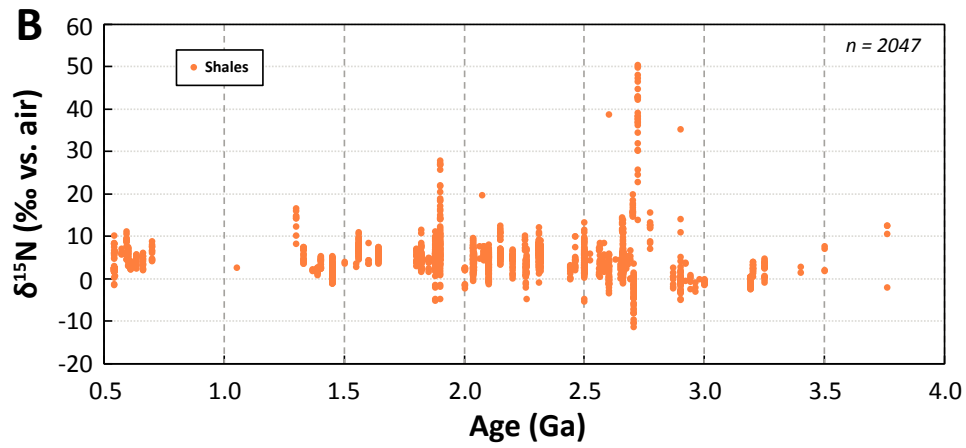
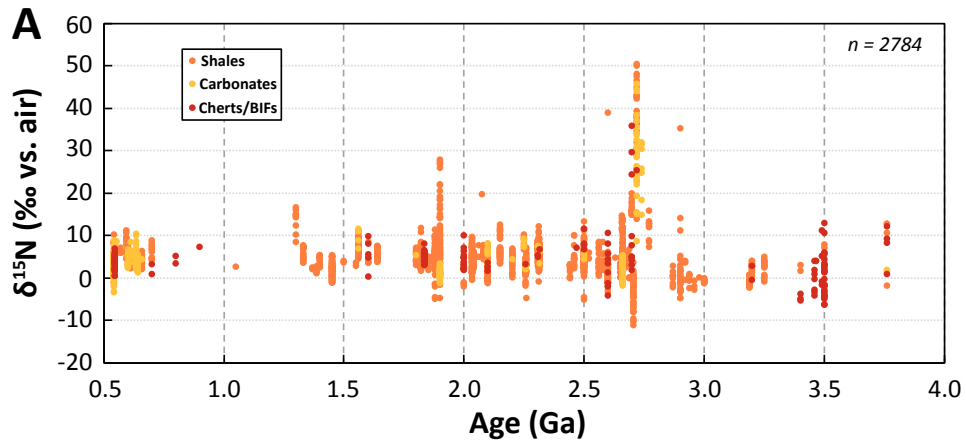


Fig. 3.6. Secular trends in $\delta^{15}\text{N}$ data through the Precambrian (4.0-0.5 Ga) for: (A) all $\delta^{15}\text{N}$ data sorted according to lithology (shales, carbonates, cherts/BIFs); (B) shales; (C) carbonates; (D) cherts/BIFs. n indicates the number of data points for each graph.

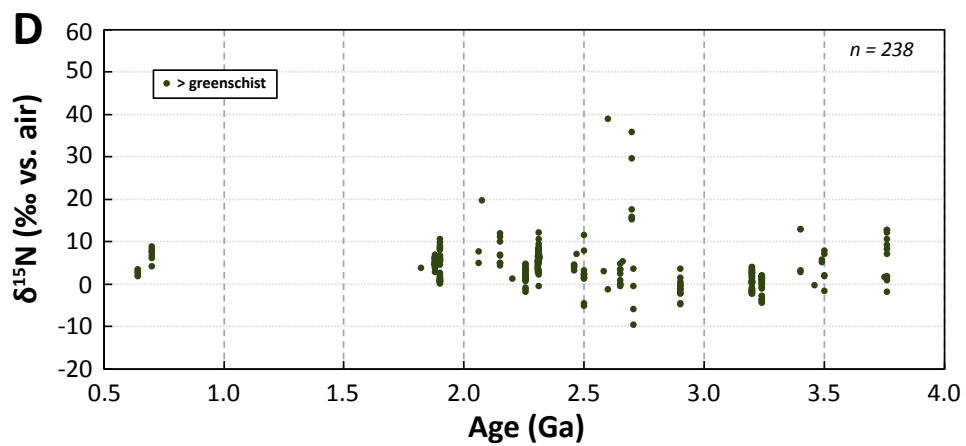
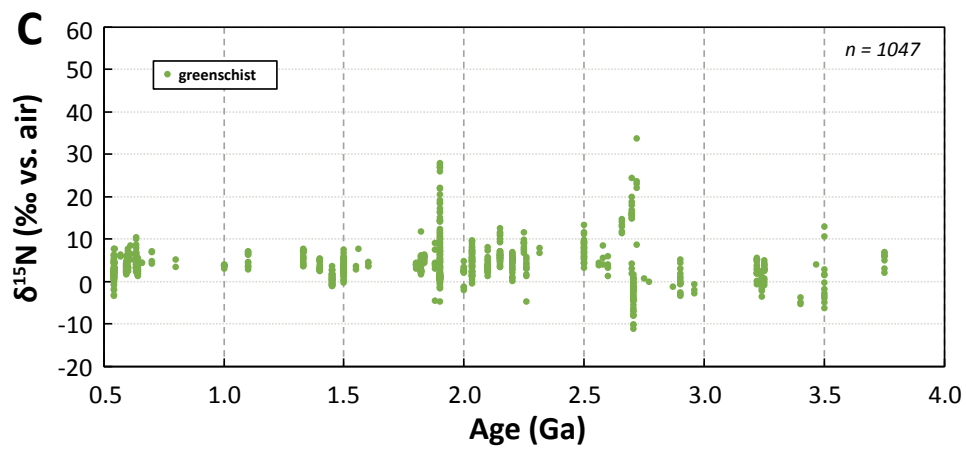
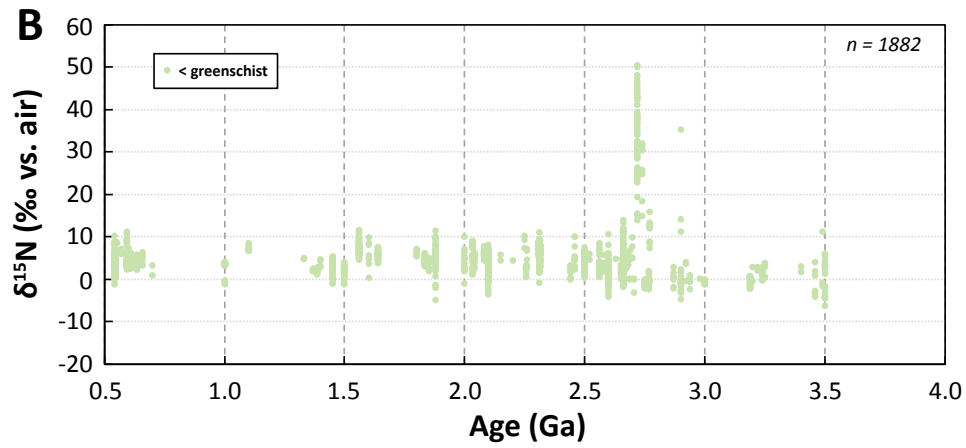
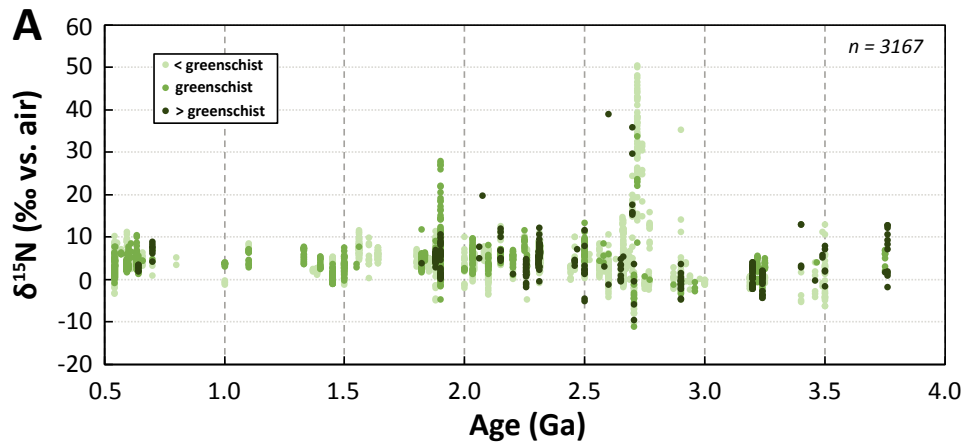


Fig. 3.7. Secular trends in $\delta^{15}\text{N}$ data through the Precambrian (4.0-0.5 Ga) for: (A) all $\delta^{15}\text{N}$ data sorted according to metamorphic grade (lower than greenschist, greenschist, higher than greenschist); (B) lower than greenschist; (C) greenschist; (D) higher than greenschist. n indicates the number of data points for each graph.

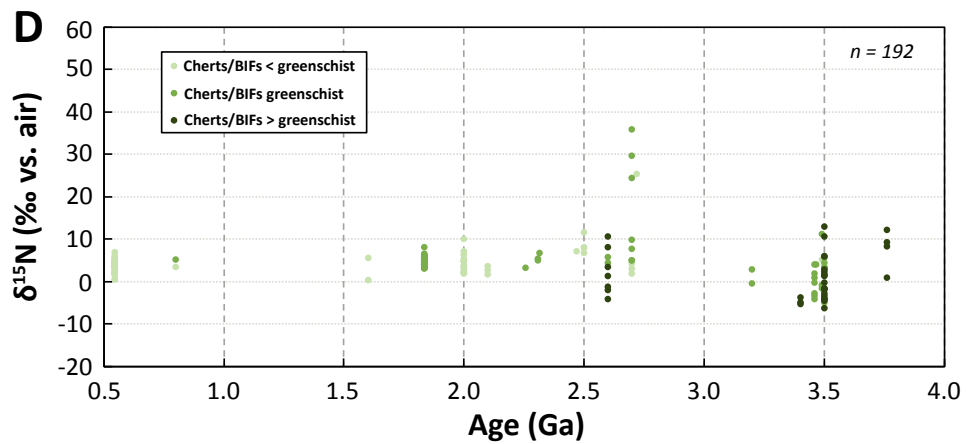
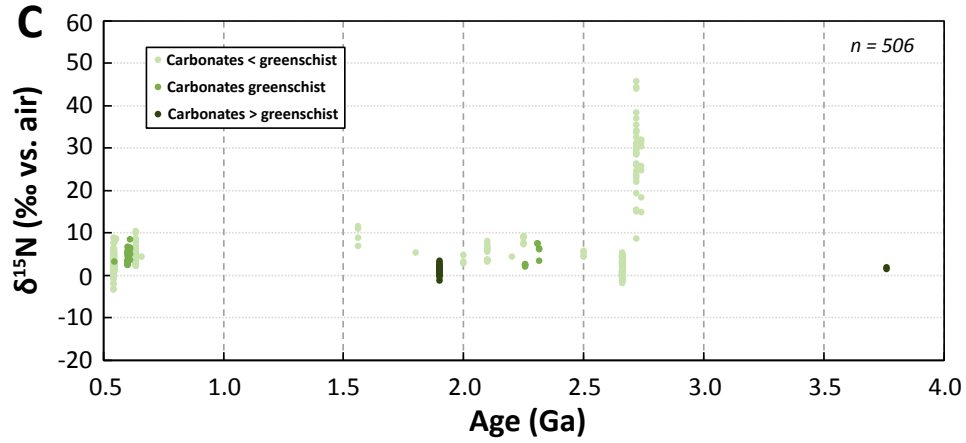
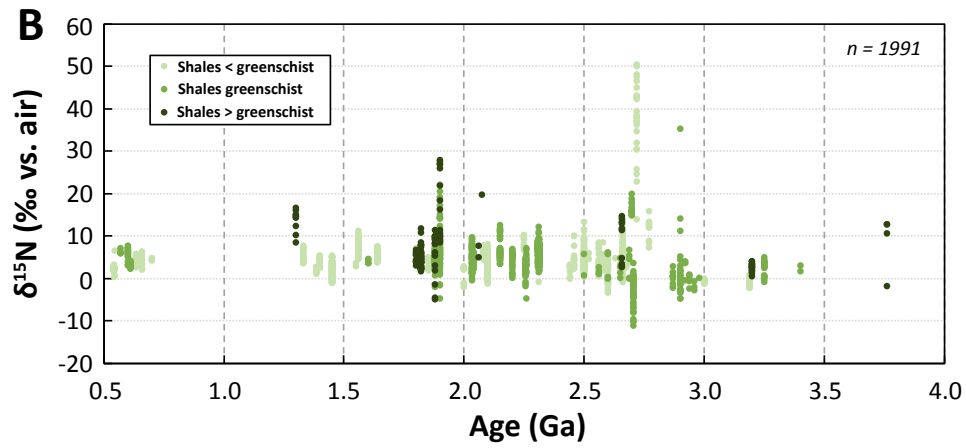
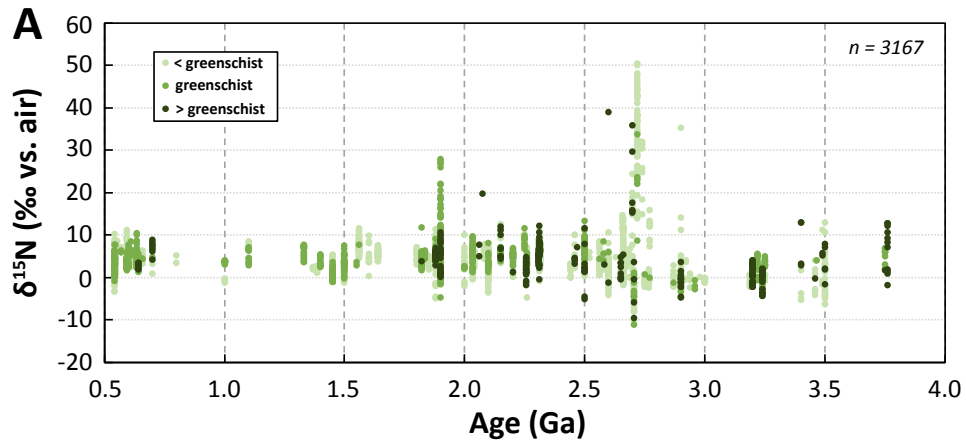


Fig. 3.8. Secular trends in $\delta^{15}\text{N}$ data through the Precambrian (4.0-0.5 Ga) for $\delta^{15}\text{N}$ data sorted according to metamorphic grade (lower than greenschist, greenschist, higher than greenschist) for (A) all lithologies; (B) shales; (C) carbonates; (D) cherts/BIFs. n indicates the number of data points for each graph.

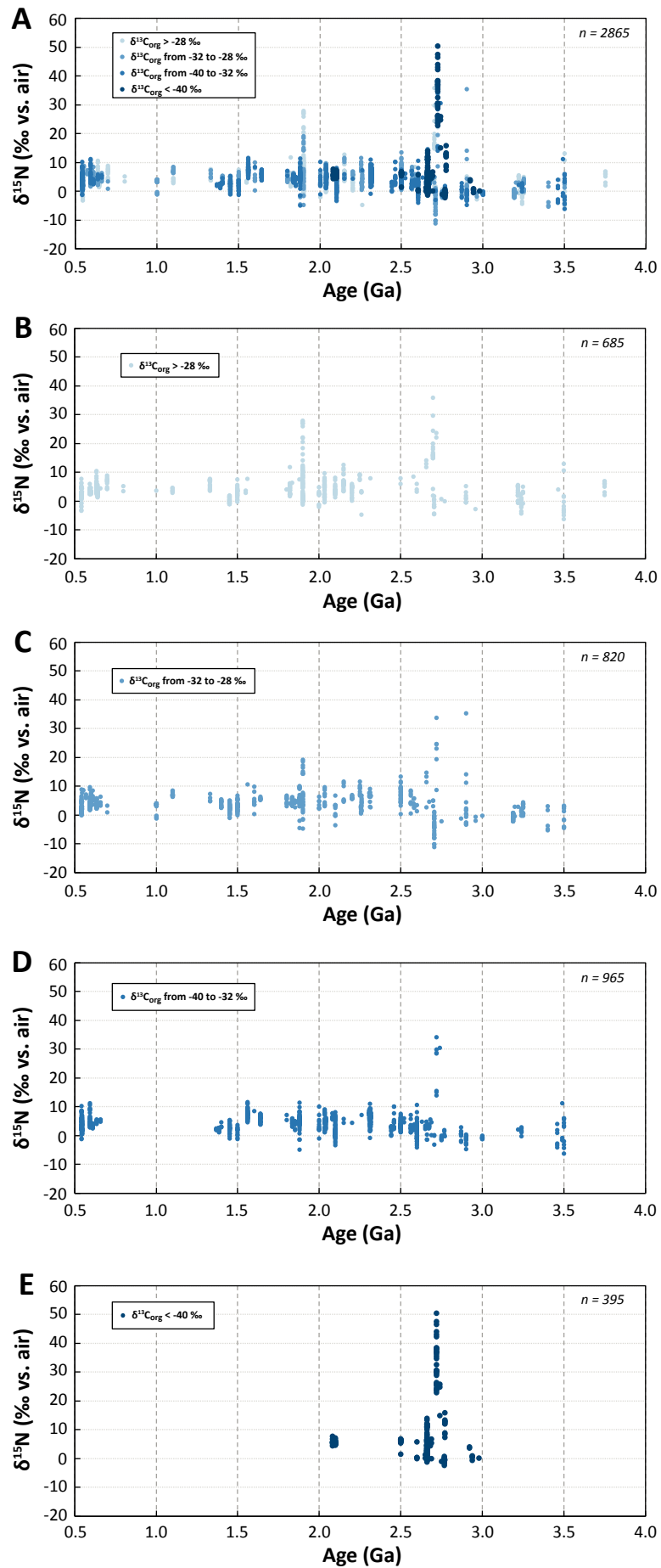


Fig. 3.9. Secular trends in $\delta^{15}\text{N}$ data through the Precambrian (4.0-0.5 Ga) for $\delta^{15}\text{N}$ data sorted according to paired $\delta^{13}\text{C}_{\text{org}}$ values for: (A) all $\delta^{13}\text{C}_{\text{org}}$ ranges of values; (B) $\delta^{13}\text{C}_{\text{org}}$ values above -28‰; (C) $\delta^{13}\text{C}_{\text{org}}$ values between -28‰ and -32‰; (D) $\delta^{13}\text{C}_{\text{org}}$ values between -32‰ and -40‰; (E) $\delta^{13}\text{C}_{\text{org}}$ values below -40‰. n indicates the number of data points for each graph.

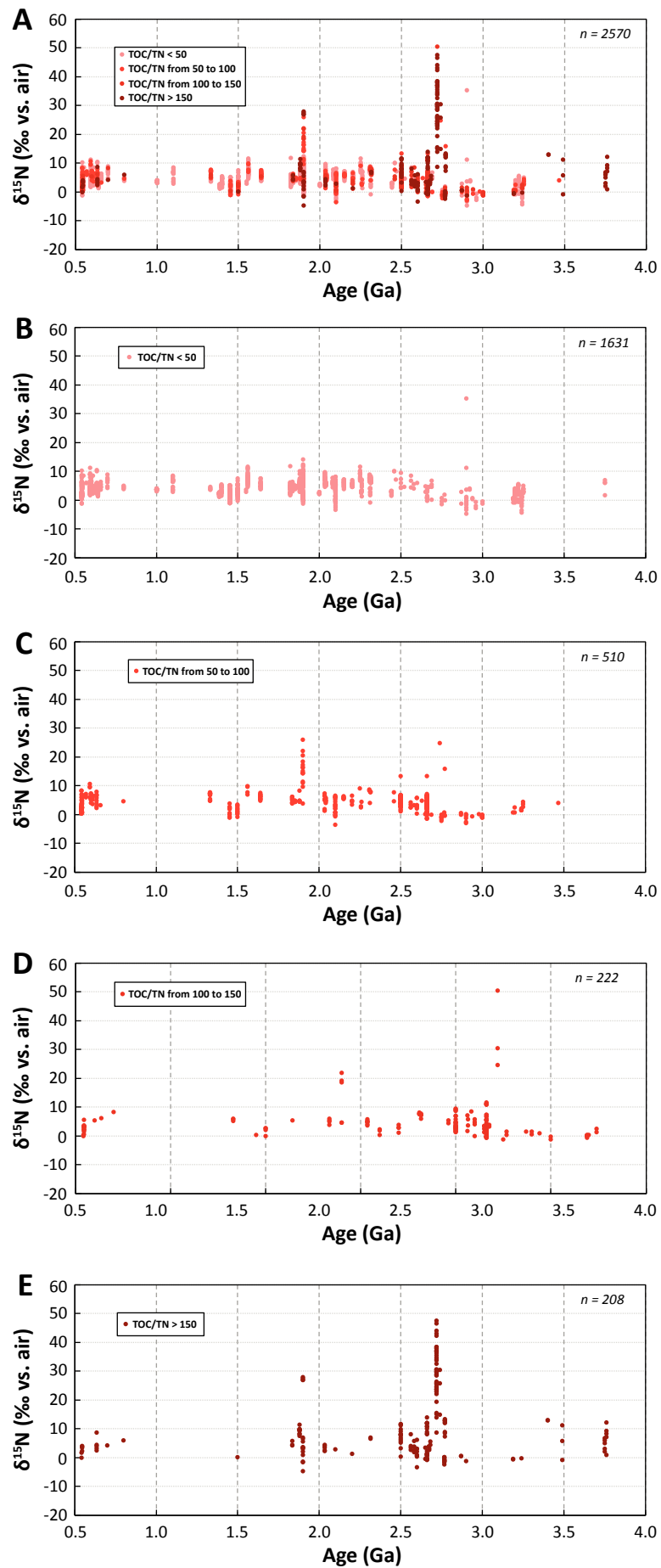


Fig. 3.10. Secular trends in $\delta^{15}\text{N}$ data through the Precambrian (4.0-0.5 Ga) for $\delta^{15}\text{N}$ data sorted according to TOC/TN ratios: (A) all TOC/TN ranges of values; (B) TOC/TN values below 50; (C) TOC/TN values between 50 and 100; (D) TOC/TN values between 100 and 150; (E) TOC/TN values above 150. n indicates the number of data points for each graph.

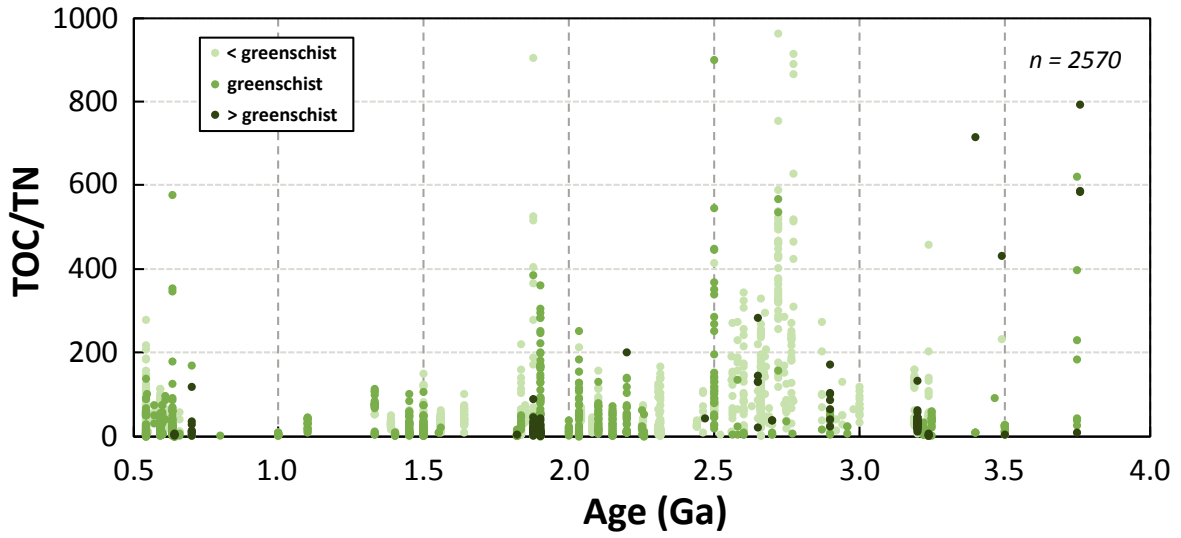


Fig. 3.11. Secular trends in TOC/TN data through the Precambrian (4.0-0.5 Ga) sorted according to metamorphic grade (lower than greenschist, greenschist, higher than greenschist). n indicates the number of data points for each graph.

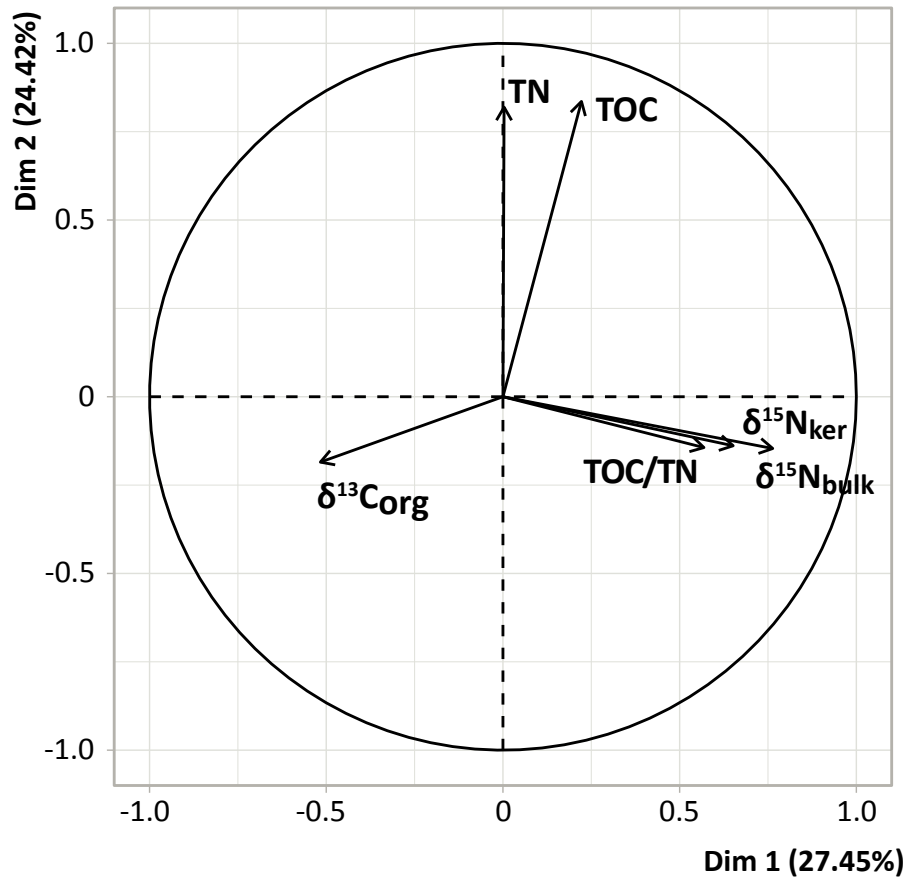


Fig. 3.12. Biplot of the variables ($\delta^{15}\text{N}_{\text{bulk}}$, $\delta^{15}\text{N}_{\text{ker}}$, $\delta^{13}\text{C}_{\text{org}}$, TOC, TN, and TOC/TN) with respect to the principal components for the whole dataset. 51.87% of the variability is explained by the plane, which can be considered significant. Variables that are grouped together are positively correlated to each other, while variables that are negatively correlated are displayed to the opposite sides of the biplot's origin. the higher the distance between the variable and the origin, the better that variable is represented.

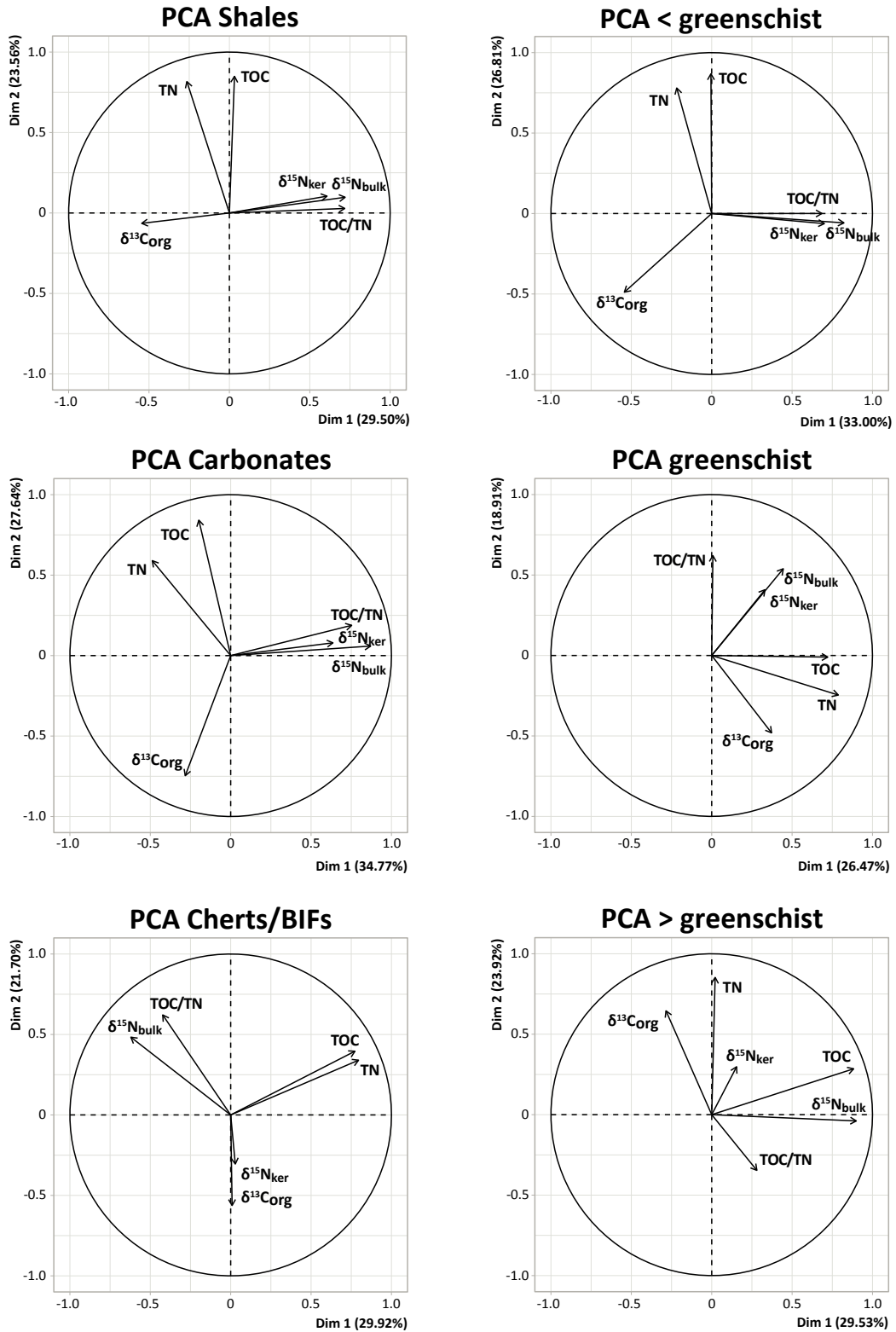
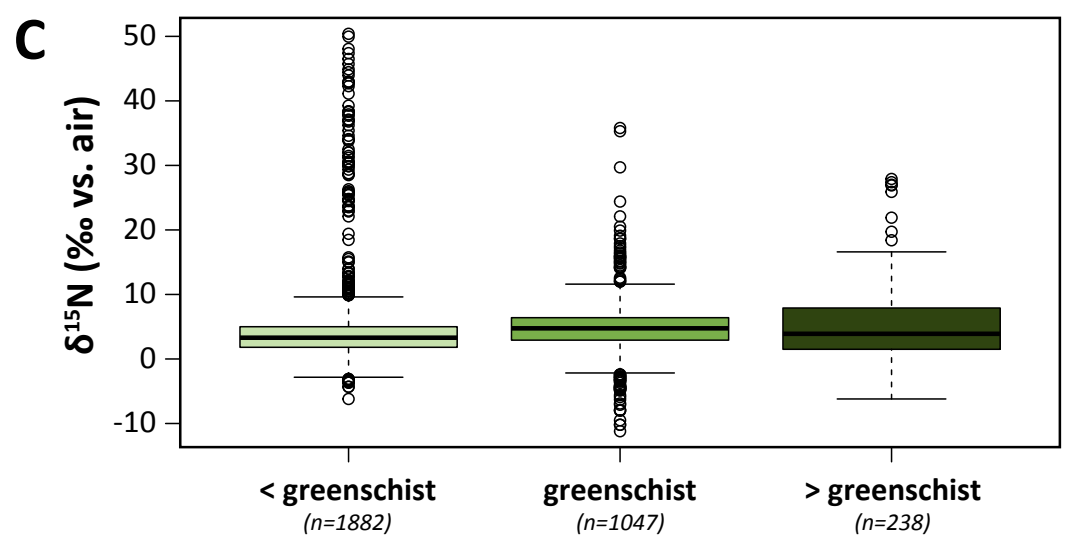
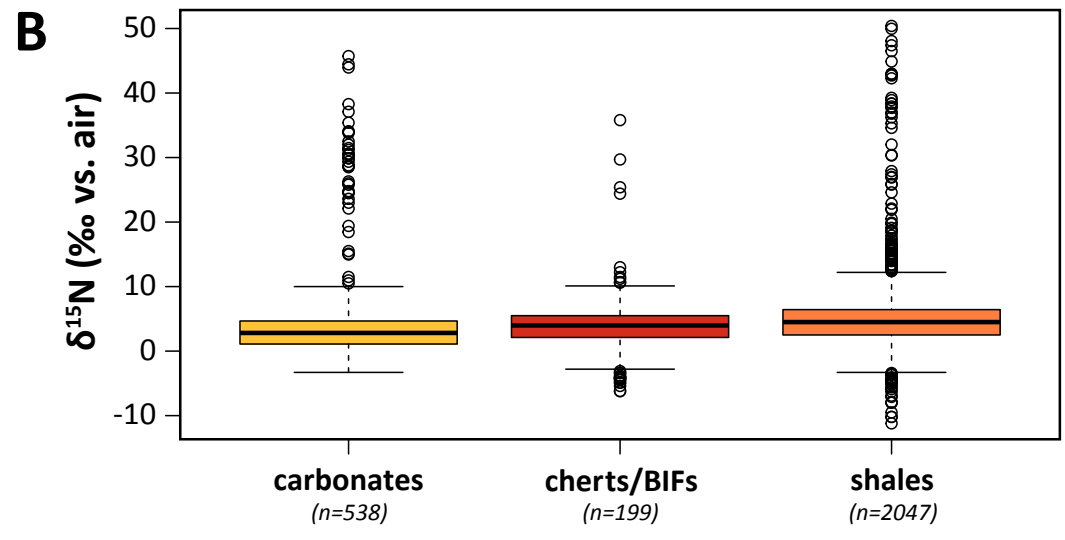
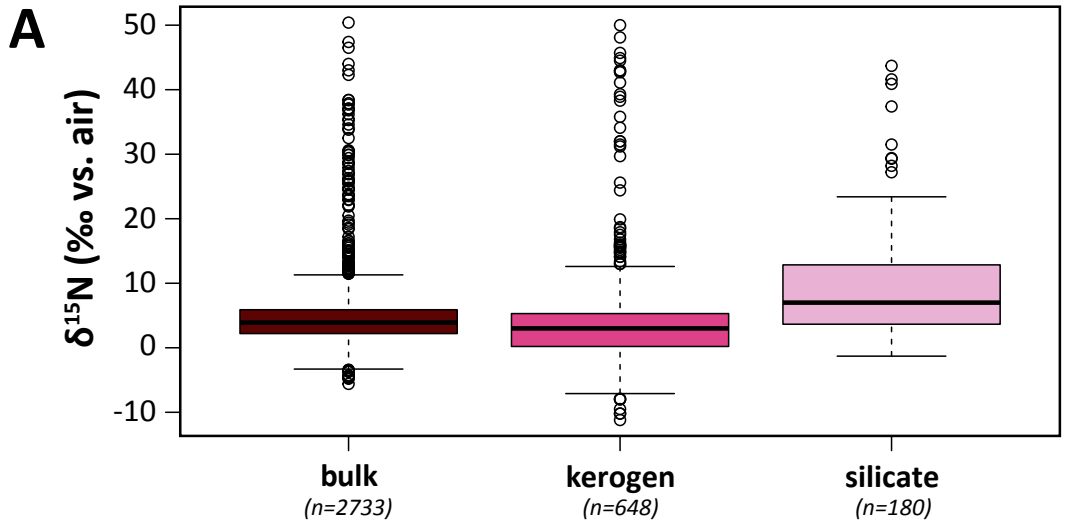


Fig. 3.13. Biplot of the variables ($\delta^{15}N_{bulk}$, $\delta^{15}N_{ker}$, $\delta^{13}C_{org}$, TOC, TN, and TOC/TN) with respect to the principal components for the three main lithologies (shales, carbonates, and cherts/BIFs) and the three main metamorphic grades (lower than greenschist, greenschist, higher than greenschist). Concerning the lithology, 53.06%, 62.41% and 51.62% of the variability is explained by the plane for shales, carbonates

and cherts/BIFs, respectively, which can be considered significant. Concerning the metamorphic grade, 59.81%, 45.38% and 53.45% of the variability is explained by the plane for samples lower than greenschist, greenschist and higher than greenschist, respectively, which can also be considered significant. Variables that are grouped together are positively correlated to each other, while variables that are negatively correlated are displayed to the opposite sides of the biplot's origin. the higher the distance between the variable and the origin, the better that variable is represented.



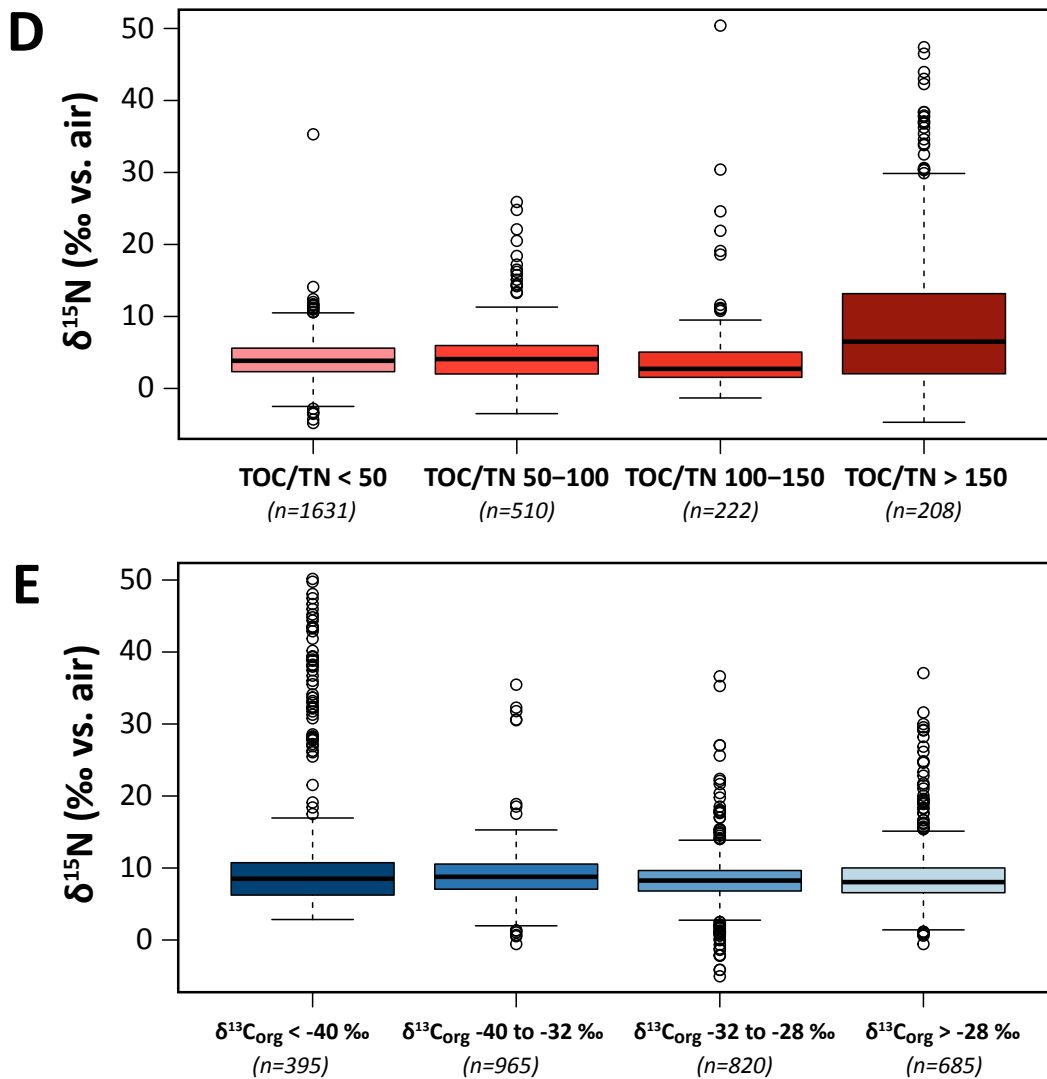


Fig. 3.14. Boxplots showing how the $\delta^{15}\text{N}$ distribution differs across: (A) the analyzed phase: bulk, kerogen or silicate; (B) the lithology: carbonates, cherts/BIFs or shales; (C) the metamorphic grade: lower than greenschist, greenschist, higher than greenschist; (D) TOC/TN ratio ranges; and (E) $\delta^{13}\text{C}_{\text{org}}$ ranges. The box in the boxplot extends from the lower quartile to the upper quartile, with the line in between showing the median of the distribution. Horizontal dashed lines, known as “whiskers”, extend to one and a half times the interquartile range, but are limited to reaching actual data points. Any value falling outside the range of the whiskers is an outlier. n indicates the number of data for each category.

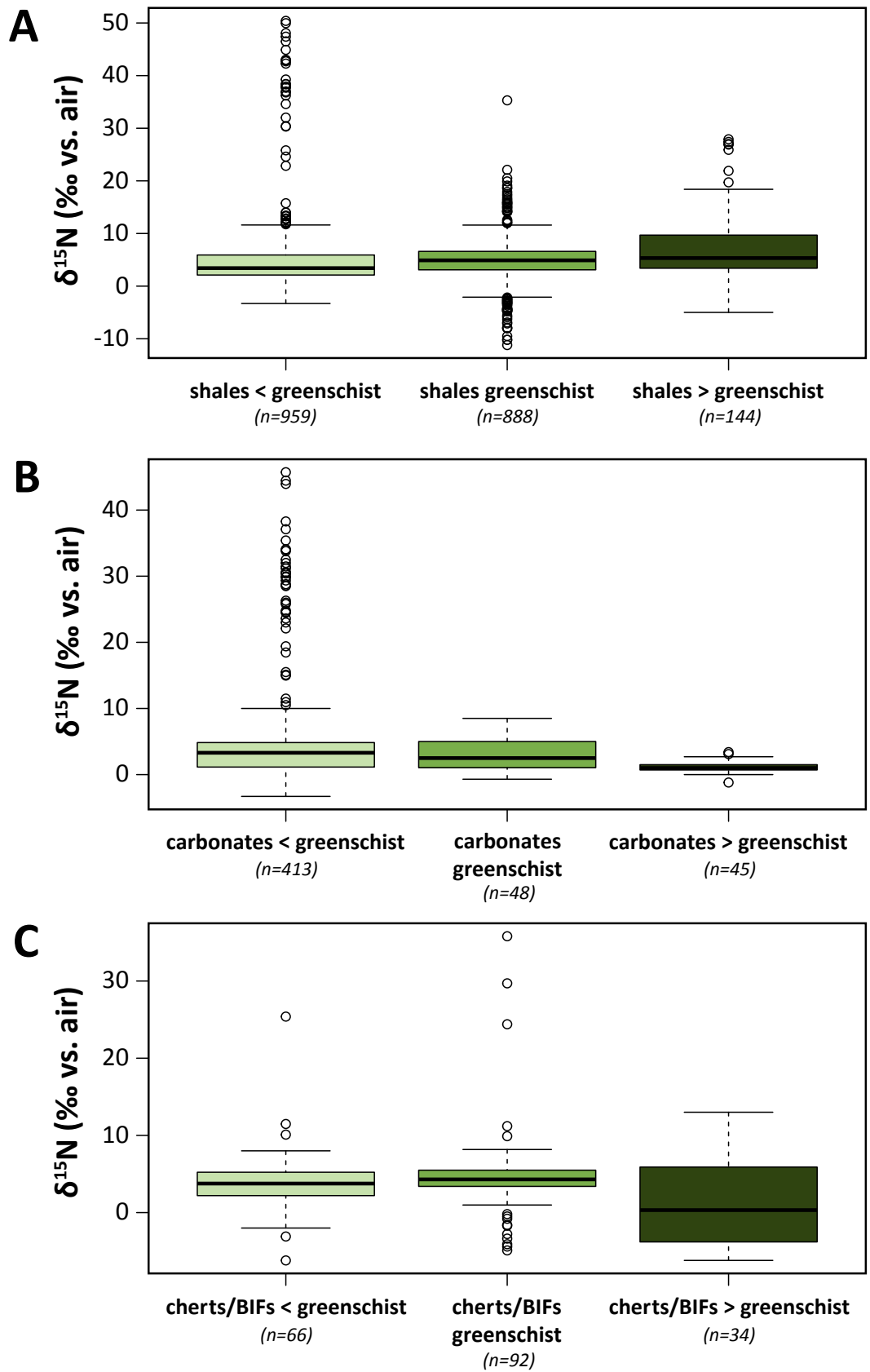


Fig. 3.15. Boxplots showing how the $\delta^{15}\text{N}$ distribution differs across metamorphic grades (lower than greenschist, greenschist, higher than greenschist) for three lithologies: (A) shales, (B) carbonates, and

(C) cherts/BIFs. The box in the boxplot extends from the lower quartile to the upper quartile, with the line in between showing the median of the distribution. Horizontal dashed lines, known as “whiskers”, extend to one and a half times the interquartile range, but are limited to reaching actual data points. Any value falling outside the range of the whiskers is an outlier. n indicates the number of data for each category.

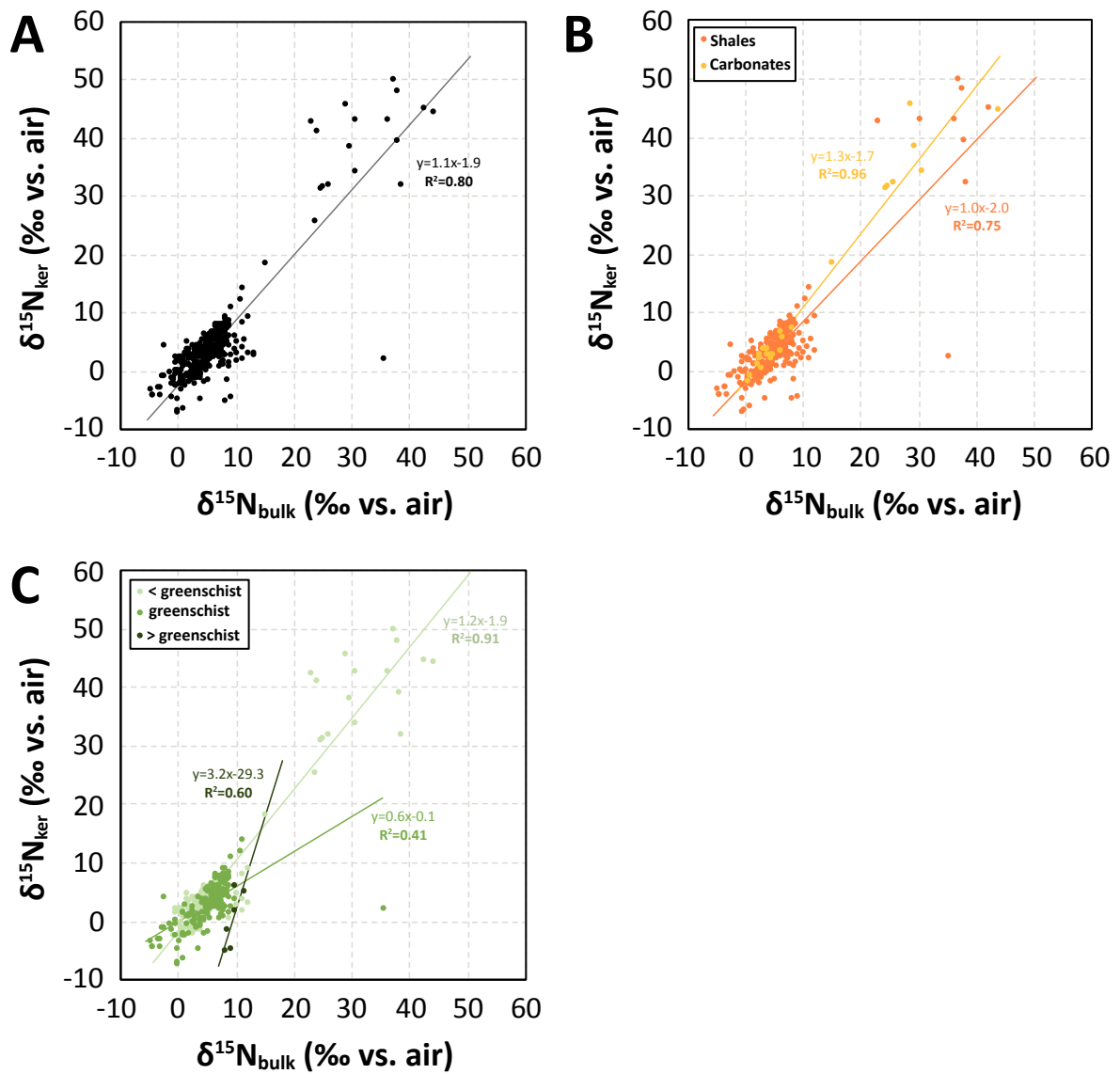


Fig. 3.16. Crossplots showing paired $\delta^{15}\text{N}_{\text{bulk}}$ - $\delta^{15}\text{N}_{\text{ker}}$ values: (A) unfiltered; (B) filtered according to lithology (shales and carbonates); (C) filtered according to metamorphic grade (lower than greenschist, greenschist, higher than greenschist).

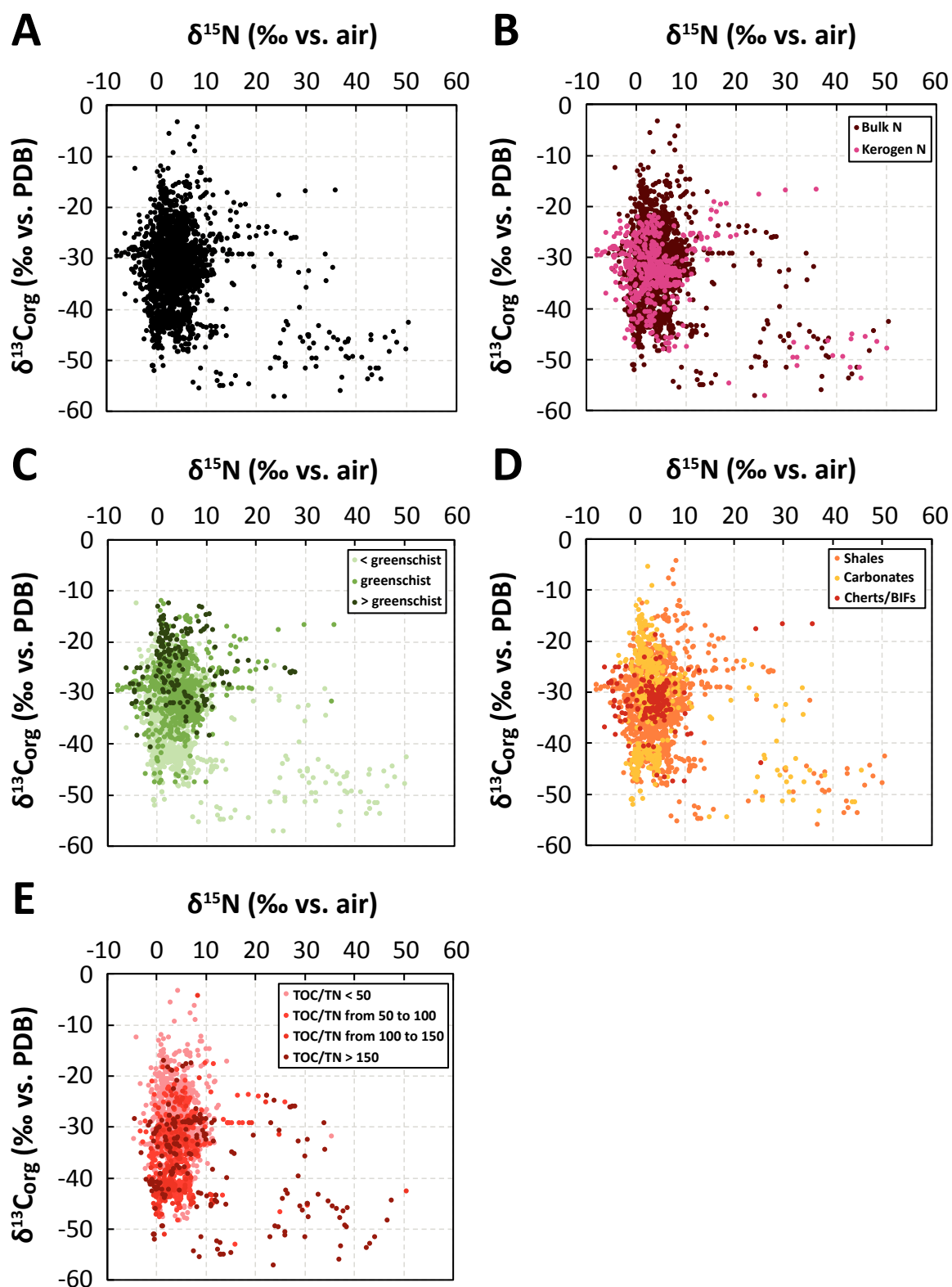


Fig. 3.17. Crossplots showing paired $\delta^{15}\text{N}$ - $\delta^{13}\text{C}_{\text{org}}$ values: (A) unfiltered; (B) filtered according to the analyzed phase (bulk N, kerogen N); (C) filtered according to metamorphic grade (lower than greenschist, greenschist, higher than greenschist); (D) filtered according to lithology (shales, carbonates, cherts/BIFs); (E) filtered according to TOC/TN ratios.

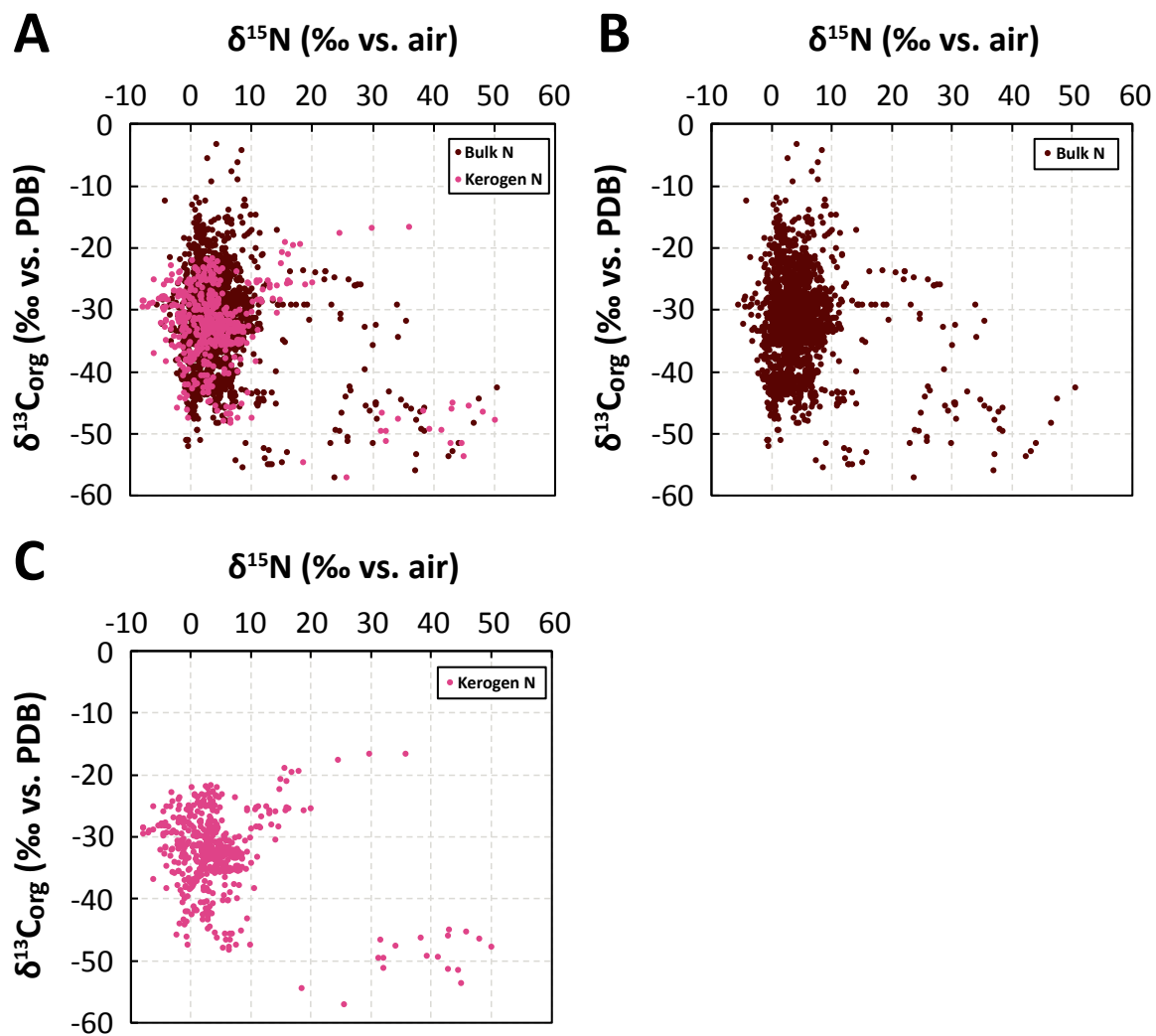


Fig. 3.18. Crossplots showing paired $\delta^{15}\text{N}$ - $\delta^{13}\text{C}_{\text{org}}$, filtered according to the analyzed phase for: (A) all N phases; (B) bulk N; (C) kerogen N.

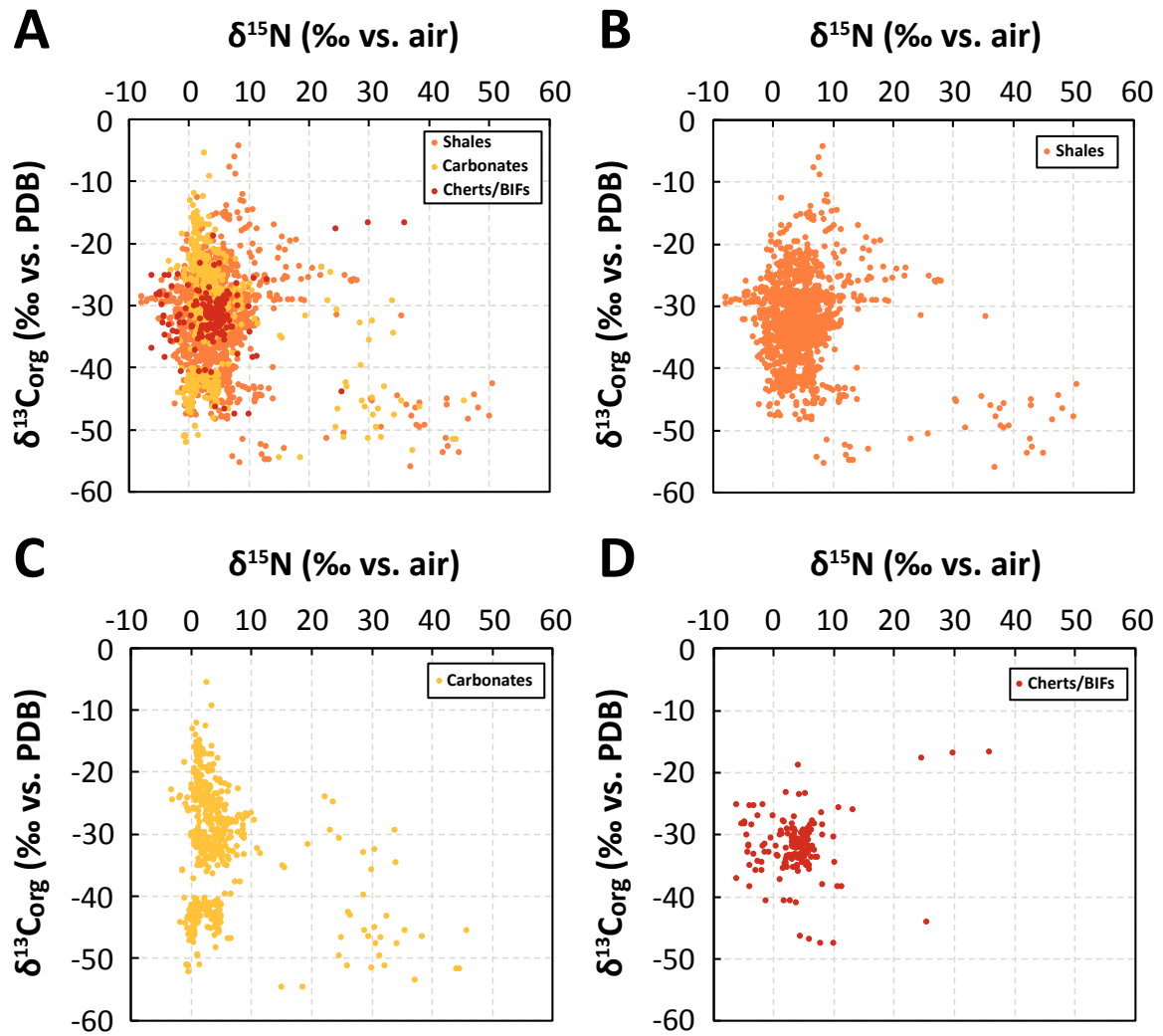


Fig. 3.19. Crossplots showing paired $\delta^{15}\text{N}$ - $\delta^{13}\text{C}_{\text{org}}$, filtered according to lithology (shales, carbonates, cherts/BIFs): (A) all lithologies; (B) shales; (C) carbonates; (D) cherts/BIFs.

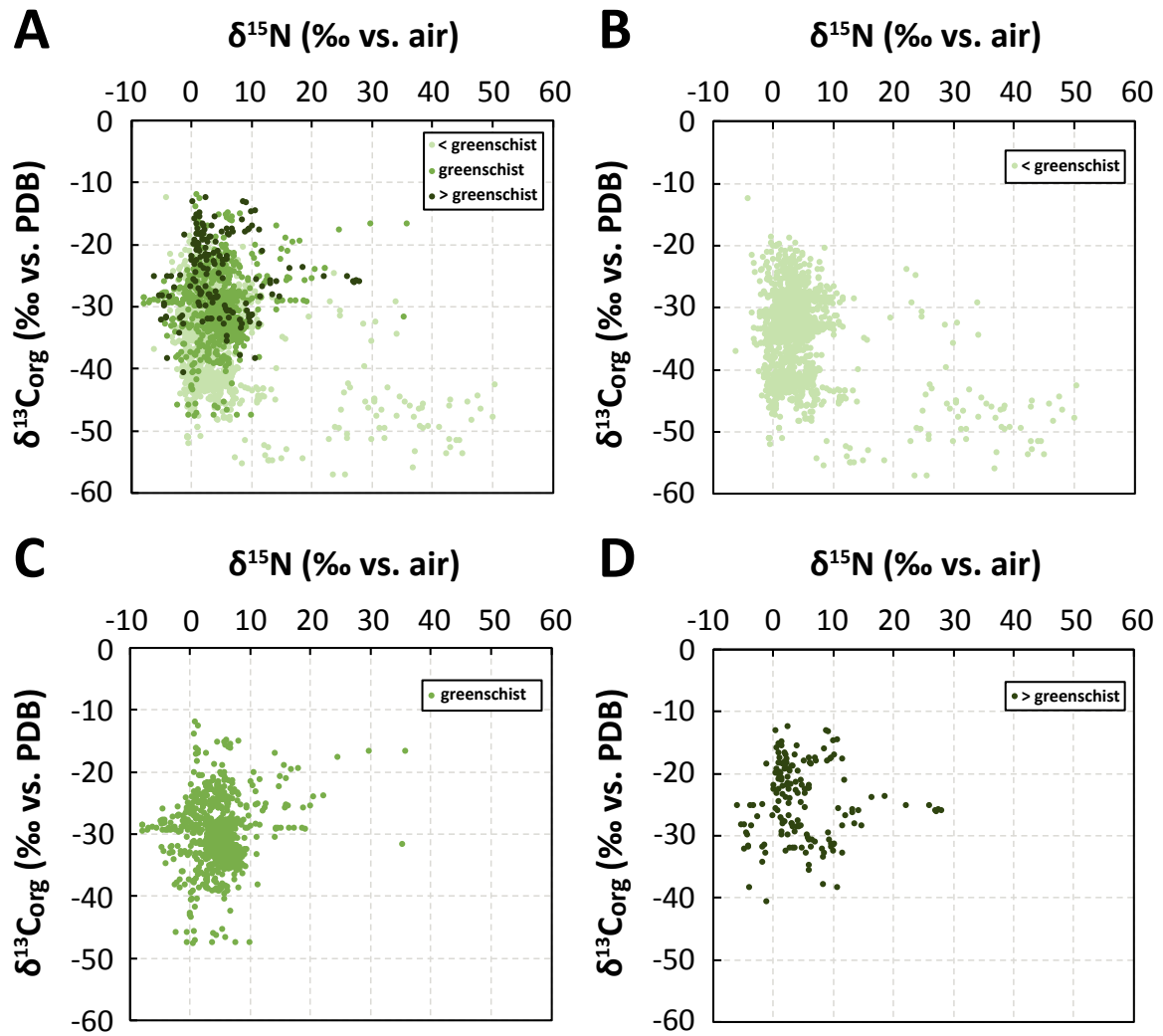


Fig. 3.20. Crossplots showing paired $\delta^{15}\text{N}$ - $\delta^{13}\text{C}_{\text{org}}$, filtered according to metamorphic grade (lower than greenschist, greenschist, higher than greenschist): (A) all metamorphic grades; (B) lower than greenschist; (C) greenschist; (D) higher than greenschist.

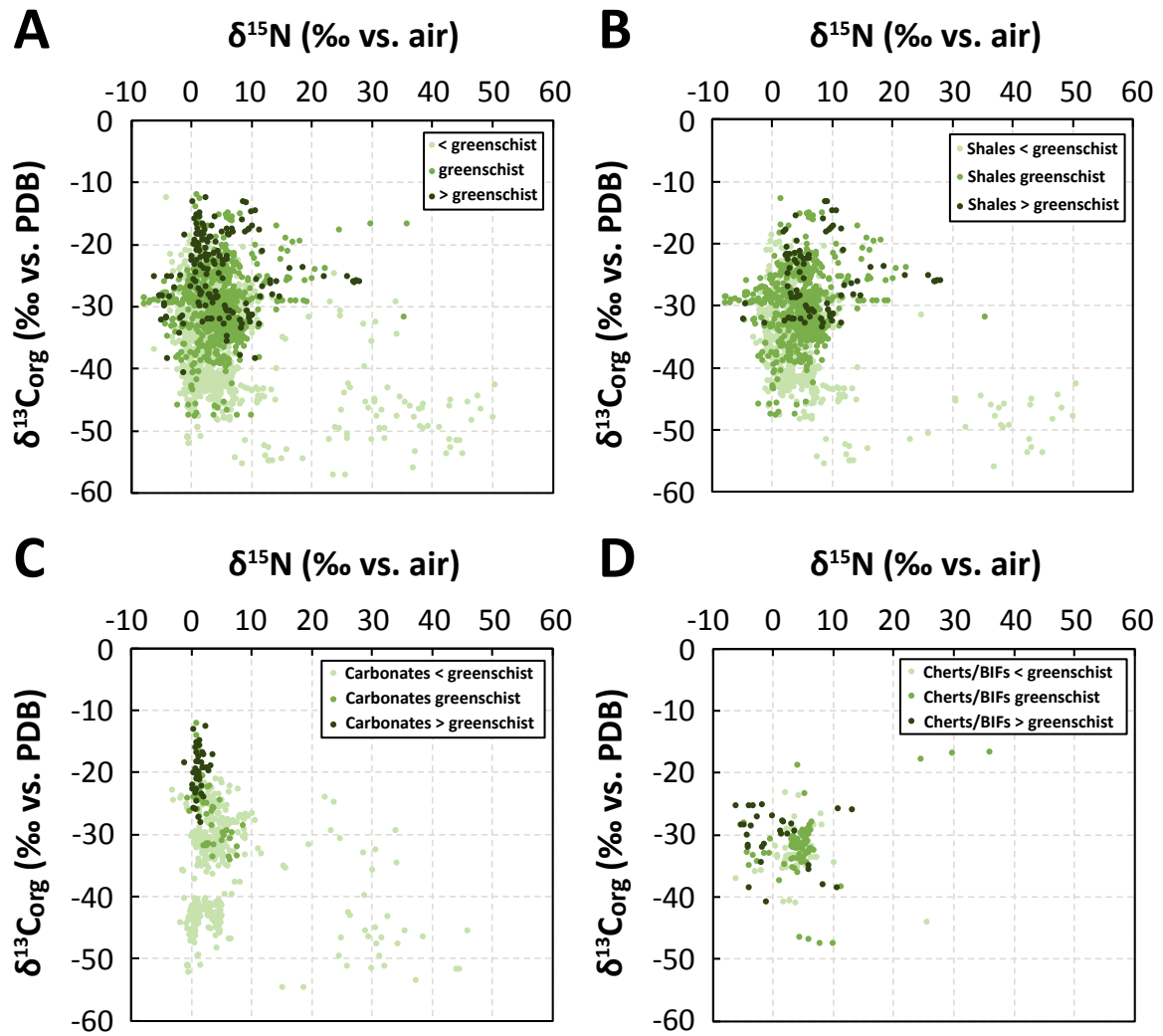


Fig. 3.21. Crossplots showing paired $\delta^{15}\text{N}$ - $\delta^{13}\text{C}_{\text{org}}$, filtered according to metamorphic grade (lower than greenschist, greenschist, higher than greenschist) for : (A) all lithologies; (B) shales; (C) carbonates; (D) cherts/BIFs.

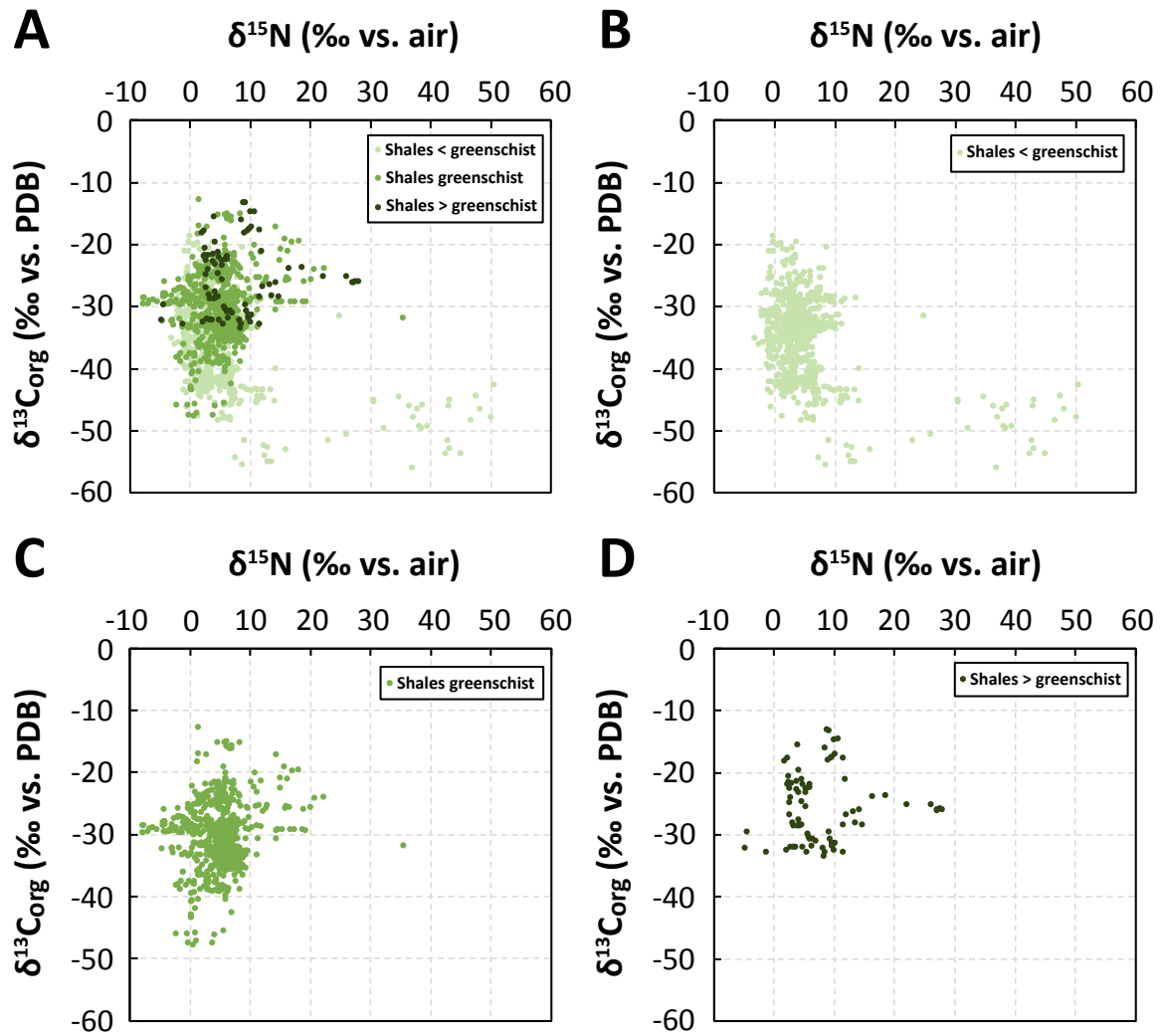


Fig. 3.22. Crossplots showing paired $\delta^{15}\text{N}$ - $\delta^{13}\text{C}_{\text{org}}$, filtered according to metamorphic grade (lower than greenschist, greenschist, higher than greenschist) for: (A) all shales; (B) shales lower than greenschist; (C) shales in the greenschist facies; (D) shales higher than greenschist.

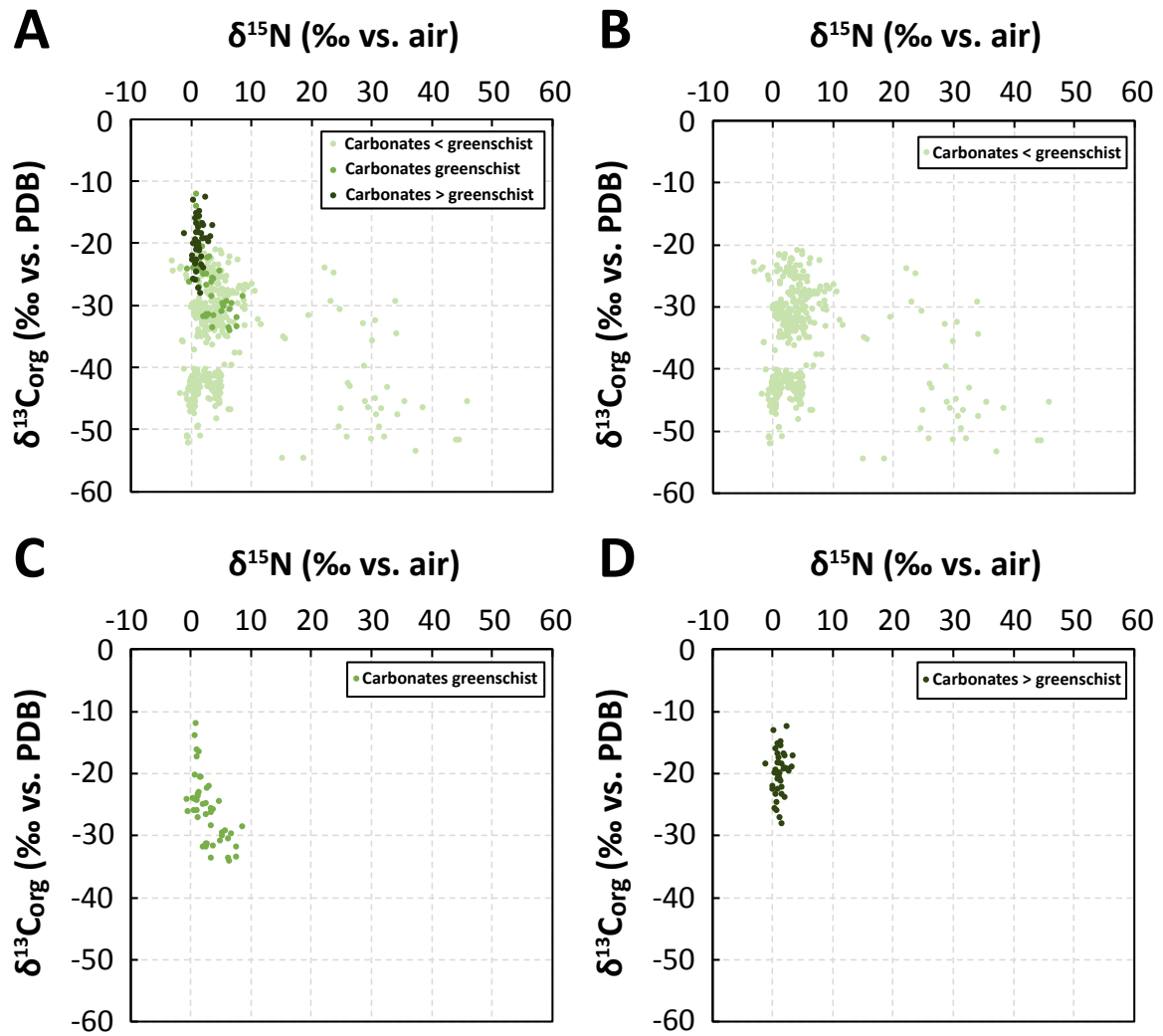


Fig. 3.23. Crossplots showing paired $\delta^{15}\text{N}$ - $\delta^{13}\text{C}_{\text{org}}$, filtered according to metamorphic grade (lower than greenschist, greenschist, higher than greenschist) for: (A) all carbonates; (B) carbonates lower than greenschist; (C) carbonates in the greenschist facies; (D) carbonates higher than greenschist.

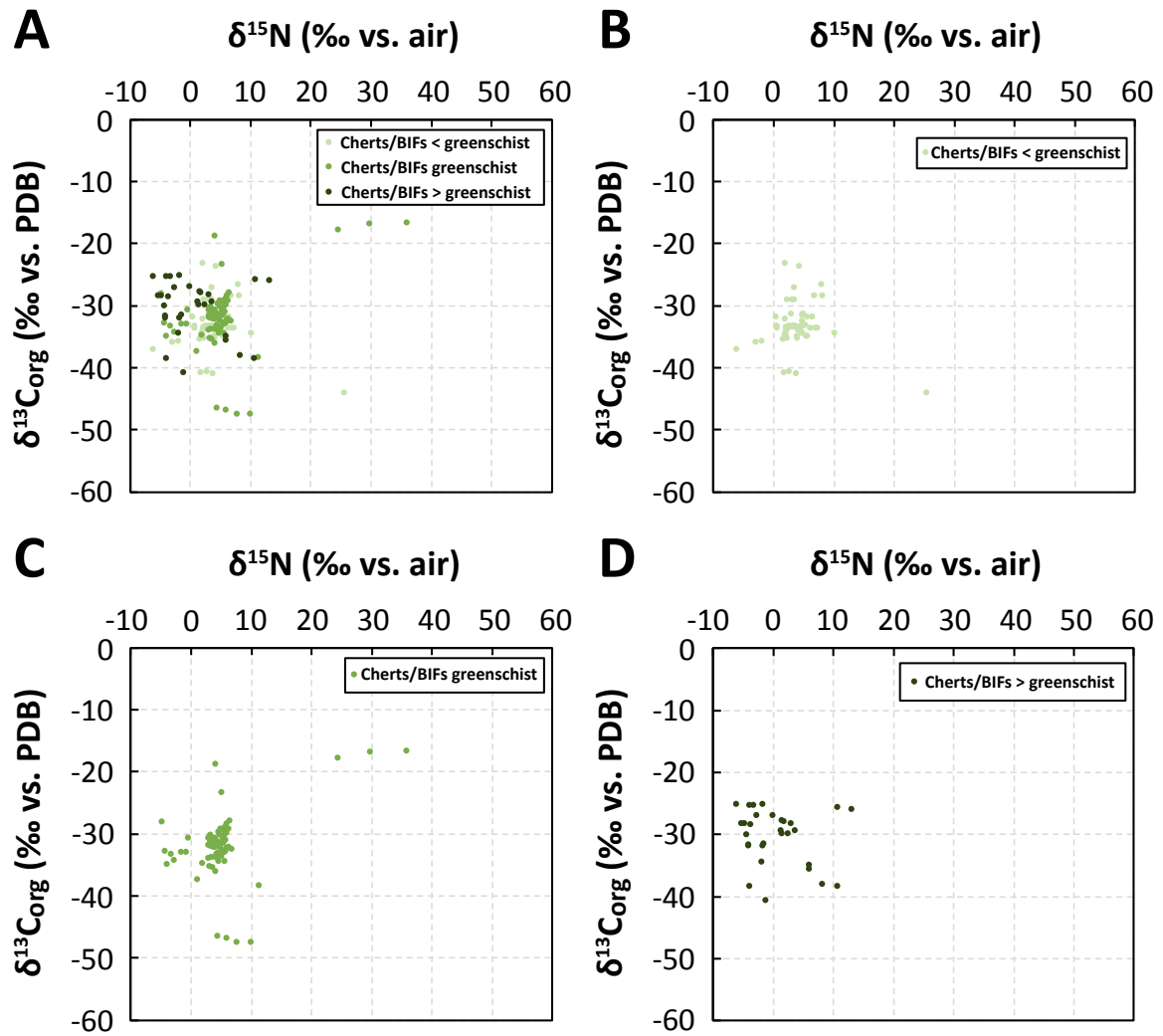


Fig. 3.24. Crossplots showing paired $\delta^{15}\text{N}$ - $\delta^{13}\text{C}_{\text{org}}$, filtered according to metamorphic grade (lower than greenschist, greenschist, higher than greenschist) for: (A) all cherts/BIFs; (B) cherts/BIFs lower than greenschist; (C) cherts/BIFs in the greenschist facies; (D) cherts/BIFs higher than greenschist.

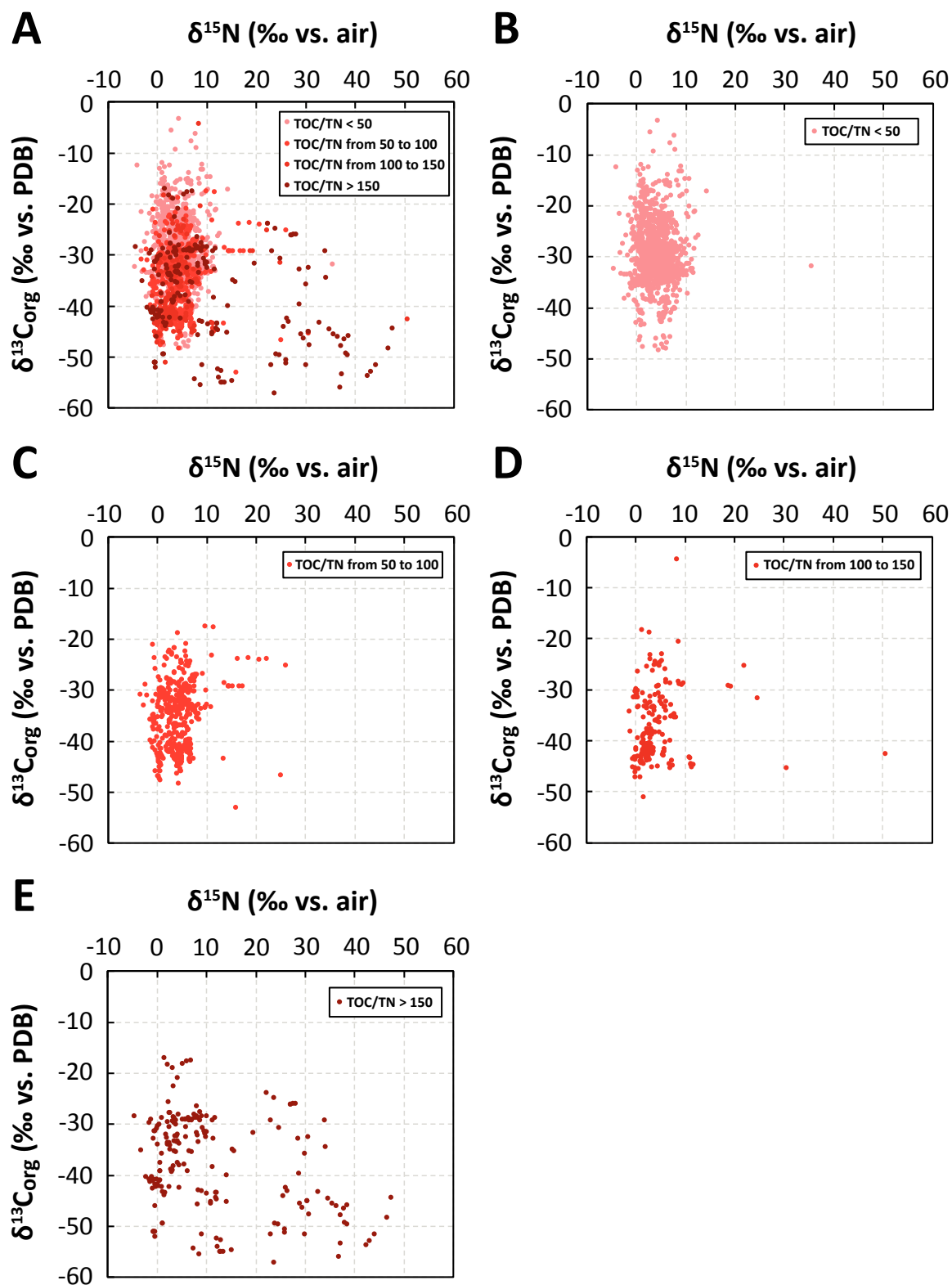


Fig. 3.25. Crossplots showing paired $\delta^{15}\text{N}$ - $\delta^{13}\text{C}_{\text{org}}$, filtered according to TOC/TN ratios (A) all TOC/TN ratios; (B) TOC/TN lower than 50; (C) TOC/TN between 50 and 100; (D) TOC/TN between 100 and 150; (E) TOC/TN above 150.

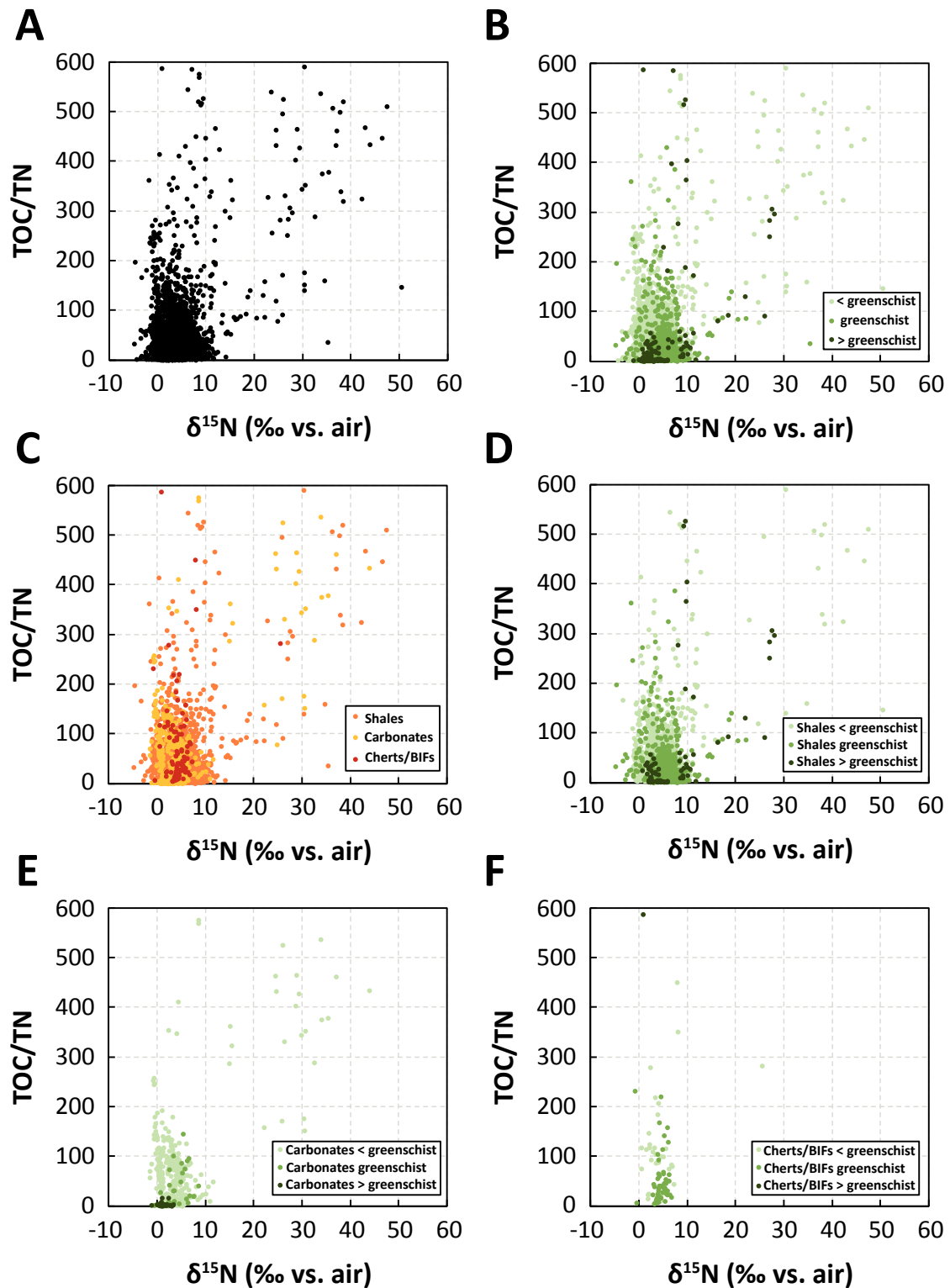


Fig. 3.26. Crossplots showing paired $\delta^{15}\text{N}$ -TOC/TN values: (A) unfiltered; (B) filtered according to metamorphic grade (lower than greenschist, greenschist, higher than greenschist); (C) filtered according to lithology (shales, carbonates, cherts/BIFs); (D) filtered according to metamorphic grade in shales (lower than greenschist, greenschist, higher than greenschist); (E) filtered according to metamorphic grade in carbonates (lower than greenschist, greenschist, higher than greenschist); (F) filtered according to metamorphic grade in cherts/BIFs (lower than greenschist, greenschist, higher than greenschist).

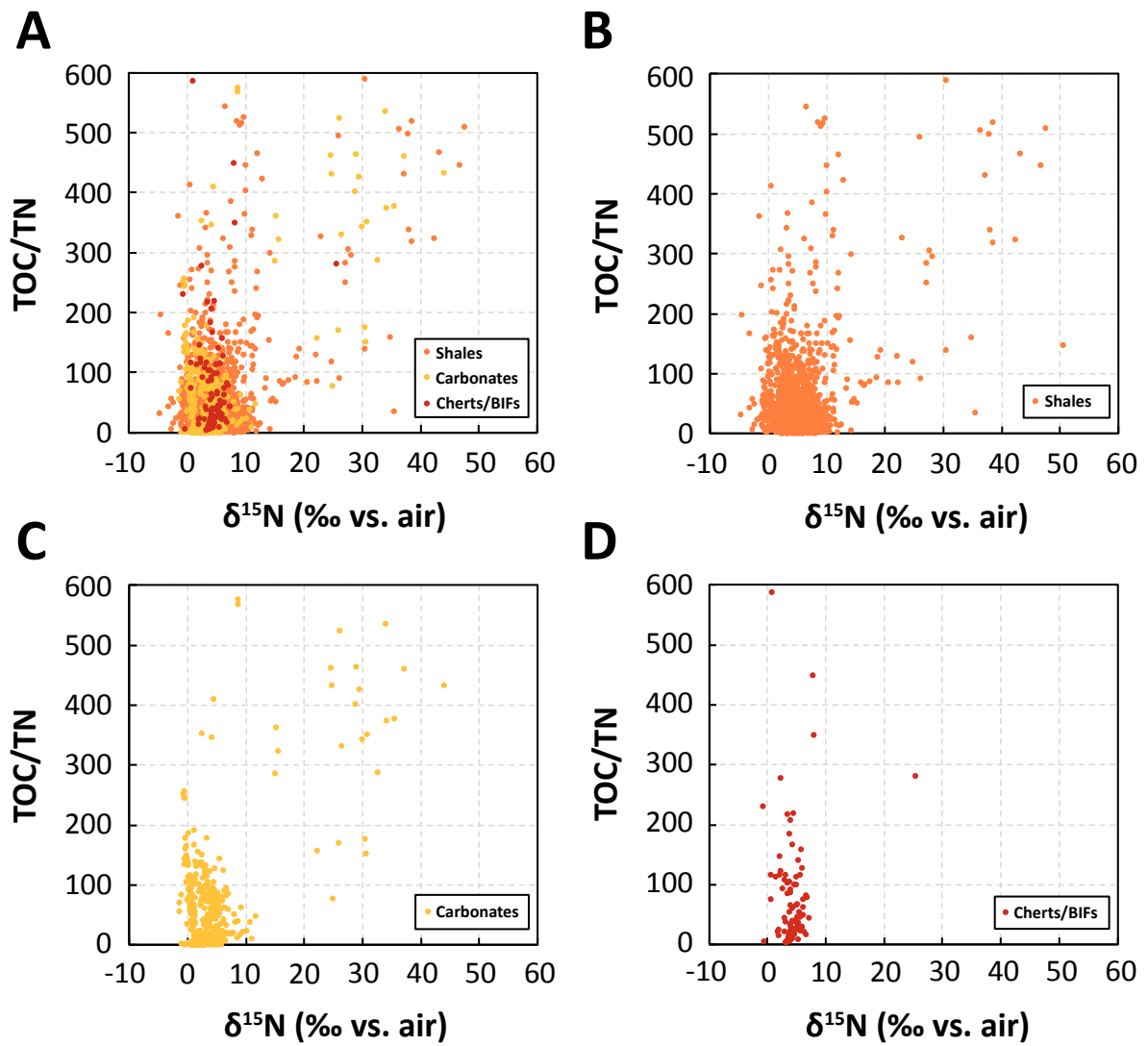


Fig. 3.27. Crossplots showing paired $\delta^{15}\text{N}$ -TOC/TN, filtered according to lithology (shales, carbonates, cherts/BIFs): (A) all lithologies; (B) shales; (C) carbonates; (D) cherts/BIFs.

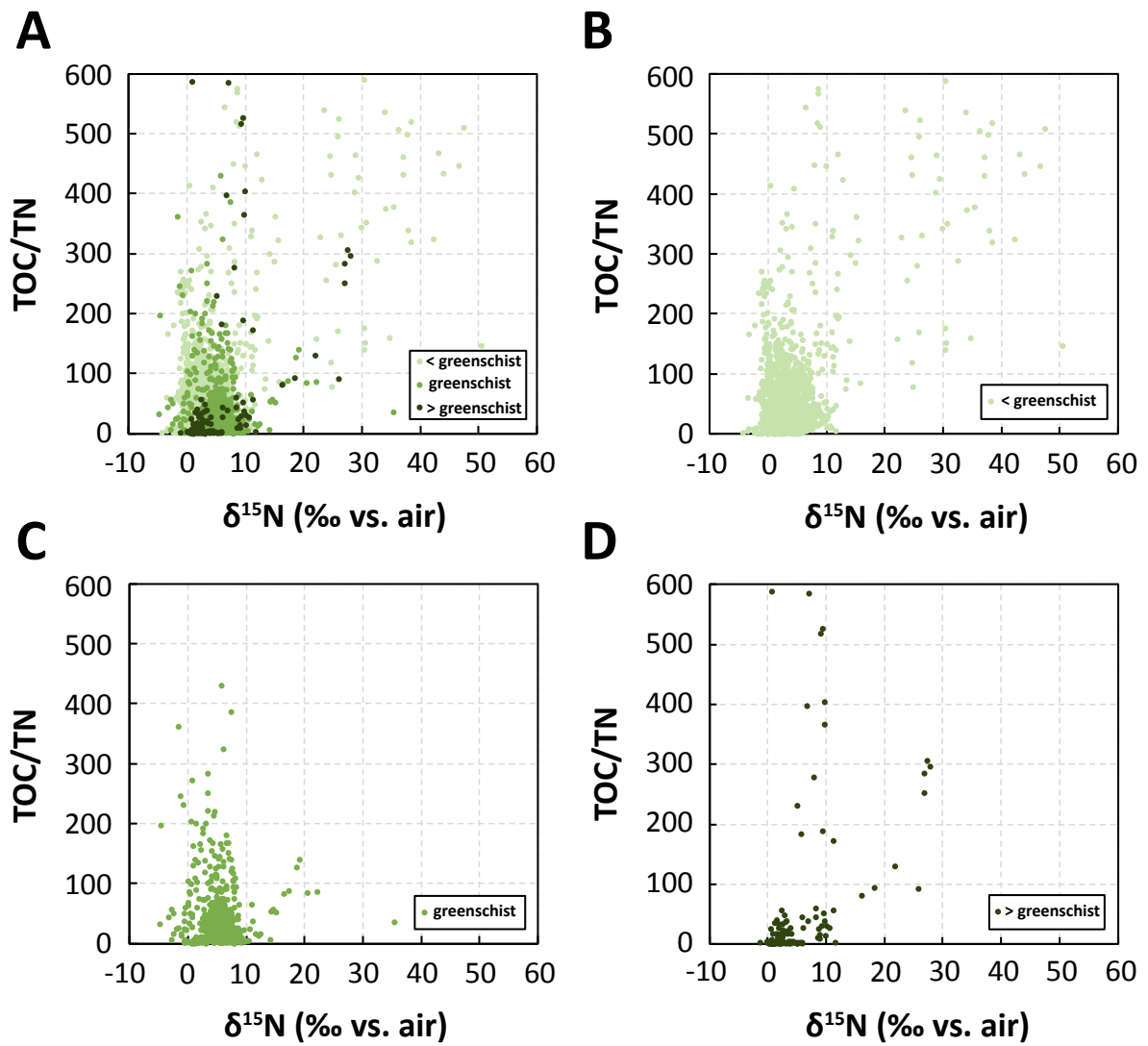


Fig. 3.28. Crossplots showing paired $\delta^{15}\text{N}$ -TOC/TN, filtered according to metamorphic grade (lower than greenschist, greenschist, higher than greenschist): (A) all metamorphic grades; (B) lower than greenschist; (C) greenschist; (D) higher than greenschist.

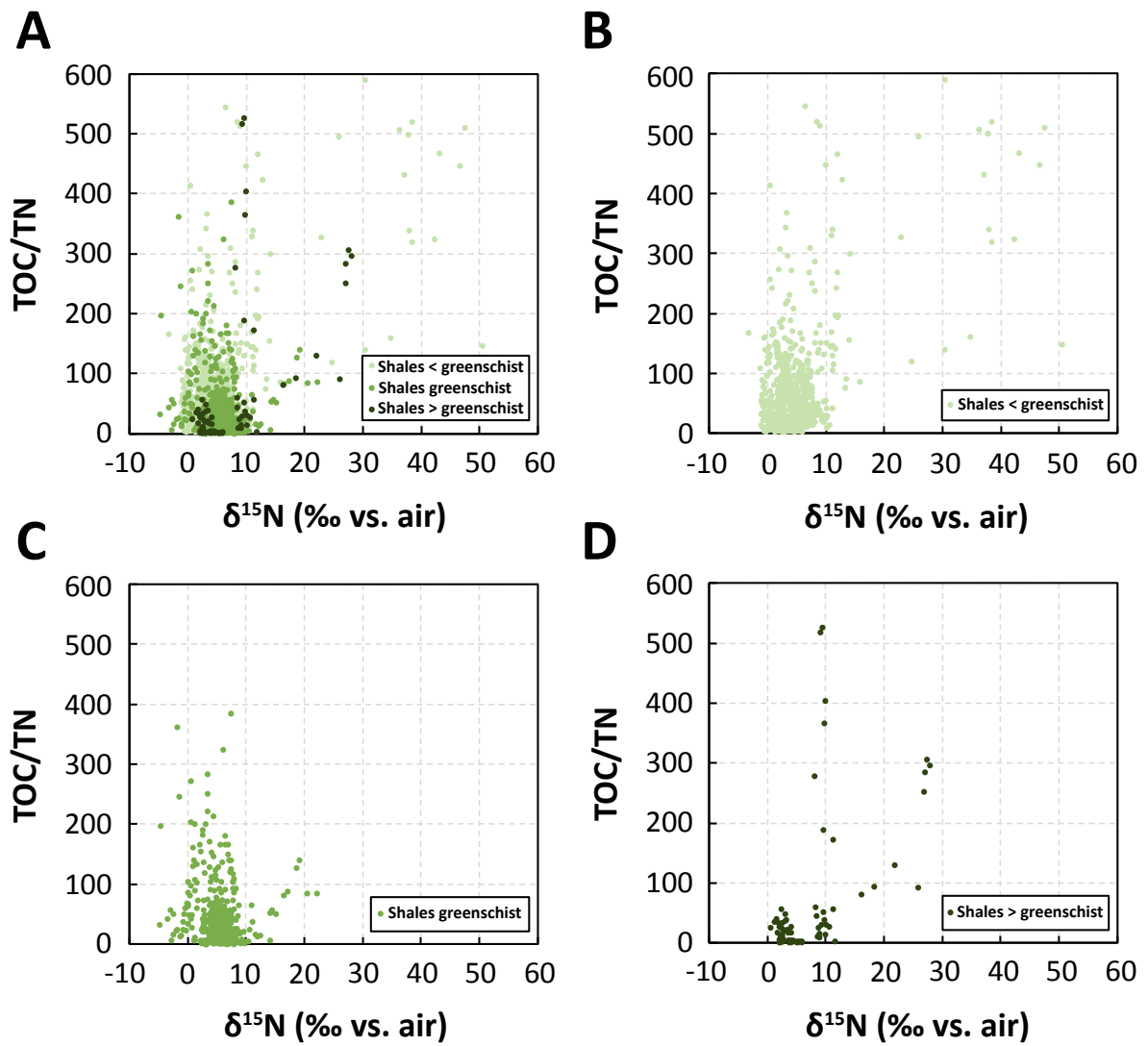


Fig. 3.29. Crossplots showing paired $\delta^{15}\text{N}$ -TOC/TN, filtered according to metamorphic grade (lower than greenschist, greenschist, higher than greenschist) for: (A) all shales; (B) shales lower than greenschist; (C) shales in the greenschist facies; (D) shales higher than greenschist.

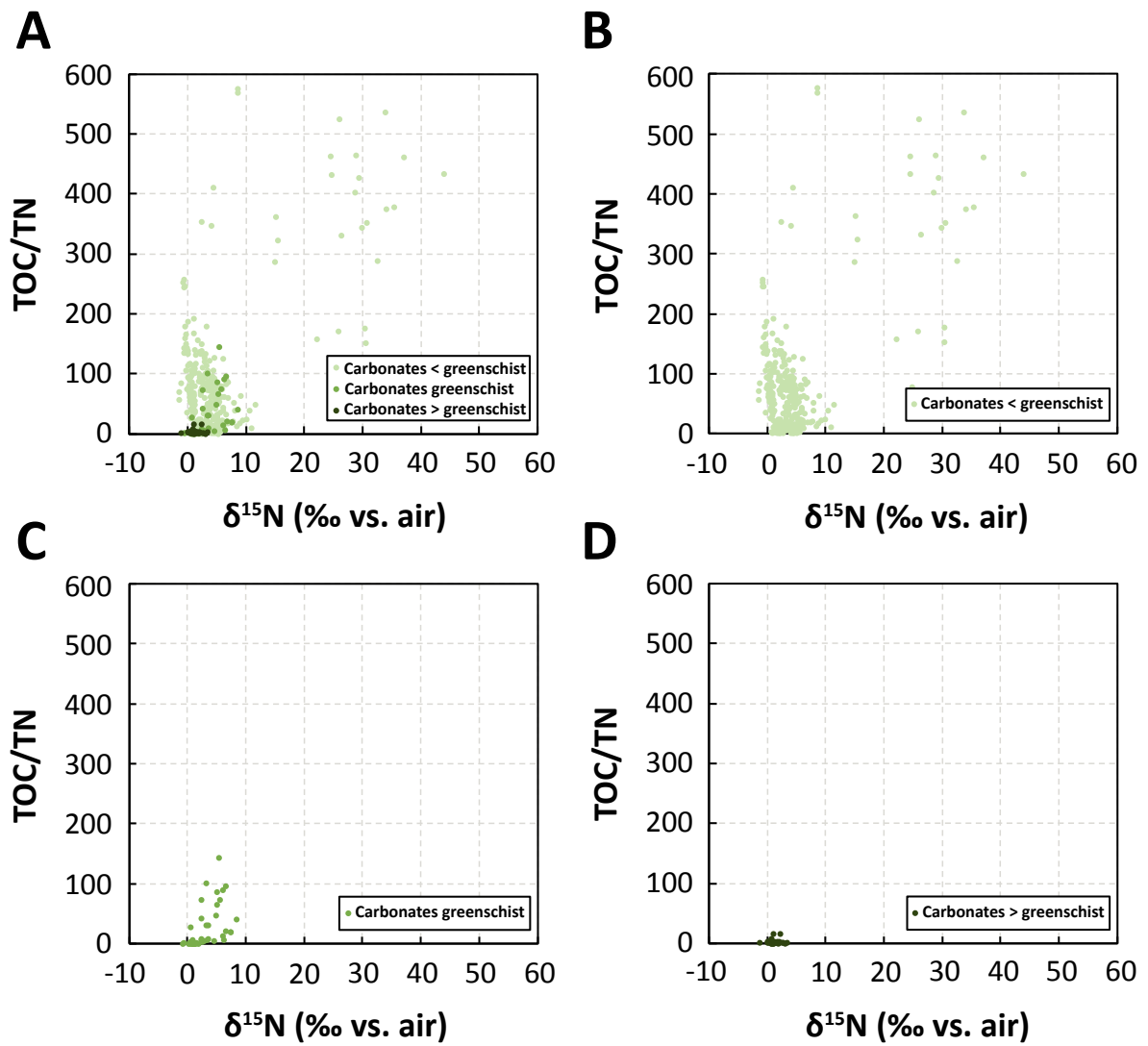


Fig. 3.30. Crossplots showing paired $\delta^{15}\text{N}$ -TOC/TN, filtered according to metamorphic grade (lower than greenschist, greenschist, higher than greenschist) for: (A) all carbonates; (B) carbonates lower than greenschist; (C) carbonates in the greenschist facies; (D) carbonates higher than greenschist.

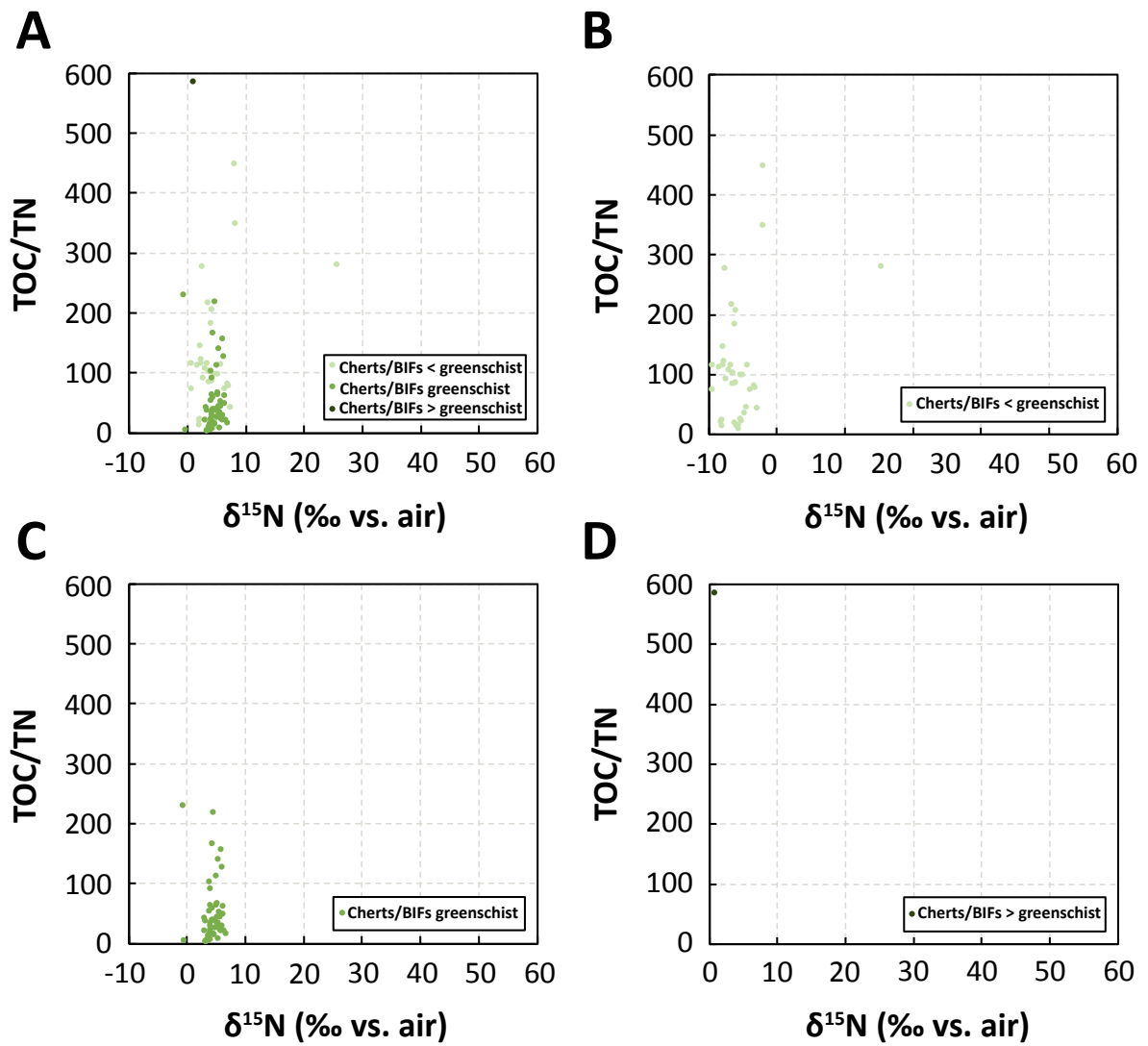


Fig. 3.31. Crossplots showing paired $\delta^{15}\text{N}$ -TOC/TN, filtered according to metamorphic grade (lower than greenschist, greenschist, higher than greenschist) for: (A) all cherts/BIFs; (B) cherts/BIFs lower than greenschist; (C) cherts/BIFs in the greenschist facies; (D) cherts/BIFs higher than greenschist.

References

- Ader, M., Boudou, J.-P., Javoy, M., Goffe, B., Daniels, E., 1998. Isotope study on organic nitrogen of Westphalian anthracites from the Western Middle field of Pennsylvania (U.S.A.) and from the Bramsche Massif (Germany). *Organic Geochemistry, Advances in Organic Geochemistry 1997 Proceedings of the 18th International Meeting on Organic Geochemistry Part I. Petroleum Geochemistry* 29, 315–323. [https://doi.org/10.1016/S0146-6380\(98\)00072-2](https://doi.org/10.1016/S0146-6380(98)00072-2)
- Ader, M., Cartigny, P., Boudou, J.-P., Oh, J.-H., Petit, E., Javoy, M., 2006. Nitrogen isotopic evolution of carbonaceous matter during metamorphism: Methodology and preliminary results. *Chemical Geology* 232, 152–169. <https://doi.org/10.1016/j.chemgeo.2006.02.019>
- Ader, M., Thomazo, C., Sansjofre, P., Busigny, V., Papineau, D., Laffont, R., Cartigny, P., Halverson, G.P., 2016. Interpretation of the nitrogen isotopic composition of Precambrian sedimentary rocks: Assumptions and perspectives. *Chemical Geology* 429, 93–110. <https://doi.org/10.1016/j.chemgeo.2016.02.010>
- Bebout, G.E., Cooper, D.C., Bradley, A.D., Sadofsky, S.J., 1999. Nitrogen-isotope record of fluid-rock interactions in the Skiddaw Aureole and granite, English Lake District. *American Mineralogist* 84, 1495–1505. <https://doi.org/10.2138/am-1999-1002>
- Bebout, G.E., Fogel, M.L., 1992. Nitrogen-isotope compositions of metasedimentary rocks in the Catalina Schist, California: Implications for metamorphic devolatilization history. *Geochimica et Cosmochimica Acta* 56, 2839–2849. [https://doi.org/10.1016/0016-7037\(92\)90363-N](https://doi.org/10.1016/0016-7037(92)90363-N)
- Boocock, T.J., Mikhail, S., Prytulak, J., Di Rocco, T., Stüeken, E.E., 2020. Nitrogen Mass Fraction and Stable Isotope Ratios for Fourteen Geological Reference Materials: Evaluating the Applicability of Elemental Analyser Versus Sealed Tube Combustion Methods. *Geostandards and Geoanalytical Research* 44, 537–551. <https://doi.org/10.1111/ggr.12345>
- Boudou, J.-P., Schimmelmann, A., Ader, M., Mastalerz, M., Sebito, M., Gengembre, L., 2008. Organic nitrogen chemistry during low-grade metamorphism. *Geochimica et Cosmochimica Acta* 72, 1199–1221. <https://doi.org/10.1016/j.gca.2007.12.004>
- Boyd, S.R., Philippot, P., 1998. Precambrian ammonium biogeochemistry: a study of the Moine metasediments, Scotland. *Chemical Geology* 144, 257–268. [https://doi.org/10.1016/S0009-2541\(97\)00135-6](https://doi.org/10.1016/S0009-2541(97)00135-6)
- Busigny, V., Ader, M., Cartigny, P., 2005. Quantification and isotopic analysis of nitrogen in rocks at the ppm level using sealed tube combustion technique: A prelude to the study of altered oceanic crust. *Chemical Geology* 223, 249–258. <https://doi.org/10.1016/j.chemgeo.2005.08.002>
- Glasmacher, U.A., Zentilli, M., Ryan, R., 2003. Nitrogen distribution in Lower Palaeozoic slates/phyllites of the Meguma Supergroup, Nova Scotia, Canada: implications for Au and Zn–Pb mineralisation and exploration. *Chemical Geology* 194, 297–329. [https://doi.org/10.1016/S0009-2541\(02\)00322-4](https://doi.org/10.1016/S0009-2541(02)00322-4)

- Haendel, D., Mühle, K., Nitzsche, H.-M., Stiehl, G., Wand, U., 1986. Isotopic variations of the fixed nitrogen in metamorphic rocks. *Geochimica et Cosmochimica Acta* 50, 749–758. [https://doi.org/10.1016/0016-7037\(86\)90351-0](https://doi.org/10.1016/0016-7037(86)90351-0)
- Havig, J.R., Hamilton, T.L., Bachan, A., Kump, L.R., 2017. Sulfur and carbon isotopic evidence for metabolic pathway evolution and a four-stepped Earth system progression across the Archean and Paleoproterozoic. *Earth-Science Reviews* 174, 1–21. <https://doi.org/10.1016/j.earscirev.2017.06.014>
- Hurley, S.J., Wing, B.A., Jasper, C.E., Hill, N.C., Cameron, J.C., 2021. Carbon isotope evidence for the global physiology of Proterozoic cyanobacteria. *Science Advances* 7, eabc8998. <https://doi.org/10.1126/sciadv.abc8998>
- Jia, Y., 2006. Nitrogen isotope fractionations during progressive metamorphism: A case study from the Paleozoic Cooma metasedimentary complex, southeastern Australia. *Geochimica et Cosmochimica Acta* 70, 5201–5214. <https://doi.org/10.1016/j.gca.2006.08.004>
- Jia, Y., Kerrich, R., 2000. Giant quartz vein systems in accretionary orogenic belts: the evidence for a metamorphic fluid origin from $\delta^{15}\text{N}$ and $\delta^{13}\text{C}$ studies. *Earth and Planetary Science Letters* 184, 211–224. [https://doi.org/10.1016/S0012-821X\(00\)00320-4](https://doi.org/10.1016/S0012-821X(00)00320-4)
- Jia, Y., Kerrich, R., 1999. Nitrogen isotope systematics of mesothermal lode gold deposits: Metamorphic, granitic, meteoric water, or mantle origin? *Geology* 27, 1051–1054. [https://doi.org/10.1130/0091-7613\(1999\)027<1051:NISOML>2.3.CO;2](https://doi.org/10.1130/0091-7613(1999)027<1051:NISOML>2.3.CO;2)
- Kipp, M.A., Stüeken, E.E., Yun, M., Bekker, A., Buick, R., 2018. Pervasive aerobic nitrogen cycling in the surface ocean across the Paleoproterozoic Era. *Earth and Planetary Science Letters* 500, 117–126. <https://doi.org/10.1016/j.epsl.2018.08.007>
- Kitchen, N.E., Valley, J.W., 1995. Carbon isotope thermometry in marbles of the Adirondack Mountains, New York. *Journal of Metamorphic Geology* 13, 577–594. <https://doi.org/10.1111/j.1525-1314.1995.tb00244.x>
- Koehler, M.C., Stüeken, E.E., Kipp, M.A., Buick, R., Knoll, A.H., 2017. Spatial and temporal trends in Precambrian nitrogen cycling: A Mesoproterozoic offshore nitrate minimum. *Geochimica et Cosmochimica Acta* 198, 315–337. <https://doi.org/10.1016/j.gca.2016.10.050>
- Mingram, B., Bräuer, K., 2001. Ammonium concentration and nitrogen isotope composition in metasedimentary rocks from different tectonometamorphic units of the European Variscan Belt. *Geochimica et Cosmochimica Acta* 65, 273–287. [https://doi.org/10.1016/S0016-7037\(00\)00517-2](https://doi.org/10.1016/S0016-7037(00)00517-2)
- Mingram, B., Hoth, P., Lüders, V., Harlov, D., 2005. The significance of fixed ammonium in Palaeozoic sediments for the generation of nitrogen-rich natural gases in the North German Basin. *Int J Earth Sci (Geol Rundsch)* 94, 1010–1022. <https://doi.org/10.1007/s00531-005-0015-0>
- Papineau, D., Purohit, R., Goldberg, T., Pi, D., Shields, G.A., Bhu, H., Steele, A., Fogel, M.L., 2009. High primary productivity and nitrogen cycling after the Paleoproterozoic phosphogenic event in the Aravalli Supergroup, India. *Precambrian Research* 171, 37–56. <https://doi.org/10.1016/j.precamres.2009.03.005>

- Pitcairn, I.K., Teagle, D.A.H., Kerrich, R., Craw, D., Brewer, T.S., 2005. The behavior of nitrogen and nitrogen isotopes during metamorphism and mineralization: Evidence from the Otago and Alpine Schists, New Zealand. *Earth and Planetary Science Letters* 233, 229–246. <https://doi.org/10.1016/j.epsl.2005.01.029>
- Plessen, B., Harlov, D.E., Henry, D., Guidotti, C.V., 2010. Ammonium loss and nitrogen isotopic fractionation in biotite as a function of metamorphic grade in metapelites from western Maine, USA. *Geochimica et Cosmochimica Acta* 74, 4759–4771. <https://doi.org/10.1016/j.gca.2010.05.021>
- Schidlowski, M., 2001. Carbon isotopes as biogeochemical recorders of life over 3.8 Ga of Earth history: evolution of a concept. *Precambrian Research* 106, 117–134. [https://doi.org/10.1016/S0301-9268\(00\)00128-5](https://doi.org/10.1016/S0301-9268(00)00128-5)
- Schimmelmann, A., Mastalerz, M., Gao, L., Sauer, P.E., Topalov, K., 2009. Dike intrusions into bituminous coal, Illinois Basin: H, C, N, O isotopic responses to rapid and brief heating. *Geochimica et Cosmochimica Acta* 73, 6264–6281. <https://doi.org/10.1016/j.gca.2009.07.027>
- Sterne, E.J., Reynolds, R.C., Zantop, H., 1982. Natural Ammonium Illites from Black Shales Hosting a Stratiform Base Metal Deposit, Delong Mountains, Northern Alaska. *Clays Clay Miner.* 30, 161–166. <https://doi.org/10.1346/CCMN.1982.0300301>
- Stüeken, E. E., Buick, R., Anderson, R.E., Baross, J.A., Planavsky, N.J., Lyons, T.W., 2017. Environmental niches and metabolic diversity in Neoproterozoic lakes. *Geobiology* 15, 767–783. <https://doi.org/10.1111/gbi.12251>
- Stüeken, E.E., Buick, R., Schauer, A.J., 2015. Nitrogen isotope evidence for alkaline lakes on late Archean continents. *Earth and Planetary Science Letters* 411, 1–10. <https://doi.org/10.1016/j.epsl.2014.11.037>
- Stüeken, E.E., Kipp, M.A., Koehler, M.C., Buick, R., 2016. The evolution of Earth's biogeochemical nitrogen cycle. *Earth-Science Reviews* 160, 220–239. <https://doi.org/10.1016/j.earscirev.2016.07.007>
- Stüeken, Eva E., Zaloumis, J., Meixnerová, J., Buick, R., 2017. Differential metamorphic effects on nitrogen isotopes in kerogen extracts and bulk rocks. *Geochimica et Cosmochimica Acta* 217, 80–94. <https://doi.org/10.1016/j.gca.2017.08.019>
- Svensen, H., Bebout, G., Kronz, A., Li, L., Planke, S., Chevallier, L., Jamtveit, B., 2008. Nitrogen geochemistry as a tracer of fluid flow in a hydrothermal vent complex in the Karoo Basin, South Africa. *Geochimica et Cosmochimica Acta* 72, 4929–4947. <https://doi.org/10.1016/j.gca.2008.07.023>
- Thomazo, C., Ader, M., Philippot, P., 2011. Extreme ¹⁵N-enrichments in 2.72-Gyr-old sediments: evidence for a turning point in the nitrogen cycle. *Geobiology* 9, 107–120. <https://doi.org/10.1111/j.1472-4669.2011.00271.x>
- Wada, H., Tomita, T., Matsuura, K., Tuchi, K., Ito, M., Morikiyo, T., 1994. Graphitization of carbonaceous matter during metamorphism with references to carbonate and pelitic rocks of contact and regional metamorphisms, Japan. *Contr. Mineral. and Petrol.* 118, 217–228. <https://doi.org/10.1007/BF00306643>

Yamaguchi, K., 2002. Geochemistry of Archean–Paleoproterozoic Black Shales: The Early Evolution of the Atmosphere, Oceans, and Biosphere.

Yang, J., Junium, C.K., Grassineau, N.V., Nisbet, E.G., Izon, G., Mettam, C., Martin, A., Zerkle, A.L., 2019. Ammonium availability in the Late Archaean nitrogen cycle. *Nat. Geosci.* 12, 553–557. <https://doi.org/10.1038/s41561-019-0371-1>

Yui, T.-F., Kao, S.-J., Wu, T.-W., 2009. Nitrogen and N-isotope variation during low-grade metamorphism of the Taiwan mountain belt. *Geochemical Journal* 43, 15–27. <https://doi.org/10.2343/geochemj.1.0003>

Zerkle, A.L., Poulton, S.W., Newton, R.J., Mettam, C., Claire, M.W., Bekker, A., Junium, C.K., 2017. Onset of the aerobic nitrogen cycle during the Great Oxidation Event. *Nature* 542, 465–467. <https://doi.org/10.1038/nature20826>

Supplementary Table 8.1. Precambrian $\delta^{15}\text{N}$ database (provided separately as a .xlsx document)

Supplementary Information: list of references used in the Precambrian $\delta^{15}\text{N}$ database

Ader, M., Sansjofre, P., Halverson, G.P., Busigny, V., Trindade, R.I.F., Kunzmann, M., Nogueira, A.C.R., 2014. Ocean redox structure across the Late Neoproterozoic Oxygenation Event: A nitrogen isotope perspective. *Earth and Planetary Science Letters* 396, 1–13. <https://doi.org/10.1016/j.epsl.2014.03.042>

Ader, M., Thomazo, C., Sansjofre, P., Busigny, V., Papineau, D., Laffont, R., Cartigny, P., Halverson, G.P., 2016. Interpretation of the nitrogen isotopic composition of Precambrian sedimentary rocks: Assumptions and perspectives. *Chemical Geology* 429, 93–110. <https://doi.org/10.1016/j.chemgeo.2016.02.010>

Aubineau, J., El Albani, A., Chi Fru, E., Kipp, M.A., Ngwal'ghoubou Ikouanga, J., Bekker, A., 2021. Benthic redox conditions and nutrient dynamics in the ca. 2.1 Ga Franceville sub-basin. *Precambrian Research* 360, 106234. <https://doi.org/10.1016/j.precamres.2021.106234>

Beaumont, V., Robert, F., 1999. Nitrogen isotope ratios of kerogens in Precambrian cherts: a record of the evolution of atmosphere chemistry? *Precambrian Research* 96, 63–82. [https://doi.org/10.1016/S0301-9268\(99\)00005-4](https://doi.org/10.1016/S0301-9268(99)00005-4)

Bebout, G.E., Cooper, D.C., Bradley, A.D., Sadofsky, S.J., 1999. Nitrogen-isotope record of fluid-rock interactions in the Skiddaw Aureole and granite, English Lake District. *American Mineralogist* 84, 1495–1505. <https://doi.org/10.2138/am-1999-1002>

Bebout, G.E., Fogel, M.L., 1992. Nitrogen-isotope compositions of metasedimentary rocks in the Catalina Schist, California: Implications for metamorphic devolatilization history. *Geochimica et Cosmochimica Acta* 56, 2839–2849. [https://doi.org/10.1016/0016-7037\(92\)90363-N](https://doi.org/10.1016/0016-7037(92)90363-N)

Boyd, S.R., Philippot, P., 1998. Precambrian ammonium biogeochemistry: a study of the Moine metasediments, Scotland. *Chemical Geology* 144, 257–268. [https://doi.org/10.1016/S0009-2541\(97\)00135-6](https://doi.org/10.1016/S0009-2541(97)00135-6)

Busigny, V., Cartigny, P., Philippot, P., Ader, M., Javoy, M., 2003. Massive recycling of nitrogen and other fluid-mobile elements (K, Rb, Cs, H) in a cold slab environment: evidence from HP to UHP oceanic metasediments of the Schistes Lustrés nappe (western Alps, Europe). *Earth and Planetary Science Letters* 215, 27–42. [https://doi.org/10.1016/S0012-821X\(03\)00453-9](https://doi.org/10.1016/S0012-821X(03)00453-9)

Busigny, V., Lebeau, O., Ader, M., Krapež, B., Bekker, A., 2013. Nitrogen cycle in the Late Archean ferruginous ocean. *Chemical Geology, Special Issue dedicated to H.D. Holland: Evolution of the atmosphere and ocean through time* 362, 115–130. <https://doi.org/10.1016/j.chemgeo.2013.06.023>

Chen, Y., Diamond, C.W., Stüeken, E.E., Cai, C., Gill, B.C., Zhang, F., Bates, S.M., Chu, X., Ding, Y., Lyons, T.W., 2019. Coupled evolution of nitrogen cycling and redoxcline dynamics on the Yangtze Block across the Ediacaran-Cambrian transition. *Geochimica et Cosmochimica Acta* 257, 243–265. <https://doi.org/10.1016/j.gca.2019.05.017>

- Cheng, C., Busigny, V., Ader, M., Thomazo, C., Chaduteau, C., Philippot, P., 2019. Nitrogen isotope evidence for stepwise oxygenation of the ocean during the Great Oxidation Event. *Geochimica et Cosmochimica Acta* 261, 224–247. <https://doi.org/10.1016/j.gca.2019.07.011>
- Cox, G.M., Sansjofre, P., Blades, M.L., Farkas, J., Collins, A.S., 2019. Dynamic interaction between basin redox and the biogeochemical nitrogen cycle in an unconventional Proterozoic petroleum system. *Sci Rep* 9, 5200. <https://doi.org/10.1038/s41598-019-40783-4>
- Cremonese, L., Shields-Zhou, G., Struck, U., Ling, H.-F., Och, L., Chen, X., Li, D., 2013. Marine biogeochemical cycling during the early Cambrian constrained by a nitrogen and organic carbon isotope study of the Xiaotan section, South China. *Precambrian Research, Biogeochemical changes across the Ediacaran-Cambrian transition in South China* 225, 148–165. <https://doi.org/10.1016/j.precamres.2011.12.004>
- Cremonese, L., Shields-Zhou, G.A., Struck, U., Ling, H.-F., Och, L.M., 2014. Nitrogen and organic carbon isotope stratigraphy of the Yangtze Platform during the Ediacaran–Cambrian transition in South China. *Palaeogeography, Palaeoclimatology, Palaeoecology, Cambrian Bioradiation* 398, 165–186. <https://doi.org/10.1016/j.palaeo.2013.12.016>
- Fike, D.A., 2007. Carbon and sulfur isotopic constraints on Ediacaran biogeochemical processes, Huqf supergroups, Sultanate of Oman (Thesis). Massachusetts Institute of Technology.
- Fraga-Ferreira, P.L., Ader, M., Caetano-Filho, S., Sansjofre, P., Paula-Santos, G.M., Babinski, M., Guacaneme, C., Bedoya-Rueda, C., Rojas, V., Reis, H.L.S., Kuchenbecker, M., Trindade, R.I.F., 2021. The Nitrogen Cycle in an Epeiric Sea in the Core of Gondwana Supercontinent: A Study on the Ediacaran-Cambrian Bambuí Group, East-central Brazil. *Frontiers in Earth Science* 9.
- Garvin, J., Buick, R., Anbar, A.D., Arnold, G.L., Kaufman, A.J., 2009. Isotopic Evidence for an Aerobic Nitrogen Cycle in the Latest Archean. *Science* 323, 1045–1048. <https://doi.org/10.1126/science.1165675>
- Godfrey, L.V., Falkowski, P.G., 2009. The cycling and redox state of nitrogen in the Archaean ocean. *Nature Geoscience* 2, 725–729. <https://doi.org/10.1038/ngeo633>
- Godfrey, L.V., Poulton, S.W., Bebout, G.E., Fralick, P.W., 2013. Stability of the nitrogen cycle during development of sulfidic water in the redox-stratified late Paleoproterozoic Ocean. *Geology* 41, 655–658. <https://doi.org/10.1130/G33930.1>
- Haendel, D., Mühle, K., Nitzsche, H.-M., Stiehl, G., Wand, U., 1986. Isotopic variations of the fixed nitrogen in metamorphic rocks. *Geochimica et Cosmochimica Acta* 50, 749–758. [https://doi.org/10.1016/0016-7037\(86\)90351-0](https://doi.org/10.1016/0016-7037(86)90351-0)
- Hallmann, C., Grosjean, E., Shapiro, N.D., Kashiyama, Y., Chikaraishi, Y., Fike, D.A., Ohkouchi, N., Summons, R.E., 2021. Redox-Controlled Ammonium Storage and Overturn in Ediacaran Oceans. *Frontiers in Earth Science* 9.
- Hayes, J.M., Wedeking, W., Kaplan, I.R., 1983. Precambrian organic geochemistry, preservation of the record. In: Schopf WJ (ed) *Earth's earliest biosphere*. Princeton University Press, Princeton, pp 291-301.

- Homann, M., Sansjofre, P., Zuilen, M.V., Heubeck, C., Gong, J., Killingsworth, B., Foster, I.S., Airo, A., Kranendonk, M.J.V., Ader, M., Lalonde, S.V., 2018. Microbial life and biogeochemical cycling on land 3,220 million years ago. *Nature Geoscience* 11, 665. <https://doi.org/10.1038/s41561-018-0190-9>
- Jia, Y., 2006. Nitrogen isotope fractionations during progressive metamorphism: A case study from the Paleozoic Cooma metasedimentary complex, southeastern Australia. *Geochimica et Cosmochimica Acta* 70, 5201–5214. <https://doi.org/10.1016/j.gca.2006.08.004>
- Jia, Y., Kerrich, R., 2004. Nitrogen 15–enriched Precambrian kerogen and hydrothermal systems. *Geochemistry, Geophysics, Geosystems* 5. <https://doi.org/10.1029/2004GC000716>
- Johnson, B.W., Mettam, C., Poulton, S.W., 2022. Combining Nitrogen Isotopes and Redox Proxies Strengthens Paleoenvironmental Interpretations: Examples From Neoproterozoic Snowball Earth Sediments. *Frontiers in Earth Science* 10.
- Kerrich, R., Jia, Y., Manikyamba, C., Naqvi, S.M., 2006. Secular variations of N-isotopes in terrestrial reservoirs and ore deposits. *Geological Society of America Bulletin* 118, 1198–1214. [https://doi.org/10.1130/2006.1198\(05\)](https://doi.org/10.1130/2006.1198(05))
- Kikumoto, R., Tahata, M., Nishizawa, M., Sawaki, Y., Maruyama, S., Shu, D., Han, J., Komiya, T., Takai, K., Ueno, Y., 2014. Nitrogen isotope chemostratigraphy of the Ediacaran and Early Cambrian platform sequence at Three Gorges, South China. *Gondwana Research* 25, 1057–1069. <https://doi.org/10.1016/j.gr.2013.06.002>
- Kipp, M.A., Stüeken, E.E., Yun, M., Bekker, A., Buick, R., 2018. Pervasive aerobic nitrogen cycling in the surface ocean across the Paleoproterozoic Era. *Earth and Planetary Science Letters* 500, 117–126. <https://doi.org/10.1016/j.epsl.2018.08.007>
- Koehler, M.C., Buick, R., Kipp, M.A., Stüeken, E.E., Zaloumis, J., 2018. Transient surface ocean oxygenation recorded in the ~2.66-Ga Jeerinah Formation, Australia. *Proceedings of the National Academy of Sciences* 115, 7711–7716. <https://doi.org/10.1073/pnas.1720820115>
- Koehler, M.C., Stüeken, E.E., Kipp, M.A., Buick, R., Knoll, A.H., 2017. Spatial and temporal trends in Precambrian nitrogen cycling: A Mesoproterozoic offshore nitrate minimum. *Geochimica et Cosmochimica Acta* 198, 315–337. <https://doi.org/10.1016/j.gca.2016.10.050>
- Kump, L.R., Junium, C., Arthur, M.A., Brasier, A., Fallick, A., Melezhik, V., Lepland, A., CČrne, A.E., Luo, G., 2011. Isotopic Evidence for Massive Oxidation of Organic Matter Following the Great Oxidation Event. *Science* 334, 1694–1696. <https://doi.org/10.1126/science.1213999>
- Liu, Y., Stüeken, E.E., Wang, D., Tang, X., Nie, H., Dang, W., Zhang, J., 2022. A potential linkage between excess silicate-bound nitrogen and N₂-rich natural gas in sedimentary reservoirs. *Chemical Geology* 600, 120864. <https://doi.org/10.1016/j.chemgeo.2022.120864>
- Luo, G., Hallmann, C., Xie, S., Ruan, X., Summons, R.E., 2015. Comparative microbial diversity and redox environments of black shale and stromatolite facies in the Mesoproterozoic Xiamaling Formation. *Geochimica et Cosmochimica Acta* 151, 150–167. <https://doi.org/10.1016/j.gca.2014.12.022>

- Luo, G., Junium, C.K., Izon, G., Ono, S., Beukes, N.J., Algeo, T.J., Cui, Y., Xie, S., Summons, R.E., 2018. Nitrogen fixation sustained productivity in the wake of the Palaeoproterozoic Great Oxygenation Event. *Nat Commun* 9, 978. <https://doi.org/10.1038/s41467-018-03361-2>
- Mettam, C., Zerkle, A.L., Claire, M.W., Prave, A.R., Poulton, S.W., Junium, C.K., 2019. Anaerobic nitrogen cycling on a Neoproterozoic ocean margin. *Earth and Planetary Science Letters* 527, 115800. <https://doi.org/10.1016/j.epsl.2019.115800>
- Mingram, B., Bräuer, K., 2001. Ammonium concentration and nitrogen isotope composition in metasedimentary rocks from different tectonometamorphic units of the European Variscan Belt. *Geochimica et Cosmochimica Acta* 65, 273–287. [https://doi.org/10.1016/S0016-7037\(00\)00517-2](https://doi.org/10.1016/S0016-7037(00)00517-2)
- Nishizawa, M., Takahata, N., Terada, K., Komiya, T., Ueno, Y., Sano, Y., 2005. Rare-Earth Element, Lead, Carbon, and Nitrogen Geochemistry of Apatite-Bearing Metasediments from the ~3.8 Ga Isua Supracrustal Belt, West Greenland. *International Geology Review* 47, 952–970. <https://doi.org/10.2747/0020-6814.47.9.952>
- Ossa Ossa, F., Hofmann, A., Spangenberg, J.E., Poulton, S.W., Stüeken, E.E., Schoenberg, R., Eickmann, B., Wille, M., Butler, M., Bekker, A., 2019. Limited oxygen production in the Mesoarchean ocean. *Proceedings of the National Academy of Sciences* 116, 6647–6652. <https://doi.org/10.1073/pnas.1818762116>
- Ossa Ossa, F., Spangenberg, J.E., Bekker, A., König, S., Stüeken, E.E., Hofmann, A., Poulton, S.W., Yierpan, A., Varas-Reus, M.I., Eickmann, B., Andersen, M.B., Schoenberg, R., 2022. Moderate levels of oxygenation during the late stage of Earth's Great Oxidation Event. *Earth and Planetary Science Letters* 594, 117716. <https://doi.org/10.1016/j.epsl.2022.117716>
- Palya, A.P., Buick, I.S., Bebout, G.E., 2011. Storage and mobility of nitrogen in the continental crust: Evidence from partially melted metasedimentary rocks, Mt. Stafford, Australia. *Chemical Geology* 281, 211–226. <https://doi.org/10.1016/j.chemgeo.2010.12.009>
- Papineau, D., De Gregorio, B., Fearn, S., Kilcoyne, D., McMahon, G., Purohit, R., Fogel, M., 2016. Nanoscale petrographic and geochemical insights on the origin of the Palaeoproterozoic stromatolitic phosphorites from Aravalli Supergroup, India. *Geobiology* 14, 3–32. <https://doi.org/10.1111/gbi.12164>
- Papineau, D., Mojzsis, S.J., Karhu, J.A., Marty, B., 2005. Nitrogen isotopic composition of ammoniated phyllosilicates: case studies from Precambrian metamorphosed sedimentary rocks. *Chemical Geology* 216, 37–58. <https://doi.org/10.1016/j.chemgeo.2004.10.009>
- Papineau, D., Purohit, R., Fogel, M.L., Shields-Zhou, G.A., 2013. High phosphate availability as a possible cause for massive cyanobacterial production of oxygen in the Paleoproterozoic atmosphere. *Earth and Planetary Science Letters* 362, 225–236. <https://doi.org/10.1016/j.epsl.2012.11.050>
- Papineau, D., Purohit, R., Goldberg, T., Pi, D., Shields, G.A., Bhu, H., Steele, A., Fogel, M.L., 2009. High primary productivity and nitrogen cycling after the Paleoproterozoic phosphogenic event in the Aravalli Supergroup, India. *Precambrian Research* 171, 37–56. <https://doi.org/10.1016/j.precamres.2009.03.005>

- Pinti, D.L., Hashizume, K., Matsuda, J., 2001. Nitrogen and argon signatures in 3.8 to 2.8 Ga metasediments: clues on the chemical state of the Archean ocean and the deep biosphere. *Geochimica et Cosmochimica Acta* 65, 2301–2315. [https://doi.org/10.1016/S0016-7037\(01\)00590-7](https://doi.org/10.1016/S0016-7037(01)00590-7)
- Pinti, D.L., Hashizume, K., Sugihara, A., Massault, M., Philippot, P., 2009. Isotopic fractionation of nitrogen and carbon in Paleoarchean cherts from Pilbara craton, Western Australia: Origin of ¹⁵N-depleted nitrogen. *Geochimica et Cosmochimica Acta* 73, 3819–3848. <https://doi.org/10.1016/j.gca.2009.03.014>
- Sadofsky, S.J., Bebout, G.E., 2000. Ammonium partitioning and nitrogen-isotope fractionation among coexisting micas during high-temperature fluid-rock interactions: examples from the New England Appalachians. *Geochimica et Cosmochimica Acta* 64, 2835–2849. [https://doi.org/10.1016/S0016-7037\(00\)00393-8](https://doi.org/10.1016/S0016-7037(00)00393-8)
- Spangenberg, J.E., Bagnoud-Velásquez, M., Boggiani, P.C., Gaucher, C., 2014. Redox variations and bioproductivity in the Ediacaran: Evidence from inorganic and organic geochemistry of the Corumbá Group, Brazil. *Gondwana Research* 26, 1186–1207. <https://doi.org/10.1016/j.gr.2013.08.014>
- Stüeken, E.E., 2013. A test of the nitrogen-limitation hypothesis for retarded eukaryote radiation: Nitrogen isotopes across a Mesoproterozoic basinal profile. *Geochimica et Cosmochimica Acta* 120, 121–139. <https://doi.org/10.1016/j.gca.2013.06.002>
- Stüeken, E.E., Boocock, T., Szilas, K., Mikhail, S., Gardiner, N.J., 2021a. Reconstructing Nitrogen Sources to Earth's Earliest Biosphere at 3.7 Ga. *Frontiers in Earth Science* 9.
- Stüeken, E.E., Boocock, T.J., Robinson, A., Mikhail, S., Johnson, B.W., 2021b. Hydrothermal recycling of sedimentary ammonium into oceanic crust and the Archean ocean at 3.24 Ga. *Geology* 49, 822–826. <https://doi.org/10.1130/G48844.1>
- Stüeken, E.E., Buick, R., 2018. Environmental control on microbial diversification and methane production in the Mesoarchean. *Precambrian Research* 304, 64–72. <https://doi.org/10.1016/j.precamres.2017.11.003>
- Stüeken, E. E., Buick, R., Anderson, R.E., Baross, J.A., Planavsky, N.J., Lyons, T.W., 2017. Environmental niches and metabolic diversity in Neoarchean lakes. *Geobiology* 15, 767–783. <https://doi.org/10.1111/gbi.12251>
- Stüeken, E.E., Buick, R., Guy, B.M., Koehler, M.C., 2015a. Isotopic evidence for biological nitrogen fixation by molybdenum-nitrogenase from 3.2 Gyr. *Nature* 520, 666–669. <https://doi.org/10.1038/nature14180>
- Stüeken, E. E., Buick, R., Schauer, A.J., 2015. Nitrogen isotope evidence for alkaline lakes on late Archean continents. *Earth and Planetary Science Letters* 411, 1–10. <https://doi.org/10.1016/j.epsl.2014.11.037>
- Stüeken, E.E., Buick, R., Schauer, A.J., 2015b. Nitrogen isotope evidence for alkaline lakes on late Archean continents. *Earth and Planetary Science Letters* 411, 1–10. <https://doi.org/10.1016/j.epsl.2014.11.037>

- Stüeken, E.E., Gregory, D.D., Mukherjee, I., McGoldrick, P., 2021c. Sedimentary exhalative venting of bioavailable nitrogen into the early ocean. *Earth and Planetary Science Letters* 565, 116963. <https://doi.org/10.1016/j.epsl.2021.116963>
- Stüeken, E.E., Kipp, M.A., Koehler, M.C., Buick, R., 2016. The evolution of Earth's biogeochemical nitrogen cycle. *Earth-Science Reviews* 160, 220–239. <https://doi.org/10.1016/j.earscirev.2016.07.007>
- Stüeken, E.E., Kuznetsov, A.B., Vasilyeva, I.M., Krupenin, M.T., Bekker, A., 2021d. Transient deep-water oxygenation recorded by rare Mesoproterozoic phosphorites, South Urals. *Precambrian Research* 360, 106242. <https://doi.org/10.1016/j.precamres.2021.106242>
- Stüeken, E.E., Prave, A.R., 2022. Diagenetic nutrient supplies to the Proterozoic biosphere archived in divergent nitrogen isotopic ratios between kerogen and silicate minerals. *Geobiology* 20, 623–633. <https://doi.org/10.1111/gbi.12507>
- Stüeken, E.E., Viehmann, S., Hohl, S.V., 2022. Contrasting nutrient availability between marine and brackish waters in the late Mesoproterozoic: Evidence from the Paranoá Group, Brazil. *Geobiology* 20, 159–174. <https://doi.org/10.1111/gbi.12478>
- Stüeken, E.E., Zaloumis, J., Meixnerová, J., Buick, R., 2017. Differential metamorphic effects on nitrogen isotopes in kerogen extracts and bulk rocks. *Geochimica et Cosmochimica Acta* 217, 80–94. <https://doi.org/10.1016/j.gca.2017.08.019>
- Thomas, K.S., 2011. Organic Geochemistry and Stable Isotope Constraints on Precambrian Biogeochemical Processes: Examples of the Late Proterozoic Coppercap Formation, NWT Canada and Archean Gorge Creek Group, Pilbara. Master thesis, Massachusetts Institute of Technology.
- Thomazo, C., Ader, M., Philippot, P., 2011. Extreme ^{15}N -enrichments in 2.72-Gyr-old sediments: evidence for a turning point in the nitrogen cycle. *Geobiology* 9, 107–120. <https://doi.org/10.1111/j.1472-4669.2011.00271.x>
- Ueno, Y., Yoshioka, H., Maruyama, S., Isozaki, Y., 2004. Carbon isotopes and petrography of kerogens in ~3.5-Ga hydrothermal silica dikes in the North Pole area, Western Australia. *Geochimica et Cosmochimica Acta* 68, 573–589. [https://doi.org/10.1016/S0016-7037\(03\)00462-9](https://doi.org/10.1016/S0016-7037(03)00462-9)
- Van Zuilen, M.A., Mathew, K., Wopenka, B., Lepland, A., Marti, K., Arrhenius, G., 2005. Nitrogen and argon isotopic signatures in graphite from the 3.8-Ga-old Isua Supracrustal Belt, Southern West Greenland. *Geochimica et Cosmochimica Acta* 69, 1241–1252. <https://doi.org/10.1016/j.gca.2004.08.033>
- Wang, X., Shi, X., Tang, D., Zhang, W., 2015. Nitrogen Isotope Evidence for Redox Variations at the Ediacaran-Cambrian Transition in South China. *The Journal of Geology*. <https://doi.org/10.1086/671396>
- Wang, Z., Wang, X., Shi, X., Tang, D., Stüeken, E.E., Song, H., 2020. Coupled Nitrate and Phosphate Availability Facilitated the Expansion of Eukaryotic Life at Circa 1.56 Ga. *Journal of Geophysical Research: Biogeosciences* 125, e2019JG005487. <https://doi.org/10.1029/2019JG005487>

Xu, D., Wang, X., Shi, X., Peng, Y., Stüeken, E.E., 2021. Feedback Between Carbon and Nitrogen Cycles During the Ediacaran Shuram Excursion. *Frontiers in Earth Science* 9.

Yamaguchi, K., 2002. Geochemistry of Archean–Paleoproterozoic black shales: The early evolution of the atmosphere, oceans, and biosphere.

Yang, J., Junium, C.K., Grassineau, N.V., Nisbet, E.G., Izon, G., Mettam, C., Martin, A., Zerkle, A.L., 2019. Ammonium availability in the Late Archaean nitrogen cycle. *Nat. Geosci.* 12, 553–557. <https://doi.org/10.1038/s41561-019-0371-1>

Zerkle, A.L., Poulton, S.W., Newton, R.J., Mettam, C., Claire, M.W., Bekker, A., Junium, C.K., 2017. Onset of the aerobic nitrogen cycle during the Great Oxidation Event. *Nature* 542, 465–467. <https://doi.org/10.1038/nature20826>

Zhang, D., 1988. Nitrogen concentrations and isotopic compositions of some terrestrial rocks. PhD, The University of Chicago.

CHAPTER 4. GEOLOGICAL CONTEXT OF THE STUDIED SAMPLES

4.1. Selection criteria for investigating grey areas of the Archean biogeochemical nitrogen cycle	141
4.2. The Buck Reef Chert Formation (3.4 Ga, South Africa)	144
4.2.1. Regional context	144
4.2.2. Stratigraphic framework of the Buck Reef Chert	147
4.2.3. Petrographic features and sedimentary facies.....	150
4.2.4. Paleoenvironment and chemical conditions.....	153
4.3. The Serra Sul Formation (2.7 Ga, Brazil).....	156
4.3.1. Regional context	156
4.3.2. Stratigraphic framework and geochronological constraints	157
4.3.3. Petrographic features and sedimentary facies.....	161
4.3.4. Paleoenvironments of the Serra Sul Formation	167
4.4. The Malmani Subgroup (2.5 Ga, South Africa).....	168
4.4.1. Regional context	168
4.4.2. Stratigraphic framework of the studied samples.....	170
4.4.3. Petrographic features and sedimentary facies.....	173
4.4.4. Paleoenvironments and chemical conditions	176

CHAPTER 4. GEOLOGICAL CONTEXT OF THE STUDIED SAMPLES

4.1. Selection criteria for investigating grey areas of the Archean biogeochemical nitrogen cycle

Three study sites were selected in the attempt to get some insights into early processes governing the N-biogeochemical cycle, in particular (i) detecting the onset of oxidative nitrogen cycling, (ii) exploring the relationship between the nitrogen cycle and biology, and (iii) assessing the emergence of biological pathways of the nitrogen cycle.

Beyond practical constraints, including sample availability (through various research projects mentioned in Chapter 5) and the limits of analytical setups (mostly with regards to the N content of the samples, Chapter 2), a number of parameters narrowed my research.

First, the three study sites span the Archean, from the Paleoproterozoic Buck Reef Chert sedimentary succession to the early Neoproterozoic Serra Sul Formation to the late Neoproterozoic Malmani Subgroup. They also fill in some temporal gaps in the nitrogen isotope geological record, sparse around those time periods (Fig. 4.1). Besides, the three study sites may be emblematic of three previously identified key time periods concerning the Archean N-biogeochemical cycle (Chapter 3). The first one, represented by the Buck Reef Chert, is emblematic of an anoxic world in which reduced N species were dominant. The second key time period is around 2.7 Ga, where a “ $\delta^{15}\text{N}$ anomaly” showing extremely positive nitrogen isotope compositions has been observed. Occurring in a single location, the Australian Tumbiana Formation, it is a peculiar feature of the Archean N isotope record and deserves some attention as to the processes behind such a signal. The c.a. 2.7 Ga Serra Sul Formation gives perspectives to dive deeper into those processes. Finally, the 2.5 Ga carbonates of the Malmani Subgroup have been deposited at the eve of the GOE, a period where changes in the N-biogeochemical cycle are expected, with the rise oxidized N species and more generally oxidants in the environment.

Alongside temporal gaps, the nitrogen isotope record suffers from important spatial gaps, with most key time intervals represented by samples from a single locality or rocks from a single craton. Our samples fill in some spatial gaps to get a wider coverage that may be more representative of the global oceanic conditions on the early Earth. Samples from the 2.68 Ga Serra Sul Formation, Amazonian Craton, Brazil will provide a comparison with the 2.72 Ga

Australian Tumbiana Formation in the Pilbara Craton, while the 3.42 Ga Buck Reef Chert in the South African Kaapvaal Craton can be compared to the 3.48 Ga Dresser Formation in the Pilbara Craton, Australia.

Moreover, when looking at geochemical features of Archean rocks, one of the key selection criteria concerns the preservation of the primary signature. Concerning the nitrogen isotope composition, the effects of diagenetic and metamorphic alteration have been discussed in Chapter 2. To the best of sample availability, we have selected sediments that have not been highly metamorphosed and avoided the most recrystallized samples. Metamorphism for each study site is discussed in this chapter.

The three study sites also allow to explore the Archean N isotope record for different lithologies: cherts/BIFs for the Buck Reef Chert, shales and detrital material in the Serra Sul Formation and carbonates in the Malmani Subgroup. This diversity of lithologies also means a variety of depositional environments, with both proximal and distal settings. In addition, the Buck Reef Chert will provide some insight into the effect of peculiar chemical conditions on the N cycle, in that case iron abundance and a ferruginous depositional environment.

One last interesting feature of the studied set of samples are potential traces of life. Biofilms have been described in the Buck Reef Chert (Alleon et al., 2021; Tice and Lowe, 2004) and the Malmani Subgroup comprises centimetric to metric stromatolitic domes. Meanwhile, the two studied drill cores of the Serra Sul Formation are devoid of microbial mats, although some have been identified in nearby samples. Therefore, these samples might be appropriate for exploring biological pathways of the early nitrogen cycle, whether anoxic or oxidative.

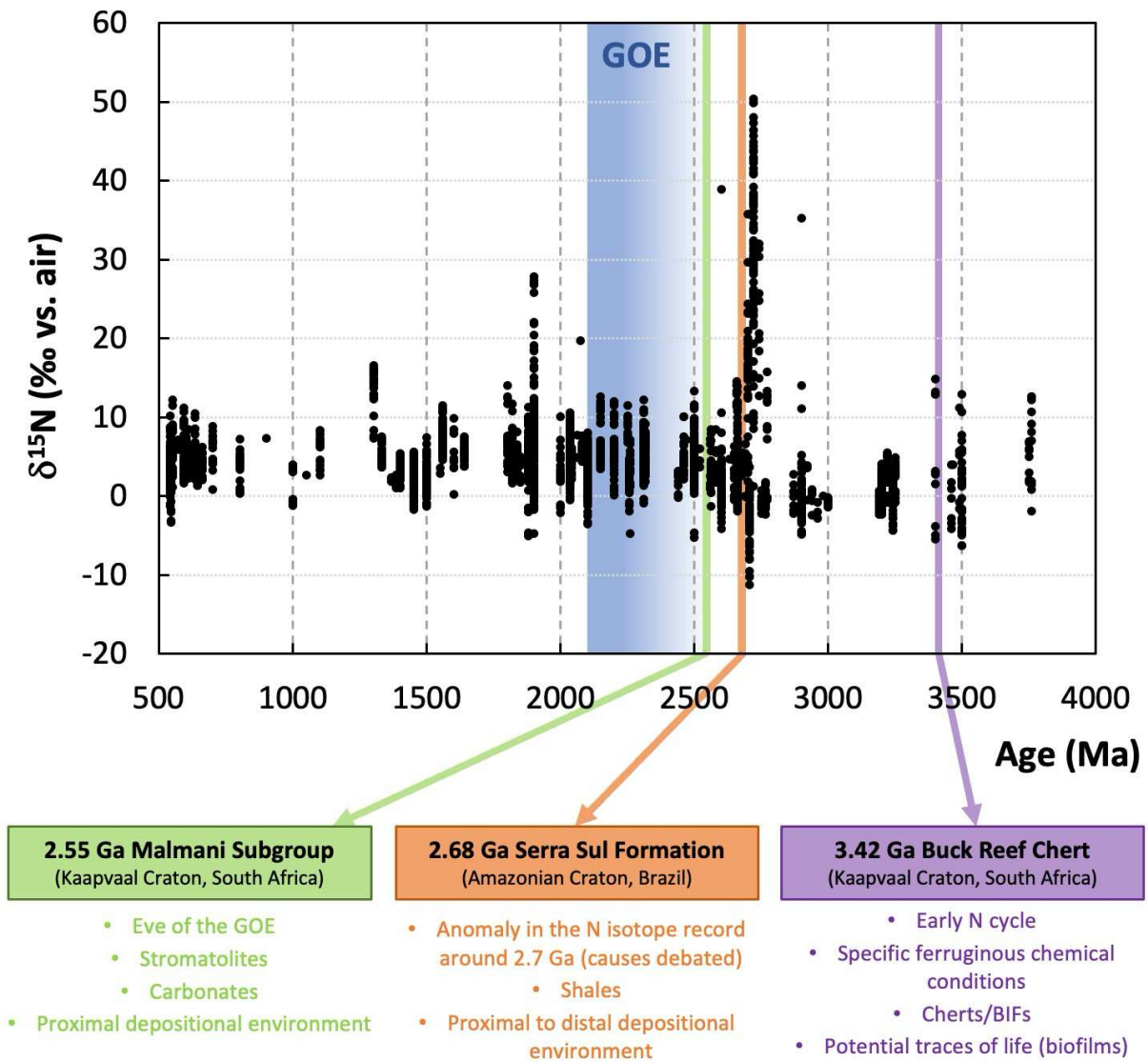


Fig. 4.1. Compilation of published Precambrian $\delta^{15}\text{N}$ data with the time intervals of the three study sites, including the main features of interests regarding our understanding of the early N-biogeochemical cycle. The time interval usually considered for the Great Oxidation Event (GOE, Lyons et al., 2014) is shown in blue.

4.2. The Buck Reef Chert Formation (3.4 Ga, South Africa)

Although they are a prevalent feature of Archean Greenstone Belts, chert deposits remain enigmatic regarding their primary or diagenetic origin, the mode of silicification and the origin of the banding. Therefore, they provide a sedimentary archive worth exploring, as it is necessary to determine the extent to which they can be informative to reconstruct paleoenvironments.

4.2.1. Regional context

The Barberton Greenstone Belt (BGB), located in the Eastern part of the Kaapvaal craton (Fig. 4.2), outcropping in North Eastern South Africa and Swaziland, is one of the few places where the early history of Earth's surface, older than 3.1 Ga, can be studied. Sedimentary and volcanic rocks of the BGB are well-preserved for their age and represent diverse environments, allowing us to study surface processes such as the composition and physical specifications of the oceans and atmosphere, and parameters governing the development of early life and associated metabolisms. The BGB comprises the 3.55 to 3.22 Ga supracrustal rocks of the Swaziland Supergroup, which is subdivided into the Onverwacht Group, the Fig Tree Group and the Moodies Group (Fig. 4.2-4.3, Lowe and Byerly, 1999; Lowe and Worrell, 1999). The 3.55 to 3.30 Ga Onverwacht Group (Fig. 4.2-4.4) is dominated by submarine ultramafic to mafic volcanic rocks, minor felsic volcanic rocks and sedimentary rocks. The 3.26 to 3.23 Ga Fig Tree Group (Fig. 4.2-4.3) is composed of siliclastic sedimentary rocks with minor Banded Iron Formations, supposedly shallower than those of the Onverwacht Group. Finally, the uppermost 3.22 Ga Moodies Group (Fig. 4.2-4.3) consists of shallow-water to fluvial sandstone and conglomerates with minor shales and Banded Iron Formations. Cherts are a prevalent feature of the Onverwacht and lower part of the Fig Tree groups, and become scarce or absent towards the Moodies Group (Hofmann et al., 2013). The central part of the BGB was affected by lower greenschist facies metamorphism, and locally reaches up to the amphibolite facies (Tice et al., 2004).

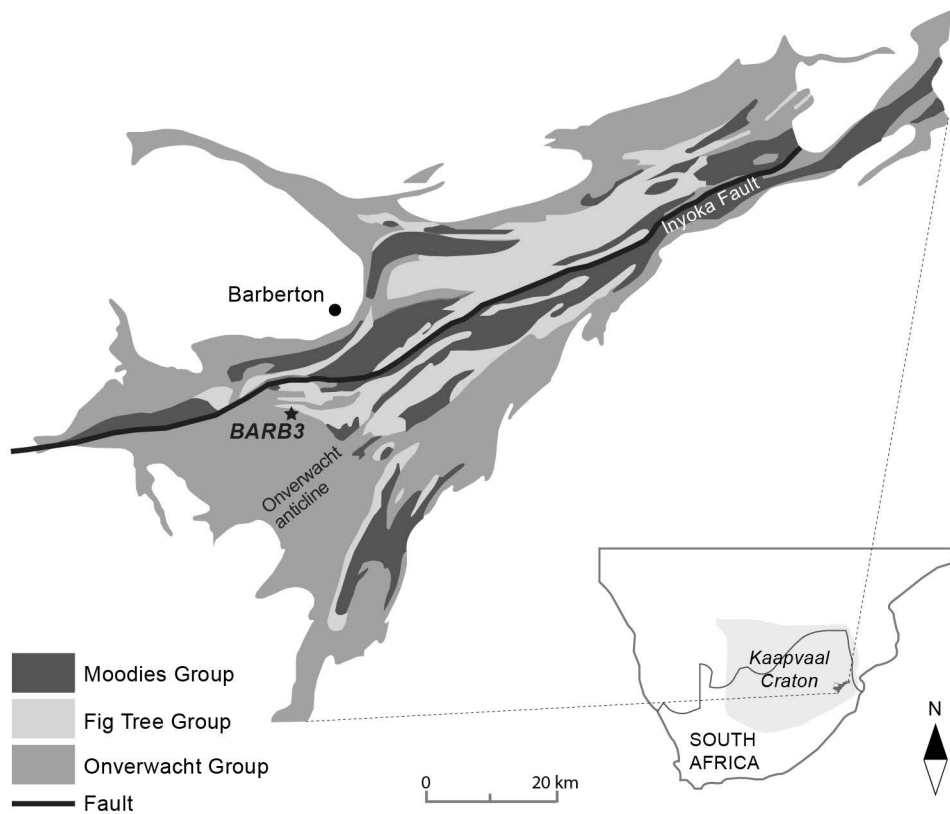


Fig. 4.2. Geological map of the Barberton Greenstone Belt (BGB) and its localization in the Kaapvaal Craton spread across South Africa and Swaziland (Greco et al., 2018; modified after Homann et al., 2015). The BARB3 drill core, located in the Onverwacht Group, is identified by a star.

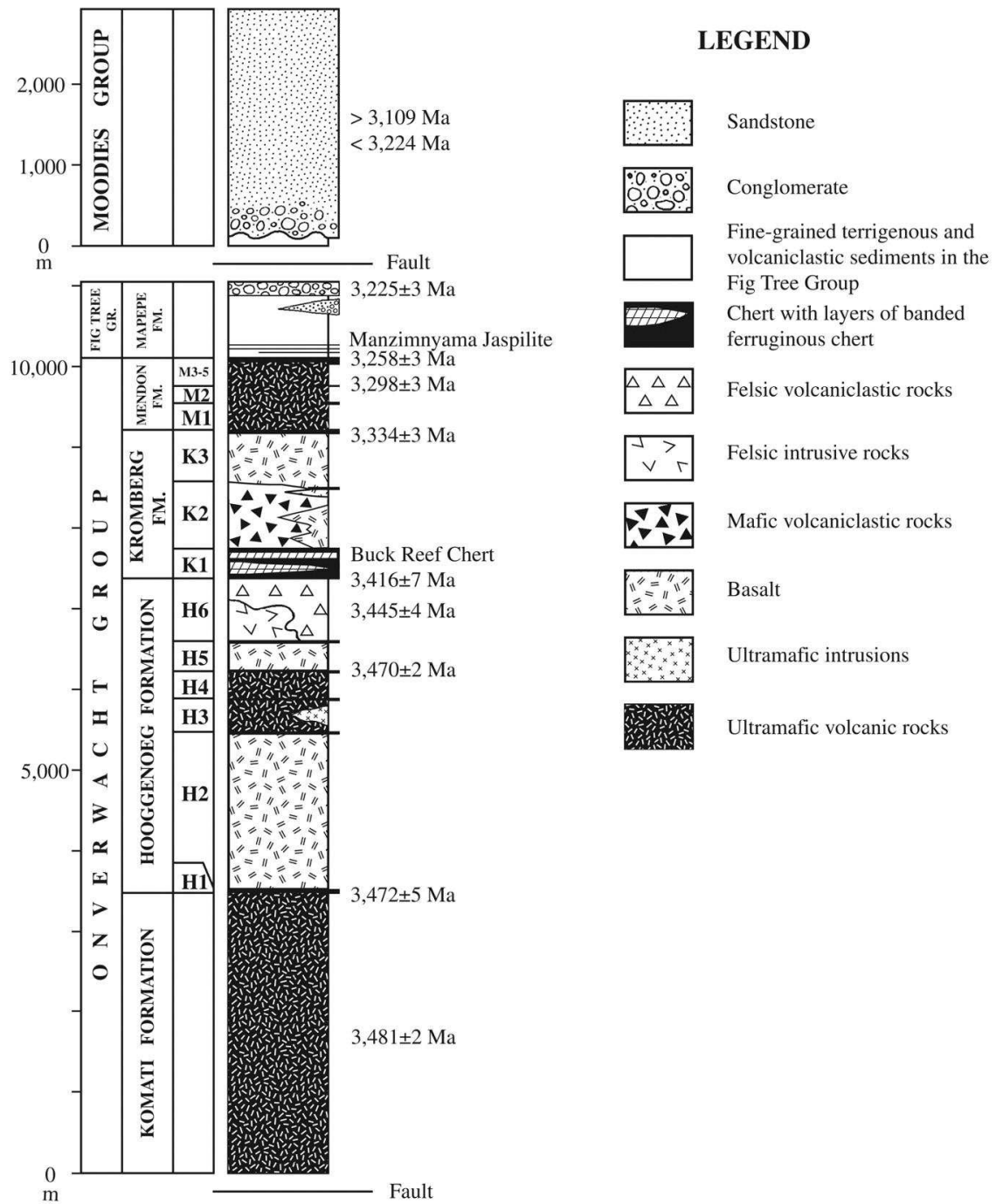


Fig. 4.3. Stratigraphy of the Barberton Greenstone Belt (BGB), missing the Sandspruit and Theespruit Formations (Lowe and Byerly, 2007).

4.2.2. Stratigraphic framework of the Buck Reef Chert

Among the BGB, in the Kromberg Formation of the Onverwacht Group, the 3416 ± 5 Ma (Krüner et al., 1991) Buck Reef Chert (BRC) is the largest chert deposit (Lowe and Worrell, 1999). The BRC is a thick sequence of up to 350m, composed of black and white banded cherts and ferruginous cherts (Fig. 4.5). Steeply dipping, it overlies a shallow intrusive to extrusive sequence of dacitic volcanic rocks of the Hooggenoeg Formation and is separated from ultramafic lapillistone of the Kromberg Formation by a >150 m thick ultramafic sill (Fig. 4.3-4.4). The BRC is assigned to the lowermost part of the Kromberg Formation (K1 Member, de Vries et al., 2010; Kröner et al., 2016; Lowe and Byerly, 1999).

The BRC represents one of the few well-preserved Paleoproterozoic sedimentary sequences on Earth, with a low metamorphic grade in the lower greenschist facies (Tice et al., 2004).

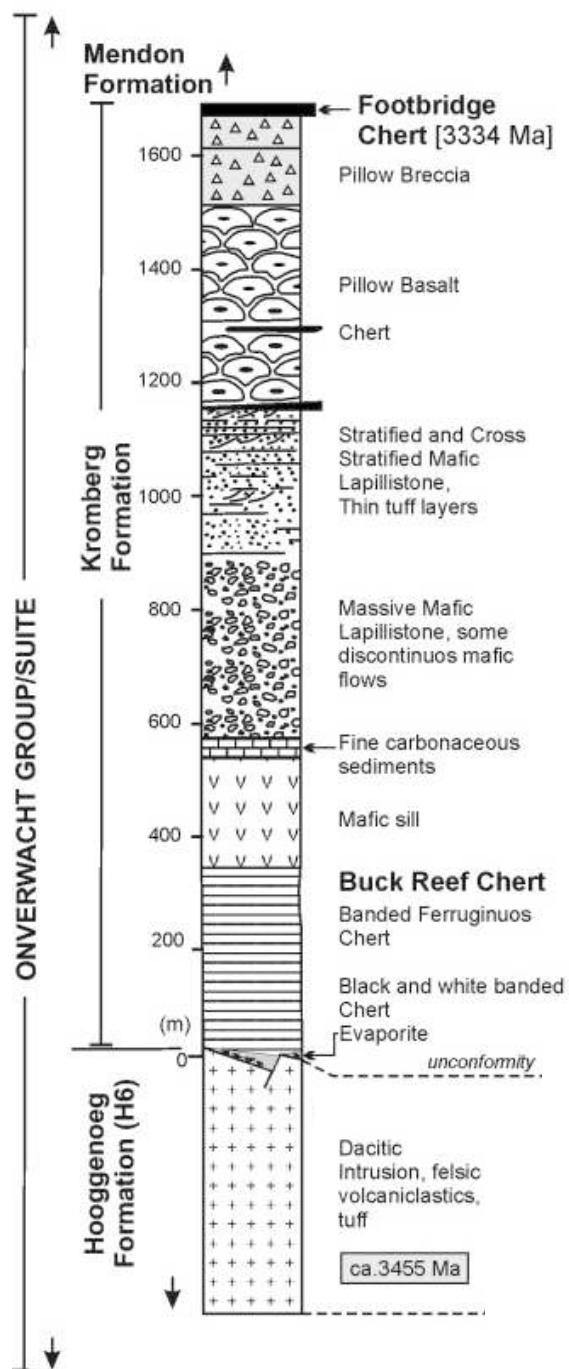


Fig. 4.4. Stratigraphy model for the part of the Onverwacht Group where the Buck Reef Chert sedimentary sequence is located (modified after Grosch et al., 2011; Lowe, 1999).

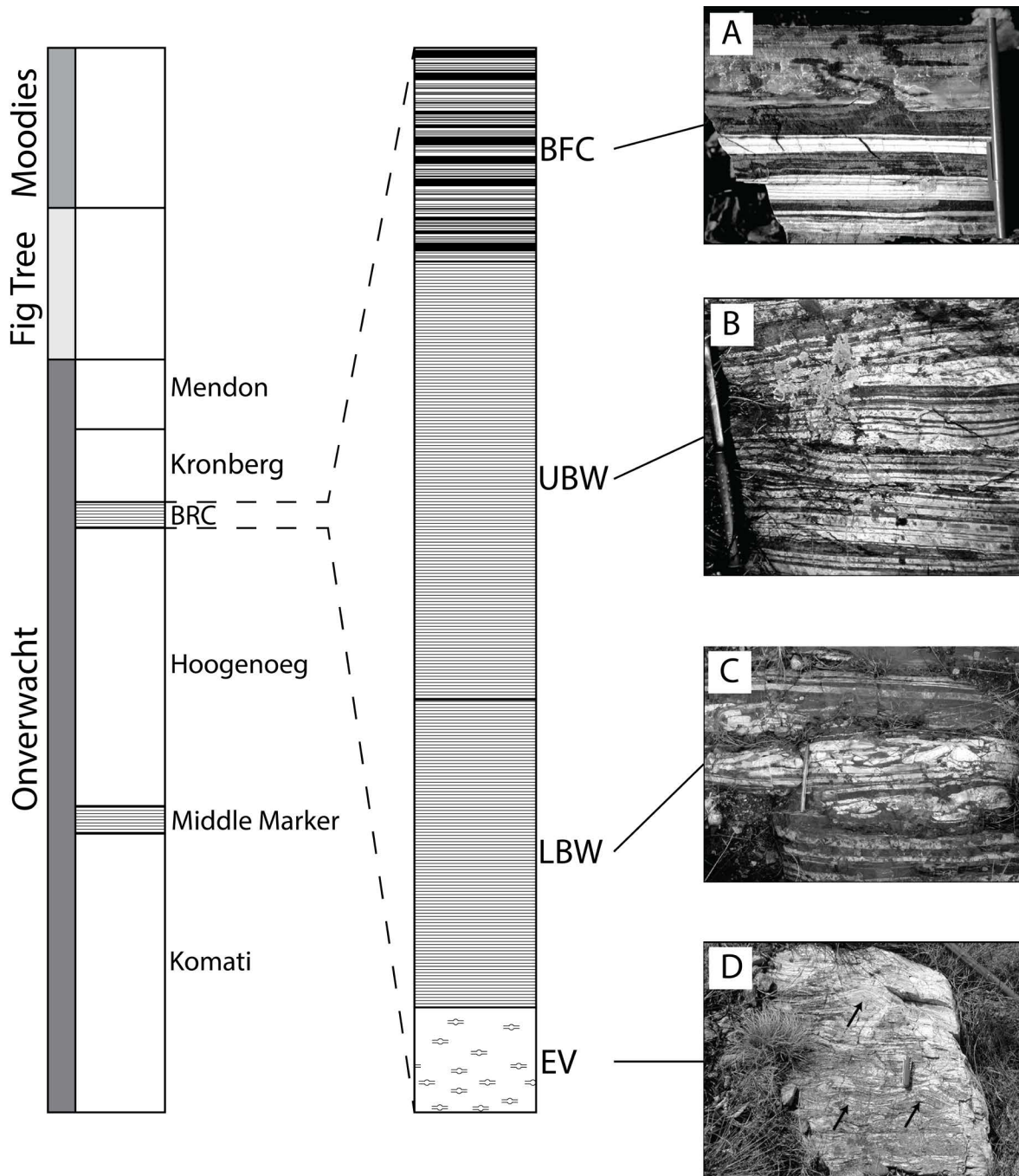


Fig. 4.5. Main facies observed in the Buck Reef Chert (BRC) from outcrop. (A) banded ferruginous chert (BFC), with rust-colored bands, (B) upper black and white banded chert facies (UBW) displaying clear, undisturbed bedding, (C) lower black and white banded chert facies (LBW), displaying chert brecciation in a black chert matrix, and (D) evaporitic facies with arrows pointing to visible ripple marks (modified from Tice and Lowe, 2006a).

4.2.3. Petrographic features and sedimentary facies

The 900-meters depth ICDP-sponsored BARB3 drill core (Barberton drilling project, Hofmann et al., 2013; Fig. 4.6) through the BRC sedimentary deposit intersected ca. 200 m of serpentinized peridotite before a 700 m pile of cherts displaying a variety of lithofacies (Fig. 4.5-4.6). Minor igneous/mafic intrusions punctuate this pile. The base of the BRC Formation, where evaporites were described on outcrop samples (Fig. 4.4-4.5; Tice and Lowe, 2006a) was unfortunately not intersected by the drill core. The aim of this drilling project was to provide insights into environmental conditions prevailing in marine Archean settings, exploring potential traces of early life, (bio)geochemical cycles and the influence of hydrothermalism (Hofmann et al., 2013). The abundance variations in Fe-bearing carbonates, organic matter and sulfides in the different chert facies was interpreted as potential changes in these parameters, to be explored through sedimentological, mineralogical and geochemical studies (Hofmann et al., 2013). Microscopic observations on the studied BARB3 drill core (Fig. 4.7) match detailed facies studies performed on outcrop samples (Fig. 4.5) by Tice and Lowe (2006a), except for the evaporitic facies that has not been intersected.

In terms of sedimentology, the BARB3 drill core records a transition between two sedimentary units (Fig. 4.6): a basal chert-dominated unit from 900 to 600 meters depth and a BIF-dominated unit from 600 to 400 meters depth. The chert-dominated unit consists of a succession of black and white banded cherts with silica grains and occurrences of carbonaceous-rich clots and laminae, ferruginous cherts, granular cherts, breccia and a few occurrences of siderite layers (Fig. 4.7-4.8). The BIF-dominated unit is mainly composed of thick layers of siderite alternating with a smaller proportion of chert beds (Fig. 4.7-4.8). Siderite occurs as densely packed rhombic and spherulitic crystals, typical of early diagenetic processes (Fig. 4.7). A distinctive feature of the BIF-dominated unit is the occurrence of thin layers, ≈ 1 cm thick, of microcrystalline quartz and carbonate characterized by subspherical domains (25 μm) containing micron to sub-micron inclusions of red iron oxides (Fig. 4.7). Single quartz crystals 50 μm in diameter enclose the spheres. These jasper layers are located in the depth intervals of 580-560, 545-500 and 480-400 meters (Fig. 4.6, 4.7C, 4.8C). Euhedral iron-rich carbonate crystals in jasper occur in varying amounts (ca. 5-10%) and are either disseminated or in lenticular clusters, suggesting their early diagenetic origin. The jasper layers are unrelated to any zones where oxic groundwaters could have circulated at depth, which suggests they are primary. Carbonaceous matter is present throughout the BARB3 drill core, with some occasional organic-rich centimetric layers, as well

as some carbonaceous clots and laminae (Fig. 4.9) disseminated in the quartz and sideritic matrix (Greco et al., 2018; Tice and Lowe, 2006a).

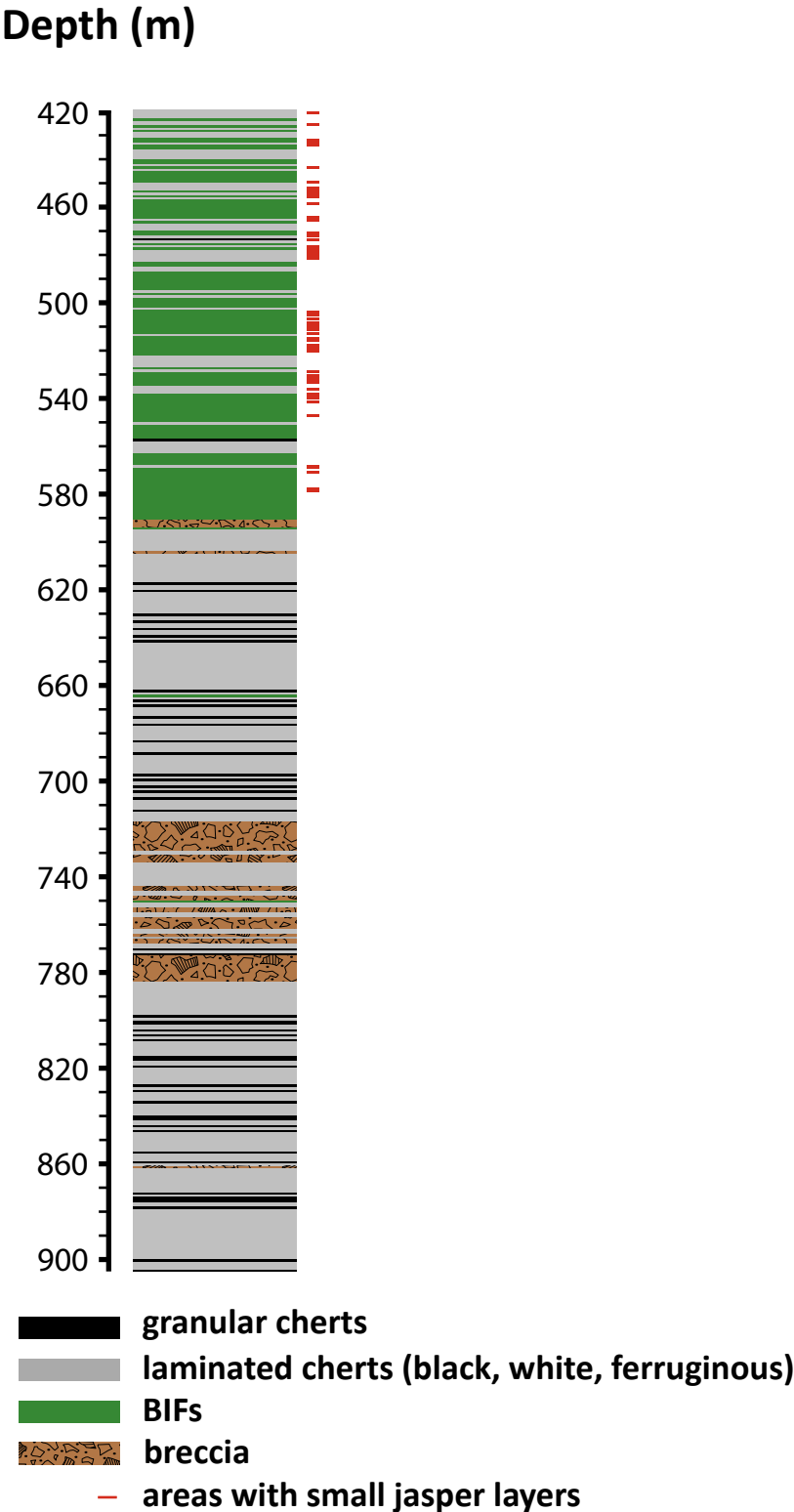


Fig. 4.6. Facies of the BARB3 drill core depths studied in this work (420-900m). Areas containing centimetric jasper layers are displayed with fine red lines (modified from Pellerin et al., 2023).

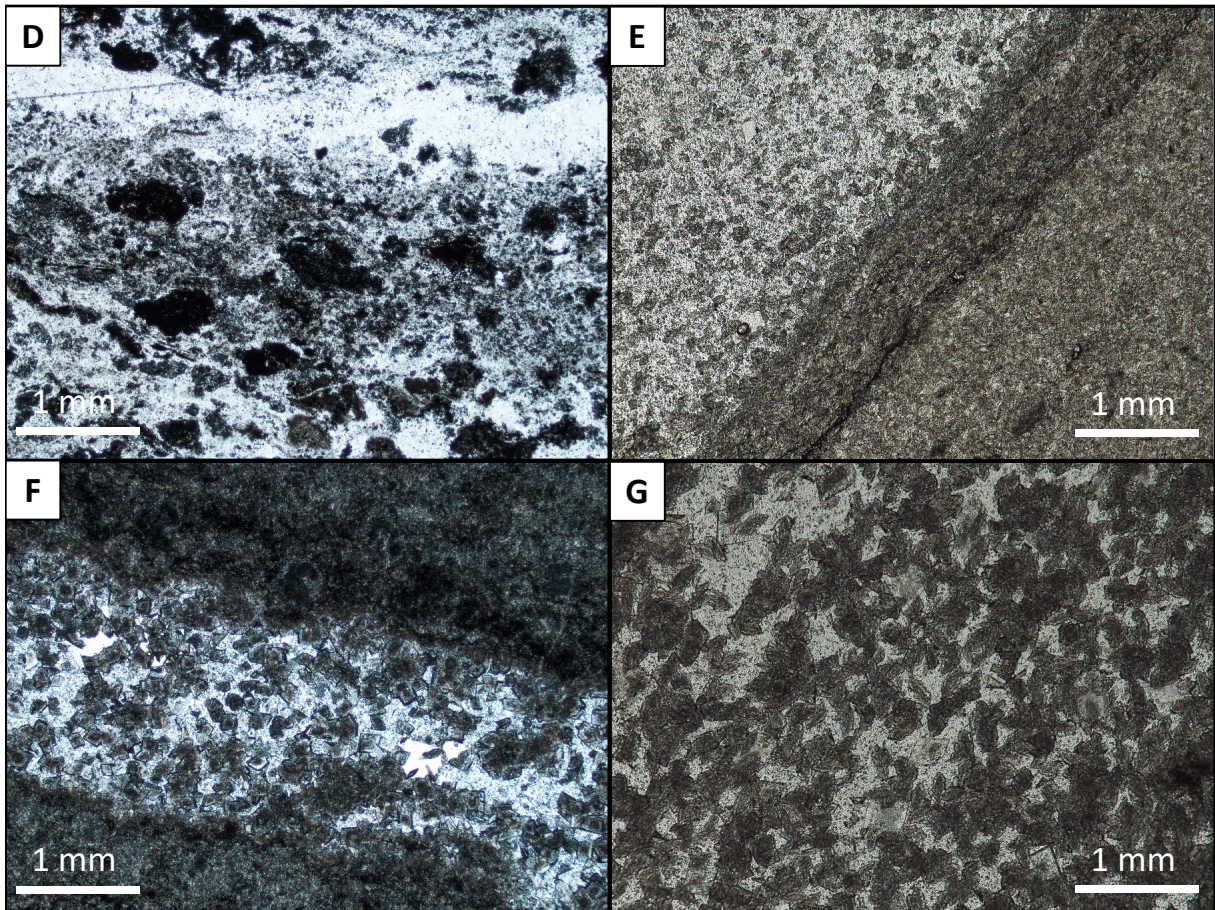
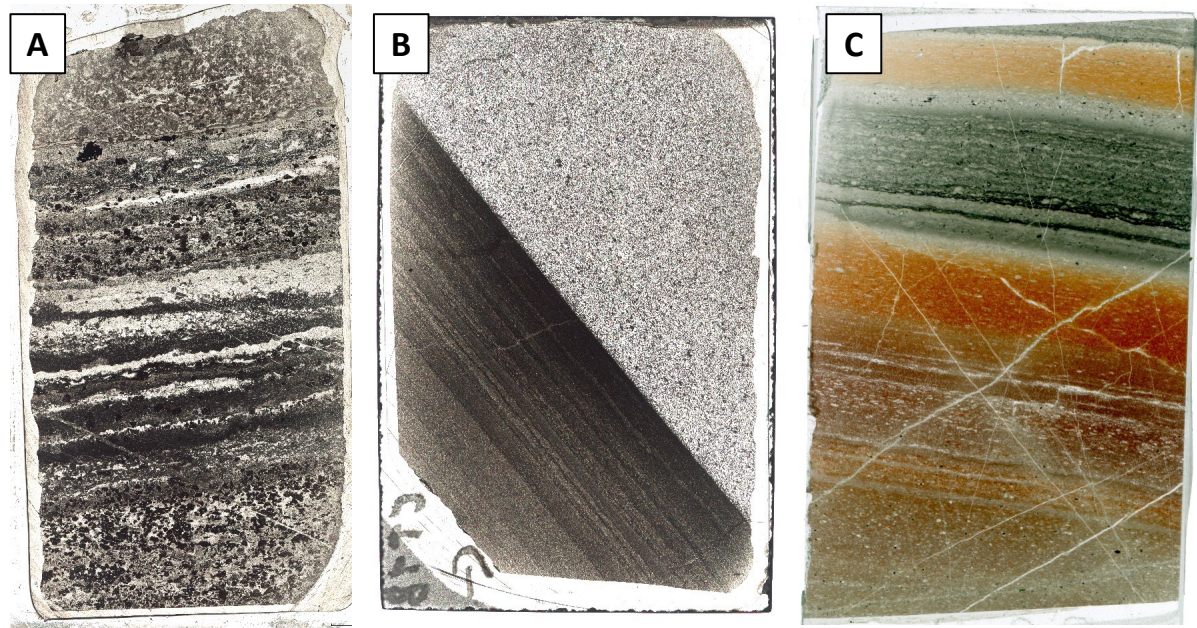


Fig. 4.7. Thin sections representative of the three main units of the BRC (Pellerin et al., 2023): the chert-dominated unit (A), the BIF-dominated unit with alternating chert and siderite layers (B) and the jasper layers of the upper BIF-dominated unit (C). D: Carbonaceous grains and laminae embedded in the siliceous matrix of the chert-dominated unit (874.87m). E: Contact between a chert layer (left) and a

siderite layer (right, 471.05m). F: Chert layer with disseminated siderite crystals between two siderite layers with laminated carbonaceous material (573.11m). G: Siderite crystals in a chert matrix (437.27m).

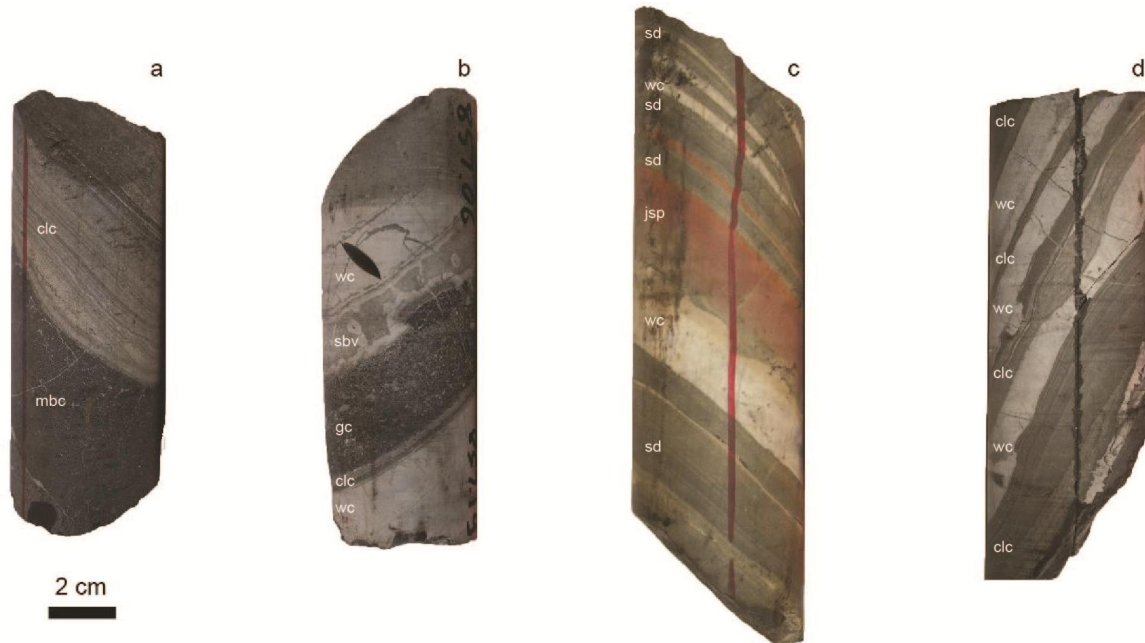


Fig. 4.8. BARB3 core samples representative of the different facies of the BRC (Greco, 2018). (a) Sample from 865.76-865.63m, displaying a lower massive black chert (mbc) and an overlying greenish-grey crinkly laminated chert (clc); (b) sample from 857.19-865.06m, displaying a stratiform botryoidal quartz vein (sbv) filled by a 4 cm-thick layer of black granular chert (gc) which is overlying a thin band of crinkly laminated chert; the top of the core sample is composed of white bedded chert (wc) bands; (c) sample from 538.30-538.08m, displaying white banded chert (wc) and siderite bands (sd) with sparse jasper mesobands (jsp); (d) sample from 256.29-256.10 displays bands of greenish-grey crinkly laminated ferruginous chert and white bedded chert mesobands.

4.2.4. Paleoenvironment and chemical conditions

The transition between the chert-dominated unit and the BIF-dominated unit is thought to record a temporal and environmental change from a wave-dominated shallow platform to a deeper low-energy basinal depositional environment (Tice and Lowe, 2004), but could also reflect chemical variability linked to variable supply of dissolved iron through hydrothermal discrete pulses (Pellerin et al., 2023).

The origin of the BRC silicified laminations is variously interpreted in the literature, and four main hypotheses stand out: (i) water column chemical precipitation (Ledevin et al., 2019), (ii) secondary silicification of a laminated sedimentary or volcano-sedimentary precursor (de Vries

et al., 2006), (iii) segregation from an initial homogenous mixing of silica and other components during early diagenesis (Tice and Lowe, 2006a), (iv) pulses of hydrothermal silicification (Geilert et al., 2014).

The origin of siderite in the BIF-dominated unit is also debated, as it can either precipitate directly in a stratified water column rich in dissolved iron (Klein and Beukes, 1989) or form in the sediment close to the sediment-water interface during early diagenesis (Heimann et al., 2010). A hydrothermal origin for siderite has also been suggested for some Archean BIFs (Bolhar et al., 2005).

Carbonaceous-rich laminae of the BRC have been interpreted as microbial mats built by anoxygenic photoautotrophs (Tice and Lowe, 2006b). Those carbonaceous laminae were likely preserved within the cherts at the time of their formation, attesting to their primary origin (Alleon et al., 2021).

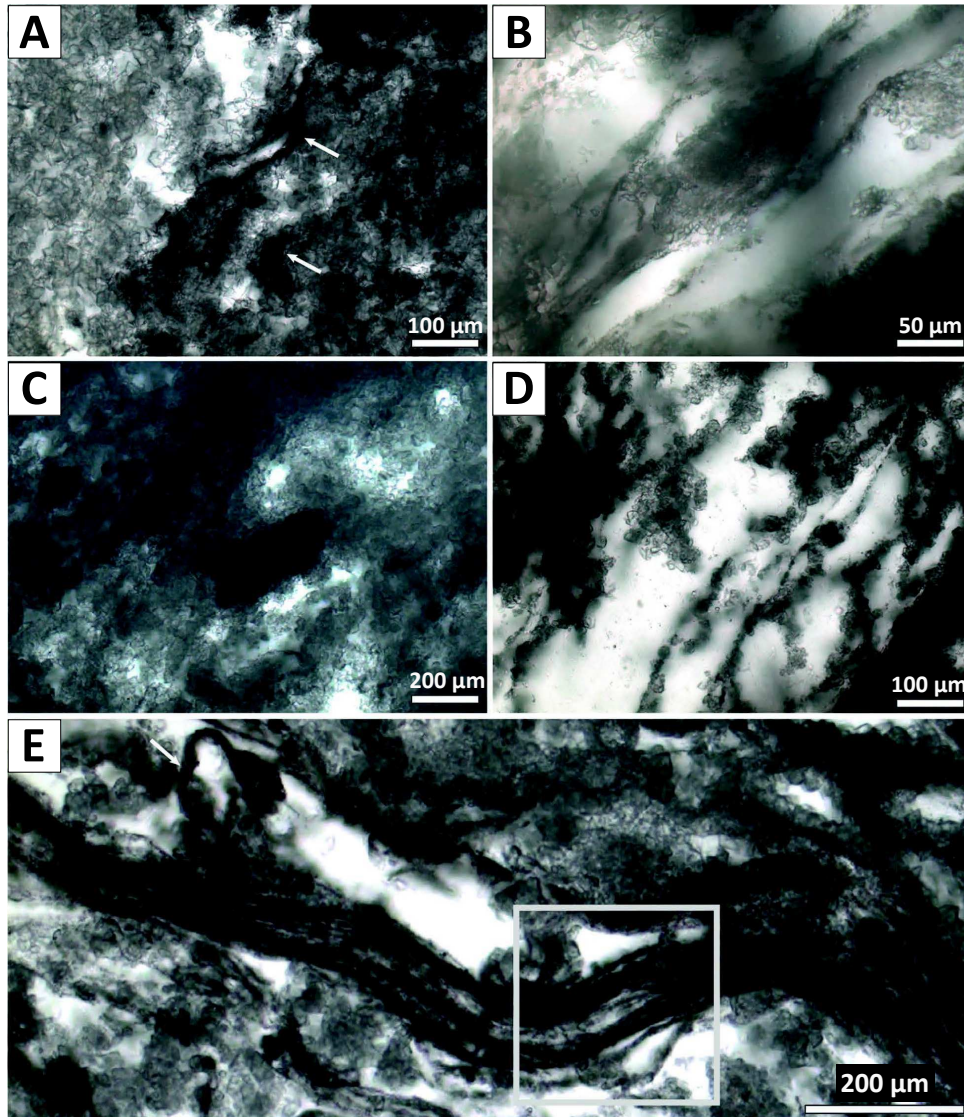


Fig. 4.9. Microphotographs of siderite-bearing laminated cherts (modified from Greco et al., 2018). (A) microbands of siderite-rich chert and carbonaceous matter (CM) locally forming grains and laminae (arrows); (B) CM-rich laminae draping siderite; (C) grain of CM; (D) siderite crystals associated with CM-rich laminations; (E) CM laminae.

4.3. The Serra Sul Formation (2.7 Ga, Brazil)

4.3.1. Regional context

The Neoproterozoic Serra Sul Formation is located in the Central Brazilian Shield of the Amazonian Craton, Brazil. The Archean basement is outcropping within the Carajás Province, among which the Carajás Basin makes up a small portion (Fig 4.10).

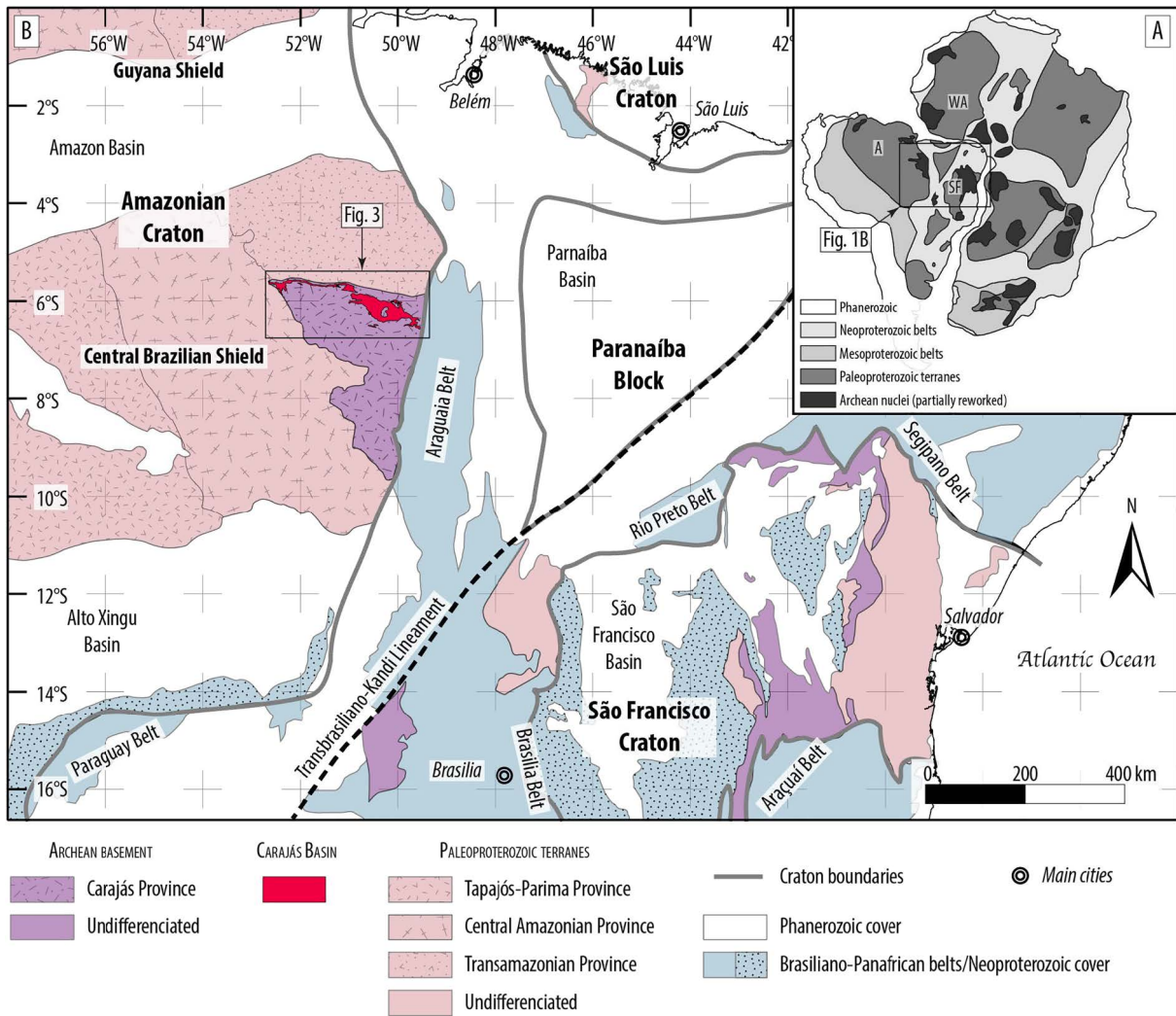


Fig. 4.10. Geological framework of the Amazonian Craton and the Carajás Basin. (A) Schematic West Gondwana reconstruction of the main tectonic elements of South America and Africa. From Rossignol et al. (2020), modified after Cordani et al. (2016). A: Amazonian Craton; SF: São Francisco Craton; WA: West African Craton. (B) Location of the Carajás Basin within the Amazonian Craton. From Rossignol et al. (2020), adapted after Almeida et al. (2013), Cordani et al. (2016), Almeida et al. (2000) and Santos et al. (2000).

The Carajás structural domain, elongated West to East, hosts major Fe, Au, Cu and Mn ore deposits as well as Banded Iron Formations (reviewed in Rossignol et al., 2020). It is delimited by the Canaã dos Carajás Shear Zone to the South and the Cinzento Strike-Slip System to the North (Fig 4.11). The basement of the Carajás Domain, dated around 3.0 Ga and made up of migmatites, mafic granulites and metavolcanic rocks was later intruded by tonalites, trondhjemites and granodiorites (TTGs) and other magmatic rocks from 2.9 to 2.6 Ga (Feio et al., 2013; Machado et al., 1991). The volcanic succession studied in this work was deposited north of the Carajás Domain around 2.77 Ga (Toledo et al., 2019). After being affected by major faults and shear zones during several Neoproterozoic and Paleoproterozoic tectonic events affecting the basement and its overlying supracrustal units, the Carajás Domain has remained relatively stable since 1.9 Ga (Pinheiro and Holdsworth, 1997). Paleomagnetic investigations indicate that at about 2.75 Ga the Carajás Basin was located at a low latitude ($3.4 \pm 8.5^\circ$, Martins et al., 2021).

4.3.2. Stratigraphic framework and geochronological constraints

In this work we will follow the stratigraphic subdivisions of the Carajás Basin recently proposed by Rossignol et al. (2020), updated from Araújo and Nogueira (2019). The main sedimentary units of the Carajás Basin and their time constraints are represented in Fig 4.12-4.13. The Serra Sul Formation was deposited in the Carajás Basin between 2684 ± 10 Ma (U-Pb dating on detrital zircon, Rossignol et al., 2020) and 2627 ± 11 Ma (Re-Os dating on molybdenite, Perelló et al., 2023). The Carajás Basin comprises various Meso- to Neoproterozoic rocks (Vasquez and Rosa-Costa, 2008) capping the 4 to 6 km thick basaltic series of the ca. 2.75 Ga Parauapebas Large Igneous Province (PLIP, Fig. 4.11-4.12, Rossignol et al., 2023). Soon after the main magmatic pulse of the PLIP, infilling of the rift initiated with the deposition of iron formations (IFs) of the Carajás Formation (Fig. 4.12). Whereas some stratigraphic relationships between the Serra Sul Formation and other sedimentary units remain unclear due to difficulties in mapping the region, it appears that the Serra Sul Formation unconformably overlies the Grão Pará Group (Fig 4.12). The transition from the Carajás to Serra Sul formations is marked by several IFs layers up to 10 m thick, grading upward into detrital terrigenous sedimentary rocks including sandstones, siltstones, conglomerates and flat pebble conglomerates (Dreher et al., 2008, 2005; Galarza et al., 2008; Melo et al., 2019; Ronzê et al., 2000; Rossignol et al., 2020).

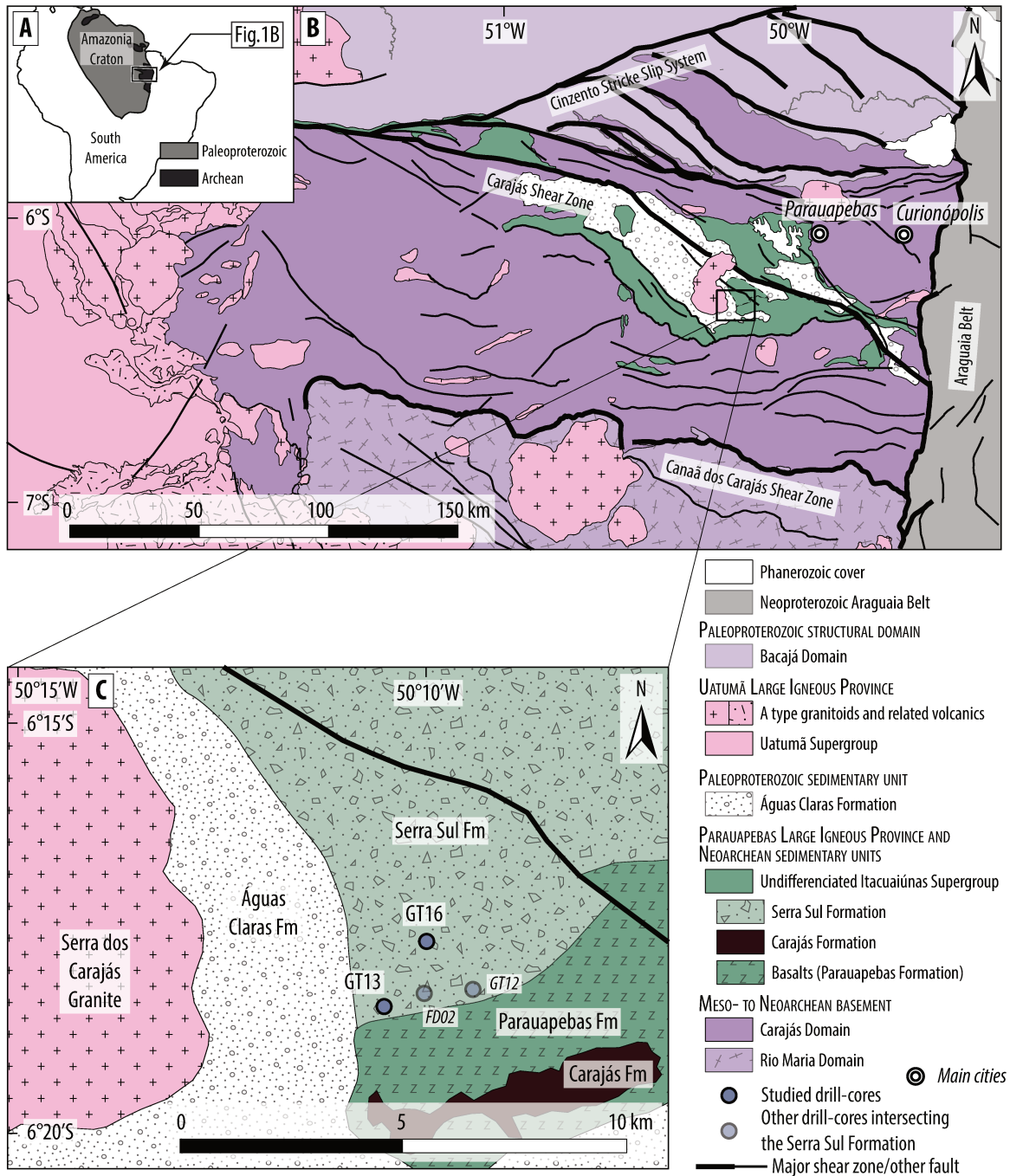


Fig. 4.11. Location of the Carajás Basin. (A) Main tectonic elements of South America (Cordani et al., 2016); (B) Geological map of the Carajás Basin (Vasquez et al., 2008); (C) Location of the drill-cores (Rossignol et al., 2020).

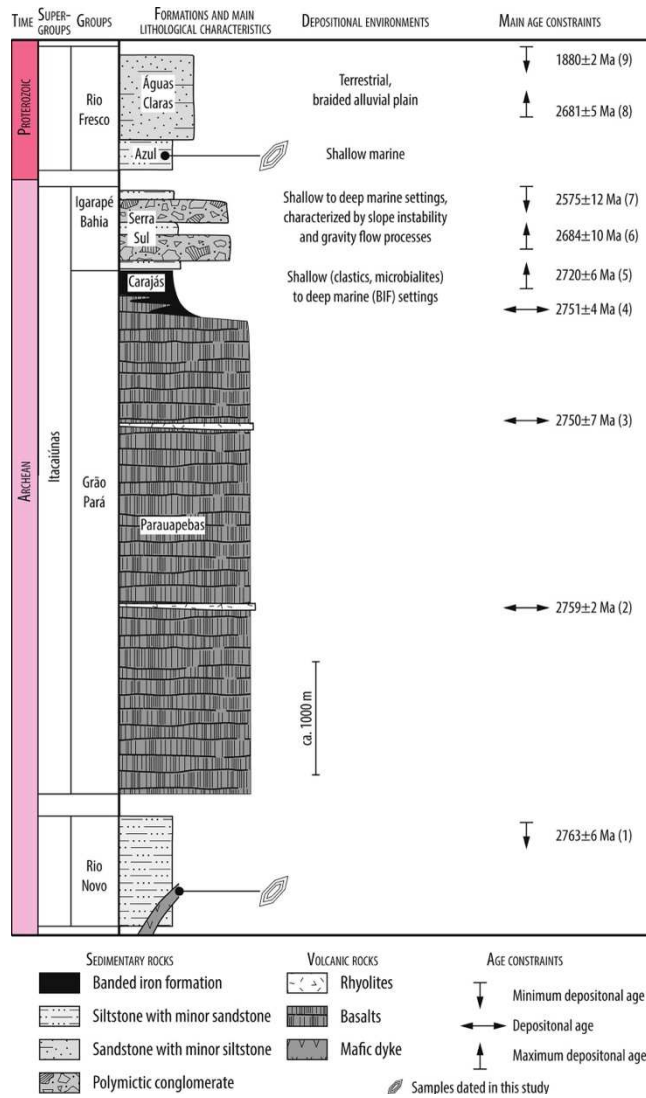


Fig. 4.12. Main sedimentary units of the Carajás Basin. Stratigraphic column from Rossignol et al. (2022), adapted after Araújo Filho et al. (2020), Araújo and Nogueira (2019), Klein and Ladeira (2002), Machado et al. (1991), and Trendall et al. (1998). References for age constraints are given in Rossignol et al. (2022).

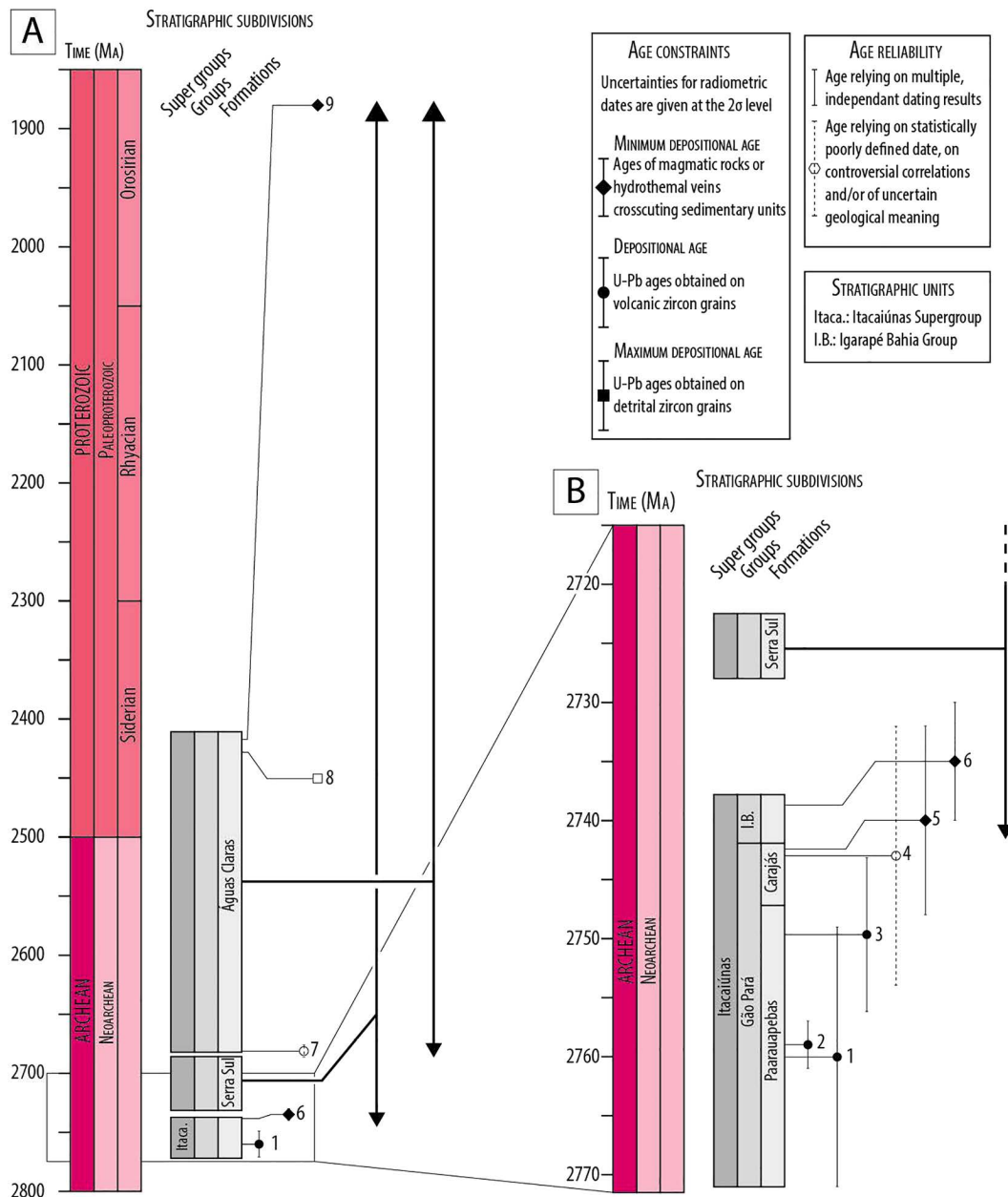


Fig. 4.13. Chronological framework for the main sedimentary units of the Carajás Basin (Rossignol et al., 2020). Arrows indicate the range of potential depositional ages for sedimentary units described in Rossignol et al. (2020). Stratigraphic chart is based on the International Chronostratigraphic Chart v2020/01 (Cohen et al., 2013).

4.3.3. Petrographic features and sedimentary facies

The Serra Sul Formation experienced low-grade greenschist metamorphism (<300°C, based on metamorphic minerals, Figueiredo e Silva et al., 2020; Martins et al., 2017; Rossignol et al., 2020). Metamorphism has affected sedimentary rocks of the Serra Sul Formation, with occurrences of deformation, foliation and pressure shadows (Araújo and Nogueira, 2019).

Based on sedimentological characteristics, 9 facies were defined in the Serra Sul Formation (Rossignol et al., 2020): conglomerates, flat pebbles, sandstones, slumped beds, greyish siltstones, blackish siltstones, fine to medium sandstones, fine sandstones alternating with thin organic-rich layers, and organic-rich clots embedded into a carbonated matrix. Those facies were then integrated into 3 facies associations (Table 4.1) to reconstruct depositional environments (Rossignol et al., 2020) The first facies association (FA1) comprises polymictic conglomerate interbedded with sandstone and siltstone, while the second (FA2) displays flat pebbles conglomerate and slumped deposits, and the third is characterized by fine-grained sediments with microbial deposits (FA3) (Table 4.1). FA1 represents deep water sediments deposited by subaqueous mass flow or debris flow, including syn-sedimentary small faults in the finely laminated siltstones and sandstones interpreted as representing downward sedimentary movement along a slope (Rossignol et al., 2020). FA2 represents relatively shallow water environments of shoreface to upper offshore with limited transport by mass movement (Rossignol et al., 2020). FA3 is representative of a shallow and low-energy subaqueous environment above fair-weather wave base, where microbial mats can develop in the photic zone (Rossignol et al., 2020).

Analyses performed in this work were conducted on samples taken from two diamond-drilled cores separated by about 1.75 km from each other and intersecting the Serra Sul Formation in the east of the Carajás Basin (Fig. 4.11C). These drill-cores (GT-41-FURO-13 and GT-41-FURO-16; see Rossignol et al. (2020) for location) have been selected due to their low metamorphic and hydrothermal overprints, with only rare occurrences of quartz-chlorite-bearing micro-veins. Both drill-cores, named thereafter GT13 and GT16, exhibit similar lithologies and sedimentary facies, but no attempt was made to correlate them, so that their relative stratigraphic positions remain unconstrained. A detailed description of sedimentary facies is presented in Rossignol et al. (2020), in Fig. 4.14 and summarized below.

The most common facies association (FA1, Table 4.1) comprises polymictic conglomerates interbedded with sandstones and siltstones with various sedimentary features attesting an overall excellent preservation state (Fig. 4.15-4.17). This facies association is interpreted to represent a deep-water environment where conglomerates and coarse sandstones were deposited by subaqueous mass flow, cohesive debris flow or hyper-concentrated density flow (Fig. 4.18; Lowe, 1982; Mulder and Alexander, 2001; Nemeč and Steel, 1984; Postma et al., 2014; Postma and Cartigny, 2014; Walker, 1975). The other facies association identified (FA2, Table 4.1) consists of sandstone, siltstone and flat pebble conglomerates made up of intraclastic granules to pebbles (Fig. 4.15-4.17). Flat pebble conglomerates are interpreted to result from the failure and subsequent reworking of compacted to loosely consolidated shoreface deposits (Myrow et al., 2004). The limited transport by mass movement of shoreface deposits and occurrence of wave ripples in sandstones and siltstones suggest relatively shallow water environments (shoreface to upper offshore, Fig. 4.18). FA3 is not displayed in the studied drill cores.

Code	Facies association	Depositional environment
FA1	Conglomerates, sandstones, greyish and blackish siltstones	Deep water
FA2	Flat pebbles, sandstones, slumped beds, rare occurrences of conglomerates	Shoreface to upper offshore, high-energy environment
FA3	Siltstones and fine sandstones with organic-rich clots and layers, rare occurrences of slumped beds	Shallow water, low-energy environment with the development of microbialites

Table 4.1. Facies associations of the Serra Sul Formation (Rossignol et al., 2020).

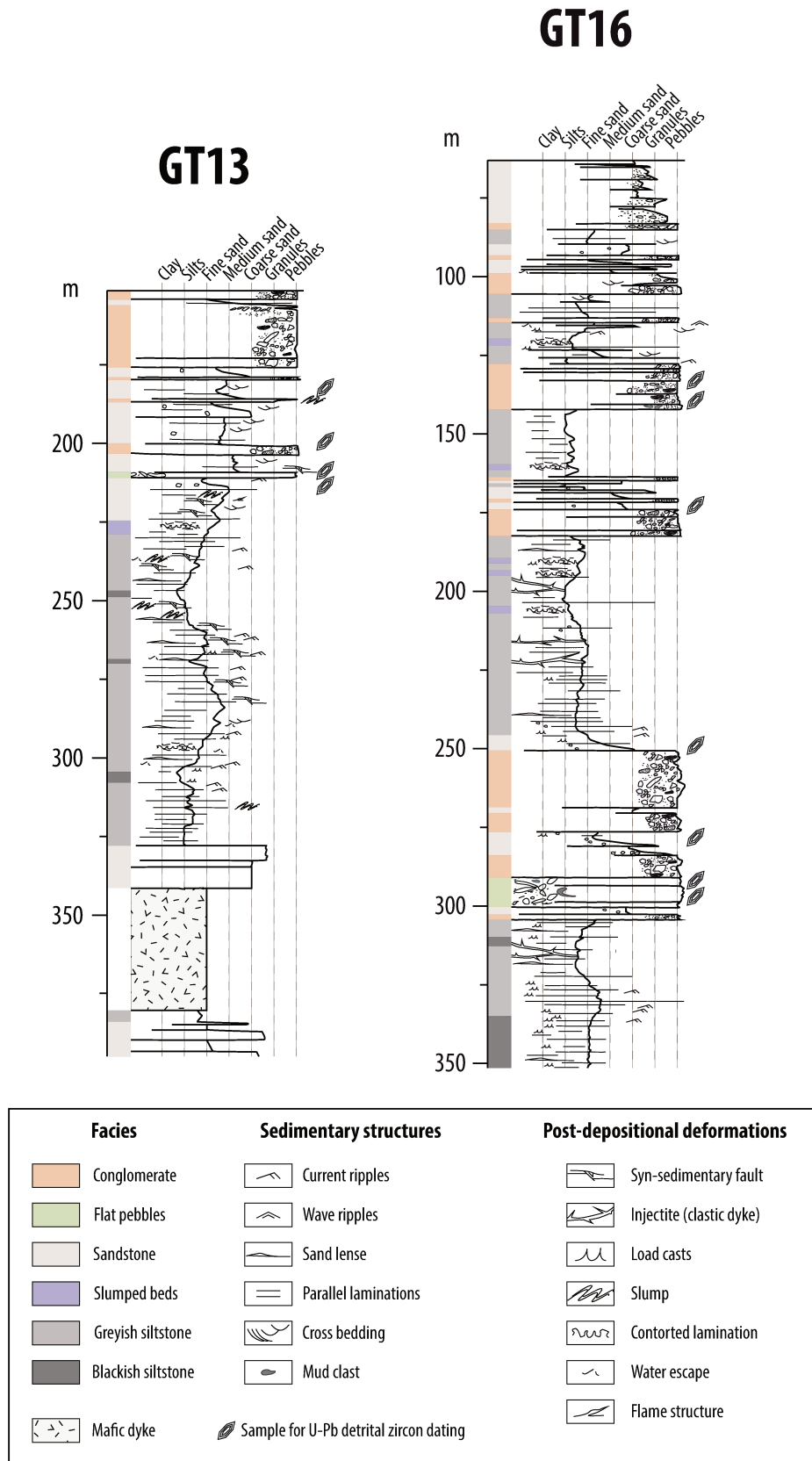


Fig. 4.14. Sedimentological logs of the GT13 and GT16 drill cores intersecting the Serra Sul Formation, along with locations of the dated samples (modified from Rossignol et al., 2020).

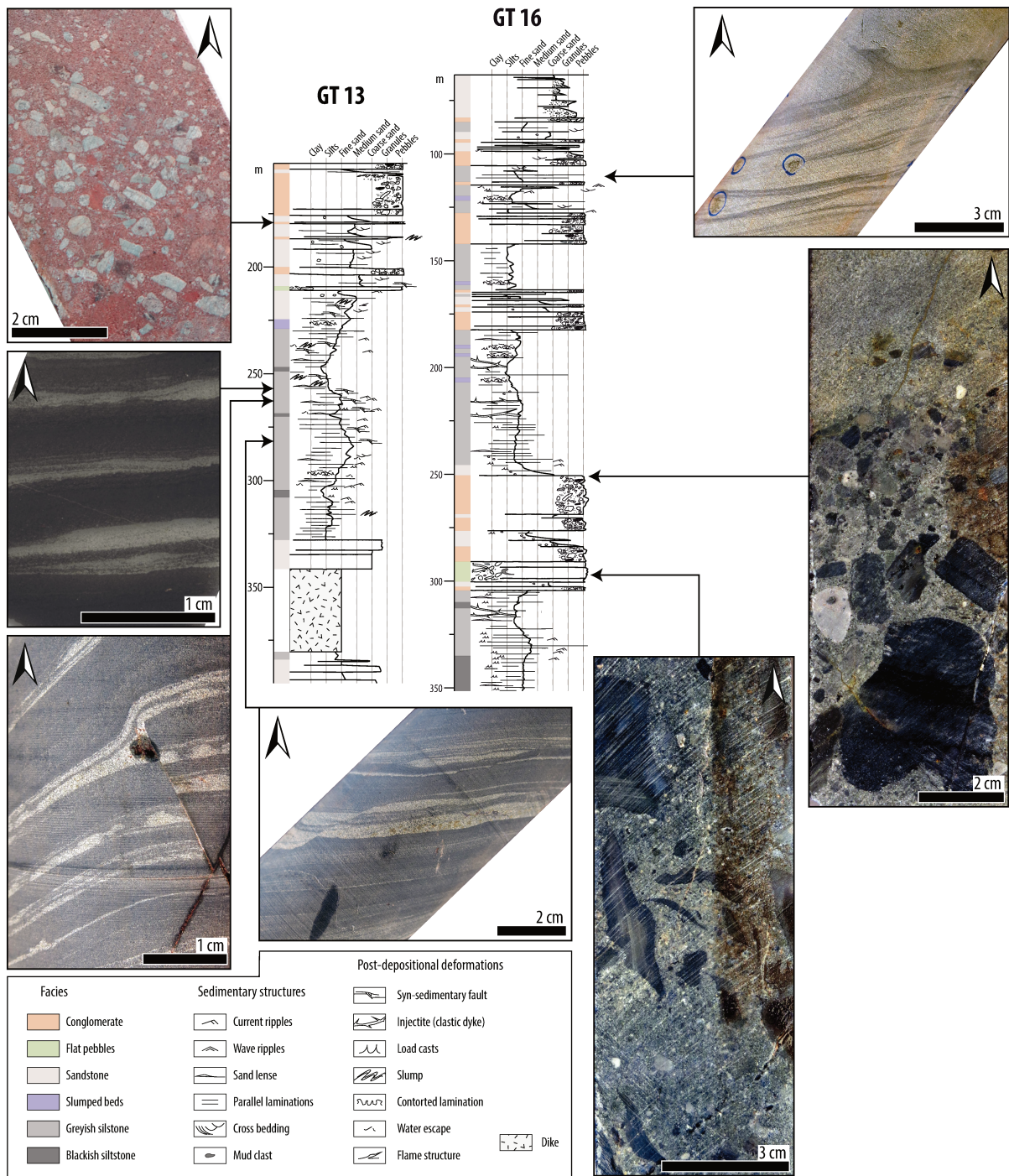


Fig. 4.15. Sedimentological logs of drill cores GT13 and GT16 (modified from Rossignol et al., 2020), with photographs of the main facies and sedimentary structures. Arrows point to the stratigraphic top. Top left photograph: conglomerate with oriented clasts and sandy matrix; middle left: alternations of siltstone and fine sandstone; bottom left and middle: syn-sedimentary, centimetric-scale faults within fine sandstone to siltstone. Top right: sandstone with wave ripples, framboidal pyrite (blue circles) and load casts. Middle right: normally graded conglomerate with rounded quartz pebbles and sub-angular sedimentary clasts, grading to coarse sandstone. Bottom right: flat pebble conglomerate comprising elongated and deformed intraformational clasts.

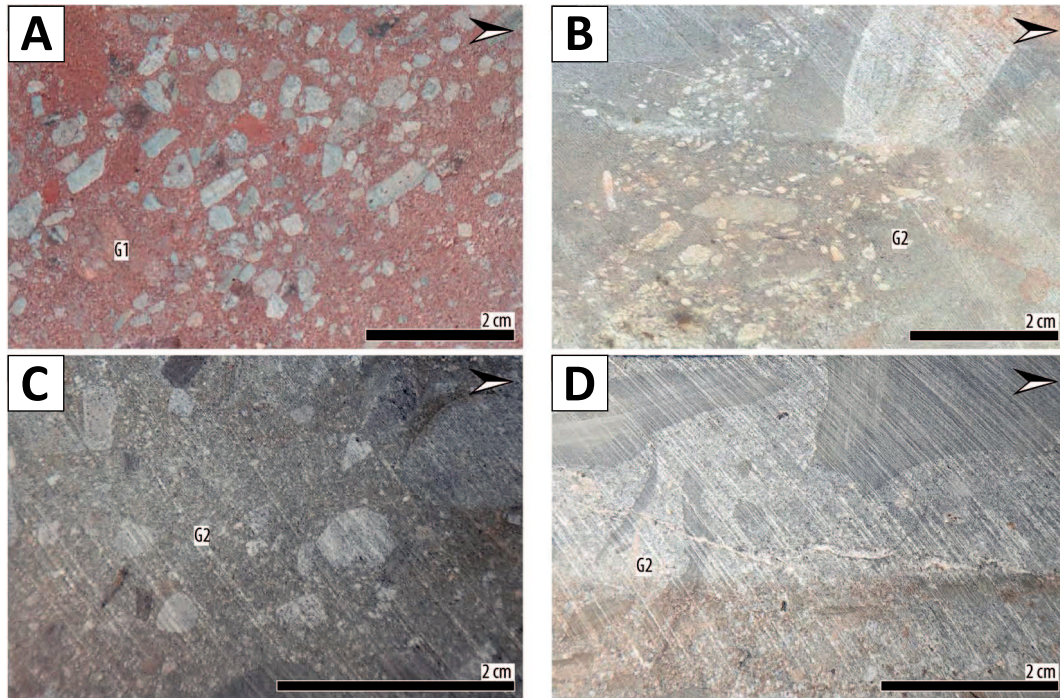


Fig. 4.16. Overview photographs of the conglomeratic facies identified in drill cores GT13 and GT16 (Rossignol et al., 2020). Arrows point to the stratigraphic up. (A) Sample GT13_187.50: polyimictic conglomerate with oriented clasts displaying various shapes. (B) Sample GT13_210.50: flat pebble conglomerate displaying elongated, sub-angular to sub-rounded clasts embedded within a greenish matrix. (C) Sample GT16_297.55: flat pebble conglomerate displaying mainly rounded to sub-angular clasts embedded within a greenish matrix. (D) Sample GT16_296.50: flat pebble conglomerate displaying elongated, plastically deformed angular clasts embedded within a coarse greenish matrix.

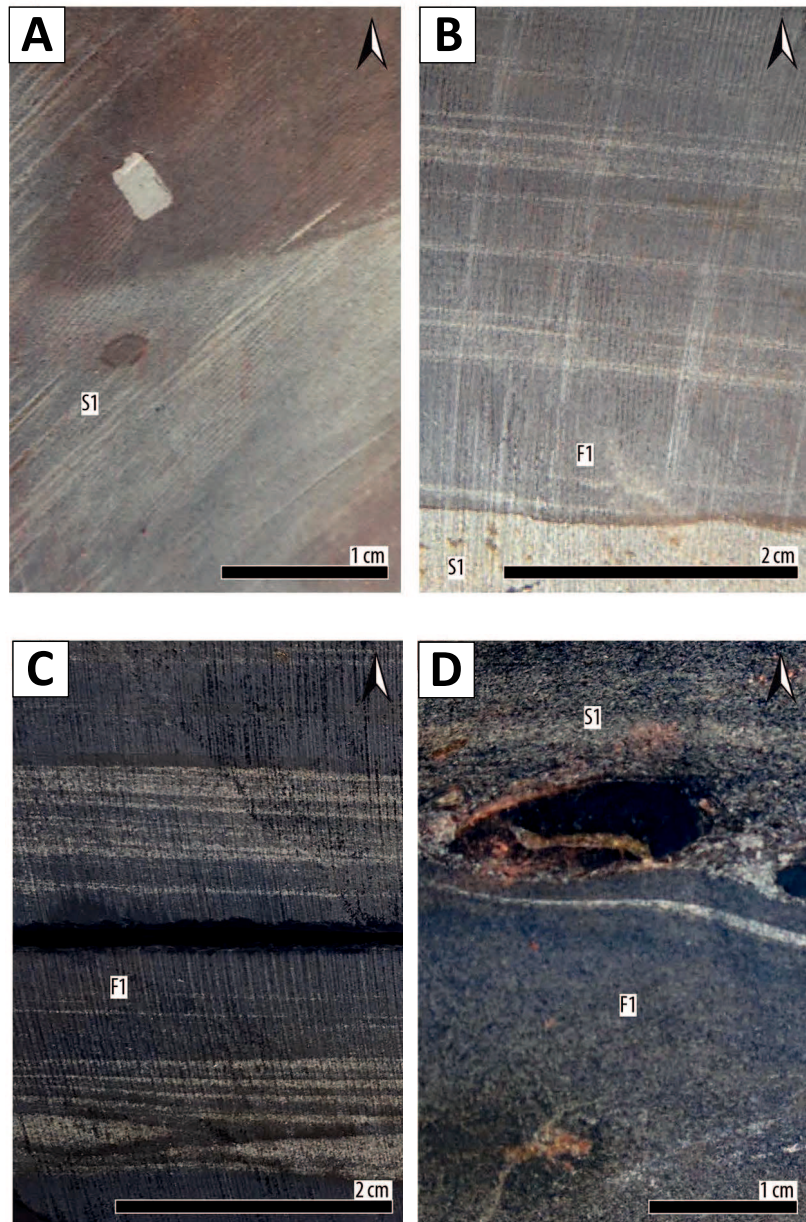


Fig. 4.17. Overview photographs of the sandstones and fine-grained facies identified in drill cores GT13 and GT16 (Rossignol et al., 2020). Arrows point to the stratigraphic up. (A) Sample GT16_210.10: massive, medium-grained sandstone with floating clast. (B) Sample GT13_267.00: planar lamination underlined by fine sandstone to siltstone layers, the coarser layers (S1 facies) usually contain numerous diagenetic pyrite. (C) Sample GT13_267.40: F1 facies with starved ripples made up of fine sandstone alternating with black siltstone. (D) Sample GT13_215.15: coarser layer (S1 facies) with slightly erosive base comprising well rounded clasts.

4.3.4. Paleoenvironments of the Serra Sul Formation

The presence of BIFs at the base of the Serra Sul Formation (Melo et al., 2019) indicates marine environments, and the different sedimentary features of this formation point toward subaqueous environments ranging from shallow to deep water settings influenced by slope instability and gravity flow processes (Fig. 4.18; Dreher et al., 2008, 2005; Rossignol et al., 2020). The BIFs are characterized by strong positive Eu anomalies indicating the influence of high-temperature hydrothermal fluids in seawater (Rego et al., 2021), absence of Ce anomalies arguing for ambient reducing conditions during deposition (Rego et al., 2021), and occurrence of positive La and Y anomalies (Rego et al., 2021) typical of chemical sediments deposited in oceanic settings (Kamber et al., 2014). In addition, Fe and C isotope data indicate that deposition of the IFs was mediated by anoxygenic photosynthetic organisms (Rego et al., 2021). The Serra Sul Formation does not preserve evidence of contemporaneous volcanic activity (Rossignol et al., 2020). The sedimentary facies and depositional environments of the Serra Sul Formation, as well as the fact that detrital zircons indicate an infilling of the basin by local sources, suggest that the Serra Sul Formation was deposited during an active extensional tectonic phase (Rossignol et al., 2020).

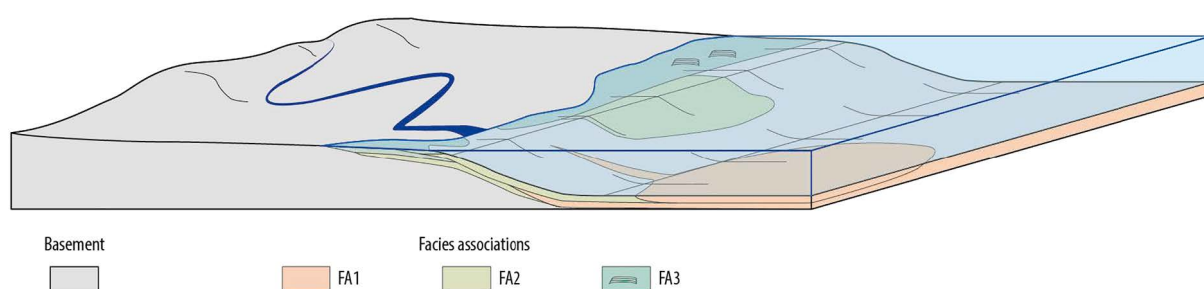


Fig. 4.18. Reconstruction of the depositional environments of the Serra Sul Formation (Rossignol et al., 2020). The different facies associations (FA) defining each depositional environment are described in Table 1. Only FA1 and FA2 are represented in drill cores GT13 and GT16.

4.4. The Malmani Subgroup (2.5 Ga, South Africa)

There are very few occurrences of well-preserved Neoproterozoic stromatolitic carbonates in the geological record. In that respect, samples from the 2.5 Ga Malmani Subgroup represent an opportunity to study shallow stromatolitic dolostone deposits, while broadening the geochemical dataset along the various depths of this major carbonate platform (Eroglu et al., 2015, 2017; Godfrey and Falkowski, 2009).

4.4.1. Regional context

In the South African Kaapvaal Craton, the ca. 2.67 to ca. 2.46 (U-Pb dating on zircons; Altermann and Nelson, 1998) Lower Transvaal Supergroup (LTS) holds a mixture of siliciclastic and carbonated sedimentary rocks overlain by deep subtidal banded iron formation (Sumner and Beukes, 2006). The siliciclastic-carbonate ramp grades upwards into the Campbellrand-Malmani carbonate platform (CMCP), which represents a major carbonate buildup. Indeed, it covers an area of 190 000 km² with a thickness averaging 1500 to 1700 m. Beukes (1987) estimated that the original carbonate deposit probably covered the entire 600 000 km² surface area of the Kaapvaal craton. The CMCP stretches along two basins, namely the Griqualand West Basin in the western part of the craton and the Transvaal Basin in the eastern part of the craton (Beukes, 1987; Fig. 4.19). Beukes (1987) correlated the different units of the Campbellrand Subgroup with the Malmani Subgroup in the Transvaal Basin using carbonate facies and stromatolite morphology. The CMCP has experienced metamorphism in the greenschist facies, with additional contact metamorphism in areas close to the 2.06 Ga intrusion of the Bushveld complex (Cawthorn, 2015). In terms of depositional environments, the northeastern part of the CMCP corresponds to shallow peritidal to subtidal facies evolving towards slope and basinal facies in the southwestern part of the platform (Fig. 4.19-4.20) (Beukes, 1987).

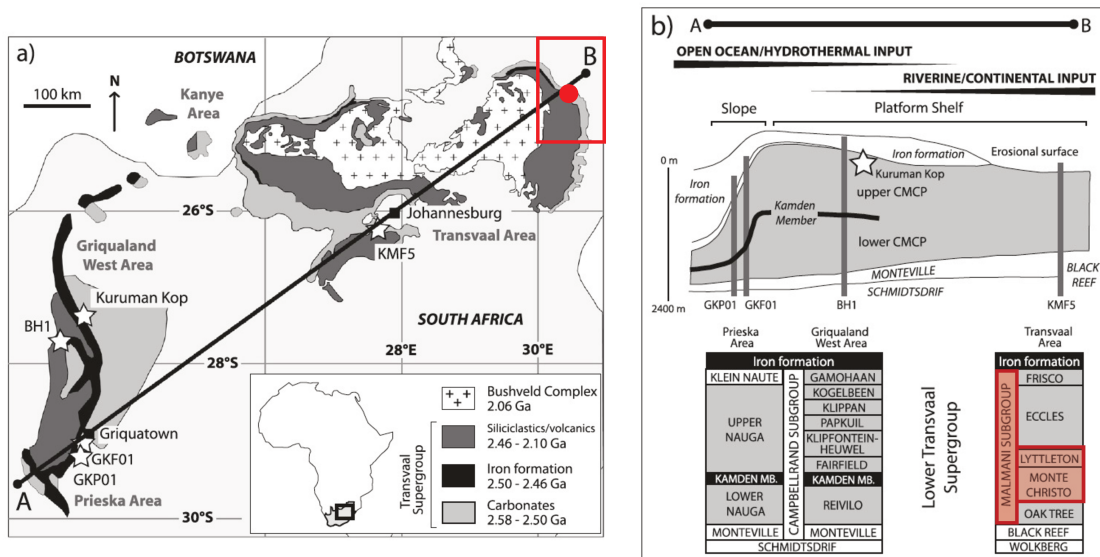


Fig. 4.19. (a) Geological overview of Transvaal Supergroup lithologies and the Bushveld igneous complex in South Africa and (b) Cross section through chemical sediments of the Lower Transvaal Supergroup. From Eroglu et al. (2017). The localization of the studied section (Transvaal area, Malmani Subgroup, Upper Monte Christo Formation) is identified in red in both (a) and (b).

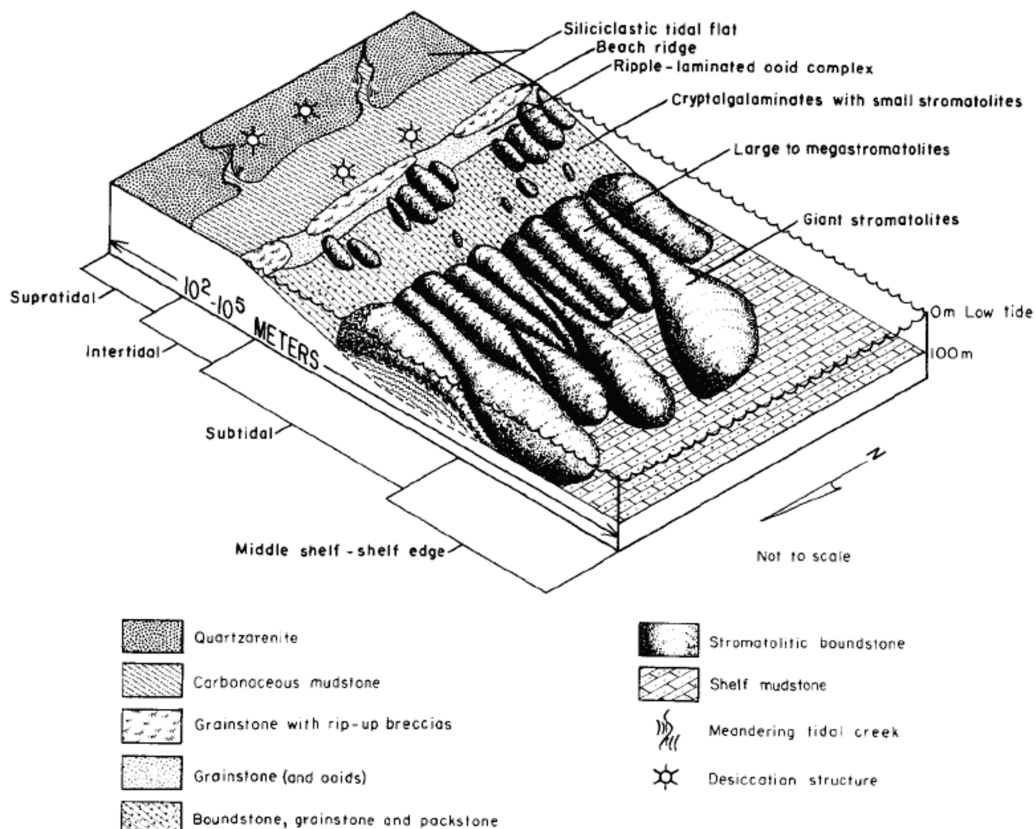
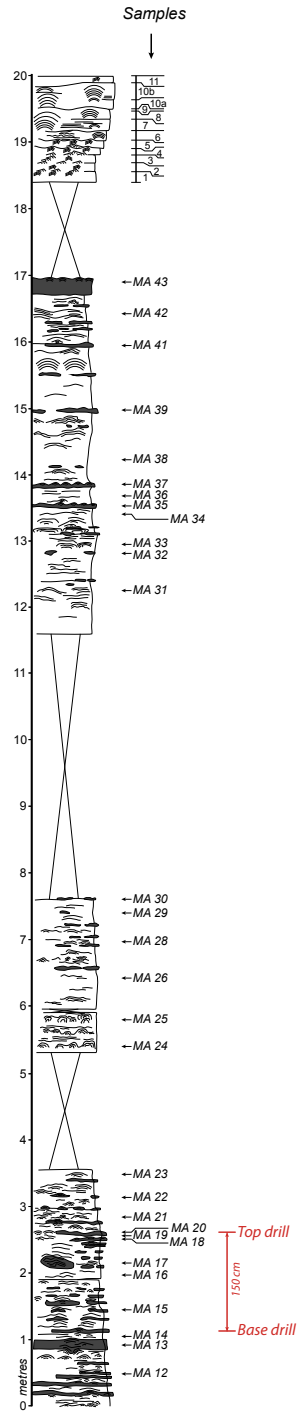


Fig. 4.20. Carbonate platform model for the Malmani Dolomite Subgroup, Transvaal Supergroup (Tyler and Tyler, 1996). In the Eastern Transvaal, the carbonate sequence was deposited on a laterally extensive platform under supratidal to deep subtidal shelf-edge conditions.

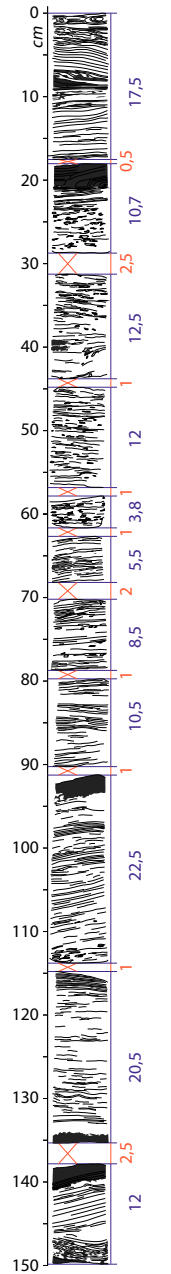
4.4.2. Stratigraphic framework of the studied samples

Samples for this study were collected during a field trip conducted in 2019 in the Barberton area. They belong to the Malmani Subgroup, which is located in the Transvaal Basin and stratigraphically correlated with the Campbellrand Subgroup in the Griqualand West Basin. The age at the base of the Malmani subgroup in the Transvaal Basin has been estimated at 2550 ± 3 Ma (Walraven, 1995). Out of the five Formations dividing the Malmani Subgroup (Oaktree, Monte Christo, Lyttleton, Eccles and Frisco; Fig. 4.19), field observations place the described section in the 2.55 Ga Upper Monte Christo Formation (Decraene, 2022). This Formation contains wavy laminations interbedded with rippled ooid grainstones, as well as columnar and megadomal stromatolites, and is representative of shallow subtidal settings (Button, 1973; Tyler and Tyler, 1996). Outcrop samples were collected along a 20m-long sedimentary section ($25^{\circ}21.561\text{S}$, $30^{\circ}42.956\text{E}$, Fig. 4.21-4.22) representative of shallow carbonate facies with dolomitized and partially silicified stromatolites. In addition, a 1.5-m core was drilled in the first meters of the outcropping chosen section (Fig. 4.21-4.23).

Field Log



Drill Log



Lithologies	Sedimentary structures	Microbial structures
Dolomite	Climbing ripple	Domal stromatolite
Chert	Asymmetrical ripple	Wavy laminae

Silicified limestones
Laminated stromatolites
Fenestral stromatolites

Fig. 4.21. Field log and drill log of the studied outcrop section. The location of the drill core in the studied section is shown in red.

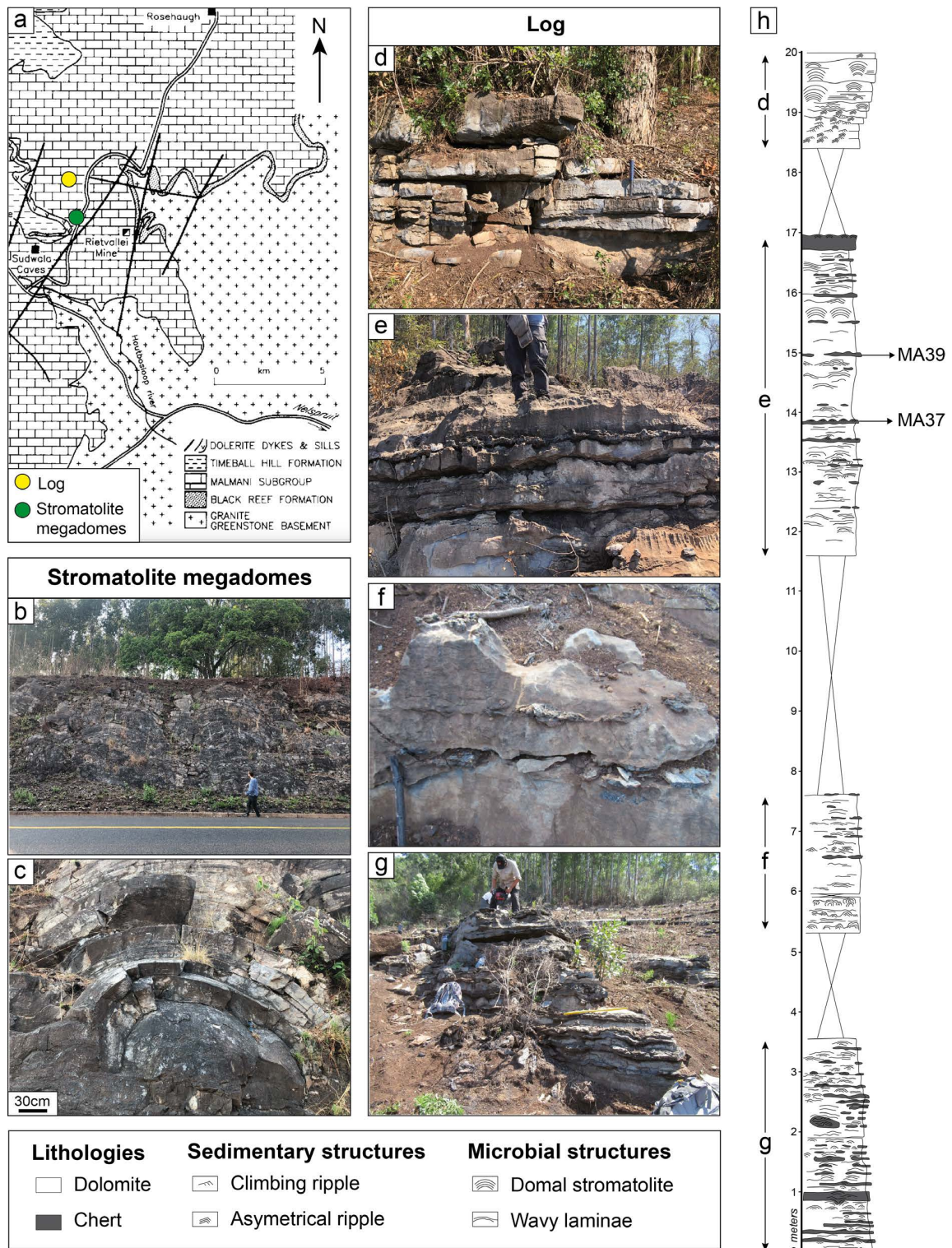


Fig. 4.22. (a) Geological map of the studied area with location of the sedimentary section and the stromatolite megadomes. From Decraene (2022), modified from Tyler and Tyler (1996). (b) Large view of an outcrop along the road made of pluri-meter large stromatolite megadomes (Decraene, 2022). (c) Zoom on a domal stromatolite (Decraene, 2022). (d) to (g) Pictures of the different outcrops which compose the log, with rippled-dolomite (non-bioconstructed facies FA1) and stromatolites (bioconstructed facies FA2) at the top and stromatolites with various degrees of silicification through the rest of the section (Decraene, 2022).

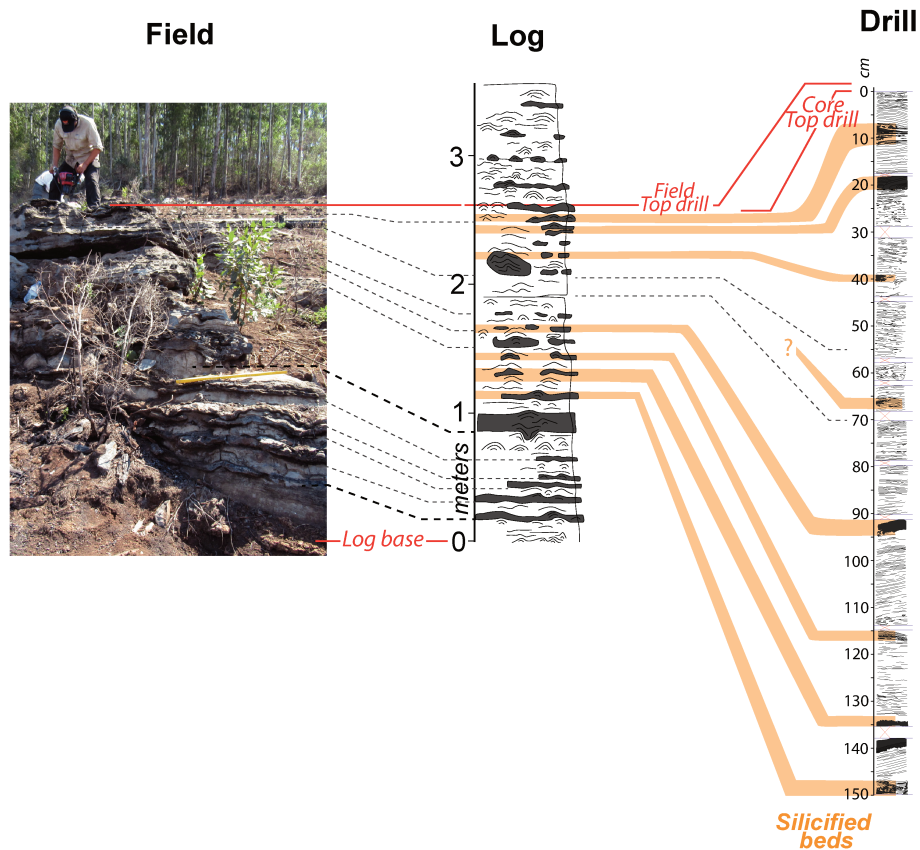


Fig. 4.23. Correspondence between the field view, the outcrop section and the drill core log. Silicified beds are shown in orange and black.

4.4.3. Petrographic features and sedimentary facies

The CMCP buildup is composed of two main lithofacies assemblages: a basinal, non-stromatolitic, laminated carbonate and shale sequence, with minor chert, iron formations and mafic tuff occurrences, and a shallow-water stromatolitic carbonated sequence. Most of the Malmani carbonates have been replaced by dolomite and/or chert, especially in the peritidal facies (Eriksson et al., 1975; Eriksson, 1977), while the Campbellrand Subgroup has preserved more limestones (Beukes, 1987; Sumner and Grotzinger, 2004).

Along the studied outcrop, two facies can be set apart (Fig. 4.22, 4.24): (i) a detrital facies with climbing ripples at the top, that is non-bioconstructed (FA1) and (ii) a bioconstructed facies with fenestral stromatolites (FA2). Stromatolitic laminations are mostly carbonated with a few silicified layers (Fig. 4.24). Carbonates are identified as dolomite, probably resulting from an early and incomplete dolomitization, followed by an early phase of silicification affecting the remaining primary carbonates (Fig. 4.25; Decraene, 2022; Lawnizack, 2022). Some later fluid

circulation episodes are indicated by cross-cutting silica veins and the presence of oxides (Fig. 4.25).

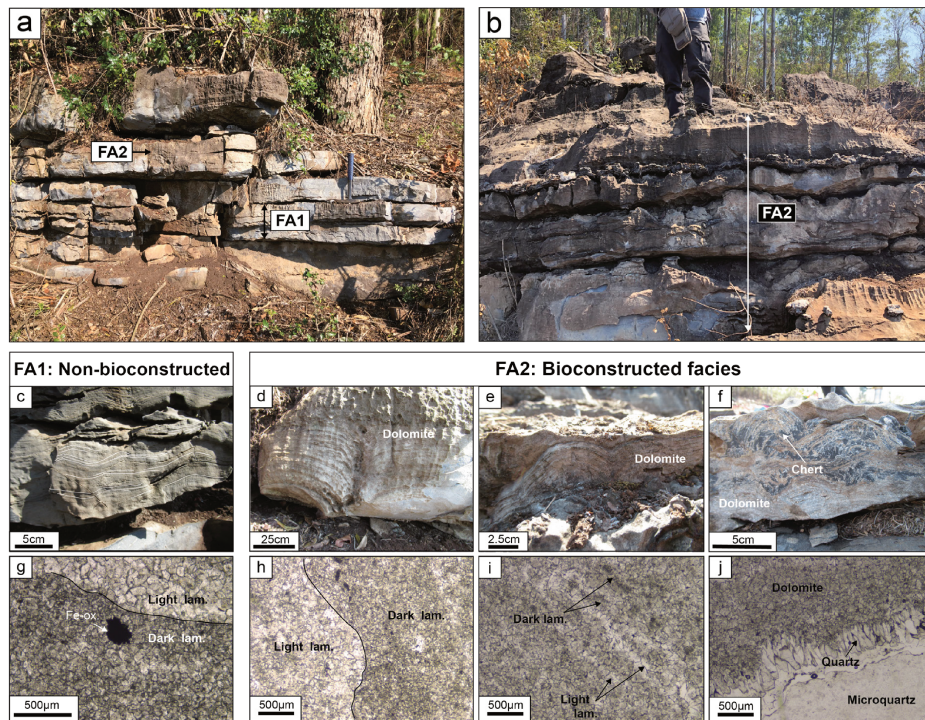


Fig. 4.24. Field views of the two facies associations of the studied section: (a) the non-bioconstructed FA1 facies with climbing ripples, and (a and b) the bioconstructed FA2 facies with stromatolites (Decraene, 2022). (c) climbing ripples in FA1. (g) dark and light laminae in FA1. (d and e) dolomitized stromatolite in FA2. (f) domal stromatolites partially silicified. (h, i, j) microscopic views of laminae and dolomite-quartz limits.

Carbonaceous matter has been observed in dark laminae of both FA1 and FA2 facies. Raman spectra display features of graphitized organic carbon, with peak temperature estimates of $395 \pm 30^\circ\text{C}$ (Decraene, 2022) following the methodology described in Kouketsu et al. (2014). This temperature estimation is higher than the greenschist metamorphic grade dominant throughout the whole platform (Miyano and Beukes, 1984), and rather corresponds to temperature estimates for higher metamorphism associated with the intrusion of the Bushveld complex (Cawthorn, 2015; Frauenstein et al., 2009). Petrographic observations are still ongoing and should provide a clearer syn- and post-depositional sedimentation model. However, preliminary work from the master's student thesis of Lawnizack (2022) argue for a complex post-depositional history that can be divided into several episodes, including (i) cementation, (ii) dolomitization, (iii) two successive stages of silicification, and (iv) a second stage of dolomitization in veins (Fig. 4.26).

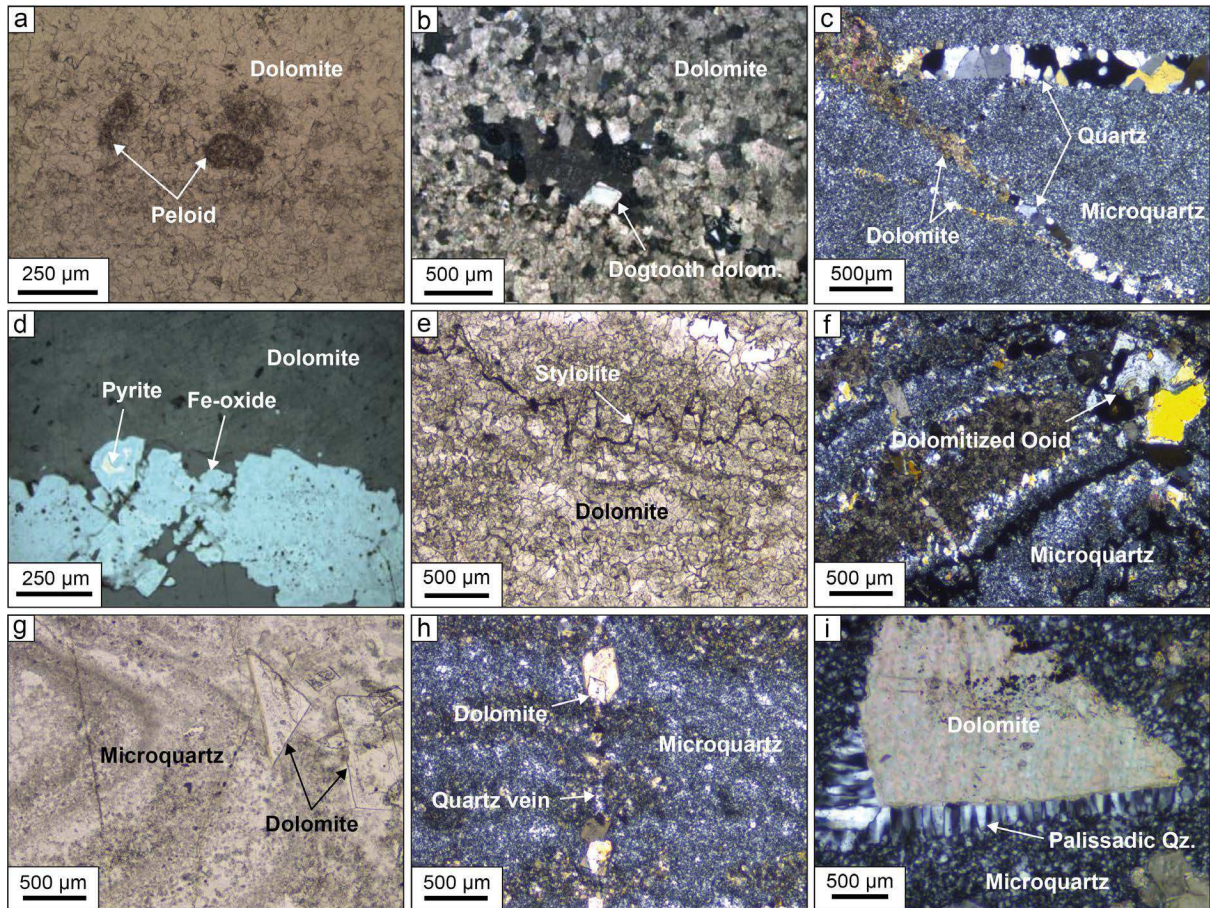


Fig. 4.25. Pictures illustrating primary and secondary features observed in the studied samples (Decraene, 2022). (a) Peloid in dolomite from FA1. (b) Example of a fenestrae with dogtooth crystals of dolomite on the edge. (c) Quartz and dolomite veins crosscutting the microquartz in a silicified stromatolite sample. (d) Large oxidized pyrite. (e) Stylolite in a sample from FA2. (f) Dolomitized ooid in a partially silicified stromatolite sample. (g) Large dolomite crystal in the microquartz. (h) Large crystals of dolomite following a cross-cutting quartz vein. (i) Palissadic quartz crystals between a large dolomite crystal and the microquartz.

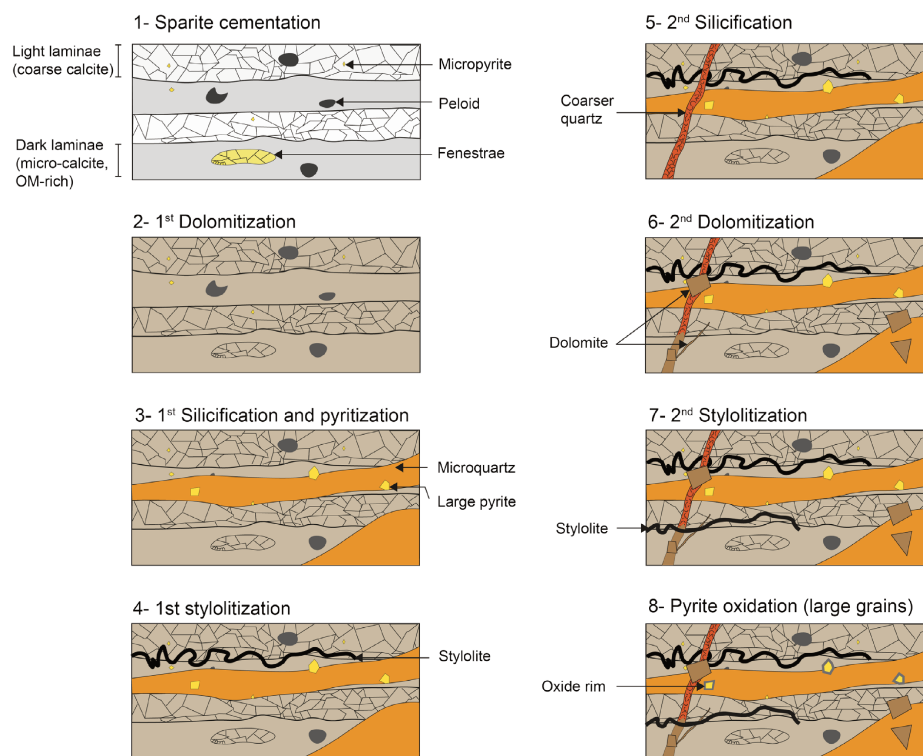


Fig. 4.26. Diagrams illustrating the inferred post-depositional history of the studied drill core samples. Not to scale. Modified from Lawnizack (2022). Coarse calcite = sparite; micro-calcite = micro-sparite.

4.4.4. Paleoenvironments and chemical conditions

In the CMCP, a depth-dependent carbon isotope trend has been shown from deep depositional settings towards the platform shelf (Eroglu et al., 2017), and interpreted as a change from anaerobic (e.g., methanogenesis and methanotrophy) to aerobic ecosystems (e.g. oxygenic photosynthesis), suggesting that various carbon fixation pathways operated in the ocean at that time. The inferred depositional environment for the studied samples was likely coastal and shallow, characterized by weak currents and a fluctuating sedimentary load with high suspension fallout rates for climbing ripples and low ones for stromatolites. As to chemical conditions, the existence of such a large-scale stromatolitic carbonate platform with partially silicified horizons raises the question of carbonate precipitation in a system where the pH was supposedly circumneutral (pH=7, Halevy and Bachan, 2017), and the processes and timing of silicification.

References

- Alleon, J., Bernard, S., Olivier, N., Thomazo, C., Marin-Carbonne, J., 2021. Inherited geochemical diversity of 3.4 Ga organic films from the Buck Reef Chert, South Africa. *Communications Earth & Environment* 2, 1–7. <https://doi.org/10.1038/s43247-020-00066-7>
- Almeida, F.F.M. de, Brito Neves, B.B. de, Dal Ré Carneiro, C., 2000. The origin and evolution of the South American Platform. *Earth-Science Reviews* 50, 77–111. [https://doi.org/10.1016/S0012-8252\(99\)00072-0](https://doi.org/10.1016/S0012-8252(99)00072-0)
- Almeida, J. de A.C. de, Dall’Agnol, R., Leite, A.A. da S., 2013. Geochemistry and zircon geochronology of the Archean granite suites of the Rio Maria granite-greenstone terrane, Carajás Province, Brazil. *Journal of South American Earth Sciences* 42, 103–126. <https://doi.org/10.1016/j.jsames.2012.10.008>
- Altermann, W., Nelson, D.R., 1998. Sedimentation rates, basin analysis and regional correlations of three Neoproterozoic and Palaeoproterozoic sub-basins of the Kaapvaal craton as inferred from precise U–Pb zircon ages from volcanoclastic sediments. *Sedimentary Geology* 120, 225–256. [https://doi.org/10.1016/S0037-0738\(98\)00034-7](https://doi.org/10.1016/S0037-0738(98)00034-7)
- Araújo Filho, R.C., Nogueira, A.C.R., Araújo, R.N., 2020. New stratigraphic proposal of a Paleoproterozoic siliciclastic succession: Implications for the evolution of the Carajás Basin, Amazonian craton, Brazil. *Journal of South American Earth Sciences* 102, 102665. <https://doi.org/10.1016/j.jsames.2020.102665>
- Araújo, R., Nogueira, A., 2019. Serra Sul diamictite of the Carajás Basin (Brazil): A Paleoproterozoic glaciation on the Amazonian craton. *Geology* 47, 1166–1170. <https://doi.org/10.1130/G46923.1>
- Beukes, N.J., 1987. Facies relations, depositional environments and diagenesis in a major early Proterozoic stromatolitic carbonate platform to basal sequence, Campbellrand Subgroup, Transvaal Supergroup, Southern Africa. *Sedimentary Geology* 54, 1–46. [https://doi.org/10.1016/0037-0738\(87\)90002-9](https://doi.org/10.1016/0037-0738(87)90002-9)
- Bolhar, R., Van Kranendonk, M.J., Kamber, B.S., 2005. A trace element study of siderite–jasper banded iron formation in the 3.45 Ga Warrawoona Group, Pilbara Craton—Formation from hydrothermal fluids and shallow seawater. *Precambrian Research* 137, 93–114. <https://doi.org/10.1016/j.precamres.2005.02.001>
- Button, A., 1973. The stratigraphic history of the Malmani dolomite in the Eastern and North-Eastern Transvaal.
- Cawthorn, R.G., 2015. The Bushveld Complex, South Africa, in: Charlier, B., Namur, O., Latypov, R., Tegner, C. (Eds.), *Layered Intrusions*, Springer Geology. Springer Netherlands, Dordrecht, pp. 517–587. https://doi.org/10.1007/978-94-017-9652-1_12
- Cohen, K.M., Finney, S.C., Gibbard, P.L., Fan, J.-X., 2013. The ICS International Chronostratigraphic Chart. *Episodes Journal of International Geoscience* 36, 199–204. <https://doi.org/10.18814/epiiugs/2013/v36i3/002>
- Cordani, U.G., Ramos, V.A., Fraga, L.M., Cegarra, M., Delgado, I., Souza, K.G. de, Gomes,

F.E.M., Schobbenhaus, C., 2016. Tectonic map of South America = Mapa tectônico da América do Sul.

de Vries, S.T., Nijman, W., Armstrong, R.A., 2006. Growth-fault structure and stratigraphic architecture of the Buck Ridge volcano-sedimentary complex, upper Hooggenoeg Formation, Barberton Greenstone Belt, South Africa. *Precambrian Research* 149, 77–98. <https://doi.org/10.1016/j.precamres.2006.04.005>

de Vries, S.T., Nijman, W., de Boer, P.L., 2010. Sedimentary geology of the Palaeoarchean Buck Ridge (South Africa) and Kittys Gap (Western Australia) volcano-sedimentary complexes. *Precambrian Research* 183, 749–769. <https://doi.org/10.1016/j.precamres.2010.09.005>

Decraene, M.-N., 2022. Biological vs. Diagenetic Controls in Microbialites from Spatially Resolved Iron Isotopes in Pyrite. *Unil*.

Dreher, A.M., Xavier, R.P., Martini, S.L., 2005. Fragmental rocks of the Igarapé Bahia CU-AU deposit, Carajas Mineral Province, Brazil. *RBG* 35, 359–368. <https://doi.org/10.25249/0375-7536.2005353359368>

Dreher, A.M., Xavier, R.P., Taylor, B.E., Martini, S.L., 2008. New geologic, fluid inclusion and stable isotope studies on the controversial Igarapé Bahia Cu–Au deposit, Carajás Province, Brazil. *Miner Deposita* 43, 161–184. <https://doi.org/10.1007/s00126-007-0150-6>

Eriksson, K.A., 1977. Tidal flat and subtidal sedimentation in the 2250 M.Y. Malmani Dolomite, Transvaal, South Africa. *Sedimentary Geology, Tidal Sedimentation* 18, 223–244. [https://doi.org/10.1016/0037-0738\(77\)90013-6](https://doi.org/10.1016/0037-0738(77)90013-6)

Eriksson, K.A., McCarthy, T.S., Truswell, J.F., 1975. Limestone formation and dolomitization in a lower Proterozoic succession from South Africa. *Journal of Sedimentary Research* 45, 604–614. <https://doi.org/10.1306/212F6DED-2B24-11D7-8648000102C1865D>

Eroglu, S., Schoenberg, R., Wille, M., Beukes, N., Taubald, H., 2015. Geochemical stratigraphy, sedimentology, and Mo isotope systematics of the ca. 2.58-2.50 Ga-old Transvaal Supergroup carbonate platform, South Africa. *Precambrian Research* 266, 27–46. <https://doi.org/10.1016/j.precamres.2015.04.014>

Eroglu, S., van Zuilen, M.A., Taubald, H., Drost, K., Wille, M., Swanner, E.D., Beukes, N.J., Schoenberg, R., 2017. Depth-dependent $\delta^{13}\text{C}$ trends in platform and slope settings of the Campbellrand-Malmani carbonate platform and possible implications for Early Earth oxygenation. *Precambrian Research* 302, 122–139. <https://doi.org/10.1016/j.precamres.2017.09.018>

Feio, G.R.L., Dall’Agnol, R., Dantas, E.L., Macambira, M.J.B., Santos, J.O.S., Althoff, F.J., Soares, J.E.B., 2013. Archean granitoid magmatism in the Canaã dos Carajás area: Implications for crustal evolution of the Carajás province, Amazonian craton, Brazil. *Precambrian Research, Precambrian Accretionary Orogens* 227, 157–185. <https://doi.org/10.1016/j.precamres.2012.04.007>

Figueiredo e Silva, R.C., Lobato, L.M., Zucchetti, M., Hagemann, S., Vennemann, T., 2020. Geotectonic signature and hydrothermal alteration of metabasalts under- and overlying the giant Serra Norte iron deposits, Carajás mineral Province. *Ore Geology Reviews* 120, 103407.

<https://doi.org/10.1016/j.oregeorev.2020.103407>

Frauenstein, F., Veizer, J., Beukes, N., Van Niekerk, H.S., Coetzee, L.L., 2009. Transvaal Supergroup carbonates: Implications for Paleoproterozoic $\delta^{18}\text{O}$ and $\delta^{13}\text{C}$ records. *Precambrian Research* 175, 149–160. <https://doi.org/10.1016/j.precamres.2009.09.005>

Galarza, M.A., Macambira, M.J.B., Villas, R.N., 2008. Dating and isotopic characteristics (Pb and S) of the Fe oxide-Cu-Au-U-REE Igarapé Bahia ore deposit, Carajás mineral province, Pará state, Brazil. *Journal of South American Earth Sciences* 25, 377–397. <https://doi.org/10.1016/j.jsames.2007.07.006>

Geilert, S., Vroon, P.Z., van Bergen, M.J., 2014. Silicon isotopes and trace elements in chert record early Archean basin evolution. *Chemical Geology* 386, 133–142. <https://doi.org/10.1016/j.chemgeo.2014.07.027>

Godfrey, L.V., Falkowski, P.G., 2009. The cycling and redox state of nitrogen in the Archean ocean. *Nature Geoscience* 2, 725–729. <https://doi.org/10.1038/ngeo633>

Greco, F., 2018. The origin and significance of carbonaceous matter within Palaeoarchean marine environments of the Barberton Greenstone Belt, South Africa (Tesi di dottorato). [10.6092/unibo/amsdottorato/8555](https://doi.org/10.6092/unibo/amsdottorato/8555).

Greco, F., Cavalazzi, B., Hofmann, A., Hickman-Lewis, K., 2018. 3.4 Ga biostructures from the Barberton greenstone belt of South Africa: new insights into microbial life. *Bollettino della Società Paleontologica Italiana* 59–74. <https://doi.org/10.4435/BSPI.2018.04>

Grosch, E.G., Kosler, J., McLoughlin, N., Drost, K., Slama, J., Pedersen, R.B., 2011. Paleoarchean detrital zircon ages from the earliest tectonic basin in the Barberton Greenstone Belt, Kaapvaal craton, South Africa. *Precambrian Research* 191, 85–99. <https://doi.org/10.1016/j.precamres.2011.09.003>

Halevy, I., Bachan, A., 2017. The geologic history of seawater pH. *Science* 355, 1069–1071. <https://doi.org/10.1126/science.aal4151>

Heimann, A., Johnson, C.M., Beard, B.L., Valley, J.W., Roden, E.E., Spicuzza, M.J., Beukes, N.J., 2010. Fe, C, and O isotope compositions of Banded Iron Formation carbonates demonstrate a major role for dissimilatory iron reduction in ~2.5 Ga marine environments. *Earth and Planetary Science Letters* 294, 8–18. <https://doi.org/10.1016/j.epsl.2010.02.015>

Hofmann, A., Bolhar, R., Orberger, B., Foucher, F., 2013. Cherts of the Barberton Greenstone Belt, South Africa: petrology and trace-element geochemistry of 3.5 to 3.3 Ga old silicified volcanoclastic sediments. *South African Journal of Geology* 116, 297–322. <https://doi.org/10.2113/gssajg.116.2.297>

Hofmann, A., Karykowski, B., Mason, P., Chunnet, G., Arndt, N., 2013. Barberton drilling project - Buck Reef Chert core BARB3 15, EGU2013-12227.

Homann, M., Heubeck, C., Airo, A., Tice, M.M., 2015. Morphological adaptations of 3.22 Ga-old tufted microbial mats to Archean coastal habitats (Moodies Group, Barberton Greenstone Belt, South Africa). *Precambrian Research* 266, 47–64. <https://doi.org/10.1016/j.precamres.2015.04.018>

- Kamber, B.S., Webb, G.E., Gallagher, M., 2014. The rare earth element signal in Archaean microbial carbonate: information on ocean redox and biogenicity. *Journal of the Geological Society* 171, 745–763. <https://doi.org/10.1144/jgs2013-110>
- Klein, C., Beukes, N.J., 1989. Geochemistry and sedimentology of a facies transition from limestone to iron-formation deposition in the early Proterozoic Transvaal Supergroup, South Africa. *Economic Geology* 84, 1733–1774. <https://doi.org/10.2113/gsecongeo.84.7.1733>
- Klein, C., Ladeira, E.A., 2002. Petrography and geochemistry of the least altered banded iron-formation of the Archean Carajás Formation, Northern Brazil. *Economic Geology* 97, 643–651. <https://doi.org/10.2113/gsecongeo.97.3.643>
- Kouketsu, Y., Nishiyama, T., Ikeda, T., Enami, M., 2014. Evaluation of residual pressure in an inclusion–host system using negative frequency shift of quartz Raman spectra. *American Mineralogist* 99, 433–442. <https://doi.org/10.2138/am.2014.4427>
- Kröner, A., Anhaeusser, C.R., Hoffmann, J.E., Wong, J., Geng, H., Hegner, E., Xie, H., Yang, J., Liu, D., 2016. Chronology of the oldest supracrustal sequences in the Palaeoarchaean Barberton Greenstone Belt, South Africa and Swaziland. *Precambrian Research* 279, 123–143. <https://doi.org/10.1016/j.precamres.2016.04.007>
- Krüner, A., Byerly, G.R., Lowe, D.R., 1991. Chronology of early Archaean granite-greenstone evolution in the Barberton Mountain Land, South Africa, based on precise dating by single zircon evaporation. *Earth and Planetary Science Letters* 103, 41–54. [https://doi.org/10.1016/0012-821X\(91\)90148-B](https://doi.org/10.1016/0012-821X(91)90148-B)
- Lawnizack, G., 2022. Étude des stromatolithes archéens (Malmani Subgroup, Afrique du Sud, 2,58-2,5 Ga) : caractérisation pétrographique et processus post-dépôt.
- Ledevin, M., Arndt, N., Chauvel, C., Jaillard, E., Simionovici, A., 2019. The Sedimentary Origin of Black and White Banded Cherts of the Buck Reef, Barberton, South Africa. *Geosciences* 9, 424. <https://doi.org/10.3390/geosciences9100424>
- Lowe, D.R., 1999. Geologic evolution of the Barberton Greenstone Belt and vicinity, in: Lowe, D.R., Byerly, G.R. (Eds.), *Geologic Evolution of the Barberton Greenstone Belt, South Africa*. Geological Society of America, p. 0. <https://doi.org/10.1130/0-8137-2329-9.287>
- Lowe, D.R., 1982. Sediment gravity flows; II, Depositional models with special reference to the deposits of high-density turbidity currents. *Journal of Sedimentary Research* 52, 279–297. <https://doi.org/10.1306/212F7F31-2B24-11D7-8648000102C1865D>
- Lowe, D.R., Byerly, G.R., 2007. Chapter 5.3 An Overview of the Geology of the Barberton Greenstone Belt and Vicinity: Implications for Early Crustal Development, in: van Kranendonk, M.J., Smithies, R.H., Bennett, V.C. (Eds.), *Developments in Precambrian Geology, Earth's Oldest Rocks*. Elsevier, pp. 481–526. [https://doi.org/10.1016/S0166-2635\(07\)15053-2](https://doi.org/10.1016/S0166-2635(07)15053-2)
- Lowe, D.R., Byerly, G.R., 1999. *Geologic Evolution of the Barberton Greenstone Belt, South Africa*. Geological Society of America.
- Lowe, D.R., Worrell, G.F., 1999. Sedimentology, mineralogy, and implications of silicified evaporites in the Kromberg Formation, Barberton Greenstone Belt, South Africa, in: *Geologic*

Evolution of the Barberton Greenstone Belt, South Africa. Geological Society of America. <https://doi.org/10.1130/0-8137-2329-9.167>

Lyons, T.W., Reinhard, C.T., Planavsky, N.J., 2014. The rise of oxygen in Earth's early ocean and atmosphere. *Nature* 506, 307–315. <https://doi.org/10.1038/nature13068>

Machado, N., Lindenmayer, Z., Krogh, T.E., Lindenmayer, D., 1991. U-Pb geochronology of Archean magmatism and basement reactivation in the Carajás area, Amazon shield, Brazil. *Precambrian Research* 49, 329–354. [https://doi.org/10.1016/0301-9268\(91\)90040-H](https://doi.org/10.1016/0301-9268(91)90040-H)

Martins, P.L.G., Toledo, C.L.B., Silva, A.M., Antonio, P.Y.J., Chemale, F., Assis, L.M., Trindade, R.I.F., 2021. Low paleolatitude of the Carajás Basin at ~2.75 Ga: Paleomagnetic evidence from basaltic flows in Amazonia. *Precambrian Research* 365, 106411. <https://doi.org/10.1016/j.precamres.2021.106411>

Martins, P.L.G., Toledo, C.L.B., Silva, A.M., Chemale Jr, F., Santos, J.O.S., Assis, L.M., 2017. Neoproterozoic magmatism in the southeastern Amazonian Craton, Brazil: Petrography, geochemistry and tectonic significance of basalts from the Carajás Basin. *Precambrian Research* 302, 340–357. <https://doi.org/10.1016/j.precamres.2017.10.013>

Melo, G.H.C. de, Monteiro, L.V.S., Xavier, R.P., Moreto, C.P.N., Arquaz, R.M., Silva, M.A.D., 2019. Evolution of the Igarapé Bahia Cu-Au deposit, Carajás Province (Brazil): Early syngenetic chalcopyrite overprinted by IOCG mineralization. *Ore Geology Reviews* 111, 102993. <https://doi.org/10.1016/j.oregeorev.2019.102993>

Miyano, T., Beukes, N.J., 1984. Phase relations of stilpnomelane, ferri-annite, and riebeckite in very low-grade metamorphosed iron-formations. *Transactions of the Geological Society of South Africa*.

Mulder, T., Alexander, J., 2001. The physical character of subaqueous sedimentary density flows and their deposits. *Sedimentology* 48, 269–299. <https://doi.org/10.1046/j.1365-3091.2001.00360.x>

Myrow, P.M., Tice, L., Archuleta, B., Clark, B., Taylor, J.F., Ripperdan, R.L., 2004. Flat-pebble conglomerate: its multiple origins and relationship to metre-scale depositional cycles. *Sedimentology* 51, 973–996. <https://doi.org/10.1111/j.1365-3091.2004.00657.x>

Nemec, W., Steel, R.J., 1984. Alluvial and Coastal Conglomerates: Their Significant Features and Some Comments on Gravelly Mass-Flow Deposits 1–31.

Pellerin, A., Thomazo, C., Ader, M., Marin-Carbonne, J., Alleon, J., Vennin, E., Hofmann, A., 2023. Iron-mediated anaerobic ammonium oxidation recorded in the early Archean ferruginous ocean. *Geobiology* 21, 277–289. <https://doi.org/10.1111/gbi.12540>

Perelló, J., Zulliger, G., García, A., Creaser, R.A., 2023. Revisiting the IOCG geology and age of Alemão in the Igarapé Bahia camp, Carajás province, Brazil. *Journal of South American Earth Sciences* 124, 104273. <https://doi.org/10.1016/j.jsames.2023.104273>

Pinheiro, R.V.L., Holdsworth, R.E., 1997. Reactivation of Archaean strike-slip fault systems, Amazon region, Brazil. *Journal of the Geological Society* 154, 99–103. <https://doi.org/10.1144/gsjgs.154.1.0099>

- Postma, G., Cartigny, M.J.B., 2014. Supercritical and subcritical turbidity currents and their deposits—A synthesis. *Geology* 42, 987–990. <https://doi.org/10.1130/G35957.1>
- Postma, G., Kleverlaan, K., Cartigny, M.J.B., 2014. Recognition of cyclic steps in sandy and gravelly turbidite sequences, and consequences for the Bouma facies model. *Sedimentology* 61, 2268–2290. <https://doi.org/10.1111/sed.12135>
- Rego, E.S., Busigny, V., Lalonde, S.V., Philippot, P., Bouyon, A., Rossignol, C., Babinski, M., de Cássia Zapparoli, A., 2021. Anoxygenic photosynthesis linked to Neoproterozoic iron formations in Carajás (Brazil). *Geobiology* 19, 326–341. <https://doi.org/10.1111/gbi.12438>
- Ronzê, P.C., Soares, A.D., Santos, M. dos, Barreira, C.F., 2000. Alemão copper-gold (U-REE) deposit, Carajás, Brazil. Hydrothermal iron oxide copper-gold & related deposits: a global perspective. Australian Mineral Foundation, Adelaide 191–202.
- Rossignol, C., Antonio, P.Y.J., Narduzzi, F., Rego, E.S., Teixeira, L., de Souza, R.A., Ávila, J.N., Silva, M.A.L., Lana, C., Trindade, R.I.F., Philippot, P., 2022. Unraveling one billion years of geological evolution of the southeastern Amazonia Craton from detrital zircon analyses. *Geoscience Frontiers* 13, 101202. <https://doi.org/10.1016/j.gsf.2021.101202>
- Rossignol, C., Rego, E.S., Philippot, P., Narduzzi, F., Teixeira, L., Silva, M.A.L., Ávila, J.N., Lana, C., Trindade, R.F., 2023. Neoproterozoic environments associated with the emplacement of a large igneous province: Insights from the Carajás Basin, Amazonia Craton. *Journal of South American Earth Sciences* 130, 104574. <https://doi.org/10.1016/j.jsames.2023.104574>
- Rossignol, C., Siciliano Rego, E., Narduzzi, F., Teixeira, L., Ávila, J.N., Silva, M.A.L., Lana, C., Philippot, P., 2020. Stratigraphy and geochronological constraints of the Serra Sul Formation (Carajás Basin, Amazonian Craton, Brazil). *Precambrian Research* 351, 105981. <https://doi.org/10.1016/j.precamres.2020.105981>
- Santos, J.O.S., Hartmann, L.A., Gaudette, H.E., Groves, D.I., McNaughton, N.J., Fletcher, I.R., 2000. A New Understanding of the Provinces of the Amazon Craton Based on Integration of Field Mapping and U-Pb and Sm-Nd Geochronology. *Gondwana Research* 3, 453–488. [https://doi.org/10.1016/S1342-937X\(05\)70755-3](https://doi.org/10.1016/S1342-937X(05)70755-3)
- Sumner, D.Y., Beukes, N.J., 2006. Sequence Stratigraphic Development of the Neoproterozoic Transvaal carbonate platform, Kaapvaal Craton, South Africa. *South African Journal of Geology* 109, 11–22. <https://doi.org/10.2113/gssajg.109.1-2.11>
- Sumner, D.Y., Grotzinger, J.P., 2004. Implications for Neoproterozoic ocean chemistry from primary carbonate mineralogy of the Campbellrand-Malmani Platform, South Africa. *Sedimentology* 51, 1273–1299. <https://doi.org/10.1111/j.1365-3091.2004.00670.x>
- Tice, M.M., Bostick, B.C., Lowe, D.R., 2004. Thermal history of the 3.5–3.2 Ga Onverwacht and Fig Tree Groups, Barberton greenstone belt, South Africa, inferred by Raman microspectroscopy of carbonaceous material. *Geology* 32, 37–40. <https://doi.org/10.1130/G19915.1>
- Tice, M.M., Lowe, D.R., 2006a. The origin of carbonaceous matter in pre-3.0 Ga greenstone terrains: A review and new evidence from the 3.42 Ga Buck Reef Chert. *Earth-Science Reviews* 76, 259–300. <https://doi.org/10.1016/j.earscirev.2006.03.003>

- Tice, M.M., Lowe, D.R., 2006b. Hydrogen-based carbon fixation in the earliest known photosynthetic organisms. *Geology* 34, 37–40. <https://doi.org/10.1130/G22012.1>
- Tice, M.M., Lowe, D.R., 2004. Photosynthetic microbial mats in the 3,416-Myr-old ocean. *Nature* 431, 549–552. <https://doi.org/10.1038/nature02888>
- Toledo, P.I., Penteado Natividade Moreto, C., Xavier, R.P., Gao, J., da Silva Nogueira de Matos, J.H., de Melo, G.H.C., 2019. Multistage Evolution of the Neoproterozoic (ca. 2.7 Ga) Igarapé Cinzento (GT-46) Iron Oxide Copper-Gold Deposit, Cinzento Shear Zone, Carajás Province, Brazil. *Economic Geology* 114, 1–34. <https://doi.org/10.5382/econgeo.2019.4617>
- Trendall, A.F., Basei, M.A.S., de Laeter, J.R., Nelson, D.R., 1998. SHRIMP zircon U–Pb constraints on the age of the Carajás formation, Grão Pará Group, Amazon Craton. *Journal of South American Earth Sciences* 11, 265–277. [https://doi.org/10.1016/S0895-9811\(98\)00015-7](https://doi.org/10.1016/S0895-9811(98)00015-7)
- Tyler, R., Tyler, N., 1996. Stratigraphic and structural controls on gold mineralization in the Pilgrim’s Rest goldfield, eastern Transvaal, South Africa. *Precambrian Research, Geology and Geochemistry of the Transvaal Supergroup* 79, 141–169. [https://doi.org/10.1016/0301-9268\(95\)00092-5](https://doi.org/10.1016/0301-9268(95)00092-5)
- Vasquez, M.L., Rosa-Costa, L.T. da, 2008. Geologia e recursos minerais do estado do Pará (Technical Report). CPRM.
- Vasquez, M.L., Sousa, C.S., Carvalho, J.M.A., 2008. Mapa geológico e de recursos minerais do Estado do Pará, escala 1: 1.000. 000. Programa Geologia do Brasil, Belém, CPRM.
- Walker, R.G., 1975. Generalized Facies Models for Resedimented Conglomerates of Turbidite Association. *GSA Bulletin* 86, 737–748. [https://doi.org/10.1130/0016-7606\(1975\)86<737:GFMFRC>2.0.CO;2](https://doi.org/10.1130/0016-7606(1975)86<737:GFMFRC>2.0.CO;2)
- Walraven, F., 1995. Zircon Pb-evaporation age determinations of the Oak Tree Formation, Chuniespoort group, Transvaal sequence: implications for Transvaal-Griqualand West Basin correlations. *South African Journal of Geology* 98, 58–67.

CHAPTER 5. ANALYTICAL TECHNIQUES

5.1. Introduction.....	186
5.2. Sampling	187
5.3. Petrographic observations.....	187
5.4. Mineralogy.....	188
5.4.1. X-Ray Diffraction (XRD).....	188
5.4.2. Raman spectroscopy	188
5.5. Elemental analyses.....	189
5.5.1. Major, minor and trace element concentrations.....	189
5.5.2. Electron Probe Micro-Analyses (EPMA).....	189
5.5.3. Scanning Electron Microscopy (SEM).....	190
5.5.4. Micro X-Ray Fluorescence (μ XRF).....	190
5.6. Carbon and nitrogen geochemical analyses.....	191
5.6.1. Sample preparation and chemical treatment.....	191
5.6.1.1. Decarbonated samples	191
5.6.1.2. Kerogen extracts	193
5.6.2. Carbon analyses : concentrations and isotope compositions	193
5.6.2.1. General principles of EA-IRMS	193
5.6.2.2. Total Organic Carbon (TOC) content and $\delta^{13}\text{C}_{\text{org}}$	194
5.6.2.3. Inorganic carbon content and $\delta^{13}\text{C}_{\text{carb}}$	194
5.6.3. Nitrogen analyses: concentrations and isotope compositions.....	195
5.6.3.1. Reliable N isotope measurements of small N quantities	195
5.6.3.2. Sealed tube combustion	196
5.6.3.2.1. Preparation of the sealed tubes	196
5.6.3.2.2. Reagents.....	197
5.6.3.2.3. Quantity of powder	197

5.6.3.2.4. Degassing under vacuum and sealing	197
5.6.3.2.5. Combustion	198
5.6.3.3. Extraction and purification on the vacuum line	198
5.6.3.4. Isotopic analysis by dual-inlet IRMS	199
5.6.3.6. Correction of $\delta^{15}\text{N}$ values of the blank contribution	200
References	201

CHAPTER 5. ANALYTICAL TECHNIQUES

5.1. Introduction

Measuring the nitrogen isotope composition of Archean sedimentary rocks represents an analytical challenge, as the nitrogen content of such rocks is usually low (reviewed in Ader et al., 2016; Stüeken et al., 2016), with most TN contents below 0.1% (Fig. 5.1). This is mainly due to a loss of N during their post-depositional history (Chapter 2). This chapter details how such nitrogen-poor samples were analyzed, and the confidence with which the resulting isotopic values can be interpreted.

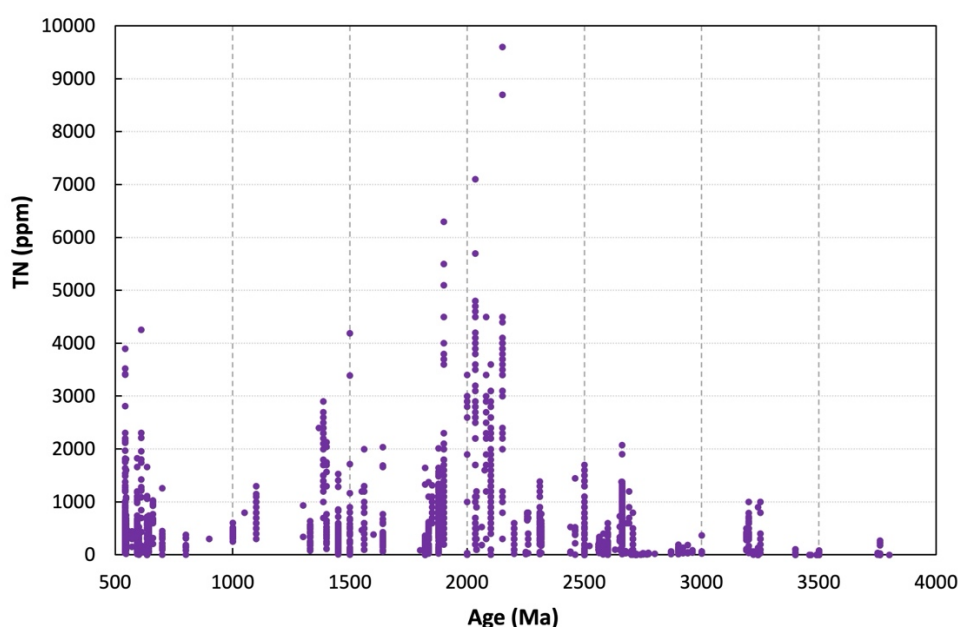


Fig. 5.1. Variation of TN contents (ppm) of Precambrian sedimentary rocks.

Although the aim of this work was to measure the nitrogen isotope signature of Archean samples, a large range of complementary indicators were obtained when those were not available in the literature. These include first and most importantly the organic carbon isotope composition of the studied samples. Additionally, the petrology, mineralogy, major and trace elements abundances were also investigated through various techniques that are detailed in this chapter. The purpose was always to provide complementary information about the depositional environment or chemical conditions that could shed light on the interpretation of the nitrogen isotope composition, e.g. arguing for the most plausible scenario when several hypotheses remained or pointing at inconsistencies between the nitrogen isotope signature and other geochemical tracers.

Among the data that is presented in this dissertation, I was directly involved in the chemical preparation of the samples for the isotope analyses and the subsequent measurements. For X-Ray Diffraction (XRD) analyses, Raman spectroscopy, Electron Probe Micro-Analyses (EPMA), Scanning Electron Microscopy (SEM), and Micro X-Ray Fluorescence (μ XRF), I was involved in the preparation and analyses, but required assisted qualified technical help. Some analyses and preparations presented in this work were outsourced, among which sample collection, thin section preparation, major and trace element analyses, and kerogen extractions.

5.2. Sampling

For the samples analyzed in this thesis, no systematic sampling technique was applied. Sampling largely depended on sample availability. Along drill cores, samples were chosen according to their observed or supposed high organic matter content, giving the most likely chance of organic matter abundance in order to contain enough nitrogen to analyze. Given the amount of sample powder necessary for a single nitrogen measurement (up to 400 mg bulk powder, [5.6.3.2.1](#)), samples were also chosen according to their available amount.

Sample provenance and details on specific sampling methods and programs are given in the Methods section for each study site. Access to the samples was made possible thanks to collaborations from various research projects: the ICDP-sponsored BARB3 drilling program (Hofmann et al., 2013) for the Buck Reef Chert samples (Chapter 6), the innovation program ERC (STROMATA, grant agreement 759289) for the Buck Reef Chert and Malmani samples (Chapter 6 & Chapter 8), and the FAPESP program (Fundação de Amparo à Pesquisa do Estado de São Paulo, Grant/Award Number: 2019/16271-0, 2018/05892-0, 2015/16235-2 and 2018/02645-2) for the Serra Sul samples (Chapter 7).

5.3. Petrographic observations

Petrographic observations were carried out on polished thin sections commercially produced by Lithologie Bourgogne (LithoB, Dijon, France), using a Nikon AZ100 Multizoom macro/micro optical microscope at the Biogéosciences Laboratory (GISMO platform, University of Burgundy, France). Thin sections were observed under plane-polarized light and cross-polarized light. Images were captured with a Tucsen TrueChrome 4K Pro camera.

5.4. Mineralogy

Mineralogy was investigated on bulk powders using X-Ray Diffraction in order to get an overview of the dominant mineral phases and using Raman spectroscopy for specific determinations at the mineral scale.

5.4.1. X-Ray Diffraction (XRD)

Mineralogical assemblages of bulk powders were determined before chemical treatment using X-Ray Diffraction (XRD) at the Biogéosciences Laboratory (University of Burgundy, France). Diffractograms were obtained with a Bruker D8 Endeavor diffractometer with $\text{CuK}\alpha$ radiation, LynxEye XE-T detector and Ni filter, under 40 kV voltage and 25 mA intensity. The goniometer scanned from 2° to 65° 2θ for each run. Identification of crystalline phases was based on the position and area of their respective mean basal reflections on the Diffrac.EVA software, compared to reference minerals from the COD (“Crystallography Open Database”) and the RRUFFTM Project mineralogy databases. Semi-quantitative estimations of mineral abundances were performed using the MacDiff and Profex (Doebelin and Kleeberg, 2015) softwares. For carbonated samples, a second XRD analysis was performed after HCl digestion (5.6.1.1) in order to verify the efficiency of the inorganic carbon removal process.

5.4.2. Raman spectroscopy

Raman spectroscopy was used to characterize carbonates and organic matter. Raman data were obtained at ISTE, Unil, Switzerland, by Dr. Julien Alleon, using a Horiba Jobin Yvon LabRAM 800 HR spectrometer in a confocal configuration equipped with an Ar⁺ laser (532 nm) excitation source and a Peltier Cooled CCD detector. Raman microspectroscopy measurements were performed on polished thin sections at constant room temperature, with a laser beam focused on the sample using a 300 μm confocal hole with a long working distance x100 objective (NA = 0.8). This configuration provides a ≈ 1 μm spot size for a laser power delivered at the sample surface below 1 mW, thereby preventing irreversible laser-induced thermal damage (Bernard et al., 2008; Beyssac et al., 2003). A 1800 grooves/mm diffraction grating was used to provide better light dispersion. A circularly polarized laser using a quarter wavelength plate limits polarization effects. A calibrated edge high band filter (lowest wavenumber: ≈ 70 cm^{-1}) has been used to minimize the elastic backscattered signal (Ferralis et al., 2016). The collected Raman spectra were used (1) to locate carbonaceous matter and differentiate it from

other dark and amorphous material such as oxides, in order to document the structural organization of the aromatic skeleton of carbonaceous matter, and (2) to characterize the nature of the carbonates at a small scale, differentiating between calcite, dolomite, ankerite and siderite, and determine if several types of carbonates could be identified at the thin section scale, XRD only providing bulk carbonate estimations. Phase identification and mineral chemistry of the carbonates were done thanks to the RRUFFTM Project mineralogy database, to Rividi et al. (2010), who proposed a calibration for extracting carbonate composition on solid solutions in the Ca-Mg-Fe-Mn carbonate system, and to Boulard et al. (2012), who provided a calibration procedure to extract the Fe content together with structural information from Raman peak positions of Fe-Mg-bearing carbonates.

5.5. Elemental analyses

Complementary to mineralogy investigations by microscopic observations, XRD and Raman determinations of the mineralogy, elemental analyses were performed to better constrain the chemical and redox properties of the studied samples' depositional environments.

5.5.1. Major, minor and trace element concentrations

Whole-rock concentrations of major and trace elements were measured on bulk powders via ICP-AES and ICP-MS at the Service d'Analyse des Roches et des Minéraux (SARM) of the Centre de Recherches Pétrographiques et Géochimiques (CRPG, Vandoeuvre-Lès-Nancy, France), following the method described in Carignan et al. (2001). Analytical precision and detection limits for major element concentrations are typically better than $\pm 10\%$.

5.5.2. Electron Probe Micro-Analyses (EPMA)

The chemical composition of carbonates performed for two Buck Reef Chert samples on thin section mounted into indium was investigated by Electron Probe Micro-Analyzer (EPMA) using a JEOL JXA-8530F at the Institute of Geological Science, University of Lausanne. Sample preparation was performed thanks to the assistance and supervision of Dr. Thomas Bovay. It consisted of manually polishing thin sections with diamond paste, with a sequential decrease in grain size of the diamond paste from 10 to 6 to 3 to 1 μm . Then, millimeter-sized thin section chips were cut using a precision diamond dicing saw. Thin section chips and

standard grains of iron carbonates (ankerite and siderite) were subsequently embedded into indium mounts using a hydraulic press at the Swiss SIMS Facility.

EPMA spot analyses of carbonates were performed by Dr. Martin Robyr, using 15 keV accelerating voltage at 15 nA, and 60 s dwell time (15 s for each background after 30 s on peak). For the carbonates a 5 μm diameter beam was used and six oxide components were obtained using synthetic and natural standards: olivine (MgO), anorthite (SiO_2), fayalite (FeO), calcite (CaO), benitoite (BaO), and rhodonite (MnO).

Quantitative compositional maps were generated from X-ray intensity maps using spot analyses acquired in the same area as internal standards. The X-ray maps were measured by WDS with 15 keV accelerating voltage at 50 nA, with various dwell time and resolutions. Four elements (Ca, Fe, Mg, Mn) were measured at the specific wavelength in two successive passes (with Ca analyzed on the first scan). Compositional maps were processed using XMapTools 3.2.1 (Lanari et al., 2014, 2019). Representative compositions of Fe-Mg-rich carbonates growth zones were obtained by averaging pixels from manually selected areas.

5.5.3. Scanning Electron Microscopy (SEM)

SEM observations of polished thin sections were performed to locate iron-bearing minerals and phases in two selected samples from the Serra Sul Formation. High-resolution images were obtained with a JEOL JSM 6400F Field Emission SEM equipped with an Oxford INCA Energy 300 X-ray Energy Dispersive Spectrometer (EDS) system for all chemical analyses at the ARCEN platform (Laboratory Institut Carnot de Bourgogne, University of Burgundy, Dijon, France). The thin sections were prepared for SEM analyses and were subsequently coated with ~ 10 nm of graphite using a High Resolution Ion Beam Coater GATAN 681. The high-resolution images were taken in back-scatter electron imaging mode to enhance the compositional contrast. These facilities were used to identify rock textures and to examine pyrite morphologies in samples from the studied section.

5.5.4. Micro X-Ray Fluorescence (μXRF)

2D elemental mapping on polished surfaces of five half-split core sections from the BRC Formation was performed by Dr. Christophe Durllet using a Bruker® M4 Tornado table-top

energy-dispersive μ XRF scanner to characterize the distribution of Ag, Al, As, Ba, Ca, Cd, Cl, Co, Cr, Cu, Fe, Hg, K, La, Mg, Mn, Na, Ni, P, S, Si, Ti, Zn, and Zr. The resolution was 20 μ m.

5.6. Carbon and nitrogen geochemical analyses

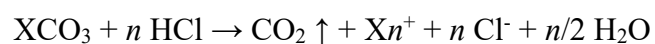
5.6.1. Sample preparation and chemical treatment

Samples were first crushed into a ≈ 60 μ m powder using a ring and puck mill at the Biogéosciences Laboratory (University of Burgundy, France). Samples were ground using an agate grinding set to avoid metal contamination, except for chert samples of the Buck Reef Chert Formation whose hardness required the use of a steel grinding set.

Chemical treatment prior to C_{org} and N elemental and isotopic measurements included either a two-step HCl digestion, for bulk nitrogen and organic carbon analyses, or a kerogen extraction, for organic nitrogen and organic carbon analyses.

5.6.1.1. Decarbonated samples

To avoid measuring an isotopic mixture between the inorganic and organic carbon phases, carbonate-free residues were obtained by HCl digestion following this reaction:



Sample powders were mixed with 6N HCl for 24h at room temperature to remove calcium carbonates. A second step of 6N HCl digestion at 80°C for 4h was needed to remove potential magnesium and/or iron carbonates. The residual powder was then rinsed with deionized distilled water to a neutral pH and centrifugated at 2300 g. After the removal of excess water, powders were oven-dried at 40°C for 48h. Carbonate content, expressed in weight percent (wt.%), was evaluated through gravimetric mass balance before and after HCl digestion. The reliability of this carbonate estimation depends on the mineral assemblages of the studied samples. While it matches semi-quantitative carbonates estimations from bulk XRD analyses in chert and carbonates samples (Table 5.1, Fig. 5.2), it can yield overestimated carbonate contents for clay- or oxide-rich samples, which can be partly digested by this procedure (Table 5.1, Fig. 5.2).

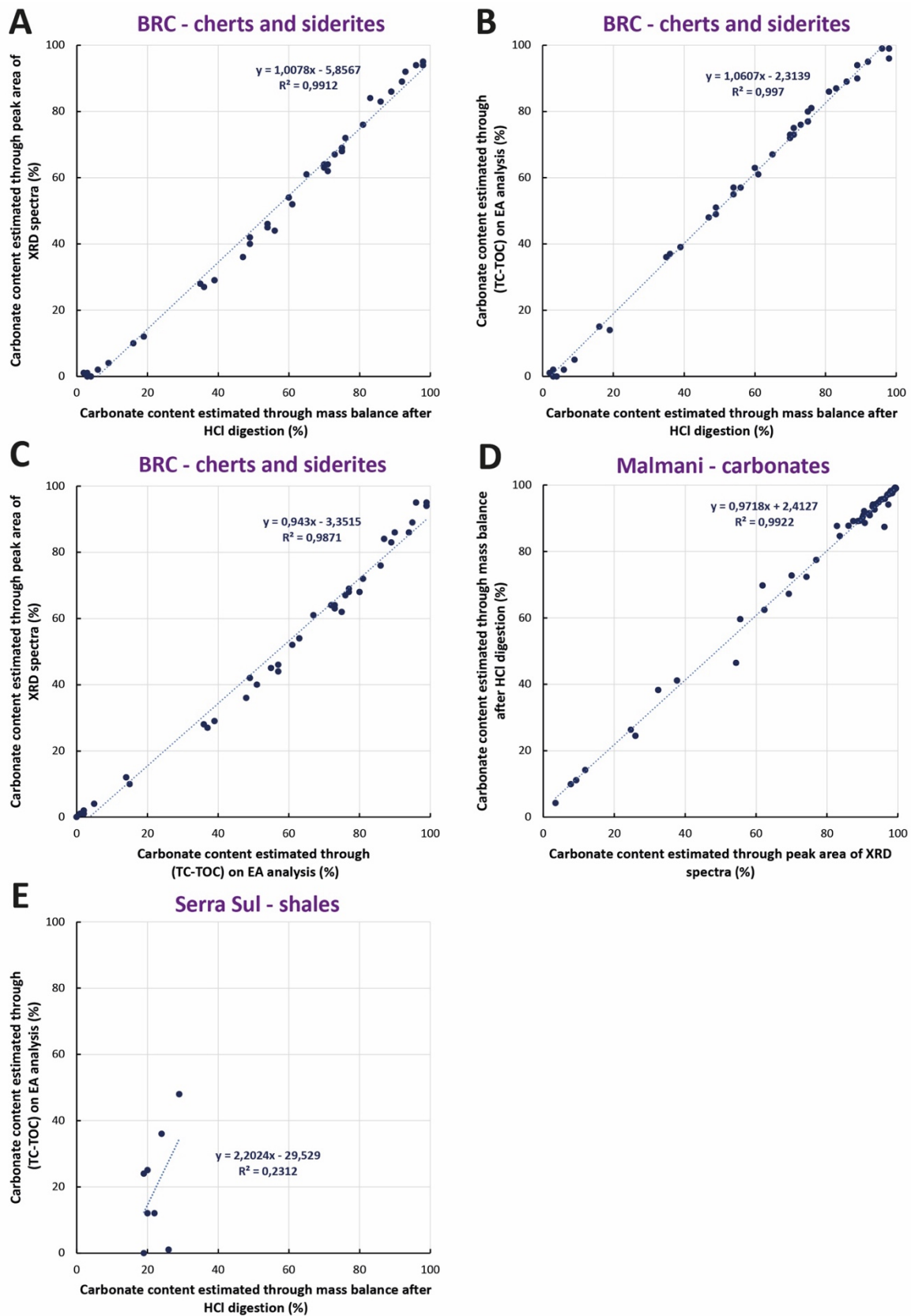


Fig. 5.2. Estimation of the samples' carbonate content (%) for the three studied Formations using different analytical techniques: gravimetric mass balance after HCl digestion, (TOC-TOC) using EA analyses, and peak area of XRD spectra. Correlation between methods are indicated by R^2 values.

5.6.1.2. Kerogen extracts

Kerogen extracts were commercially produced by Global Geolab Ltd, Alberta, Canada. Bulk powders were digested using HCl and HF, and kerogens were separated out by heavy liquid separation with zinc bromide.

5.6.2. Carbon analyses : concentrations and isotope compositions

5.6.2.1. General principles of EA-IRMS

Elemental and isotopic abundances were obtained through an Elemental Analyzer (EA) and an Isotopic Ratio Mass Spectrometre (IRMS), respectively. IRMS allows the separation and collection of the isotopes of a given element according to differences of mass-to-charge ratio (m/z) of ionized samples. An IRMS includes (i) an ion source that ionizes the sample, (ii) an analyzer that accelerates and separates the ions produced according to their m/z ratio and, (iii) a series of collectors that count the ions and amplify the generated electric signal (Fig. 5.3).

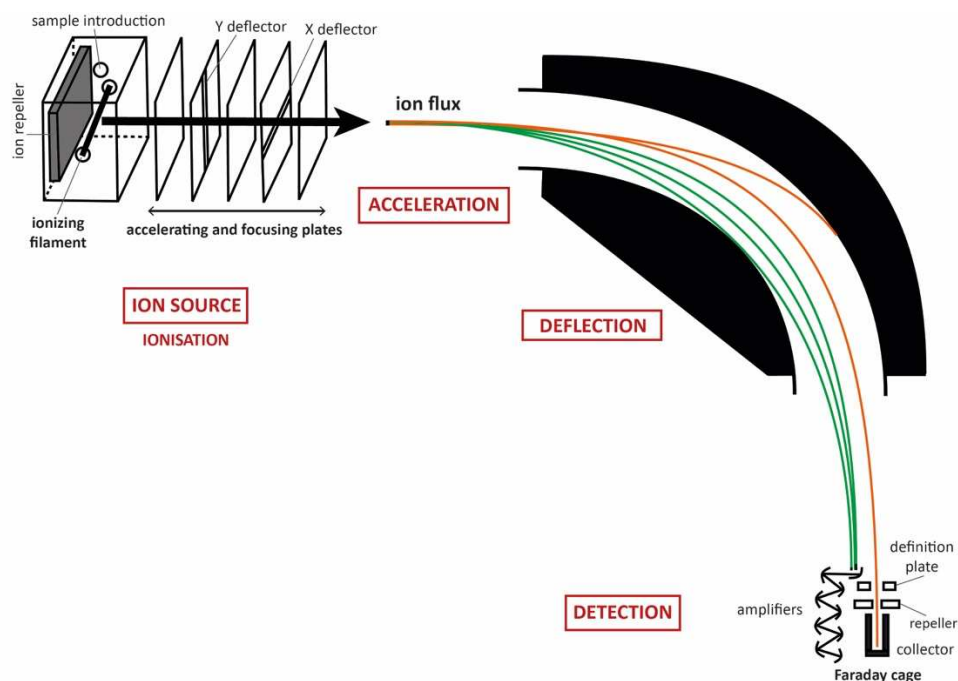


Fig. 5.3. Diagram showing the different IRMS areas: ionization, acceleration, deflection and detection.

5.6.2.2. Total Organic Carbon (TOC) content and $\delta^{13}\text{C}_{\text{org}}$

150 samples were analyzed (285 analyses with replicates) for their total organic carbon (TOC) content and their organic carbon isotope composition ($\delta^{13}\text{C}_{\text{org}}$). Aliquots of dried decarbonated residues were poured into tin capsules (20 to 80 mg of powder) and weighed using a Sartorius M2P ultra-balance before TOC and $\delta^{13}\text{C}_{\text{org}}$ measurements were performed using a Thermo Fisher Scientific Flash Smart elemental analyser, coupled in continuous flow mode to a Thermo Fisher Scientific Delta V isotope ratio mass spectrometer (EA-IRMS) via a ConFlo IV interface, or an Elementar Vario Micro Cube elemental analyser, coupled in continuous flow mode to an IsoPrime isotope ratio mass spectrometer (EA-IRMS) at the Biogéosciences Laboratory (GISMO platform, University of Burgundy, France). These instruments were run by Anne-Lise Santoni. Certified USGS40 ($\delta^{13}\text{C}_{\text{org}}=-26.39\text{‰}$, TOC=40.82 wt.%), caffeine IAEA-600 ($\delta^{13}\text{C}_{\text{org}}=-27.77\text{‰}$, TOC=49.48 wt.%) and wheat flour ($\delta^{13}\text{C}_{\text{org}}=-27.21\text{‰}$, TOC=39.38 wt.%) reference materials were used for the calibration. These standards had a mean reproducibility of 1.3 wt.% for the TOC content and 0.4‰ for the $\delta^{13}\text{C}_{\text{org}}$ (USGS40), 4.8 wt.% for the TOC content and 0.8‰ for the $\delta^{13}\text{C}_{\text{org}}$ (caffeine IAEA-600) and 4.2 wt.% for the TOC content and 0.7‰ for the $\delta^{13}\text{C}_{\text{org}}$ (wheat flour) (Table 5.2). Deviations from reference materials were 0.6 wt.% for the TOC content and 0.2‰ for the $\delta^{13}\text{C}_{\text{org}}$ (USGS40), 2.5 wt.% for the TOC content and 1.6‰ for the $\delta^{13}\text{C}_{\text{org}}$ (caffeine IAEA-600) and 2.3 wt.% for the TOC content and 0.6‰ for the $\delta^{13}\text{C}_{\text{org}}$ (wheat flour) (Table 5.2). TOC contents are expressed in dry weight percentage (wt.%) of the non-decarbonated bulk powder and isotope results are reported in delta-notation relative to V-PDB. The mean external reproducibility (2σ), based on all sample replicate analyses, is ± 0.06 wt.% for the TOC content and $\pm 0.9\text{‰}$ for the $\delta^{13}\text{C}_{\text{org}}$ ($n=61$) for the BRC Formation samples, ± 0.01 wt.% for the TOC content and $\pm 0.3\text{‰}$ for the $\delta^{13}\text{C}_{\text{org}}$ ($n=23$) for the Serra Sul Formation samples, and ± 57 ppm for the TOC content and $\pm 0.6\text{‰}$ for the $\delta^{13}\text{C}_{\text{org}}$ ($n=53$) for the Malmani Subgroup samples. This external reproducibility includes resampling and chemical treatment; it thus may in part reflect sample heterogeneity.

5.6.2.3. Inorganic carbon content and $\delta^{13}\text{C}_{\text{carb}}$

An estimation of total carbonate contents of the samples was provided by weighing samples before and after the HCl digestion procedure described in [4.6.1.1](#). However, this estimation has limits. Indeed, it yields reliable results for samples containing negligible amounts of clays and oxides. For example, for the Buck Reef Chert and the Malmani carbonated samples, semi-

quantitative carbonate estimations by XRD match carbonate contents calculated by mass-balance calculations after HCl digestion (Table 5.1, Fig. 5.2), as well as carbonate contents calculated by measuring the difference between total carbon and organic carbon contents using the EA (Table 5.1, Fig. 5.2). However, for the Serra Sul samples, carbonate contents calculated by mass-balance calculations after HCl digestion deviate from semi-quantitative carbonate estimations by XRD and EA total carbon results by 13% on average ($n=8$, Table 5.1). It is likely that the digestion procedure described in [4.6.1.1](#) removed a significant percentage of clays and iron oxides, which make an important fraction of the sample. If the samples contain only calcium carbonates, carbonate contents should be estimated by using a less concentrated HCl digestion. However, as the samples likely contain Mg and Fe carbonates, the HCl 6N at 80°C digestion procedure needs to be used. This might be a problem to get accurate carbonate contents for Archean rock samples.

For $\delta^{13}\text{C}_{\text{carb}}$ measurements, samples were ground, homogenized and oven-dried at 80°C for 4 hours. Aliquots of 1.850 to 2.075 mg were weighed and transferred into 12 mL Labco™ Exetainers™. Atmospheric gases were flushed from the tubes and replaced with a CO₂-free synthetic atmosphere (80 % N₂ and 20 % O₂) using the automated air sampler flushing program of an IRIS Delta Ray™ (ThermoScientific™). An excess of 0.25 mL of H₃PO₄ (100%) was manually injected into each tube. After reacting for 12 hours at 80°C, the carbon isotopic composition ($\delta^{13}\text{C}_{\text{carb}}$) and the quantity of CO₂ released from the sample were measured by IRIS (ThermoScientific™ Delta Ray™). Aliquots of a calibrated reference gas (Bio ; $\delta^{13}\text{C} = -25.5$ ‰VPDB) and a solid standard of calcite put through the same chemical treatment as the samples (NBS19 ; $\delta^{13}\text{C} = +1.95$ ‰VPDB) were used for calibrating the measurements on the VPDB international scale and to estimate the internal error (< 0.1 ‰, 2σ).

5.6.3. Nitrogen analyses: concentrations and isotope compositions

5.6.3.1. Reliable N isotope measurements of small N quantities

As most samples contain less than 200 ppm N, the abovedescribed EA-IRMS method used for carbon isotopes is not sensitive enough to yield reliable bulk nitrogen isotopic analyses (Ader et al., 2016; Boocock et al., 2020). Samples were therefore analyzed at IPGP (Paris, France) using the “sealed tubes method” as described in Ader et al. (2014, 2016), in which N₂ is

produced offline through sealed-tube Dumas combustion and cryogenically purified in a vacuum line.

5.6.3.2. Sealed tube combustion

Sealed-tube Dumas combustion (Dumas, 1826) consists in heating a powder sample to a high temperature in the presence of oxygen and in a sealed glass tube vacuumed beforehand, in order to release the gases contained in the sample. It allows to subsequently separate those gases chemically for quantification and analysis.

5.6.3.2.1. Preparation of the sealed tubes

Quartz tubes with an external diameter of 6 mm and an internal diameter of 4 mm ($D_1=6\text{mm}$, $d_1=4\text{mm}$) were cut to a 30 cm length and sealed to one end using a blowtorch. Similarly, smaller quartz tubes with an external diameter of 3 mm ($D_2=3\text{mm}$) were cut to a length of a few centimeters and sealed to one end using a blowtorch. Up to 400 mg of decarbonated residual powder was put into several small quartz tubes, each partially obstructed with quartz wool or alumina (aluminium oxide) wool to prevent the powder from coming out. Each larger quartz tube is filled from bottom to top with: 3 to 4 cm of CuO wires, the smaller quartz tubes turned upside down and 1 to 2 cm of Cu wires (Fig. 5.4). All quartz tubes, CuO wires, Cu wires and alumina/quartz wool were purified beforehand at 900°C for 2h in a muffle furnace to prevent contamination. For each series of sealed tubes, a few « blank » tubes containing the reagents but no powder sample are prepared following the same procedure.

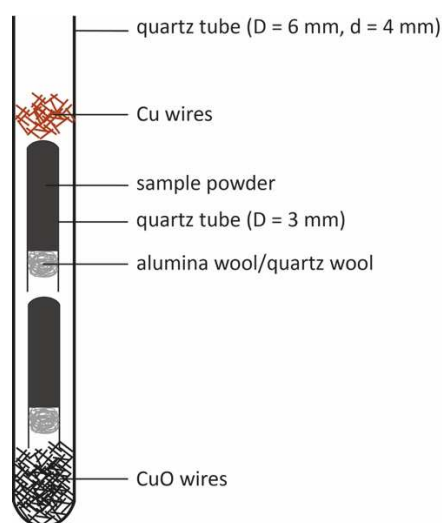
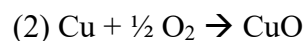
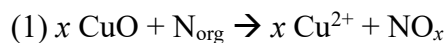


Fig. 5.4. Diagram of sample preparation showing a sample inside a sealed tube with reagents.

5.6.3.2.2. Reagents

CuO wires provide oxygen for the combustion (1), while Cu reduces nitrous oxides and traps residual oxygen at the end of the reaction (2).



Standard analytical procedures for nitrogen usually include CaO in the reagents to trap gaseous CO₂ and H₂O liberated from samples (Kendall and Grim, 1990), but given that Busigny et al. (2005) have shown that it significantly contributes to analytical blanks, we performed a few tests on selected samples which show that the addition of CaO does not yield significant $\delta^{15}\text{N}$ differences (Table 5.3). Samples were consequently analyzed without the addition of CaO, except for the kerogen extracts.

5.6.3.2.3. Quantity of powder

The quantity of powder in the quartz tube was determined so as to yield 1 micromole of N₂ or more, when possible. The tubes maximal capacity is around 400 mg of powder, depending on the density of the sample.

5.6.3.2.4. Degassing under vacuum and sealing

Quartz tubes filled with sample powder and reagents were connected to the vacuum line (Fig. 5.5) using a heat-shrinkable sleeve. Samples were degassed for 12h at 150°C using under vacuum to remove adsorbed atmospheric N₂ and organics. When a vacuum of 3×10^{-6} mbar was reached, usually after 12 hours, tubes were sealed directly under vacuum using a blowtorch.

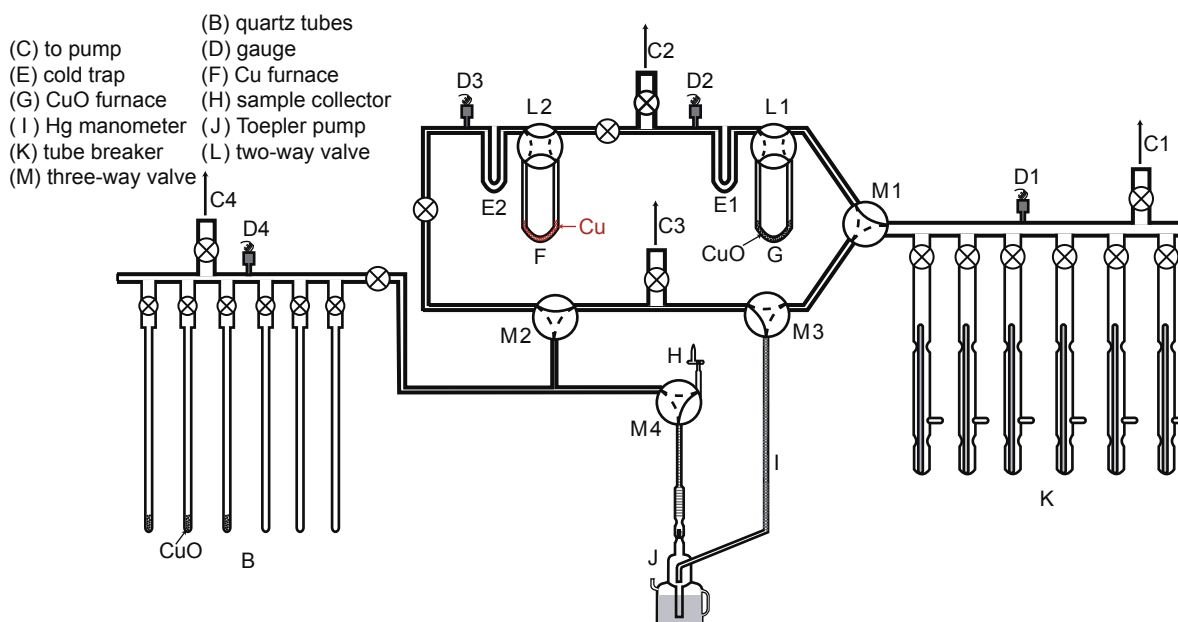


Fig. 5.5. Diagram of the vacuum line used for sample preparation (degassing) and extraction. (B) quartz tubes; (C) to pump; (D) gauge; (E) cold trap; (F) Cu furnace; (G) CuO furnace; (H) sample collector; (I) Hg manometer; (J) Toepler pump; (K) tube cracker; (L) two-way valve; (M) three-way valve.

5.6.3.2.5. Combustion

Sealed tubes were combusted in a muffle furnace at 950°C for 6h under oxidizing conditions by oxygen liberated from the CuO wires, then cooled at 600°C for 2h, allowing residual oxygen to combine with cupric oxide and nitrous oxide to be reduced by copper, and finally cooled to ambient temperature (Kendall and Grim, 1990). Busigny et al. (2005) have shown that the extraction yield for this protocol is 100% for both organic and mineral nitrogen, including ammonium in minerals such as phyllosilicates. During this step, a high PCO₂ buildup can cause the tubes to explode, either due to a high TOC/TN ratio or to the presence of inorganic carbon if carbonates have not previously been removed. Therefore, individual metal sheaths were placed around each tube to prevent damaging other tubes in case of explosion.

5.6.3.3. Extraction and purification on the vacuum line

The content of each quartz tube is liberated in the vacuum line (Fig. 5.5) with a tube cracker (Fig. 5.6), where CO₂ and H₂O are trapped cryogenically. The purified incondensable N₂ gas is concentrated into a calibrated volume for quantification using a Toepler pump (Hg manometer)

and assuming ideal gas law (i.e. $PV=nRT$, where P is the pressure, V the volume, T the temperature, n the amount of N and R the ideal gas constant).

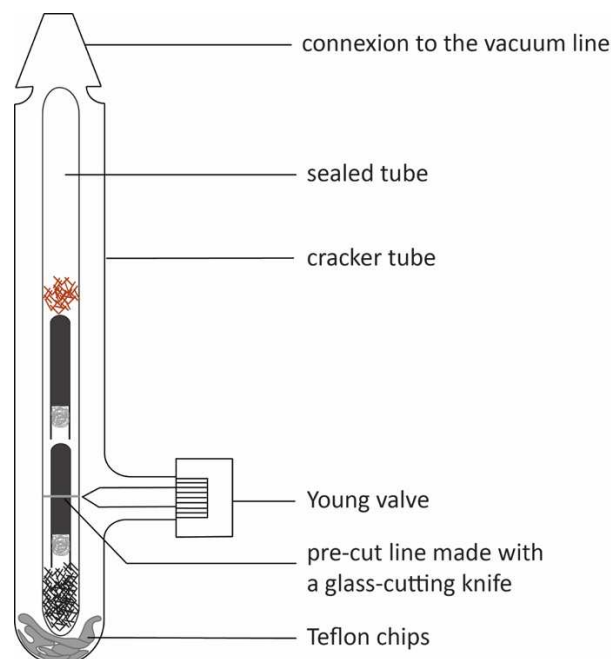


Fig. 5.6. Diagram of the tube cracker containing a sealed tube.

5.6.3.4. Isotopic analysis by dual-inlet IRMS

Purified N_2 is analyzed by dual-inlet mass spectrometry using a ThermoFinnigan DeltaPlus XP IRMS. Possible air contamination and isobaric interferences due to CO are monitored by scanning of m/z 12 (C from CO_2 , CO, CH_4 or organic compounds), 18 (H_2O), 30 ($C^{18}O$), 32 (O_2), 40 (atmospheric Ar) and 44 (CO_2).

5.6.3.5. Precision on $\delta^{15}N$ measurements

External $\delta^{15}N$ reproducibility ranged between 0.1 and 1.0‰ with a mean of $0.4 \pm 0.3\text{‰}$ ($n = 14$) for the BRC Formation samples, between 0.1 and 3.5‰ with a mean of $1.5 \pm 1.5\text{‰}$ ($n = 6$) for the Serra Sul Formation samples. Replicates are reported in data tables for each study site. This external reproducibility includes resampling and chemical treatment; it thus may in part reflect sample heterogeneity.

Kerogen extracts yield TN contents and $\delta^{15}N$ values comparable to their bulk counterparts (Table 5.4).

5.6.3.6. Correction of $\delta^{15}\text{N}$ values of the blank contribution

Analytical blanks for the entire procedure are <0.02 micromoles N, which represents a mean of 6% of the gas (33% of the gas for the smallest sample and less than 0.3% for the more concentrated samples). TN and $\delta^{15}\text{N}$ values have been individually corrected from the blank contribution (Table 5.5), using the reference blank value of $\delta^{15}\text{N} = -3.7\text{‰}$ measured by Busigny et al. (2005). On average, blank-corrected $\delta^{15}\text{N}$ values are 0.8‰ higher than their raw counterparts, but can be up to 4.1‰ in the smallest sample.

References

- Ader, M., Sansjofre, P., Halverson, G.P., Busigny, V., Trindade, R.I.F., Kunzmann, M., Nogueira, A.C.R., 2014. Ocean redox structure across the Late Neoproterozoic Oxygenation Event: A nitrogen isotope perspective. *Earth and Planetary Science Letters* 396, 1–13. <https://doi.org/10.1016/j.epsl.2014.03.042>
- Ader, M., Thomazo, C., Sansjofre, P., Busigny, V., Papineau, D., Laffont, R., Cartigny, P., Halverson, G.P., 2016. Interpretation of the nitrogen isotopic composition of Precambrian sedimentary rocks: Assumptions and perspectives. *Chemical Geology* 429, 93–110. <https://doi.org/10.1016/j.chemgeo.2016.02.010>
- Bernard, S., Beyssac, O., Benzerara, K., 2008. Raman Mapping Using Advanced Line-Scanning Systems: Geological Applications. *Appl Spectrosc* 62, 1180–1188. <https://doi.org/10.1366/000370208786401581>
- Beyssac, O., Goffé, B., Petit, J.-P., Froigneux, E., Moreau, M., Rouzaud, J.-N., 2003. On the characterization of disordered and heterogeneous carbonaceous materials by Raman spectroscopy. *Spectrochimica Acta Part A: Molecular and Biomolecular Spectroscopy*, Georaman 2002, Fifth International Conference on Raman Spectroscopy Applied to the Earth Sciences 59, 2267–2276. [https://doi.org/10.1016/S1386-1425\(03\)00070-2](https://doi.org/10.1016/S1386-1425(03)00070-2)
- Boocock, T.J., Mikhail, S., Prytulak, J., Di Rocco, T., Stüeken, E.E., 2020. Nitrogen Mass Fraction and Stable Isotope Ratios for Fourteen Geological Reference Materials: Evaluating the Applicability of Elemental Analyser Versus Sealed Tube Combustion Methods. *Geostandards and Geoanalytical Research* 44, 537–551. <https://doi.org/10.1111/ggr.12345>
- Boulard, E., Guyot, F., Fiquet, G., 2012. The influence on Fe content on Raman spectra and unit cell parameters of magnesite–siderite solid solutions. *Phys Chem Minerals* 39, 239–246. <https://doi.org/10.1007/s00269-011-0479-3>
- Busigny, V., Ader, M., Cartigny, P., 2005. Quantification and isotopic analysis of nitrogen in rocks at the ppm level using sealed tube combustion technique: A prelude to the study of altered oceanic crust. *Chemical Geology* 223, 249–258. <https://doi.org/10.1016/j.chemgeo.2005.08.002>
- Carignan, J., Hild, P., Mevelle, G., Morel, J., Yeghicheyan, D., 2001. Routine Analyses of Trace Elements in Geological Samples using Flow Injection and Low Pressure On-Line Liquid Chromatography Coupled to ICP-MS: A Study of Geochemical Reference Materials BR, DR-N, UB-N, AN-G and GH. *Geostandards Newsletter* 25, 187–198. <https://doi.org/10.1111/j.1751-908X.2001.tb00595.x>
- Doebelin, N., Kleeberg, R., 2015. Profex: a graphical user interface for the Rietveld refinement program BGMN. *J Appl Cryst* 48, 1573–1580. <https://doi.org/10.1107/S1600576715014685>
- Dumas, A., 1826. *Annales de Chimie*, 33, 342.
- Ferralis, N., Matys, E.D., Knoll, A.H., Hallmann, C., Summons, R.E., 2016. Rapid, direct and non-destructive assessment of fossil organic matter via microRaman spectroscopy. *Carbon* 108, 440–449. <https://doi.org/10.1016/j.carbon.2016.07.039>

Hofmann, A., Karykowski, B., Mason, P., Chunnet, G., Arndt, N., 2013. Barberton drilling project - Buck Reef Chert core BARB3 15, EGU2013-12227.

Kendall, C., Grim, E., 1990. Combustion tube method for measurement of nitrogen isotope ratios using calcium oxide for total removal of carbon dioxide and water. *Analytical Chemistry*.

Lanari, P., Vho, A., Bovay, T., Airaghi, L., Centrella, S., 2019. Quantitative compositional mapping of mineral phases by electron probe micro-analyser. *Geological Society, London, Special Publications* 478, 39–63. <https://doi.org/10.1144/SP478.4>

Lanari, P., Vidal, O., De Andrade, V., Dubacq, B., Lewin, E., Grosch, E.G., Schwartz, S., 2014. XMapTools: A MATLAB©-based program for electron microprobe X-ray image processing and geothermobarometry. *Computers & Geosciences* 62, 227–240. <https://doi.org/10.1016/j.cageo.2013.08.010>

Rividi, N., van Zuilen, M., Philippot, P., Ménez, B., Godard, G., Poidatz, E., 2010. Calibration of Carbonate Composition Using Micro-Raman Analysis: Application to Planetary Surface Exploration. *Astrobiology* 10, 293–309. <https://doi.org/10.1089/ast.2009.0388>

Stüeken, E.E., Kipp, M.A., Koehler, M.C., Buick, R., 2016. The evolution of Earth's biogeochemical nitrogen cycle. *Earth-Science Reviews* 160, 220–239. <https://doi.org/10.1016/j.earscirev.2016.07.007>

Sample	Carbonate content (%) estimated through mass balance after HCl digestion	Carbonate content (%) estimated through (TC-TOC) on EA analysis	Carbonate content (%) estimated through peak area of XRD spectra
BRC_CT19U	93		92
BRC_CT19L	54	57	46
BRC_CT18U	83	87	84
BRC_CT18L	65	67	61
BRC_CT17	86	89	83
BRC_CT16	70	73	63
BRC_CT15	35	36	28
BRC_CT114U	60	63	54
BRC_CT14M	81	86	76
BRC_CT14L	73	76	67
BRC_CT13	36	37	27
BRC_CT5U_U	39	39	29
BRC_CT5U_M	75	80	68
BRC_CT5U_L	47	48	36
BRC_CT5L_U	76	81	72
BRC_CT5L_M	49	51	40
BRC_CT5L_L	96	99	94
BRC_CT6U	71	75	62
BRC_CT6L	89	94	86
BRC_CT7	75	77	69
BRC_CT12U	98	99	94
BRC_CT12L	89	90	86
BRC_CT11U	70	72	64
BRC_CT11M	92	95	89
BRC_CT11L	71	73	64
BRC_CT10	98	96	95
BRC_CT9	54	55	45
BRC_CT8U_U	61	61	52
BRC_CT8U_L	49	49	42
BRC_CT8L_U	98	99	95
BRC_CT8L_M	75	77	68
BRC_CT8L_L	56	57	44
BRC_CT4U	19	14	12
BRC_CT4L_U	9	5	4
BRC_CT4L_L	2	1	1
BRC_CT3U	4	0	0
BRC_CT3L	3	0	0
BRC_CT2U	2	1	1
BRC_CT2L	16	15	10
BRC_CT1U	6	2	2
BRC_CT1L	3	2	1
MA10b-2	99		99
MA10b-1	98		99
MA7bas	99		99
MA6	99		99
MA3	99		100
MA1	99		99
MA43	10		8
MA37	77		77
MA35	38		32
MA32	11		9
MA30	99		99
MA28	98		99
MA24	99		99

MA23	97		98
11d	89		87
11c	84		
11b	96		95
MA18	67		69
11a2	98		98
11a1	73		70
10b	41		38
10a2	93		93
10a1	92		92
9c	87		96
9b	88		83
9a	92		91
8d	94		94
8c	97		98
8b	98		99
8a	98		98
7	91		92
6b	88		86
6a	62		62
5c	94		93
5b	85		84
5a	89		91
4c	97		97
4b	90		90
4a	98		99
3h	14		12
3g	93		93
3f	96		96
3e	94		97
3d	96		96
3c	97		
3b	98		98
3a	89		89
2b3	60		56
MA15	24		26
2b2	91		90
2b1	89		89
2a3	97		97
2a2	95		95
2a1	72		74
1c	46		54
1b	99		
1a	70		62
MA13	26		25
MA12	4		3
GT16_122.05	24	36	
GT16_159.885	29	48	
GT16_208.61	19	24	
GT16_312.005	22	12	
GT16_348.805	26	1	
GT13_211.45	20	25	
GT13_277.175	19	0	
GT13_301.81	20	12	

Table 5.1. Estimation of the samples' carbonate content (%) using different analytical techniques: gravimetric mass balance after HCl digestion, (TC-TOC) using EA analyses, and peak area of XRD spectra.

Standard	Date	TOC (%)	$\delta^{13}\text{C}_{\text{org}}$ (‰ vs. PDB)	Deviation TOC (%)	Deviation $\delta^{13}\text{C}_{\text{org}}$ (‰)
Ref.				40.82	-26.39
USGS40	25/01/2021	40.53	-26.29	0.29	0.10
USGS40	25/01/2021	40.91	-26.41	0.09	0.02
USGS40	25/01/2021	41.03	-26.38	0.21	0.01
USGS40	25/01/2021	41.09	-26.44	0.27	0.05
USGS40	25/01/2021	41.03	-26.41	0.21	0.02
USGS40	25/01/2021	40.93	-26.43	0.11	0.04
USGS40	25/01/2021	40.82	-26.36	0	0.03
USGS40	22/02/2021	39.50	-26.42	1.32	0.03
USGS40	22/02/2021	39.54	-26.47	1.28	0.08
USGS40	22/02/2021	39.46	-26.28	1.36	0.11
USGS40	22/02/2021	39.50	-26.25	1.32	0.14
USGS40	22/02/2021	39.59	-26.24	1.23	0.15
USGS40	22/02/2021	39.50	-26.39	1.32	0.00
USGS40	22/02/2021	41.00	-26.93	0.18	0.54
USGS40	16/03/2021	39.82	-27.47	1	1.08
USGS40	16/03/2021	39.75	-27.20	1.07	0.81
USGS40	16/03/2021	39.72	-27.13	1.1	0.74
USGS40	16/03/2021	39.47	-26.39	1.35	0.00
USGS40	16/03/2021	39.67	-29.13	1.15	2.74
USGS40	16/03/2021	39.66	-27.32	1.16	0.93
USGS40	15/03/2021		-26.44		0.05
USGS40	15/03/2021		-26.33		0.06
USGS40	15/03/2021		-26.42		0.03
USGS40	15/03/2021		-26.32		0.07
USGS40	15/03/2021		-26.44		0.05
USGS40	15/03/2021		-26.39		0.00
USGS40	19/03/2021	36.28	-26.46	4.54	0.07
USGS40	19/03/2021	36.16	-26.23	4.66	0.16
USGS40	19/03/2021	36.12	-26.47	4.7	0.08
USGS40	19/03/2021	36.12	-26.39	4.7	0.00
USGS40	19/03/2021		-27.23		0.84
USGS40	26/11/2021	40.82	-26.41	0.00	0.02
USGS40	26/11/2021	40.82	-26.37	0.00	0.02
USGS40	26/11/2021	40.82	-26.38	0.00	0.01
USGS40	26/11/2021	40.82	-26.41	0.00	0.02
USGS40	26/11/2021	40.82	-26.39	0.00	0.00
USGS40	10/12/2021	40.82	-26.45	0.00	0.06
USGS40	10/12/2021	40.82	-26.36	0.00	0.03
USGS40	10/12/2021	40.82	-26.35	0.00	0.04
USGS40	10/12/2021	40.82	-26.39	0.00	0.00
USGS40	10/12/2021	40.82	-26.38	0.00	0.01
USGS40	15/12/2021	40.82	-26.44	0.00	0.05
USGS40	15/12/2021	40.82	-26.32	0.00	0.07
USGS40	15/12/2021	40.82	-26.41	0.00	0.02
USGS40	15/12/2021	40.82	-26.38	0.00	0.01
USGS40	15/12/2021	40.82	-26.40	0.00	0.01
USGS40	15/12/2021	40.82	-26.38	0.00	0.01
USGS40	15/12/2021	40.82	-26.39	0.00	0.00
USGS40	15/12/2021	40.82	-26.39	0.00	0.00
USGS40	15/12/2021	40.82	-26.40	0.00	0.01
USGS40	15/12/2021	40.82	-26.40	0.00	0.01
USGS40	10/01/2022	40.82	-26.28	0.00	0.11
USGS40	10/01/2022	40.82	-26.43	0.00	0.04
USGS40	10/01/2022	40.82	-26.45	0.00	0.06
USGS40	10/01/2022	40.82	-26.39	0.00	0.00
USGS40	10/01/2022	40.82	-26.40	0.00	0.01
USGS40	14/01/2022	40.82	-26.40	0.00	0.01
USGS40	14/01/2022	40.82	-26.38	0.00	0.01
USGS40	14/01/2022	40.82	-26.38	0.00	0.01
USGS40	14/01/2022	40.82	-26.39	0.00	0.00
USGS40	14/01/2022	40.82	-26.34	0.00	0.05
USGS40	Mean	40.22	-26.51	0.64	0.16
USGS40	SD	1.28	0.43		

Standard	Date	TOC (%)	$\delta^{13}\text{C}_{\text{org}}$ (‰ vs. PDB)	Deviation TOC (%)	Deviation $\delta^{13}\text{C}_{\text{org}}$ (‰)
Ref.				49.48	-27.77
Caffeine IAEA-600	16/10/2020	48.00	-27.55	1.48	0.22
Caffeine IAEA-600	16/10/2020	49.00	-28.00	0.48	0.23
Caffeine IAEA-600	16/10/2020	48.90	-27.49	0.58	0.28
Caffeine IAEA-600	16/10/2020	48.50	-27.91	0.98	0.14
Caffeine IAEA-600	16/10/2020	48.40	-27.55	1.08	0.22
Caffeine IAEA-600	25/01/2021	48.59	-27.73	0.89	0.04
Caffeine IAEA-600	25/01/2021	48.23	-28.75	1.25	0.98
Caffeine IAEA-600	25/01/2021	48.80	-28.77	0.68	1.00
Caffeine IAEA-600	25/01/2021	49.25	-28.86	0.23	1.09
Caffeine IAEA-600	25/01/2021	51.23	-29.49	1.75	1.72
Caffeine IAEA-600	22/02/2021	46.81	-28.28	2.67	0.51
Caffeine IAEA-600	22/02/2021	46.94	-27.63	2.54	0.14
Caffeine IAEA-600	22/02/2021	47.59	-27.21	1.89	0.56
Caffeine IAEA-600	22/02/2021	47.09	-27.64	2.39	0.13
Caffeine IAEA-600	15/03/2021		-27.45		0.32
Caffeine IAEA-600	15/03/2021		-27.76		0.01
Caffeine IAEA-600	16/03/2021	46.66	-28.32	2.82	0.55
Caffeine IAEA-600	16/03/2021	47.84	-30.61	1.64	2.84
Caffeine IAEA-600	19/03/2021	47.72	-27.55	1.76	0.22
Caffeine IAEA-600	19/03/2021		-27.61		0.16
Caffeine IAEA-600	15/12/2021	49.50	-27.73	0.02	0.04
Caffeine IAEA-600	15/12/2021	49.73	-27.71	0.25	0.06
Caffeine IAEA-600	15/12/2021	52.95	-27.22	3.47	0.55
Caffeine IAEA-600	15/12/2021	67.28	-27.53	17.8	0.24
Caffeine IAEA-600	10/01/2022	49.31	-27.77	0.17	
Caffeine IAEA-600	10/01/2022	59.85	-28.88	10.37	1.11
Caffeine IAEA-600	Mean	49.92	-28.04	2.49	1.58
Caffeine IAEA-600	SD	4.76	0.79		

Standard	Date	TOC (%)	$\delta^{13}\text{C}_{\text{org}}$ (‰ vs. PDB)	Deviation TOC (%)	Deviation $\delta^{13}\text{C}_{\text{org}}$ (‰)
Ref.				39.38	-27.21
Wheat flour	25/01/2021	41.97	-27.50	2.59	0.29
Wheat flour	25/01/2021	39.38	-27.52		0.31
Wheat flour					
Wheat flour	15/03/2021		-28.36		1.15
Wheat flour	15/03/2021		-28.32		1.11
Wheat flour	15/03/2021		-28.20		0.99
Wheat flour	15/03/2021		-26.15		1.06
Wheat flour					
Wheat flour	16/03/2021	39.38	-29.08		1.87
Wheat flour	16/03/2021	39.38	-28.29		1.08
Wheat flour	16/03/2021	39.38	-27.64		0.43
Wheat flour	16/03/2021	39.38	-27.22		0.01
Wheat flour					
Wheat flour	26/11/2021	35.30	-27.43	4.08	0.22
Wheat flour	26/11/2021	28.41	-27.47	10.97	0.26
Wheat flour					
Wheat flour	10/12/2021	43.78	-27.45	4.40	0.24
Wheat flour	10/12/2021	38.22	-27.47	1.16	0.26
Wheat flour					
Wheat flour	14/01/2022		-27.42		0.21
Wheat flour	14/01/2022		-26.68		0.53
Wheat flour					
Wheat flour	Mean	38.46	-27.64	2.32	0.63
Wheat flour	SD	4.22	0.72		

Table 5.2. Standard reproducibility for TOC content and $\delta^{13}\text{C}_{\text{org}}$. For the three standards (USGS 40, caffeine IAEA-600 and wheat flour) used during the course of this study, the date of analysis, TOC content, $\delta^{13}\text{C}_{\text{org}}$ value and deviations from TOC content and $\delta^{13}\text{C}_{\text{org}}$ of the reference material are indicated.

Sample	Weight (mg)	Raw N (μ moles)	Blank-corrected N (μ moles)	Raw TN (ppm)	Blank-corrected TN (ppm)	Raw $\delta^{15}\text{N}$ (‰ vs. air)	IRMS I28 intensity (mV)	CaO addition
			0.018					
75A_(1)	56.5	5.5	5.5	2745	2736	5.1	611	
75A_(2)	39.8	3.8	3.8	2703	2690	4.7	705	
75A_(3)	9.8	1.0	1.0	2861	2809	3.2	172	
75A_(4)	6.4	0.6	0.6	2582	2503	3.9	101	
75A_(5)	20.5	1.9	1.9	2573	2549	3.7	346	
75A_(6)	48.4	4.5	4.5	2598	2587	4.0	909	CaO
75A_(7)	10.3	1.0	0.9	2589	2540	3.3	163	CaO
75A_(8)	21.2	1.8	1.8	2345	2322	3.6	333	CaO
75A_(9)	4.4	0.4	0.4	2680	2565	4.7	76	CaO
75A_(10)	45.7	4.1	4.1	2540	2529	3.9	662	CaO

Mean 75A	2621	2583	4.0
SD	138	136	0.6

Mean 75A without CaO	2693	2657	4.1
SD	120	128	0.8

Mean 75A with CaO	2550	2508	3.9
SD	125	107	0.5

Sample	Weight (mg)	Raw N (μ moles)	Blank-corrected N (μ moles)	Raw TN (ppm)	Blank-corrected TN (ppm)	Raw $\delta^{15}\text{N}$ (‰ vs. air)	IRMS I28 intensity (mV)	CaO addition
			0.018					
73A_(1)	33.5	2.0	2.0	1695	1679	3.0	384	
73A_(2)	31.7	2.0	1.9	1720	1705	2.4	370	CaO
73A_(3)	42.8	2.8	2.8	1854	1842	3.0	475	CaO

Mean 73A	1756	1742	2.8
SD	86	88	0.3

Mean 73A with CaO	1787	1773	2.7
SD	94	97	0.4

Table 5.3. Effect of CaO addition on TN and $\delta^{15}\text{N}$ values for two selected BRC samples (75A and 73A).

Sample	Fraction analyzed	TOC (wt. %)	TN (wt. ppm)	TOC/TN	$\delta^{13}\text{C}_{\text{org}}$ (‰ vs. PDB)	$\delta^{15}\text{N}$ (‰ vs. air)
CT18U	bulk	0.69	114	60	-28.13	-0.27
CT18U	kerogen	0.68	94	73	-28.09	-0.26
CT16	bulk	0.55	90	61	-29.78	1.1
CT16	kerogen	0.39	56	70	-30.05	0.83

Table 5.4. Comparison between TN and $\delta^{15}\text{N}$ of samples CT18U and CT16 (BRC) for kerogen extracts vs. bulk rock.

Blank = 0.018 μ moles ; $\delta^{15}\text{N} = -3.7\text{‰}$ (Busigny et al., 2005)					
Sample ID	μ moles N	Raw $\delta^{15}\text{N}$ (‰ vs. air)	Blank contribution (%)	Blank-corrected $\delta^{15}\text{N}$ (‰ vs. air)	$\Delta^{15}\text{N}$ blank (‰)
GT13 211.45	0.22	27.9	8	30.6	2.77
GT13 211.45	0.38	29.5	5	31.1	1.67
GT13 229.27	0.33	32.1	5	34.2	2.07
GT13 237.735	0.22	28.3	8	31.1	2.81
GT13 237.735	0.38	31.6	5	33.4	1.78
GT13 247.82	0.29	27.2	6	29.2	2.08
GT13 258.165	0.27	32.8	7	35.5	2.66
GT13 266.32	0.31	35.1	6	37.5	2.41
GT13 277.175	0.27	32.8	7	35.3	2.56
GT13 287.305	0.26	26.4	7	28.7	2.23
GT13 301.81	0.38	35.0	5	37	1.94
GT13 306.175	0.35	31.2	5	33.1	1.91
GT13 306.175	0.63	32	3	33.3	1.06
GT13 319.46	0.38	26.2	5	27.7	1.50
GT16 122.05	0.28	25.5	6	27.4	1.98
GT16 152.775	0.15	17.1	12	19.9	2.87
GT16 152.775	0.16	17.8	11	20.5	2.72
GT16 159.885	0.27	21.7	7	23.6	1.85
GT16 166.05	0.23	31.7	8	34.6	2.95
GT16 195.97	0.11	16.5	16	20.4	3.90
GT16 208.61	0.18	13.1	10	14.9	1.81
GT16 224.11	0.22	27.9	8	30.8	2.88
GT16 234.725	0.24	24.1	7	26.3	2.24
GT16 234.725	0.39	29.6	5	31.2	1.59
GT16 244.845	0.10	10.9	17	13.9	3.03
GT16 290.835	0.26	23.7	7	25.8	2.05
GT16 312.005	0.31	22.9	6	24.6	1.65
GT16 324.595	0.23	27.1	8	29.6	2.56
GT16 324.595	0.38	23.9	5	25.3	1.39
GT16 348.805	0.17	24.3	10	27.6	3.28
11A2	0.23	3.6	8	4.2	0.61
10A2	0.40	-0.2	4	-0.1	0.16
10A1	0.45	-0.5	4	-0.4	0.13
9C	0.17	-2.4	11	-2.2	0.16
9B	0.16	2.1	12	2.9	0.76
9A	0.22	0.1	8	0.4	0.33
9A	0.38	-1.8	5	-1.7	0.10
8B	0.11	2.3	16	3.4	1.16
8A	0.13	0.2	14	0.9	0.64
7	0.39	1.2	5	1.4	0.23
6B	0.33	-0.6	6	-0.4	0.18
4C	0.50	-3.7	4	-3.7	0.00
4A	0.26	2.8	7	3.2	0.48
3C	0.17	2.8	10	3.5	0.76
3B	0.38	0.4	5	0.6	0.21
2A3	0.44	-1.6	4	-1.5	0.09
2A2	0.28	-2.1	6	-2	0.11
2A1	0.15	2.4	12	3.2	0.84
1B	0.17	0.4	10	0.9	0.48
36A	1.38	-0.3	1		
36A	1.14	-0.9	2	-0.9	0.04
36A	0.87	-0.2	2	-0.1	0.07
36B	0.32	1.7	6	2	0.33
36B	0.37	1.1	5	1.4	0.25
36B	0.21	2.2	8	2.7	0.54
27A	1.77	-0.3	1	-0.2	0.04
CT19U	1.28	0.2	1	0.3	0.06
CT19L	0.43	0.2	4	0.3	0.17
CT18U	1.57	-0.3	1	-0.3	0.04

CT18U	2.24	-0.2	1	-0.2	0.03
CT18U ker	3.88	-0.2	0	-0.2	0.02
CT18L	0.79	-0.1	2	0	0.08
CT17	0.88	0.4	2	0.4	0.08
CT17	2.90	0.7	1	0.7	0.03
CT17	2.32	0.8	1	0.8	0.03
CT16	0.61	1.0	3	1.1	0.14
CT16	2.25	1.3	1	1.4	0.04
CT16	1.89	1.0	1	1	0.05
CT16 ker	3.17	0.9	1	0.9	0.03
CT15	1.63	0.6	1	0.6	0.05
CT15	0.58	1.0	3	1.2	0.15
CT14U	0.27	3.3	7	3.8	0.49
CT14M	0.53	1.3	3	1.5	0.18
CT14M	0.63	1.7	3	1.8	0.16
CT14L	0.56	2.9	3	3.2	0.22
CT13	0.43	1.2	4	1.4	0.21
CT13	0.47	0.3	4	0.4	0.16
75A	5.54	5.1	0	5.1	0.03
75A	3.84	4.7	0	4.7	0.04
75A	1.01	3.2	2	3.3	0.13
75A	0.59	3.9	3	4.2	0.24
75A	1.88	3.7	1	3.7	0.07
75A	4.49	4.0	0	4	0.03
75A	0.95	3.3	2	3.5	0.14
75A	1.78	3.6	1	3.7	0.07
75A	0.42	4.7	4	5.1	0.38
75A	4.14	3.9	0	3.9	0.03
CT5U_U	0.33	6.1	5	6.6	0.56
CT5U_M	0.94	4.5	2	4.7	0.16
CT5U_L	0.27	5.0	7	5.6	0.63
CT5L_U	0.79	4.9	2	5.1	0.20
CT5L_M	0.44	3.4	4	3.7	0.30
CT5L_L	3.20	4.4	1	4.5	0.05
73A	2.03	3.0	1	3	0.06
73A	1.95	2.4	1	2.5	0.06
73A	2.84	3.0	1	3	0.04
CT6U	0.53	1.6	3	1.8	0.19
CT6L	1.13		2		
CT6L	2.68	1.8	1	1.9	0.04
CT6L	1.09	2.1	1	2.1	0.05
72B	0.83	2.9	2	3	0.14
21A	0.62		3		
CT7	0.79	1.9	2	2	0.13
20A	0.32	3.8	6	4.2	0.44
CT12U	3.29	4.3	1	4.3	0.04
CT12L	1.03	5.2	2	5.4	0.16
CT11U	0.32	5.3	6	5.8	0.54
CT11M	1.38	5.0	1	5.1	0.11
CT11L	0.27	5.4	7	6.1	0.65
CT10	0.57	3.3	3	3.5	0.23
CT9	0.91	-1.5	2	-1.4	0.04
CT9	0.30	3.4	6	3.9	0.46
CT8U_U	0.17		10		
CT8U_U	0.40	4.1	5	4.5	0.37
CT8U_L	0.25		7		
CT8U_L	0.38	5.1	5	5.5	0.44
CT8U_L	0.39	4.9	5	5.3	0.42
CT8L_U	1.62	4.3	1	4.4	0.09
CT8L_M	0.51	4.3	4	4.6	0.29
CT8L_L	0.40	3.9	5	4.2	0.36
18A	0.42	4.5	4	4.9	0.37
17A	1.64	4.6	1	4.7	0.09
17A	1.76	4.5	1	4.6	0.09
17A	0.81	3.6	2	3.8	0.17
16A	0.90	2.7	2	2.8	0.13

61A	1.68	3.4	1	3.4	0.08
58A	1.94	2.6	1	2.7	0.06
58A	2.58	1.2	1	1.2	0.03
CT4U	0.26		7		
CT4U	0.14		13		
CT4L_U	0.33	2.0	5	2.4	0.33
CT4L_L	0.34	3.6	5	4	0.41
9A	1.20	3.3	1	3.4	0.11
9A	1.15	2.3	2	2.4	0.09
CT3U	0.87	5.8	2	6	0.20
CT3L	1.09	5.6	2	5.7	0.16
49A	0.11		17		
49A	0.15		12		
CT2U	0.59	3.3	3	3.5	0.22
CT2L	0.27		7		
CT2L	0.37	2.0	5	2.2	0.29
CT2L	0.43	0.8	4	1	0.19
CT1U	0.79	1.3	2	1.5	0.12
CT1L	0.14		13		
1A	1.07	3.9	2	4	0.13
DH02 111.765	0.29	6.9	6	7.6	0.70
DH02 111.765	0.55	7.0	3	7.4	0.36
DH02 122.86	0.36	7.4	5	7.9	0.57
DH02 128.19	0.30	7.1	6	7.8	0.68
DH02 128.19	0.43	9.0	4	9.5	0.55
DH02 135.98	0.39	9.0	5	9.6	0.61
DH02 145.84	0.35	9.1	5	9.8	0.69
DH02 145.84	0.46	8.5	4	9	0.50
DH02 155.47	0.34	7.4	5	8	0.63
DH02 163.105	0.40	9.1	5	9.7	0.61
DH02 163.105	0.46	8.7	4	9.2	0.50
DH02 171.835	0.40	9.8	5	10.4	0.64
DH02 185.82	0.38	11.1	5	11.9	0.74
DH02 203.95	0.33	10.4	5	11.1	0.80
FD52 317.54	0.11	17.0	16	21	3.99
FD52 317.54	0.17	20.5	10	23.3	2.82
FD52 508.05	0.09		19		
FD52 508.05	0.10	15.9	17	20	4.09
FD52 623.655	0.06		28		
FD52 646.045	0.05		33		
FD55 479.43	0.06		28		
FD55 516.38	0.11	10.1	16	12.8	2.69
FD55 517.675	0.11	11.6	16	14.6	2.97
MMJ4	0.16	1.2	12	1.9	0.65
MM07_12	0.11		16		
	All data	Mean	6		1.33
		SD	5		0.62
		Min	0.3		0.48
		Max	33		4.09
	Published values	Mean	5		0.48
		SD	4		0.04
		Min	0.3		0.48
		Max	17		0.48

Table 5.5. Blank contribution for each of the studied samples, including blank-corrected $\delta^{15}\text{N}$ values and deviation from the raw $\delta^{15}\text{N}$.

CHAPTER 6. THE 3.4 GA BUCK REEF CHERT FORMATION, A WINDOW INTO THE PALEOARCHEAN N CYCLE IN ANOXIC & FERRUGINOUS CONDITIONS

Introductory summary

The aim of this PhD work is to improve our understanding of the timing and processes of early oceans oxygenation, and to identify changes in the activity of microbial metabolisms operating the N-cycle, using the nitrogen isotopic composition. Indeed, because the Paleoarchean nitrogen isotopic record remains sparse due to the difficulty of analyzing nitrogen-poor samples, uncertainties regarding early nitrogen pathways linger. In particular, despite the abundance of dissolved iron in Archean oceans, the links between the iron and nitrogen cycles remain to be explored. This chapter aims at providing elements of answers concerning such links.

It consists of an article published in *Geobiology* in 2023, entitled “***Iron-mediated ammonium oxidation recorded in the early Archean ferruginous ocean***”. It includes the main text and figures, a separate methods section and supplementary information, all of which are available in open access.

The article reports $\delta^{15}\text{N}$ results obtained on more than 50 samples from the 3.4 Ga Buck Reef Chert (BRC), Kaapvaal Craton, South Africa. With its good preservation and reported occurrence of microbial activity, this thick sedimentary deposit composed of ferruginous cherts and iron carbonates offers a unique opportunity to peer into early pathways of the biogeochemical nitrogen cycle in anoxic and ferruginous conditions.

The Buck Reef Chert sedimentary deposit was chosen as representative of a period where low $\delta^{15}\text{N}$ values close to 0‰, typical of a reducing N cycle with N_2 fixation dominating the isotopic signal, are expected. Instead, we measured positive $\delta^{15}\text{N}$ values of up to +6.1‰ (Fig. 6.0), that are best explained by non-quantitative oxidation of ammonium coupled to Fe(III) reduction in the presence of iron oxides, through the Feammox metabolic pathway. These findings thus draw attention to possible interactions between the iron and nitrogen cycles in the Archean ferruginous oceans, where iron availability and speciation, rather than oxygen, could have controlled the sedimentary nitrogen isotopic signature. Most importantly, it calls for careful reconsideration of positive $\delta^{15}\text{N}$ signatures previously reported in Archean sediments, that have

commonly been interpreted as reflecting the stability of a nitrate pool in the water column, which in turn implies partial oxygenation.

Ultimately, this article paves the way towards a **new understanding of the nitrogen cycle in reducing and ferruginous conditions, which are relevant for most Paleoproterozoic depositional environments.**

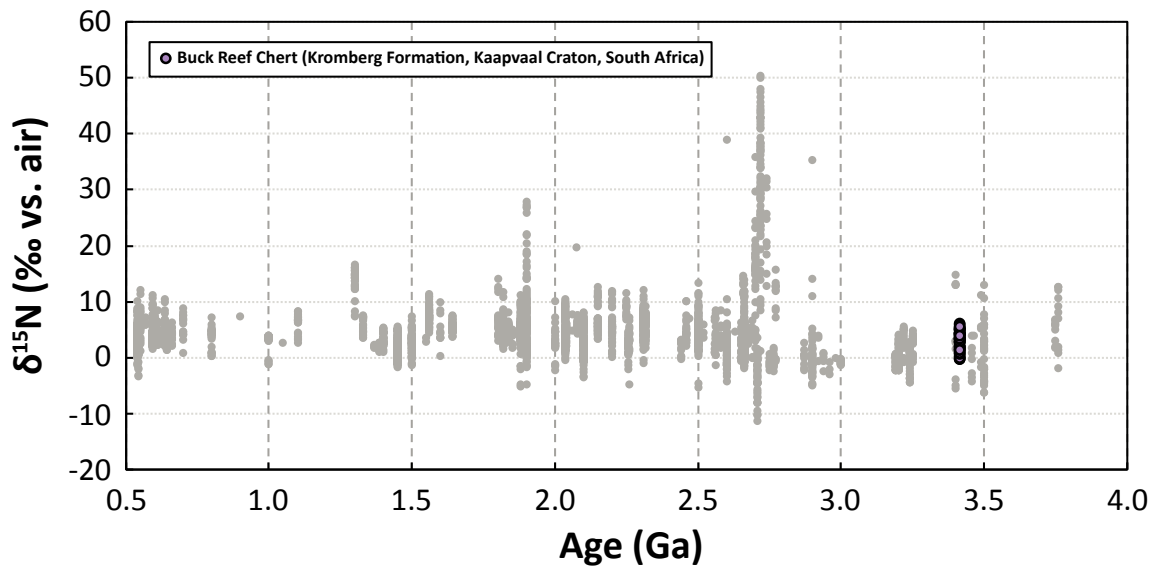


Fig. 6.0. Nitrogen isotope signature of the BRC (purple) among all Precambrian sedimentary $\delta^{15}\text{N}$ data.




**CHAPTER 6. THE 3.4 GA BUCK REEF CHERT, A WINDOW INTO THE
PALEOARCHEAN N CYCLE IN ANOXIC & FERRUGINOUS CONDITIONS**

6.1. Article published in <i>Geobiology</i>	215
6.2. Methods.....	228
6.3. Supplementary Information	230
References.....	234

**CHAPTER 6. THE 3.4 GA BUCK REEF CHERT, A WINDOW INTO THE
PALEOARCHEAN N CYCLE IN ANOXIC & FERRUGINOUS CONDITIONS**

REPORT

Iron-mediated anaerobic ammonium oxidation recorded in the early Archean ferruginous ocean

Alice Pellerin¹  | Christophe Thomazo^{1,2} | Magali Ader³  |
 Johanna Marin-Carbonne⁴  | Julien Alleon^{4,5} | Emmanuelle Vennin¹ | Axel Hofmann⁶

¹Laboratoire Biogéosciences, UMR CNRS 6282, Université de Bourgogne Franche-Comté, Dijon, France

²Institut Universitaire de France (IUF), Paris, France

³Université Paris Cité, Institut de Physique du Globe de Paris, CNRS, Paris, France

⁴Institut des Sciences de la Terre, University of Lausanne, Lausanne, Switzerland

⁵Université de Lyon, ENS de Lyon, Université Lyon 1, CNRS, LGL-TPE, Lyon, France

⁶Department of Geology, University of Johannesburg, Johannesburg, South Africa

Correspondence

Alice Pellerin, Laboratoire Biogéosciences, UMR CNRS 6282, Université de Bourgogne Franche-Comté, Dijon, France.
 Email: alice.pellerin-lefevre@u-bourgogne.fr

Abstract

The nitrogen isotopic composition of organic matter is controlled by metabolic activity and redox speciation and has therefore largely been used to uncover the early evolution of life and ocean oxygenation. Specifically, positive $\delta^{15}\text{N}$ values found in well-preserved sedimentary rocks are often interpreted as reflecting the stability of a nitrate pool sustained by water column partial oxygenation. This study adds much-needed data to the sparse Paleoproterozoic record, providing carbon and nitrogen concentrations and isotopic compositions for more than fifty samples from the 3.4 Ga Buck Reef Chert sedimentary deposit (BRC, Barberton Greenstone Belt). In the overall anoxic and ferruginous conditions of the BRC depositional environment, these samples yield positive $\delta^{15}\text{N}$ values up to +6.1‰. We argue that without a stable pool of nitrates, these values are best explained by non-quantitative oxidation of ammonium via the Feammox pathway, a metabolic co-cycling between iron and nitrogen through the oxidation of ammonium in the presence of iron oxides. Our data contribute to the understanding of how the nitrogen cycle operated under reducing, anoxic, and ferruginous conditions, which are relevant to most of the Archean. Most importantly, they invite to carefully consider the meaning of positive $\delta^{15}\text{N}$ signatures in Archean sediments.

KEYWORDS

ammonium oxidation, biogeochemistry, Buck Reef Chert, Feammox, ferruginous ocean, nitrogen isotopes, Paleoproterozoic

1 | INTRODUCTION

Nitrogen is an essential nutrient for all living organisms, and its availability strongly influences biological productivity. As water column redox speciation controls active metabolic pathways of the biogeochemical nitrogen cycle, the nitrogen isotopic composition of sedimentary rocks can record oceanic redox changes in the early oceans.

On the modern Earth, the atmosphere is the main surface nitrogen reservoir, where N is present mostly as gaseous dinitrogen N_2 (Ward, 2012, $\delta^{15}\text{N} = 0\text{‰}$). However, nitrogen in its N_2 form can only be assimilated by diazotrophs, prokaryotic organisms who possess the nitrogenase enzyme and are thus capable of biological N_2 fixation (Raymond et al., 2004). Bioavailable “fixed” forms of nitrogen are therefore almost exclusively provided to the biosphere by N_2 -fixating

This is an open access article under the terms of the [Creative Commons Attribution-NonCommercial](https://creativecommons.org/licenses/by-nc/4.0/) License, which permits use, distribution and reproduction in any medium, provided the original work is properly cited and is not used for commercial purposes.

© 2023 The Authors. *Geobiology* published by John Wiley & Sons Ltd.

diazotrophs and their mineralization in the water column or in the sediment, referred to as ammonification (Sigman et al., 2009). Fractionations imparted by biological N_2 fixation with classical Mo-based nitrogenase range from -2% to $+2\%$, whereas alternative nitrogenases using Fe or V as cofactors can impart negative fractionations as large as -8% (Zhang et al., 2014). In the modern ocean, transfers between the different oceanic nitrogen reservoirs (N_2 , NH_4^+ , NO_3^- and dissolved and particulate organic nitrogen DON and PON) are mainly controlled by biological processes involving redox reactions. The isotopic composition of these nitrogen sources determines the isotopic composition of primary producers and therefore the sedimentary $\delta^{15}N$. Ammonium release during organic matter remineralization (ammonification) does not impart significant isotope fractionation (Möbius, 2013), and ammonium is rapidly assimilated into the biomass, as it is the preferred inorganic nitrogen source for many organisms. Consequently, even if ammonium assimilation preferentially incorporates ^{14}N , its fractionation is almost never expressed. In oxic conditions prevailing during the Phanerozoic, ammonium can also be successively nitrified to nitrites NO_2^- and nitrates NO_3^- , which are either assimilated by photosynthetic organisms or biologically reduced through denitrification or anaerobic ammonium oxidation (anammox) in dysoxic and anoxic conditions (Dalsgaard & Thamdrup, 2002; Sigman et al., 2009). Denitrification and anammox release N_2O or N_2 , which are subsequently lost to the atmosphere, making them the major oceanic sinks of fixed nitrogen. As denitrification imparts a large nitrogen isotope fractionation of $\approx 30\%$ (Sigman et al., 2009), modern and by extension Phanerozoic sedimentary $\delta^{15}N$ values around $+5\%$ result from the balance between N_2 fixation inputs and denitrification/anammox outputs.

The Archean biogeochemical nitrogen cycle is thought to have been very different from the Phanerozoic, as the redox states of the ocean and the atmosphere have evolved together with rising oxygen levels, impacting environmental conditions and biological evolution. The analysis of 3.5 Ga fluid inclusions containing N_2 (Nishizawa et al., 2007) points toward a stable isotopic composition of atmospheric nitrogen ($\delta^{15}N_{N_2} = 0\%$) at least since the Paleoproterozoic. Without oxygen levels significant enough to allow nitrification, nitrites and nitrates were likely scarce or absent. Therefore, ammonium is often assumed to have been the dominant form of fixed N prior to the rise of oxygen levels (Beaumont & Robert, 1999; Canfield et al., 2010). Potential abiotic sources of ammonium, including hydrothermal reduction, lightning, and volcanic eruptions, have been reviewed in Stüeken et al. (2016) and their magnitude was deemed too small to have sustained the Archean biosphere. The range of Paleoproterozoic sedimentary $\delta^{15}N$ values (reviewed in Ader et al., 2016) centers around 0% , which is compatible with a primitive nitrogen cycle dominated by biological N_2 fixation, ammonification, and ammonium assimilation. The rise of oceanic oxidants preceding the Great Oxidation Event (GOE) might have initiated nitrification/denitrification during the Neoproterozoic, when positive $\delta^{15}N$ values have been observed (Garvin et al., 2009; Godfrey & Falkowski, 2009; Stüeken et al., 2015; Thomazo et al., 2011), paving the way towards an aerobic nitrogen cycle similar to modern environments.

The first nitrogen isotope Precambrian time series was published by Beaumont and Robert (1999). Since then a lot of data have been acquired but only a few for the Paleoproterozoic (reviewed in Ader et al., 2016; Mettam & Zerkle, 2021; Stüeken et al., 2016). This is due to the scarcity of well-preserved Paleoproterozoic geological formations and the difficulty of analyzing nitrogen-poor samples. Therefore, the exceptionally well-preserved and continuous sedimentary record provided by the 900 m BARB3 drill core through the 3.4 Ga Buck Reef Chert offers a unique opportunity to gain some insight into Paleoproterozoic environments in which an early biosphere could have developed. Moreover, it opens a deep-time window to explore early nitrogen cycle mechanisms such as the onset of N_2 fixation and redox reactions.

2 | GEOLOGICAL CONTEXT

The 3416 ± 5 Ma (Krüner et al., 1991) Buck Reef Chert (BRC) is the largest chert deposit of the Kromberg Formation in the Onverwacht Group, located in the Barberton Greenstone Belt, Kaapvaal craton, South Africa (Lowe & Worrell, 1999). The ICDP-sponsored BARB3 drill core (Hofmann et al., 2013) through the BRC sedimentary deposit records a transition between two sedimentary units: a basal chert-dominated unit from 900 to 600 m depth and a BIF-dominated unit from 600 to 400 m depth. Microscopic observations on the studied BARB3 samples matches detailed facies studies performed on outcrop samples by Tice and Lowe (2006a), except for the evaporitic facies that has not been intersected by the drill core.

The chert-dominated unit consists of a succession of black and white banded cherts with sand-sized carbonaceous grains and laminae, granular cherts, chert breccia and ferruginous cherts with intercalated siderite layers (Figure 1; Figure S1).

The BIF-dominated unit is mainly composed of thick layers of iron-rich carbonates alternating with a smaller proportion of chert beds. Siderite occurs as densely packed rhombic and spherulitic crystals, typical of early diagenetic siderite.

A distinctive feature of the BIF-dominated unit is the occurrence of thin layers ≈ 1 cm thick of microcrystalline quartz and carbonate characterized by subspherical domains ($25 \mu m$) containing micron to sub-micron-sized inclusions of red iron oxides. Single quartz crystals $50 \mu m$ in diameter enclose the spheres. These jasper layers are located in the depth intervals of 580–560, 545–500, and 480–400 m (Figure 1, Figure S1). Euhedral iron-rich carbonate crystals in jasper occur in varying amounts (ca. 5%–10%) and are either disseminated or in lenticular clusters, suggesting their early diagenetic nature. The jasper layers are unrelated to any zones where oxic groundwaters could have circulated at depth, which suggests they are primary.

The transition between the chert- and BIF-dominated units is thought to record a temporal and environmental change from a wave-dominated shallow platform to a deeper low-energy basinal depositional environment (Tice & Lowe, 2004) and could also reflect chemical variability linked to an increased supply of dissolved iron through hydrothermal pulses. The origin of the BRC silicified

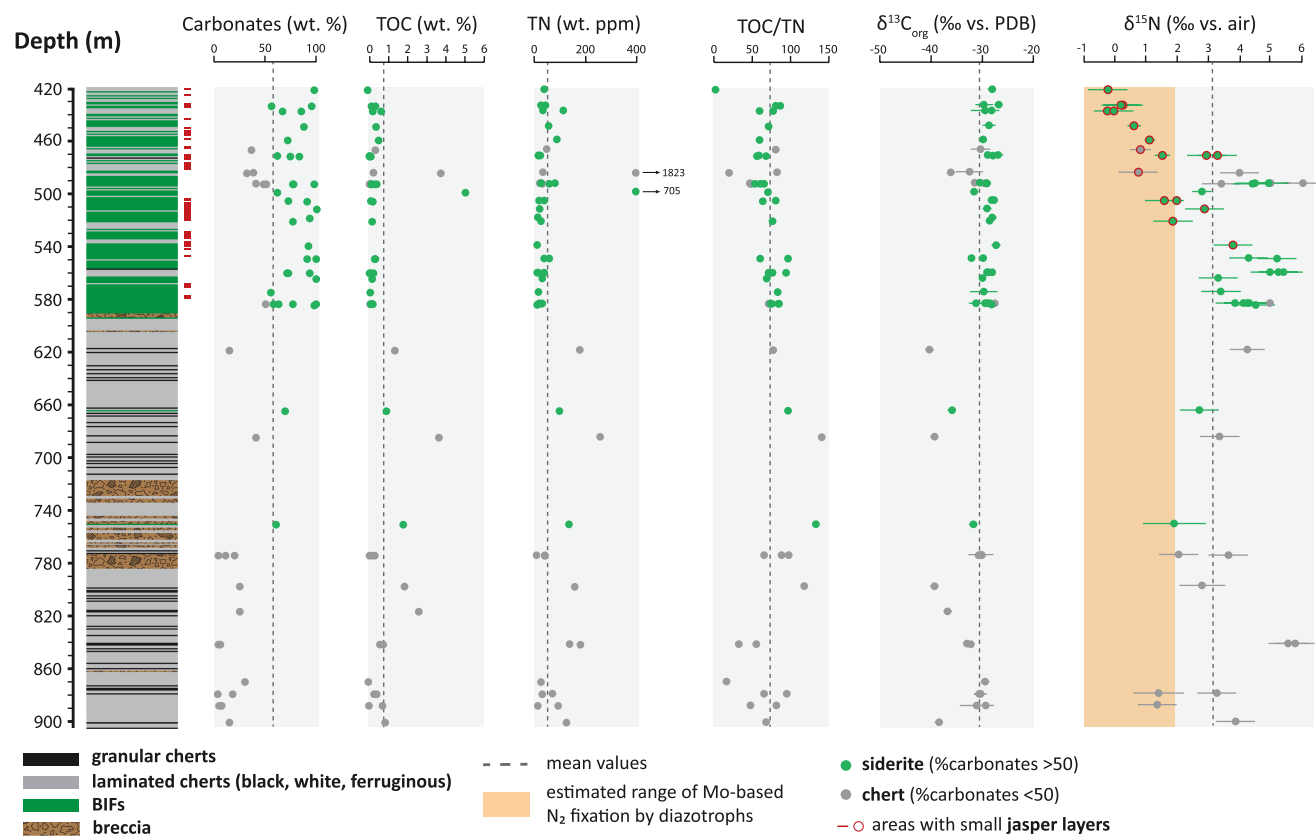


FIGURE 1 Stratigraphic evolution of carbonate content (wt. %), TOC (wt. %), TN (ppm), TOC/TN, $\delta^{13}\text{C}_{\text{org}}$ (‰ vs. PDB), and $\delta^{15}\text{N}$ (‰ vs. air) along the BARB3 drill core.

laminations is variously interpreted in the literature, and four main hypotheses stand out: (i) water column chemical precipitation (Ledevin et al., 2019), (ii) secondary and late silicification of a laminated sedimentary or volcano-sedimentary precursor (de Vries et al., 2006), (iii) segregation from an initial homogenous mix of silica and other components during early diagenesis (Tice & Lowe, 2006a), (iv) pulses of hydrothermal silicification (Geilert et al., 2014). The origin of siderite in the BIF-dominated unit is also debated, as iron-rich carbonates can either precipitate directly in a stratified water column rich in dissolved iron (Klein & Beukes, 1989) or form in the sediment close to the sediment–water interface during diagenesis (Heimann et al., 2010). A hydrothermal origin for siderite has also been suggested for some Archean BIFs (Bolhar et al., 2005).

Regional metamorphism does not exceed the greenschist facies (Tice et al., 2004), with peak temperatures of $310 \pm 50^\circ\text{C}$, according to Raman geothermometry of carbonaceous matter (Alleon et al., 2021).

3 | METHODS

3.1 | Sampling

Fifty-one samples were chosen along the drill core according to their organic matter content (TOC > 0.1% in the digestion residue) that mostly reflects their potential in containing enough nitrogen

to analyze. Those samples are composed of various proportions of bands of chert and siderite. Only samples CT6, CT7, and CT18 contain jasper layers. Accordingly, the amount of carbonates in the samples has been used to define two lithological endmembers: “chert” (when carbonates range from 0 to 50 wt. %) and “siderite” (when carbonates range from 50 to 100 wt. %).

3.2 | Mineralogy

Mineralogy was investigated before and after chemical treatment using X-Ray Diffraction (XRD) at the Biogéosciences Laboratory (Université de Bourgogne Franche-Comté, France). Diffractograms were obtained with a Bruker D8 Endeavor diffractometer with CuK α radiation, LynxEye XE-T detector and Ni filter, under 40kV voltage and 25 mA intensity. The goniometer scanned from 2° to 65° 2θ for each run. Identification of crystalline phases was based on the position and area of their respective mean basal reflections.

3.3 | Chemical treatment

Samples were first crushed into powder using a ring and puck mill at the Biogéosciences Laboratory (Université de Bourgogne Franche-Comté) in order to obtain sample powder smaller than $60\mu\text{m}$. Carbonate-free residues were obtained by mixing sample powders

with 6 N HCl for 24 h, followed by a second step of digestion at 80°C for 4 h. The powder was then rinsed with deionized distilled water to a neutral pH and oven-dried at 40°C for 48 h. Carbonate content, expressed in weight percent (wt. %), was evaluated through gravimetric mass balance after HCl digestion. Some kerogen extracts were commercially produced by Global Geolab Ltd, Alberta, Canada. Powders were digested using HCl and HF, and kerogens were separated out by heavy liquid separation with zinc bromide.

3.4 | C isotopic analyses

The decarbonated residues were poured into tin capsules (20 to 80 mg of powder) and weighted using a Sartorius M2P ultra-balance before TOC and $\delta^{13}\text{C}_{\text{org}}$ measurements were performed using a Thermo Fisher Scientific Flash Smart elemental analyzer, coupled to a Thermo Fisher Scientific Delta V isotope ratio mass spectrometer (EA-IRMS) via a ConFlo IV interface at the Biogéosciences laboratory. Certified USGS40 ($\delta^{13}\text{C}_{\text{org}} = -26.2\text{‰}$, TOC = 40.82 wt. %) and caffeine IAEA-600 ($\delta^{13}\text{C}_{\text{org}} = -27.77\text{‰}$) reference materials were used for the calibration. Total organic carbon (TOC) contents are expressed in dry weight percentage (wt. %) of the non-decarbonated bulk powder and isotope results are reported in delta-notation relative to V-PDB. Each measurement session included three to four standard measurements at the beginning and at the end, as well as one standard measurement every 10 samples. The mean $\delta^{13}\text{C}_{\text{org}}$ precision for standards is 0.8‰ and the mean accuracy 0.5‰. The number of replicates for each sample is shown in Table 1. The mean external reproducibility (2σ), based on sample replicate analyses and including powder resampling and reprocessing via chemical treatment, is ± 0.06 wt. % for the TOC content and $\pm 0.86\text{‰}$ for the $\delta^{13}\text{C}_{\text{org}}$. The $\delta^{13}\text{C}_{\text{org}}$ of 10 kerogen extracts (Table 1) has also been measured following the same procedure mentioned above: their average deviation from corresponding bulk $\delta^{13}\text{C}_{\text{org}}$ measurements is on average $0.63 \pm 0.68\text{‰}$.

3.5 | N isotopic analyses

As most samples contain less than 200 ppm N (Table 1) and the proportion of silicate-bound nitrogen is unknown, the above-described EA-IRMS method is not sensitive enough for reliable bulk nitrogen isotopic analyses (Ader et al., 2016; Boocock et al., 2020). Samples were therefore analyzed using the "classical method" developed at IPGP described in Ader et al. (2014, 2016), in which N_2 is produced offline through sealed-tube Dumas combustion and cryogenically purified in a vacuum line. Up to 200 mg of decarbonated residual powder was put into a quartz tube with CuO and Cu wires, purified beforehand at 900°C for 2 h in a muffle furnace to prevent contamination. Samples were degassed for 12 h at 150°C under vacuum to remove adsorbed atmospheric N_2 and organics. Quartz tubes were then sealed directly under vacuum and combusted in a muffle furnace at 950°C for 6 h under oxidizing conditions by oxygen liberated

from the CuO wires, then cooled at 600°C for 2 h, allowing residual oxygen to combine with cupric oxide and nitrous oxide to be reduced by copper, and finally cooled to ambient temperature (Beaumont & Robert, 1999; Kendall and Grim, 1990). This allows the chemical separation of gaseous products. Busigny et al. (2005) have shown that the extraction yield for this protocol is 100% for both organic and mineral nitrogen, including ammonium in minerals such as phyllosilicates. The content of each quartz tube is liberated in the vacuum line with a tube cracker, where CO_2 and H_2O are trapped cryogenically to avoid any isobaric interferences. The purified incondensable N_2 gas is concentrated into a calibrated volume for quantification using a Toepler pump (Hg manometer). Standard analytical procedures for nitrogen usually include CaO in the reagents to trap gaseous CO_2 and H_2O liberated from samples (Kendall and Grim, 1990), but given that Busigny et al. (2005) have shown that it significantly contributes to analytical blanks, we performed a few tests on samples from the BRC which show that the addition of CaO does not yield significant $\delta^{15}\text{N}$ differences. Most samples were consequently analyzed without the addition of CaO, except for the two kerogen extracts. Analytical blanks for the entire procedure are < 0.05 micromoles N, which represents less than 10% of the gas for smaller samples and less than 1% for more concentrated samples. Purified N_2 is analyzed by dual-inlet mass spectrometry using a ThermoFinnigan DeltaPlus XP IRMS. Possible air contamination and isobaric interferences due to CO are monitored by scanning of m/z 12 (C from CO_2 , CO, CH_4 , or organic compounds), 18 (H_2O), 30 (C^{18}O), 32 (O_2), 40 (atmospheric Ar), and 44 (CO_2). External $\delta^{15}\text{N}$ reproducibility falls between 0.10 and 1.02‰ with a mean of $0.44 \pm 0.29\text{‰}$ ($n = 14$). Samples that were replicated are reported in Table 1. Samples with no external reproducibility are reported with an error of $\pm 0.63\text{‰}$, which is the external reproducibility of sample 75A replicated 10 times at different concentrations (Table S1). Kerogen extracts of two samples (CT16 and CT18U) yield TN contents and $\delta^{15}\text{N}$ values identical within external reproducibility to those measured on their decarbonated counterparts (Table S2).

4 | RESULTS

Iron-rich carbonate throughout the BRC is identified mostly as siderite, with a few samples containing ankerite, based on XRD analyses (Figures S2 and S3; Table S3), which is consistent with previous investigations (Tice et al., 2004; Tice & Lowe, 2006a; Tice & Lowe, 2006b). Carbonate content obtained through HCl digestion is highly variable (2% to 99%) depending on the relative proportions of bands of chert versus siderite. Total organic carbon (TOC) contents vary between 0.01% and 5.01% with a mean value of $0.66 \pm 1.01\%$ ($n = 52$). Total nitrogen (TN) content ranges from 11 to 259 ppm with a mean of 55 ± 53 ppm ($n = 55$), excluding two N-rich outliers (samples 75A and 73A showing TN contents of 1823 and 705 ppm, respectively). TOC/TN ratios are below 150, which is relatively low for Archean sedimentary rocks (Yamaguchi, 2002); it ranges from 3 to 141 with a mean TOC/TN of 72 ± 24 ($n = 51$).

TABLE 1 Summary data table featuring the depth (m), carbonate content (wt. %), TOC (wt. %) with its standard deviation (SD) and number of replicates, TN (wt. ppm) with its standard deviation (SD) and number of replicates, $\delta^{13}\text{C}_{\text{org}}$ (‰ vs. PDB) with its standard deviation (SD) and number of replicates, $\delta^{15}\text{N}$ (‰ vs. air) with its standard deviation (SD) and number of replicates, for each sample analyzed along the BARB3 drill core.

Sample	Depth (m)	Carbonate content (wt. %)	TOC (wt. %)	SD	Nb repl.	TN (wt. ppm)	SD	Nb repl.	TOC/TN	$\delta^{13}\text{C}_{\text{org}}$ (‰ vs. PDB)	SD	Nb repl.	$\delta^{15}\text{N}$ (‰ vs. air)	SD	Nb repl.
27A ^a	421.37	96	0.01		1	41		1	3	-27.96	0.84	1	-0.3	0.63	1
CT19U ^a	433.18	93	0.40	0.14	2	45		1	87	-26.68	0.84	1	0.2	0.63	1
CT19L ^a	433.24	54	0.21	0.02	3	26		1	81	-29.58	1.73	3	0.2	0.63	1
CT18U ^a	437.27	83	0.69	0.21	2	114		2	60	-28.13	0.35	2	-0.3	0.10	2
CT18L ^a	437.36	65	0.28	0.02	3	35		1	78	-29.37	2.77	3	-0.1	0.63	1
CT17 ^a	448.64	86	0.42	0.07	3	58		3	73	-28.59	1.23	2	0.6	0.22	3
CT16 ^a	459.03	70	0.55	0.15	2	90		3	61	-29.78	0.39	2	1.1	0.18	3
CT15 ^a	466.33	35	0.41	0.01	3	50		1	81	-30.23	1.93	3	0.8	0.34	2
CT14U ^a	470.82	60	0.11	0.02	3	18		1	60	-28.81	0.39	2	3.3	0.63	1
CT14M ^a	470.94	81	0.10	0.01	3	18		2	57	-26.82	1.11	3	1.5	0.25	2
CT14L ^a	471.05	73	0.17	0.02	3	24		1	69	-27.84	0.40	3	2.9	0.63	1
CT13 ^a	483.39	36	0.30	0.15	3	36		2	83	-32.45	2.69	3	0.7	0.64	2
75A	483.81	30	3.77		1	1823	96	10	21	-36.11	0.84	1	4.0	0.63	10
CT5U_U	491.66	39	0.14	0.04	3	29		1	48	-31.42	0.29	3	6.1	0.63	1
CT5U_M	491.74	75	0.45	0.09	3	82		1	55	-30.43	0.83	3	4.5	0.63	1
CT5U_L	491.82	47	0.11	0.01	3	22		1	49	-29.17	0.21	3	5.0	0.63	1
CT5L_U	491.9	76	0.18	0.02	3	28		1	66	-29.14	0.17	3	4.9	0.63	1
CT5L_M	491.98	49	0.16	0.03	3	32		1	49	-29.54	0.22	3	3.4	0.63	1
CT5L_L	492.04	96	0.37	0.25	2	61		1	61	-28.93	0.71	2	4.4	0.63	1
73A	498.09	60	5.01		1	705	34	3	71	-31.53	0.84	1	2.8	0.31	3
CT6U ^a	504.68	71	0.16	0.01	3	20		1	82	-27.51	0.36	3	1.6	0.63	1
CT6L ^a	504.8	89	0.26	0.08	3	40		2	65	-28.13	0.36	3	2.0	0.19	2
72B ^a	511.05	99				23		1		-28.97	0.84	1	2.9	0.63	1
21A	517.53	92				16		1		-27.91	0.84	1			
CT7 ^a	520.05	75	0.22	0.01	3	28		1	77	-28.44	0.61	3	1.9	0.63	1
20A ^a	538.26	90				13		1		-27.17	0.84	1	3.8	0.63	1
CT12U	548.08	98	0.37	0.28	2	60		1	61	-29.80	0.84	1	4.3	0.63	1
CT12L	548.15	89	0.38	0.03	3	40		1	97	-32.08	0.19	3	5.2	0.63	1
CT11U	558.62	70	0.16	0.01	3	17		1	95	-27.93	0.50	3	5.3	0.63	1

(Continues)

TABLE 1 (Continued)

Sample	Depth (m)	Carbonate content (wt. %)	TOC (wt. %)	SD	Nb repl.	TN (wt. ppm)	SD	Nb repl.	TOC/TN	$\delta^{13}\text{C}_{\text{org}}$ (‰ vs. PDB)	SD	Nb repl.	$\delta^{15}\text{N}$ (‰ vs. air)	SD	Nb repl.
CT11M	558.68	92	0.31	0.04	3	40		1	77	-29.01	0.25	3	5.0	0.63	1
CT11L	558.75	71	0.09	0.02	3	13		1	73	-28.68	0.15	3	5.4	0.63	1
CT10	562.96	98	0.23	0.08	3	32		1	70	-29.82	0.01	2	3.3	0.63	1
CT9	573.11	54	0.14	0.00	3	17		1	84	-29.62	2.69	3	3.4	0.63	1
CT8U_U	581.76	61	0.17	0.05	3	23	4	2	76	-31.16	1.42	3	4.1	0.63	1
CT8U_L	581.88	49	0.14	0.01	3	20	2	3	72	-27.48	0.20	3	5.0	0.12	2
CT8L_U	581.93	98	0.27	0.05	3	32		1	85	-28.43	0.84	1	4.3	0.63	1
CT8L_M	581.96	75	0.18	0.01	3	21		1	85	-28.92	0.28	3	4.3	0.63	1
CT8L_L	582	56	0.23	0.02	3	30		1	75	-29.31	0.14	3	3.9	0.63	1
18A	583.03	96				12		1		-28.10	0.84	1	4.5	0.63	1
17A	616.77	13	1.41		1	180	7	3	78	-40.35	0.84	1	4.3	0.57	3
16A	662.32	68	0.96		1	99		1	98	-35.91	0.84	1	2.7	0.63	1
61A	682	39	3.65		1	259		1	141	-39.40	0.84	1	3.4	0.63	1
58A	747.59	59	1.83		1	137		2	134	-31.72	0.84	1	1.9	1.02	2
CT4U	770.65	19	0.11	0.04	2	11		1	99	-30.18	2.47	2			
CT4L_U	770.8	9	0.37	0.05	2	41		1	89	-30.01	0.33	2	2.0	0.63	1
CT4L_L	770.95	2	0.28	0.00	3	42		1	66	-30.68	0.03	2	3.6	0.63	1
9A	794.12	23	1.89		1	159	2	2	118	-39.39	0.84	1	2.8	0.75	2
52A	813.05	23	2.61		1					-36.77	0.84	1			
CT3U	837.32	4	0.78	0.03	2	140		1	56	-33.01	0.32	2	5.8	0.63	1
CT3L	837.51	3	0.62	0.06	2	181		1	34	-32.15	0.45	2	5.6	0.63	1
49A	865.76	29	0.05		1	27	18	2	17	-29.37	0.84	1			
CT2U	874.65	2	0.47	0.06	2	71		1	66	-30.52	0.99	2	3.3	0.63	1
CT2L	874.87	16	0.32	0.01	2	33	4	3	96	-30.24	1.28	2	1.4	0.82	2
CT1U	883.47	6	0.78	0.05	2	94		1	83	-30.99	3.43	2	1.3	0.63	1
CT1L	883.65	3	0.08	0.01	2	16		1	49	-29.25	0.04	2			
1A	896	13	0.88		1	128		1	69	-38.49	0.84	1	3.9	0.63	1

^aSamples containing jasper layers.

Note: Green shade indicates Cherts (carbonates <50wt. %); Grey shade indicates Siderites (carbonates >50wt. %).

Along the drill core, $\delta^{15}\text{N}$ values ($n = 51$) range between -0.3‰ and $+6.1\text{‰}$ with a mean $\delta^{15}\text{N}$ of $3.1 \pm 1.8\text{‰}$. $\delta^{15}\text{N}$ variations are not correlated with either organic carbon ($R^2 = .0308$) or nitrogen concentrations ($R^2 = .0043$) (Figure 3). The average $\delta^{15}\text{N}$ value in the chert-dominated unit does not significantly differ from the average $\delta^{15}\text{N}$ value in the BIF-dominated unit, nor do $\delta^{15}\text{N}$ values in chert samples significantly differ from $\delta^{15}\text{N}$ values in siderite samples (Figure 2, $p > .05$). However, $\delta^{15}\text{N}$ values ($n = 17$) from the BIF-dominated unit with jasper layers are significantly different (Figure 2, $p < .05$) from $\delta^{15}\text{N}$ values ($n = 34$) in core intervals lacking jasper, with a mean $\delta^{15}\text{N}$ of 1.3‰ and 4.0‰ respectively. $\delta^{15}\text{N}$ values display stratigraphic variations along the BARB3 drill core, with markedly positive values in most of the core, and values decreasing toward 0‰ in the upper part, between depths of 400 and 500 m.

$\delta^{13}\text{C}_{\text{org}}$ in the BIF-dominated unit and in the chert-dominated unit show close mean values of $-29.3 \pm 1.8\text{‰}$ ($n = 39$) and $-33.4 \pm 4.0\text{‰}$ ($n = 17$) respectively, but the latter displays a much larger range of variations (from -40.4‰ to -29.3‰), whereas values in the BIF-dominated unit are much more homogenous (from -32.5‰ to -26.7‰ leaving out one outlier). The same $\delta^{13}\text{C}_{\text{org}}$ variations hold true for chert and siderite samples (Figure 2).

5 | DISCUSSION

The potential impact of post-depositional processes on the $\delta^{15}\text{N}$ is discussed in Supplementary Information. All indicators point to a good preservation of the BRC samples primary nitrogen isotopic signature. Besides, even if metamorphic processes in the greenschist

facies may have slightly shifted the $\delta^{15}\text{N}$ ($<2\text{‰}$), they cannot account for the large range of values observed in the BRC and their rapid stratigraphic variations.

5.1 | A biotic organic source of N

Nitrogen-bearing organic molecules produced in organic hazes such as in Titan's atmosphere (tholins) are mentioned as an abiotic alternative to organic matter production during the Archean (Izon et al., 2015; Trainer et al., 2006). However, organic molecules generated through experimental aerosols production set-ups in plasma or photochemical flow reactors are depleted in ^{15}N (from 0.8‰ to -25.5‰) compared with the initial N_2 gas from which they precipitated (Kuga et al., 2014; Sebree et al., 2016). If the $\delta^{15}\text{N}_{\text{N}_2}$ value of the Archean atmosphere was similar to that of the present-day atmosphere ($\delta^{15}\text{N}_{\text{N}_2} = 0\text{‰}$, Nishizawa et al., 2007), then the range of $\delta^{15}\text{N}$ values observed in the BRC is not consistent with a significant contribution of ^{15}N -depleted abiotic organic matter. The relatively stable TN along the drill core would also mean a sustained abiotic production of these organic molecules, which seems unlikely given the suggested rapid oscillations between hazy and haze-free states evidenced for the Neoproterozoic atmosphere (Izon et al., 2015; Zerkle et al., 2012). Indeed, oscillations that have only been observed over stratigraphic intervals of a few dozens of meters are hard to reconcile with the 350-m-thick BRC, even if the sedimentation rate remains poorly constrained.

While hydrothermal activity may have been widespread on Archean oceans seafloor and fluid circulations have likely

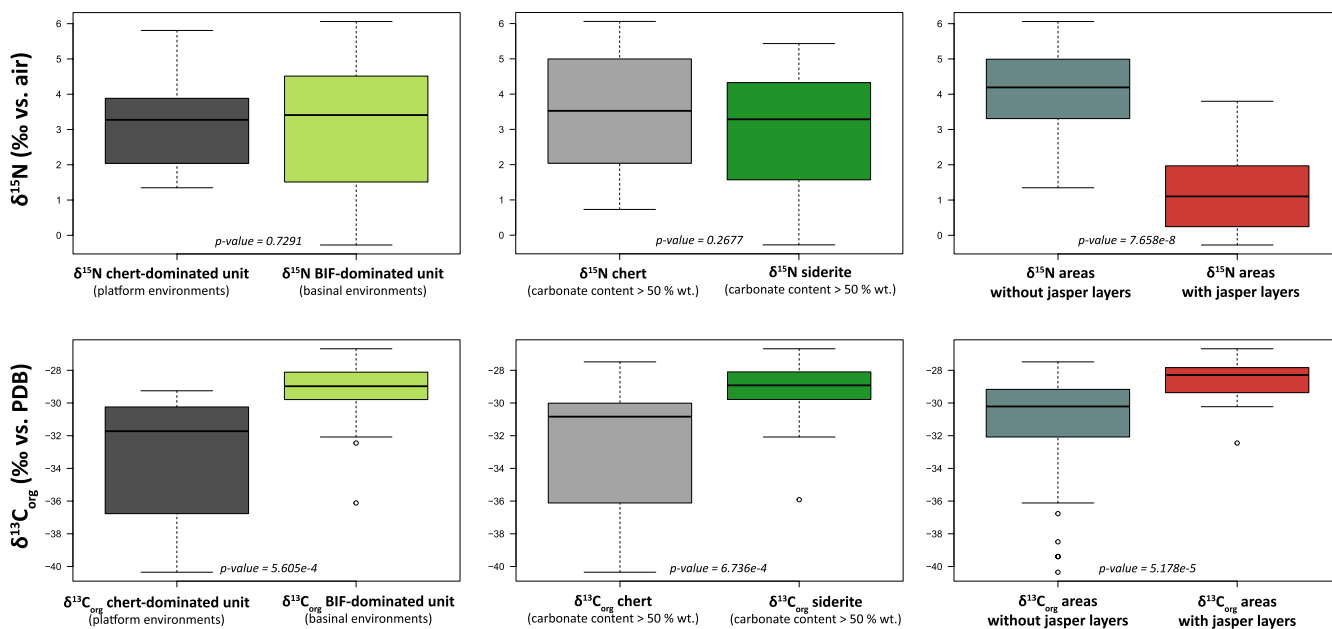


FIGURE 2 Boxplots showing the $\delta^{15}\text{N}$ and $\delta^{13}\text{C}_{\text{org}}$ range of values and means between (1) the chert-dominated unit and the BIF-dominated unit, (2) chert samples and siderite samples and (3) areas of the drill core with or without jasper layers.

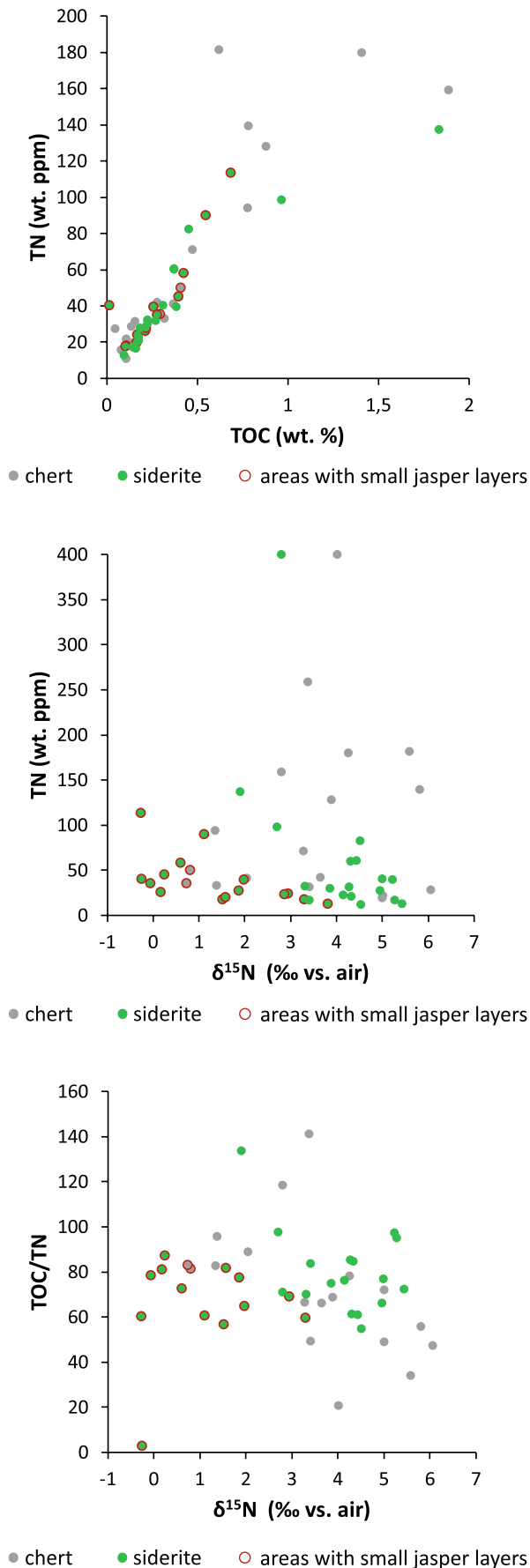


FIGURE 3 Crossplots: TOC (wt. %) vs. TN (wt. ppm); $\delta^{15}\text{N}$ (‰ vs. air) vs. TN (wt. ppm); $\delta^{15}\text{N}$ (‰ vs. air) vs. TOC/TN.

influenced the availability of nutrients like dissolved iron (Poulton & Canfield, 2011), it seems unlikely that hydrothermal circulations either made a strong contribution of abiotic organic nitrogen to the BRC or that it significantly shifted its bulk $\delta^{15}\text{N}$ signal. Indeed, the contribution of mantellic N to hydrothermal systems seems low compared to hydrothermal remobilization of previously sedimented nitrogen (Stüeken et al., 2021). Neither typical mantellic $\delta^{15}\text{N}$ values around -5% (Cartigny & Marty, 2013) nor $\delta^{15}\text{N}$ values measured for altered oceanic crust (ranging from -12% to $+8\%$, Li et al., 2007) have been found in the BRC samples. Instead, the BRC lowest $\delta^{15}\text{N}$ values are consistent with the range of fractionation displayed by Mo-based biological fixation of N_2 by diazotrophs (Nishizawa et al., 2014; Sigman et al., 2009; Zhang et al., 2014).

Abiotic graphite formation has been identified in highly metamorphosed, siderite-bearing sedimentary rocks of the Eoarchean Isua Supracrustal Belt (van Zuilen et al., 2003). In the BRC, organic matter is not preferentially associated with siderite layers, which suggests that it was not formed by thermal decomposition of siderite.

Therefore, the most probable hypothesis is that nitrogen found in the BRC samples has a biotic source, namely biological N_2 fixation by diazotrophs in the photic zone, followed by organic matter mineralization in the water column or the sediment.

5.2 | Anoxic and reducing paleoenvironmental conditions

The lithologies of the BRC (mainly chert and siderite), the lack of Ce anomalies (Tice & Lowe, 2006b), and the presence of mass-independent fractionation of sulfur isotopes in sulfides (S-MIF, Galić, 2015) are consistent with overall reducing and anoxic conditions. The thin jasper layers within the BIF-dominated unit indicate that iron oxidation may nonetheless have taken place punctually, possibly due to anoxygenic photosynthesis (Tice & Lowe, 2006b) or UV photolysis (Konhauser et al., 2007).

The Archean ocean was likely saturated in silica, which either could have precipitated in the water column or formed silica gels at the sediment surface (Ledevin et al., 2019). The main iron source in Archean oceans is likely Fe(II) provided by hydrothermalism (Poulton & Canfield, 2011). The siderite enrichment in the BIF-dominated unit could either indicate deepening of the water column such that the depositional setting was overlain by Fe(II)-rich bottom waters in a stratified ocean (Tice & Lowe, 2004), or periods of increased hydrothermal activity releasing large quantities of dissolved Fe, indicating a chemical shift from a silica-rich to a carbonate-rich fluid.

5.3 | Nitrogen cycling in the Paleoproterozoic BRC

In the anoxic and ferruginous environmental context of the BRC, nitrites and nitrates would not have been thermodynamically stable. Therefore, the water column nitrogen pool was most probably fixed ammonium (Beaumont & Robert, 1999; Canfield et al., 2010), either released during the degradation of organic matter or released from lithified sediments through fluid circulations (Stüeken et al., 2021).

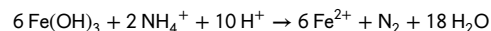
Nevertheless, nitrification in a stratified ocean with an oxic surface layer has been proposed for some Neoproterozoic and Paleoproterozoic settings (Garvin et al., 2009; Godfrey & Falkowski, 2009; Kipp et al., 2018; Koehler et al., 2018). While the production of small amounts of nitrates cannot be fully ruled out, it is unlikely that nitrification could have been sustained in the reducing and anoxic conditions of the depositional environment of the Paleoproterozoic BRC. Indeed, an anoxic atmosphere evidenced by the S-MIF data (Galić, 2015) seems incompatible with an oceanic surface layer hosting a stable nitrate reservoir. In addition, the small range of pyrites $\delta^{34}\text{S}$ values (Galić, 2015) indicate that sulfates were scarce, further supporting the absence of significant concentrations of oxidized anions in the BRC water column. Therefore, without a stable pool of nitrates that could explain the enrichment in ^{15}N of a residual nitrate pool through denitrification and its subsequent assimilation by primary producers, a mechanism that can fractionate NH_4^+ before its assimilation is required to explain the observed positive nitrogen isotopic signatures.

Partial biological assimilation of NH_4^+ can enrich residual organic matter in ^{14}N ($\epsilon \approx -4\%$ to -27% , Hoch et al., 1992), if the pool of ammonium is not quantitatively consumed, which might be possible in upwelling regions. However, the expected distribution of $\delta^{15}\text{N}$ values should be centered around 0% , displaying both the upwelled ^{15}N -depleted and the sinking ^{15}N -enriched pools of ammonium. While this mechanism has been proposed to explain the negative and near zero $\delta^{15}\text{N}$ values found in the Paleoproterozoic (Ader et al., 2016; Beaumont & Robert, 1999), $\delta^{15}\text{N}$ values in the BRC are centered around 3.3% with no negative values. This means that in the BRC depositional environment, an additional mechanism enriching residual ammonium in ^{15}N was operating at a regional scale.

The hypothesis of positive ammonium $\delta^{15}\text{N}$ values resulting from NH_3 degassing at high pH (Stüeken et al., 2015) ($\text{pH} > 9.2$) is compatible with the precipitation of iron-rich carbonates but seems unlikely in the context of the BRC given that positive $\delta^{15}\text{N}$ values are also found in chert layers (Figure 1), which require decreasing pH values (Wright, 2022).

The oxidation of ammonium is therefore the only remaining mechanism capable of producing a $^{15}\text{NH}_4^+$ -enriched pool that could have been recorded in the BRC organic N after assimilation.

Most metabolic pathways oxidizing NH_4^+ need free O_2 , and even classic anaerobic ammonium oxidation (anammox) requires the presence of nitrites, which cannot be produced without O_2 (Grotzinger & Kasting, 1993). However, in anoxic and ferruginous conditions, NH_4^+ can be oxidized to N_2 in the presence of iron oxides through the Feammox reaction (Stüeken et al., 2016):



This reaction has only recently been described in modern environments, namely in iron-rich conditions in wetland soils and marine sediments (Rios-Del Toro et al., 2018; Yang et al., 2012). Such a metabolism is compatible with Eh-pH conditions and iron speciation during the Archean period, as it is thermodynamically favored when Fe^{2+} concentrations are below $100 \mu\text{M}$ and NH_4^+ concentrations are above $1 \mu\text{M}$, for pH between 6 and 8 (Stüeken et al., 2016). These conditions were probably achieved in the Paleoproterozoic seafloor, given the available constraints on its pH values around 6.5 to 7 (Halevy & Bachan, 2017). Ammonium and iron concentrations measured in modern anoxic and ferruginous environments (Petrasch et al., 2022) and estimated for ancient environments (Canfield, 2005; Tosca et al., 2019) are also in accordance with this hypothesis.

Jasper layers observed in the BRC suggest that iron redox cycling (from anoxygenic photosynthesis or UV photolysis) was occurring and could have provided iron oxides to the Feammox reaction. Ammonium released from biomass degradation during diagenesis could have been in direct contact with iron oxides in the sediment, allowing Feammox to operate while residual ^{15}N -enriched ammonium could have exchanged isotopically with organic matter or been assimilated by benthic organisms. Feammox is also capable of producing N_2 at rates that can outcompete denitrification in iron-rich tropical soils (Yang et al., 2012). It therefore provides a return nitrogen flux to the atmosphere before the spread of denitrification, which is consistent with a stable atmospheric N_2 reservoir from 3.5 Ga (Nishizawa et al., 2007).

While the fractionation factor for Feammox remains to be determined, all known ammonium oxidation pathways enrich residual NH_4^+ in ^{15}N . In particular, anammox fractionation can equal that of denitrification (Brunner et al., 2013). The assimilation of the residual ^{15}N -enriched ammonium into the biomass will then lead to positive sedimentary $\delta^{15}\text{N}$ values (Figure 4).

Such positive values in the BRC are observed where jasper layers are absent, indicating limited iron oxide availability and/or reduction in those iron oxides by reactions with organic matter or sulfide during diagenesis. By contrast, the lowest $\delta^{15}\text{N}$ values are observed in the intervals of the BIF-dominated unit that contain jasper layers, that is, in environments where iron oxides were either abundant or well preserved. The return to a diazotrophic environment could either mean that the Feammox reaction did not take place in settings where waters were saturated in Fe^{2+} to concentrations capable of inhibiting this metabolic pathway or that iron oxides were not scavenged by sulfides and abundant enough to allow NH_4^+ to be entirely consumed by the Feammox reaction, leaving no detectable fractionation (Figure 4).

As to organic carbon isotopic signatures, $\delta^{13}\text{C}_{\text{org}}$ values in the BIF-dominated unit are centered around -30% , which is consistent with carbon fixation through the Calvin cycle, a pathway that exists in both chemoautotrophs and photosynthesizers, either anoxygenic or oxygenic. Such values fall in the typical range for photosynthesis,

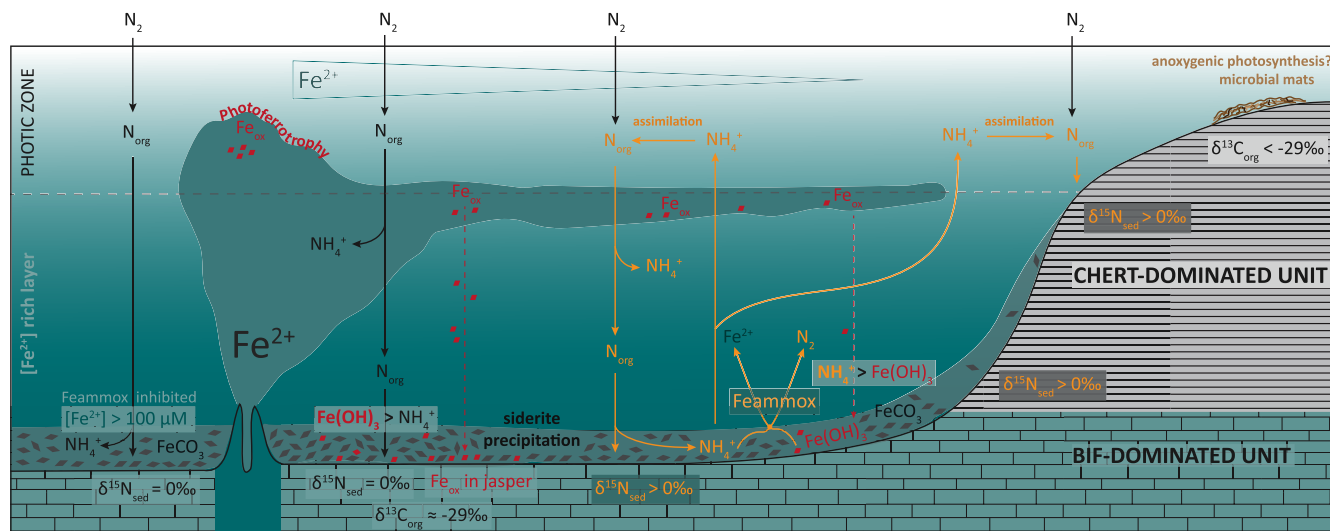


FIGURE 4 Schematic model illustrating how the iron and nitrogen cycles could have interacted in an anoxic and ferruginous Archean ocean, as recorded in the BRC formation. Following the sedimentary model described by Tice and Lowe (2004), the chert-dominated unit is related to platform settings and gives way to the BIF-dominated unit as depth increases toward basin settings. The water column is chemostratified, with a lower Fe^{2+} -rich layer supplied by hydrothermal iron fluxes. Siderite precipitates either at the chemocline or in the sediment and accumulates on the seafloor, forming the BIF-dominated unit. The abundance of siderite follows a gradient away from the hydrothermal discharge zones. In the absence of free O_2 in the water column, iron oxides observed in the BRC jasper layers can be produced through photoferrotrophy when dissolved Fe^{2+} reaches the photic zone. Organic nitrogen is sourced to the water column by diazotrophic N_2 fixation and is either consumed by organisms or ammonified as NH_4^+ . In the chert-dominated unit, iron oxides are scarce and therefore quantitatively consumed by Feammox. The residual ammonium becomes enriched in ^{15}N and can carry this enrichment to organic matter when reassimilated, which would produce positive sedimentary $\delta^{15}\text{N}$ values. In the iron-rich settings of the BIF-dominated unit, $\delta^{15}\text{N}$ values are close to 0‰ , recording only biological N_2 fixation by diazotrophs. This could either result from quantitative consumption of NH_4^+ by Feammox due to an excess of iron oxides or to an inhibition of Feammox by dissolved Fe^{2+} concentrations exceeding $100\ \mu\text{M}$.

likely anoxygenic given other oxidation indicators. The chert-dominated unit displays more variable $\delta^{13}\text{C}_{\text{org}}$ values, which points toward a larger diversity of metabolisms in shallow depositional environments, possibly within benthic communities of biomats (Tice & Lowe, 2004). Some of the strongly negative values, down to -40‰ , are consistent with methanotrophy/methanogenesis, which is all the more interesting because iron oxides can also be used to oxidize methane (Lepot, 2020). These strongly negative $\delta^{13}\text{C}_{\text{org}}$ values are thus consistent with Fe(III)-driven oxidation of organic products, including methane and ammonium.

6 | CONCLUSION

Carbon and nitrogen isotopic compositions in the 3.4 Ga Buck Reef Chert display a large range of variations. However, while the sedimentary $\delta^{13}\text{C}_{\text{org}}$ signal seems to change with the depositional environment or chemical conditions, the bulk sedimentary $\delta^{15}\text{N}$ signal seems to rather primarily reflect iron oxides availability. $\delta^{15}\text{N}$ values are consistently positive and reach up to $+6.1\text{‰}$ in both jasper-free cherts and siderites of the two main sedimentary units, whereas they display a distinctive diazotrophic Mo-based N_2 fixation signature close to 0‰ in the jasper-bearing facies of the upper BIF-dominated unit. Positive $\delta^{15}\text{N}$ values observed in sediments that are more scarce in iron could have resulted from the partial oxidation

of NH_4^+ to N_2 through the Feammox reaction, whereas sediments deposited in an environment saturated in Fe^{2+} would show no isotopic nitrogen fractionation, either from direct Feammox inhibition or from complete consumption of the ammonium pool. Accordingly, these findings suggest that iron availability could have controlled the nitrogen isotopic signature recorded in sediments through an ammonium oxidative pathway. More importantly, these results call for careful consideration of the meaning of positive $\delta^{15}\text{N}$ signatures in Archean ferruginous sediments. Indeed, while ^{15}N -enriched sedimentary organic matter has often been used as a redox indicator of a stable pool of nitrates in "oxygen oases," this study shows that in anoxic settings where Fe(III) minerals are present, the oxidation of ammonium can lead to similar positive $\delta^{15}\text{N}$ signatures. As anoxic and ferruginous conditions are thought to have been widespread in the Archean ocean, it might be necessary to carefully consider iron abundance and speciation when interpreting the nitrogen isotopic signatures and to rely on complementary redox indicators.

ACKNOWLEDGMENTS

This work is a contribution to the Institut Universitaire de France project EVOLINES. It was supported by the Observatoire des Sciences de l'Univers Terre Homme Environnement Temps Astronomie of Bourgogne-Franche-Comté (OSU THETA). For technical support, the authors would like to thank Anne-Lise Santoni, Ludovic Bruneau and the GISMO platform (Université de Bourgogne Franche-Comté,

France), and Virginia Rojas (Institut de Physique du Globe de Paris, France). AH acknowledges the DSI-NRF Centre of Excellence in Palaeosciences (Grant 86073). Drilling in the Barberton greenstone belt was supported by the International Continental Scientific Drilling Program (ICDP). JMC acknowledges the innovation program ERC (STROMATA, grant agreement 759289).

DATA AVAILABILITY STATEMENT

The data that supports the findings of this study are available in the supplementary material of this article.

ORCID

Alice Pellerin  <https://orcid.org/0000-0001-6828-5899>

Magali Ader  <https://orcid.org/0000-0002-9239-1509>

Johanna Marin-Carbonne  <https://orcid.org/0000-0002-4265-1595>

REFERENCES

- Ader, M., Thomazo, C., Sansjofre, P., Busigny, V., Papineau, D., Laffont, R., Cartigny, P., & Halverson, G. P. (2016). Interpretation of the nitrogen isotopic composition of Precambrian sedimentary rocks: Assumptions and perspectives. *Chemical Geology*, 429, 93–110. <https://doi.org/10.1016/j.chemgeo.2016.02.010>
- Alleon, J., Bernard, S., Olivier, N., Thomazo, C., & Marin-Carbonne, J. (2021). Inherited geochemical diversity of 3.4 Ga organic films from the Buck Reef Chert. *South Africa. Communications Earth & Environment*, 2, 1–7. <https://doi.org/10.1038/s43247-020-00066-7>
- Beaumont, V., & Robert, F. (1999). Nitrogen isotope ratios of kerogens in Precambrian cherts: A record of the evolution of atmosphere chemistry? *Precambrian Research*, 96, 63–82. [https://doi.org/10.1016/S0301-9268\(99\)00005-4](https://doi.org/10.1016/S0301-9268(99)00005-4)
- Bolhar, R., Van Kranendonk, M. J., & Kamber, B. S. (2005). A trace element study of siderite–jasper banded iron formation in the 3.45Ga Warrawoona group, Pilbara craton—Formation from hydrothermal fluids and shallow seawater. *Precambrian Research*, 137, 93–114. <https://doi.org/10.1016/j.precamres.2005.02.001>
- Boocock, T. J., Mikhail, S., Prytulak, J., Di Rocco, T., & Stüeken, E. E. (2020). Nitrogen mass fraction and stable isotope ratios for fourteen geological reference materials: Evaluating the applicability of elemental Analyser versus sealed tube combustion methods. *Geostandards and Geoanalytical Research*, 44, 537–551. [10.1111/ggr.12345](https://doi.org/10.1111/ggr.12345)
- Brunner, B., Contreras, S., Lehmann, M. F., Matantseva, O., Rollog, M., Kalvelage, T., Klockgether, G., Lavik, G., Jetten, M. S. M., Kartal, B., & Kuypers, M. M. M. (2013). Nitrogen isotope effects induced by anammox bacteria. *Proceedings of the National Academy of Sciences of the United States of America*, 110, 18994–18999. <https://doi.org/10.1073/pnas.1310488110>
- Busigny, V., Ader, M., & Cartigny, P. (2005). Quantification and isotopic analysis of nitrogen in rocks at the ppm level using sealed tube combustion technique: A prelude to the study of altered oceanic crust. *Chemical Geology*, 223, 249–258. [10.1016/j.chemgeo.2005.08.002](https://doi.org/10.1016/j.chemgeo.2005.08.002)
- Canfield, D. E. (2005). THE EARLY HISTORY OF ATMOSPHERIC OXYGEN: Homage to Robert M. Garrels. *Annual Review of Earth and Planetary Sciences*, 33, 1–36. <https://doi.org/10.1146/annurev.earth.33.092203.122711>
- Canfield, D. E., Glazer, A. N., & Falkowski, P. G. (2010). The evolution and future of Earth's nitrogen cycle. *Science*, 330, 192–196. <https://doi.org/10.1126/science.1186120>
- Cartigny, P., & Marty, B. (2013). Nitrogen isotopes and mantle geodynamics: The emergence of life and the atmosphere–crust–mantle connection. *Elements*, 9, 359–366. <https://doi.org/10.2113/gselements.9.5.359>
- Dalsgaard, T., & Thamdrup, B. (2002). Factors controlling anaerobic ammonium oxidation with nitrite in marine sediments. *Applied and Environmental Microbiology*, 68, 3802–3808. <https://doi.org/10.1128/AEM.68.8.3802-3808.2002>
- e Vries, S. T., Nijman, W., & Armstrong, R. A. (2006). Growth-fault structure and stratigraphic architecture of the Buck Ridge volcano-sedimentary complex, upper Hoogenoeg formation, Barberton Greenstone Belt, South Africa. *Precambrian Research*, 149, 77–98. <https://doi.org/10.1016/j.precamres.2006.04.005>
- Galić, A. (2015). *Unravelling atmospheric photolysis and ocean redox chemistry from Paleoproterozoic pyrite: A multiple sulfur and iron stable isotope study*. PhD thesis. Universiteit Utrecht.
- Garvin, J., Buick, R., Anbar, A. D., Arnold, G. L., & Kaufman, A. J. (2009). Isotopic evidence for an aerobic nitrogen cycle in the latest Archean. *Science*, 323, 1045–1048. <https://doi.org/10.1126/science.1165675>
- Geilert, S., Vroon, P. Z., & van Bergen, M. J. (2014). Silicon isotopes and trace elements in chert record early Archean basin evolution. *Chemical Geology*, 386, 133–142. <https://doi.org/10.1016/j.chemgeo.2014.07.027>
- Godfrey, L. V., & Falkowski, P. G. (2009). The cycling and redox state of nitrogen in the Archean ocean. *Nature Geoscience*, 2, 725–729. <https://doi.org/10.1038/ngeo633>
- Grotzinger, J. P., & Kasting, J. F. (1993). New constraints on Precambrian ocean composition. *The Journal of Geology*, 101, 235–243. <https://doi.org/10.1086/648218>
- Halevy, I., & Bachan, A. (2017). The geologic history of seawater pH. *Science*, 355, 1069–1071. <https://doi.org/10.1126/science.aal4151>
- Heimann, A., Johnson, C. M., Beard, B. L., Valley, J. W., Roden, E. E., Spicuzza, M. J., & Beukes, N. J. (2010). Fe, C, and O isotope compositions of banded iron formation carbonates demonstrate a major role for dissimilatory iron reduction in ~2.5Ga marine environments. *Earth and Planetary Science Letters*, 294, 8–18. <https://doi.org/10.1016/j.epsl.2010.02.015>
- Hoch, M. P., Fogel, M. L., & Kirchman, D. L. (1992). Isotope fractionation associated with ammonium uptake by a marine bacterium. *Limnology and Oceanography*, 37, 1447–1459. <https://doi.org/10.4319/lo.1992.37.7.1447>
- Hofmann, A., Karykowski, B., Mason, P., Chunnnet, G., & Arndt, N. (2013). *Barberton drilling project - Buck Reef Chert core BARB3*. 15, EGU2013-12227.
- Izon, G., Zerkle, A. L., Zhelezinskaia, I., Farquhar, J., Newton, R. J., Poulton, S. W., Eigenbrode, J. L., & Claire, M. W. (2015). Multiple oscillations in Neoproterozoic atmospheric chemistry. *Earth and Planetary Science Letters*, 431, 264–273. <https://doi.org/10.1016/j.epsl.2015.09.018>
- Kendall, C., & Grim, E. (1990). Combustion tube method for measurement of nitrogen isotope ratios using calcium oxide for total removal of carbon dioxide and water. *Analytical Chemistry*, 62, 526–529.
- Kipp, M. A., Stüeken, E. E., Yun, M., Bekker, A., & Buick, R. (2018). Pervasive aerobic nitrogen cycling in the surface ocean across the Paleoproterozoic era. *Earth and Planetary Science Letters*, 500, 117–126. <https://doi.org/10.1016/j.epsl.2018.08.007>
- Klein, C., & Beukes, N. J. (1989). Geochemistry and sedimentology of a facies transition from limestone to iron-formation deposition in the early Proterozoic Transvaal supergroup, South Africa. *Economic Geology*, 84, 1733–1774. <https://doi.org/10.2113/gsecongeo.84.7.1733>
- Koehler, M. C., Buick, R., Kipp, M. A., Stüeken, E. E., & Zalomus, J. (2018). Transient surface ocean oxygenation recorded in the ~2.66-Ga Jeerinah formation, Australia. *Proceedings of the National Academy of Sciences*, 115, 7711–7716. <https://doi.org/10.1073/pnas.1720820115>
- Konhäuser, K. O., Amskold, L., Lalonde, S. V., Posth, N. R., Kappler, A., & Anbar, A. (2007). Decoupling photochemical Fe(II) oxidation from

- shallow-water BIF deposition. *Earth and Planetary Science Letters*, 258, 87–100. <https://doi.org/10.1016/j.epsl.2007.03.026>
- Krüner, A., Byerly, G. R., & Lowe, D. R. (1991). Chronology of early Archaean granite-greenstone evolution in the Barberton Mountain land, South Africa, based on precise dating by single zircon evaporation. *Earth and Planetary Science Letters*, 103, 41–54. [https://doi.org/10.1016/0012-821X\(91\)90148-B](https://doi.org/10.1016/0012-821X(91)90148-B)
- Kuga, M., Carrasco, N., Marty, B., Marrocchi, Y., Bernard, S., Rigaudier, T., Fleury, B., & Tissandier, L. (2014). Nitrogen isotopic fractionation during abiotic synthesis of organic solid particles. *Earth and Planetary Science Letters*, 393, 2–13. <https://doi.org/10.1016/j.epsl.2014.02.037>
- Ledevin, M., Arndt, N., Chauvel, C., Jaillard, E., & Simionovici, A. (2019). The sedimentary origin of black and white banded cherts of the Buck Reef, Barberton, South Africa. *Geosciences*, 9, 424. <https://doi.org/10.3390/geosciences9100424>
- Lepot, K. (2020). Signatures of early microbial life from the Archean (4 to 2.5 Ga) eon. *Earth-Science Reviews*, 209, 103296. <https://doi.org/10.1016/j.earscirev.2020.103296>
- Li, L., Bebout, G. E., & Idleman, B. D. (2007). Nitrogen concentration and $\delta^{15}\text{N}$ of altered oceanic crust obtained on ODP legs 129 and 185: Insights into alteration-related nitrogen enrichment and the nitrogen subduction budget. *Geochimica et Cosmochimica Acta*, 71, 2344–2360. <https://doi.org/10.1016/j.gca.2007.02.001>
- Lowe, D. R., & Worrell, G. F. (1999). Sedimentology, mineralogy, and implications of silicified evaporites in the Kromberg formation, Barberton Greenstone Belt, South Africa. *Special Paper-Geological Society of America*, 329, 167–188.
- Mettam, C., & Zerkle, A. L. (2021). *Nitrogen isotopes in deep time*. Cambridge University Press.
- Möbius, J. (2013). Isotope fractionation during nitrogen remineralization (ammonification): Implications for nitrogen isotope biogeochemistry. *Geochimica et Cosmochimica Acta*, 105, 422–432. <https://doi.org/10.1016/j.gca.2012.11.048>
- Nishizawa, M., Miyazaki, J., Makabe, A., Koba, K., & Takai, K. (2014). Physiological and isotopic characteristics of nitrogen fixation by hyperthermophilic methanogens: Key insights into nitrogen anaerobism of the microbial communities in Archean hydrothermal systems. *Geochimica et Cosmochimica Acta*, 138, 117–135. <https://doi.org/10.1016/j.gca.2014.04.021>
- Nishizawa, M., Sano, Y., Ueno, Y., & Maruyama, S. (2007). Speciation and isotope ratios of nitrogen in fluid inclusions from seafloor hydrothermal deposits at ~3.5 Ga. *Earth and Planetary Science Letters*, 254, 332–344. <https://doi.org/10.1016/j.epsl.2006.11.044>
- Petrash, D. A., Steenbergen, I. M., Valero, A., Meador, T. B., Pačes, T., & Thomazo, C. (2022). Aqueous system-level processes and prokaryote assemblages in the ferruginous and sulfate-rich bottom waters of a post-mining lake. *Biogeosciences*, 19, 1723–1751. <https://doi.org/10.5194/bg-19-1723-2022>
- Poulton, S. W., & Canfield, D. E. (2011). Ferruginous conditions: A dominant feature of the ocean through Earth's history. *Elements*, 7, 107–112. <https://doi.org/10.2113/gselements.7.2.107>
- Raymond, J., Siefert, J. L., Staples, C. R., & Blankenship, R. E. (2004). The natural history of nitrogen fixation. *Molecular Biology and Evolution*, 21, 541–554. <https://doi.org/10.1093/molbev/msh047>
- Rios-Del Toro, E. E., Valenzuela, E. I., López-Lozano, N. E., Cortés-Martínez, M. G., Sánchez-Rodríguez, M. A., Calvario-Martínez, O., Sánchez-Carrillo, S., & Cervantes, F. J. (2018). Anaerobic ammonium oxidation linked to sulfate and ferric iron reduction fuels nitrogen loss in marine sediments. *Biodegradation*, 29, 429–442. <https://doi.org/10.1007/s10532-018-9839-8>
- Sebree, J. A., Stern, J. C., Mandt, K. E., Domagal-Goldman, S. D., & Trainer, M. G. (2016). ^{13}C and ^{15}N fractionation of CH_4/N_2 mixtures during photochemical aerosol formation: Relevance to Titan. *Icarus, Titan's Surface and Atmosphere*, 270, 421–428. <https://doi.org/10.1016/j.icarus.2015.04.016>
- Sigman, D. M., Karsh, K. L., & Casciotti, K. L. (2009). Nitrogen isotopes in the ocean. In J. H. Steele, S. A. Thorpe, & K. K. Turekian (Eds.), *Encyclopedia of ocean sciences* (pp. 40–54). Academic Press. <https://doi.org/10.1016/B978-012374473-9.00632-9>
- Stüeken, E. E., Boocock, T. J., Robinson, A., Mikhail, S., & Johnson, B. W. (2021). Hydrothermal recycling of sedimentary ammonium into oceanic crust and the Archean Ocean at 3.24 Ga. *Geology*, 49, 822–826. <https://doi.org/10.1130/G48844.1>
- Stüeken, E. E., Buick, R., & Schauer, A. J. (2015). Nitrogen isotope evidence for alkaline lakes on late Archean continents. *Earth and Planetary Science Letters*, 411, 1–10. <https://doi.org/10.1016/j.epsl.2014.11.037>
- Stüeken, E. E., Kipp, M. A., Koehler, M. C., & Buick, R. (2016). The evolution of Earth's biogeochemical nitrogen cycle. *Earth-Science Reviews*, 160, 220–239. <https://doi.org/10.1016/j.earscirev.2016.07.007>
- Thomazo, C., Ader, M., & Philippot, P. (2011). Extreme ^{15}N -enrichments in 2.72-Gyr-old sediments: Evidence for a turning point in the nitrogen cycle. *Geobiology*, 9, 107–120. <https://doi.org/10.1111/j.1472-4669.2011.00271.x>
- Tice, M. M., Bostick, B. C., & Lowe, D. R. (2004). Thermal history of the 3.5–3.2 Ga Onverwacht and fig tree groups, Barberton greenstone belt, South Africa, inferred by Raman microspectroscopy of carbonaceous material. *Geology*, 32, 37–40. <https://doi.org/10.1130/G19915.1>
- Tice, M. M., & Lowe, D. R. (2004). Photosynthetic microbial mats in the 3,416-Myr-Old ocean. *Nature*, 431, 549–552. <https://doi.org/10.1038/nature02888>
- Tice, M. M., & Lowe, D. R. (2006a). The origin of carbonaceous matter in pre-3.0 Ga greenstone terrains: A review and new evidence from the 3.42 Ga Buck Reef Chert. *Earth-Science Reviews*, 76, 259–300. <https://doi.org/10.1016/j.earscirev.2006.03.003>
- Tice, M. M., & Lowe, D. R. (2006b). Hydrogen-based carbon fixation in the earliest known photosynthetic organisms. *Geology*, 34, 37–40. <https://doi.org/10.1130/G22012.1>
- Tosca, N. J., Jiang, C. Z., Rasmussen, B., & Muhling, J. (2019). Products of the iron cycle on the early earth. *Free Radical Biology and Medicine*, 140, 138–153. <https://doi.org/10.1016/j.freeradbio.2019.05.005>
- Trainer, M. G., Pavlov, A. A., DeWitt, H. L., Jimenez, J. L., McKay, C. P., Toon, O. B., & Tolbert, M. A. (2006). Organic haze on Titan and the early Earth. *PNAS*, 103, 18035–18042. <https://doi.org/10.1073/pnas.0608561103>
- van Zuilen, M. A., Lepland, A., Teranes, J., Finarelli, J., Wahlen, M., & Arrhenius, G. (2003). Graphite and carbonates in the 3.8 Ga old Isua Supracrustal Belt, southern West Greenland. *Precambrian Research*, 126, 331–348. [https://doi.org/10.1016/S0301-9268\(03\)00103-7](https://doi.org/10.1016/S0301-9268(03)00103-7)
- Ward, B. (2012). The global nitrogen cycle. In A. H. Knoll, D. E. Canfield, & K. O. Konhauser (Eds.), *Fundamentals of geobiology* (pp. 36–48). John Wiley & Sons, Ltd. <https://doi.org/10.1002/9781118280874.ch4>
- Wright, V. P. (2022). The mantle, CO_2 and the giant Aptian chemogenic lacustrine carbonate factory of the South Atlantic: Some carbonates are made, not born. *Sedimentology*, 69, 47–73. <https://doi.org/10.1111/sed.12835>
- Yamaguchi, K. (2002). *Geochemistry of Archean-Paleoproterozoic black shales: The early evolution of the atmosphere, oceans, and biosphere*. Pennsylvania State University.
- Yang, W. H., Weber, K. A., & Silver, W. L. (2012). Nitrogen loss from soil through anaerobic ammonium oxidation coupled to iron reduction. *Nature Geoscience*, 5, 538–541. <https://doi.org/10.1038/ngeo1530>
- Zerkle, A. L., Claire, M. W., Domagal-Goldman, S. D., Farquhar, J., & Poulton, S. W. (2012). A bistable organic-rich atmosphere on the Neoproterozoic Earth. *Nature Geoscience*, 5, 359–363. <https://doi.org/10.1038/ngeo1425>
- Zhang, X., Sigman, D. M., Morel, F. M. M., & Kraepiel, A. M. L. (2014). Nitrogen isotope fractionation by alternative nitrogenases and past ocean anoxia. *PNAS*, 111, 4782–4787. <https://doi.org/10.1073/pnas.1402976111>

Ader, M., Sansjofre, P., Halverson, G. P., Busigny, V., Trindade, R. I. F., Kunzmann, M., & Nogueira, A. C. R. (2014). Ocean redox structure across the late Neoproterozoic oxygenation event: A nitrogen isotope perspective. *Earth and Planetary Science Letters*, 396, 1–13 [10.1016/j.epsl.2014.03.042](https://doi.org/10.1016/j.epsl.2014.03.042)

SUPPORTING INFORMATION

Additional supporting information can be found online in the Supporting Information section at the end of this article.

How to cite this article: Pellerin, A., Thomazo, C., Ader, M., Marin-Carbonne, J., Alleon, J., Vennin, E., & Hofmann, A. (2023). Iron-mediated anaerobic ammonium oxidation recorded in the early Archean ferruginous ocean. *Geobiology*, 00, 1–13. <https://doi.org/10.1111/gbi.12540>

Methods

Sampling. Fifty-one samples were chosen along the drill core according to their organic matter content (TOC>0.1% in the digestion residue), that mostly reflects their potential in containing enough nitrogen to analyze. Those samples are composed of various proportions of bands of chert and siderite. Only samples CT6, CT7 and CT18 contain jasper layers. Accordingly, the amount of carbonates in the samples has been used to define two lithological endmembers: “chert” (when carbonates range from 0 to 50 wt.%) and “siderite” (when carbonates range from 50 to 100 wt.%).

Mineralogy. Mineralogy was investigated before and after chemical treatment using X-ray Diffraction (XRD) at the Biogéosciences Laboratory (Université de Bourgogne Franche-Comté, France). Diffractograms were obtained with a Bruker D8 Endeavor diffractometer with CuK α radiation, LynxEye XE-T detector and Ni filter, under 40 kV voltage and 25 mA intensity. The goniometer scanned from 2° to 65° 2 θ for each run. Identification of crystalline phases was based on the position and area of their respective mean basal reflections.

Chemical treatment. Samples were first crushed into powder using a ring and puck mill at the Biogéosciences Laboratory (Université de Bourgogne Franche-Comté, France) in order to obtain sample powder smaller than 60 μ m. Carbonate-free residues were obtained by mixing sample powders with 6N HCl for 24h, followed by a second step of digestion at 80°C for 4h. The powder was then rinsed with deionized distilled water to a neutral pH and oven-dried at 40°C for 48h. Carbonate content, expressed in weight percent (wt.%), was evaluated through gravimetric mass balance after HCl digestion. Some kerogen extracts were commercially produced by Global Geolab Ltd, Alberta, Canada. Powders were digested using HCl and HF, and kerogens were separated out by heavy liquid separation with zinc bromide.

C isotopic analyses. The decarbonated residues were poured into tin capsules (20 to 80 mg of powder) and weighted using a Sartorius M2P ultra-balance before TOC and $\delta^{13}\text{C}_{\text{org}}$ measurements were performed using a Thermo Fisher Scientific Flash Smart elemental analyser, coupled to a Thermo Fisher Scientific Delta V isotope ratio mass spectrometer (EA-IRMS) via a ConFlo IV interface at the Biogéosciences laboratory. Certified USGS40 ($\delta^{13}\text{C}_{\text{org}}=-26.2\%$, TOC=40.82 wt.%) and caffeine IAEA-600 ($\delta^{13}\text{C}_{\text{org}}=-27.77\%$) reference materials were used for the calibration. Total organic carbon (TOC) contents are expressed in dry weight percentage (wt.%) of the non-decarbonated bulk powder and isotope results are reported in

delta-notation relative to V-PDB. The mean external reproducibility (2σ), based on sample replicate analyses, is ± 0.06 wt.% for the TOC content and $\pm 0.86\text{‰}$ for the $\delta^{13}\text{C}_{\text{org}}$. Note that external reproducibility includes chemical treatment, and may also reflect sample heterogeneity.

N isotopic analyses. As most samples contain less than 200 ppm N (Table 1) and the proportion of silicate-bound nitrogen is unknown, the above-described EA-IRMS method is not sensitive enough for reliable bulk nitrogen isotopic analyses (Ader et al., 2016; Boocock et al., 2020). Samples were therefore analyzed using the “classical method” developed at IPGP described in Ader et al. (2014, 2016), in which N_2 is produced offline through sealed-tube Dumas combustion and cryogenically purified in a vacuum line. Up to 200 mg of decarbonated residual powder was put into a quartz tube with CuO and Cu, purified beforehand at 900°C for 2h in a muffle furnace to prevent contamination. Samples were degassed for 12h at 150°C under vacuum to remove adsorbed atmospheric N_2 and organics. Quartz tubes were then sealed directly under vacuum and combusted in a muffle furnace at 950°C for 6h, then cooled at 600°C for 2h, allowing residual oxygen to combine with cupric oxide and nitrous oxide to be reduced by copper, and finally cooled to ambient temperature. This allows the chemical separation of gaseous products. Busigny et al. (2005) have shown that the extraction yield for this protocol is 100% for mineral and organic N. The content of each quartz tube is liberated in the vacuum line with a tube cracker, where CO_2 and H_2O are trapped cryogenically to avoid any isobaric interferences. The purified incondensable N_2 gas is concentrated into a calibrated volume for quantification using a Toepler pump (Hg manometer). Standard analytical procedures for nitrogen usually include CaO in the reagents to trap gaseous CO_2 and H_2O liberated from samples (Kendall and Grim, 1990), but given that Busigny et al. (2005) have shown that it significantly contributes to analytical blanks, we performed a few tests on samples from the BRC which show that the addition of CaO does not yield significant $\delta^{15}\text{N}$ differences. Most samples were consequently analyzed without the addition of CaO, except for the two kerogen extracts. Analytical blanks for the entire procedure are <0.05 micromoles N, which represents less than 10% of the gas for smaller samples and less than 1% for more concentrated samples. Purified N_2 is analyzed by dual-inlet mass spectrometry using a ThermoFinnigan DeltaPlus XP IRMS. Possible air contamination and isobaric interferences due to CO are monitored by scanning of m/z 12 (C from CO_2 , CO, CH_4 or organic compounds), 18 (H_2O), 30 (C^{18}O), 32 (O_2), 40 (atmospheric Ar) and 44 (CO_2). External $\delta^{15}\text{N}$ reproducibility falls between 0.10 and 1.02‰ with a mean of $0.44 \pm 0.29\text{‰}$ ($n=14$). Samples that were replicated are reported in Table 1. Samples with no external reproducibility are reported with an error of $\pm 0.63\text{‰}$, which is the

external reproducibility of sample 75A replicated 10 times at different concentrations (Supplementary Table 1). Kerogen extracts of two samples (CT16 and CT18U) yield TN contents and $\delta^{15}\text{N}$ values identical within external reproducibility to those measured on their decarbonated counterparts (Supplementary Table 2).

SIMS S isotopes analyses. Multiple S isotope compositions have been measured in situ in pyrite grains at the SwissSIMS (UNIL, Lausanne) following the method described in Whitehouse (2013) and Marin-Carbonne et al. (2014, 2020). Briefly, a Cs^+ beam of 5 nA intensity was focused to a spot of 25 μm with electron gun to compensate charge on sample surface. $^{32}\text{S}^-$, $^{33}\text{S}^-$ and $^{34}\text{S}^-$ were simultaneous detected on three of axis Faraday cups in multi-collection mode. Typical $^{32}\text{S}^-$ intensity was around 10.10^8 counts per second (cps). Typical analyses consisted of 2 minutes of presputtering in raster mode (20 x 20 μm) followed by data acquisition in 40 cycles of 3 seconds each. The background of the detectors was measured during presputtering and was then corrected for each analysis. Several pyrite standards (Maine, ($\delta^{34}\text{S} = -20.61\%$, $\Delta^{33}\text{S} = -10.63\%$), Spain ($\delta^{34}\text{S} = -1.56\%$ and $\Delta^{33}\text{S} = -0.78\%$) and Balmat ($\delta^{34}\text{S} = 15.84\%$ and $\Delta^{33}\text{S} = 8.12\%$) were used to determine (i) the instrumental mass fractionation, and (ii) the reference mass discrimination line, from which $\Delta^{33}\text{S}$ values were calculated. The internal precision achieved under these conditions was better than $\pm 0.05\%$ for $\delta^{34}\text{S}$ and better than $\pm 0.03\%$ for $\Delta^{33}\text{S}$ values (2σ). The external precision was $\pm 0.40\%$ (2σ) for $\delta^{34}\text{S}$ and $\pm 0.1\%$ (2σ) for $\Delta^{33}\text{S}$ values. All data are given in delta notation, with the international standard V-CDT. The average value is given for each sample.

Supplementary Information

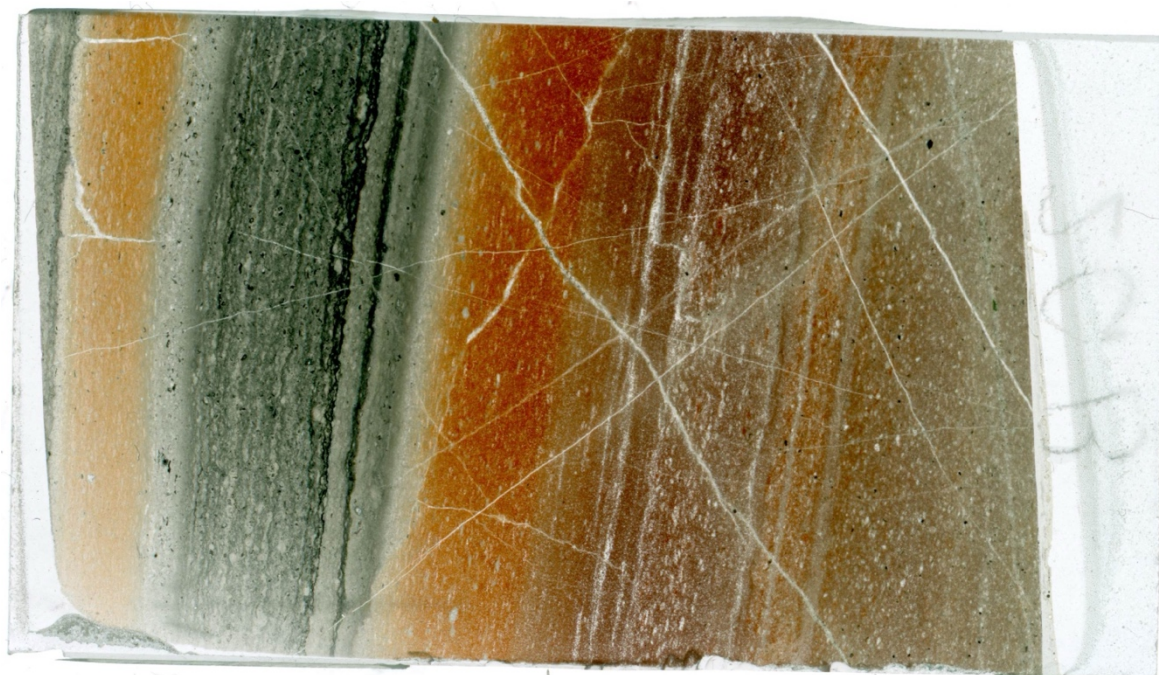
Preservation of the isotopic signature: impact of post-depositional processes on the $\delta^{15}\text{N}$

As post-depositional modifications of sedimentary $\delta^{15}\text{N}$ can occur during diagenesis and metamorphism, it is essential to evaluate the impact of these processes. Organic N and mineral N (fixed NH_4^+ that substitutes for K^+ in some phyllosilicates) are affected differently by post-depositional processes. In the set of samples studied here, organic N seems to dominate and is likely the only nitrogen phase in most samples. Indeed, analyses of kerogen extracts and bulk rocks yield slightly lower TN and higher TOC/TN in the kerogens, but very similar $\delta^{15}\text{N}$ values (Supplementary Table 2) compared to the bulk rock. Moreover, XRD analyses do not show any K-bearing phyllosilicates (clays or micas) in the BRC sediments (Supplementary Fig. 2), as chlorite is the only identified phyllosilicate, and the TOC vs. TN crossplot (Fig. 3) shows a good

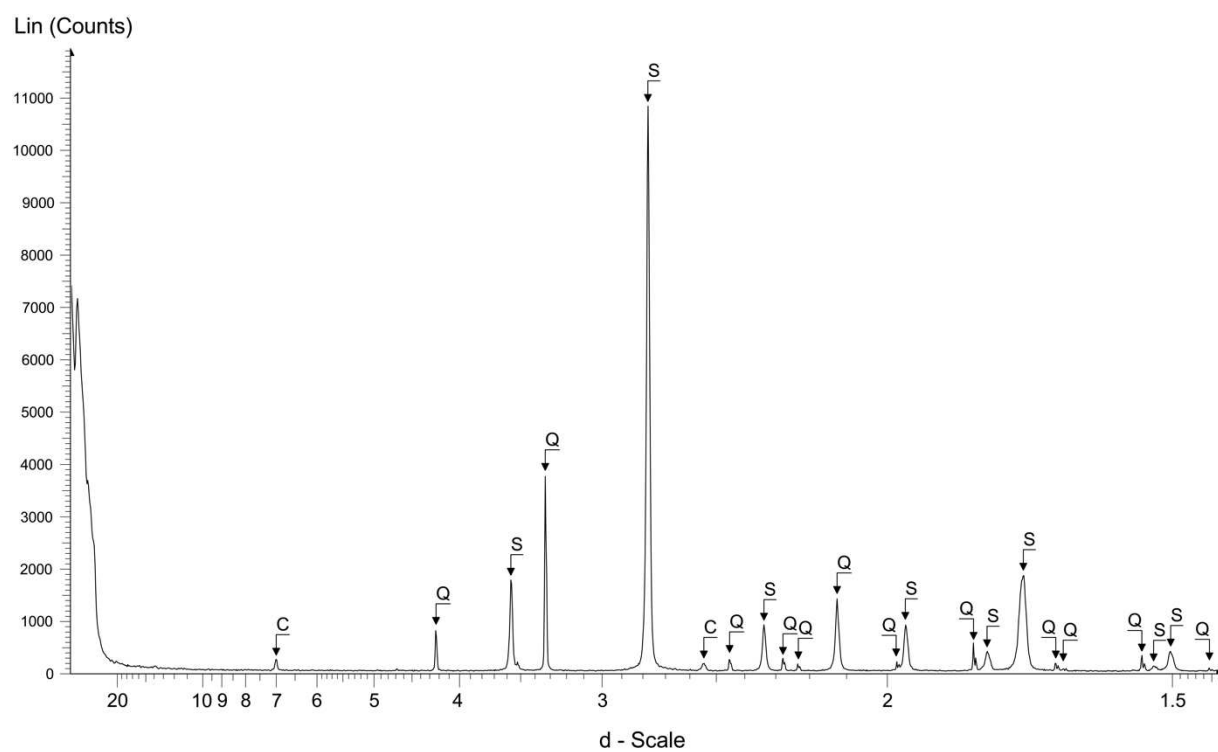
correlation ($R^2=0.78$). It therefore seems unlikely that organic matter remineralization during diagenesis significantly impacted the BRC $\delta^{15}\text{N}$ record since early diagenesis under anoxic conditions does not seem to shift organic matter $\delta^{15}\text{N}$ values by more than 1‰ (Lehmann et al., 2002).

As for metamorphism, the BRC formation has undergone low-grade metamorphism in the greenschist facies, reaching peak temperatures of 350°C (Tice et al., 2004; Greco et al., 2018; Alleon et al., 2021). While an increase in $\delta^{15}\text{N}$ and a decrease in TN is usually seen during prograde metamorphism (Haendel et al., 1986; Bebout and Fogel, 1992; Boyd and Philippot, 1998; Jia, 2006), studies on coal series show that nitrogen loss from organic matter during anthracitization is not associated with significant $\delta^{15}\text{N}$ increase (Ader et al., 1998, 2006; Boudou et al., 2008). The absence of covariation between $\delta^{15}\text{N}$ and TOC/TN in the BRC argues against a strong modification of $\delta^{15}\text{N}$ values due to metamorphic N-loss (Fig. 3). Moreover, maximum isotopic enrichments documented for greenschist facies metamorphism are below 2‰ (Jia, 2006; Stüeken et al., 2017), which is small compared to the reported range of measured $\delta^{15}\text{N}$ in the BRC (between -0.5‰ and +6.1‰). Secondary modification of $\delta^{15}\text{N}$ values can also occur during metasomatic ammonium addition through hydrothermal recycling, which tends to decrease the TOC/TN and either increase or decrease the $\delta^{15}\text{N}$ depending on the isotopic signature of recycled sediments (Stüeken et al., 2021a, 2021b). The negligible amount of phyllosilicates, none K-bearing, in the BRC suggests that such secondary modifications were absent or very limited. Besides, despite evidence of fluid circulation through cross-cutting veins, TOC/TN remains relatively constant along the core, arguing against any heterogeneous secondary overprint of the nitrogen record, either by metamorphism or by metasomatism. Finally, the absence of significant $\delta^{15}\text{N}$ differences between chert and siderite samples also argues against a metamorphic or metasomatic modification, as chert and siderite would react very differently to thermal alteration.

Supplementary Figures



Supplementary Fig. 1. Photography of a thin section showing centimetric layers of jasper (iron oxide-bearing red chert) observed in the BRC.



Supplementary Fig. 2. XRD diffractogram of sample CT17, representative of the main crystalline phases of the BRC: quartz (Q), siderite (S) and chlorite (C).

Supplementary Tables

Sample	Weight (mg)	Extracted N (μ moles)	TN residue (ppm)	$\delta^{15}\text{N}$ (‰ vs. air)
75A	56	5.54	2745	5.1
75A	48	4.49	2598	4
75A	46	4.14	2540	3.9
75A	40	3.84	2703	4.7
75A	21	1.78	2345	3.6
75A	20	1.88	2573	3.7
75A	10	1.01	2861	3.2
75A	10	0.95	2589	3.3
75A	6	0.59	2582	3.9
75A	4	0.42	2680	4.7
Mean			2622\pm138	4.0\pm0.6

Supplementary Table 1. External reproducibility for TN and $\delta^{15}\text{N}$ of sample 75A at different initial powder weights.

Sample	Fraction analyzed	TOC (wt. %)	TN (wt. ppm)	TOC/TN	$\delta^{13}\text{C}_{\text{org}}$ (‰ vs. PDB)	$\delta^{15}\text{N}$ (‰ vs. air)
CT18U	bulk	0.69	114	60	-28.13	-0.27
CT18U	kerogen	0.68	94	73	-28.09	-0.26
CT16	bulk	0.55	90	61	-29.78	1.1
CT16	kerogen	0.39	56	70	-30.05	0.83

Supplementary Table 2. Comparison between TN and $\delta^{15}\text{N}$ of samples CT18U and CT16 for kerogen extracts vs. bulk rock.

Sample	Depth (m)	Lithology	$\delta^{34}\text{S}$ (‰ vs. VCDT)	SD	$\Delta^{33}\text{S}$ (‰ vs. VCDT)	SD	Nb. of pyrites analyzed
75A	483.81	BIFs	+1.59	1.55	+0.36	0.32	56
17A	616.77	Laminated chert	+1.20	1.05	+0.29	0.47	48
9A	794.12	Granular chert	-1.59	1.28	+1.20	0.36	26

Supplementary Table 3. Average S isotope compositions of pyrite grains from 3 BRC samples showing mass-independent fractionation (S-MIF).

References

- Ader, M., Boudou, J.-P., Javoy, M., Goffe, B., Daniels, E., 1998. Isotope study on organic nitrogen of Westphalian anthracites from the Western Middle field of Pennsylvania (U.S.A.) and from the Bramsche Massif (Germany). *Organic Geochemistry, Advances in Organic Geochemistry 1997 Proceedings of the 18th International Meeting on Organic Geochemistry Part I. Petroleum Geochemistry* 29, 315–323. [https://doi.org/10.1016/S0146-6380\(98\)00072-2](https://doi.org/10.1016/S0146-6380(98)00072-2)
- Ader, M., Cartigny, P., Boudou, J.-P., Oh, J.-H., Petit, E., Javoy, M., 2006. Nitrogen isotopic evolution of carbonaceous matter during metamorphism: Methodology and preliminary results. *Chemical Geology* 232, 152–169. <https://doi.org/10.1016/j.chemgeo.2006.02.019>
- Ader, M., Sansjofre, P., Halverson, G.P., Busigny, V., Trindade, R.I.F., Kunzmann, M., Nogueira, A.C.R., 2014. Ocean redox structure across the Late Neoproterozoic Oxygenation Event: A nitrogen isotope perspective. *Earth and Planetary Science Letters* 396, 1–13. <https://doi.org/10.1016/j.epsl.2014.03.042>
- Ader, M., Thomazo, C., Sansjofre, P., Busigny, V., Papineau, D., Laffont, R., Cartigny, P., Halverson, G.P., 2016. Interpretation of the nitrogen isotopic composition of Precambrian sedimentary rocks: Assumptions and perspectives. *Chemical Geology* 429, 93–110. <https://doi.org/10.1016/j.chemgeo.2016.02.010>
- Alleon, J., Bernard, S., Olivier, N., Thomazo, C., Marin-Carbonne, J., 2021. Inherited geochemical diversity of 3.4 Ga organic films from the Buck Reef Chert, South Africa. *Communications Earth & Environment* 2, 1–7. <https://doi.org/10.1038/s43247-020-00066-7>
- Bebout, G.E., Fogel, M.L., 1992. Nitrogen-isotope compositions of metasedimentary rocks in the Catalina Schist, California: Implications for metamorphic devolatilization history. *Geochimica et Cosmochimica Acta* 56, 2839–2849. [https://doi.org/10.1016/0016-7037\(92\)90363-N](https://doi.org/10.1016/0016-7037(92)90363-N)
- Boocock, T.J., Mikhail, S., Prytulak, J., Di Rocco, T., Stüeken, E.E., 2020. Nitrogen Mass Fraction and Stable Isotope Ratios for Fourteen Geological Reference Materials: Evaluating the Applicability of Elemental Analyser Versus Sealed Tube Combustion Methods. *Geostandards and Geoanalytical Research* 44, 537–551. <https://doi.org/10.1111/ggr.12345>
- Boudou, J.-P., Schimmelmann, A., Ader, M., Mastalerz, M., Sebito, M., Gengembre, L., 2008. Organic nitrogen chemistry during low-grade metamorphism. *Geochimica et Cosmochimica Acta* 72, 1199–1221. <https://doi.org/10.1016/j.gca.2007.12.004>
- Boyd, S.R., Philippot, P., 1998. Precambrian ammonium biogeochemistry: a study of the Moine metasediments, Scotland. *Chemical Geology* 144, 257–268. [https://doi.org/10.1016/S0009-2541\(97\)00135-6](https://doi.org/10.1016/S0009-2541(97)00135-6)
- Busigny, V., Ader, M., Cartigny, P., 2005. Quantification and isotopic analysis of nitrogen in rocks at the ppm level using sealed tube combustion technique: A prelude to the study of altered oceanic crust. *Chemical Geology* 223, 249–258. <https://doi.org/10.1016/j.chemgeo.2005.08.002>

Greco, F., Cavalazzi, B., Hofmann, A., Hickman-Lewis, K., 2018. 3.4 Ga biostructures from the Barberton greenstone belt of South Africa: new insights into microbial life. *Bollettino della Società Paleontologica Italiana* 59–74. <https://doi.org/10.4435/BSPI.2018.04>

Haendel, D., Mühle, K., Nitzsche, H.-M., Stiehl, G., Wand, U., 1986. Isotopic variations of the fixed nitrogen in metamorphic rocks. *Geochimica et Cosmochimica Acta* 50, 749–758. [https://doi.org/10.1016/0016-7037\(86\)90351-0](https://doi.org/10.1016/0016-7037(86)90351-0)

Jia, Y., 2006. Nitrogen isotope fractionations during progressive metamorphism: A case study from the Paleozoic Cooma metasedimentary complex, southeastern Australia. *Geochimica et Cosmochimica Acta* 70, 5201–5214. <https://doi.org/10.1016/j.gca.2006.08.004>

Kendall, C., Grim, E., 1990. Combustion tube method for measurement of nitrogen isotope ratios using calcium oxide for total removal of carbon dioxide and water. *Analytical Chemistry*.

Lehmann, M.F., Bernasconi, S.M., Barbieri, A., McKenzie, J.A., 2002. Preservation of organic matter and alteration of its carbon and nitrogen isotope composition during simulated and in situ early sedimentary diagenesis. *Geochimica et Cosmochimica Acta* 66, 3573–3584. [https://doi.org/10.1016/S0016-7037\(02\)00968-7](https://doi.org/10.1016/S0016-7037(02)00968-7)

Marin-Carbonne, J., Busigny, V., Miot, J., Rollion-Bard, C., Muller, E., Drabon, N., Jacob, D., Pont, S., Robyr, M., Bontognali, T.R., 2020. In Situ Fe and S isotope analyses in pyrite from the 3.2 Ga Mendon Formation (Barberton Greenstone Belt, South Africa): Evidence for early microbial iron reduction. *Geobiology* 18, 306–325.

Marin-Carbonne, J., Rollion-Bard, C., Bekker, A., Rouxel, O., Agangi, A., Cavalazzi, B., Wohlgemuth-Ueberwasser, C.C., Hofmann, A., McKeegan, K.D., 2014. Coupled Fe and S isotope variations in pyrite nodules from Archean shale. *Earth and Planetary Science Letters* 392, 67–79.

Stüeken, E.E., Boocock, T.J., Robinson, A., Mikhail, S., Johnson, B.W., 2021a. Hydrothermal recycling of sedimentary ammonium into oceanic crust and the Archean ocean at 3.24 Ga. *Geology* 49, 822–826. <https://doi.org/10.1130/G48844.1>

Stüeken, E.E., Gregory, D.D., Mukherjee, I., McGoldrick, P., 2021b. Sedimentary exhalative venting of bioavailable nitrogen into the early ocean. *Earth and Planetary Science Letters* 565, 116963. <https://doi.org/10.1016/j.epsl.2021.116963>

Stüeken, E.E., Zaloumis, J., Meixnerová, J., Buick, R., 2017. Differential metamorphic effects on nitrogen isotopes in kerogen extracts and bulk rocks. *Geochimica et Cosmochimica Acta* 217, 80–94. <https://doi.org/10.1016/j.gca.2017.08.019>

Tice, M.M., Bostick, B.C., Lowe, D.R., 2004. Thermal history of the 3.5–3.2 Ga Onverwacht and Fig Tree Groups, Barberton greenstone belt, South Africa, inferred by Raman microspectroscopy of carbonaceous material. *Geology* 32, 37–40. <https://doi.org/10.1130/G19915.1>

Whitehouse, M.J., 2013. Multiple sulfur isotope determination by SIMS: evaluation of reference sulfides for $\Delta^{33}\text{S}$ with observations and a case study on the determination of $\Delta^{36}\text{S}$. *Geostandards and Geoanalytical Research* 37, 19–33.

CHAPTER 7. NEOARCHEAN OXYGEN-BASED NITROGEN CYCLE EN ROUTE TO THE GREAT OXIDATION EVENT

Introductory summary

At the beginning of the Neoproterozoic, the most extreme positive nitrogen isotope values have been measured (Fig. 7.0). Stemming from a single formation in the Pilbara Craton, their interpretation remains debated between a biotic O₂-related signal, i.e. an onset of oceanic oxygenation, and an abiotic, pH-dependent process specific to the depositional environment. Since these extremely positive $\delta^{15}\text{N}$ values are unique in the Archean rock record, the question, although crucial to our understanding of the first steps of the oxidative N cycle, has remained open.

In an article entitled “*Neoproterozoic oxygen-based nitrogen cycle en route to the Great Oxidation Event*”, currently under review in *Nature*, we reexamine this anomaly in the Neoproterozoic nitrogen isotope record using a new set of carbon and nitrogen isotope results (Fig. 7.0) from the 2.68 Ga Serra Sul Formation (Carajás Basin, Amazonian Craton, Brazil). These show a rare combination of extremely positive nitrogen ($\delta^{15}\text{N}$ up to +37.5‰) and extremely negative organic carbon ($\delta^{13}\text{C}_{\text{org}}$ down to -51.8‰) isotope values similar to those previously reported for the Tumbiana Formation (Thomazo et al., 2011). We propose to name this time period at around 2.7 Ga, which harbor occurrences of extreme $\delta^{15}\text{N}$ values in addition to those of the Precambrian usual range, the **Nitrogen Isotope Event (NIE)**. We suggest that it reflects the onset of ammonium oxidation on a global scale. This peculiar NIE, seemingly unique in Earth’s history, testifies that the emergence of N oxidative pathways predates the GOE by at least 200 Ma and adds evidence for Neoproterozoic “whiffs of oxygen” based on trace metal element concentrations and isotopes (Anbar et al., 2007).

Moreover, this onset of ammonium oxidation around 2.7 Ga has major implications for the history of oceanic and atmospheric oxygenation. It is likely to have resulted in nutrient-depleted conditions by consuming part of the ammonium that previously fueled primary productivity. This biologically-mediated negative feedback on primary productivity could have limited the activity of oxygenic phototrophs, thereby delaying the accumulation of oxygen in the oceans and atmosphere.

The findings presented in this article are a breakthrough in the understanding of the early evolution of the nitrogen biogeochemical cycle and of the mechanisms that could have delayed Earth's oxygenation.

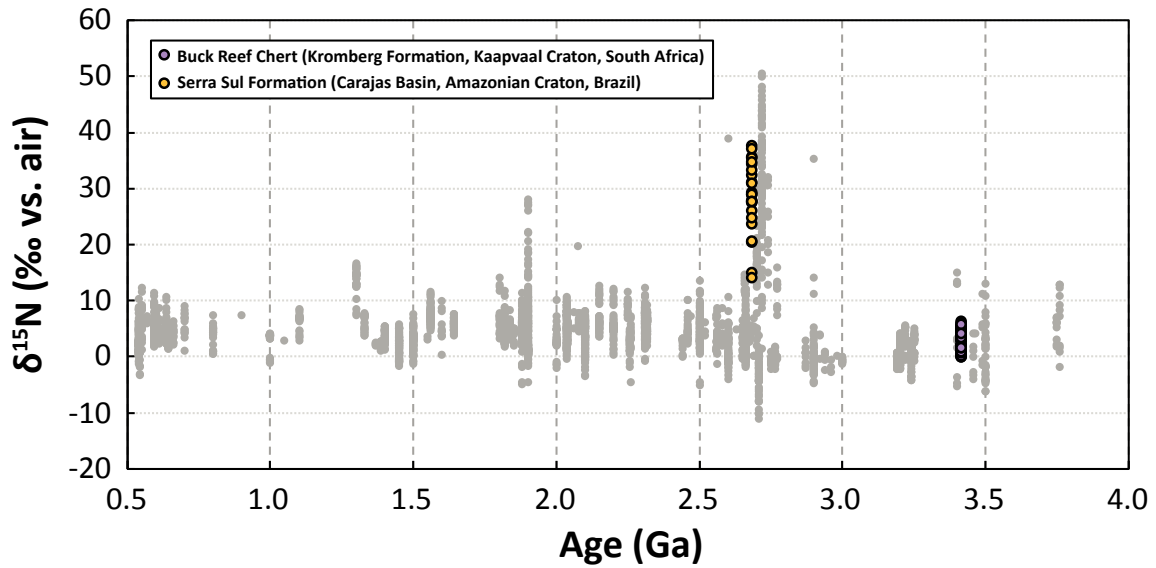


Fig. 7.0. Nitrogen isotope signature of the Serra Sul Formation (orange) among all Precambrian sedimentary $\delta^{15}\text{N}$ data.

**CHAPTER 7. NEOARCHEAN OXYGEN-BASED NITROGEN CYCLE EN ROUTE
TO THE GREAT OXIDATION EVENT**

<i>Abstract</i>	239
7.1. Nitrogen isotopes record water column oxidation.....	239
7.2. Extreme positive $\delta^{15}\text{N}$ values unique to the Neoproterozoic sedimentary record	240
7.3. Defining a Nitrogen Isotope Event (NIE).....	243
7.4. A transitional state in the evolution of the N-biogeochemical cycle	246
7.5. From the NIE to the GOE	248
7.6. Methods.....	250
7.7. Supplementary Information	252
7.7.1. Geological context of the Serra Sul and Tumbiana Formations	256
7.7.2. Studied drill-cores.....	257
7.7.3. Preservation of the primary N isotope signature.....	261
References.....	262

CHAPTER 7. NEOARCHEAN OXYGEN-BASED NITROGEN CYCLE EN ROUTE TO THE GREAT OXIDATION EVENT

Abstract

The nitrogen isotopic composition of sedimentary rocks ($\delta^{15}\text{N}$) can be used to trace redox-dependent biological pathways and early Earth oxygenation (Ader et al., 2016; Stüeken et al., 2016). Previous studies reported extremely positive $\delta^{15}\text{N}$ values in rocks deposited between 2.8 and 2.6 Ga, but their origin and spatial extent remains uncertain (Stüeken et al., 2015; Thomazo et al., 2011). Here we report a new occurrence of extremely positive $\delta^{15}\text{N}$ values ($> 30\%$) in the ca. 2.68 Ga old shallow to deep marine sedimentary deposit of the Serra Sul Formation (Rossignol et al., 2020), Amazonian Craton, Brazil. These results are best explained by regionally variable extents of ammonium oxidation to N_2 or N_2O tied to a cryptic oxygen cycle, implying that oxygenic photosynthesis was operating 2.7 Ga ago. Molecular oxygen production likely shifted the redox potential so that an intermediate N cycle based on ammonium oxidation developed well before nitrate accumulation in surface waters. We propose to name this unique period, when extreme positive nitrogen isotopic compositions are superimposed to the usual range of Precambrian $\delta^{15}\text{N}$ values, the Nitrogen Isotope Event (NIE). We suggest that it marks the earliest steps of the major biogeochemical reorganizations that led to surface waters and subsequent atmospheric oxygenation, the so-called Great Oxidation Event.

Nitrogen isotopes record water column oxidation

Nitrogen is an essential nutrient for the biosphere, exerting a strong control on biological productivity through the availability of its “fixed” bioavailable forms, including ammonium (NH_4^+), nitrite (NO_2^-) and nitrate (NO_3^-), which can all be readily uptaken by primary producers. The nitrogen isotope composition ($\delta^{15}\text{N} = [({}^{15}\text{N}/{}^{14}\text{N})_{\text{sample}}/({}^{15}\text{N}/{}^{14}\text{N})_{\text{standard}}] - 1$) of these nitrogen forms is controlled by microbially-mediated metabolic reactions, most of them sensitive to the redox state of the water column. When assimilated, N species transfer their isotope signature to the organic matter, which can subsequently be preserved in sedimentary rocks (Altabet and Francois, 1994). Nitrogen isotopes in the sedimentary record thus represent an ideal tool for investigating the joint temporal evolution of surface environments oxidation and primary productivity.

Despite being largely present in the atmosphere as gaseous N_2 ($\delta^{15}N=0\text{‰}$), nitrogen in this form can only be assimilated by diazotrophs, nitrogenase-bearing prokaryotes capable of biological N_2 fixation. Fractionation imparted by biological N_2 fixation with classical Mo-based nitrogenase ranges from -2‰ to $+2\text{‰}$, whereas alternative nitrogenase using Fe or V as cofactors can impart negative fractionation as large as -8‰ (Zhang et al., 2014). The mineralization of organic matter derived from diazotrophic activity in the water column or in sediments, namely ammonification (Sigman et al., 2009), provides most of the bioavailable nitrogen to the biosphere as ammonium (NH_4^+) without significant isotope fractionation (Möbius, 2013). In anoxic conditions, ammonium released during organic matter mineralization is rapidly and quantitatively assimilated into the biomass. Hence, even if ammonium assimilation preferentially incorporates ^{14}N , its fractionation is rarely expressed in the sedimentary record. In oxic conditions, ammonium can either be assimilated or nitrified to nitrite and nitrate, enriching residual ammonium by up to $+35\text{‰}$ (Mariotti et al., 1981). In modern environments, where oxygen levels are in excess, ammonium is oxidized quantitatively, preventing the fractionation associated with ammonium oxidation from being expressed. Nitrite and nitrate are in turn assimilated by photosynthetic organisms or biologically reduced, either through denitrification or anaerobic ammonium oxidation (anammox) in dysoxic and anoxic conditions (Dalsgaard and Thamdrup, 2002; Sigman et al., 2009). Denitrification and anammox are the major oceanic sinks of fixed nitrogen, releasing N_2O or N_2 back to the atmosphere. Both of these sinks impart a large nitrogen isotope fractionation of around $+30\text{‰}$ (Sigman et al., 2009), leaving behind ^{15}N -enriched residual nitrate that can be uptaken by primary producers and subsequently transferred to the sediments. In modern environments, and by extension any sediment deposited under oxic conditions, $\delta^{15}N$ values around $+5\text{‰}$ are interpreted to reflect the balance between N_2 fixation inputs and denitrification/anammox outputs from the water column and surface sediments.

Extreme positive $\delta^{15}N$ values unique to the Neoproterozoic sedimentary record

The secular evolution of sedimentary $\delta^{15}N$ values shifts from a mode of $+2\text{‰}$ between 3.8 and 2.8 Ga in the Archean to a mode of $+5\text{‰}$ between 2.5 and 1.8 Ga (Ader et al., 2016). Based on this framework, and assuming that (i) atmospheric N_2 isotope composition ($\delta^{15}N_{N_2}=0\text{‰}$) has remained stable since the Paleoproterozoic (Marty et al., 2013; Nishizawa et al., 2007), and that (ii) N_2 assimilation through biological nitrogen fixation provides the fixed-N source needed to sustain biomass production since at least 3.2 Ga (Stüeken et al., 2015; Stüeken et al., 2016), this

evolution has mostly been attributed to a major change in the nitrogen biogeochemical cycle. From being ammonium-dominated in the essentially anoxic Archean oceans and lakes, including in their surface waters, the N-biogeochemical cycle would have evolved to nitrate-dominated after 2.5 Ga in transiently oxic surface waters of oceans and lakes (Ader et al., 2016; Garvin et al., 2009; Godfrey and Falkowski, 2009; Kipp et al., 2018; Koehler et al., 2018; Stüeken et al., 2016; Zerkle et al., 2017). Intriguingly, there is no significant change in the sedimentary $\delta^{15}\text{N}$ record across the Great Oxidation Event (GOE, e.g. Lyons et al., 2014; Fig. 7.1A), which is widely considered as the most prominent redox change in the Earth history. This argues for a temporal decoupling between the emergence of the first oxygen-based oxidative pathway of the biogeochemical nitrogen cycle and the accumulation of free oxygen in the atmosphere after 2.5 Ga.

The transition between both states (occurring in the 2.8-2.6 Ga time interval), displays strongly positive $\delta^{15}\text{N}$ values (between +10 and +50‰, Fig. 7.1A) recorded in sedimentary rocks deposited between 2.8 and 2.6 Ga in at least 5 different locations (Beaumont and Robert, 1999; Jia and Kerrich, 2004; Kerrich et al., 2006; E. E. Stüeken et al., 2015, 2017; Thomazo et al., 2011; Supplementary Table S1). They have been interpreted in various ways (Supplementary Table S1), including: (i) metamorphic alteration of the original isotopic signature (Beaumont and Robert, 1999), (ii) a ^{15}N -enriched atmospheric reservoir derived from chondrite-like material (Jia and Kerrich, 2004; Kerrich et al., 2006), (iii) the onset of an oxidative pathway in the nitrogen cycle, arguing for the presence of cryptic oxygen in an otherwise anoxic ocean, prior to the oxygenation of the atmosphere (Thomazo et al., 2011), and more recently (iv) NH_3 degassing from alkaline waters of restricted lacustrine environments (Stüeken et al., 2015, 2017). This latter hypothesis has gained momentum because the most positive $\delta^{15}\text{N}$ values reported so far are associated with extreme negative $\delta^{13}\text{C}_{\text{org}}$ values (Hayes, 1994; Fig. 7.1B) and stem from the Tumbiana Formation in the Pilbara Craton, now firmly demonstrated to have been deposited in an alkaline lake (Awramik and Buchheim, 2009). Yet it implies that the relative synchronicity of these positive $\delta^{15}\text{N}$ values and their occurrence right at the transition between the two $\delta^{15}\text{N}$ distribution modes would have happened incidentally.

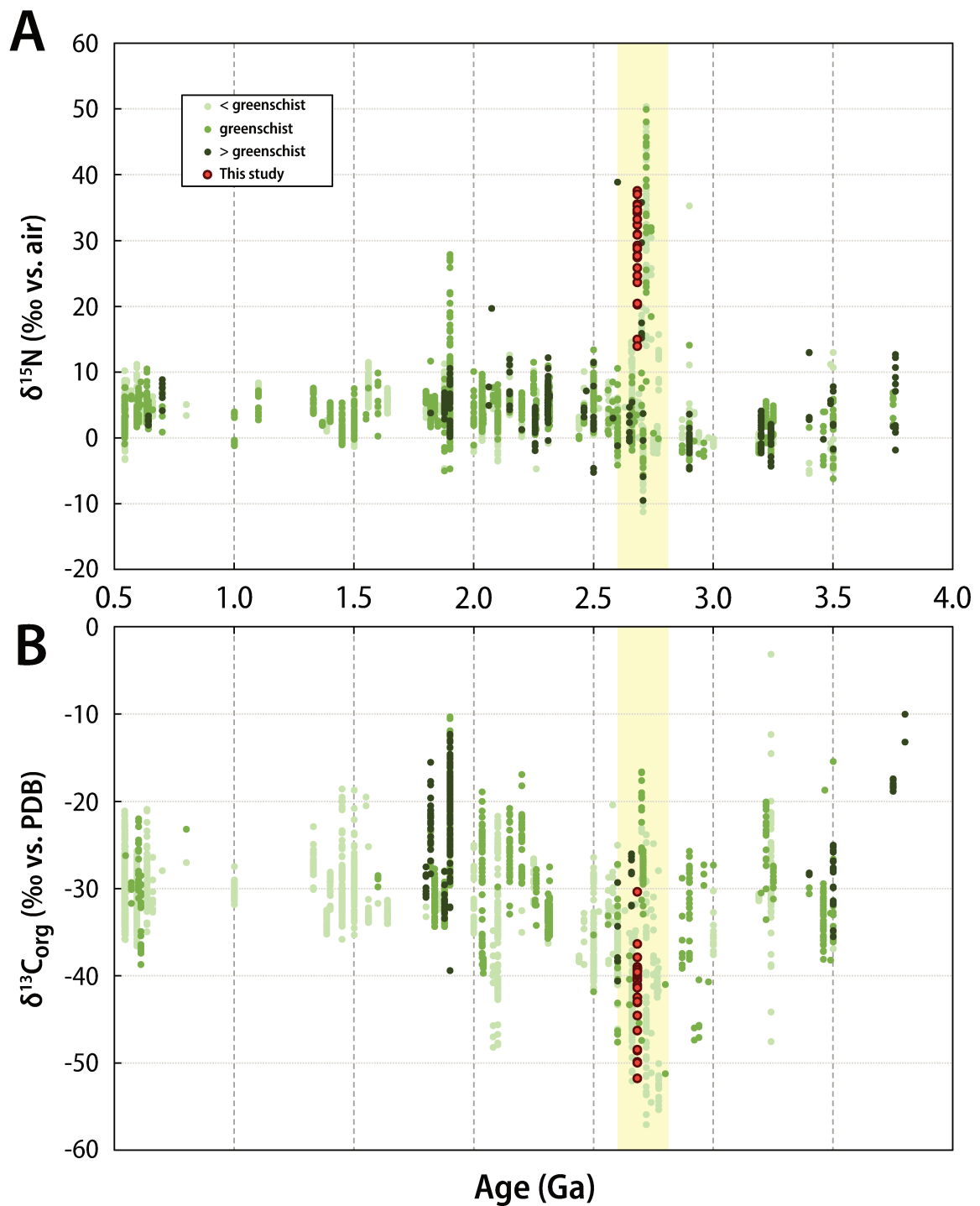


Fig. 7.1. Compilation of paired Precambrian sedimentary $\delta^{15}\text{N}$ (a) and $\delta^{13}\text{C}_{\text{org}}$ (b) data, including all lithologies. The different colors represent the various metamorphic grades (lower than greenschist (light green), greenschist (medium green), higher than greenschist (dark green) facies). The studied samples are represented by circled red dots. They experienced only limited metamorphic conditions, not higher than greenschist facies.

Here we take the opportunity of the discovery of a new occurrence of extreme $\delta^{15}\text{N}$ and $\delta^{13}\text{C}_{\text{org}}$ values from the Serra Sul Formation, Amazonian Craton, Brazil, deposited between 2684 ± 10 Ma and 2627 ± 11 Ma (Perelló et al., 2023; Rossignol et al., 2021, 2020), to reassess the significance of these positive $\delta^{15}\text{N}$ values. This Neoproterozoic formation is representative of a marine shelf system with a sedimentary sequence ranging from shallow to deep-water environments with slope instabilities and debris flow (Rossignol et al., 2020; Supplementary Information). Two drill cores intercepting the Serra Sul Formation, GT13 and GT16 (Supplementary Information, Supplementary Fig. S4), were studied. They display polygenic and flat-pebbles conglomerates interbedded with fine-grained siliciclastic sediments (Rossignol et al., 2020) indicating the presence of sediments from both shallow and deep water environments, respectively (Fig. 7.2; Supplementary Information; Supplementary Fig. S4).

Organic carbon and nitrogen concentrations and isotopic compositions for the two studied drill cores are reported in Table 1, Fig. 7.1 and Fig. 7.2. For both drill cores, $\delta^{15}\text{N}$ values are markedly positive, from +13.9 to +37.5‰, with mean values of $+32.9 \pm 3.4\text{‰}$ ($n = 11$) and $+24.6 \pm 6.0\text{‰}$ ($n = 13$) for GT13 and GT16, respectively. $\delta^{13}\text{C}_{\text{org}}$ values are ^{13}C -depleted, ranging from -30.4 to -51.8‰, with comparable mean values ($-40.0 \pm 1.2\text{‰}$ for GT13 and $-44.1 \pm 6.1\text{‰}$ for GT16). Overall, carbon and nitrogen concentrations and isotopic compositions appear relatively homogeneous throughout drill core GT13, compared to the more scattered signal in drill core GT16. No variations were observed with respect to lithological features or facies changes (Fig. 7.2).

Defining a Nitrogen Isotope Event (NIE)

Overall, despite different geological settings, depositional environments, and paleogeography, this new occurrence of a paired $\delta^{15}\text{N}$ - $\delta^{13}\text{C}_{\text{org}}$ excursion recorded in the Amazonian Craton is within the range of the one reported in the Pilbara Craton, suggesting that these extremely positive $\delta^{15}\text{N}$ values are inherent to the 2.8-2.6 Ga time interval. Importantly, since these extreme values coexist with $\delta^{15}\text{N}$ values falling within the usual range for the sub-greenschist facies Archean record (Fig. 7.1; i.e. roughly from -1 to +6‰, Ader et al., 2016), regional controls must be at play. This extreme range of $\delta^{15}\text{N}$ values seems to be unique in the geological record and we propose to single it out as the Nitrogen Isotope Event (NIE).

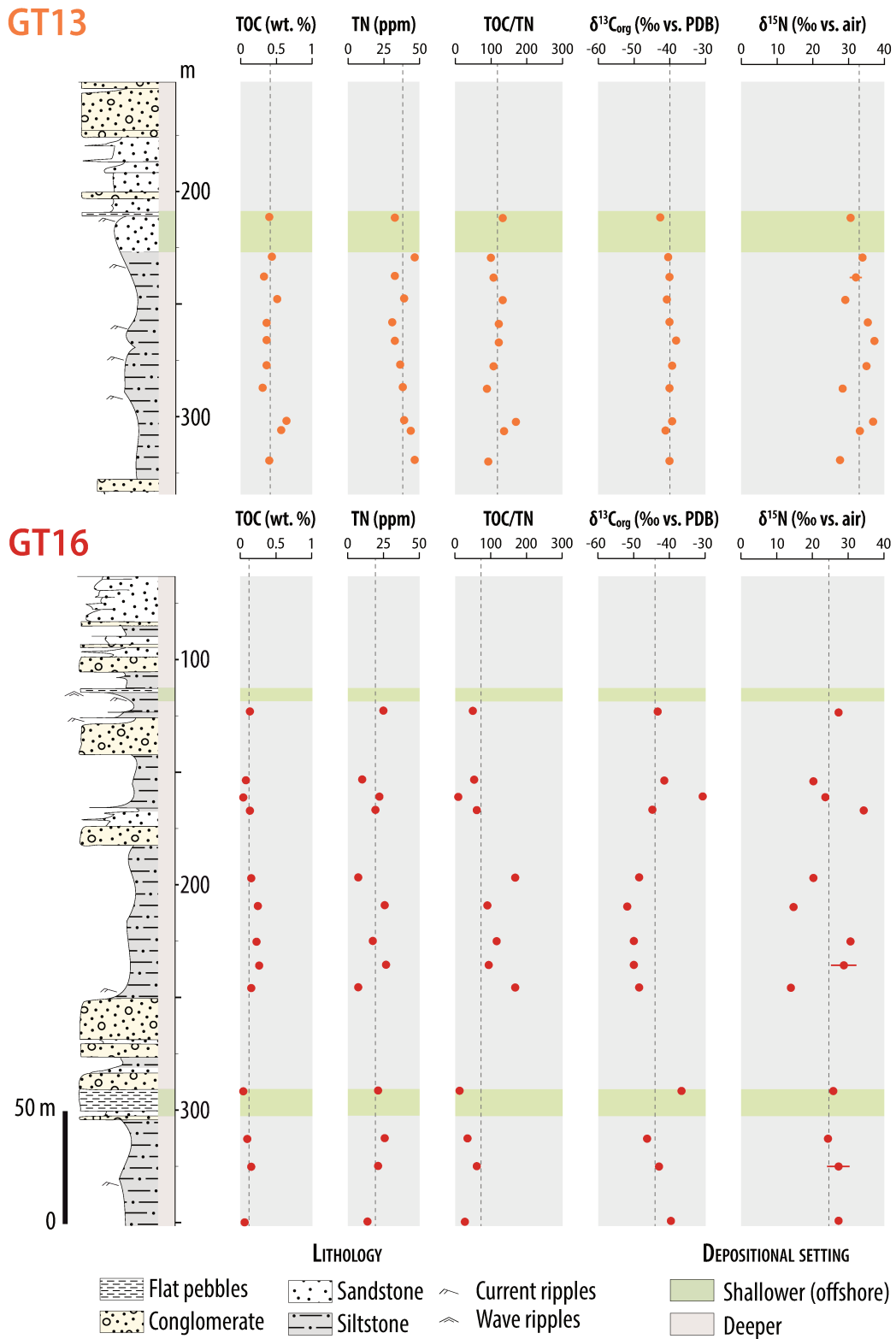


Fig. 7.2. Carbon and nitrogen geochemical and isotopic profiles for drill cores GT13 and GT16. Stratigraphic logs simplified from Rossignol et al. (2020). Dotted lines correspond to mean values.

Drill core	Depth (m)	TOC (wt. %)	SD	Nb repl.	TN (ppm)	SD	Nb repl.	TOC/TN	$\delta^{13}\text{C}_{\text{org}}$ (‰ vs. PDB)	SD	Nb repl.	$\delta^{15}\text{N}_{\text{bulk}}$ (‰ vs. air)	SD	Nb repl.
GT13	211.45	0.42	0.108	2	32	5	2	132	-42.5	0.23	2	30.9	0.4	2
GT13	229.27	0.45	0.009	2	46		1	97	-40.2	0.05	2	34.2		1
GT13	237.735	0.34	0.006	2	32	2	2	107	-40.0	0.05	2	32.3	1.6	2
GT13	247.82	0.52	0.025	2	39		1	133	-40.5	0.23	2	29.2		1
GT13	258.165	0.38	0.013	2	31		1	121	-40.0	0.07	2	35.5		1
GT13	266.32	0.38	0.010	2	32		1	119	-37.9	0.08	2	37.5		1
GT13	277.175	0.38	0.015	2	36		1	106	-39.0	0.04	2	35.3		1
GT13	287.305	0.33	0.004	2	38		1	88	-40.0	0.18	2	28.7		1
GT13	301.81	0.65	0.015	2	39		1	167	-39.3	0.19	2	37.0		1
GT13	306.175	0.58	0.001	2	43	1	2	135	-41.1	0.07	2	33.2	0.1	2
GT13	319.46	0.42	0.009	2	46		1	92	-39.8	0.08	2	27.7		1
GT16	122.05	0.13		1	25		1	51	-43.1		1	27.4		1
GT16	152.775	0.06	0.003	2	11	1	2	54	-41.4	0.21	2	20.2	0.4	2
GT16	159.885	0.02	0.002	2	23		1	8	-30.4	0.08	2	23.6		1
GT16	166.05	0.12	0.000	2	20		1	61	-44.6	0.01	2	34.6		1
GT16	195.97	0.13	0.002	2	8		1	166	-48.6	0.07	2	20.4		1
GT16	208.61	0.24	0.001	2	26		1	91	-51.8	0.03	2	14.9		1
GT16	224.11	0.21	0.002	2	18		1	115	-49.9	0.52	2	30.8		1
GT16	234.725	0.25	0.024	2	27	3	2	94	-50.0	1.73	2	28.8	3.5	2
GT16	244.845	0.13	0.002	2	8		1	167	-48.5	0.21	2	13.9		1
GT16	290.835	0.03	0.000	2	22		1	14	-36.4	0.48	2	25.8		1
GT16	312.005	0.09	0.001	2	26		1	35	-46.3	0.09	2	24.6		1
GT16	324.595	0.14	0.010	2	22	4	2	62	-43.0	0.67	2	27.5	3.1	2
GT16	348.805	0.04	0.007	2	14		1	27	-39.6	0.54	2	27.6		1

Table 7.1. Data featuring drill core ID, sample depth (m), TOC (wt. %, wholerock), TN (ppm, wholerock), TOC/TN, $\delta^{13}\text{C}_{\text{org}}$ (‰ vs. PDB), and $\delta^{15}\text{N}_{\text{bulk}}$ (‰ vs. air), for all samples analyzed along the GT13 and GT16 drill cores. Standard deviation (SD) and number of replicates (Nb repl.) are given for all parameters.

In order to investigate the nature of this NIE, we can first focus on the significance of the extremely positive $\delta^{15}\text{N}$ values, starting with the reassessment of previously proposed hypotheses. The hypothesis of a ^{15}N -enriched atmospheric reservoir derived from chondrite-like material (Jia and Kerrich, 2004; Kerrich et al., 2006) can be ruled out because (i) such a contribution from ^{15}N -enriched extraterrestrial material should be observed well before 2.8 Ga (Fig. 7.1) and (ii) the abundance of $\delta^{15}\text{N}$ extreme values should decrease with time, in contrast with the unique sharp peak recorded between 2.8 and 2.6 Ga (Fig. 7.1). Furthermore, while micrometeorites have been reported in the Tumbiana Formation (Tomkins et al., 2016), there is no evidence for contribution of extraterrestrial material within the Serra Sul Formation.

Several lines of evidence can also be used to rule out metamorphic alteration as the mechanism responsible for extreme $\delta^{15}\text{N}$ values, at least in the Serra Sul Formation. Indeed, no known diagenetic, metamorphic or hydrothermal process has the capacity to enrich sedimentary nitrogen in ^{15}N to an extent of more than 10‰ (Ader et al., 2016; Stüeken et al., 2021a), while $\delta^{15}\text{N}$ values in the Serra Sul Formation range from +14 to +38‰. Moreover, metamorphism in the Serra Sul Formation does not exceed the greenschist facies (Supplementary Information), implying a negligible impact of post-depositional processes on the studied samples (Figueiredo

e Silva et al., 2020; Martins et al., 2021). Last but not least, no correlations were observed between Total N content (TN) and $\delta^{15}\text{N}$ ($R^2 < 0.14$), Total Organic Carbon content (TOC)/TN ratios and $\delta^{15}\text{N}$ ($R^2 < 0.20$), or $\delta^{15}\text{N}$ and $\delta^{13}\text{C}_{\text{org}}$ ($R^2 < 0.26$) (Supplementary Fig. S1).

Finally, the hypothesis of positive ammonium $\delta^{15}\text{N}$ values resulting from NH_3 degassing at high pH (Stüeken et al., 2015, 2017) proposed as an explanation for extreme $\delta^{15}\text{N}$ values in the 2.72 Ga Tumbiana Formation does not hold for the Serra Sul Formation, unless the ocean also had a high pH at the time. Indeed, at $\text{pH} > 9.2$, NH_4^+ dissociates to NH_3 , which can degas to the atmosphere with a strong isotope fractionation (+45‰ at 23°C, Li et al., 2012). When assimilated, the residual ^{15}N -enriched NH_4^+ transfers its signature to the organic matter, which can subsequently be preserved in sedimentary rocks. Although such strong fractionations have never been recorded in modern alkaline environments, this hypothesis is well suited for the Tumbiana Formation, which was deposited in a restricted lacustrine setting with a substratum made of alkaline rocks (Awramik and Buchheim, 2009). The abiotic loss of nitrogen from the water column caused by ammonia degassing also provides a consistent explanation for the low TN and high TOC/TN of sediments from this formation (Stüeken et al., 2015). However, samples from the Serra Sul Formation analyzed here neither show a strong TN depletion compared to other Neoproterozoic sedimentary rocks, nor any evidence of being deposited under a highly alkaline water column. They are representative of shallow to deep marine depositional environments, with neither evaporitic facies nor carbonates (Supplementary Information). If we assume that the ocean pH at the time was lower than 9.2 (Halevy and Bachan, 2017), NH_3 degassing cannot solely account for the extremely positive $\delta^{15}\text{N}$ values of the Serra Sul Formation.

Accordingly, none of these hypotheses can explain the NIE. The only one left to explore is a change in the biological nitrogen cycle, which is shown from today's sedimentary record (Tesdal et al., 2013) and likely also in the Precambrian (Ader et al., 2016), to be regionally controlled.

A transitional state in the evolution of the N-biogeochemical cycle

Only a few metabolic pathways of the N-biogeochemical cycle can lead to a ^{15}N -enrichment of fixed nitrogen species. N_2 fixation with classic Fe-Mo nitrogenase does not impart any significant fractionation (Sigman et al., 2009), and Fe-Fe or Fe-V alternative nitrogenases generate organic matter with a negative $\delta^{15}\text{N}$ (Zhang et al., 2014). Ammonification has a

negligible impact on the $\delta^{15}\text{N}$ (Sigman et al., 2009). Partial biological assimilation of NH_4^+ can enrich organic matter in ^{14}N ($\epsilon \approx -4\text{‰}$ to -27‰ , Hoch et al., 1992) if the pool of ammonium is progressively distilled but not quantitatively consumed (Papineau et al., 2009). However, the expected distribution of $\delta^{15}\text{N}$ values following partial assimilation alone should be centered around 0‰ , displaying both the upwelled ^{15}N -depleted and the sinking ^{15}N -enriched pools of ammonium. This mechanism has been proposed to explain a single set of Neoproterozoic $\delta^{15}\text{N}$ values (Yang et al., 2019), yet the two complementary fractions have never been recovered from the same study site. Our reported $\delta^{15}\text{N}$ data from the Serra Sul Formation are centered around $+28\text{‰}$, with no negative values (Fig. 7.2). Therefore, they are inconsistent with the distillation of an NH_4^+ reservoir by a simple assimilation process. None of the above-mentioned pathways can produce the extremely positive $\delta^{15}\text{N}$ values recorded in the Serra Sul Formation. An oxidative pathway that strongly fractionates N isotopes must therefore have been at play.

The strongly fractionating metabolism commonly considered for the moderately positive $\delta^{15}\text{N}$ values recorded from 2.5 Ga onwards is non-quantitative denitrification (Garvin et al., 2009; Godfrey and Falkowski, 2009; Kipp et al., 2018; Koehler et al., 2018), which in the modern ocean occurs in dysoxic parts of the water column. It requires both nitrification and a large and consistently oxic surface water layer where nitrate can accumulate. In this case, it is the isotope composition of the enriched residual nitrate that is expressed and recorded in the sediments. Although denitrification can induce isotope fractionation by as much as 30‰ in nitrate-replete conditions (Saitoh et al., 2023), the observed range of $\delta^{15}\text{N}$ values should be significantly smaller, as it depends on the isotope mass balance between N_2 -fixation and denitrification in Oxygen Minimum Zones (OMZs) or sediments. As an example, in the modern ocean where nitrate is stable both in the photic zone and in deeper waters, and thus not fully denitrified, $\delta^{15}\text{N}$ values only reach up to $+15\text{‰}$ in OMZs (Saitoh et al., 2023; Sigman et al., 2009; Tesdal et al., 2013).

For both drill-core samples of the Serra Sul Formation, ammonium is expected to be the dominant fixed nitrogen species (Canfield et al., 2010). We thus propose a scenario where the mechanism responsible for the positive $\delta^{15}\text{N}$ values is ammonium oxidation to N_2 , N_2O , or NO_2^- , tied to a cryptic oxygen cycle. Ammonium oxidation isotope fractionation can reach up to $+55\text{‰}$ when ammonium is co-oxidized with methane by methanotrophs (Mandernack et al., 2009) and up to $+38\text{‰}$ when ammonium is oxidized by ammonium-oxidizing bacteria and archaea (Casciotti, 2009). Importantly, as for denitrification, the isotope expression of this oxidative pathway requires ammonium oxidation to be non-quantitative.

In the anoxic ocean of the early Neoproterozoic, ammonium oxidation can only take place in the photic zone where photosynthesis occurs and generates the electrochemical potential necessary to oxidize ammonium. In this photic zone, ammonium oxidation must be in competition with ammonium assimilation, since photosynthesizers require N for their growth. From there, several cases can be envisioned. If photosynthesis hardly generates the necessary oxidants for ammonium oxidation, then ammonium is essentially assimilated by photosynthesizers and, depending on its rate of assimilation, its ^{15}N -enrichment will be low to null. ^{15}N -depletion can even happen, which may explain the slightly negative $\delta^{15}\text{N}$ values reported during the NIE (Yang et al., 2019). If photosynthesis generates enough oxidants to oxidize much of the ammonium before it can be assimilated, ^{15}N -enrichments will also be low or null as N would be supplied by N_2 -fixation. As a result, a nitrogen cycle comprising the different pathways of ammonium oxidation to gaseous N-species continuously escaping the system can generate all the range of $\delta^{15}\text{N}$ values reported during the NIE, from mildly negative to extremely positive depending on regional controls on primary productivity and ammonium supply.

In summary, similarly to nitrate-dominated environments where $\delta^{15}\text{N}_{\text{NO}_3^-}$ values are regionally controlled (ranging from 0 to 15‰) and depend on the mass and isotope balance between N sources (N_2 -fixation and nitrate supply) and N sinks (denitrification in the water column, in the sediments and nitrate assimilation), in an ammonium-dominated environment, the $\delta^{15}\text{N}_{\text{NH}_4}$ values would depend on the mass and isotope balance between N_2 -fixation, ammonium supply, ammonium oxidation and ammonium assimilation. The extreme range of $\delta^{15}\text{N}$ values recorded in the Tumbiana Formation is even better explained by ammonia degassing occurring alongside ammonium oxidation, which together could drive $\delta^{15}\text{N}$ values up to +50‰.

From the NIE to the GOE

For such a transitional state to occur during the Neoproterozoic, photosynthesis must have been generating oxidants able to oxidize ammonium into volatile gaseous species. Most metabolic pathways oxidizing ammonium need O_2 . Even canonical anaerobic ammonium oxidation (anammox) requires the presence of nitrite, which cannot be produced without O_2 (Grotzinger and Kasting, 1993). In a fully anoxic world, in the absence of oxygenic photosynthesis, only the Feammox reaction has been suggested as a biological mechanism associated with ammonium oxidation (Pellerin et al., 2023). However, this pathway has been substantiated for

iron-rich depositional environments and associated with only slightly positive $\delta^{15}\text{N}$ values (Pellerin et al., 2023).

Dioxygen is therefore necessary to account for ammonium oxidation during the NIE. The preservation of a S-MIF signal in both the Serra Sul and Tumbiana sediments (Bouyon et al., 2018; Thomazo et al., 2009) indicates, however, that free O_2 was not accumulating in the ocean and atmosphere at that time. Free O_2 must have been present at a low level but in sufficient amounts to fuel ammonium oxidation. Indeed, in modern nitrite-rich anoxic marine zones (AMZs), ammonium oxidation occurs at nanomolar oxygen concentrations, compatible with anoxic surrounding waters (Ulloa et al., 2012). The overall low levels of O_2 would also prevent the accumulation of nitrate if any was formed, which would have been quantitatively converted into N_2 or N_2O .

This intermediate state of the N-cycle would have ended progressively as O_2 supply in the photic zone surpassed ammonium supply. With increasing O_2 concentrations, ammonium oxidation would have proceeded up to nitrate production in dysoxic surface water masses. As their size grew, these dysoxic surface water masses became connected, and extended deeper than the photic zone. Nitrate was able to accumulate, turning the N-cycle to a new steady state where denitrification and anammox became the main drivers of the $\delta^{15}\text{N}$ sedimentary record.

We conclude that the extreme range of nitrogen isotope signatures recorded in the 2.8-2.6 Ga time interval reflect micro-aerobic conditions prone to the emergence of ammonium oxidation. The NIE would thus mark the emergence of biological oxidative nitrogen cycling in surface oceans transitioning from fully anoxic to coexisting anoxic and dysoxic water masses and might underline one of the very first steps of the GOE.

Methods

Sampling. Twenty-four samples were chosen along the two studied drill cores (11 samples for drill core GT13 and 13 samples for drill core GT16) according to their organic matter content (TOC > 0.02% in the digestion residue), that mostly reflects their potential in containing enough nitrogen for analysis.

Chemical treatment prior to C and N analyses. Samples were first crushed into powder using a ring and puck mill in order to obtain sample powder smaller than 60 μm . Carbonate-free residues were obtained by mixing sample powders with 6N HCl for two successive digestion steps: first at room temperature for 24h, then at 80°C for 4h. Samples were then rinsed with deionized distilled water to a neutral pH and oven-dried at 40°C for 48h.

C isotopic analyses. The decarbonated residues were poured into tin capsules (50 to 80 mg of powder) and weighted using a Sartorius M2P ultra-balance before TOC and $\delta^{13}\text{C}_{\text{org}}$ measurements were performed using a Thermo Fisher Scientific Flash Smart elemental analyser, coupled to a Thermo Fisher Scientific Delta V isotope ratio mass spectrometer (EA-IRMS) via a ConFlo IV interface. Certified USGS40 ($\delta^{13}\text{C}_{\text{org}} = -26.39\text{‰}$, TOC = 40.82 wt.%) and caffeine IAEA-600 ($\delta^{13}\text{C}_{\text{org}} = -27.77\text{‰}$, TOC = 49.48 wt.%) reference materials were used for the calibration. Total organic carbon (TOC) contents are expressed in dry weight percentage (wt.%) of the non-decarbonated bulk powder and isotope results are reported in delta-notation relative to V-PDB. Each measurement session included three to four standards measurements at the beginning and at the end, as well as one standard measurement every 12 samples. The mean $\delta^{13}\text{C}_{\text{org}}$ precision for standards is better than 0.35‰ and the mean accuracy better than 0.28‰. Each sample was duplicated. The mean external reproducibility (2σ), based on sample replicate analyses and including powder resampling and reprocessing via chemical treatment, is ± 0.012 wt.% for the TOC content and $\pm 0.26\text{‰}$ for the $\delta^{13}\text{C}_{\text{org}}$.

N isotopic analyses. As all samples contain less than 50 ppm N, the EA-IRMS method applied for carbon analyses is not sensitive enough for reliable bulk nitrogen isotopic analyses (Ader et al., 2016; Boocock et al., 2020). Samples were therefore analyzed at IPGP using the “classical sealed-tube combustion method” as described in Ader et al. (2014, 2016). In brief, N_2 was produced offline through sealed-tube Dumas combustion and cryogenically purified in a vacuum line. Up to 400 mg of decarbonated residual powder was put into a quartz tube with CuO and Cu wires, purified beforehand at 900°C for 2h in a muffle furnace to prevent

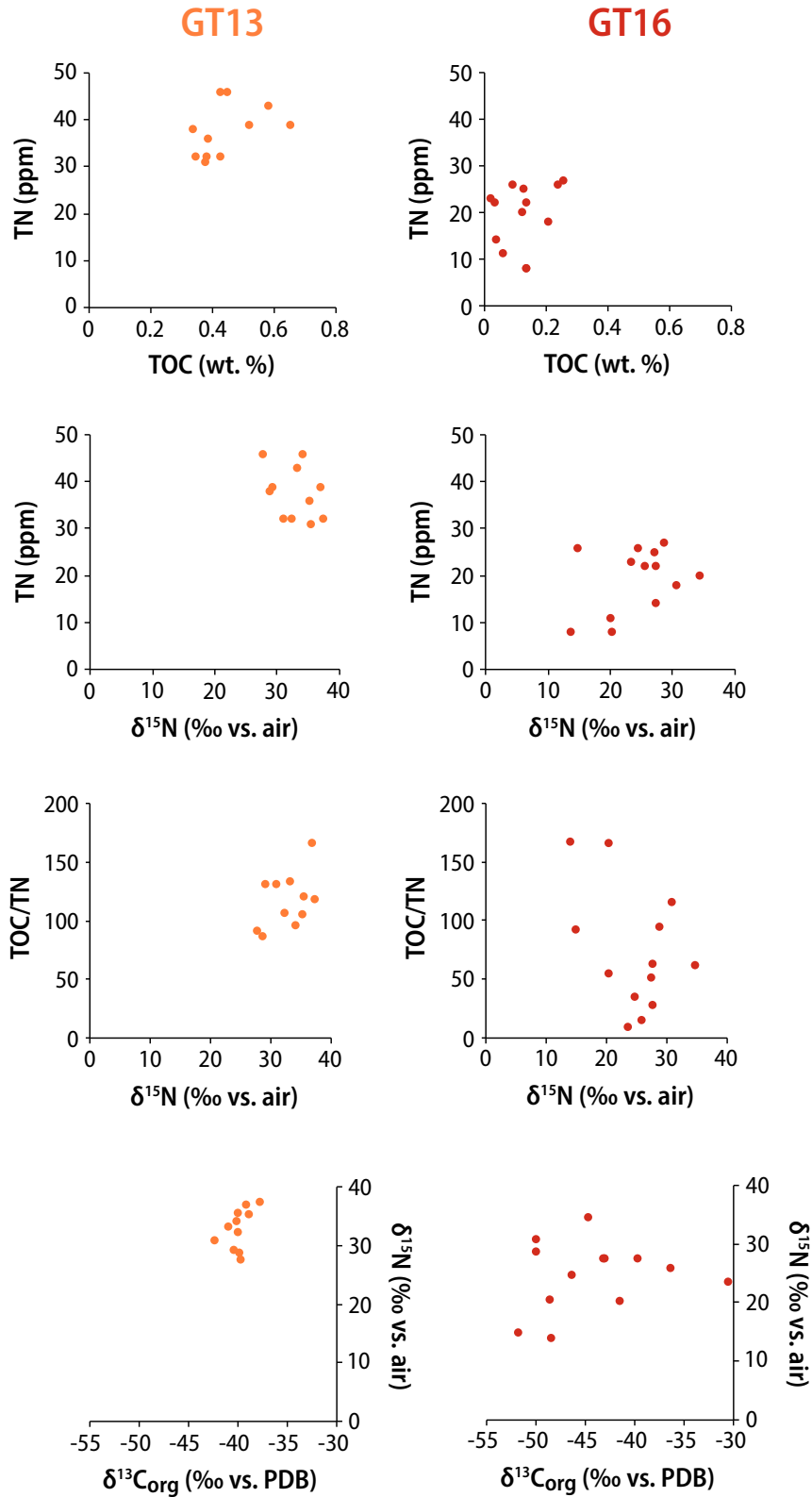
contamination. Samples were degassed for 12h at 150°C under vacuum to remove adsorbed atmospheric N₂ and organics. Quartz tubes were then sealed directly under vacuum and combusted in a muffle furnace at 950°C for 6h under oxidizing conditions by oxygen liberated from the CuO wires, then cooled at 600°C for 2h, allowing residual oxygen to combine with cupric oxide and nitrous oxide to be reduced by copper, and finally cooled to ambient temperature (Kendall and Grim, 1990). The extraction yield for this protocol is 100% for both organic and mineral nitrogen (Busigny et al., 2005), including ammonium in minerals such as phyllosilicates. The content of each quartz tube was released in the vacuum line with a tube cracker, where CO₂ and H₂O were trapped cryogenically to avoid any subsequent isobaric interferences. The purified incondensable N₂ gas was concentrated into a calibrated volume for quantification using a Toepler pump (Hg manometer). Standard analytical procedures for nitrogen usually include CaO in the reagents to trap gaseous CO₂ and H₂O from the samples (Kendall and Grim, 1990). Given that the addition of CaO significantly contributes to analytical blanks (Busigny et al., 2005), we performed a few tests which show that the addition of CaO does not yield significant $\delta^{15}\text{N}$ differences (Chapter 5). Samples were consequently analyzed without the addition of CaO. Purified N₂ was analyzed by dual-inlet mass spectrometry using a ThermoFinnigan DeltaPlus XP IRMS. Possible air contamination and isobaric interferences (due to CO) were monitored by scanning of m/z 12 (C from CO₂, CO, CH₄ or organic compounds), 18 (H₂O), 30 (C¹⁸O), 32 (O₂), 40 (atmospheric Ar) and 44 (CO₂). Analytical blanks for the entire procedure are <0.02 micromoles N, which represents a mean of 7% of the gas (17% of the gas for the smallest sample and less than 3% for more concentrated samples). TN and $\delta^{15}\text{N}$ values have been individually corrected from the blank contribution, using the reference blank value of $\delta^{15}\text{N} = -3.7\text{‰}$ measured by Busigny et al. (2005). On average, blank-corrected $\delta^{15}\text{N}$ values are 2.3‰ higher than their raw counterparts (from 1.2‰ to 3.9‰ higher). External $\delta^{15}\text{N}$ reproducibility ranged between 0.1 and 3.5‰ with a mean of $1.5 \pm 1.5\text{‰}$ ($n = 6$). Samples that were replicated are reported in Table 1.

Supplementary Information

Supplementary Table S1. Compilation of Neoproterozoic nitrogen isotope studies (from 2.90 to 2.66 Ga) featuring the age of studied samples, reference, location, mean and range of values for $\delta^{15}\text{N}$ (‰ vs. air), TN (ppm), $\delta^{13}\text{C}_{\text{org}}$ (‰ vs. PDB), TOC (%), TOC/TN, metamorphic grade, lithology, depositional environment and interpretation for the nitrogen isotopic signature.

TN (ppm)	$\delta^{15}\text{N}_{\text{org}}$ (‰ vs. PDB)	TOC (%)	TOC/TN	Metamorphism	Lithology	Depositional environment	Interpretation
TN = 7839 ppm (n=18) (range from 16 to 150 ppm)	$\delta^{15}\text{N}_{\text{org}}$ = -31.15±3.82‰ (n=20) (range from -38.10 to -25.70‰)	TOC = 0.30±0.16% (n=22) (range from 0.01 to 0.64%)	(TOC/TN) _{bulk} = 34±18 (n=18) (range from 3 to 60)	lower greenschist	shale	shallow marine above wave base	Fe and Mn redox indicate "oxygen oasis" but $\delta^{15}\text{N}$ data indicate a Mo-based diazotrophic biosphere with no evidence for an aerobic N cycling. O_2 levels deemed too low to have sustained a stable nitrate reservoir, possible nutrient limitation by P rather than N
TN = 40±20 ppm (n=7) (range from 17 to 67 ppm)	$\delta^{15}\text{N}_{\text{org}}$ = -35.86±3.71‰ (n=7) (range from -39.11 to -28.80‰)	TOC = 0.35±0.27% (n=7) (range from 0.03 to 0.75%)	(TOC/TN) _{bulk} = 114±92 (n=7) (range from 15 to 272)	greenschist	shale	fluvial and shallow marine	Biological N_2 fixation
TN = 29±7 ppm (n=10) (range from 16 to 40 ppm)	$\delta^{15}\text{N}_{\text{org}}$ = -53.33±1.61‰ (n=13) (range from -55.34 to -50.06‰)	TOC = 1.23±0.64% (n=13) (range from 0.16 to 2.23%)	(TOC/TN) _{bulk} = 561±269 (n=10) (range from 85 to 915)	sub-greenochist	silty mudrocks; siliclastic and silticlastic	non-marine, shallow ponds subject to evaporation; paleosols	Dominance of methanotrophy and NH_4^+ loss under alkaline conditions
TN = 22±3 ppm (n=3) (range from 19 to 25 ppm)	$\delta^{15}\text{N}_{\text{org}}$ = -36.26±7.33‰ (n=3) (range from -41.71 to -27.93‰)	TOC = 1.1±0.10% (n=3) (range from 0.01 to 0.19%)	(TOC/TN) _{bulk} = 604±7 (n=3) (range from 6 to 89)	Prehnite-pump. (<300°C)	sandstones and thin mudstones; conglomerates; siliclastic	open fluvio-lacustrine system	Biological N_2 fixation
TN = 16±4 ppm (n=17) (range from 9 to 22 ppm)	$\delta^{15}\text{N}_{\text{org}}$ = -40.76±1.02‰ (n=17) (range from -42.46 to -38.28‰)	TOC = 0.28±0.14% (n=17) (range from 0.03 to 0.48%)	(TOC/TN) _{bulk} = 191±69 (n=17) (range from 31 to 271)	sub-greenochist	sandstone	open, braided fluvial system; fluvio-lacustrine	Dominance of methanogenesis and biological N_2 fixation
TN = 22±8 ppm (n=10) (range from 10 to 35 ppm)	$\delta^{15}\text{N}_{\text{org}}$ = -35.88±5.04‰ (n=10) (range from -41.18 to -24.85‰)	TOC = 0.12±0.07% (n=10) (range from 0.03 to 0.26%)	(TOC/TN) _{bulk} = 65±30 (n=10) (range from 19 to 124)	Prehnite-pump. (<300°C)	sandstone	open fluvio-lacustrine system	Biological N_2 fixation
TN = 4±2 ppm (n=4) (range from 2 to 6 ppm)	$\delta^{15}\text{N}_{\text{org}}$ = -46.15±9.71‰ (n=4) (range from -54.49 to -32.42‰)	TOC = 0.05±0.03% (n=4) (range from 0.02 to 0.09%)	(TOC/TN) _{bulk} = 122±86 (n=4) (range from 78 to 286)	Prehnite-pump. (<300°C)	thin stromatolitic carbonate intercalated with shale and volcanoclastic material	shallow lacustrine; evaporitic	Dominance of methanotrophy and NH_4^+ loss under alkaline conditions
TN = 8±6 ppm (n=17) (range from 1 to 21 ppm)	$\delta^{15}\text{N}_{\text{org}}$ = -48.88±3.43‰ (n=17) (range from -57.07 to -43.90‰)	TOC = 0.28±0.22% (n=17) (range from 0.03 to 0.76%)	(TOC/TN) _{bulk} = 405±96 (n=17) (range from 256 to 589)	Prehnite-pump. (<300°C)	stromatolitic carbonate (calcite, shale, tuff, chert)	shallow lacustrine; closed evaporitic lakes	Dominance of methanotrophy and NH_4^+ loss under alkaline conditions; oxidative processes and multiple carbon fixation pathways
TN = 5±3 ppm (n=30) (range from 1 to 14 ppm)	$\delta^{15}\text{N}_{\text{org}}$ = -39.46±8.66‰ (n=30) (range from -55.90 to -23.80‰)	TOC = 0.15±0.09% (n=30) (range from 0.04 to 0.40%)	(TOC/TN) _{bulk} = 272±99 (n=30) (range from 119 to 1719)	Prehnite-pump. (<300°C)	carbonate, shale, siltstone	shallow water	^{15}N enrichments record the onset of nitrification coupled to the continuous removal of its derivatives (nitrite and nitrate) by denitrification; increase in the availability of electron acceptors and probably oxygen in the depositional environment
TN = 25±158 ppm (n=35) (range from 100 to 800 ppm)	$\delta^{15}\text{N}_{\text{org}}$ = -28.30±1.46‰ (n=42) (range from -32.90 to -25.60‰)	TOC = 0.54±0.32% (n=43) (range from 0.02 to 1.70%)	(TOC/TN) _{bulk} = 25±14 (n=25) (range from 6 to 60)	lowermost greenschist	shale, stromatolitic limestone	continental shelf; deep shelf settings below wave base	Dominantly anaerobic marine N cycle with a transient oxygen oasis above ammonium-rich ferruginous waters; NH_4^+ assimilation (locally non-limiting NH_4^+ concentrations, with 70-90% of the NH_4^+ assimilated)
TN = 56±17 ppm (n=3) (range from 46 to 76 ppm)	$\delta^{15}\text{N}_{\text{org}}$ = -16.97±0.55‰ (n=3) (range from -17.60 to -16.60‰)	TOC = 0.18±0.06% (n=3) (range from 0.15 to 0.25%)	(TOC/TN) _{bulk} = 38±0 (n=3) (range from 38 to 38)	greenschist	BIF	meta-volcanic unit	Metamorphic alteration of the $\delta^{15}\text{N}$ values
TN = 6±0 ppm (n=2) (range from 6 to 6 ppm)	$\delta^{15}\text{N}_{\text{org}}$ = -31.30±0% (n=2) (range from -31.30 to -31.30‰)			greenschist	chert		Shift of the $\delta^{15}\text{N}$ of sedimentary organic matter towards positive values from the early Archean to the Phanerozoic, linked to the evolution of the oxidation state of surface environments
TN = 5±0 ppm (n=2) (range from 5 to 5 ppm)	$\delta^{15}\text{N}_{\text{org}}$ = -47.40±0% (n=2) (range from -47.40 to -47.40‰)	TOC = 0.01±0% (n=2) (range from 0.01 to 0.01%)	(TOC/TN) _{bulk} = 28±0 (n=2) (range from 28 to 28)	prehnite-pump/late to lower greenschist	stromatolitic chert	shallow-water marine	Shift of the $\delta^{15}\text{N}$ of sedimentary organic matter towards positive values from the early Archean to the Phanerozoic, linked to the evolution of the oxidation state of surface environments
TN = 23±14 ppm (n=3) (range from 7 to 33 ppm)	$\delta^{15}\text{N}_{\text{org}}$ = -25.17±3.24‰ (n=3) (range from -28.90 to -23.10‰)	TOC = 0.01±0.01% (n=3) (range from 0.01 to 0.02%)	(TOC/TN) _{bulk} = 6±2 (n=3) (range from 5 to 9)	sub-greenochist	black chert	meta-volcanic unit	Shift of the $\delta^{15}\text{N}$ of sedimentary organic matter towards positive values from the early Archean to the Phanerozoic, linked to the evolution of the oxidation state of surface environments

range from 100 to 600 ppm) (n=5) 6 ¹³ C _{org} = -40.44±2.41‰ (n=5)	(range from -47.60 to -43.10‰)	TOC = 2.98±1.49% (n=5)	(range from 0.74 to 4.45%)	(TOC/TN) _{bulk} = 1.32±1.09 (n=5)	(range from 62 to 324)	lower greenschist	black shale	deep marine
range from 18 to 169 ppm) (n=6) 6 ¹³ C _{org} = -36.69±3.73‰ (n=6)	(range from -46.09 to -37.36‰)	TOC = 3.18±2.86% (n=6)	(range from 0.10 to 10.91%)	(TOC/TN) _{bulk} = 2.48±7.0 (n=6)	(range from 167 to 343)	sub-greenschist	shales, carbonates	shallow subtidal, intertidal or lagoonal
range from 110 to 410 ppm) (n=10) 6 ¹³ C _{org} = -35.01±3.84‰ (n=10)	(range from -39.00 to -25.00‰)	TOC = 2.02±0.79% (n=10)	(range from 0.15 to 2.94%)	(TOC/TN) _{bulk} = 1.00±5.9 (n=10)	(range from 9 to 215)	<70°C	shale	subtidal to deep subtidal
range from 3 to 11 ppm) (n=9) TN = 6±3 ppm (n=9)	(range from -46.70 to -29.30‰)	TOC = 0.01±0.0% (n=9)	(range from 0 to 0.02%)	(TOC/TN) _{bulk} = 1.6±9 (n=9)	(range from 5 to 27)	lower greenschist to amphibolite	chert, stromatolitic	playa lake to marine
range from 100 to 100 ppm) (n=4) TN = 10±0 ppm (n=4)	(range from -43.30 to -37.70‰)	TOC = 0.56±0.34% (n=4)	(range from 0.19 to 0.93%)	(TOC/TN) _{bulk} = 65±39 (n=4)	(range from 22 to 109)	lower greenschist	black shale	shallow marine
range from 256 to 730 ppm) (n=4) TN = 46±23 ppm (n=4)		TOC = 5.99±1.70% (n=4)	(range from 4.08 to 8.17%)	(TOC/TN) _{bulk} = 172±74 (n=4)	(range from 130 to 282)			
range from 811 to 867 ppm) (n=4) TN = 84±23 ppm (n=4)	(range from -32.00 to -31.90‰)	TOC = 0.55±0.04% (n=4)	(range from 0.50 to 0.58%)	(TOC/TN) _{bulk} = 8±0 (n=4)	(range from 7 to 8)	greenschist to mid-amphibolite	black shale	Phanerozoic oilfield brines that penetrated the Archean basement. Secondary hydrocarbon signature = perceptible for Proterozoic
range from 57 to 88 ppm) (n=6) TN = 73±11 ppm (n=6)	(range from -28.30 to -26.00‰)	TOC = 2.81±0.7% (n=6)	(range from 1.12 to 2.12%)	(TOC/TN) _{bulk} = 302±92 (n=6)	(range from 179 to 433)	greenschist to mid-amphibolite	black shale	Secular trend from positive δ ¹⁵ N values in the Archean to intermediate δ ¹⁵ N values in Proterozoic deposits to finally reach the Phanerozoic mean δ ¹⁵ N value around +5‰ Bioprobe using a ¹⁵ N-enriched atmospheric reservoir derived from a secondary atmosphere with C-chondrite-like material and comets with a δ ¹⁵ N of +3.0 to +4.2‰
range from 14 to 2078 ppm) (n=266) 6 ¹³ C _{org} = -42.74±2.33‰ (n=266)	(range from -52.03 to -35.64‰)	TOC = 4.96±2.51% (n=265)	(range from 0.06 to 12.51%)	(TOC/TN) _{bulk} = 101±45 (n=265)	(range from 2 to 330)	premitic-pumpellyite	basinal BIFs and sulfidic kerogenous shales, stromatolitic carbonates	Transient surface aerobic nitrogen cycling with free oxygen in the upper water column Secondary surface ocean oxygenation; positive δ ¹⁵ N values interpreted as recording aerobic nitrogen cycling with free oxygen in the upper water column
range from 30 to 70 ppm) (n=8) TN = 44±4 ppm (n=8)	(range from -47.40 to -31.80‰)	TOC = 0.56±0.20% (n=8)	(range from 0.25 to 0.85%)	(TOC/TN) _{bulk} = 163±73 (n=8)	(range from 49 to 296)	<170°C	shale	subtidal to deep subtidal
range from 8 to 46 ppm) (n=24) TN = 28±11 ppm (n=24)	(range from -51.76 to -30.40‰)	TOC = 2.27±0.18% (n=24)	(range from 0.02 to 0.65%)	(TOC/TN) _{bulk} = 93±47 (n=24)	(range from 8 to 167)	greenschist	shale	shallow to deep marine
range from 600 to 1200 ppm) (n=5) TN = 800±255 ppm (n=5)	(range from -45.40 to -39.10‰)	TOC = 3.15±2.10% (n=5)	(range from 1.56 to 6.83%)	(TOC/TN) _{bulk} = 43±15 (n=5)	(range from 30 to 66)	lower greenschist	black shale	shallow marine
range from 10 to 47 ppm) (n=10) TN = 24±2 ppm (n=10)						greenschist	volcanogenic massive sulfide (VMS) and gold deposits	¹⁵ N-enriched values attributed to a different Archean N cycle with large biologicaly-mediated fractionations OR Bioprobe using a ¹⁵ N-enriched atmospheric reservoir derived from a secondary atmosphere with C-chondrite-like material and comets with a δ ¹⁵ N of +3.0 to +4.2‰
range from 97 to 310 ppm) (n=10) TN = 209±79 ppm (n=10)	(range from -22.40 to -19.00‰)	TOC = 3.20±1.27% (n=6)	(range from 1.46 to 24.25%)	(TOC/TN) _{bulk} = 537±283 (n=6)	(range from 66 to 928)	premitic-pumpellyite to	black shales	¹⁵ N-enriched values attributed to a different Archean N cycle with large biologicaly-mediated fractionations OR Bioprobe using a ¹⁵ N-enriched atmospheric reservoir derived from a secondary atmosphere with C-chondrite-like material and comets with a δ ¹⁵ N of +3.0 to +4.2‰
range from 26 to 60 ppm) (n=5) TN = 39±14 ppm (n=5)	(range from -25.56±0.19‰)	TOC = 0.08±0.07% (n=5)	(range from 0.03 to 0.18%)	(TOC/TN) _{bulk} = 283±231 (n=5)	(range from 134 to 685)	premitic-pumpellyite to	black shales	¹⁵ N-enriched values attributed to a different Archean N cycle with large biologicaly-mediated fractionations. Bioprobe using a ¹⁵ N-enriched atmospheric reservoir derived from a secondary atmosphere with C-chondrite-like material and comets with a δ ¹⁵ N of +3.0 to +4.2‰



Supplementary Figure S1. Crossplots for drill cores GT13 (orange) and GT16 (red): TOC (wt. %) vs. TN (ppm); $\delta^{15}\text{N}$ (‰ vs. air) vs. TN (ppm); $\delta^{15}\text{N}$ (‰ vs. air) vs. TOC/TN and $\delta^{13}\text{C}_{\text{org}}$ (‰ vs. PDB) vs. $\delta^{15}\text{N}$ (‰ vs. air).

Geological context of the Serra Sul and Tumbiana Formations

Here we present a short description of the geological context of the Serra Sul Formation, Amazonian Craton (Supplementary Fig. S2A), and point out the main similarities and differences with the Tumbiana Formation, Pilbara Craton, where similar strongly positive $\delta^{15}\text{N}$ values have been reported (Stüeken et al., 2015; Thomazo et al., 2011). The age of the Serra Sul Formation is constrained between 2684 ± 10 Ma (U-Pb on detrital zircon, Rossignol et al., 2020) and 2627 ± 11 Ma (Re-Os dating on molybdenite, Perelló et al., 2023; Supplementary Fig. S3). This indicates that the Serra Sul Formation is slightly younger than the Tumbiana Formation, which was deposited around 2724 ± 5 Ma (U-Pb on volcanic zircon, Blake et al., 2004) to $\leq 2715 \pm 6$ Ma (U-Pb on detrital zircon, Arndt et al., 1991). Importantly, paleomagnetic investigations indicate that at about 2.75 Ga the Carajás Basin was located at a low latitude ($3.4 \pm 8.5^\circ$, Martins et al., 2021), whereas the Hamersley Basin in which the Tumbiana Formation deposited was located at high to mid paleolatitude (between $51.5 \pm 7.0^\circ$ and $32.1 \pm 5.7^\circ$, Kasbohm et al., 2023). Both the Serra Sul (Figueiredo e Silva et al., 2020; Martins et al., 2017; Rossignol et al., 2020) and the Tumbiana (Lepot et al., 2008) formations experienced low-grade ($\leq 300^\circ\text{C}$) greenschist facies metamorphism.

The Serra Sul Formation was deposited in the Carajás Basin, southeast Amazonian Craton (Supplementary Fig. S2A, B). The basement of the basin comprises various Meso- to Neoproterozoic rocks (Vasquez and Rosa-Costa, 2008) capped by a 4 to 6 km thick basaltic series of the ca. 2.75 Ga Parauapebas Large Igneous Province (PLIP, Rossignol et al., 2022). Soon after the main magmatic pulse of the PLIP, infilling of the rift initiated with the deposition of iron formations (IFs) of the Carajás Formation (Supplementary Fig. S3). These IFs are characterized by strong positive Eu anomalies indicating the influence of high-temperature hydrothermal fluids in seawater (Rego et al., 2021), absence of Ce anomalies arguing for ambient reducing conditions during deposition (Rego et al., 2021), and occurrence of positive La and Y anomalies (Rego et al., 2021) typical of chemical sediments deposited in oceanic setting (Kamber et al., 2014). In addition, Fe and C isotope data indicate that deposition of the IFs was mediated by anoxygenic photosynthetic organisms (Rego et al., 2021). The transition from the Carajás to Serra Sul formations is marked by several IFs layers up to 10 m thick, grading upward into detrital terrigenous sedimentary rocks including sandstones, siltstones, conglomerates and flat pebble conglomerates (Dreher et al., 2005, 2008; Galarza et al., 2008; Melo et al., 2019; Ronzê et al., 2000; Rossignol et al., 2020). The presence of BIFs at the base of the Serra Sul Formation (Melo et al., 2019) indicates marine environments, and the different

sedimentary features of this formation point toward subaqueous environments ranging from shallow to deep water settings influenced by slope instability and gravity flow processes (Dreher et al., 2005, 2008; Rossignol et al., 2020). The Serra Sul Formation does not preserve evidence of contemporaneous volcanic activity (Rossignol et al., 2020).

These lithologies and environments contrast with those of the Tumbiana Formation, which comprises mainly stromatolitic and fenestrate carbonates, calcareous sandstones, various volcanic and volcanoclastic rocks including tuffs, lapillis and tuffaceous sandstones, and other detrital facies including conglomerates and flat pebbles conglomerates (Awramik and Buchheim, 2009; Coffey et al., 2013; Lepot et al., 2008; Stüeken et al., 2015; Thomazo et al., 2011). Contrarily to the Serra Sul Formation, the presence of tuffs and lapillis argues for active volcanic activity during the deposition of the Tumbiana Formation (Coffey et al., 2013). Various sedimentary structures such as desiccation cracks point to shallow subaqueous environments subjected to frequent emersion (Awramik and Buchheim, 2009; Coffey et al., 2013). Geochemical characteristics of chemical sedimentary rocks of the Tumbiana Formation, such as nearly chondritic Y/Ho and the absence of positive Y anomaly, point to lacustrine subaqueous environments (Awramik and Buchheim, 2009; Coffey et al., 2013), and strongly positive $\delta^{15}\text{N}$ values have been suggested to evidence alkaline waters (Stüeken et al., 2015).

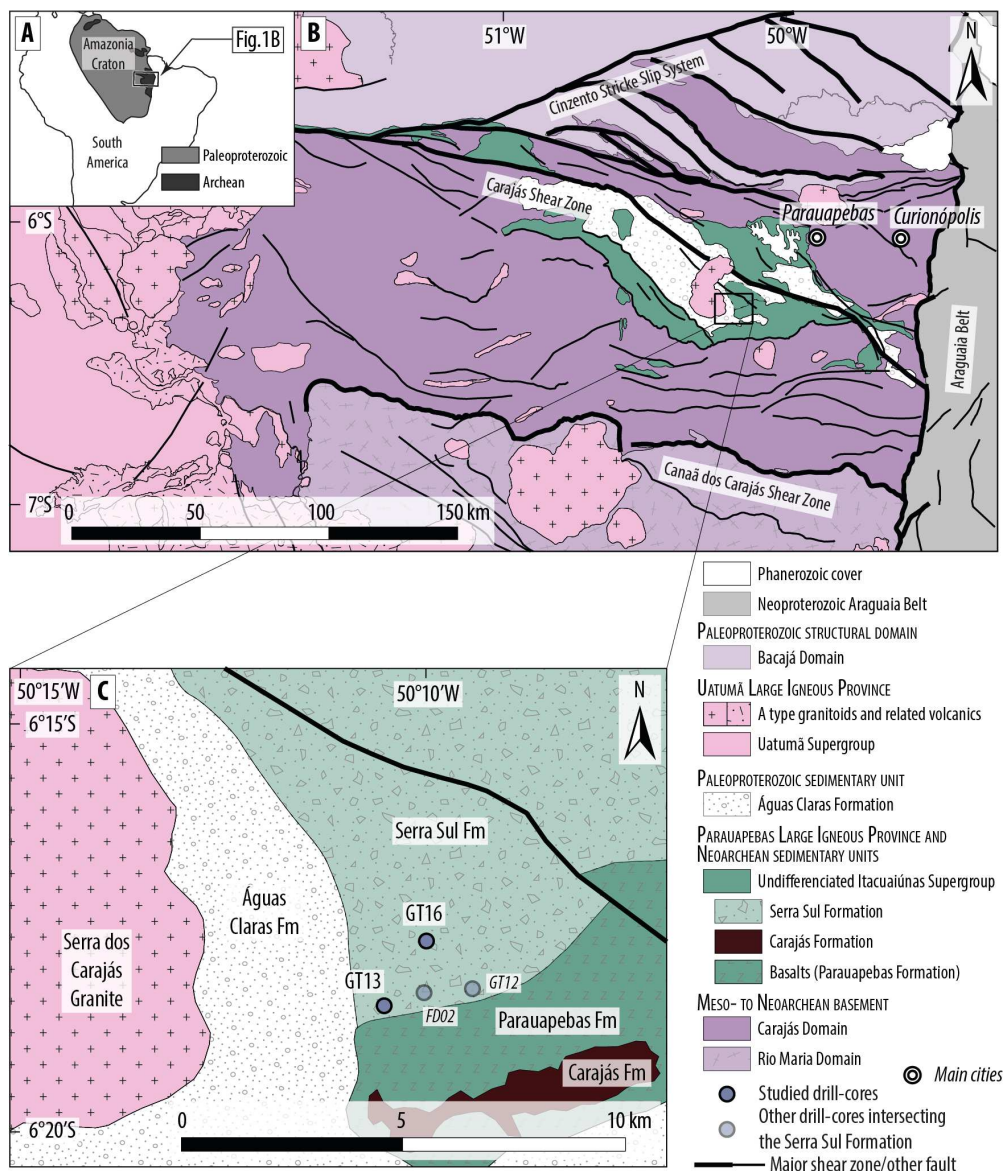
Studied drill-cores

Samples were collected from two diamond-drilled cores separated by about 1.75 km from each other and intersecting the Serra Sul Formation in the east of the Carajás Basin (Supplementary Fig. S2C). These drill-cores (GT-41-FURO-13 and GT-41-FURO-16) have been selected due to their low metamorphic and hydrothermal overprints, with only rare occurrences of quartz-chlorite-bearing micro-veins. Both drill-cores, named thereafter GT13 and GT16, exhibit similar lithologies and sedimentary facies, but no attempt was made to correlate them, so that their relative stratigraphic positions remain unconstrained. A detailed description of sedimentary facies is presented in Rossignol et al. (2020) and summarized below.

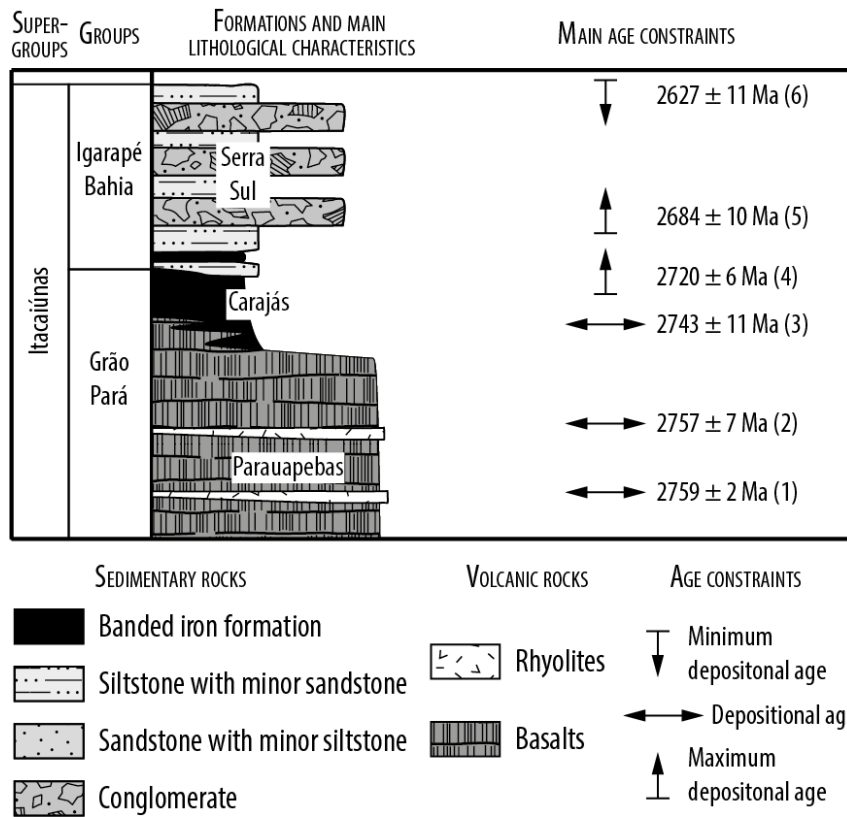
The most common facies association comprises polymictic conglomerates interbedded with sandstones and siltstones with various sedimentary features attesting an overall excellent preservation state (Supplementary Fig. S4). This facies association is interpreted to represent deep water environment, where conglomerates and coarse sandstones were deposited by subaqueous mass flow, cohesive debris flow or hyper-concentrated density flow (Lowe, 1982;

Mulder and Alexander, 2001; Nemeč and Steel, 1984; Postma et al., 2014; Postma and Cartigny, 2014; Walker, 1975).

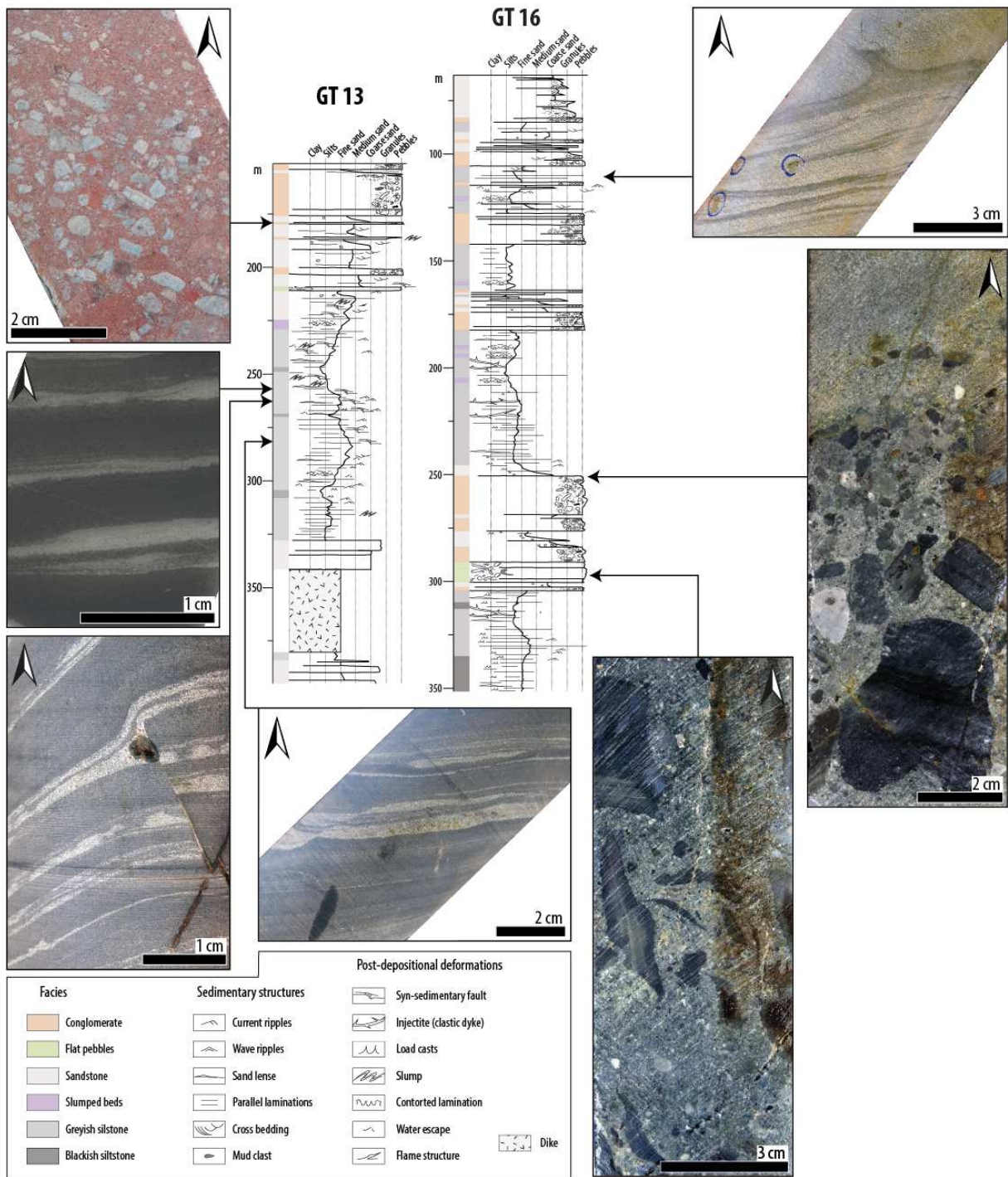
The other facies association identified consists of sandstone, siltstone and flat pebble conglomerates made up of intraclastic granules to pebbles (Supplementary Fig. S4). Flat pebble conglomerates are interpreted to result from the failure and subsequent reworking of compacted to loosely consolidated shoreface deposits (Myrow et al., 2004). The limited transport by mass movement of shoreface deposits and occurrence of wave ripples in sandstones and siltstones suggest relatively shallow water environments (shoreface to upper offshore).



Supplementary Fig. S2. Maps illustrating the location of the Carajás Basin. (A) Main tectonic elements of South America (Cordani et al., 2016). (B) Geological map of the Carajás Basin (Vasquez et al., 2008). (C) Location of the drill-cores.



Supplementary Fig. S3. Main sedimentary units of the Carajás Basin and age constraints. (1) Machado et al. (1991); (2, 3) Trendall et al. (1998); (4) Rossignol et al. (2023); (5) Rossignol et al. (2020); (6) Perelló et al. (2023).



Supplementary Fig. S4. Sedimentological logs of the drill-cores GT13 and GT16 with photographs of the main facies and sedimentary structures. Arrows point to the stratigraphic top. Top left photograph: conglomerate with oriented clasts and sandy matrix; middle left: alternations of siltstone and fine sandstone; bottom left and middle: syn-sedimentary, centimetric-scale faults within fine sandstone to siltstone. Top right: sandstone with wave ripples, framboidal pyrite (blue circles) and load casts. Middle right: normally graded conglomerate with rounded quartz pebbles and sub-angular sedimentary clasts, grading to coarse sandstone. Bottom right: flat pebble conglomerate comprising elongated and deformed intraformational clasts.

Preservation of the primary N isotope signature

As post-depositional modifications of sedimentary $\delta^{15}\text{N}$ can occur during diagenesis and metamorphism, it is essential to evaluate the effects of such processes. It seems unlikely that organic matter remineralization during diagenesis significantly impacted the Serra Sul Formation $\delta^{15}\text{N}$ record since early diagenesis under anoxic conditions does not seem to shift organic matter $\delta^{15}\text{N}$ values by more than 1‰ (Lehmann et al., 2002), and the measured values range from +10 to +35‰.

The Serra Sul Formation has undergone metamorphism in the greenschist facies (Rossignol et al., 2020). While an increase in $\delta^{15}\text{N}$ and a decrease in TN is usually seen during prograde metamorphism (Bebout and Fogel, 1992; Boyd and Philippot, 1998; Haendel et al., 1986; Jia, 2006), studies on coal series show that nitrogen loss from organic matter during anthracitization is not associated with significant $\delta^{15}\text{N}$ increase (Ader et al., 1998, 2006; Boudou et al., 2008). The absence of covariation between $\delta^{15}\text{N}$ and TOC/TN in the Serra Sul Formation argues against a strong modification of $\delta^{15}\text{N}$ values due to metamorphic N-loss (Supplementary Figure S1). Moreover, maximum isotopic enrichments documented for greenschist facies metamorphism are below 2‰ (Jia, 2006; Stüeken et al., 2017), which is small compared to the reported range of measured $\delta^{15}\text{N}$ in the Serra Sul Formation (between +10‰ and +35‰). Secondary modification of $\delta^{15}\text{N}$ values can also occur during metasomatic ammonium addition through hydrothermal recycling, which tends to decrease the TOC/TN and either increase or decrease the $\delta^{15}\text{N}$ depending on the isotopic signature of recycled sediments (Stüeken et al., 2021a, 2021b). The relative constancy of TOC/TN along the core argues against any heterogeneous secondary overprint of the nitrogen record, either by metamorphism or by metasomatism. Finally, the absence of significant $\delta^{15}\text{N}$ differences between facies also argues against a metamorphic or metasomatic modification, as samples of different lithologies would react differently to thermal alteration.

References

- Ader, M., Boudou, J.-P., Javoy, M., Goffe, B., Daniels, E., 1998. Isotope study on organic nitrogen of Westphalian anthracites from the Western Middle field of Pennsylvania (U.S.A.) and from the Bramsche Massif (Germany). *Organic Geochemistry, Advances in Organic Geochemistry 1997 Proceedings of the 18th International Meeting on Organic Geochemistry Part I. Petroleum Geochemistry* 29, 315–323. [https://doi.org/10.1016/S0146-6380\(98\)00072-2](https://doi.org/10.1016/S0146-6380(98)00072-2)
- Ader, M., Cartigny, P., Boudou, J.-P., Oh, J.-H., Petit, E., Javoy, M., 2006. Nitrogen isotopic evolution of carbonaceous matter during metamorphism: Methodology and preliminary results. *Chemical Geology* 232, 152–169. <https://doi.org/10.1016/j.chemgeo.2006.02.019>
- Ader, M., Sansjofre, P., Halverson, G.P., Busigny, V., Trindade, R.I.F., Kunzmann, M., Nogueira, A.C.R., 2014. Ocean redox structure across the Late Neoproterozoic Oxygenation Event: A nitrogen isotope perspective. *Earth and Planetary Science Letters* 396, 1–13. <https://doi.org/10.1016/j.epsl.2014.03.042>
- Ader, M., Thomazo, C., Sansjofre, P., Busigny, V., Papineau, D., Laffont, R., Cartigny, P., Halverson, G.P., 2016. Interpretation of the nitrogen isotopic composition of Precambrian sedimentary rocks: Assumptions and perspectives. *Chemical Geology* 429, 93–110. <https://doi.org/10.1016/j.chemgeo.2016.02.010>
- Altabet, M.A., Francois, R., 1994. Sedimentary nitrogen isotopic ratio as a recorder for surface ocean nitrate utilization. *Global Biogeochemical Cycles* 8, 103–116. <https://doi.org/10.1029/93GB03396>
- Arndt, N.T., Nelson, D.R., Compston, W., Trendall, A.F., Thorne, A.M., 1991. The age of the Fortescue Group, Hamersley Basin, Western Australia, from ion microprobe zircon U-Pb results. *Australian Journal of Earth Sciences* 38, 261–281. <https://doi.org/10.1080/08120099108727971>
- Awramik, S.M., Buchheim, H.P., 2009. A giant, Late Archean lake system: The Meentheena Member (Tumbiana Formation; Fortescue Group), Western Australia. *Precambrian Research* 174, 215–240. <https://doi.org/10.1016/j.precamres.2009.07.005>
- Beaumont, V., Robert, F., 1999. Nitrogen isotope ratios of kerogens in Precambrian cherts: a record of the evolution of atmosphere chemistry? *Precambrian Research* 96, 63–82. [https://doi.org/10.1016/S0301-9268\(99\)00005-4](https://doi.org/10.1016/S0301-9268(99)00005-4)
- Bebout, G.E., Fogel, M.L., 1992. Nitrogen-isotope compositions of metasedimentary rocks in the Catalina Schist, California: Implications for metamorphic devolatilization history. *Geochimica et Cosmochimica Acta* 56, 2839–2849. [https://doi.org/10.1016/0016-7037\(92\)90363-N](https://doi.org/10.1016/0016-7037(92)90363-N)
- Blake, T.S., Buick, R., Brown, S.J.A., Barley, M.E., 2004. Geochronology of a Late Archaean flood basalt province in the Pilbara Craton, Australia: constraints on basin evolution, volcanic and sedimentary accumulation, and continental drift rates. *Precambrian Research* 133, 143–173. <https://doi.org/10.1016/j.precamres.2004.03.012>
- Boocock, T.J., Mikhail, S., Prytulak, J., Di Rocco, T., Stüeken, E.E., 2020. Nitrogen Mass Fraction and Stable Isotope Ratios for Fourteen Geological Reference Materials: Evaluating the

Applicability of Elemental Analyser Versus Sealed Tube Combustion Methods. *Geostandards and Geoanalytical Research* 44, 537–551. <https://doi.org/10.1111/ggr.12345>

Boudou, J.-P., Schimmelmann, A., Ader, M., Mastalerz, M., Sebito, M., Gengembre, L., 2008. Organic nitrogen chemistry during low-grade metamorphism. *Geochimica et Cosmochimica Acta* 72, 1199–1221. <https://doi.org/10.1016/j.gca.2007.12.004>

Bouyon, A., Cartigny, P., Avila, J., Rego, E.S., Rossignol, C., Philippot, P., Trindade, R.I., Hühn, S.R., 2018. Multiple sulfur isotope record from the Precambrian of South America shows an unusual trend. 2018, V31B-04.

Boyd, S.R., Philippot, P., 1998. Precambrian ammonium biogeochemistry: a study of the Moine metasediments, Scotland. *Chemical Geology* 144, 257–268. [https://doi.org/10.1016/S0009-2541\(97\)00135-6](https://doi.org/10.1016/S0009-2541(97)00135-6)

Busigny, V., Ader, M., Cartigny, P., 2005. Quantification and isotopic analysis of nitrogen in rocks at the ppm level using sealed tube combustion technique: A prelude to the study of altered oceanic crust. *Chemical Geology* 223, 249–258. <https://doi.org/10.1016/j.chemgeo.2005.08.002>

Canfield, D.E., Glazer, A.N., Falkowski, P.G., 2010. The Evolution and Future of Earth's Nitrogen Cycle. *Science* 330, 192–196. <https://doi.org/10.1126/science.1186120>

Casciotti, K.L., 2009. Inverse kinetic isotope fractionation during bacterial nitrite oxidation. *Geochimica et Cosmochimica Acta* 73, 2061–2076. <https://doi.org/10.1016/j.gca.2008.12.022>

Coffey, J.M., Flannery, D.T., Walter, M.R., George, S.C., 2013. Sedimentology, stratigraphy and geochemistry of a stromatolite biofacies in the 2.72 Ga Tumbiana Formation, Fortescue Group, Western Australia. *Precambrian Research* 236, 282–296. <https://doi.org/10.1016/j.precamres.2013.07.021>

Cordani, U.G., Ramos, V.A., Fraga, L.M., Cegarra, M., Delgado, I., Souza, K.G. de, Gomes, F.E.M., Schobbenhaus, C., 2016. Tectonic map of South America = Mapa tectônico da América do Sul.

Dalsgaard, T., Thamdrup, B., 2002. Factors Controlling Anaerobic Ammonium Oxidation with Nitrite in Marine Sediments. *Applied and Environmental Microbiology*. <https://doi.org/10.1128/AEM.68.8.3802-3808.2002>

Dreher, A.M., Xavier, R.P., Martini, S.L., 2005. Fragmental rocks of the Igarapé Bahia CU-AU deposit, Carajas Mineral Province, Brazil. *RBG* 35, 359–368. <https://doi.org/10.25249/0375-7536.2005353359368>

Dreher, A.M., Xavier, R.P., Taylor, B.E., Martini, S.L., 2008. New geologic, fluid inclusion and stable isotope studies on the controversial Igarapé Bahia Cu–Au deposit, Carajás Province, Brazil. *Miner Deposita* 43, 161–184. <https://doi.org/10.1007/s00126-007-0150-6>

Figueiredo e Silva, R.C., Lobato, L.M., Zucchetti, M., Hagemann, S., Vennemann, T., 2020. Geotectonic signature and hydrothermal alteration of metabasalts under- and overlying the giant Serra Norte iron deposits, Carajás mineral Province. *Ore Geology Reviews* 120, 103407. <https://doi.org/10.1016/j.oregeorev.2020.103407>

- Galarza, M.A., Macambira, M.J.B., Villas, R.N., 2008. Dating and isotopic characteristics (Pb and S) of the Fe oxide-Cu-Au-U-REE Igarapé Bahia ore deposit, Carajás mineral province, Pará state, Brazil. *Journal of South American Earth Sciences* 25, 377–397. <https://doi.org/10.1016/j.jsames.2007.07.006>
- Garvin, J., Buick, R., Anbar, A.D., Arnold, G.L., Kaufman, A.J., 2009. Isotopic Evidence for an Aerobic Nitrogen Cycle in the Latest Archean. *Science* 323, 1045–1048. <https://doi.org/10.1126/science.1165675>
- Godfrey, L.V., Falkowski, P.G., 2009. The cycling and redox state of nitrogen in the Archaean ocean. *Nature Geoscience* 2, 725–729. <https://doi.org/10.1038/ngeo633>
- Grotzinger, J.P., Kasting, J.F., 1993. New Constraints on Precambrian Ocean Composition. *The Journal of Geology* 101, 235–243. <https://doi.org/10.1086/648218>
- Haendel, D., Mühle, K., Nitzsche, H.-M., Stiehl, G., Wand, U., 1986. Isotopic variations of the fixed nitrogen in metamorphic rocks. *Geochimica et Cosmochimica Acta* 50, 749–758. [https://doi.org/10.1016/0016-7037\(86\)90351-0](https://doi.org/10.1016/0016-7037(86)90351-0)
- Halevy, I., Bachan, A., 2017. The geologic history of seawater pH. *Science* 355, 1069–1071. <https://doi.org/10.1126/science.aal4151>
- Hayes, J.M., 1994. Global methanotrophy at the Archean-Proterozoic transition. *Early Life on Earth, Nobel Symposium No. 84* 220–236.
- Hoch, M.P., Fogel, M.L., Kirchman, D.L., 1992. Isotope fractionation associated with ammonium uptake by a marine bacterium. *Limnology and Oceanography* 37, 1447–1459. <https://doi.org/10.4319/lo.1992.37.7.1447>
- Jia, Y., 2006. Nitrogen isotope fractionations during progressive metamorphism: A case study from the Paleozoic Cooma metasedimentary complex, southeastern Australia. *Geochimica et Cosmochimica Acta* 70, 5201–5214. <https://doi.org/10.1016/j.gca.2006.08.004>
- Jia, Y., Kerrich, R., 2004. Nitrogen 15-enriched Precambrian kerogen and hydrothermal systems. *Geochemistry, Geophysics, Geosystems* 5. <https://doi.org/10.1029/2004GC000716>
- Kamber, B.S., Webb, G.E., Gallagher, M., 2014. The rare earth element signal in Archaean microbial carbonate: information on ocean redox and biogenicity. *Journal of the Geological Society* 171, 745–763. <https://doi.org/10.1144/jgs2013-110>
- Kasbohm, J., Schoene, B., Maclennan, S.A., Evans, D.A.D., Weiss, B.P., 2023. Paleogeography and high-precision geochronology of the Neoproterozoic Fortescue Group, Pilbara, Western Australia. *Precambrian Research* 394, 107114. <https://doi.org/10.1016/j.precamres.2023.107114>
- Kendall, C., Grim, E., 1990. Combustion tube method for measurement of nitrogen isotope ratios using calcium oxide for total removal of carbon dioxide and water. *Analytical Chemistry*.
- Kerrich, R., Jia, Y., Manikyamba, C., Naqvi, S.M., 2006. Secular variations of N-isotopes in terrestrial reservoirs and ore deposits. *Geological Society of America Bulletin* 118, 1071–1083. [https://doi.org/10.1130/2006.1198\(05\)](https://doi.org/10.1130/2006.1198(05))

Kipp, M.A., Stüeken, E.E., Yun, M., Bekker, A., Buick, R., 2018. Pervasive aerobic nitrogen cycling in the surface ocean across the Paleoproterozoic Era. *Earth and Planetary Science Letters* 500, 117–126. <https://doi.org/10.1016/j.epsl.2018.08.007>

Koehler, M.C., Buick, R., Kipp, M.A., Stüeken, E.E., Zaloumis, J., 2018. Transient surface ocean oxygenation recorded in the ~2.66-Ga Jeerinah Formation, Australia. *Proceedings of the National Academy of Sciences* 115, 7711–7716. <https://doi.org/10.1073/pnas.1720820115>

Lehmann, M.F., Bernasconi, S.M., Barbieri, A., McKenzie, J.A., 2002. Preservation of organic matter and alteration of its carbon and nitrogen isotope composition during simulated and in situ early sedimentary diagenesis. *Geochimica et Cosmochimica Acta* 66, 3573–3584. [https://doi.org/10.1016/S0016-7037\(02\)00968-7](https://doi.org/10.1016/S0016-7037(02)00968-7)

Lepot, K., Benzerara, K., Brown, G.E., Philippot, P., 2008. Microbially influenced formation of 2,724-million-year-old stromatolites. *Nature Geosci* 1, 118–121. <https://doi.org/10.1038/ngeo107>

Li, L., Lollar, B.S., Li, H., Wortmann, U.G., Lacrampe-Couloume, G., 2012. Ammonium stability and nitrogen isotope fractionations for NH_4^+ – $\text{NH}_3(\text{aq})$ – $\text{NH}_3(\text{gas})$ systems at 20–70°C and pH of 2–13: Applications to habitability and nitrogen cycling in low-temperature hydrothermal systems. *Geochimica et Cosmochimica Acta* 84, 280–296. <https://doi.org/10.1016/j.gca.2012.01.040>

Lowe, D.R., 1982. Sediment gravity flows; II, Depositional models with special reference to the deposits of high-density turbidity currents. *Journal of Sedimentary Research* 52, 279–297. <https://doi.org/10.1306/212F7F31-2B24-11D7-8648000102C1865D>

Lyons, T.W., Reinhard, C.T., Planavsky, N.J., 2014. The rise of oxygen in Earth's early ocean and atmosphere. *Nature* 506, 307–315. <https://doi.org/10.1038/nature13068>

Machado, N., Lindenmayer, Z., Krogh, T.E., Lindenmayer, D., 1991. U-Pb geochronology of Archean magmatism and basement reactivation in the Carajás area, Amazon shield, Brazil. *Precambrian Research* 49, 329–354. [https://doi.org/10.1016/0301-9268\(91\)90040-H](https://doi.org/10.1016/0301-9268(91)90040-H)

Mandernack, K.W., Mills, C.T., Johnson, C.A., Rahn, T., Kinney, C., 2009. The $\delta^{15}\text{N}$ and $\delta^{18}\text{O}$ values of N_2O produced during the co-oxidation of ammonia by methanotrophic bacteria. *Chemical Geology, Combined Ecological and Geologic Perspectives in Ecosystem Studies* 267, 96–107. <https://doi.org/10.1016/j.chemgeo.2009.06.008>

Mariotti, A., Germon, J.C., Hubert, P., Kaiser, P., Letolle, R., Tardieux, A., Tardieux, P., 1981. Experimental determination of nitrogen kinetic isotope fractionation: Some principles; illustration for the denitrification and nitrification processes. *Plant Soil* 62, 413–430. <https://doi.org/10.1007/BF02374138>

Martins, P.L.G., Toledo, C.L.B., Silva, A.M., Antonio, P.Y.J., Chemale, F., Assis, L.M., Trindade, R.I.F., 2021. Low paleolatitude of the Carajás Basin at ~2.75 Ga: Paleomagnetic evidence from basaltic flows in Amazonia. *Precambrian Research* 365, 106411. <https://doi.org/10.1016/j.precamres.2021.106411>

Martins, P.L.G., Toledo, C.L.B., Silva, A.M., Chemale Jr, F., Santos, J.O.S., Assis, L.M., 2017. Neoproterozoic magmatism in the southeastern Amazonian Craton, Brazil: Petrography,

geochemistry and tectonic significance of basalts from the Carajás Basin. *Precambrian Research* 302, 340–357. <https://doi.org/10.1016/j.precamres.2017.10.013>

Marty, B., Zimmermann, L., Pujol, M., Burgess, R., Philippot, P., 2013. Nitrogen Isotopic Composition and Density of the Archean Atmosphere. *Science* 342, 101–104. <https://doi.org/10.1126/science.1240971>

Melo, G.H.C. de, Monteiro, L.V.S., Xavier, R.P., Moreto, C.P.N., Arquaz, R.M., Silva, M.A.D., 2019. Evolution of the Igarapé Bahia Cu-Au deposit, Carajás Province (Brazil): Early syngenetic chalcopyrite overprinted by IOCG mineralization. *Ore Geology Reviews* 111, 102993. <https://doi.org/10.1016/j.oregeorev.2019.102993>

Möbius, J., 2013. Isotope fractionation during nitrogen remineralization (ammonification): Implications for nitrogen isotope biogeochemistry. *Geochimica et Cosmochimica Acta* 105, 422–432. <https://doi.org/10.1016/j.gca.2012.11.048>

Mulder, T., Alexander, J., 2001. The physical character of subaqueous sedimentary density flows and their deposits. *Sedimentology* 48, 269–299. <https://doi.org/10.1046/j.1365-3091.2001.00360.x>

Myrow, P.M., Tice, L., Archuleta, B., Clark, B., Taylor, J.F., Ripperdan, R.L., 2004. Flat-pebble conglomerate: its multiple origins and relationship to metre-scale depositional cycles. *Sedimentology* 51, 973–996. <https://doi.org/10.1111/j.1365-3091.2004.00657.x>

Nemec, W., Steel, R.J., 1984. Alluvial and Coastal Conglomerates: Their Significant Features and Some Comments on Gravelly Mass-Flow Deposits 1–31.

Nishizawa, M., Sano, Y., Ueno, Y., Maruyama, S., 2007. Speciation and isotope ratios of nitrogen in fluid inclusions from seafloor hydrothermal deposits at ~ 3.5 Ga. *Earth and Planetary Science Letters* 254, 332–344. <https://doi.org/10.1016/j.epsl.2006.11.044>

Papineau, D., Purohit, R., Goldberg, T., Pi, D., Shields, G.A., Bhu, H., Steele, A., Fogel, M.L., 2009. High primary productivity and nitrogen cycling after the Paleoproterozoic phosphogenic event in the Aravalli Supergroup, India. *Precambrian Research* 171, 37–56. <https://doi.org/10.1016/j.precamres.2009.03.005>

Pellerin, A., Thomazo, C., Ader, M., Marin-Carbonne, J., Alleon, J., Vennin, E., Hofmann, A., 2023. Iron-mediated anaerobic ammonium oxidation recorded in the early Archean ferruginous ocean. *Geobiology* 21, 277–289. <https://doi.org/10.1111/gbi.12540>

Perelló, J., Zulliger, G., García, A., Creaser, R.A., 2023. Revisiting the IOCG geology and age of Alemão in the Igarapé Bahia camp, Carajás province, Brazil. *Journal of South American Earth Sciences* 124, 104273. <https://doi.org/10.1016/j.jsames.2023.104273>

Postma, G., Cartigny, M.J.B., 2014. Supercritical and subcritical turbidity currents and their deposits—A synthesis. *Geology* 42, 987–990. <https://doi.org/10.1130/G35957.1>

Postma, G., Kleverlaan, K., Cartigny, M.J.B., 2014. Recognition of cyclic steps in sandy and gravelly turbidite sequences, and consequences for the Bouma facies model. *Sedimentology* 61, 2268–2290. <https://doi.org/10.1111/sed.12135>

Rego, E.S., Busigny, V., Lalonde, S.V., Philippot, P., Bouyon, A., Rossignol, C., Babinski, M., de Cássia Zapparoli, A., 2021. Anoxygenic photosynthesis linked to Neoproterozoic iron formations in Carajás (Brazil). *Geobiology* 19, 326–341. <https://doi.org/10.1111/gbi.12438>

Ronzê, P.C., Soares, A.D., Santos, M. dos, Barreira, C.F., 2000. Alemão copper-gold (U-REE) deposit, Carajás, Brazil. *Hydrothermal iron oxide copper-gold & related deposits: a global perspective*. Australian Mineral Foundation, Adelaide 191–202.

Rossignol, C., Antonio, P.Y.J., Narduzzi, F., Rego, E.S., Teixeira, L., de Souza, R.A., Ávila, J.N., Silva, M.A.L., Lana, C., Trindade, R.I.F., Philippot, P., 2022. Unraveling one billion years of geological evolution of the southeastern Amazonia Craton from detrital zircon analyses. *Geoscience Frontiers* 13, 101202. <https://doi.org/10.1016/j.gsf.2021.101202>

Rossignol, C., Antonio, P.Y.J., Narduzzi, F., Rego, E.S., Teixeira, L., de Souza, R.A., Ávila, J.N., Silva, M.A.L., Lana, C., Trindade, R.I.F., Philippot, P., 2021. Unraveling one billion years of geological evolution of the southeastern Amazonia Craton from detrital zircon analyses. *Geoscience Frontiers*. <https://doi.org/10.1016/j.gsf.2021.101202>

Rossignol, C., Rego, E.S., Philippot, P., Narduzzi, F., Teixeira, L., Silva, M.A.L., Ávila, J.N., Lana, C., Trindade, R.F., 2023. Neoproterozoic environments associated with the emplacement of a large igneous province: Insights from the Carajás Basin, Amazonia Craton. *Journal of South American Earth Sciences* 130, 104574. <https://doi.org/10.1016/j.jsames.2023.104574>

Rossignol, C., Siciliano Rego, E., Narduzzi, F., Teixeira, L., Ávila, J.N., Silva, M.A.L., Lana, C., Philippot, P., 2020. Stratigraphy and geochronological constraints of the Serra Sul Formation (Carajás Basin, Amazonian Craton, Brazil). *Precambrian Research* 351, 105981. <https://doi.org/10.1016/j.precamres.2020.105981>

Saitoh, M., Nishizawa, M., Ozaki, K., Ikeda, M., Ueno, Y., Takai, K., Isozaki, Y., 2023. Nitrogen Isotope Record From a Mid-oceanic Paleo-Atoll Limestone to Constrain the Redox State of the Panthalassa Ocean in the Capitanian (Late Guadalupian, Permian). *Paleoceanography and Paleoclimatology* 38, e2022PA004573. <https://doi.org/10.1029/2022PA004573>

Sigman, D.M., Karsh, K.L., Casciotti, K.L., 2009. Nitrogen Isotopes in the Ocean. *Encyclopedia of Ocean Sciences* 40–54. <https://doi.org/10.1016/B978-012374473-9.00632-9>

Stüeken, E.E., Boocock, T.J., Robinson, A., Mikhail, S., Johnson, B.W., 2021a. Hydrothermal recycling of sedimentary ammonium into oceanic crust and the Archean ocean at 3.24 Ga. *Geology* 49, 822–826. <https://doi.org/10.1130/G48844.1>

Stüeken, E.E., Buick, R., Anderson, R.E., Baross, J.A., Planavsky, N.J., Lyons, T.W., 2017. Environmental niches and metabolic diversity in Neoproterozoic lakes. *Geobiology* 15, 767–783. <https://doi.org/10.1111/gbi.12251>

Stüeken, E.E., Buick, R., Guy, B.M., Koehler, M.C., 2015. Isotopic evidence for biological nitrogen fixation by molybdenum-nitrogenase from 3.2 Gyr. *Nature* 520, 666–669. <https://doi.org/10.1038/nature14180>

Stüeken, E.E., Buick, R., Schauer, A.J., 2015. Nitrogen isotope evidence for alkaline lakes on late Archean continents. *Earth and Planetary Science Letters* 411, 1–10. <https://doi.org/10.1016/j.epsl.2014.11.037>

- Stüeken, E.E., Gregory, D.D., Mukherjee, I., McGoldrick, P., 2021b. Sedimentary exhalative venting of bioavailable nitrogen into the early ocean. *Earth and Planetary Science Letters* 565, 116963. <https://doi.org/10.1016/j.epsl.2021.116963>
- Stüeken, E.E., Kipp, M.A., Koehler, M.C., Buick, R., 2016. The evolution of Earth's biogeochemical nitrogen cycle. *Earth-Science Reviews* 160, 220–239. <https://doi.org/10.1016/j.earscirev.2016.07.007>
- Stüeken, E.E., Zaloumis, J., Meixnerová, J., Buick, R., 2017. Differential metamorphic effects on nitrogen isotopes in kerogen extracts and bulk rocks. *Geochimica et Cosmochimica Acta* 217, 80–94. <https://doi.org/10.1016/j.gca.2017.08.019>
- Tesdal, J.-E., Galbraith, E., Kienast, M., 2013. Nitrogen isotopes in bulk marine sediment: Linking seafloor observations with subseafloor records 10. <https://doi.org/10.5194/bg-10-101-2013>
- Thomazo, C., Ader, M., Farquhar, J., Philippot, P., 2009. Methanotrophs regulated atmospheric sulfur isotope anomalies during the Mesoarchean (Tumbiana Formation, Western Australia). *Earth and Planetary Science Letters* 279, 65–75. <https://doi.org/10.1016/j.epsl.2008.12.036>
- Thomazo, C., Ader, M., Philippot, P., 2011. Extreme ¹⁵N-enrichments in 2.72-Gyr-old sediments: evidence for a turning point in the nitrogen cycle. *Geobiology* 9, 107–120. <https://doi.org/10.1111/j.1472-4669.2011.00271.x>
- Tomkins, A.G., Bowlt, L., Genge, M., Wilson, S., Brand, H.E.A., Wykes, J.L., 2016. Ancient micrometeorites suggestive of an oxygen-rich Archaean upper atmosphere. *Nature* 533, 235–238. <https://doi.org/10.1038/nature17678>
- Trendall, A.F., Basei, M.A.S., de Laeter, J.R., Nelson, D.R., 1998. SHRIMP zircon U–Pb constraints on the age of the Carajás formation, Grão Pará Group, Amazon Craton. *Journal of South American Earth Sciences* 11, 265–277. [https://doi.org/10.1016/S0895-9811\(98\)00015-7](https://doi.org/10.1016/S0895-9811(98)00015-7)
- Ulloa, O., Canfield, D.E., DeLong, E.F., Letelier, R.M., Stewart, F.J., 2012. Microbial oceanography of anoxic oxygen minimum zones. *Proceedings of the National Academy of Sciences* 109, 15996–16003. <https://doi.org/10.1073/pnas.1205009109>
- Vasquez, M.L., Rosa-Costa, L.T. da, 2008. Geologia e recursos minerais do estado do Pará (Technical Report). CPRM.
- Vasquez, M.L., Sousa, C.S., Carvalho, J.M.A., 2008. Mapa geológico e de recursos minerais do Estado do Pará, escala 1: 1.000. 000. Programa Geologia do Brasil, Belém, CPRM.
- Walker, R.G., 1975. Generalized Facies Models for Resedimented Conglomerates of Turbidite Association. *GSA Bulletin* 86, 737–748. [https://doi.org/10.1130/0016-7606\(1975\)86](https://doi.org/10.1130/0016-7606(1975)86)
- Yang, J., Junium, C.K., Grassineau, N.V., Nisbet, E.G., Izon, G., Mettam, C., Martin, A., Zerkle, A.L., 2019. Ammonium availability in the Late Archaean nitrogen cycle. *Nat. Geosci.* 12, 553–557. <https://doi.org/10.1038/s41561-019-0371-1>
- Zerkle, A.L., Poulton, S.W., Newton, R.J., Mettam, C., Claire, M.W., Bekker, A., Junium, C.K., 2017. Onset of the aerobic nitrogen cycle during the Great Oxidation Event. *Nature* 542, 465–467. <https://doi.org/10.1038/nature20826>

Zhang, X., Sigman, D.M., Morel, F.M.M., Kraepiel, A.M.L., 2014. Nitrogen isotope fractionation by alternative nitrogenases and past ocean anoxia. PNAS 111, 4782–4787. <https://doi.org/10.1073/pnas.1402976111>

CHAPTER 8.

ARE STROMATOLITIC CARBONATES IDEAL CANDIDATES TO STUDY THE ARCHEAN N-BIOGEOCHEMICAL CYCLE?

INSIGHTS FROM THE 2.5 GA MALMANI SUBGROUP, SOUTH AFRICA

Introductory summary

Neoproterozoic stromatolites from shallow platform depositional environments, often considered to be niches for early aerobic systems, provide seemingly ideal settings to explore the timing of biological oxygen production in the interval leading to and across the Great Oxidation Event (GOE). Intriguingly, few $\delta^{15}\text{N}$ data stem from stromatolitic carbonates compared to shales. This might be because, in addition to the lack of preserved carbonate platforms from the Precambrian and the paucity of nitrogen in remaining samples, metamorphism might have significantly altered the geochemical footprint of organic matter in carbonates, as it is the case for the $\delta^{13}\text{C}_{\text{org}}$.

In an article entitled “*Are stromatolitic carbonates ideal candidates to study the Archean N-biogeochemical cycle? Insights from the 2.5 Ga Malmani Subgroup, South Africa*”, close to submission, we explore the nitrogen isotope signature of stromatolitic carbonates from shallow depositional settings of the Campbellrand-Malmani carbonate platform (CMCP).

While positive $\delta^{15}\text{N}$ values recorded in deeper basinal parts of the CMCP have been interpreted as reflecting the onset of oxidative nitrogen cycling with a nitrate pool sufficiently stable to sustain denitrification overtime (Godfrey and Falkowski, 2009), we report $\delta^{15}\text{N}$ values centered around 0‰ from dolomitized stromatolites, representative of proximal depositional environments. Such data invite us to wonder why, despite the presence of undisputed photosynthetic microbial remains and a $\delta^{13}\text{C}_{\text{org}}$ signature compatible with the development of an aerobic biosphere (Eroglu et al., 2017), the oxidative part of the nitrogen cycle is not expressed in this sedimentary rock record. Several hypotheses are examined, including alternative metabolisms such as anoxygenic photosynthesis, the presence of quantitatively consumed “cryptic” oxygen, and sampling bias, in an attempt to determine whether stromatolitic carbonates provide the ideal tool to target Early Earth oxygenation.

The Malmani isotopic signal might be explained by variable ammonium assimilation rates in the microbial mats or in their vicinity, i.e. in a proximal depositional environment isolated from oceanic processes, that, contrary to basinal shales, does not readily record the N-cycle dynamics of the open ocean water column. This finding suggests that stromatolitic carbonates would be good proxies of local processes happening in the depositional environment on shorter temporal timescales, whereas shales from deeper depositional settings preferentially record a homogenized mean signal of processes happening in the water column on larger timescales. If so, different lithologies could record different parts of the N-biogeochemical cycle, which invites careful considerations of this parameter.

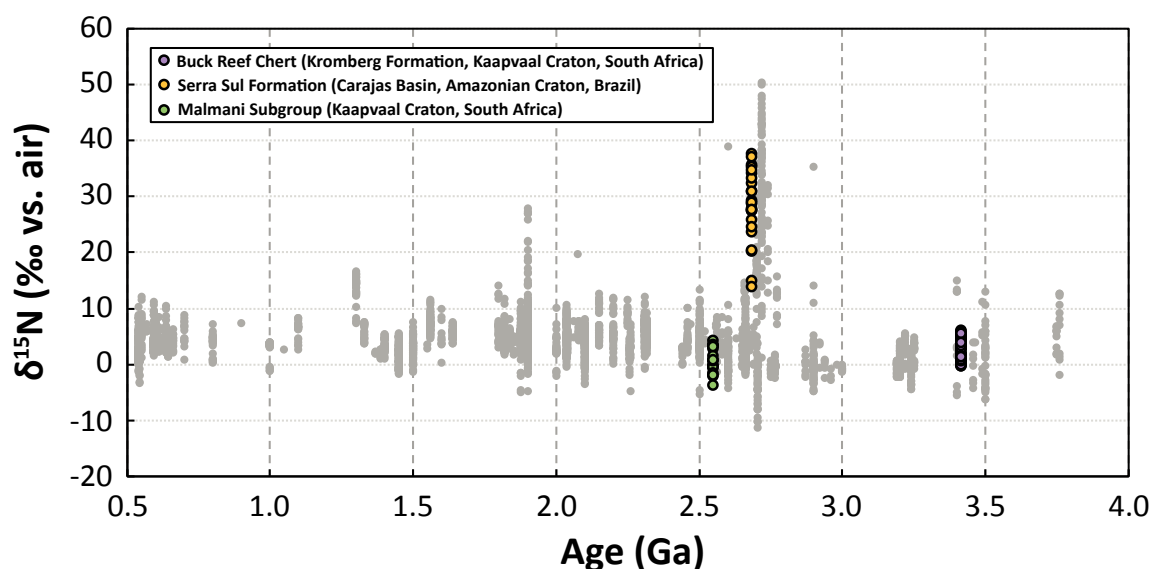


Fig. 8.0. Nitrogen isotope signature of the Malmani Subgroup (green) among all Precambrian sedimentary $\delta^{15}\text{N}$ data.

CHAPTER 8.

ARE STROMATOLITIC CARBONATES IDEAL CANDIDATES TO STUDY THE ARCHEAN N-BIOGEOCHEMICAL CYCLE?

INSIGHTS FROM THE 2.5 GA MALMANI SUBGROUP, SOUTH AFRICA

Abstract.....	273
8.1. Introduction.....	273
8.2. Geological context.....	277
8.3. Methods.....	283
8.4. Results.....	286
8.5. Discussion.....	294
8.5.1. A primary nitrogen isotope signature despite potential organic carbon resetting.	294
8.5.2. Oxidative pathways of the N-biogeochemical cycle are not recorded in the Malmani carbonates	300
8.5.3. A record of ammonium assimilation inside the microbial mats.....	301
8.6. Conclusions.....	302
References.....	306

CHAPTER 8.

ARE STROMATOLITIC CARBONATES IDEAL CANDIDATES TO STUDY THE ARCHEAN N-BIOGEOCHEMICAL CYCLE?

INSIGHTS FROM THE 2.5 GA MALMANI SUBGROUP, SOUTH AFRICA

Abstract

Often considered to be niches for early aerobic systems, Precambrian stromatolites from shallow platform depositional environments provide an ideal target to explore the timing of oxygen production in the interval leading to the Great Oxidation Event (GOE). The carbon and nitrogen isotope compositions preserved in shallow stromatolitic carbonates from the 2.55 Ga Malmani Subgroup, South Africa, were analyzed in an attempt to uncover carbon fixation pathways and oceanic redox changes associated with the evolution of the biosphere at the eve of the GOE. While the $\delta^{13}\text{C}_{\text{org}}$ signal seems partially reset, $\delta^{15}\text{N}$ values are likely preserved, but lack the positive isotopic signal typical of an oxygenated water column that has been recorded in deeper parts of the Campbellrand-Malmani carbonate platform. After examining several hypotheses, we argue that nitrogen isotopes in the studied stromatolitic carbonate samples record variable ammonium assimilation rates in the microbial mats or in their vicinity, i.e. in a proximal environment isolated from oceanic processes, that, contrary to basinal shales, do not reliably record the N-cycle dynamics of the open ocean water column. This finding suggests that stromatolitic carbonates would be good proxies of local processes happening in the depositional environment on shorter temporal timescales, whereas shales from deeper depositional settings preferentially record a homogenized mean signal of processes happening in the water column on larger timescales. If so, different lithologies could record different parts of the N-biogeochemical cycle, which invites careful considerations of this parameter.

8.1. Introduction

Nitrogen is an essential nutrient for all living organisms, and its availability strongly influences biological productivity. Additionally, the nitrogen isotopic composition of organic matter is controlled by both metabolic activity and redox speciation, as key biologically-mediated pathways of the oceanic nitrogen cycle are redox-dependent. As such, the nitrogen isotopic signature preserved in sedimentary rocks has become a standard tool for uncovering redox changes in the oceans associated with the evolution of the biosphere (Ader et al., 2016; Stüeken

et al., 2016). Specifically, positive $\delta^{15}\text{N}$ values found in well-preserved samples are often interpreted as reflecting the stability of a nitrate reservoir, partially consumed through active denitrification in dysoxic parts of an otherwise oxygenated water column (Altabet and Francois, 1994).

Indeed, nitrogen, in its atmospheric and dissolved oceanic N_2 form ($\delta^{15}\text{N}=0\text{‰}$, Ward (2012)), is assimilated almost exclusively by diazotrophs, prokaryotes capable of biological N_2 fixation thanks to the nitrogenase enzyme (Raymond et al., 2004). Bioavailable “fixed” nitrogen is therefore provided to the biosphere by diazotrophic N_2 -fixation and ammonium (NH_4^+) release through mineralization in the water column or in the sediment (Sigman et al., 2009). Fractionations imparted by biological N_2 fixation with classical Mo-based nitrogenase range from -2‰ to $+2\text{‰}$, whereas alternative nitrogenases using Fe or V as cofactors can impart negative fractionations as large as -8‰ (Zhang et al., 2014). In the modern ocean, transfers between the different oceanic nitrogen reservoirs (N_2 , NH_4^+ , NO_3^- and dissolved and particulate organic nitrogen DON and PON) are mainly controlled by biological processes involving redox reactions. The isotopic composition of these nitrogen sources determines the isotopic composition of primary producers and therefore the sedimentary $\delta^{15}\text{N}$. Ammonium assimilation preferentially incorporates ^{14}N , but its isotope fractionation ($+4$ to $+27\text{‰}$, Hoch et al. (1992)) can rarely be expressed in the sediment. Indeed, ammonium being the preferred inorganic nitrogen source for many organisms, its incorporation into the biomass is often rapid and quantitative. The only potential recordings of ammonium assimilation in the Precambrian rock record stem from rare negative $\delta^{15}\text{N}$ values found in shales from the 2.7 Ga Manjeri Formation in Zimbabwe (Yang et al., 2019), and from unusual stromatolitic phosphorite deposits of the 1.9 Ga Aravalli Supergroup in India (Papineau et al., 2009). However, for both cases, the complementary ^{15}N -enriched or ^{15}N -depleted reservoir has never been evidenced on site. When oxygen is present, ammonium can also be successively nitrified to nitrite NO_2^- and nitrate NO_3^- , which are either assimilated by photosynthetic organisms or biologically reduced through denitrification or anaerobic ammonium oxidation (anammox) in dysoxic and anoxic conditions (Dalsgaard and Thamdrup, 2002; Sigman et al., 2009). Denitrification and anammox release N_2O or N_2 , which are subsequently lost to the atmosphere, making them the major oceanic sinks of fixed nitrogen. Denitrification imparts a large nitrogen isotope fractionation of $\approx +30\text{‰}$ (Sigman et al., 2009), leaving residual nitrate enriched in ^{15}N . If assimilated into the organic matter, this ^{15}N -enriched pool of nitrate leaves a positive nitrogen isotope signature in the sediment. Ultimately, it is the balance between N_2 fixation inputs and denitrification/anammox

outputs that determines sedimentary $\delta^{15}\text{N}$ values, around +5‰ in modern sediments under oxic conditions. The first isotopic evidence for biological nitrogen fixation by the nitrogenase enzyme dates back to 3.2 Ga (Stüeken et al., 2015). From then on, the contribution of abiotic processes to the overall fixed nitrogen budget must have been minimal (Stüeken et al., 2016). During most of the Archean, oxygen was likely absent from the oceans (Lyons et al., 2014). Therefore, before the rise of oxygen levels significant enough to allow nitrification, nitrite and nitrate had to be scarce enough to be consumed quantitatively. Hence ammonium is assumed to have been the dominant form of fixed nitrogen prior to the Great Oxidation Event (GOE) (Fig. 8.1; Beaumont and Robert, 1999; Canfield et al., 2010). The rise of oceanic oxidants ultimately leading to the GOE might have initiated its oxidation during the Neoproterozoic (Fig. 8.1), when extreme positive $\delta^{15}\text{N}$ values have been observed (Stüeken et al., 2015; Thomazo et al., 2011; Pellerin et al., *in review*) An aerobic nitrogen cycle similar to modern environments where nitrate accumulated, at least in surface waters, may have been established at ca. 2.5 Ga (Garvin et al., 2009; Godfrey and Falkowski, 2009; Zerkle et al., 2017). From being ammonium-dominated in the anaerobic Archean oceans, the N-biogeochemical cycle would have evolved to nitrate-dominated and aerobic (Fig. 8.1) during the Phanerozoic and possibly the Proterozoic, at least in surface waters (Ader et al., 2016; Garvin et al., 2009; Godfrey and Falkowski, 2009; Kipp et al., 2018; Koehler et al., 2017, 2018; Stüeken et al., 2016; Zerkle et al., 2017). This redox shift may have impacted nutrient availability by rerouting a significant portion of the ammonium pool to energy-yielding reactions using nitrate.

As the accumulation of biologically produced oxygen in the early oceans is widely seen as the driving factor leading to the GOE (Lyons et al., 2014), oxygen production has been linked to the evolution of carbon fixation pathways, in particular the appearance of oxygenic photosynthesis. Shallow platform settings are often considered to be niches for early aerobic systems as early as 2.9 Ga (Planavsky et al., 2014). Among these settings, Precambrian stromatolites have been the focus of a number of geochemical studies targeting the link between biological innovations and Earth's protracted oxygenation (reviewed in Lepot, 2020).

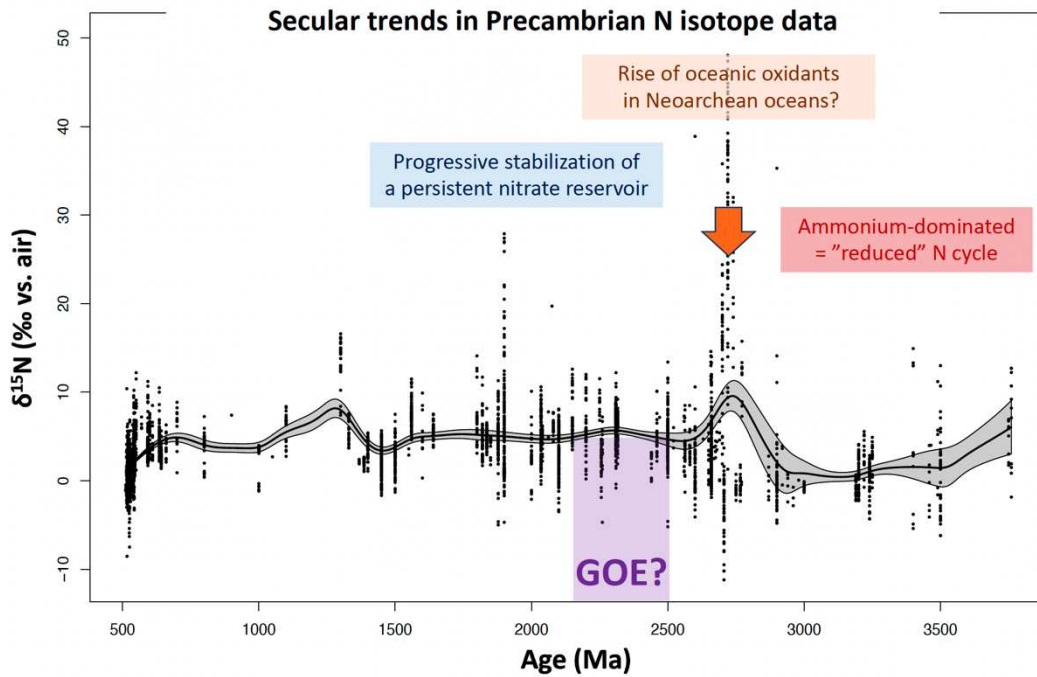


Fig. 8.1. Secular trends in Precambrian N isotope data with the inferred interpretations about the evolution of the marine N-biogeochemical cycle: an ammonium-dominated “reduced” N cycle in pre-GOE anoxic oceans, a rise of oceanic oxidants during the Neoproterozoic some time before the GOE, possibly around 2.7 Ga, followed by the progressive stabilization of a persistent nitrate reservoir in oxygenated surface waters. Smoothed curve and 95% confidence intervals are generated using kernel regressions with a bandwidth (h) of 100 Ma.

The ca. 2.58-2.50 Ga Campbellrand-Malmani carbonate platform (Transvaal Supergroup, South Africa) represents an opportunity to explore the timing of oxygen accumulation in the oceans during the protracted interval of the major redox transition on Earth, the GOE. It is also a preferential location to examine how the carbon and nitrogen biogeochemical cycles operated at various water depths along a carbonate platform. In addition, as there are very few occurrences of well-preserved Neoproterozoic carbonates in the geological record, it provides a case study to assess the effect of lithology on C- and N-isotope biogeochemical signatures.

Previous studies have shown a depth-dependent trend from lower $\delta^{13}\text{C}_{\text{org}}$ values around -40‰ in deeper depositional settings to higher $\delta^{13}\text{C}_{\text{org}}$ values close to -25‰ towards the platform shelf (Eroglu et al., 2017). This trend has been interpreted as a change from anaerobic (i.e., methanogenesis and methanotrophy) to aerobic ecosystems (i.e. oxygenic photosynthesis), suggesting that various carbon fixation pathways operated in the ocean at that time. In shales from slope settings, heavy nitrogen isotope signatures centred around +5‰ and reaching up to +10‰ have been interpreted to record oxidative nitrogen cycling with a nitrate pool sufficiently

stable to sustain denitrification over time (Godfrey and Falkowski, 2009). Molybdenum isotope compositions of Campbellrand carbonates and shales also seem to indicate redox cycling and transient free oxygen in the atmosphere-oceans system at that time (Voegelin et al., 2010; Wille et al., 2007), but secondary processes during diagenesis might have overprinted this signature (Eroglu et al., 2015). It is possible that the Campbellrand carbonates underwent redox changes within microbial mats and surrounding sediments during diagenesis (Eroglu et al., 2015).

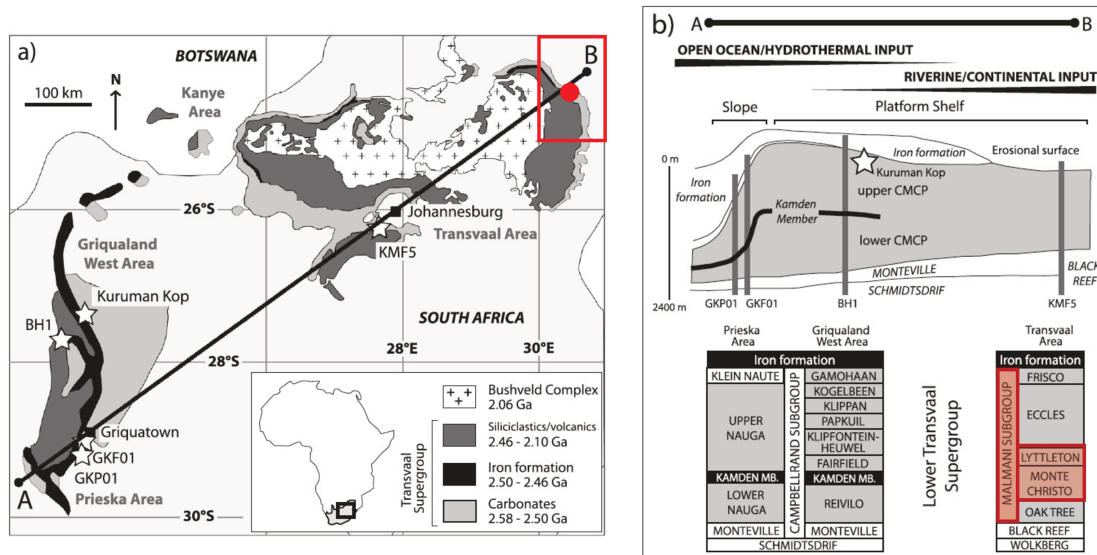
The present study analyses the paired carbon and nitrogen isotopes of a meter-scale drill core and a few outcrop samples retrieved from an unexplored part of the Campbellrand-Malmani platform harboring very shallow stromatolitic dolostone deposits. It aims to broaden the dataset along the platform to explore the impact of lithology and water depth on the carbon and nitrogen biogeochemical pathways.

8.2. Geological context

The Campbellrand-Malmani carbonate platform (CMCP) is part of the Lower Transvaal Supergroup that belongs to the South African Kaapvaal Craton. Deposited between 2.65 and 2.50 Ga (U-Pb dating on zircons; Altermann and Nelson, 1998), the CMCP stretches along two basins, namely the Griqualand West Basin in the western part of the craton and the Transvaal Basin in the eastern part of the craton (Beukes, 1987; Fig. 8.2). From northeast to southwest, some outcrops are preserved over 190 000 km², but studies have estimated that the platform could have extended over the entire surface of the craton, spanning about 600 000 km² (Beukes, 1987). The CMCP has experienced metamorphism in the greenschist facies, with additional contact metamorphism in areas close to the 2.06 Ga intrusion of the Bushveld complex (Cawthorn, 2015). In terms of depositional environments, the northeastern part of the CMCP corresponds to shallow peritidal to subtidal facies evolving towards slope and basinal facies in the southwestern part of the platform (Beukes, 1987).

Samples for this study were collected during a field trip conducted in 2019 in the Barberton area. They belong to the Malmani Subgroup, which is located in the Transvaal Basin and stratigraphically correlated with the Campbellrand Subgroup in the Griqualand West Basin. Out of the five Formations dividing the Malmani Subgroup (Oaktree, Monte Christo, Lyttleton, Eccles and Frisco; Fig. 8.2), field observations place the described section in the 2.55 Ga Upper Monte Christo Formation (Decraene, 2022; Altermann, *pers. com.*). This Formation contains wavy laminations interbedded with rippled ooid grainstones, as well as columnar stromatolites,

and is representative of shallow subtidal settings (Button, 1973; Tyler and Tyler, 1996). Outcrop samples were collected along a 20m-long sedimentary section (25° 21.561S, 30° 42.956E, Fig. 8.3) representative of shallow carbonate facies with dolomitized and partially silicified stromatolites. In addition, a 1.5-m core was drilled in the first meters of the outcrop (Fig. 8.4).



Eroglu et al., 2017

Fig. 8.2. (a) Geological overview of Transvaal Supergroup lithologies and the Bushveld igneous complex in South Africa and (b) Cross section through chemical sediments of the Lower Transvaal Supergroup. From Eroglu et al. (2017). The localization of the studied section (Transvaal area, Malmani Subgroup, Upper Monte Christo Formation) is identified in red in both (a) and (b).

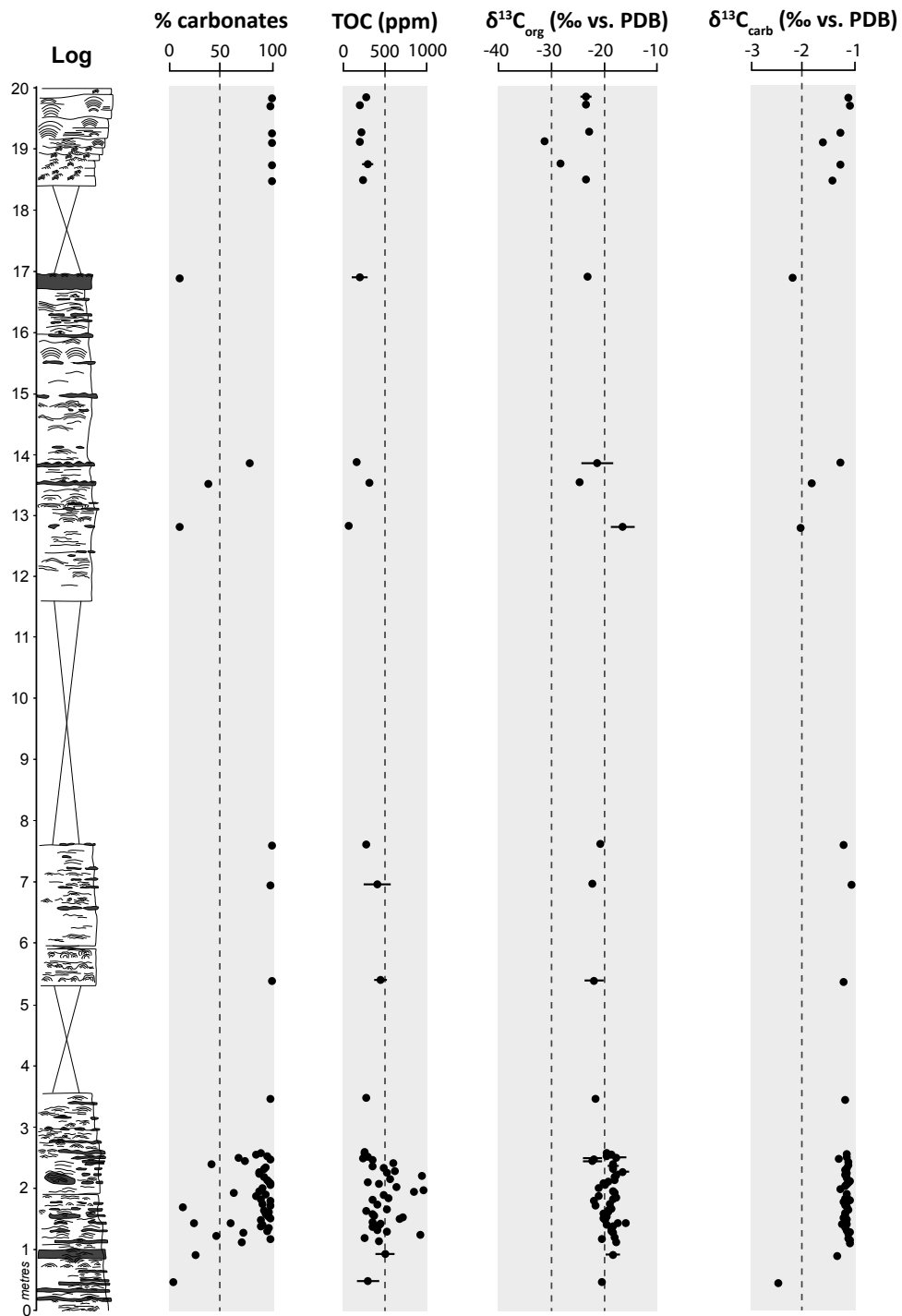


Fig. 8.3. Stratigraphic evolution of carbonate content (wt. %), TOC (ppm), $\delta^{13}\text{C}_{\text{org}}$ (‰ vs. PDB), and $\delta^{13}\text{C}_{\text{carb}}$ (‰ vs. PDB) along the studied outcrop section. Error bars indicate external reproducibility. When not visible external reproducibility is included within the data points.

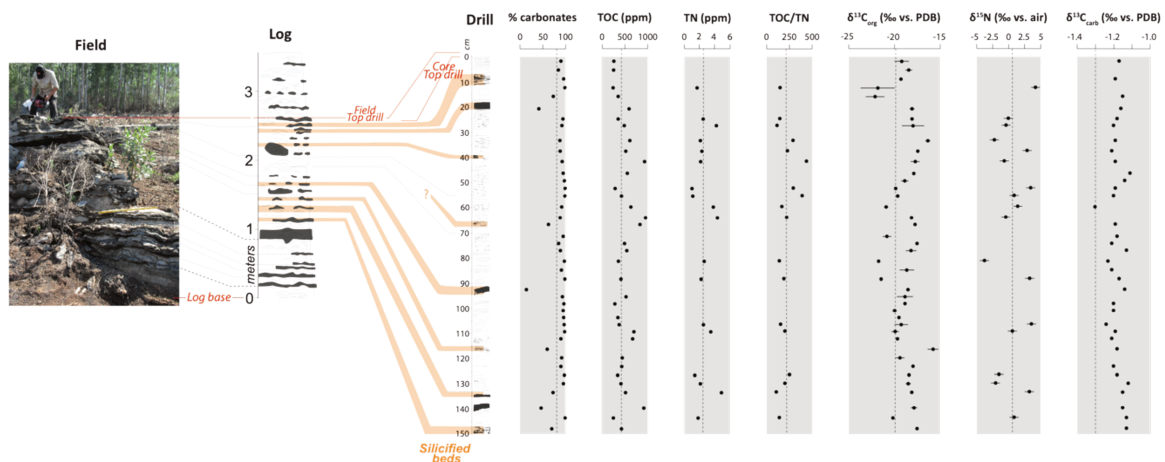


Fig. 8.4. Stratigraphic evolution of carbonate content (wt. %), TOC (ppm), TN (ppm), TOC/TN, $\delta^{13}\text{C}_{\text{org}}$ (‰ vs. PDB), $\delta^{15}\text{N}$ (‰ vs. air) and $\delta^{13}\text{C}_{\text{carb}}$ (‰ vs. PDB) along the studied drill core. Dotted lines indicate mean values. Error bars indicate external reproducibility. When not visible external reproducibility is included within the data points.

Along the outcrop, two facies can be set apart (Fig. 8.5): (i) a detrital facies with climbing ripples at the top (FA1) and (ii) a bioconstructed facies with fenestral stromatolites (FA2). Stromatolitic laminations are mostly carbonated with a few silicified layers (Fig. 8.5). Carbonates are identified as dolomite, probably resulting from an early and incomplete dolomitization, followed by an early phase of silicification replacing part of the remaining primary carbonates (Fig. 8.6; Decraene, 2022; Lawnizack, 2022). Some later fluid circulation episodes are indicated by cross-cutting silica veins and the presence of oxides (Fig. 8.6). Carbonaceous matter has been observed in dark laminae of both FA1 and FA2 facies. Raman spectra (Fig. 8.7-8.8) obtained from a peloid sample at 1.30 m depth display features of graphitized organic carbon, with peak temperature estimates of $395 \pm 30^\circ\text{C}$ following the methodology described in Kouketsu et al. (2014). This temperature estimation is higher than the greenschist metamorphic grade dominant throughout the whole platform (Miyano and Beukes, 1984), and rather corresponds to temperature estimates for the higher metamorphism created by the intrusion of the Bushveld complex (Cawthorn, 2015; Frauenstein et al., 2009). This means that the studied sedimentary section is located in a rather altered part of the platform compared to the studies of Eroglu et al. (2015, 2017) and Godfrey and Falkowski (2009). Petrographic observations are still ongoing and should provide a clearer syn- and post-depositional sedimentation model. However, preliminary work from the master's student thesis

of Lawnizack (2022) argue for a complex post-depositional history that can be divided into several episodes, including (i) cementation, (ii) dolomitization, (iii) two successive stages of silicification, and (iv) a second stage of dolomitization in veins (Fig. 8.6).

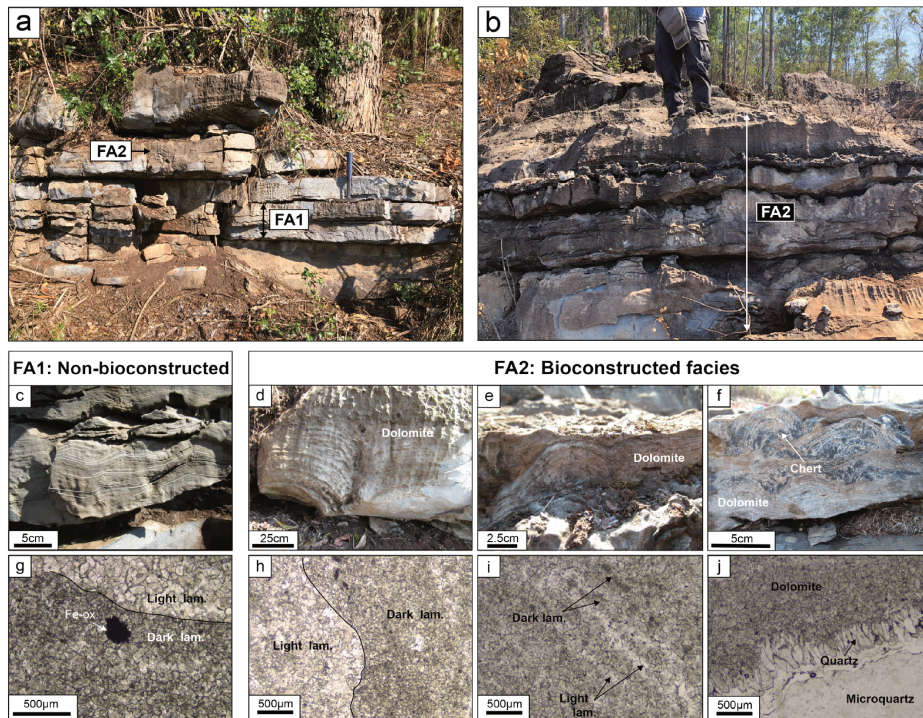


Fig. 8.5. Field views of the two facies associations of the studied section: the non-bioconstructed FA1 facies with climbing ripples (a) and the bioconstructed FA2 facies with stromatolites (a and b) (Decraene, 2022). (c) climbing ripples in FA1. (g) dark and light laminae in FA1. (d and e) dolomitized stromatolite in FA2. (f) dolomitic stromatolites partially silicified. (h, i, j) microscopic views of laminae and dolomite-quartz limits.

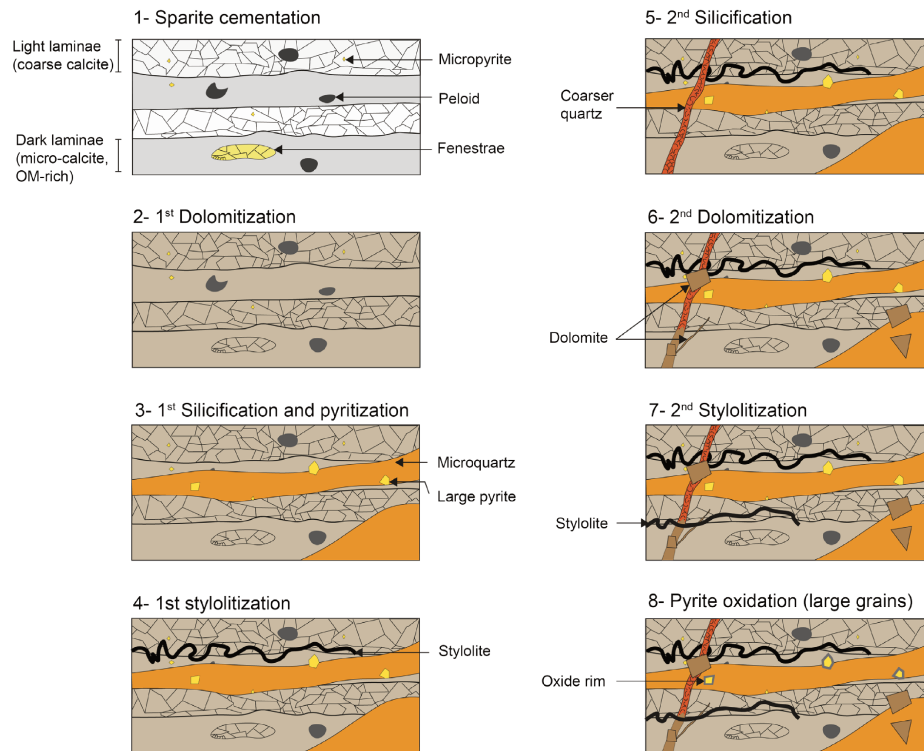


Fig. 8.6. Diagrams illustrating the inferred post-depositional history of the studied samples. Not to scale. Modified from Lawnizack (2022).

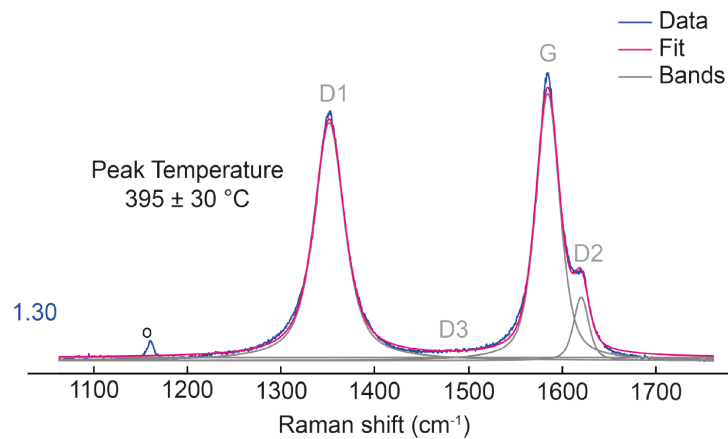


Fig. 8.7. Raman spectra of carbonaceous matter from sample 2a at 1.30 m depth of the drill core (partially silicified stromatolite), fitted to the theoretical G and D bands. Peak temperature estimation of $395 \pm 30^\circ\text{C}$ is calculated using the method described in Kouketsu et al. (2014).

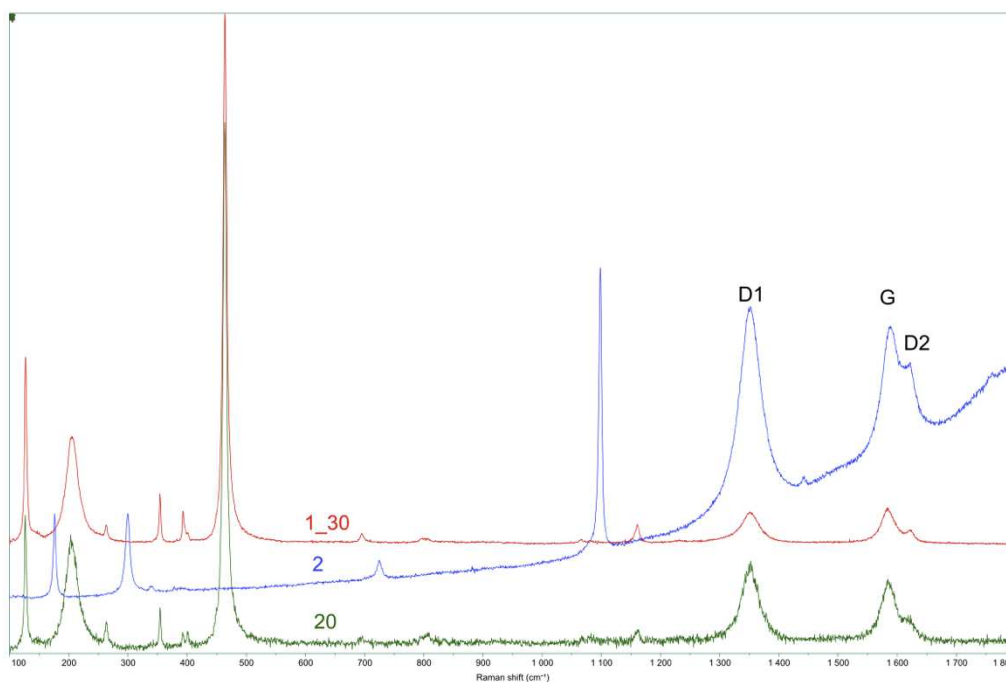


Fig. 8.8. Three Raman spectra of carbonaceous matter, associated to quartz in samples 1.30 and 20, and associated to carbonates in sample 2. Raman spectra are similar. G, D1 and D2 bands are identified. G band is centered around 1587 cm^{-1} , and D2 can be easily identified, typical of a partially graphitized carbon. The reorganization in the aromatic structure indicates that the samples have likely been affected by regional metamorphism. Peak temperatures are estimated around $395 \pm 30^\circ\text{C}$ for samples 1.30 and 20 (carbon associated to quartz).

8.3. Methods

Sampling. 41 samples were chosen regularly along a 1.5 m drill core so as to get a stratigraphic resolution of a few centimeters. In addition, 18 outcrop samples were collected along a 20 m long section (Fig. 8.3), to compare and complement the signal from the drill core. Core depths and log positions of each sample are indicated in Table 8.1. All samples were analyzed for their major and trace element composition, carbonate content, carbon content, and both organic and inorganic carbon isotope compositions. For nitrogen, a subset of 18 core samples were selected according to their organic matter content ($\text{TOC} > 0.5\%$ in the digestion residue), that mostly reflects their potential in containing enough nitrogen for analysis.

Chemical treatment prior to C and N analyses. Samples were first crushed into powder using a ring and puck mill in order to obtain sample powder smaller than $60\ \mu\text{m}$. Carbonate-free residues were obtained by mixing sample powders with 6N HCl for two successive digestion

steps: first at room temperature for 24h, then at 80°C for 4h. Samples were then rinsed with deionized distilled water to a neutral pH and oven-dried at 40°C for 48h.

Mineralogy. Mineralogy was investigated before and after chemical treatment using X-Ray Diffraction (XRD) at the Biogéosciences Laboratory (Université de Bourgogne, France). Diffractograms were obtained with a Bruker D8 Endeavor diffractometer with CuK α radiation, LynxEye XE-T detector and Ni filter, under 40 kV voltage and 25 mA intensity. The goniometer scanned from 2° to 65° 2 θ for each run. Identification of crystalline phases was based on the position and area of their respective mean basal reflections. Semi-quantitative estimates (Supplementary Table 8.1) of the two main mineral phases were made using the open source XRD refinement software Profex (Doebelin and Kleeberg, 2015). Accordingly, the amount of carbonates in the samples has been used to define two lithological endmembers: “cherts” (when carbonates range from 0 to 80 wt.%) and “carbonates” (when carbonates range from 80 to 100 wt.%).

Organic C isotopic analyses. The decarbonated residues were poured into tin capsules (50 to 80 mg of powder) and weighted using a Sartorius M2P ultra-balance. TOC and $\delta^{13}\text{C}_{\text{org}}$ measurements were performed at the Biogéosciences Laboratory (Université de Bourgogne, France) using a Thermo Fisher Scientific Flash Smart elemental analyser, coupled to a Thermo Fisher Scientific Delta V isotope ratio mass spectrometer (EA-IRMS) via a ConFlo IV interface. Certified USGS40 ($\delta^{13}\text{C}_{\text{org}} = -26.39\text{‰}$, TOC = 40.82 wt.%) and caffeine IAEA-600 ($\delta^{13}\text{C}_{\text{org}} = -27.77\text{‰}$, TOC = 49.48 wt.%) reference materials were used for the calibration. Total organic carbon (TOC) contents are expressed in dry weight percentage (wt.%) of the non-decarbonated bulk powder and isotope results are reported in delta-notation relative to V-PDB. Each measurement session included three to four standards measurements at the beginning and at the end, as well as one standard measurement every 12 samples. The mean $\delta^{13}\text{C}_{\text{org}}$ precision for standard USGS40 is better than 0.45‰ and the mean accuracy better than 0.09‰ (Supplementary Table 8.2). Each sample was duplicated. The mean external reproducibility (2σ), based on sample replicate analyses and including powder resampling and reprocessing via chemical treatment, is ± 57 ppm for the TOC content and $\pm 0.6\text{‰}$ for the $\delta^{13}\text{C}_{\text{org}}$ (Table 8.1).

Inorganic C isotopic analyses. $\delta^{13}\text{C}_{\text{carb}}$ measurements were also performed at the Biogéosciences Laboratory (Université de Bourgogne, France). Samples were ground, homogenized and oven-dried at 80°C for 4 hours. 2 mg aliquots were weighed and transferred into 12 mL Labco™ Exetainers™. Atmospheric gases were flushed from the tubes and replaced

with a CO₂-free synthetic atmosphere (80 % N₂ and 20 % O₂) using the automated air sampler flushing program of an IRIS Delta Ray™ (ThermoScientific™). An excess of 0.25 mL of H₃PO₄ (100%) was manually injected into each tube. After reacting for 12 hours at 80°C, the carbon isotopic composition ($\delta^{13}\text{C}_{\text{carb}}$) and the quantity of CO₂ released from the sample were measured by IRIS (ThermoScientific™ Delta Ray™). Aliquots of a calibrated reference gas (Bio; $\delta^{13}\text{C} = -25.5 \text{ ‰VPDB}$) and a solid standard of calcite put through the same chemical treatment as the samples (NBS19; $\delta^{13}\text{C} = +1.95 \text{ ‰VPDB}$) were used for calibrating the measurements on the VPDB international scale and to estimate the internal error ($< 0.1 \text{ ‰}, 2\sigma$).

N isotopic analyses. As all samples contain less than 50 ppm N, the EA-IRMS method applied for carbon analyses is not sensitive enough for reliable bulk nitrogen isotopic analyses. Samples were therefore analyzed at IPGP using the “sealed-tube combustion method” as described in Ader et al. (2014, 2016). In brief, N₂ was produced offline through sealed-tube Dumas combustion (Dumas, 1826) and cryogenically purified in a vacuum line. Up to 400 mg of decarbonated residual powder was put into a quartz tube with CuO and Cu wires, purified beforehand at 900°C for 2h in a muffle furnace to prevent contamination. Samples were degassed for 12h at 150°C under vacuum to remove adsorbed atmospheric N₂ and organics. Quartz tubes were then sealed directly under vacuum and combusted in a muffle furnace at 950°C for 6h under oxidizing conditions by oxygen liberated from the CuO wires, then cooled at 600°C for 2h, allowing residual oxygen to combine with cupric oxide and nitrous oxide to be reduced by copper, and finally cooled to ambient temperature (Kendall and Grim, 1990). Busigny et al. (2005) have shown that the extraction yield for this protocol is 100% for both organic and mineral nitrogen, including ammonium in minerals such as phyllosilicates. The content of each quartz tube was released in the vacuum line with a tube cracker, where CO₂ and H₂O were trapped cryogenically to avoid any subsequent isobaric interferences. The purified incondensable N₂ gas was concentrated into a calibrated volume for quantification using a Toepler pump (Hg manometer). Standard analytical procedures for nitrogen usually include CaO in the reagents to trap gaseous CO₂ and H₂O from the samples (Kendall and Grim, 1990). Given that Busigny et al. (2005) have shown that CaO significantly contributes to analytical blanks, we performed a few tests which showed identical $\delta^{15}\text{N}$ results within the analytical precision whether CaO was added or not. Samples were thus analyzed without adding CaO. Purified N₂ was analyzed by dual-inlet mass spectrometry using a ThermoFinnigan DeltaPlus XP IRMS. Possible air contamination and isobaric interferences (due to CO) were monitored by scanning of m/z 12 (C from CO₂, CO, CH₄ or organic compounds), 18 (H₂O), 30 (C¹⁸O), 32

(O₂), 40 (atmospheric Ar) and 44 (CO₂). Analytical blanks for the entire procedure are <0.02 micromoles N which represents a mean of 8% of the gas (16% of the gas for the least concentrated sample and 4% for the most concentrated) (Supplementary Table 8.3). TN and $\delta^{15}\text{N}$ values have been individually corrected from the blank contribution (Supplementary Table 8.3), using the reference blank value of $\delta^{15}\text{N} = -3.7\text{‰}$ measured by Busigny et al. (2005). On average, blank-corrected $\delta^{15}\text{N}$ values are 0.4‰ higher than their raw counterparts (from 0‰ to 1.2‰ higher). External $\delta^{15}\text{N}$ reproducibility is only available for a single sample (Table 8.1), therefore the mean external reproducibility reported for $\delta^{15}\text{N}$ values in Fig. 8.4 is taken from Pellerin et al. (2023) and Pellerin et al. (*in review*) in which external reproducibility is determined using the same analytical technique for a range of TN values comparable to this study.

8.4. Results

Based on XRD analyses, carbonates through the entire drill core are identified as dolomite (Fig. 8.9; Supplementary Table 8.1), which is consistent with petrographic observations in microscopy (Fig. 8.5). Carbonate content obtained by gravimetric quantification after HCl digestion is highly variable (4 to 99%) depending on the relative proportions of silicified laminations (Table 8.1, Supplementary Table 8.1). Carbonate content estimated through integration of peak areas from XRD spectra yields identical results within uncertainties ($R^2=0.9922$, Fig. 8.10, Supplementary Table 8.1). Total organic carbon (TOC) contents estimated from the TOC of the decarbonated residue vary between 81 ppm and 946 ppm with a mean value of 420 ± 195 ppm ($n=52$) (Table 8.1, Fig. 8.3, Fig. 8.4). Total nitrogen (TN) content ranges from 1.0 to 4.9 ppm with a mean of 2.5 ± 1.1 ppm ($n=18$) (Table 8.1, Fig. 8.4). TOC and TN contents are poorly correlated ($R^2=0.2592$, Fig 8.11A). TOC/TN ratios are below 450, which is relatively low for Archean sedimentary rocks (Yamaguchi, 2002); it ranges from 105 to 436 with a mean TOC/TN of 212 ± 92 ($n=18$) (Table 8.1, Fig. 8.4). Along the drill core, $\delta^{15}\text{N}$ values ($n=18$) range between -3.7‰ and 4.2‰ with a mean $\delta^{15}\text{N}$ of $0.7\pm 2.3\text{‰}$ (Table 8.1, Fig. 8.4), with no clear stratigraphic trend (Fig. 8.4). $\delta^{15}\text{N}$ variations are not correlated with nitrogen concentrations ($R^2=0.0003$, Fig. 8.11B), TOC/TN ratios ($R^2=0.0275$, Fig 8.11C) or organic carbon isotope compositions ($R^2=0.0812$, Fig 8.11D). $\delta^{13}\text{C}_{\text{org}}$ values are highly variable, ranging from -31.1‰ to -15.8‰ , with a mean value of $-19.8\pm 2.7\text{‰}$ ($n=59$) (Table 8.1, Fig. 8.3-8.4). Variations do not seem to follow any stratigraphic pattern (Fig. 8.3-8.4). $\delta^{13}\text{C}_{\text{carb}}$ values range from -2.5‰ to -1.1‰ , with a mean value of $-1.3\pm 0.3\text{‰}$ ($n=53$) (Table 8.1, Fig. 8.3-8.4). They

display more variability in the outcrop section than in the drill core (Fig. 8.3). The average TOC contents, $\delta^{13}\text{C}_{\text{org}}$ and $\delta^{13}\text{C}_{\text{carb}}$ values in carbonates does not significantly differ from the average TOC contents, $\delta^{13}\text{C}_{\text{org}}$ and $\delta^{13}\text{C}_{\text{carb}}$ values in silicified samples (Fig. 8.12, $p>0.05$).

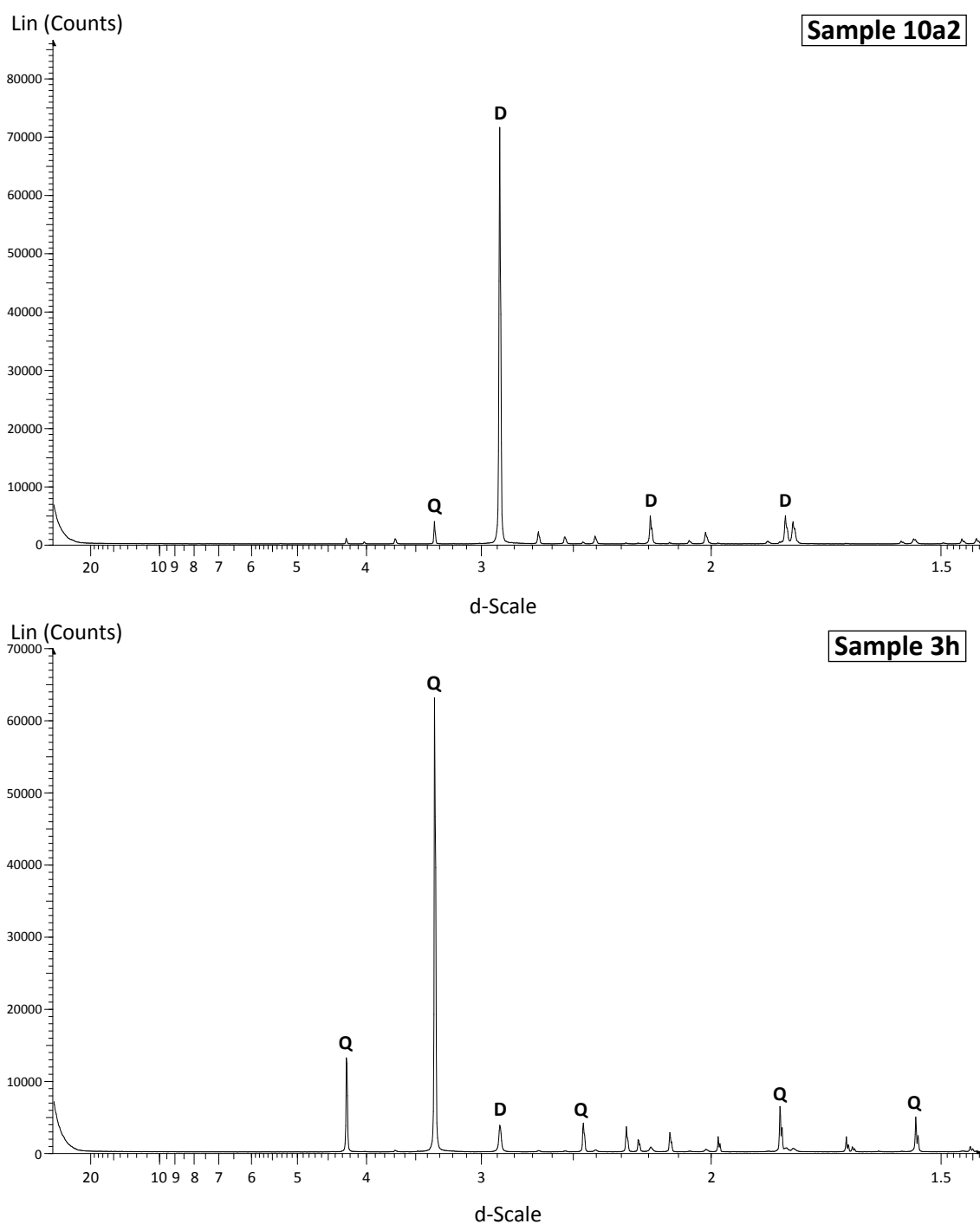


Fig. 8.9. XRD diffractograms of samples 10a2 and 3h, representative of the main crystalline phases found in the studied samples: dolomite (D) and quartz (Q).

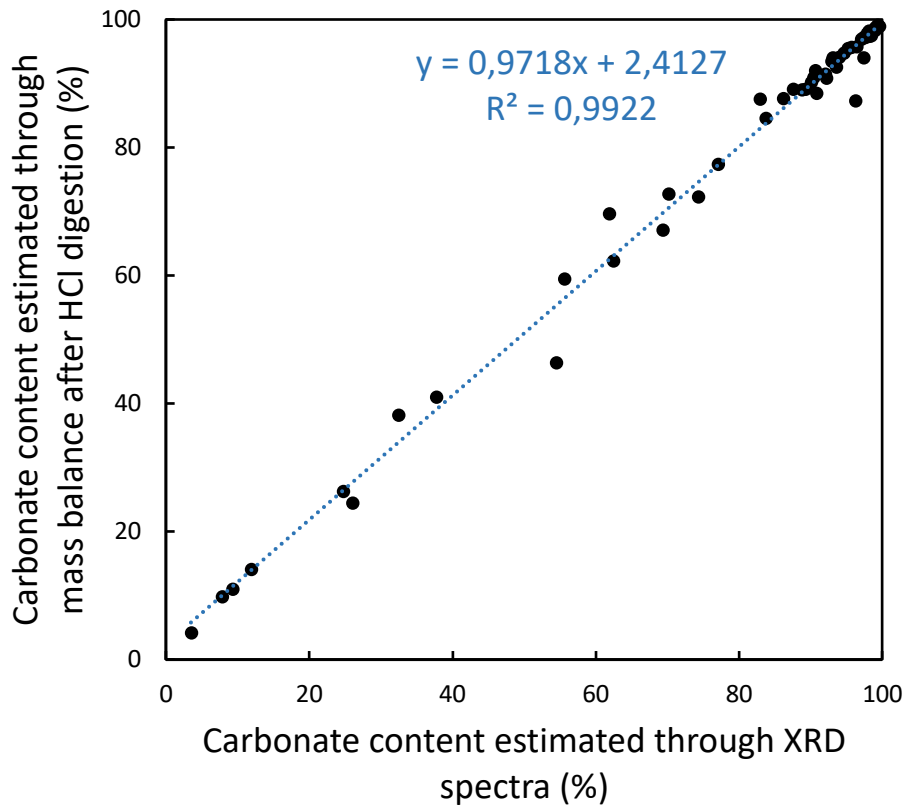
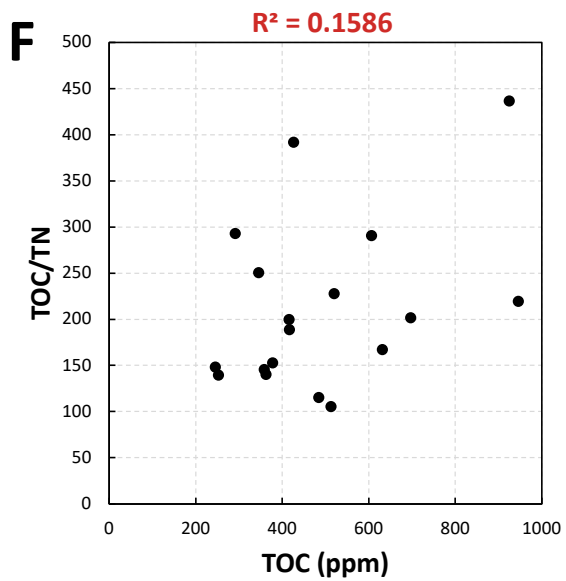
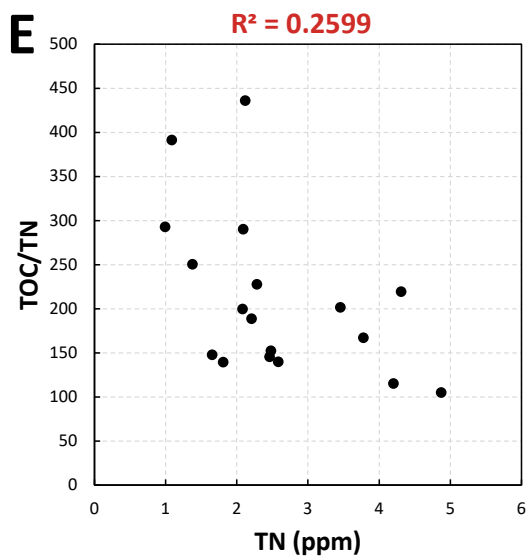
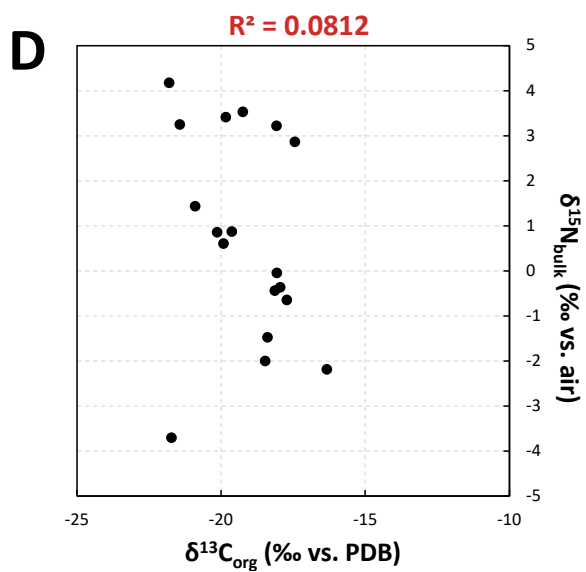
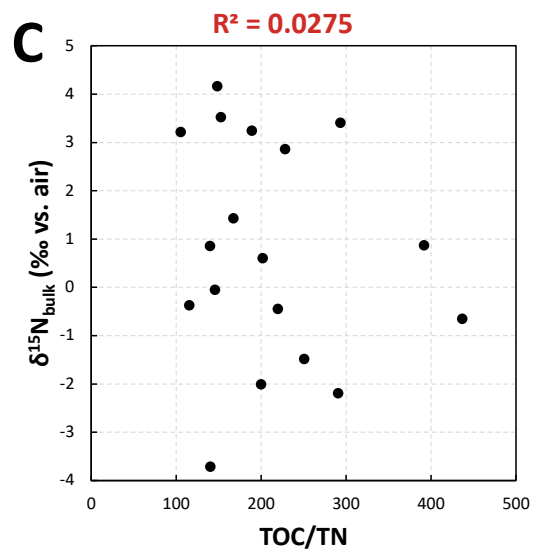
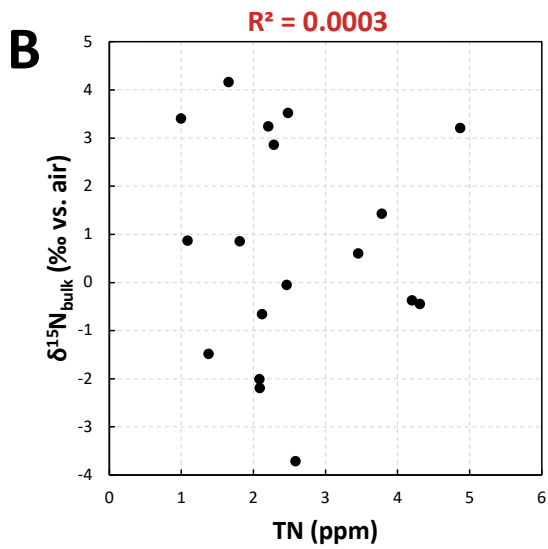
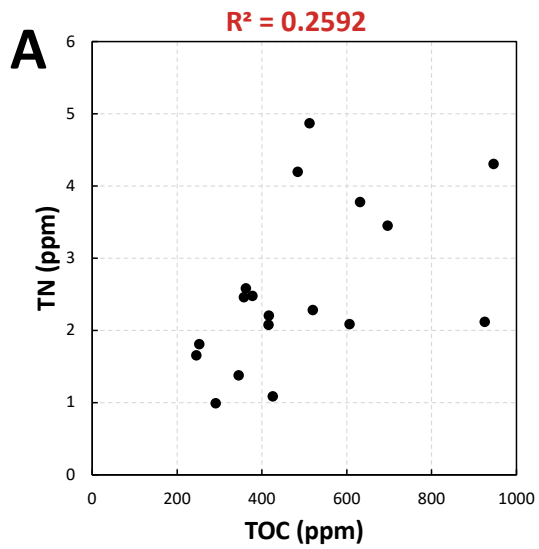


Fig. 8.10. Correlation between the carbonate content of the studied samples estimated through gravimetric mass balance after HCl digestion vs. carbonate content estimated through integration of XRD spectra peak areas using the Profex software (Doebelin and Kleeberg, 2015).



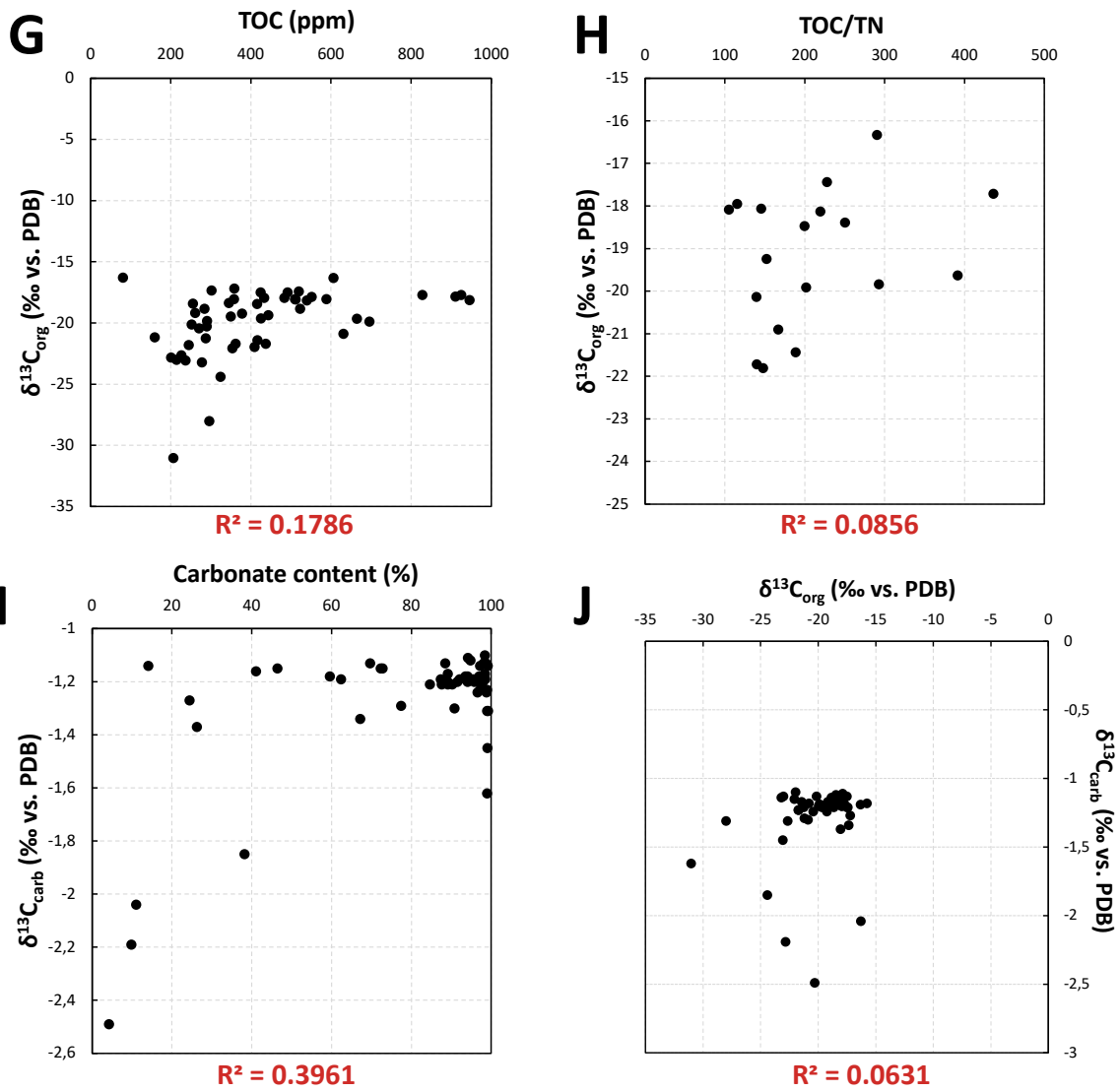


Fig. 8.11. Crossplots for the studied section with their associated correlation coefficient (R^2): (A) TOC (ppm) vs. TN (ppm); (B) TN (ppm) vs. $\delta^{15}\text{N}_{\text{bulk}}$ (‰ vs. air); (C) TOC/TN vs. $\delta^{15}\text{N}_{\text{bulk}}$ (‰ vs. air); (D) $\delta^{13}\text{C}_{\text{org}}$ (‰ vs. PDB) vs. $\delta^{15}\text{N}_{\text{bulk}}$ (‰ vs. air); (E) TN (ppm) vs. TOC/TN; (F) TOC (ppm) vs. TOC/TN; (G) TOC (ppm) vs. $\delta^{13}\text{C}_{\text{org}}$ (‰ vs. PDB); (H) TOC/TN vs. $\delta^{13}\text{C}_{\text{org}}$ (‰ vs. PDB); (I) carbonate content (wt. %) vs. $\delta^{13}\text{C}_{\text{carb}}$ (‰ vs. PDB); (J) $\delta^{13}\text{C}_{\text{org}}$ (‰ vs. PDB) vs. $\delta^{13}\text{C}_{\text{carb}}$ (‰ vs. PDB).

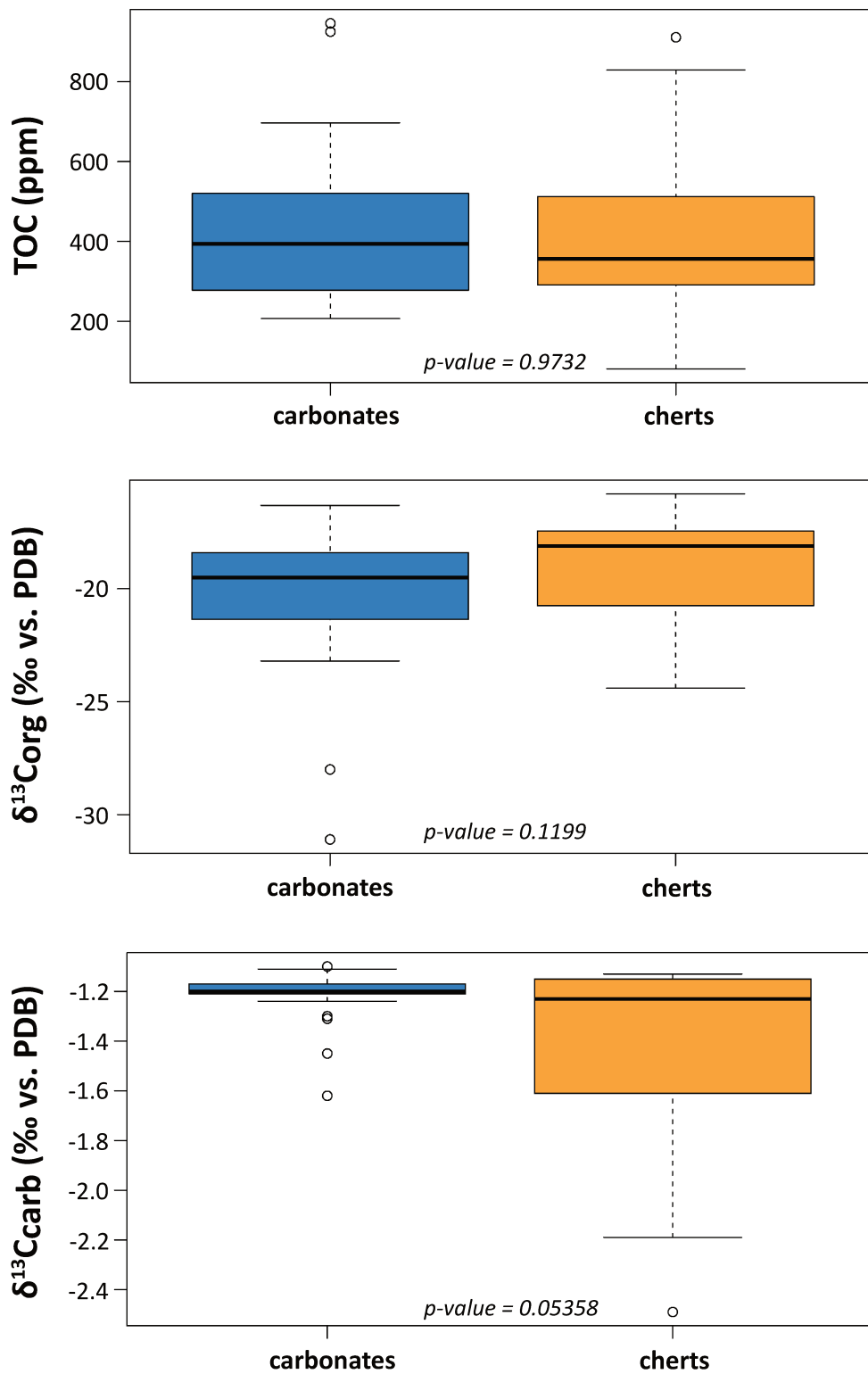


Fig. 8.12. Boxplots showing the TOC content (ppm), $\delta^{13}\text{C}_{\text{org}}$ (‰ vs. PDB) and $\delta^{13}\text{C}_{\text{carb}}$ (‰ vs. PDB) range of values and means between (1) carbonated samples (carbonates, > 80 wt.% carbonates) and (2) silicified samples (cherts, < 80 wt.% carbonates). Associated p-values are indicated in italics.

Sample	Log position (cm)	Core depth (cm)	Facies/Lithology	XRD main phase	Carbonate content (% HCl digestion)	TOC (wt. ppm)	SD	Nb repl.	TN (wt. ppm) on digestion residue	SD	Nb repl.	TN (wt. ppm)	TOC/TN	$\delta^{13}\text{C}_{org}$ (‰ vs. PDB)	SD	Nb repl.	$\delta^{15}\text{N}_{org}$ (‰ vs. air)	SD	Nb repl.	$\delta^{13}\text{C}_{carb}$ (‰ vs. PDB)	
MA10D-2	16.25		Laminated stromatolites	Dolomite	99	278	16	2					-23.2	1.0	2					-1.24	
MA10D-1	28.75		Laminated stromatolites	Dolomite	98	215	36	2					-23.0	0.1	2					-1.31	
MA10B	73.5		Laminated stromatolites	Dolomite	99	227	21	2					-22.7	0.3	2					-1.31	
MA6	89.5		Laminated stromatolites	Dolomite	99	207	22	2					-31.1	0.2	2					-1.62	
MA3	125		Climbing ripples	Dolomite	99	297	65	2					-28.0	0.8	2					-1.31	
MA1	152		Climbing ripples	Dolomite	99	237	44	2					-23.1	0.1	2					-1.45	
HABUS (150cm)																					
MA43	310		Siltified limestone	Quartz	10	201	90	2					-22.8	0.5	2					-2.19	
MA37	614		Siltified limestone	Dolomite	77	161	8	2					-21.2	2.9	2					-1.29	
MA35	647		Siltified limestone	Quartz	38	325	21	2					-24.4	0.0	2					-1.85	
MA32	719		Laminated stromatolites / Siltified limestone	Quartz	11	81	40	3					-16.3	2.23	3					-2.04	
HABUS (483cm)																					
MA30	1239		Laminated stromatolites / Siltified limestone	Dolomite	99	271	35	2					-20.4	0.2	2					-1.24	
MA28	1304		Laminated stromatolites / Siltified limestone	Dolomite	98	409	149	2					-22.0	0.2	2					-1.1	
MA24	1461		Laminated stromatolites	Dolomite	99	438	72	2					-21.7	1.8	2					-1.23	
HABUS (192cm)																					
MA23	1634		Laminated stromatolites	Dolomite	97	287	34	2					-21.3	0.4	2					-1.21	
11d	1742.75	1.75	Laminated stromatolites (more dense)	Dolomite	89	261		1					-19.2	0.8	2					-1.17	
11c	1746.25	5.25	Laminated stromatolites	Dolomite	86	235		1					-18.4	0.4	2					-1.19	
11b	1749.75	8.75	Laminated stromatolites / Siltified limestone	Dolomite	86	302	53	3					-17.4	1.8	3					-1.34	
MA19	1751		Laminated stromatolites	Dolomite	87	245		1					-17.4	1.8	3					-1.15	
11a2	1752.25	12.25	Laminated stromatolites	Dolomite	95	256		1					-22.1	1.9	2					-1.16	
11a1	1752.75	13.75	Laminated stromatolites	Dolomite	72	534		1					-18.1	1.9	2					-1.38	
109	1756.875	20.875	Siltified limestone	Dolomite	93	328		1					-17.5	0.9	2					-1.19	
108	1758.875	22.875	Festucal stromatolites	Dolomite	92	484		1					-16.2	1.2	2					-1.15	
1081	1758.875	22.875	Festucal stromatolites	Dolomite	87	607		1					-17.2	0.3	2					-1.21	
9e	1774.3	37.3	Festucal stromatolites	Dolomite	88	520		1					-17.2	0.1	2					-1.19	
9a	1778.5	41.5	Festucal stromatolites / Siltified limestone	Dolomite	92	925		2					-17.9	0.5	2					-1.11	
8d	1782.2	46.2	Festucal stromatolites	Dolomite	94	552		1					-18.9		1					-1.14	
8c	1789.2	48.2	Festucal stromatolites	Dolomite	97	291		1					-19.8	0.4	2					-1.19	
8b	1798.2	55.2	Festucal stromatolites	Dolomite	98	426		1					-19.6	1	1					-1.12	
8a	1798.2	55.2	Festucal stromatolites	Dolomite	91	632		1					-20.9	0.2	2					-1.3	
7	1800.6	59.6	Festucal stromatolites	Dolomite	98	946		1					-18.1	0.2	2					-0.4	
6a	1804.875	63.875	Festucal stromatolites	Quartz	88	829		1					-17.7	0.1	2					-1.19	
5c	1807.625	66.625	Festucal stromatolites / Siltified limestone	Dolomite	62	829		1					-20.8	0.5	2					-1.18	
5b	1812.4	71.4	Festucal stromatolites	Dolomite	85	492		1					-17.5	0.5	2					-1.21	
4c	1818	77	Laminated stromatolites	Dolomite	89	540		1					-18.2	0.1	2					-1.13	
4b	1827.25	81.25	Laminated stromatolites / Siltified limestone	Dolomite	97	362		1					-21.7	0.6	2					-1.23	
4a	1827.25	81.25	Laminated stromatolites	Dolomite	90	362		1					-18.6	0.2	2					-1.21	
3h	1829.25	88.25	Laminated stromatolites	Dolomite	98	417		1					-21.4	0.8	2					-1.17	
3g	1833.4	92.4	Siltified limestone	Quartz	14	524		1					-18.5	0.2	2					-1.14	
3f	1835.2	95.2	Laminated stromatolites	Dolomite	93	524		1					-18.8	0.2	2					-1.14	
3e	1839	98	Laminated stromatolites	Dolomite	96	284		1					-18.8	0.9	2					-1.2	
3d	1841.8	100.8	Laminated stromatolites	Dolomite	94			1					-20.0		1					-1.2	
3c	1844.6	103.6	Laminated stromatolites	Dolomite	96	350		1					-19.5	0.2	2					-1.24	
3b	1847.4	106.4	Laminated stromatolites	Dolomite	97	378		1					-19.2	0.1	2					-1.24	
3a	1850.2	109.2	Laminated stromatolites	Dolomite	98	697		1					-19.9	0.7	2					-1.19	
2b	1853.05	112.05	Laminated stromatolites	Dolomite	89	665		1					-19.7	0.4	2					-1.21	
2b3	1857.4	116.2	Laminated stromatolites	Quartz	60			1					-15.8		1						-1.18
MA15	1857.4	116.2	Laminated stromatolites / Siltified limestone	Quartz	24	359	76	3					-17.2	1.3	3					-1.27	
2b2	1860.6	119.6	Laminated stromatolites	Dolomite	91	444		1					-19.4	0.6	2					-1.2	
2b1	1864	123	Laminated stromatolites	Dolomite	89	444		1					-18.0	0.5	2					-1.2	
2b3	1867.4	126.4	Laminated stromatolites	Dolomite	97	345		1					-18.4	0.5	2					-1.18	
2a2	1870.8	129.8	Laminated stromatolites / Siltified limestone	Dolomite	95	416		1					-18.5	0.1	2					-1.12	
2a1	1874.25	133.25	Laminated stromatolites	Dolomite	72	512		1					-18.1	0.3	2					-1.15	
1c	1880.5	139.5	Siltified limestone	Quartz	46	911		1					-17.8	0.0	2					-1.15	
1b	1884.5	143.5	Laminated stromatolites	Dolomite	70	253		1					-20.1	0.3	2					-1.13	
1a	1888.75	147.75	Laminated stromatolites / Siltified limestone	Dolomite	99	424		1					-17.5	0.3	2					-1.13	
MA13	1911		Siltified limestone	Quartz	26	511	106	2					-18.1	1.3	3					-1.37	
MA12	1954		Laminated stromatolites / Siltified limestone	Quartz	4	291	133	2					-20.3	0.3	2					-2.49	

Table 8.1. Data featuring sample ID, log position along the outcrop section (cm), core depth (cm), facies/lithology, main mineral identified on XRD spectra, carbonate content estimated through gravimetric mass balance after HCl digestion (%), TOC (ppm, wholerock), TN (ppm, digestion residue), TN (ppm, wholerock), TOC/TN, $\delta^{13}\text{C}_{\text{org}}$ (‰ vs. PDB), $\delta^{15}\text{N}_{\text{bulk}}$ (‰ vs. air), and $\delta^{13}\text{C}_{\text{carb}}$ (‰ vs. PDB) for all samples analyzed along the studied outcrop section and drill core. Standard deviation (SD) and number of replicates (Nb repl.) are given after selected parameters when samples were replicated.

8.5. Discussion

A primary nitrogen isotope signature despite potential organic carbon resetting

Before attempting to interpret the significance of the carbon and nitrogen isotopic signals, it is necessary to evaluate if and how they have been impacted by post-depositional processes. Diagenesis, metamorphism and metasomatism can shift TN, TOC/TN and $\delta^{15}\text{N}$ values either by carbonaceous nitrogen devolatilization, ammonium input and mobility through fluids and/or fractionation during these processes (reviewed in Ader et al. (2016)).

During the graphitization process that accompanies prograde metamorphism, organic matter is progressively enriched in ^{13}C (Wada et al., 1994). In carbonated rocks, this enrichment results from carbonate-graphite isotopic exchange with increasing temperatures. Fractionations can go from a few permil to 20‰, depending on the temperature, lithology and extent of the isotope exchange. Significant $\delta^{13}\text{C}_{\text{org}}$ modifications can start at 300°C with the formation of the first graphite crystals (Kitchen and Valley, 1995) but isotopic equilibrium can only be reached when all the organic matter has been graphitized. This can be achieved at temperatures as low as 500°C but in numerous cases it is not attained below 700°C (Kreulen and van Beek, 1983). In the case of the studied dolomites, Raman geothermometry of carbonaceous matter indicates peak temperatures of $395 \pm 30^\circ\text{C}$ (Fig. 8.7-8.8). Raman spectra are typical of a partially graphitized carbon (Fig. 8.7-8.8), showing that samples have likely been affected by regional metamorphism that caused a reorganization of the aromatic structure of the carbonaceous matter. The low mean $\delta^{13}\text{C}_{\text{org}}$ value of $-19.8 \pm 2.7\text{‰}$ (Fig. 8.3-8.4) in the samples studied here, that are almost pure carbonates with low TOC contents (Fig. 8.3-8.4) could point towards an onset of isotope exchange between carbonaceous matter and carbonates. Mass balance calculations integrating the measured $\delta^{13}\text{C}_{\text{carb}}$ and assuming an original organic matter with a $\delta^{13}\text{C}_{\text{org}}$ at -30‰ show that a mean 64% of the isotopic signal comes from the initial organic matter (between 51 and 100‰). In that case the $\delta^{13}\text{C}_{\text{org}}$ signature would not be interpretable in terms of the C-isotope fractionation associated with photosynthesis, e.g., carbon fixation pathways. However, it is likely that the heterogeneity shown by the large range of $\delta^{13}\text{C}_{\text{org}}$ values from -31.1‰ to -15.8‰ (Table 8.1, Fig. 8.3-8.4) is a remnant of some degree of heterogeneity in the primary $\delta^{13}\text{C}_{\text{org}}$ signal.

In the set of samples studied here, the poor correlation between TOC and TN ($R^2=0.2592$, Fig. 8.11A) probably indicates that organic N and mineral N (fixed NH_4^+ that substitutes for K^+ in

some phyllosilicates, Kemp and Mudrochova (1973)) coexist, and some of the XRD analyses show traces of phyllosilicates (clays or micas) that could host the mineral N (Supplementary Table 8.1). Organic N and mineral N can be affected differently by post-depositional processes taking place from early diagenesis to metamorphism (reviewed in Ader et al. (2016)). While early diagenesis under anoxic conditions does not seem to shift organic matter $\delta^{15}\text{N}$ values by more than 1‰ (Lehmann et al., 2002), an increase in $\delta^{15}\text{N}$ and a decrease in TN is usually seen during prograde metamorphism (Bebout and Fogel, 1992; Boyd and Philippot, 1998; Haendel et al., 1986; Jia, 2006), maximum isotopic enrichments documented for greenschist facies metamorphism are below 2‰ (Jia, 2006; Stüeken et al., 2017), which is smaller than the 8‰ range of $\delta^{15}\text{N}$ variations reported in this study. This means that although absolute values may be slightly shifted, the observed $\delta^{15}\text{N}$ variability recorded in the samples studied here is likely primary. Moreover, the absence of covariation between $\delta^{15}\text{N}$ and TOC/TN also argues against a strong modification of $\delta^{15}\text{N}$ values due to metamorphic N-loss ($R^2=0.0275$; Fig. 8.11C).

Nevertheless, most of the available Precambrian carbon and nitrogen isotope compositions were measured in shales (Chapter 3), which usually harbor larger C and N concentrations than carbonates and hence might be less sensitive to generalized secondary resetting and/or contaminations. Thus, the impact of metamorphism on $\delta^{15}\text{N}$ values may be different in the case of carbonates. When looking at available paired $\delta^{13}\text{C}_{\text{org}}-\delta^{15}\text{N}$ data, the nitrogen isotope signature recorded in carbonated samples seems to be more sensitive to metamorphism than in shales (Chapter 3). Indeed, Precambrian carbonates above the greenschist facies consistently display an increased $\delta^{13}\text{C}$ and a decreased $\delta^{15}\text{N}$ signal, which is not the case in shales (Fig. 8.13-8.14). Besides, the samples studied here fall into the range of ^{13}C -enriched and ^{15}N -depleted metamorphosed carbonates. However, contrary to most of the previous results on carbonate rocks, for which the blank contribution has likely lowered both $\delta^{15}\text{N}$ values and TOC/TN ratios (Fig. 8.15A, B, C), in the Malmani carbonates TOC/TN ratios remain as high as in unmetamorphosed samples (Fig. 8.15D), arguing against a strong resetting of the nitrogen isotope signature.

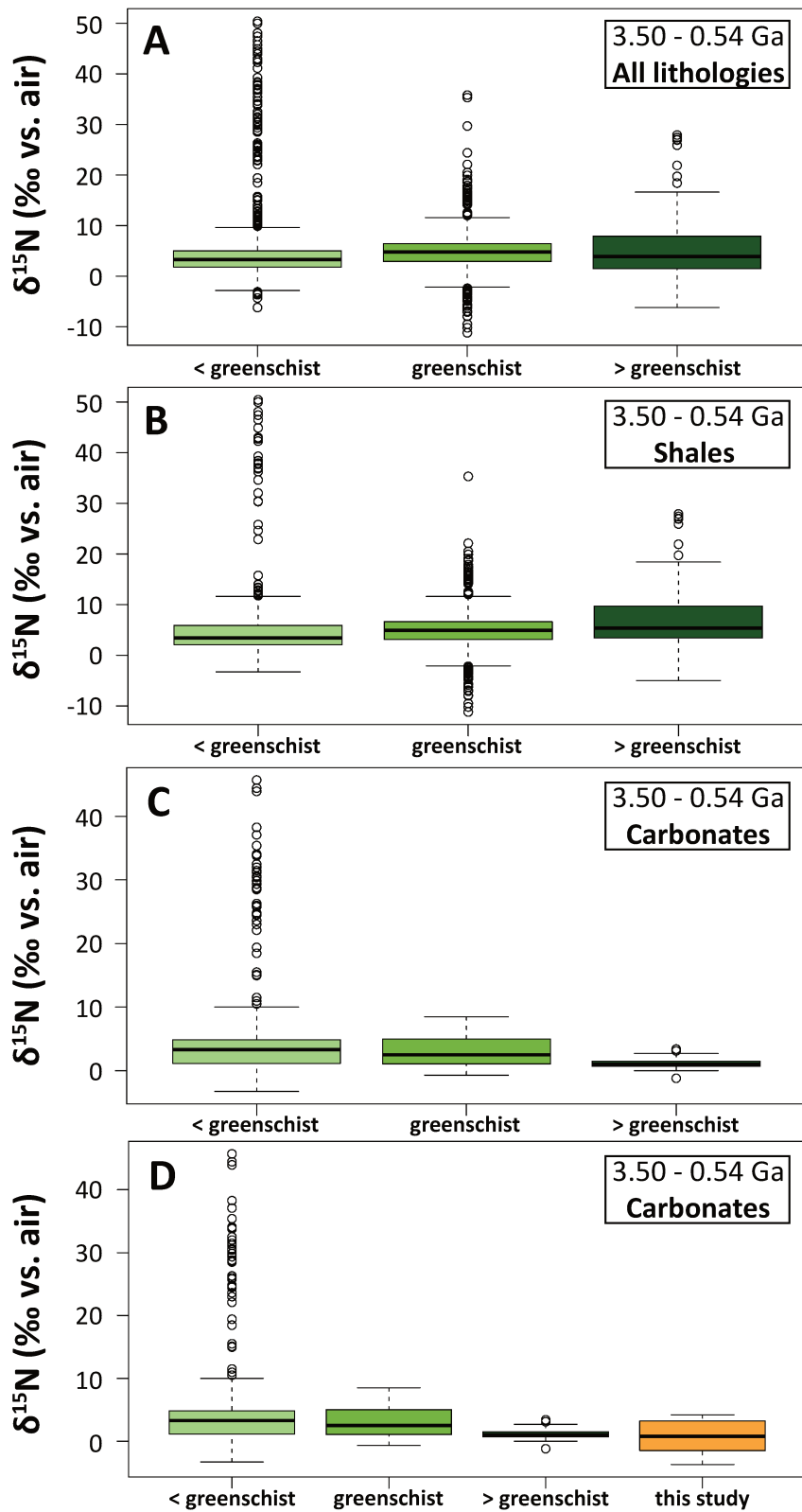
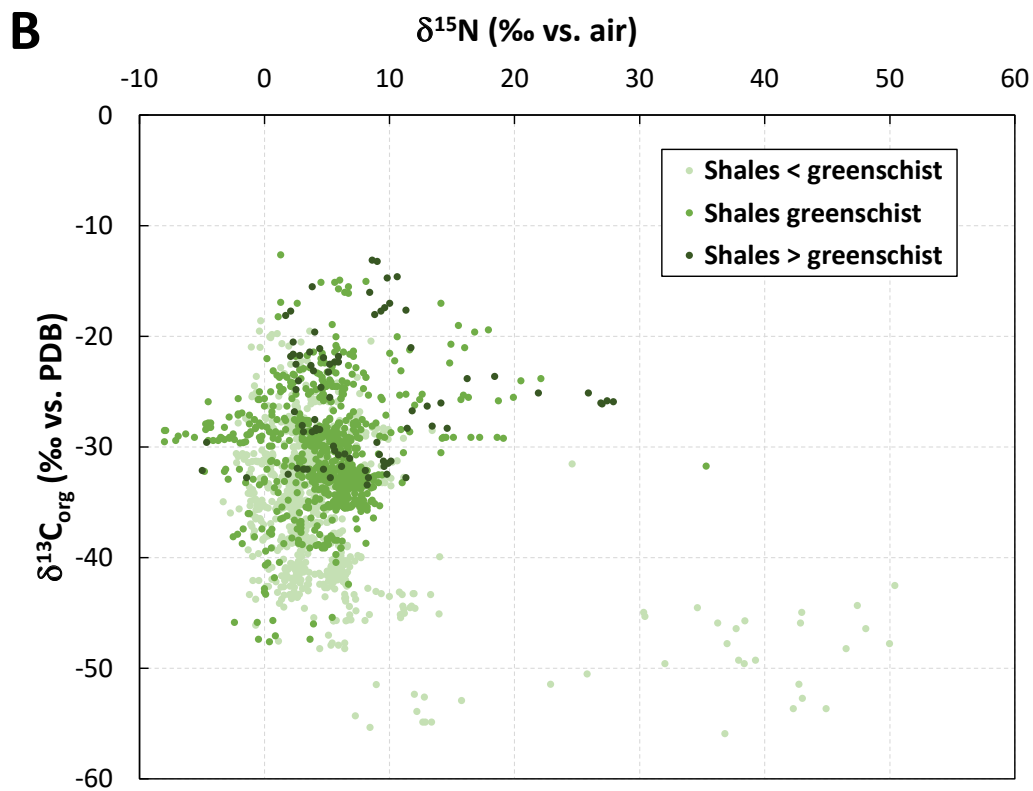
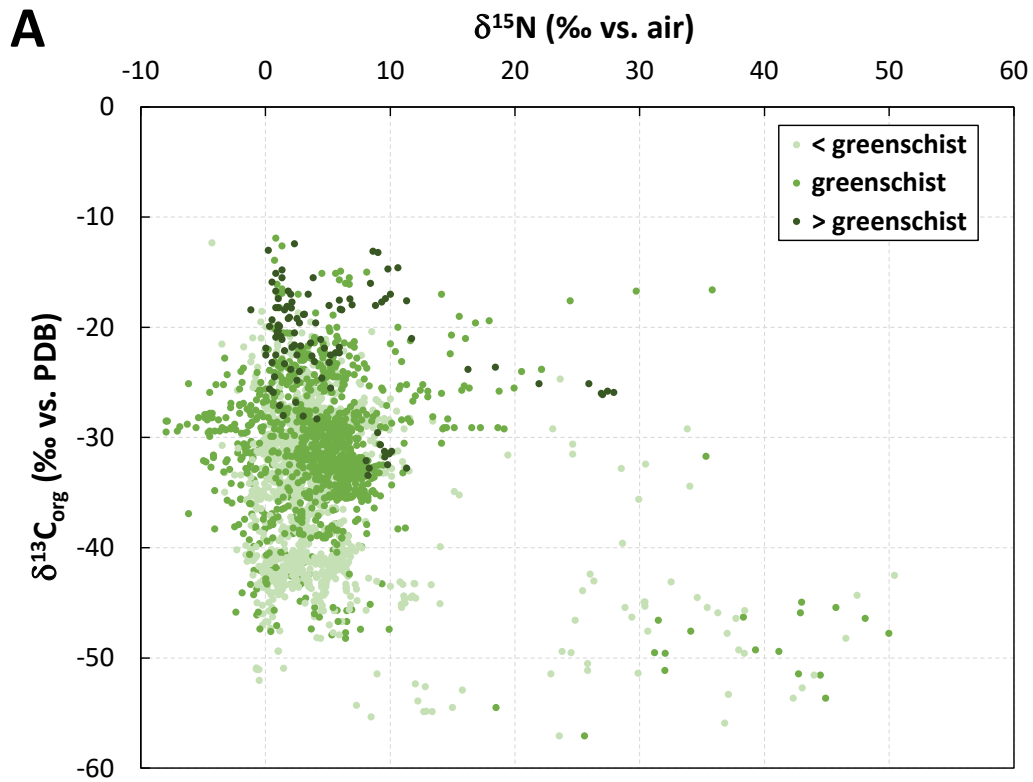


Fig. 8.13. Boxplots showing Precambrian (3.50-0.54 Ga) $\delta^{15}\text{N}$ (‰ vs. air) range of values and means sorted by metamorphic grade (lower than greenschist, greenschist, higher than greenschist) for (A) all lithologies (B) shales (C) carbonates (D) carbonates presented in this study.



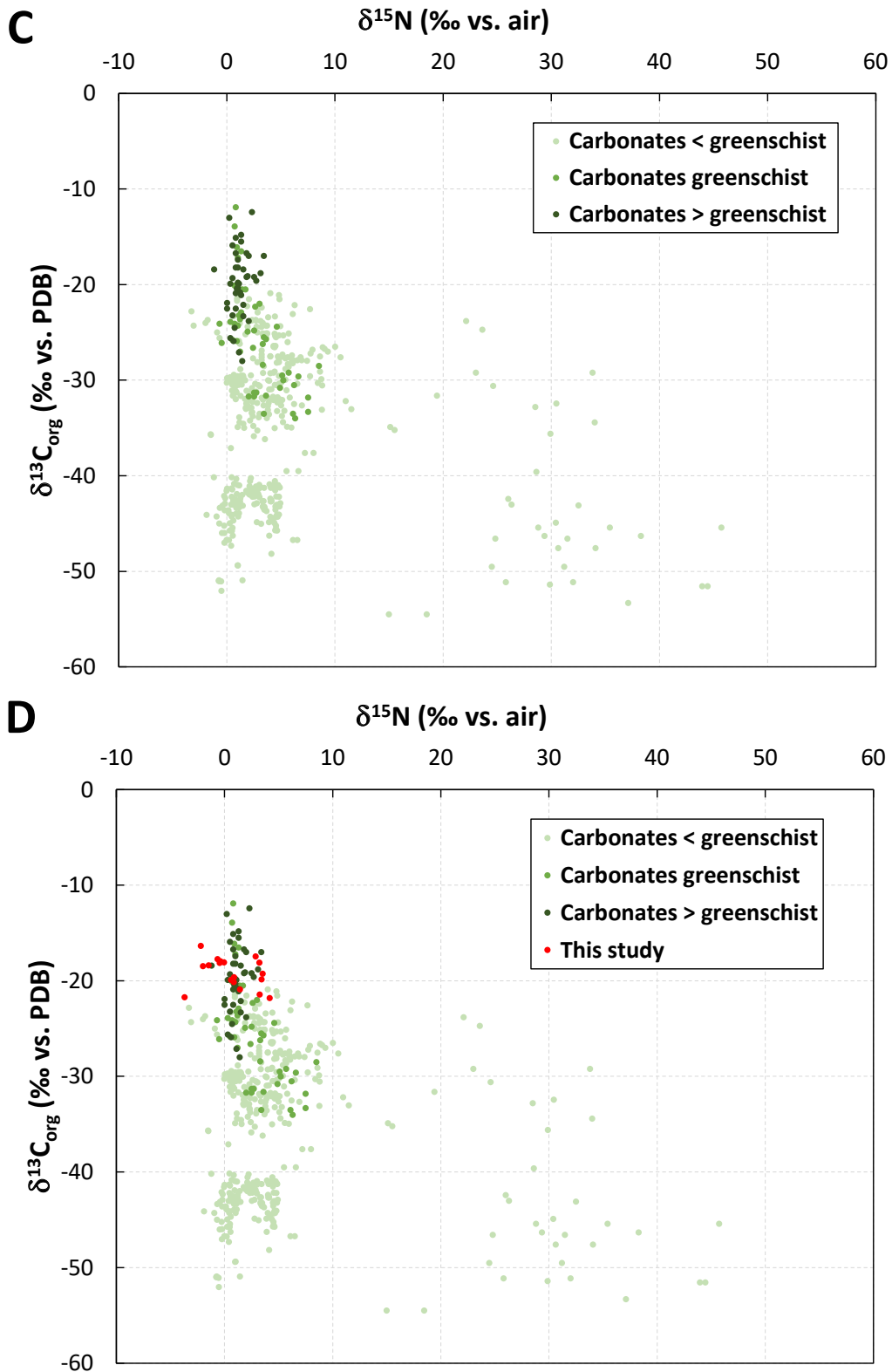


Fig. 8.14. $\delta^{15}\text{N}$ (‰ vs. air) vs. $\delta^{13}\text{C}_{\text{org}}$ (‰ vs. PDB) crossplots for Precambrian (3.5-0.54 Ga) samples, sorted by metamorphic grade (light green: lower than greenschist; green: greenschist; dark green: higher than greenschist). (A) in all lithologies. (B) in shales. (C) in carbonates. (D) in carbonates, including the studied carbonate samples in red.

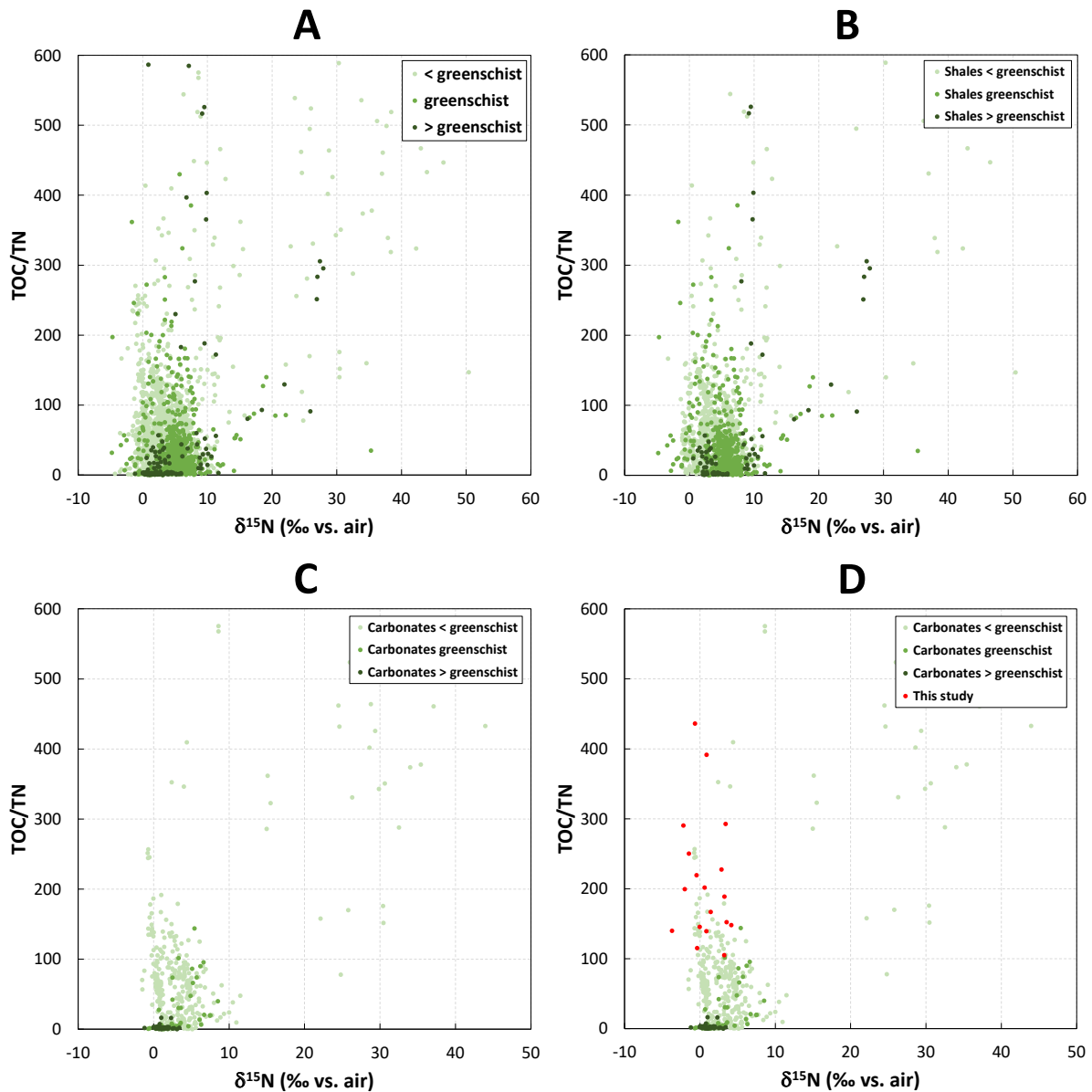


Fig. 8.15. $\delta^{15}\text{N}$ (‰ vs. air) vs. TOC/TN crossplots for Precambrian (3.5-0.54 Ga) samples, sorted by metamorphic grade (light green: lower than greenschist; green: greenschist; dark green: higher than greenschist). (A) in all lithologies. (B) in shales. (C) in carbonates. (D) in carbonates, including the studied carbonate samples in red.

Moreover, because (i) biologically-derived nitrogen is assumed to be the main nitrogen source in the studied samples, as biological nitrogen fixation has likely overtaken abiotic nitrogen sources since the Paleoproterozoic (Stüeken et al., 2016) and (ii) given the low correlation between TOC and TN ($R^2=0.0275$; Fig. 8.11C), a significant portion of nitrogen must have been transferred from organic matter to clays, generating a mineral nitrogen fraction that coexists with the organic nitrogen fraction. However, ammonification in the sediment only creates a

negligible isotope fractionation (Freudenthal et al., 2001; Möbius, 2013) that is unlikely to account for the observed variability in the sample set. We therefore assume here that, contrary to the carbon isotope signal, the nitrogen isotope signature recorded in the Malmani set of samples is primarily reflecting processes that took place at the time of deposition.

Oxidative pathways of the N-biogeochemical cycle are not recorded in the Malmani carbonates

With a mean $\delta^{15}\text{N}$ of $0.7 \pm 2.3\text{‰}$ (Fig. 8.4), the studied section contrasts with the section from slope settings for which $\delta^{15}\text{N}$ values fall between +1.8 and +10.1‰ (Godfrey and Falkowski, 2009). The consistently positive $\delta^{15}\text{N}$ values found in slope settings were interpreted as recording the presence of a sustained ^{15}N -enriched nitrate reservoir undergoing partial denitrification (Godfrey and Falkowski, 2009).

If the depositional environment of the studied samples was oxygen-depleted to fully anoxic, stromatolite-building microorganisms communities could have been dominated by anoxygenic photosynthesizers, with diazotrophs fixing N_2 whenever nitrogen becomes limiting, and using ammonium coming from organic matter degradation when available. This hypothesis would be compatible with the low $\delta^{13}\text{C}_{\text{org}}$ values centered around -20‰, that are in the range of anoxygenic photosynthesizers isotopic signature (Schidlowski, 2001).

Conversely, if free oxygen was indeed present in the Campbellrand-Malmani platform waters, the absence of consistently positive $\delta^{15}\text{N}$ values in the restricted studied shallow platform setting could result from different scenario. First, $\delta^{15}\text{N}$ values close to 0‰ could indicate that there was no nitrate supply from the main basin to the shallow part of the platform, i.e. that there was no strong upwelling reaching the shallow and/or restricted depositional environment of the studied samples. $\delta^{15}\text{N}$ values close to 0‰ could also be interpreted as recording a fully oxic reservoir in which nitrate remained stable, i.e. were not denitrified, and hence where nitrogen isotopes would only record the fractionation of N_2 -fixation, which is null (Quan and Falkowski, 2009). Finally, $\delta^{15}\text{N}$ values near 0‰ could be produced in a N-starved oligotrophic environment typical of modern microbial mats, where the N-cycle is cryptic, with quantitative nitrate consumption and/or denitrification inside the mats (e.g. Bauersachs et al., 2011).

A record of ammonium assimilation inside the microbial mats

In any case, ammonium was likely the dominant fixed nitrogen reservoir in the Malmani depositional environment. However, the 8‰ $\delta^{15}\text{N}$ variability, ranging from -3.7‰ to 4.2‰, is hard to explain by N_2 fixation alone, which typical isotope fractionation ranges from -2‰ to +2‰ (Bauersachs et al., 2009). The alternating positive and negative $\delta^{15}\text{N}$ values would reflect instead the fate of a sustained ammonium reservoir where ^{14}N -assimilation is favored, yielding primary producers with a negative $\delta^{15}\text{N}$ and increasing the residual ammonium $\delta^{15}\text{N}$ from +4‰ to +27‰ (Hoch et al., 1992). This residual ammonium could then be assimilated into a second organic pool that would be, on the other hand, ^{15}N -enriched. This scenario requires that the redox conditions of the ammonium reservoir were anoxic to the point that even ammonium oxidation did not occur. Such conditions were most certainly not met in the water column, as previous studies of the CMCP proposed that the emergence of stable shallow-water carbonate platforms in the Neoproterozoic provided ideal conditions for the evolution of early aerobic ecosystems (Eroglu et al., 2017), with trace element data supporting an increasing nutrient supply and oxidation state towards the continent (Eroglu et al., 2017). The presence of multiscale stromatolitic domes, some of the most undisputed microbial remains of photosynthesizers, also indicate at least some degree of oxidant production, possibly even O_2 . Finally, ammonium oxidation was recently proposed to have been active as early as 2.7 Ga based on extremely positive $\delta^{15}\text{N}$ values (Pellerin et al., *in review*). The ammonium pool was thus probably sheltered from oxidants and present in the interstitial fluids of the stromatolites, where it was produced by organic mineralization. It could have been quantitatively assimilated by photosynthesizers before reaching the upper part of the microbial mat. This would not have precluded diazotrophs from fixing N_2 whenever ammonium became limiting.

If stromatolitic carbonates indeed record ammonium assimilation occurring locally, they may be poor proxies of the water column N-biogeochemical cycle, which would be better recorded in shales from deeper depositional settings.

8.6. Conclusions

Although the carbon and nitrogen isotopic signatures preserved in sedimentary rocks are some of the standard tools for investigating redox changes in the ocean associated with the evolution of the biosphere, Precambrian sediments might not always provide information relevant to pinpoint Early Earth oxygenation. Indeed, stromatolitic carbonates are often targeted to investigate the onset of oxygenation, as they likely harbor the first organisms that developed oxidative metabolisms. In carbonates, the carbon isotope signature is more altered, even in the greenschist facies that a majority of Archean samples have reached. For this lithology, often N-poor, the blank contribution might also be important, obscuring the N isotopic signal. It is therefore difficult to assess if the C and N isotope signatures are primary. In the studied stromatolitic carbonates of the 2.55 Ga Malmani Subgroup, South Africa, the $\delta^{13}\text{C}_{\text{org}}$ signal seems partially reset while $\delta^{15}\text{N}$ values are likely preserved. If primary, the nitrogen isotopic signature does not argue for the presence of a persistent nitrate reservoir sustained by an oxygenated shallow water column, even partially. Hypotheses that could explain why the oxidative part of the nitrogen cycle is not expressed in the studied set of samples include (i) an anoxic environment dominated by anoxygenic photosynthesizers, (ii) a fully oxic environment where nitrate is produced but not denitrified, (iii) a cryptic oxidative N-cycle in which nitrate would be produced but quantitatively consumed, indicating an oligotrophic environment dominated by N_2 fixation, (iv) a proximal environment isolated from oceanic processes that would not reliably record the N-cycle of the water column. These various scenarios could also be operating together. In any case, ammonium was likely the dominant bioavailable N species in the depositional environment of these stromatolitic carbonates. However, the 8‰ $\delta^{15}\text{N}$ variability, ranging from -3.7‰ to 4.2‰, can hardly result from N_2 fixation alone. We argue that the Malmani stromatolitic platform records variable ammonium assimilation rates in a dynamic environment, preserving both the ^{15}N -enriched and the ^{15}N -depleted reservoirs. We argue that the studied set of samples might be a record of local processes happening in the depositional environment, either directly in the microbial mats or in their vicinity, on short, seasonal timescales, or maybe even longer climatic, astronomically driven cycles. They are unlikely to reflect the dynamics of the open ocean water column.

Sample	Log position (cm)	Core depth (cm)	Facies/Lithology	Carbonate content estimated through mass balance after HCl digestion (%)	Content estimated through XRD spectra (%)		
					Dolomite	Quartz	Phyllosilicate
MA10b-2	16.25		Laminated stromatolites	99.10	99.36	0.64	
MA10b-1	28.75		Laminated stromatolites	98.11	98.59	1.41	
MA7bas	73.50		Laminated stromatolites	99.18	99.27	0.73	traces
MA6	89.50		Laminated stromatolites	99.01	99.40	0.60	
MA3	125.00		Climbing ripples	98.96	99.50	0.50	
MA1	152.00		Climbing ripples	99.09	99.30	0.70	traces
Hiatus (150cm)							
MA43	310.00		Silicified limestone	9.84	7.78	92.22	
MA37	614.00		Silicified limestone	77.40	77.01	22.99	traces
MA35	647.00		Silicified limestone	38.23	32.46	67.54	
MA32	719.00		Laminated stromatolites / Silicified limestone	11.03	9.28	90.72	
Hiatus (203cm)							
MA30	1239.00		Laminated stromatolites / Silicified limestone	98.81	99.00	1.00	
MA28	1304.00		Laminated stromatolites / Silicified limestone	98.40	98.89	1.11	traces
MA24	1461.00		Laminated stromatolites	98.95	99.26	0.74	traces
Hiatus (192cm)							
MA23	1654.00		Laminated stromatolites	97.45	98.14	1.86	
11d	1742.75	1.75	Laminated stromatolites	89.12	87.47	12.53	traces
11c	1746.25	5.25	Laminated stromatolites	84.04			
11b	1749.75	8.75	Laminated stromatolites / Silicified limestone	95.57	95.17	4.83	
MA18	1751.00		Laminated stromatolites / Silicified limestone	67.16	69.31	30.69	
11a2	1753.25	12.25	Laminated stromatolites	98.23	98.04	1.96	traces
11a1	1756.75	15.75	Laminated stromatolites	72.75	70.11	29.89	
10b	1761.675	20.675	Silicified limestone	41.07	37.74	62.26	
10a2	1765.6875	24.6875	Fenestral stromatolites	93.49	92.89	7.11	
10a1	1768.3625	27.3625	Fenestral stromatolites	91.50	92.00	8.00	traces
9c	1774.30	33.30	Fenestral stromatolites	87.36	96.21	3.79	
9b	1778.50	37.50	Fenestral stromatolites	87.62	82.89	17.11	
9a	1782.65	41.65	Fenestral stromatolites / Silicified limestone	92.09	90.56	9.44	traces
8d	1787.20	46.20	Fenestral stromatolites	94.19	93.89	6.11	traces
8c	1790.20	49.20	Fenestral stromatolites	97.23	97.59	2.41	traces
8b	1793.20	52.20	Fenestral stromatolites	98.46	98.96	1.04	traces
8a	1796.20	55.20	Fenestral stromatolites	97.91	97.84	2.16	traces
7	1800.60	59.60	Fenestral stromatolites	90.85	92.13	7.87	traces
6b	1804.875	63.875	Fenestral stromatolites	87.71	86.16	13.84	
6a	1807.625	66.625	Fenestral stromatolites / Silicified limestone	62.34	62.41	37.59	traces
5c	1812.40	71.40	Fenestral stromatolites	94.10	93.00	7.00	
5b	1815.20	74.20	Fenestral stromatolites	84.62	83.66	16.34	
5a	1818.00	77.00	Laminated stromatolites / Silicified limestone	88.50	90.75	9.25	traces
4c	1822.25	81.25	Laminated stromatolites	97.25	97.30	2.70	traces
4b	1825.75	84.75	Laminated stromatolites	90.21	90.06	9.94	traces
4a	1829.25	88.25	Laminated stromatolites	98.39	98.91	1.09	traces
3h	1833.40	92.40	Silicified limestone	14.11	11.85	88.15	traces
3g	1836.20	95.20	Laminated stromatolites	92.62	93.48	6.52	
3f	1839.00	98.00	Laminated stromatolites	95.79	96.34	3.66	
3e	1841.80	100.80	Laminated stromatolites	94.09	97.32	2.68	
3d	1844.60	103.60	Laminated stromatolites	95.68	95.63	4.37	
3c	1847.40	106.40	Laminated stromatolites	96.59			
3b	1850.20	109.20	Laminated stromatolites	97.52	98.43	1.57	
3a	1853.05	112.05	Laminated stromatolites	89.10	88.73	11.27	
2b3	1857.20	116.20	Laminated stromatolites / Silicified limestone	59.54	55.56	44.44	
MA15	1857.40		Laminated stromatolites / Silicified limestone	24.45	26.03	73.97	
2b2	1860.60	119.60	Laminated stromatolites	90.94	90.36	9.64	
2b1	1864.00	123.00	Laminated stromatolites	89.15	89.23	10.77	
2a3	1867.40	126.40	Laminated stromatolites	96.97	96.99	3.01	
2a2	1870.80	129.80	Laminated stromatolites / Silicified limestone	94.80	94.57	5.43	
2a1	1874.25	133.25	Laminated stromatolites	72.30	74.29	25.71	traces
1c	1880.50	139.50	Silicified limestone	46.43	54.42	45.58	traces
1b	1884.50	143.50	Laminated stromatolites	98.71			
1a	1888.75	147.75	Laminated stromatolites / Silicified limestone	69.68	61.87	38.13	traces
MA13	1911.00		Silicified limestone	26.27	24.74	75.26	
MA12	1954.00		Laminated stromatolites / Silicified limestone	4.22	3.49	96.51	

Mean	80.58	79.74
SD	26.56	27.74
Min	4.22	3.49
Max	99.18	99.50

Supplementary Table 8.1. Carbonate content for each studied sample, estimated through mass balance after HCl digestion vs. estimated through XRD spectra using the open source XRD refinement software Profex (Doebelin and Kleeberg, 2015).

USGS40			
Date	TOC (%)	$\delta^{13}\text{C}_{\text{org}}$ (‰ vs. PDB)	$\delta^{13}\text{C}_{\text{org}}$ deviation from ref. value (-26.39‰)
15/12/2021	40.82	-26.44	0.05
15/12/2021	40.82	-26.32	0.07
15/12/2021	40.82	-26.41	0.02
15/12/2021	40.82	-26.38	0.01
15/12/2021	40.82	-26.4	0.01
15/12/2021	40.82	-26.38	0.01
15/12/2021	40.82	-26.39	0.00
15/12/2021	40.82	-26.39	0.00
15/12/2021	40.82	-26.4	0.01
15/12/2021	40.82	-26.4	0.01
15/03/2021		-26.44	0.05
15/03/2021		-26.33	0.06
15/03/2021		-26.42	0.03
15/03/2021		-26.32	0.07
15/03/2021		-26.44	0.05
15/03/2021		-26.39	0.00
14/01/2022		-26.4	0.01
14/01/2022		-26.38	0.01
14/01/2022		-26.38	0.01
14/01/2022		-26.39	0.00
14/01/2022		-26.34	0.05
10/01/2022	40.82	-26.28	0.11
10/01/2022	40.82	-26.43	0.04
10/01/2022	40.82	-26.45	0.06
10/01/2022	40.82	-26.39	0.00
10/01/2022	40.82	-26.4	0.01
10/12/2021	40.82	-26.45	0.06
10/12/2021	40.82	-26.36	0.03
10/12/2021	40.82	-26.35	0.04
10/12/2021	40.82	-26.39	0.00
10/12/2021	40.82	-26.38	0.01
26/11/2021	40.82	-26.41	0.02
26/11/2021	40.82	-26.37	0.02
26/11/2021	40.82	-26.38	0.01
26/11/2021	40.82	-26.41	0.02
26/11/2021	40.82	-26.39	0.00
14/01/2022	40.82	-26.4	0.01
14/01/2022	40.82	-26.38	0.01
14/01/2022	40.82	-26.38	0.01
14/01/2022	40.82	-26.39	0.00
14/01/2022	40.82	-23.69	2.7
14/01/2022	40.82	-26.34	0.05
Mean	40.82	-26.32	0.09
SD	0.00	0.42	
n=	31	42	

Supplementary Table 8.2. Standard measurements (USGS40) performed during all TOC and $\delta^{13}\text{C}_{\text{org}}$ analysis sessions, with deviation from reference $\delta^{13}\text{C}_{\text{org}}$ value for USGS 40 (-26.39‰). The mean $\delta^{13}\text{C}_{\text{org}}$ precision is 0.42‰ and the mean accuracy 0.09‰.

Sample ID	$\mu\text{moles N}$	Raw $\delta^{15}\text{N}$ (‰ vs. air)	Blank contribution (%)	Blank-corrected $\delta^{15}\text{N}$ (‰ vs. air)
11A2	0.23	3.6	8	4.2
10A2	0.40	-0.2	5	0.0
10A1	0.45	-0.5	4	-0.4
9C	0.17	-2.4	11	-2.2
9B	0.16	2.1	11	2.8
9A	0.22	0.1	8	0.4
9A	0.38	-1.8	5	-1.7
8B	0.11	2.3	16	3.4
8A	0.13	0.2	14	0.8
7	0.39	1.2	5	1.5
6B	0.33	-0.6	5	-0.4
4C	0.50	-3.7	4	-3.7
4A	0.26	2.8	7	3.3
3C	0.17	2.8	11	3.6
3B	0.38	0.4	5	0.6
2A3	0.44	-1.6	4	-1.5
2A2	0.28	-2.1	6	-2.0
2A1	0.15	2.4	12	3.2
1B	0.17	0.4	11	0.9

Mean	8
Min	4
Max	16

Supplementary Table 8.3. N analytical blank contribution and correction for the studied samples. Blank contribution (0.018 μmoles) represents a mean of 8% of the gas (16% of the gas for the least concentrated sample and 4% for the most concentrated). $\delta^{15}\text{N}$ values have been individually corrected from the blank contribution using the reference blank value of $\delta^{15}\text{N} = -3.7\text{‰}$ measured by Busigny et al. (2005). On average, blank-corrected $\delta^{15}\text{N}$ values are 0.4‰ higher than their raw counterparts (from 0‰ to 1.2‰ higher).

References

- Ader, M., Sansjofre, P., Halverson, G.P., Busigny, V., Trindade, R.I.F., Kunzmann, M., Nogueira, A.C.R., 2014. Ocean redox structure across the Late Neoproterozoic Oxygenation Event: A nitrogen isotope perspective. *Earth and Planetary Science Letters* 396, 1–13. <https://doi.org/10.1016/j.epsl.2014.03.042>
- Ader, M., Thomazo, C., Sansjofre, P., Busigny, V., Papineau, D., Laffont, R., Cartigny, P., Halverson, G.P., 2016. Interpretation of the nitrogen isotopic composition of Precambrian sedimentary rocks: Assumptions and perspectives. *Chemical Geology* 429, 93–110. <https://doi.org/10.1016/j.chemgeo.2016.02.010>
- Altabet, M.A., Francois, R., 1994. Sedimentary nitrogen isotopic ratio as a recorder for surface ocean nitrate utilization. *Global Biogeochemical Cycles* 8, 103–116. <https://doi.org/10.1029/93GB03396>
- Altermann, W., Nelson, D.R., 1998. Sedimentation rates, basin analysis and regional correlations of three Neoproterozoic and Palaeoproterozoic sub-basins of the Kaapvaal craton as inferred from precise U–Pb zircon ages from volcanoclastic sediments. *Sedimentary Geology* 120, 225–256. [https://doi.org/10.1016/S0037-0738\(98\)00034-7](https://doi.org/10.1016/S0037-0738(98)00034-7)
- Bauersachs, T., Compaoré, J., Severin, I., Hopmans, E.C., Schouten, S., Stal, L.J., Sinninghe Damsté, J.S., 2011. Diazotrophic microbial community of coastal microbial mats of the southern North Sea. *Geobiology* 9, 349–359. <https://doi.org/10.1111/j.1472-4669.2011.00280.x>
- Bauersachs, T., Schouten, S., Compaoré, J., Wollenzien, U., Stal, L.J., Sinninghe Damsté, J.S., 2009. Nitrogen isotopic fractionation associated with growth on dinitrogen gas and nitrate by cyanobacteria. *Limnology and Oceanography* 54, 1403–1411. <https://doi.org/10.4319/lo.2009.54.4.1403>
- Beaumont, V., Robert, F., 1999. Nitrogen isotope ratios of kerogens in Precambrian cherts: a record of the evolution of atmosphere chemistry? *Precambrian Research* 96, 63–82. [https://doi.org/10.1016/S0301-9268\(99\)00005-4](https://doi.org/10.1016/S0301-9268(99)00005-4)
- Bebout, G.E., Fogel, M.L., 1992. Nitrogen-isotope compositions of metasedimentary rocks in the Catalina Schist, California: Implications for metamorphic devolatilization history. *Geochimica et Cosmochimica Acta* 56, 2839–2849. [https://doi.org/10.1016/0016-7037\(92\)90363-N](https://doi.org/10.1016/0016-7037(92)90363-N)
- Beukes, N.J., 1987. Facies relations, depositional environments and diagenesis in a major early Proterozoic stromatolitic carbonate platform to basinal sequence, Campbellrand Subgroup, Transvaal Supergroup, Southern Africa. *Sedimentary Geology* 54, 1–46. [https://doi.org/10.1016/0037-0738\(87\)90002-9](https://doi.org/10.1016/0037-0738(87)90002-9)
- Boyd, S.R., Philippot, P., 1998. Precambrian ammonium biogeochemistry: a study of the Moine metasediments, Scotland. *Chemical Geology* 144, 257–268. [https://doi.org/10.1016/S0009-2541\(97\)00135-6](https://doi.org/10.1016/S0009-2541(97)00135-6)
- Busigny, V., Ader, M., Cartigny, P., 2005. Quantification and isotopic analysis of nitrogen in rocks at the ppm level using sealed tube combustion technique: A prelude to the study of altered

oceanic crust. *Chemical Geology* 223, 249–258.
<https://doi.org/10.1016/j.chemgeo.2005.08.002>

Button, A., 1973. The stratigraphic history of the Malmani dolomite in the Eastern and North-Eastern Transvaal.

Canfield, D.E., Glazer, A.N., Falkowski, P.G., 2010. The Evolution and Future of Earth's Nitrogen Cycle. *Science* 330, 192–196. <https://doi.org/10.1126/science.1186120>

Cawthorn, R.G., 2015. The Bushveld Complex, South Africa, in: Charlier, B., Namur, O., Latypov, R., Tegner, C. (Eds.), *Layered Intrusions*, Springer Geology. Springer Netherlands, Dordrecht, pp. 517–587. https://doi.org/10.1007/978-94-017-9652-1_12

Dalsgaard, T., Thamdrup, B., 2002. Factors Controlling Anaerobic Ammonium Oxidation with Nitrite in Marine Sediments. *Applied and Environmental Microbiology*. <https://doi.org/10.1128/AEM.68.8.3802-3808.2002>

Decraene, M.-N., 2022. Biological vs. Diagenetic Controls in Microbialites from Spatially Resolved Iron Isotopes in Pyrite. *Unil*.

Doebelin, N., Kleeberg, R., 2015. Profex: a graphical user interface for the Rietveld refinement program BGMN. *J Appl Cryst* 48, 1573–1580. <https://doi.org/10.1107/S1600576715014685>

Dumas, A., 1826. *Annales de Chimie*, 33, 342.

Eroglu, S., Schoenberg, R., Wille, M., Beukes, N., Taubald, H., 2015. Geochemical stratigraphy, sedimentology, and Mo isotope systematics of the ca. 2.58-2.50 Ga-old Transvaal Supergroup carbonate platform, South Africa. *Precambrian Research* 266, 27–46. <https://doi.org/10.1016/j.precamres.2015.04.014>

Eroglu, S., van Zuilen, M.A., Taubald, H., Drost, K., Wille, M., Swanner, E.D., Beukes, N.J., Schoenberg, R., 2017. Depth-dependent $\delta^{13}\text{C}$ trends in platform and slope settings of the Campbellrand-Malmani carbonate platform and possible implications for Early Earth oxygenation. *Precambrian Research* 302, 122–139. <https://doi.org/10.1016/j.precamres.2017.09.018>

Frauenstein, F., Veizer, J., Beukes, N., Van Niekerk, H.S., Coetzee, L.L., 2009. Transvaal Supergroup carbonates: Implications for Paleoproterozoic $\delta^{18}\text{O}$ and $\delta^{13}\text{C}$ records. *Precambrian Research* 175, 149–160. <https://doi.org/10.1016/j.precamres.2009.09.005>

Freudenthal, T., Wagner, T., Wenzhöfer, F., Zabel, M., Wefer, G., 2001. Early diagenesis of organic matter from sediments of the eastern subtropical Atlantic: evidence from stable nitrogen and carbon isotopes. *Geochimica et Cosmochimica Acta* 65, 1795–1808. [https://doi.org/10.1016/S0016-7037\(01\)00554-3](https://doi.org/10.1016/S0016-7037(01)00554-3)

Garvin, J., Buick, R., Anbar, A.D., Arnold, G.L., Kaufman, A.J., 2009. Isotopic Evidence for an Aerobic Nitrogen Cycle in the Latest Archean. *Science* 323, 1045–1048. <https://doi.org/10.1126/science.1165675>

Godfrey, L.V., Falkowski, P.G., 2009. The cycling and redox state of nitrogen in the Archaean ocean. *Nature Geoscience* 2, 725–729. <https://doi.org/10.1038/ngeo633>

- Haendel, D., Mühle, K., Nitzsche, H.-M., Stiehl, G., Wand, U., 1986. Isotopic variations of the fixed nitrogen in metamorphic rocks. *Geochimica et Cosmochimica Acta* 50, 749–758. [https://doi.org/10.1016/0016-7037\(86\)90351-0](https://doi.org/10.1016/0016-7037(86)90351-0)
- Hoch, M.P., Fogel, M.L., Kirchman, D.L., 1992. Isotope fractionation associated with ammonium uptake by a marine bacterium. *Limnology and Oceanography* 37, 1447–1459. <https://doi.org/10.4319/lo.1992.37.7.1447>
- Jia, Y., 2006. Nitrogen isotope fractionations during progressive metamorphism: A case study from the Paleozoic Cooma metasedimentary complex, southeastern Australia. *Geochimica et Cosmochimica Acta* 70, 5201–5214. <https://doi.org/10.1016/j.gca.2006.08.004>
- Kemp, A.L.W., Mudrochova, A., 1973. The distribution and nature of amino acids and other nitrogen-containing compounds in Lake Ontario surface sediments. *Geochimica et Cosmochimica Acta* 37, 2191–2206. [https://doi.org/10.1016/0016-7037\(73\)90016-1](https://doi.org/10.1016/0016-7037(73)90016-1)
- Kendall, C., Grim, E., 1990. Combustion tube method for measurement of nitrogen isotope ratios using calcium oxide for total removal of carbon dioxide and water. *Analytical Chemistry*.
- Kipp, M.A., Stüeken, E.E., Yun, M., Bekker, A., Buick, R., 2018. Pervasive aerobic nitrogen cycling in the surface ocean across the Paleoproterozoic Era. *Earth and Planetary Science Letters* 500, 117–126. <https://doi.org/10.1016/j.epsl.2018.08.007>
- Kitchen, N.E., Valley, J.W., 1995. Carbon isotope thermometry in marbles of the Adirondack Mountains, New York. *Journal of Metamorphic Geology* 13, 577–594. <https://doi.org/10.1111/j.1525-1314.1995.tb00244.x>
- Koehler, M.C., Buick, R., Kipp, M.A., Stüeken, E.E., Zaloumis, J., 2018. Transient surface ocean oxygenation recorded in the ~2.66 Ga Jeerinah Formation, Australia. *Proceedings of the National Academy of Sciences* 115, 7711–7716. <https://doi.org/10.1073/pnas.1720820115>
- Koehler, M.C., Stüeken, E.E., Kipp, M.A., Buick, R., Knoll, A.H., 2017. Spatial and temporal trends in Precambrian nitrogen cycling: A Mesoproterozoic offshore nitrate minimum. *Geochimica et Cosmochimica Acta* 198, 315–337. <https://doi.org/10.1016/j.gca.2016.10.050>
- Kouketsu, Y., Nishiyama, T., Ikeda, T., Enami, M., 2014. Evaluation of residual pressure in an inclusion–host system using negative frequency shift of quartz Raman spectra. *American Mineralogist* 99, 433–442. <https://doi.org/10.2138/am.2014.4427>
- Kreulen, R., van Beek, P.C.J.M., 1983. The calcite-graphite isotope thermometer; data on graphite bearing marbles from Naxos, Greece. *Geochimica et Cosmochimica Acta* 47, 1527–1530. [https://doi.org/10.1016/0016-7037\(83\)90312-5](https://doi.org/10.1016/0016-7037(83)90312-5)
- Lawnizack, G., 2022. Étude des stromatolithes archéens (Malmani Subgroup, Afrique du Sud, 2,58-2,5 Ga) : caractérisation pétrographique et processus post-dépôt.
- Lehmann, M.F., Bernasconi, S.M., Barbieri, A., McKenzie, J.A., 2002. Preservation of organic matter and alteration of its carbon and nitrogen isotope composition during simulated and in situ early sedimentary diagenesis. *Geochimica et Cosmochimica Acta* 66, 3573–3584. [https://doi.org/10.1016/S0016-7037\(02\)00968-7](https://doi.org/10.1016/S0016-7037(02)00968-7)

- Lepot, K., 2020. Signatures of early microbial life from the Archean (4 to 2.5 Ga) eon. *Earth-Science Reviews* 209, 103296. <https://doi.org/10.1016/j.earscirev.2020.103296>
- Lyons, T.W., Reinhard, C.T., Planavsky, N.J., 2014. The rise of oxygen in Earth's early ocean and atmosphere. *Nature* 506, 307–315. <https://doi.org/10.1038/nature13068>
- Miyano, T., Beukes, N.J., 1984. Phase relations of stilpnomelane, ferri-annite, and riebeckite in very low-grade metamorphosed iron-formations. *Transactions of the Geological Society of South Africa*.
- Möbius, J., 2013. Isotope fractionation during nitrogen remineralization (ammonification): Implications for nitrogen isotope biogeochemistry. *Geochimica et Cosmochimica Acta* 105, 422–432. <https://doi.org/10.1016/j.gca.2012.11.048>
- Pellerin, A., Thomazo, C., Ader, M., Marin-Carbonne, J., Alleon, J., Vennin, E., Hofmann, A., 2023. Iron-mediated anaerobic ammonium oxidation recorded in the early Archean ferruginous ocean. *Geobiology* 21, 277–289. <https://doi.org/10.1111/gbi.12540>
- Planavsky, N.J., Asael, D., Hofmann, A., Reinhard, C.T., Lalonde, S.V., Knudsen, A., Wang, X., Ossa Ossa, F., Pecoits, E., Smith, A.J.B., Beukes, N.J., Bekker, A., Johnson, T.M., Konhauser, K.O., Lyons, T.W., Rouxel, O.J., 2014. Evidence for oxygenic photosynthesis half a billion years before the Great Oxidation Event. *Nature Geosci* 7, 283–286. <https://doi.org/10.1038/ngeo2122>
- Quan, T.M., Falkowski, P.G., 2009. Redox control of N:P ratios in aquatic ecosystems. *Geobiology* 7, 124–139. <https://doi.org/10.1111/j.1472-4669.2008.00182.x>
- Raymond, J., Siefert, J.L., Staples, C.R., Blankenship, R.E., 2004. The Natural History of Nitrogen Fixation. *Mol Biol Evol* 21, 541–554. <https://doi.org/10.1093/molbev/msh047>
- Schidlowski, M., 2001. Carbon isotopes as biogeochemical recorders of life over 3.8 Ga of Earth history: evolution of a concept. *Precambrian Research* 106, 117–134. [https://doi.org/10.1016/S0301-9268\(00\)00128-5](https://doi.org/10.1016/S0301-9268(00)00128-5)
- Sigman, D.M., Karsh, K.L., Casciotti, K.L., 2009. Nitrogen Isotopes in the Ocean. *Encyclopedia of Ocean Sciences* 40–54. <https://doi.org/10.1016/B978-012374473-9.00632-9>
- Stüeken, Eva E., Buick, R., Guy, B.M., Koehler, M.C., 2015. Isotopic evidence for biological nitrogen fixation by molybdenum-nitrogenase from 3.2 Gyr. *Nature* 520, 666–669. <https://doi.org/10.1038/nature14180>
- Stüeken, E. E., Buick, R., Schauer, A.J., 2015. Nitrogen isotope evidence for alkaline lakes on late Archean continents. *Earth and Planetary Science Letters* 411, 1–10. <https://doi.org/10.1016/j.epsl.2014.11.037>
- Stüeken, E.E., Kipp, M.A., Koehler, M.C., Buick, R., 2016. The evolution of Earth's biogeochemical nitrogen cycle. *Earth-Science Reviews* 160, 220–239. <https://doi.org/10.1016/j.earscirev.2016.07.007>
- Stüeken, E.E., Zaloumis, J., Meixnerová, J., Buick, R., 2017. Differential metamorphic effects on nitrogen isotopes in kerogen extracts and bulk rocks. *Geochimica et Cosmochimica Acta* 217, 80–94. <https://doi.org/10.1016/j.gca.2017.08.019>

Thomazo, C., Ader, M., Philippot, P., 2011. Extreme ^{15}N -enrichments in 2.72-Gyr-old sediments: evidence for a turning point in the nitrogen cycle. *Geobiology* 9, 107–120. <https://doi.org/10.1111/j.1472-4669.2011.00271.x>

Tyler, R., Tyler, N., 1996. Stratigraphic and structural controls on gold mineralization in the Pilgrim's Rest goldfield, eastern Transvaal, South Africa. *Precambrian Research, Geology and Geochemistry of the transvaal supergroup* 79, 141–169. [https://doi.org/10.1016/0301-9268\(95\)00092-5](https://doi.org/10.1016/0301-9268(95)00092-5)

Voegelin, A.R., Nägler, T.F., Beukes, N.J., Lacassie, J.P., 2010. Molybdenum isotopes in late Archean carbonate rocks: Implications for early Earth oxygenation. *Precambrian Research* 182, 70–82. <https://doi.org/10.1016/j.precamres.2010.07.001>

Wada, H., Tomita, T., Matsuura, K., Tuchi, K., Ito, M., Morikiyo, T., 1994. Graphitization of carbonaceous matter during metamorphism with references to carbonate and pelitic rocks of contact and regional metamorphisms, Japan. *Contr. Mineral. and Petrol.* 118, 217–228. <https://doi.org/10.1007/BF00306643>

Ward, B., 2012. The Global Nitrogen Cycle, in: *Fundamentals of Geobiology*. John Wiley & Sons, Ltd, pp. 36–48. <https://doi.org/10.1002/9781118280874.ch4>

Wille, M., Kramers, J.D., Nägler, T.F., Beukes, N.J., Schröder, S., Meisel, Th., Lacassie, J.P., Voegelin, A.R., 2007. Evidence for a gradual rise of oxygen between 2.6 and 2.5 Ga from Mo isotopes and Re-PGE signatures in shales. *Geochimica et Cosmochimica Acta* 71, 2417–2435. <https://doi.org/10.1016/j.gca.2007.02.019>

Yamaguchi, K., 2002. *Geochemistry of Archean–Paleoproterozoic Black Shales: The Early Evolution of the Atmosphere, Oceans, and Biosphere*.

Yang, J., Junium, C.K., Grassineau, N.V., Nisbet, E.G., Izon, G., Mettam, C., Martin, A., Zerkle, A.L., 2019. Ammonium availability in the Late Archaean nitrogen cycle. *Nat. Geosci.* 12, 553–557. <https://doi.org/10.1038/s41561-019-0371-1>

Zerkle, A.L., Poulton, S.W., Newton, R.J., Mettam, C., Claire, M.W., Bekker, A., Junium, C.K., 2017. Onset of the aerobic nitrogen cycle during the Great Oxidation Event. *Nature* 542, 465–467. <https://doi.org/10.1038/nature20826>

Zhang, X., Sigman, D.M., Morel, F.M.M., Kraepiel, A.M.L., 2014. Nitrogen isotope fractionation by alternative nitrogenases and past ocean anoxia. *PNAS* 111, 4782–4787. <https://doi.org/10.1073/pnas.1402976111>

GENERAL CONCLUSIONS AND PERSPECTIVES

The nitrogen isotope signature ($\delta^{15}\text{N}$) preserved in sedimentary rocks has become one of the standard tools for investigating the joint evolution of redox changes and the biosphere. Specifically, secular changes in $\delta^{15}\text{N}$ have been interpreted as reflecting the evolution of the N-biogeochemical cycle and the redox transition of marine environments from an anoxic world to redox-stratified oceans to fully oxygenated ones comparable to modern times. During my PhD, not only did I significantly improve the temporal definition of the secular changes in $\delta^{15}\text{N}$, but I also investigated in depth the parameters that control the range of $\delta^{15}\text{N}$ for a given time period.

Starting with the buildup of an extensive Precambrian $\delta^{15}\text{N}$ database spanning from the early Archean to the late Proterozoic (i.e. from 3.8 Ga to 540 Ma), based on previous compilations and recent publications, my work identified research questions regarding the relevance of using the $\delta^{15}\text{N}$ proxy to explore early processes of the N-biogeochemical cycle, and directions that seemed to remain unresolved or ambiguous. This Precambrian compilation of $\delta^{15}\text{N}$ data allowed me to validate some previously established hypotheses and paradigms. First order secular variations of the $\delta^{15}\text{N}$ signature throughout the Precambrian seem robust, with a step change in the mode of $\delta^{15}\text{N}$ distribution from +1 to +3‰ during the Neoproterozoic, at ca. 2.8 to 2.6 Ga, and transient occurrences of extremely ^{15}N -enriched N isotope signatures at 2.7 and 1.9 Ga. Therefore, it is still meaningful to get a better temporal resolution from the early to the late Archean, especially for time intervals that potentially record important redox changes.

The three study sites chosen for this thesis targeted these three stages of the Archean, from 3.4 to 2.5 Ga. This study allowed me to improve their resolution and confirmed the previously identified temporal trends (Fig. 9.1). The 3.4 Ga Buck Reef Chert sedimentary deposit is indeed representative of a period where low $\delta^{15}\text{N}$ values close to 0‰, typical of an ammonium-dominated and reducing N cycle. The 2.7 Ga Serra Sul Formation occurs around the time where a “ $\delta^{15}\text{N}$ anomaly” with extremely positive nitrogen isotope compositions occur and provides an additional occurrence. Finally, the 2.5 Ga Malmani Subgroup, which has been deposited at the eve of the GOE shows $\delta^{15}\text{N}$ values in the lowest part of the $\delta^{15}\text{N}$ range for this period.

Additionally, these three formations span a large range of lithologies, from cherts/BIFs to shales to carbonates, all comparably metamorphosed in the greenschist facies, and reflects a variety of depositional environments, with both proximal and distal settings. This variability allowed me

to investigate the extent to which lithologies, and potentially depositional environments, control the $\delta^{15}\text{N}$ signal and to take their influence into account when interpreting $\delta^{15}\text{N}$ values in term of global changes in the oceanic nitrogen cycle linked to redox conditions (Fig. 9.2). Therefore, the three study sites provided a pertinent selection to get some insights into early processes governing the N-biogeochemical cycle, in particular (i) detecting the onset of oxidative nitrogen cycling, (ii) exploring the relationship between the nitrogen cycle and biology, and (iii) assessing the emergence of biological pathways of the nitrogen cycle.

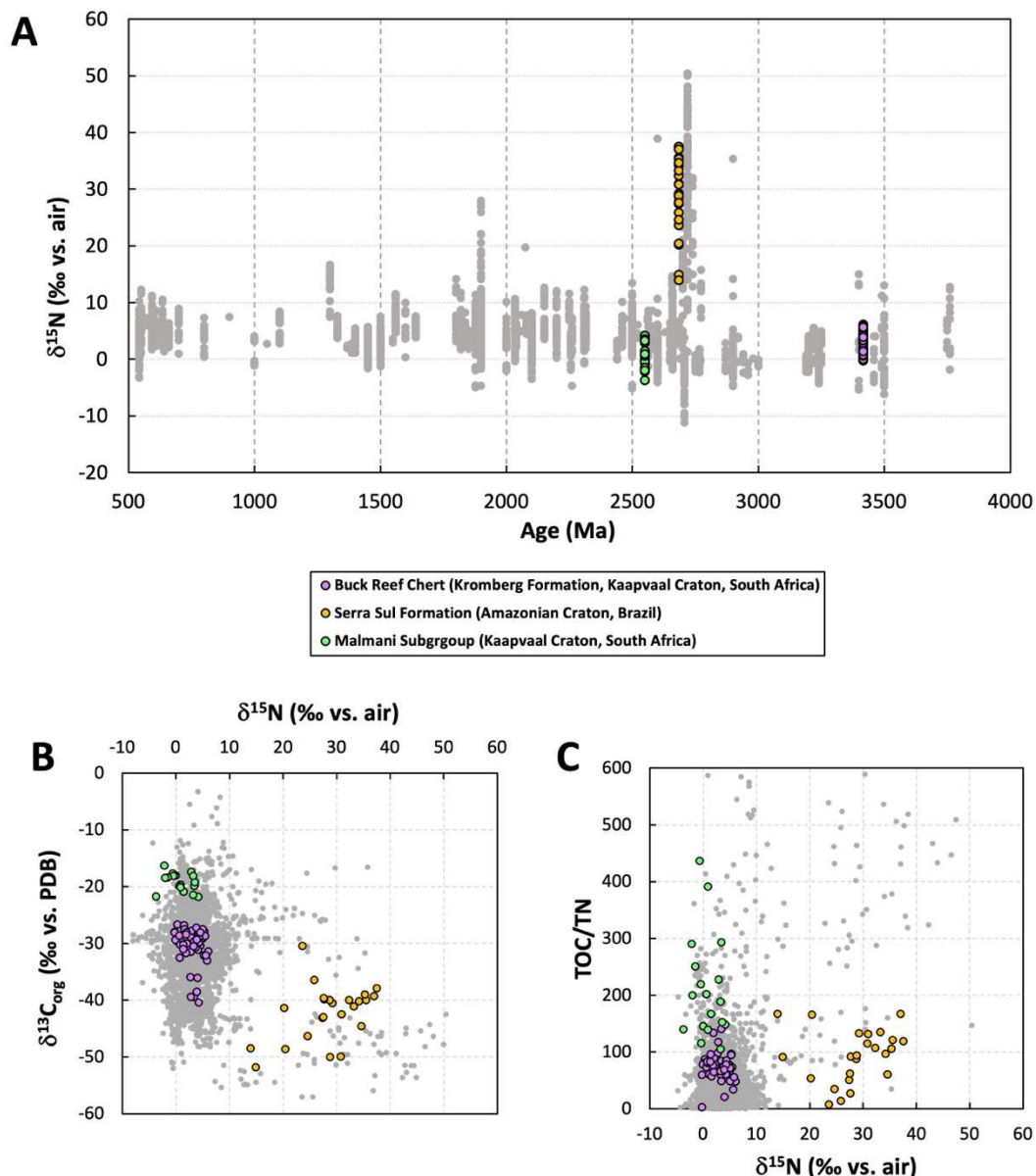


Fig. 9.1. Summary of where the three studied $\delta^{15}\text{N}$ datasets stand relative to all available Precambrian data (grey dots), in $\delta^{15}\text{N}$ versus time (A), $\delta^{13}\text{C}_{\text{org}}$ versus $\delta^{15}\text{N}$ (B), and TOC/TN versus $\delta^{15}\text{N}$ (C) diagrams.

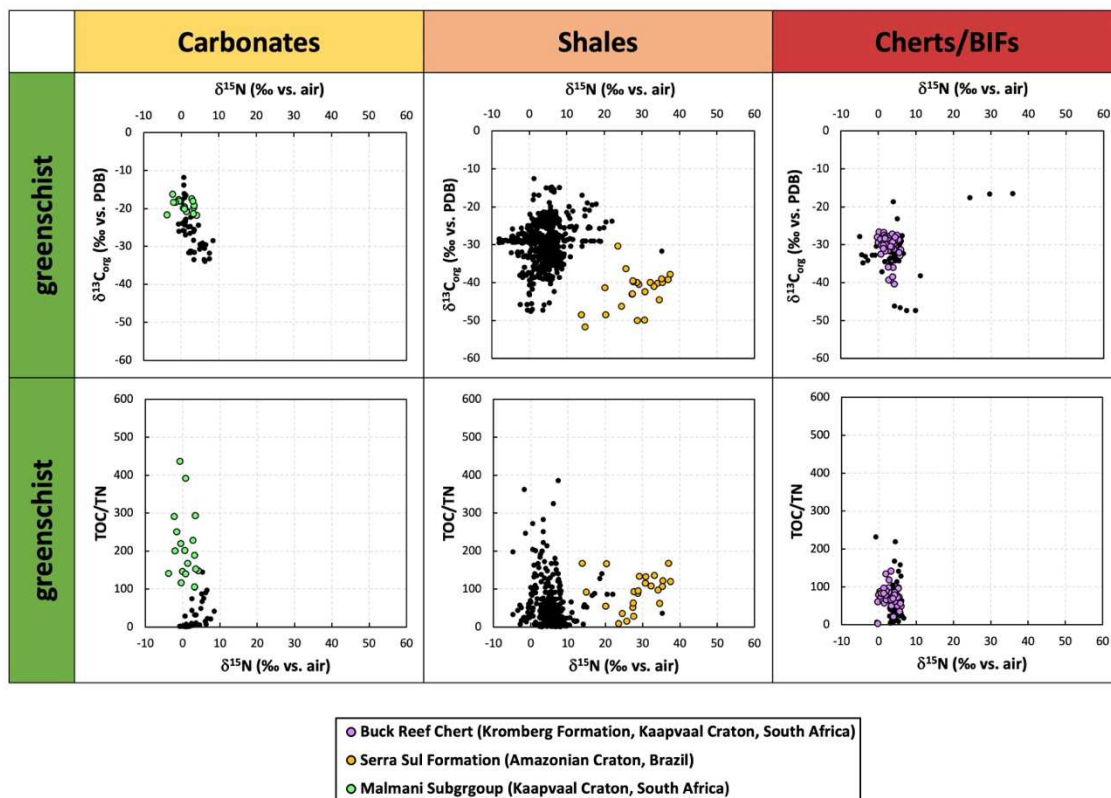


Fig. 9.2. Example of how the three studied set of samples compare to other Precambrian $\delta^{15}\text{N}$ data (black dots) of similar lithology and metamorphism, in crossplots of $\delta^{15}\text{N}$ vs. $\delta^{13}\text{C}_{\text{org}}$ and $\delta^{15}\text{N}$ vs. TOC/TN ratios.

The 3.4 Ga Buck Reef Chert sedimentary deposit (Kromberg Formation, Kaapvaal Craton, South Africa) with its iron oxides-rich sedimentary rocks, is one of the oldest testimonies of an oceanic anoxic and ferruginous environment where Fe underwent oxidation by photochemistry or photoferrotrophy. It allowed me to explore the impact of this Fe redox chemistry on the early N cycle in settings. $\delta^{15}\text{N}$ analyses have revealed positive values of up to +6‰, that fall outside the range for N_2 fixation, pointing towards an ammonium oxidizing pathway. Petrographic analyses reveal that $\delta^{15}\text{N}$ values from iron oxide-bearing chert and siderite significantly differ from iron oxide-depleted layers. This Fe- $\delta^{15}\text{N}$ relationship may indicate a linkage between iron oxides availability and metabolic N pathways. Positive $\delta^{15}\text{N}$ values observed in Fe_{ox} -poorer sediments have been interpreted as reflecting non-quantitative ammonium oxidation through the Feammox pathway, a metabolic co-cycling between iron and nitrogen in the presence of iron oxides, and the absence of nitrate. Conversely, sediments deposited in an Fe^{2+} saturated environment with $\delta^{15}\text{N}$ values near 0‰ likely reflect the prevalence of diazotrophic N_2 fixation at times of Feammox inhibition and/or the complete consumption of the residual ammonium pool. These findings suggest an early rise of biogeochemical nitrogen redox cycling, using iron

oxides as the electron acceptor, a common mineral found throughout the Archean Eon. The Buck Reef Chert draws attention to possible interactions between the iron and nitrogen cycles in anoxic and ferruginous conditions, which are relevant to most Paleoproterozoic depositional environments. $\delta^{15}\text{N}$ results for this formation invite to carefully consider the meaning of positive nitrogen isotopic signatures in Archean sediments, which do not necessarily indicate the presence of nitrate and an oxygen supply. They invite to conduct a detailed sedimentological characterization before interpreting the significance of N isotopes. In future studies, it might be worth exploring if a more systematic coupling of Fe and N occurred during the Paleoproterozoic, to assess if iron could have exerted a first-order control on the $\delta^{15}\text{N}$ signature. Fractionations associated with metabolic co-cyclings between Fe and N such as Feammox also need to be measured in modern stratified iron-rich environments, such as lake Towuti.

The ca. 2.68 Ga Serra Sul Formation (Carajás Basin, Amazonian Craton, Brazil) records a new occurrence of extremely positive Neoproterozoic $\delta^{15}\text{N}$ values. This signal seems to broadly coincide with that of the 2.72 Ga Tumbiana Formation (Pilbara Craton, Australia), making the 2.8-2.6 Ga time interval a unique feature of the Archean N isotope record. Since the two formations present very distinct geological, sedimentary and chemical features, and were deposited in contrasted depositional environments under different paleolatitudes, the signal they record cannot be tied to these features. We argue that the extreme $\delta^{15}\text{N}$ values highlight the onset of ammonium oxidation locally, reflecting a rise of oxidants in the depositional environment of the studied formations, in otherwise anoxic surroundings. It implies that oxygenic photosynthesis was already operating 2.7 Ga ago. Molecular oxygen production likely shifted the redox potential so that an intermediate N cycle based on ammonium oxidation developed well before nitrate accumulation in surface waters. We propose to name this unique period, when extreme positive nitrogen isotopic compositions are superimposed to the usual range of Precambrian $\delta^{15}\text{N}$ values, the Nitrogen Isotope Event (NIE). We suggest that it marks the earliest steps of the major biogeochemical reorganizations that led to surface waters and subsequent atmospheric oxygenation, the so-called Great Oxidation Event. This means that first-order secular variations of N isotopes hold the potential to detect oxygen production, i.e. the rise of oceanic oxidants before oxygen is supplied enough to start accumulating in the water column. A perspective to be explored is the maximization of N loss during this 2.8-2.6 Ga time interval, marking the transition from an ammonium-dominated nitrogen cycle to a mixed ammonium-nitrate cycle. The rerouting of a significant portion of the ammonium supply to nitrate used for energy production could have had major implications regarding nutrient

balance. Indeed, a system with increased fixed N loss could have strongly limited primary productivity and its associated oxidant production, thereby creating zones of delayed surface oxygenation.

Samples from the 2.55 Ga Malmani Subgroup (Campbellrand-Malmani Carbonate Platform, Kaapvaal Craton, South Africa) were chosen to explore the timing of biological O₂ production in the time interval leading to the GOE. The Neoproterozoic stromatolitic carbonates from shallow platform settings are considered to be niches for early aerobic systems, where oxygenic photosynthesizers were the most likely to thrive in otherwise still dominantly anoxic oceans. However, while in basinal shales of the Campbellrand-Malmani Carbonate Platform (CMCP), positive $\delta^{15}\text{N}$ values reaching up to +10‰ have been interpreted as recording oxidative nitrogen cycling in “oxygen oases”, the studied stromatolitic carbonates display an unexpected N isotope signature centered around 0‰, with no evidence of oxidative processes. Alongside preservation issues of the N isotope signature in carbonates compared to other lithologies, this finding raises a broader question regarding the suitability of stromatolitic carbonates to study processes of the N-biogeochemical cycle. Several hypotheses may explain why the oxidative part of the N cycle is not expressed despite the presence of undisputed microbial remains at a time close to the GOE, with oxygen oases in deeper depositional environments of the CMCP. They include sampling bias and alteration, the dominance of alternative metabolisms in shallow ecosystems, e.g. anoxygenic photosynthesis, and/or a cryptic oxidative N cycle in which oxygen would have been quantitatively consumed inside microbial mats. The N isotope signal seems primary, and could be explained by variable ammonium assimilation rates in the microbial mats or in their vicinity. This interpretation would have major consequences as to the use of carbonates for reconstructing the dynamics of the water column N-biogeochemical cycle. Indeed, it is possible that stromatolitic carbonates are more likely to record local biological processes occurring on short temporal timescales, and not a homogenized mean signal of global water column oxygenation. It stresses the importance of characterizing the depositional environment before interpreting the N isotope signature.

To conclude, confronting the three case studies spanning the Archean period to the existing Precambrian $\delta^{15}\text{N}$ record has highlighted some strengths and limits of using sedimentary $\delta^{15}\text{N}$ data as an oxygenation tracer, as well as the crucial need for context while interpreting them. In particular:

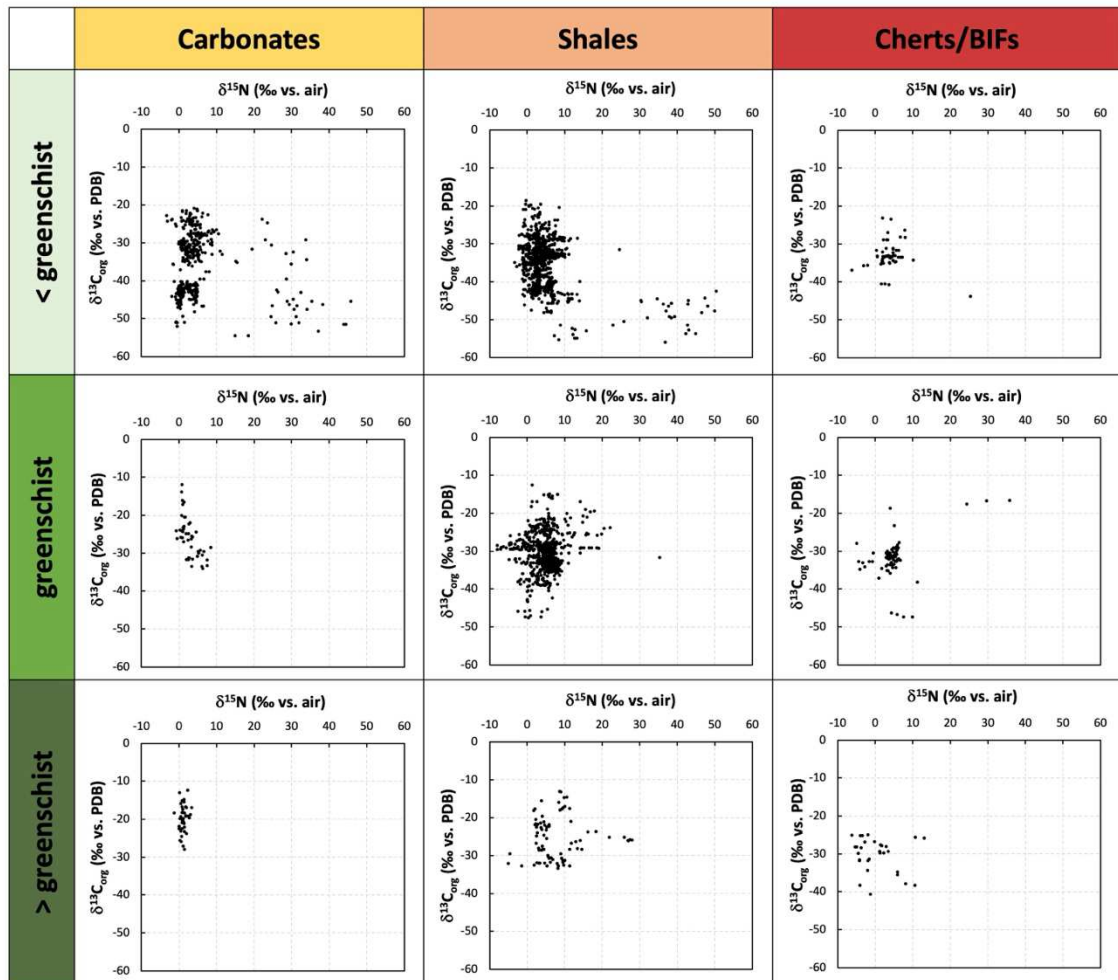
(1) N isotopes in Precambrian sedimentary rocks hold the potential to record both large scale changes in the dynamics of the Precambrian N-biogeochemical cycle, and local processes happening in a restricted depositional environment such a microbial mat. However, this $\delta^{15}\text{N}$ dependence to context is relevant only if the two can be distinguished. To this aim, parameters such as lithology, metamorphism, and, above all, the depositional environment, need to be well characterized by external indicators.

(2) Straightforward interpretations of the N isotope signature, such as considering positive $\delta^{15}\text{N}$ values to unquestionably indicate the presence of a stable nitrate pool sustained by oxygen production, while not always incorrect, need to be examined more carefully. This work has highlighted the possibility of generating positive $\delta^{15}\text{N}$ values through ammonium oxidation using iron oxides as an alternative electron acceptor (Chapter 6), but also through ammonium oxidation with a cryptic oxygen cycle (Chapter 7). Conversely, the absence of positive $\delta^{15}\text{N}$ values does not necessarily mean the absence of oxygen (Chapter 8).

(3) This PhD work has shown that shales can record the global oxidation state of the water column (Chapter 7), but that cherts/BIFs might be more representative of chemical conditions of the early ocean (Chapter 6), while stromatolites may be a better proxy for local biological processes occurring on short temporal timescales (Chapter 8). It invites careful consideration of the lithology and if possible, of the associated depositional environment, before conclusions based on N isotope data are drawn.

Finally, in light of these three takeaways, I have started building a framework for $\delta^{15}\text{N}$ interpretation in Archean sedimentary rocks, that includes lithology and metamorphism (Fig. 9.3). I hope it can serve as a starting point to reflect on any newly acquired $\delta^{15}\text{N}$ dataset. In addition to how new $\delta^{15}\text{N}$ values fall into the secular evolution of nitrogen isotopes through the Precambrian, the links between $\delta^{15}\text{N}$ and $\delta^{13}\text{C}_{\text{org}}$, or $\delta^{15}\text{N}$ and TOC/TN ratios, separated by lithology and metamorphism, are worth exploring (Chapter 3, Fig. 9.3). It could further be enriched by adding more isotopic redox and metabolic tracers, such as $\delta^{56}\text{Fe}$ or $\delta^{34}\text{S}$

measurements. An ultimate goal would be to characterize a large range of depositional environments and assess their control on the $\delta^{15}\text{N}$ signature.



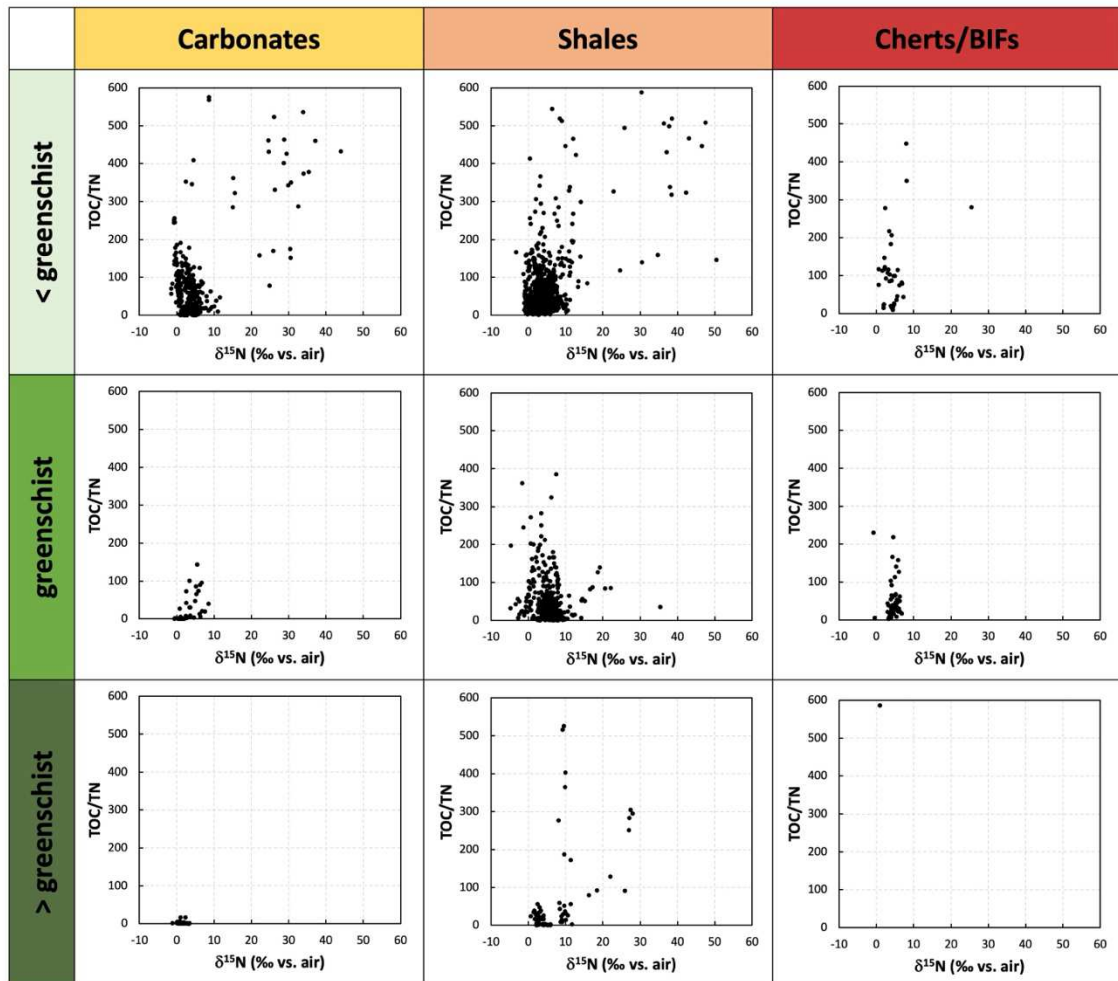


Fig. 9.3. A framework for interpreting the nitrogen isotope signature of Precambrian sedimentary rocks, depending on their lithology and metamorphism.

APPENDIX. OTHER CONTRIBUTIONS

A.1. Co-author of Tau et al., 2024 (<i>Precambrian Research</i>)	321
A.2. Book Chapter “Interactions géosphère-biosphère”, Chapter 6 “L’importance du vivant dans les cycles du carbone et de l’azote ”	338
A.3. Conference abstracts	364
A.3.1. Goldschmidt (2021, online)	364
A.3.2. M-FED Microbialites: Formation, Evolution, Diagenesis (2021, Paris, France)	366
A.3.3. Goldschmidt (2022, Honolulu, U.S.A.)	368
A.3.4. GES12: Geochemistry of the Earth’s Surface (2022, Zürich, Switzerland)	370
A.3.5. Goldschmidt (2023, Lyon, France)	372
A.3.6. M-FED Microbialites: Formation, Evolution, Diagenesis (2023, Leysin, Switzerland)	374
A.3.7. RESMO: Matière organique, environnement et société (2024, France).....	376
A.4. Reviewing activities.....	379

APPENDIX. OTHER CONTRIBUTIONS

A.1. Co-author of Tau et al., 2024 (*Precambrian Research*)

I performed the $\delta^{13}\text{C}_{\text{org}}$ measurements, and wrote the associated “Methods section/ interpretation”. I was involved in the writing and editing of the manuscript.



The Lanseria palaeosol: Implications for palaeoweathering and terrestrial life at ~2.6 Ga on the Kaapvaal Craton

Gobona L. Tau^{a,*}, Axel Hofmann^a, Jeremie Lehmann^a, Trishya Owen-Smith^a, Alice Pellerin^b, Christophe Thomazo^{b,c}, Christian Reinke^d, Allan H. Wilson^e

^a Department of Geology, University of Johannesburg, Auckland Park 2006, South Africa

^b Laboratoire Biogéosciences, Université Bourgogne Franche-Comté, Dijon, France

^c Institut Universitaire de France, 1 rue Descartes, Paris Cedex 05 75231, France

^d Spectrum, University of Johannesburg, Auckland Park 2006, South Africa

^e School of Geosciences, University of the Witwatersrand, Johannesburg 2050, South Africa

ARTICLE INFO

Keywords:

Palaeosol
Kaapvaal Craton
Archaean
Carbonaceous matter
Early terrestrial life
Black Reef Formation

ABSTRACT

Archaean palaeosols are a rare record of surface processes on the early Earth. We report on the discovery of a palaeoweathering profile developed at the contact between Mesoarchaean basement and the Neoproterozoic Transvaal Supergroup along the northern margin of the Johannesburg Dome, Kaapvaal Craton. Granodiorite ~3.1 Ga old was subjected to weathering just prior to the deposition of the ~2.6 Ga Black Reef Formation. The ~25 m-thick profile is dominated by a palaeosaprolite and organic matter-rich palaeosol remnant at the top that experienced erosion upon marine transgression on the Kaapvaal Craton. The Al concentration of the profile, sericite content and chemical index of alteration (CIA) values progressively increase from the parent granodiorite towards the nonconformity as Fe, Mg, Na and Ca concentrations decrease. The decrease of Co and Zn together with Fe and the retention of U, V and Cr collectively suggest a reducing and acidic environment at the time of weathering. Carbonaceous matter with negative $\delta^{13}\text{C}$ isotopic values (-27 to -23 ‰_{V-PDB}) in the palaeosol is compatible with the former presence of photoautotrophic microbes. Copper depletion and mobility of P may indicate the presence of organic acids that enhanced chemical weathering of the bedrock. The palaeoweathering profile was subjected to diagenetic-hydrothermal K-metasomatism, regional metamorphism and deformation, which collectively transformed the regolith into a quartz-sericite schist, as it presently occurs. Despite these modifications, the original record of palaeoweathering and microbial colonisation is well preserved. Colonisation of a large swath of the Kaapvaal Craton by terrestrial soil-dwelling microbiota at 2.60 Ga is recorded in abundant soil-derived carbonaceous matter in transgressive marine conglomerates that erosively overlie the palaeosol.

1. Introduction

Alteration zones interpreted as relict palaeo-weathering horizons and thus fossil soils and regoliths have been widely described from the Precambrian record of the Kaapvaal Craton of South Africa (Fig. 1a). The alteration zones are primarily preserved below major unconformities both within and below Archaean to Palaeoproterozoic volcano-sedimentary successions, such as the Dominion Group and the Witwatersrand, Pongola and Transvaal supergroups (Button and Tyler, 1981; Grandstaff et al., 1986; Kimberley and Grandstaff, 1986; Martini, 1994; Maynard et al., 1995; Rye and Holland, 2000a; Beukes et al., 2002;

Watanabe et al., 2000, 2004; Delvigne et al., 2016). Unconformities can be sites of enhanced fluid flow during diagenesis, metamorphism, and hydrothermal alteration, resulting in the formation of apparent palaeosols or overprinting of true palaeoweathering horizons (Maynard, 1992). However, the presence of a number of features from outcrop to microscope-scale aid in palaeosol recognition, such as differentiation into horizons variably depleted and enriched in elements or matter, palaeo-spheroidal weathering, evidence for clay illuviation, and the presence of fossil soil-dwelling biota (Retallack, 2001). Nevertheless, partial erosion of soil profiles prior to burial, metasomatism during burial and metamorphism, and even modern-day weathering can result

* Corresponding author.

E-mail address: lizziet@uj.ac.za (G.L. Tau).

<https://doi.org/10.1016/j.precamres.2024.107352>

Received 8 January 2024; Received in revised form 5 March 2024; Accepted 5 March 2024

Available online 19 March 2024

0301-9268/© 2024 The Author(s). Published by Elsevier B.V. This is an open access article under the CC BY-NC-ND license (<http://creativecommons.org/licenses/by-nc-nd/4.0/>).

in incorrect conclusions to be drawn from palaeosols (Beukes et al., 2002; Albut et al., 2018).

The majority of documented Archaean palaeoweathering profiles on the Kaapvaal Craton developed on granitoid basement and are now typified by a quartz-sericite horizon (Button and Tyler, 1981; Grandstaff et al., 1986; Kimberley and Grandstaff, 1986; Maynard et al., 1995). Palaeosols that developed on ultramafic rocks linked to Archaean greenstone belts have been described from the Schagen, Kalkkloof and Elandshoek areas in the eastern Transvaal Basin, Mpumalanga Province (red box in Fig. 1a; Martini, 1994; Watanabe et al., 2000, 2004). These palaeosols are remarkable for their abundance of organic matter, interpreted as microbial in origin.

Precambrian palaeosols are used to constrain $p\text{CO}_2$ and $p\text{O}_2$ at the time of weathering, which is useful in assessing the evolution of atmospheric conditions throughout Earth's history (Rye and Holland, 1998; Tabor and Myers, 2014; Sheldon et al., 2021). The behaviour of iron in palaeosols is a classic indicator of the rise of oxygen through time (Holland, 1984; Rye and Holland, 1998; Murakami et al., 2011), when developed in organic matter-poor palaeosols not having been waterlogged. In simple terms, ferrous iron in palaeosols that pre-date the Great Oxidation Event (GOE) in the Palaeoproterozoic experienced mobilisation and loss from weathered bedrock, suggesting reducing atmospheric conditions. On the other hand, palaeosols younger than the GOE show retention of iron and are considered to have formed under more oxygenated atmospheric conditions. Besides the mobility of iron, other proxies to evaluate palaeo-atmospheric oxygen levels include the distribution of redox-sensitive trace elements such as Cr, V, Co, Zn, U and Zr in palaeosols (Murakami et al., 2016) and their isotopic composition (Colwyn et al., 2019; Heard et al., 2021).

In addition to constraining atmospheric conditions, terrestrial microbial colonisation in the Archaean has been regarded likely in palaeosols that contain carbonaceous matter (e.g., Martini, 1994; Rye and Holland, 2000b; Watanabe et al., 2000, 2004; Finke et al., 2019). By studying the isotopic characteristics of such carbonaceous matter, we can better understand the nature of early terrestrial life through the

metabolic processes of micro-organisms found in palaeosols, which has direct implications for the evolution of the atmosphere and the carbon cycle and vice versa (Planavsky et al., 2021). In addition, soil biota may play important roles in soil formation, such as in the stabilisation of soils or in the enhancement of chemical weathering upon the release of organic acids. The mobility patterns of certain elements (e.g., P) could even serve as "organomarkers" (Neaman et al., 2005; Goynes et al., 2006). However, it is necessary to determine whether carbon-rich upper horizons in palaeosols of the Kaapvaal Craton indeed represent ancient biological soil crust or formed differently. Important carbon sources to consider are migrating hydrocarbons associated with burial diagenesis or hydrothermal-metamorphic processes, such as caused by the emplacement of the Bushveld Igneous Complex and the Vredefort Impact at ~ 2.0 Ga (Fig. 1a; Robb and Meyer, 1995; Buick et al., 1998; Drennan and Robb, 2006; Fuchs et al., 2016).

This paper documents the discovery of a ~ 2.60 Ga palaeoregolith at the contact between granitoid basement and the Black Reef Formation (BRF) of the Transvaal Supergroup along the northern margin of the Johannesburg Dome. We compare this palaeoregolith to those reported in the Schagen and Kalkkloof areas (Martini, 1994; Watanabe et al., 2000, 2004), which similarly lie beneath the Black Reef Formation and contain carbonaceous matter immediately below the nonconformity, although in larger quantities. This study presents petrographic, major and trace element, carbon isotope, total organic carbon (TOC) and Raman Spectroscopy data and addresses the surface conditions at the time of weathering and whether the carbonaceous matter in the palaeosol formed from Archaean microbial activity or hydrocarbon circulation.

2. Geology of the study area

The study area straddles the contact between granitoid-greenstone basement and Transvaal Supergroup along the northern margin of the 700 km² Johannesburg Dome (Fig. 1b). The Johannesburg Dome represents exhumed basement exposing granitoids dated between 3340 \pm

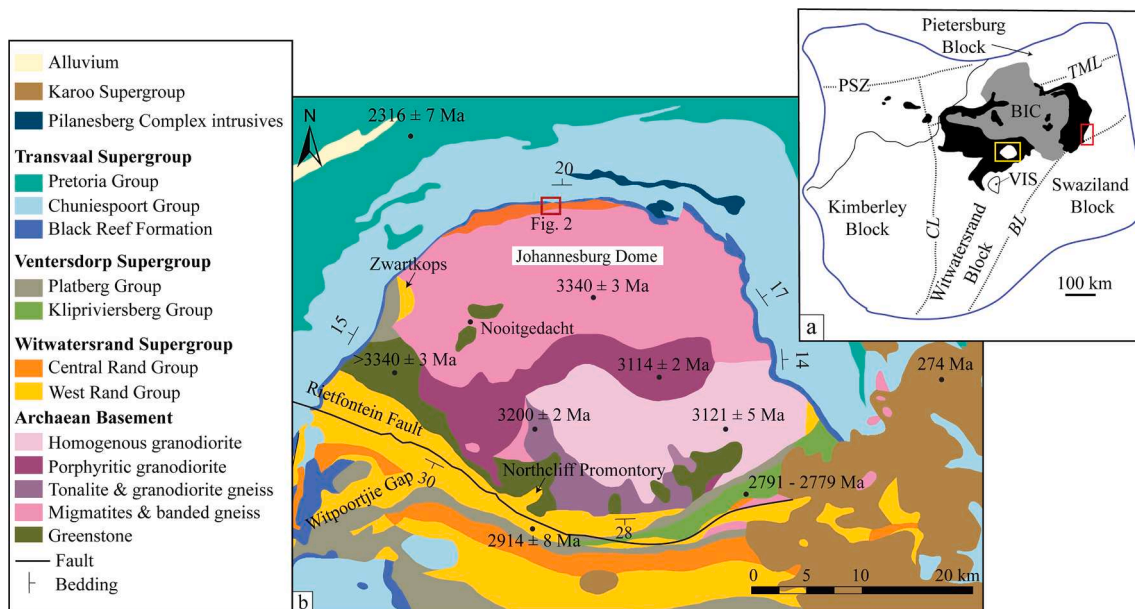


Fig. 1. (a) Sketch map of the Kaapvaal Craton (outlined in blue) with inferred accreted terranes indicated with dotted borders (modified after Eglinton and Armstrong, 2004). The black solid line is the border between Botswana and South Africa. The yellow box marks the Johannesburg Dome and the red box marks the Schagen, Kalkkloof and Elandshoek areas. The Transvaal Basin is shown in black. BL: Barberton Lineament, PSZ: Palala Shear Zone, TML: Thabazimbi-Murchison Lineament, CL: Colesberg Lineament, VIS: Vredefort Impact Structure, BIC: Bushveld Igneous Complex. (b) Expanded geological map of the yellow box in (a) that shows the Johannesburg Dome and surrounding geology (adapted from the 1:1 000 000-scale Geological Map of South Africa, <https://www.geoscience.org.za/>, Department of Mineral and Energy Affairs, 2018). Ages of the basement and cover were obtained from Bangert et al. (1999), Poujol and Anhaeusser (2001), Kositcin and Krapež (2004), Lenhardt et al. (2012) and Gumsley et al. (2020). The red box, marked Fig. 2, shows the present study area.

3 Ma and 3114 ± 2 Ma (U-Pb zircon ages) and (ultra)mafic rocks of the Kaapvaal Craton (Fig. 1a and b; Poujol and Anhaeusser, 2001; Ormond and Lehmann, 2022). The basement in the area is nonconformably overlain by meta-sedimentary rocks of the Neoarchaeon to Palaeoproterozoic Transvaal Supergroup, commencing with the siliciclastic rocks of the BRF, which are overlain by marine dolostones of the Chuniespoort Group (Fig. 2). The quartzites and slates making up the BRF were deposited in a fluvial to shallow marine setting (Eriksson and Truswell, 1974; Tyler, 1979; Obbes, 2001).

The rocks in the study area were deformed and metamorphosed under greenschist facies conditions in the Palaeoproterozoic, as suggested by the presence of low-grade metamorphic minerals such as sericite and chlorite. Shortening produced south-inclined folds in the BRF strata with an axial-planar schistosity in both the basement and cover. The gently north-dipping nonconformity is well exposed in a section of an E-W-striking ridge of BRF quartzite and basement at the confluence of the Jukskei and Crocodile rivers (Fig. 2). Here, the Lanseria palaeosol (now quartz-sericite schist, named after the Lanseria area where it occurs) can be seen below the BRF quartzites (Fig. 3a–b). The quartz-sericite schist grades downward over an effective distance of 25 m into a relatively unaltered and less deformed granodiorite (Fig. 3b). Fresh exposures of basement, quartz-sericite schist and the BRF across and along the river valley allow for comparison in mineralogy and geochemistry. Although the basement is dominated by granodiorite, exposures of medium-grained tonalite and intrusive pegmatite are present in some places in the study area, indicating some heterogeneity, but were unmapable at the scale shown in Fig. 2.

3. Sampling

We investigated a ~25 m-long inclined section at the confluence of the Crocodile and Jukskei rivers (Fig. 2, Fig. 3a–b). The section allowed systematic sampling of the palaeoregolith and 5 m of the overlying BRF. The granodiorite, unlike the palaeoregolith, was sampled in the Jukskei riverbed (Fig. 2) due to a lack of bedrock exposure at the base of the

ridge (sample numbers LT19-13 to LT19-15). Distances along the section line are considered close-to-true distances above and below the nonconformity, as the contact is gently tilted towards the north at ~13° (Fig. 3b). The section line starts at the base of the ridge on the western side of the confluence of the Crocodile and Jukskei rivers (sample numbers LT19-1 to LT19-10) and continues on the eastern side where the effective distance from the nonconformity to the base of the ridge was greater. In this way, lower levels of the quartz-sericite schist (sample numbers LT19-11 and LT19-12) were included in the section line. The nonconformity was chosen as the zero point along the section line, with positive and negative values representing close-to-true distances above and below the nonconformity, respectively. Sampling was done at regular intervals of 2.5 m along the section line. This distance was reduced between samples nearest to the nonconformity to detect subtle changes towards the contact.

4. Analytical procedures

Seventeen samples were collected for whole-rock geochemical analysis. Weathered surfaces on samples were chipped off in the field using a geological hammer. The samples were then wrapped up in plastic bags, manually crushed into gravel-sized pieces on a steel plate and pulverised to a fine powder in an agate mill at the University of Johannesburg. The powdered samples were used for major and trace element and carbon isotope analyses.

Major element concentrations for seventeen samples were analysed on fusion discs using X-ray fluorescence spectrometry at the Central Analytical Facility for the Faculty of Science (Spectrum), University of Johannesburg. Approximately 2 g of each powdered sample was dried for 24 h at 105 °C in glass vials. 1 g of the dried samples was placed in porcelain crucibles and ignited at 930 °C in a laboratory furnace to devolatilise the samples. The resultant loss on ignition (LOI) was measured using an analytical balance. Following this, 0.7 g of the ignited material was used for borate fusion. The material was first mixed with a flux comprising 0.1 g of lithium nitrate and 6 g of lithium tetraborate +

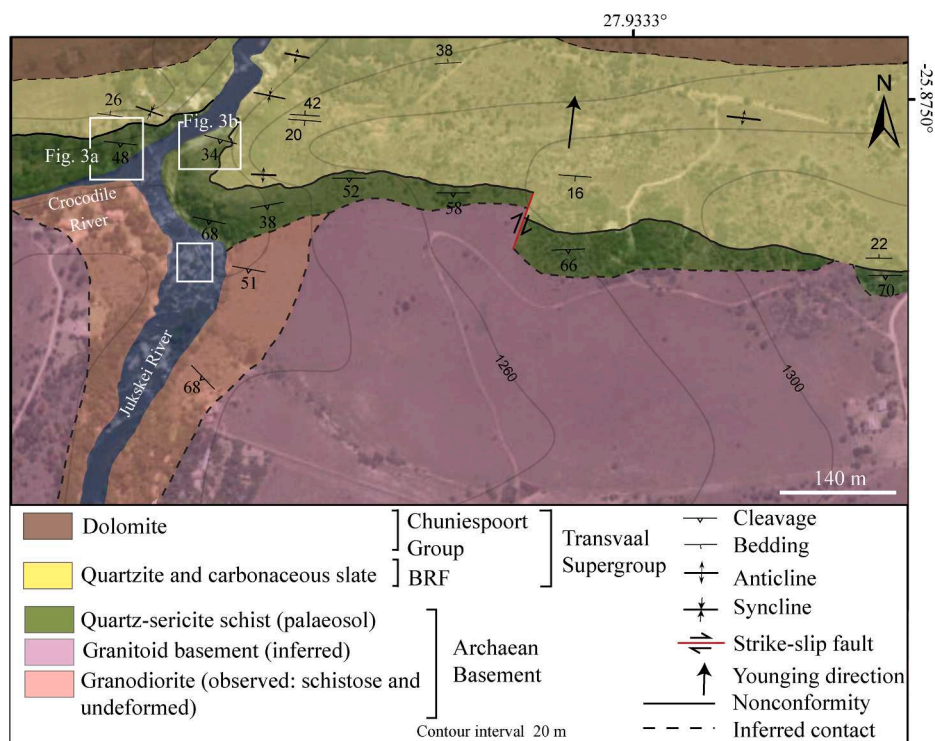


Fig. 2. Enlarged geological map of the study area shown in Fig. 1b. Contour intervals are from the 1:50000 2527DD Broederstroom geological map (Department of Mineral and Energy Affairs, Council for Geoscience, 1986). The sampling sites are shown as white boxes.

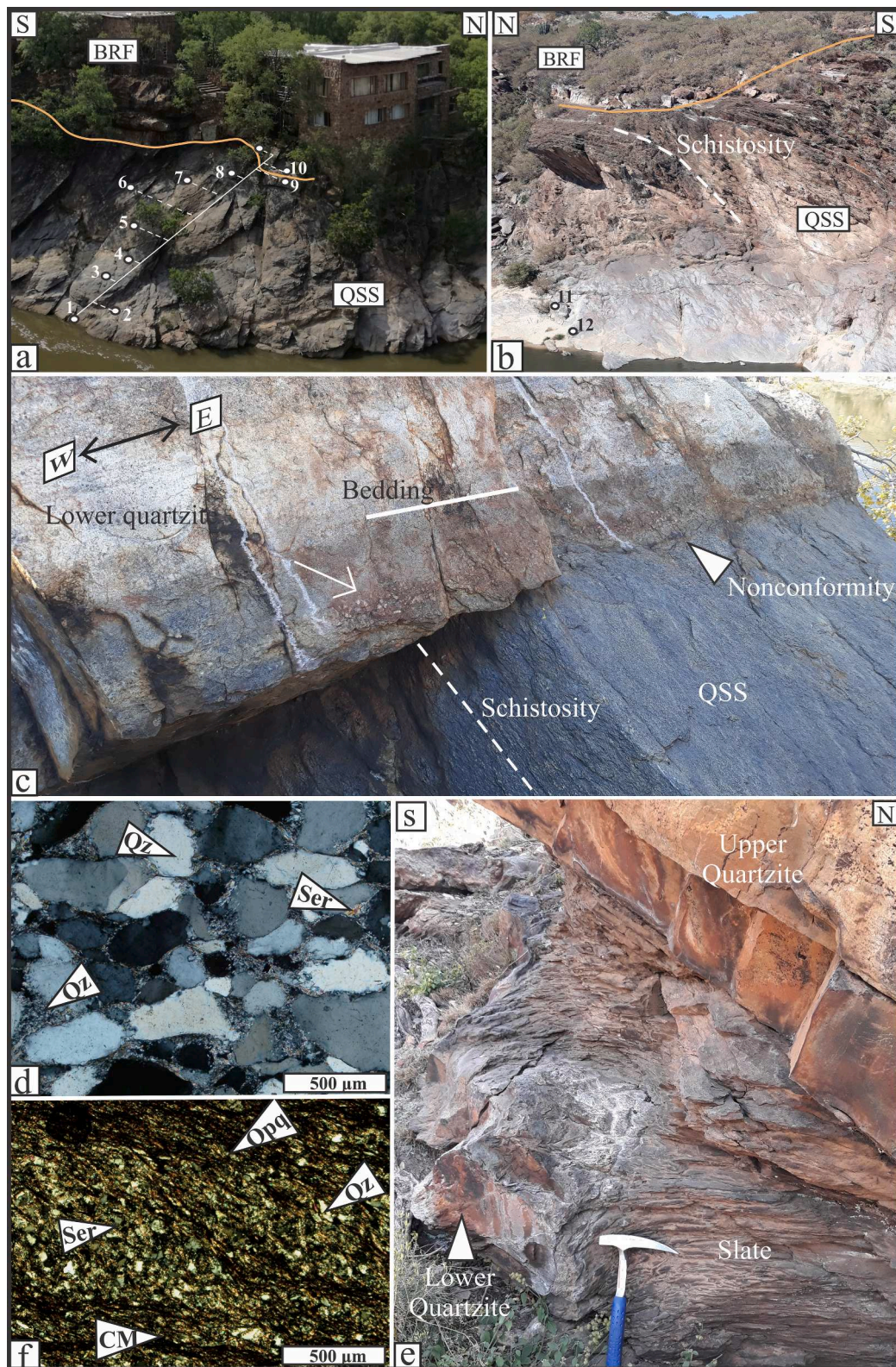


Fig. 3. (a) Sampling sites and their effective distances (dashed lines) along the section line, which is shown as a solid white line through the quartz-sericite schist (QSS) and into the Black Reef Formation (BRF). The numbers represent sample names (1 means LT19-1, 2 means LT19-2, etc.) and the orange line marks the nonconformity. This part of the section line is on the west side of the river (see Fig. 2). The field of view is 6 m. (b) View of the eastern side of the river, directly opposite photograph (a), showing sampling locations from the lower levels of the ridge. Here, the variation in the intensity of the schistosity towards the nonconformity can be seen. The field of view is ~30 m. (c) Field photograph of the basement–BRF contact taken along the nonconformity in (a). The basal matrix-supported conglomerate (Black Reef, shown by the white arrow) and abrupt termination of the cleavage in the QSS clearly define the base of the BRF. The field of view is 3 m. (d) Photomicrograph (in cross-polarized light, XPL) of sandstone matrix of basal conglomerate shown in (c). (e) Vertical outcrop view of the BRF upper quartzite and slate above the nonconformity in Fig. 3a. (f) Representative photomicrograph (XPL) of a slate sample.

lithium metaborate + lithium bromide. Fusion discs were then prepared in platinum-gold crucibles and moulds, and the material melted at 1050 °C in an electric fusion machine (TheOx) to produce the final glass discs. Wavelength dispersive X-ray fluorescence of the samples was done using a PANalytical MagiX PRO, using USGS and GSJ standard reference samples for calibration (Supplementary file, Table S1). Relative standard errors are estimated at 2 %; detection limits at 0.05 wt%.

Of the seventeen samples, eleven were selected for trace element analysis. The samples were chosen to give a representation of both the altered and relatively unweathered basement rock, and to assess adjacent samples showing large differences in major element percentages. Trace elements were determined at the School of Geosciences, University of the Witwatersrand, using a Perkin Elmer Sciex ELAN DRC-e. 50 mg of powdered sample was dissolved in a mixture of 3:2 HF and HNO₃ in a high-pressure Teflon vessel in a CEM Mars Express Microwave digester with 40-minute digestion times. Contents were evaporated to dryness in Teflon beakers during several steps of HNO₃ addition and evaporation. The samples were taken up in 300 µl of pure HNO₃ and made up to 50 ml (by weight) for analysis. Internal standards (Rh, In, Re and Bi) and calibration solutions were prepared from certified single- and multi-element Perkin Elmer and Alfa Aesar standard solutions. The quality of data was monitored using the international standards BCR-1, BHVO-1 and BIR-1. We note that microwave digestion of silicate rocks may result in incomplete digestion of some phases, specifically zircon, resulting in anomalously low Zr and Hf concentrations. However, granodiorite samples show smooth trace element patterns relative to primitive mantle composition, and quartz-sericite schists show elevated Zr and Hf concentrations (diagram not shown) due to depletion of rare earth elements during palaeoweathering. We are thus confident that the sample digestion technique completely dissolved even the most refractory minerals.

Further details of the analytical procedures and data quality can be found in [Siahi et al. \(2018\)](#). Whole-rock major and trace element data and selected indices are presented in [Tables 1 and 2](#).

Fifteen samples were selected for carbon isotope analysis: ten from the Lanseria study area (four from the quartz-sericite schist, four from basal conglomerate of the BRF, two from the BRF slate), three from the Schagen palaeosol, and two from the Kalkkloof palaeosol. TOC and $\delta^{13}\text{C}_{\text{org}}$ values from this study were compared with published data from the Schagen and Kalkkloof palaeosols ([Watanabe et al., 2000, 2004](#)) and from the BRF above the Schagen palaeosol ([Strauss and Beukes, 1996; Watanabe et al., 1997](#)).

Carbonate-free residues were obtained by mixing sample powders with 6 N HCl for 24 h at room temperature to remove calcium carbonates. A second step of 6 N HCl digestion at 80 °C for 4 h was used to remove potential magnesium and/or iron carbonates. The powder was then rinsed with deionised distilled water to a neutral pH and oven-dried at 40 °C for 48 h. The decarbonated residues were poured into tin capsules (20–80 mg of powder) and weighed using a Sartorius M2P ultra-balance before TOC and $\delta^{13}\text{C}_{\text{org}}$ measurements were performed using an Elementar Vario MICRO Cube elemental analyser, coupled to an Elementar Isoprime isotope ratio mass spectrometer (EA-IRMS) at the Biogéosciences laboratory (Université de Bourgogne Franche-Comté, France). Certified USGS40 ($\delta^{13}\text{C}_{\text{org}} = -26.2\text{‰}$, TOC = 40.82 wt%) and caffeine IAEA-600 ($\delta^{13}\text{C}_{\text{org}} = -27.77\text{‰}$) reference materials were used for the calibration. Total organic carbon (TOC) contents are expressed in dry weight percentage (wt.%) of the non-decarbonated bulk powder and isotope results are reported in delta-notation relative to V-PDB.

The distribution of carbonaceous matter (CM) and other minerals was identified by Raman Spectroscopy. Raman analyses of selected samples were carried out using a WITec alpha 300R configured with a frequency-doubled Nd-YAG laser (wavelength 532 nm) at the Department of Geology, University of Johannesburg. The analyses were made using a 5× Nikon objective with a numerical aperture of 0.4 and a maximum of 4 mW laser power to prevent thermal degradation. The system couples motorised sample positioning with a piezo-driven scan

Table 1
Whole-rock major element analyses of basement (granodiorite and quartz-sericite schist) and Black Reef Formation samples in wt%.

Sample	Basement										Black Reef Formation									
	Rock type	LT02-2	LT02-1	LT19-10	LT19-9	LT19-8	LT19-7	LT19-6	LT19-5	LT19-4	LT19-3	LT19-2	LT19-1	LT19-11	LT19-12	LT19-13	LT19-14	LT19-15		
Distance (m)	Slate	Slate	Quartzite	QSS	QSS	QSS	QSS	QSS	QSS	QSS	QSS	QSS	QSS	QSS	QSS	Granodiorite	Granodiorite	Granodiorite		
SiO ₂	65.19	66.48	89.11	65.38	66.51	66.18	66.10	65.65	64.81	64.22	66.44	69.81	64.63	65.02	71.79	72.24	72.31			
Al ₂ O ₃	19.75	18.98	3.542	23.06	21.28	21.64	22.10	22.15	22.70	22.20	20.26	16.27	19.71	19.07	14.56	14.05	14.88			
K ₂ O	6.808	6.580	1.077	6.742	6.591	6.437	6.649	6.765	6.963	6.868	6.712	5.668	6.880	7.142	3.037	2.764	3.147			
Fe ₂ O ₃	1.555	1.490	0.140	0.330	0.350	0.350	0.420	0.480	0.510	0.540	1.010	2.140	2.280	2.310	1.750	1.540	1.240			
Na ₂ O	–	–	–	0.110	0.100	0.100	0.110	0.110	0.090	0.090	0.050	–	–	–	4.370	3.710	4.500			
MgO	1.050	1.030	–	0.250	0.460	0.280	0.370	0.460	0.480	0.500	0.870	1.250	1.510	1.440	0.860	0.960	0.790			
BaO	0.080	0.080	–	–	–	–	–	–	–	–	–	–	–	0.070	–	–	–			
MnO	–	–	–	–	–	–	–	–	–	–	–	–	–	–	–	–	–			
CaO	–	–	–	–	–	–	–	–	–	–	–	–	–	–	0.560	1.350	0.270			
TiO ₂	0.580	0.560	0.160	0.410	0.350	0.420	0.390	0.410	0.420	0.400	0.340	0.150	0.340	0.320	0.220	0.150	0.210			
P ₂ O ₅	–	–	–	–	–	–	–	–	–	–	0.050	–	–	–	0.080	0.090	0.080			
Cr ₂ O ₃	–	–	–	–	–	–	–	–	–	–	–	–	–	–	–	–	–			
SO ₃	–	–	–	–	–	–	–	–	–	–	–	–	–	–	–	–	–			
V ₂ O ₅	–	–	–	–	–	–	–	–	–	–	–	–	–	–	–	–	–			
NiO	–	–	–	–	–	–	–	–	–	–	–	–	–	–	–	–	–			
LOI	4.030	3.800	0.570	2.860	2.540	2.550	2.820	2.810	2.950	2.860	2.750	2.820	2.790	2.670	1.560	2.300	1.210			
Total	99.03	99.00	94.69	99.14	98.37	97.96	98.96	98.83	98.92	97.69	98.50	98.10	98.14	98.05	98.78	99.15	98.65			
Al/Ti	–	–	–	56.24	60.80	51.52	56.67	54.02	54.05	55.50	59.59	108.47	57.97	59.59	66.18	93.67	70.86			
CIA	–	–	–	75.51	74.46	75.21	74.97	74.70	74.71	74.50	73.39	72.62	72.58	71.15	58.16	60.70	57.92			

– = values below detection limit; QSS = quartz-sericite schist; CIA = Chemical Index of Alteration; Distance (m) = negative values are depths below the nonconformity.

Table 2

Whole-rock trace element analyses of basement (granodiorite and quartz-sericite schist) and Black Reef Formation samples in ppm.

Sample Rock type Distance (m)	Black Reef Formation		Basement								
	LT02-1 Slate 1.5	LT19-10 Quartzite 0.5	LT19-9 QSS 0	LT19-7 QSS -2.5	LT19-5 QSS -7.5	LT19-3 QSS -12.5	LT19-2 QSS -15	LT19-1 QSS -17.5	LT19-12 QSS -22.5	LT19-13 Granodiorite -25	LT19-15 Granodiorite -50
Li	20.52	1.45	3.96	3.51	2.91	2.79	7.42	28.00	45.52	18.06	20.78
P	78.89	211	97.98	79.76	34.14	50.24	126	19.52	42.03	205	249
Sc	7.81	2.17	4.20	4.59	4.34	3.89	4.85	2.53	2.82	2.10	2.35
Ti	2389	388	1768	1694	1591	1655	1473	711	1652	885	919
V	60.16	7.16	33.86	26.99	35.85	34.68	27.59	10.93	29.81	14.58	15.74
Cr	161	61.26	13.13	5.47	12.21	12.05	1.56	3.81	9.08	4.90	6.47
Co	2.009	0.166	0.423	0.473	0.671	1.038	3.572	3.442	2.761	2.595	3.12
Ni	10.23	0.702	1.706	3.032	5.810	6.725	7.225	8.200	5.357	4.133	4.532
Cu	4.255	3.975	2.074	1.120	1.040	1.149	1.326	9.311	1.887	1.094	19.03
Zn	47.98	4.386	6.250	8.715	8.632	7.915	17.73	30.30	56.69	35.78	33.46
Ga	24.94	22.41	22.47	26.64	22.55	24.06	34.88	16.11	20.61	13.88	16.63
Rb	153.74	14.95	105	102	111	116	138	137	196	72.17	92.81
Sr	11.25	49.17	38.86	13.53	12.37	11.98	11.97	6.84	12.67	138	118
Y	19.30	7.84	4.12	8.73	6.03	11.44	17.99	4.65	7.64	6.87	9.71
Zr	224	170	145	219	121	144	369	91.87	146	82.86	129
Nb	18.28	22.44	9.99	10.01	9.73	8.95	7.74	7.79	11.42	6.45	9.88
Sn	8.28	33.15	2.41	6.20	2.46	2.97	8.18	3.04	2.79	1.53	3.59
Sb	0.041	0.048	0.013	0.034	0.032	0.029	0.042	0.051	0.056	0.022	0.046
Cs	3.16	0.214	0.915	1.004	1.229	1.349	2.042	2.927	4.878	1.758	1.597
Ba	579	39.17	130	128	148	185	277	231	406	393	315
La	57.08	131	47.40	83.50	15.06	47.18	137	5.16	8.88	20.50	26.10
Ce	105	269	77.29	125.00	21.55	83.80	269	10.15	19.34	32.93	41.28
Pr	11.67	31.19	6.112	9.753	1.916	8.647	29.40	1.031	1.837	3.447	4.138
Nd	40.12	98.63	12.745	20.57	5.418	29.90	109.09	3.706	6.847	12.61	14.07
Sm	7.208	9.033	0.520	1.027	0.629	5.073	19.96	0.796	1.407	2.356	2.623
Eu	1.171	2.112	0.249	0.352	0.197	1.137	4.059	0.202	0.443	0.773	0.655
Gd	5.683	6.556	0.839	1.504	0.774	3.769	13.977	0.763	1.450	2.160	2.401
Tb	0.725	0.718	0.110	0.199	0.152	0.439	1.194	0.119	0.216	0.282	0.331
Dy	4.102	3.215	0.808	1.523	1.173	2.396	4.588	0.808	1.434	1.589	1.961
Ho	0.799	0.510	0.188	0.375	0.261	0.481	0.764	0.176	0.297	0.325	0.389
Er	2.419	1.486	0.678	1.377	0.817	1.517	2.345	0.562	0.925	0.817	1.126
Tm	0.391	0.228	0.125	0.26	0.134	0.238	0.372	0.097	0.162	0.114	0.174
Yb	2.828	1.611	0.995	2.049	0.971	1.635	2.765	0.762	1.263	0.746	1.186
Lu	0.454	0.226	0.163	0.326	0.151	0.245	0.441	0.123	0.204	0.109	0.178
Hf	6.735	5.681	3.823	5.261	3.334	3.959	9.291	2.727	3.907	2.396	3.793
Ta	1.589	3.132	0.567	0.687	0.369	0.666	0.493	0.544	0.568	0.298	0.821
W	1.077	0.243	0.828	0.148	0.121	1.184	0.142	0.170	0.183	2.449	0.597
Tl	0.874	0.107	0.654	0.663	0.697	0.728	0.84	0.817	1.12	0.474	0.570
Pb	1.648	20.77	1.997	0.923	0.659	0.739	0.878	0.740	1.032	2.804	8.585
Th	14.39	111	5.830	20.57	4.768	4.746	27.419	4.284	3.649	2.025	8.878
U	5.948	29.89	4.514	4.080	1.543	1.600	3.967	1.748	1.848	0.654	2.944

QSS = quartz-sericite schist; Distance (m) = negative values are depths below the nonconformity.

platform, allowing Raman mapping from micrometre- to centimetre-scale. All our analyses were made by Raman mapping, whereby the parameters of acquisition were the same for each point and several thousands of spectra were acquired per image.

Raman geothermometry was applied to CM in three samples to evaluate its degree of crystallinity (Fig. S1, Table S2). Structural ordering of CM upon metamorphism is irreversible, which allows estimating peak temperature conditions (Beyssac et al., 2002). Point analyses of CM were taken for 10 s with 10 accumulations on average to obtain good signal-to-noise ratio. The raw data were exported to Origin Pro for processing. Baseline correction on each spectrum was done to reduce statistical bias before fitting the first-order Raman peaks and decomposition of the acquired signals into different bands. A manual baseline correction was used, keeping the number of control points at 8, and positioning them at the same points along the baselines. The Lorentz function was used to deconvolute the signal into its different components and automatically locate the bands. This function, compared to the Voigt and Gaussian, performed the curve-fitting process most effectively. The parameters used to calculate the peak temperature were obtained from this step, including the peak height/intensity, area, width and centre. These were used to calculate two essential ratios: the peak height ratio, R1 (D1/G) and peak area ratio, R2 (D1/D1 + D2 + G). Calculations were made following the method of Beyssac et al. (2002,

Supplementary file, Table S2).

5. Results

5.1. Petrography of the Black Reef Formation

The exposed BRF has a total stratigraphic thickness of ~5 m in the study area and dips gently to the north at ~13°. It consists of two quartzitic sandstone bedsets separated by slate. The base of the lower unit is a 25 cm-thick, dark grey, very coarse-grained pebbly sandstone with stringers of clast-supported quartz pebble conglomerate at the base. This carbonaceous conglomerate is regionally known as the Black Reef, with the term “reef” used to denote auriferous quartz pebble conglomerates in the Witwatersrand Basin (Robb and Meyer, 1995). It is overlain by 0.8 m-thick, very coarse-grained light grey to white pebbly sandstone (Fig. 3c). This unit consists of several tabular beds that are either massive, planar laminated or, near the top, trough cross-bedded. The Black Reef is made up of 90 vol% variably rounded quartz clasts in a carbonaceous and sericite matrix (10 vol%; Fig. 3d). Raman mapping of the samples shows that the carbonaceous matter (CM) is closely associated with sericite (Fig. 4).

An 80 cm-thick, dark grey carbonaceous slate stratigraphically overlies the quartzite along a sharp stratigraphic contact covered by

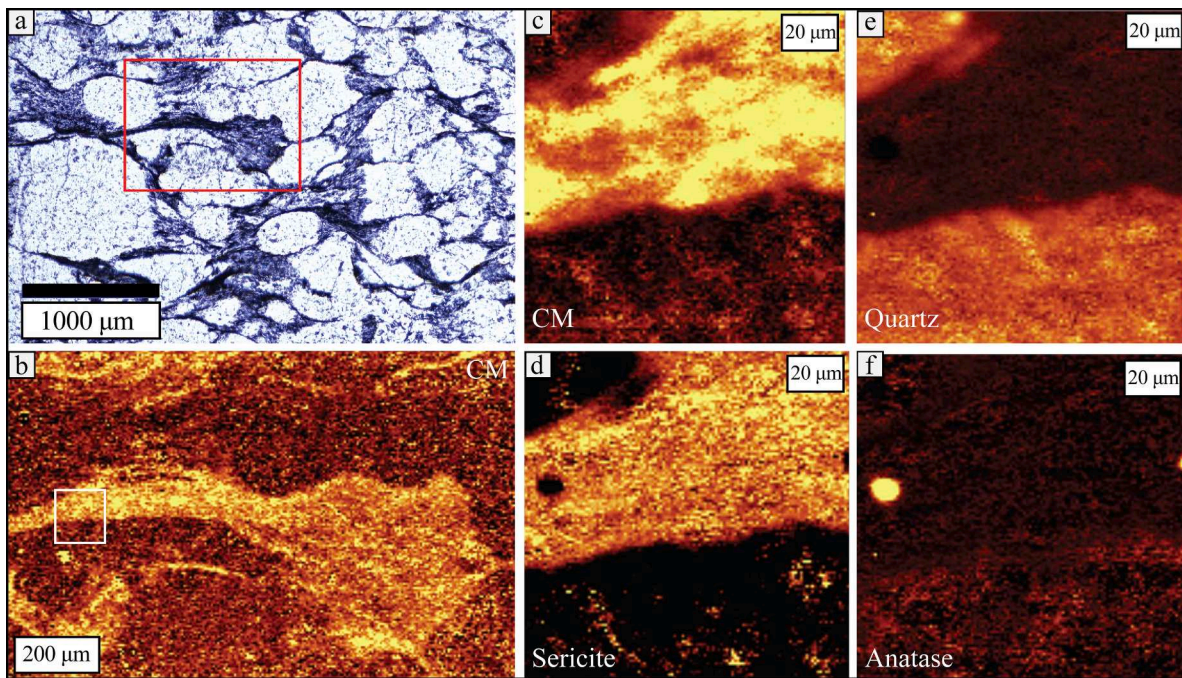


Fig. 4. Raman maps showing the distribution of minerals and carbonaceous matter in the basal conglomerate from sample LT19-10-3a at <15 cm above the nonconformity. (a) Photomicrograph in plane-polarised light (PPL) of the lower quartzite; box shows the area of Raman analysis in b. (b) Raman map of the carbonaceous matter (CM) G band at $\sim 1590\text{ cm}^{-1}$; box shows the area of Raman analyses in subsequent images. (c–f) Distribution of (c) carbonaceous matter G band at $\sim 1590\text{ cm}^{-1}$, (d) sericite major band at $\sim 260\text{ cm}^{-1}$, (e) quartz major band at $\sim 470\text{ cm}^{-1}$ and (f) anatase band (average peak position of $\sim 150\text{ cm}^{-1}$), respectively. Brighter areas within Raman maps reflect higher intensities of mineral-specific spectra.

wave-ripple bedforms (Fig. 3e). The slate contains 60 vol% phyllosilicates, 35 vol% quartz, and 5 vol% opaques and CM (Fig. 3f) and is interstratified with thin beds of cross-bedded and wave-ripple laminated sandstone. The slate is overlain by another (upper) white quartzite layer with a stratigraphic thickness of $\sim 1.8\text{ m}$ that consists of cross-bedded, very coarse-grained sandstone. The quartzite is overlain by poorly exposed slate followed by stromatolitic dolostone of the Oaktree Formation (Obbes, 2001).

5.2. Petrography of the palaeoregolith

The zone of palaeoweathering is identifiable by a grey quartz-sericite schist with a pseudo-porphroclastic texture and an intense cleavage that weakens with distance from the nonconformity (Fig. 3a–c). Greenish grey and yellow-weathering tabular bodies with a width of 10 to 90 cm and lenses in the quartz-sericite schist represent weathered dolerite and pegmatite dykes that intruded the basement. The mineralogy of the profile varies with distance from the nonconformity towards the less weathered granodiorite and is the basis for subdivision into carbon-sericite and sericite zones, a chlorite zone and relatively fresh bedrock (Fig. 5). The defining features of each of these zones are described below, from top to bottom. In comparison with modern-day regolith profiles, the carbon-sericite zone would equate with the solum, the sericite zone with saprolite, and the chlorite zone possibly with saprock (e.g., Retallack, 2001; Scott and Pain, 2009). In a strict sense, the carbon-sericite zone is thus the Lanseria palaeosol and represents the uppermost part of the Lanseria palaeoregolith.

5.2.1. Sericite zone

The 18 m-thick sericite zone makes up the bulk of the profile. This zone contains elevated (compared to the rest of the profile) concentrations of sericite (>70 vol%) surrounding ductilely deformed quartz porphyroclasts (Fig. 5a–b). Some quartz grains have been marginally replaced by sericite, giving the grains an embayed texture.

The uppermost, $\leq 1\text{ m}$ thick part of the sericite zone contains CM and

is named carbon-sericite zone to differentiate it from the carbon-absent sericite zone. This zone likely represents the B horizon of the former soil, but pervasive foliation at this level does not allow delineation of its lower contact. The thickness of this zone varies laterally and is absent in places, possibly due to erosion. The carbon-sericite zone contains 15 vol% quartz porphyroclasts in a matrix of 80 vol% sericite and 5 vol% recrystallised quartz and accessory minerals, including apatite, biotite, zircon, tourmaline, rutile, opaque minerals and CM (Fig. 5a). Sericite, recrystallised quartz and minor biotite define the intense schistosity in Figs. 3b and 5a–b. The CM is finely disseminated in the sericite matrix and is frequently concentrated in high-strain zones parallel to the schistosity, forming stringers (Figs. 5a, 6a and b). The stringers are common along quartz grain boundaries parallel to the schistosity due to the effect of contact strain and pressure dissolution, with CM becoming enriched due to its insolubility. In rare cases, mm-sized CM-rich fragments occur in the sericite matrix (Fig. 6a and f).

The lower 17 m of the sericite zone contains decreasing concentrations of sericite from top to bottom, down to 70 vol%, with 20 vol% quartz porphyroclasts, 5 vol% recrystallised quartz matrix grains of less than 500 μm , and <5 vol% biotite, apatite, rutile and zircon. It represents saprolite as indicated by the presence of variably altered pegmatites and mafic dykes.

5.2.2. Chlorite zone

The palaeosaprolite transitions into a relict parent mineralogy at $\sim 18\text{ m}$ below the nonconformity. The 5 m-thick chlorite zone contains 55 vol% sericite, 25 vol% quartz, 10 vol% K-feldspar, 5 vol% muscovite and biotite and 5 vol% chlorite with minor apatite, zircon and rutile (Fig. 5c). Partially sericitised and fractured K-feldspar porphyroclasts and muscovite crystals are $\pm 250\text{ }\mu\text{m}$ in size. Here, quartz porphyroclasts are less embayed and recrystallized than in the sericite zone. The matrix in the chlorite zone is richer in biotite compared to the sericite and carbon-sericite zones and hosts $\leq 250\text{ }\mu\text{m}$ -sized crystals of chlorite disseminated in the matrix. Unlike the parent rock, the chlorite zone is devoid of plagioclase and may be equated with saprock in modern

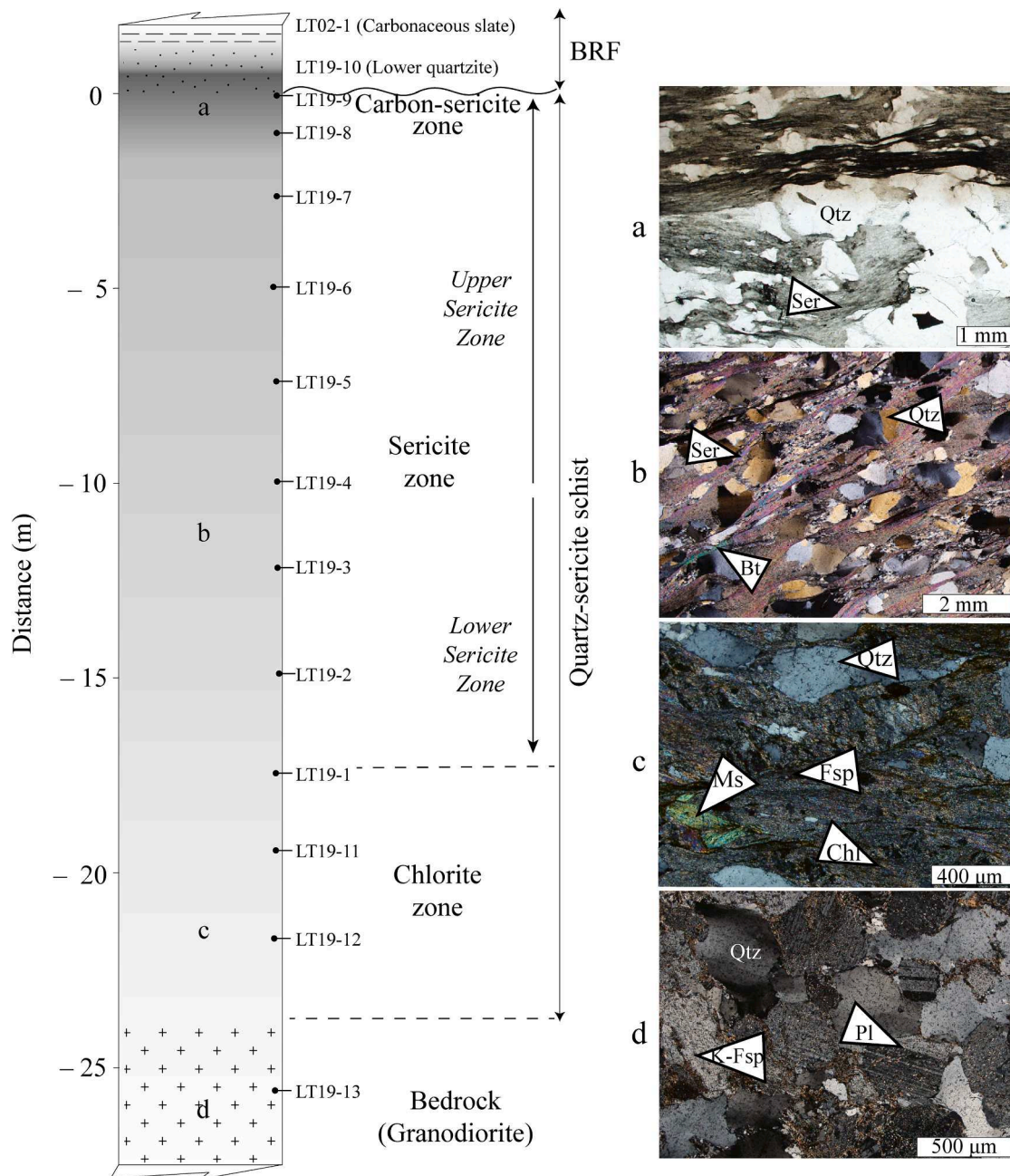


Fig. 5. The log on the left-hand side of the figure shows the different zones that make up the palaeoregolith, based on mineralogical assemblages. Labels a, b, and d correspond to photomicrographs on the right-hand side that are representative of the three different zones of the palaeoregolith and the underlying granodiorite. All photomicrographs were taken in XPL except for (a) taken in PPL. The dashed lines show the estimated gradational contacts of the different zones.

regolith profiles.

5.2.3. Bedrock

The bedrock is a medium- to coarse-grained granodiorite (Fig. 5d). The granodiorite contains 40 vol% quartz, 40 vol% plagioclase, 15 vol% K-feldspar and 5 vol% muscovite and biotite with tourmaline, zircon, chlorite, apatite and iron sulphides as accessory minerals. Here, quartz grains lack replacement textures, and the schistosity is weak to absent.

5.3. Geochemical composition of the palaeoregolith

The average composition of two granodiorite samples LT19-13 and LT19-15 is regarded as representative of the parent material, although the two samples yield Ti/Al ratios (0.016–0.017) slightly different to the

range of the palaeoregolith samples (Ti/Al = 0.019–0.021; Tables 1 and 2). Titanium is considered immobile during weathering, whereas Al can display some mobility (e.g., Brimhall and Dietrich, 1987; Driese et al., 2011), thus their ratios in both the parent and weathered product are expected to be similar. Small differences in ratios may indicate some Al depletion. Although the Ti/Al ratios do not vary significantly in the bulk of the palaeoregolith, some heterogeneity in the parent material is suggested by an anomalous value at –17.5 m, most likely a podding effect (e.g., Yang et al., 2002), the presence of altered pegmatite or due to local variations in modal percentages of major minerals.

5.3.1. Mass balance calculations

Applying a mass balance equation modified from Brimhall and Dietrich (1987, Eq. (1)) to our data shows that most of the analysed major

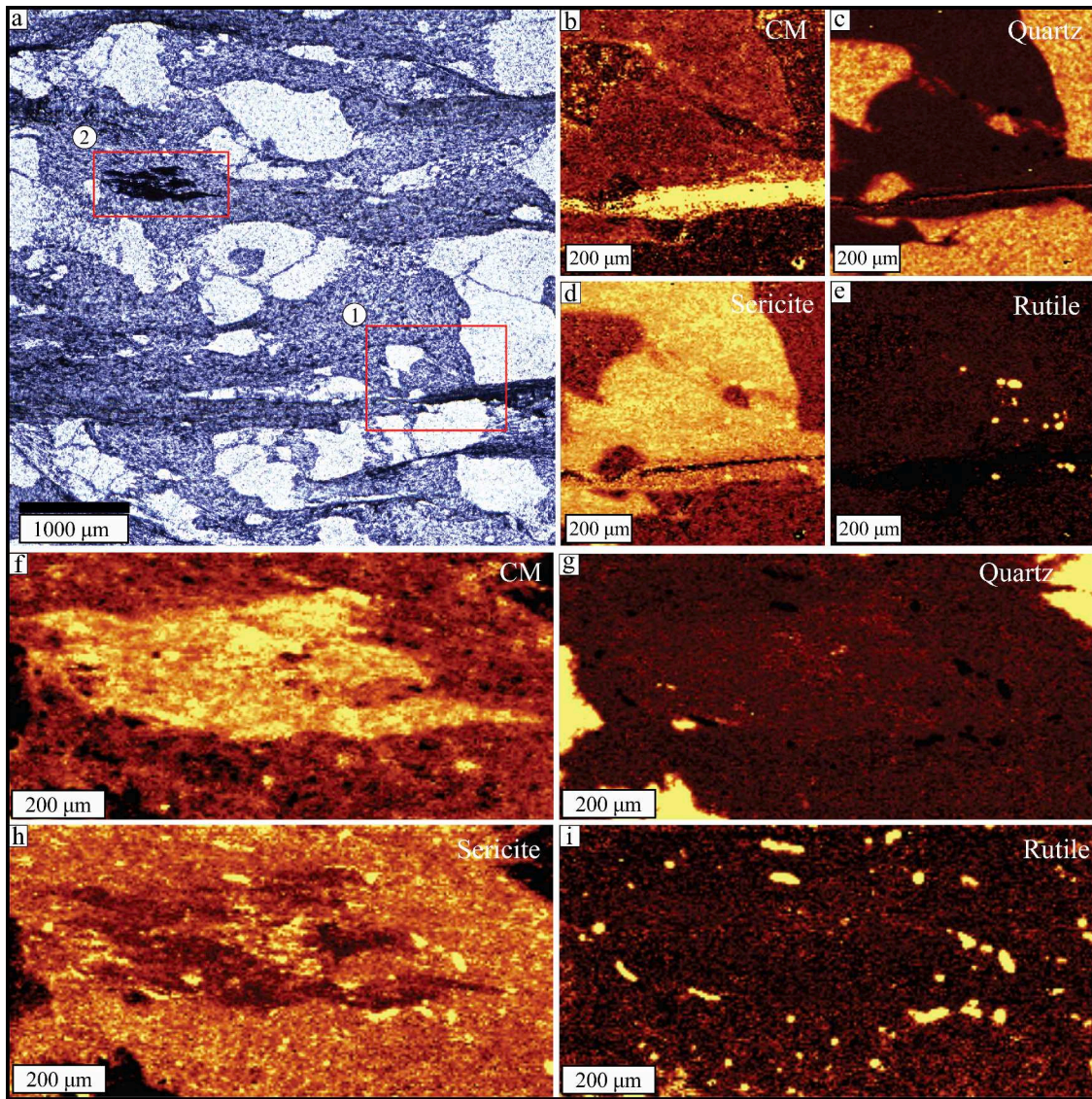


Fig. 6. Raman maps showing the distribution of minerals and carbonaceous matter in the carbon-sericite zone from sample LT19-9 at <10 cm below the nonconformity. (a) A photomicrograph (PPL) of quartz-sericite schist; red squares 1 and 2 show the areas of Raman analysis in b–e and f–i, respectively. (b–i) Raman maps of the carbonaceous matter (CM) G band at $\sim 1590\text{ cm}^{-1}$ (b and f), quartz major band at $\sim 470\text{ cm}^{-1}$ (c and g), sericite major band at $\sim 260\text{ cm}^{-1}$ (d and h), and rutile major band at $\sim 610\text{ cm}^{-1}$ (e and i). Brighter areas within Raman maps reflect higher intensities of mineral-specific spectra.

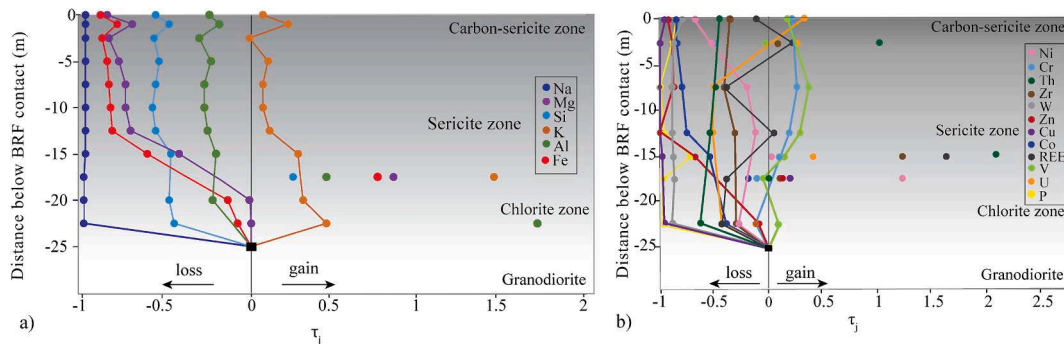


Fig. 7. (a) Mass fraction diagram normalised to Ti, showing the net gain or loss of major elements in the palaeoregolith relative to the granodiorite (shown as a black box). The anomalies at -17.5 and -22.5 m are not included in the trend lines to better visualise the trends. (b) Mass fraction diagram normalised to Ti, showing the net gain or loss of trace elements in the palaeoregolith relative to the granodiorite (shown as a black box). Samples at -17.5 , -15 and -2.5 m are excluded to better visualise the pattern without the effect of anomalous values. Average τ values in text include anomalies.

elements are depleted in the palaeoregolith relative to the parent (Fig. 7a).

$$\tau_{j,w} = \frac{[j]_w [Ti]_p}{[Ti]_w [j]_p} - 1 \quad (1)$$

j = mobile element
 Ti = immobile element
 w = weathered material
 p = parent material

We used Ti as the immobile element in the mass balance equation, as rutile occurs throughout the profile with no textural evidence of dissolution and is generally regarded immobile during weathering (e.g., Yang et al., 2002; Driese et al., 2011; Delvigne et al., 2016; Heard et al., 2021). Calcium is the most depleted element (below the detection limit of <0.05 % for CaO, Table 2) in the palaeoregolith compared to the parent rock, such that it cannot be included in Fig. 7a. Sodium yields an average τ value of -0.99 (SD = 0). Magnesium and Fe are depleted in the sericite zone and yield average τ values of -0.73 (SD = 0.13) and -0.82 (SD = 0.09), respectively. In the chlorite zone, Fe shows minor depletion (-0.20 , SD = 0.54), and Mg is neither lost nor gained at this depth. Their closely coupled behaviour seen from the similarity in patterns in Fig. 7a suggests that these elements were contained in, and lost from, ferromagnesian minerals, most likely biotite, in the granodiorite during weathering in the sericite zone. Silicon has an average τ value of -0.46 (SD = 0.24). Aluminium yields an average τ value of -0.25 (SD = 0.61), suggesting minor depletion in the palaeoregolith. Potassium shows enrichment in the palaeoregolith relative to the granodiorite, with an average τ value of 0.28 (SD = 0.41). This enrichment is greater in the chlorite zone of the palaeoregolith.

The mass fractions for selected trace elements are shown in Fig. 7b. Cu, P and W show a marked depletion and yield average τ values of -0.77 (SD = 0.36), -0.83 (SD = 0.09) and -0.83 (SD = 0.14), respectively. Zinc and Co are more depleted in the sericite zone compared to the chlorite zone and yield average τ values of -0.62 (SD = 0.43) and -0.52 (SD = 0.53), respectively. Zirconium, Th and U yield average τ values of -0.02 (SD = 0.52), -0.14 (SD = 1.03) and -0.08 (SD = 0.41), respectively. These values are close enough to 0 to consider

them immobile. Nickel shows a variable depletion trend and yields an average τ value of -0.10 (SD = 0.72). As a result, it is also considered immobile. Chromium and V have average τ values of 0.15 (SD = 0.39) and 0.11 (SD = 0.15), respectively. Similar to Th, U and Zr, these values are close to 0 and Cr and V are therefore regarded as immobile.

5.3.2. REE distribution

The rare earth element (REE) patterns of the palaeoregolith normalized to primitive mantle are generally similar, showing higher concentrations of light REE (LREE) relative to heavy REE (HREE; Fig. 8). REE concentrations are lower in the chlorite zone relative to the bedrock, while the sericite zones contain higher concentrations of REE relative to the chlorite zone and bedrock (Fig. 7b). Enrichment in LREE relative to the general trend is observed at -15 m (Fig. 8), which correlates with outliers in trace element concentrations in Fig. 7b. The enrichment is likely controlled by zircon as suggested by a higher concentration of LREE to HREE (Fig. 8) and a good general correlation between Zr and Σ REE (Fig. 9a, $R^2 = 0.96$). In addition, the sample taken at -15 m has the highest Zr concentration in the dataset. The REE patterns of the palaeoregolith normalized to parent rock shows their enrichment in the lower sericite zone and LREE and MREE depletion in the chlorite zone (Fig. 10). Significant MREE depletion is recorded in the uppermost portion of the palaeoregolith (Figs. 8 and 10).

5.3.3. Chemical index of alteration (CIA)

The CIA for the palaeoregolith was calculated using the equation defined by Nesbitt and Young (1982; Table 1; Eq. (2)):

$$CIA = \left(\frac{Al_2O_3}{Al_2O_3 + CaO + Na_2O + K_2O} \right) \times 100 \quad (2)$$

The CaO concentration used in the equation requires correction to reflect Ca in silicate minerals only. This correction was not necessary, as the palaeoregolith in question contains Ca concentrations below detection. The CIA values of the samples increase from an average of 55.9 in the granodiorite to 75.5 in the uppermost part of the profile. These increasing values correspond to the increasing degree of K-feldspar alteration and complete loss of plagioclase, resulting in the loss of Ca and

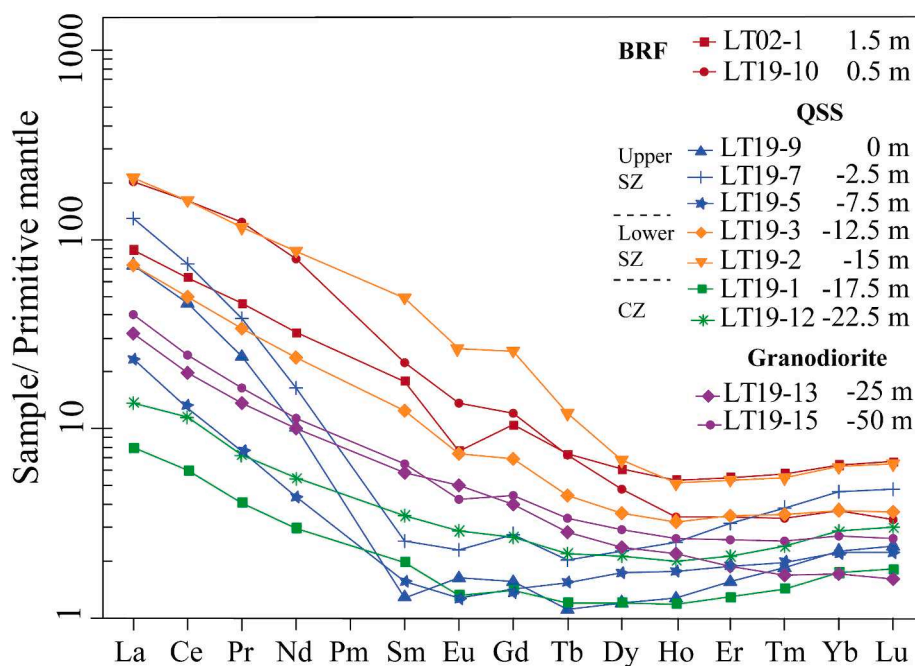


Fig. 8. Primitive mantle-normalised (McDonough and Sun, 1995) REE plot showing REE concentrations in the granodiorite, palaeoregolith (QSS; quartz-sericite schist) and Black Reef Formation (BRF). Purple: granodiorite, green: Chlorite Zone (CZ), orange: Lower Sericite Zone (SZ), blue: Upper Sericite Zone (SZ), red: Black Reef Formation (BRF).

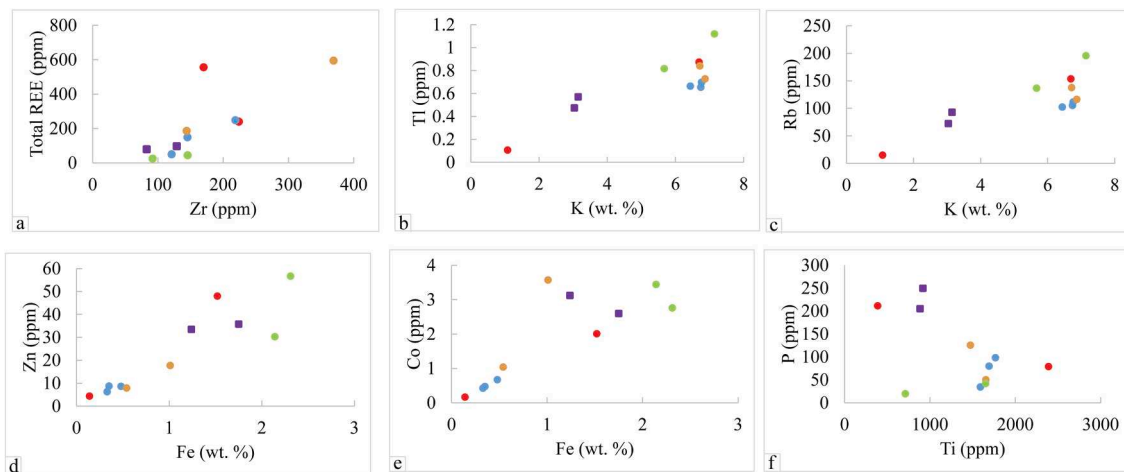


Fig. 9. Correlation diagrams of selected elements in the palaeoreolith. Purple squares: granodiorite, green circles: Chlorite Zone, orange circle: Lower Sericite Zone, blue circles: Upper Sericite Zone, red: Black Reef Formation (BRF).

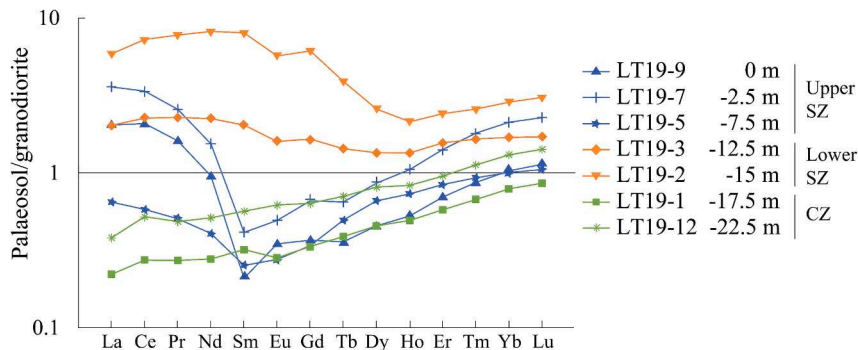


Fig. 10. REE plot of palaeoreolith samples normalised to average granodiorite. Purple: granodiorite, green: Chlorite Zone (CZ), orange: Lower Sericite Zone (SZ), blue: Upper Sericite Zone (SZ), red: Black Reef Formation (BRF).

Na towards the nonconformity. The chemical index of weathering (CIW; Harnois, 1988; Table 1), which does not utilise K_2O for determination of the degree of weathering, has values ≥ 99 .

5.4. Total organic carbon (TOC) content and $\delta^{13}C_{org}$ values

Samples from the carbon-sericite zone and basal conglomerate of the BRF have low TOC values of 0.02–0.05 wt% and similar $\delta^{13}C$ values of CM (–27 to –23 ‰ vs –25 to –22 ‰; Table 3, Fig. 11). Although the TOC contents of the Kalkkloof and Schagen palaeosol samples are in almost all cases higher, the $\delta^{13}C_{org}$ value of the Kalkkloof sample falls within the range for the carbon-sericite zone and BRF conglomerate. Schagen palaeosol samples are isotopically heavier (Table 3, Fig. 11). Compared to basal conglomerate of the BRF and the carbon-sericite zone, the BRF slates in the study area yield much lighter $\delta^{13}C_{org}$ values of –34 and –33 ‰, within the range reported by Strauss and Beukes (1996) from BRF shales collected southeast of the Johannesburg Dome. Watanabe et al. (1997) reported $\delta^{13}C$ values of –36 to –30 ‰ for the BRF slates from the eastern and central Transvaal Basin, similar to what we measured (Fig. 11).

5.5. Raman geothermometry

Raman geothermometry of CM using the model of Beyssac et al. (2002) was conducted on three samples, the basal conglomerate and slate of the Black Reef Formation and quartz-sericite schist of the palaeosol. It yields peak metamorphic temperatures of 384 ± 50 °C for conglomerate, 447 ± 50 °C for slate, and 498 ± 50 °C for quartz-sericite

schist of the palaeosol (Fig. S1, Table S2).

6. Discussion

The differentiation of the alteration profile into compositionally distinct zones, the increase in degree of alteration towards the nonconformity, the presence of organic matter at the top of the profile and as a reworked component in the overlying sedimentary rocks, and the preservation of alteration signals in deformed and metamorphosed rocks are some of the main lines of evidence that the studied section represents an ancient weathering profile.

6.1. Post-weathering alteration

6.1.1. Burial diagenesis and K-metasomatism

Feldspars weather to kaolinite under surface conditions (White et al., 2001) and the same process must have acted on granitoids of the Johannesburg Dome upon surface exposure. This loss of feldspar in the Lanseria palaeoreolith resulted in quartz grains dispersed in a clay-rich matrix, which eventually gave the palaeoweathering profile the porphyroclastic texture observed in Fig. 5a and b. During burial diagenesis, kaolinite converted to illite, a process that requires the addition of K. The A-CN-K ternary plot in Fig. 12 (adapted from Nesbitt, 1992) shows a diagenetic overprint on the profile, consistent with enrichment in K, as seen in Fig. 7a. The weathering of basement granodiorite would have given rise to an Al-rich kaolinitic residuum, as shown by Trend 1 in Fig. 12. The trend follows the weathering process expected for felsic rocks using the method of Fedo et al. (1995) and is constructed based on

Table 3

Organic C stable isotope analysis and whole-rock total organic carbon (TOC) results for the Lanseria, Schagen and Kalkkloof palaeosols, and the Black Reef Formation quartzite and slate. Only samples analysed in this study are shown.

Locality	Paleosol	Sample no.	Rock type	TOC (wt %)	d13Corg (% vs PDB)
Northern margin of JD	n.a	LT02-1	Slate	1.03	-34.96
	n.a	LT02-2	Slate	1.11	-33.25
	n.a	LT19-10-1	Quartzite	0.04	-24.77
	n.a	LT19-10-2	Quartzite	0.04	-22.12
	n.a	LT19-10-3	Quartzite	0.04	-24.56
	n.a	LT19-10-4	Quartzite	0.03	-23.32
	Lanseria	LT19-9-1	QSS	0.05	-23.82
	Lanseria	LT19-9-2	QSS	0.02	-27.01
	Lanseria	LT19-9-3	QSS	0.03	-24.65
	Lanseria	LT19-9-4	QSS	0.04	-22.62
Eastern Transvaal Basin	Schagen	SHG-1	Carbonaceous serpentinite	0.65	-17.86
	Schagen	SHG-3	Carbonaceous serpentinite	0.05	-22.16
	Schagen	SHG-6	Carbonaceous serpentinite	0.30	-16.44
	Kalkkloof	K1	Carbonaceous serpentinite	0.49	-23.95
	Kalkkloof	K2	Carbonaceous serpentinite	0.05	-21.83

n.a = not applicable; QSS = quartz-sericite schist.

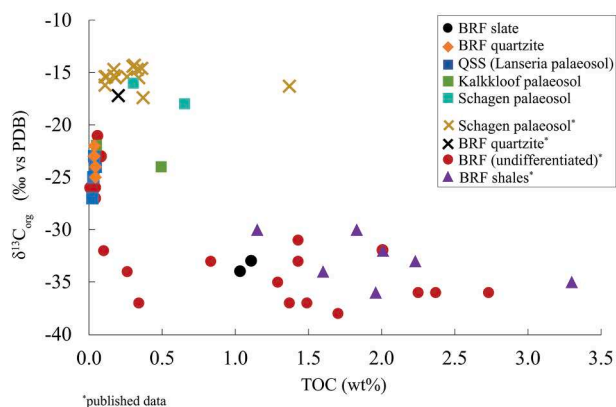


Fig. 11. Plot of total organic carbon (TOC) versus $\delta^{13}\text{C}_{\text{org}}$ for samples from the Lanseria, Schagen and Kalkkloof palaeosols, and the BRF. Note that two samples (one from Kalkkloof and the other from Schagen) overlap at -22% and $0.05\text{ wt}\%$. Additional data are from Strauss and Beukes (1996, red diamonds), Watanabe et al. (1997, purple triangles) and Watanabe et al. (2004, crosses).

the feldspar proportions of the relatively fresh (line 3) granodiorite samples (LT19-13, 14 and 15). Note that the CIA value of the granodiorite at 56 is slightly elevated relative to an unweathered felsic rock (~ 50), which may be linked to deep palaeoweathering or post-emplacement hydrothermal alteration in the subsurface. During diagenesis, the inferred Al-rich weathering product shifted towards a K-rich mineralogy in the current palaeoregolith (Trend 2, parallel to the $\text{Al}_2\text{O}_3\text{-K}_2\text{O}$ line) as kaolinite transformed to illite. Metamorphism later converted illite into sericite. Potassium was added to the palaeoregolith via K-metasomatism, a process occurring in a range of geologic settings, and commonly recorded in shales and palaeosols (Fedó et al., 1995). In

fact, K concentrations in Precambrian palaeosols are significantly higher than in modern soils (Novoselov & de Souza Filho, 2015). Rubidium and Tl correlate well with K in the Lanseria palaeoregolith (Fig. 9b–c, $R^2 = 0.62$ and 0.67 , respectively), as they can have the same valence and similar ionic radii.

6.1.2. Metamorphism and deformation

Greenschist facies metamorphism converted illite in the palaeoregolith to sericite, which assumed a preferred orientation and formed a schistosity during deformation. Calculation estimates, using Raman spectra data from CM in conglomerate, slate and quartz-sericite schist yield peak metamorphic temperatures of 384 to $498 \pm 50\text{ }^\circ\text{C}$, respectively (Supplementary file, Table S2). The temperature estimate of the conglomerate is probably closer to the true temperature, as shearing affected the CM in the palaeosol to form the quartz-sericite schist, which may have had an influence on its structural order. Temperatures in the order of $\sim 400\text{ }^\circ\text{C}$ are consistent with greenschist facies conditions inferred from petrographic analysis of rocks from the study area.

6.2. Age constraints for the palaeoweathering

The palaeoregolith was not directly dated in this study. However, the maximum deposition age of the capping Black Reef Formation of $2618 \pm 11\text{ Ma}$ (Zeh et al., 2020) provides a constraint for the maximum age of surficial weathering, which likely occurred close to the deposition age of the Black Reef Formation owing to the preservation of the palaeoregolith. The minimum age of the palaeoregolith is best constrained by the oldest U-Pb zircon age of a tuff bed in the overlying Malmani carbonates of $2588 \pm 7\text{ Ma}$ (Martin et al., 1998) and suggests that the palaeosol formed between $2618 \pm 11\text{ Ma}$ and $2588 \pm 6\text{ Ma}$ (i.e., $\sim 2.60\text{ Ga}$). Post-burial alteration contributed to the evolution of the palaeoregolith, i.e., conversion of kaolinite to illite and K-metasomatism, and likely persisted well beyond the time of deposition of the Black Reef Formation.

6.3. Palaeoenvironment and palaeoclimate

The palaeoregolith formed on basement granitoids after an interval of intense terrestrial weathering as inferred from major and trace element analyses. The BRF is interpreted to have formed in a shallow-marine environment although braided fluvial deposits occur in places (Eriksson and Truswell, 1974; Tyler, 1979; Obbes, 2001). At the studied site, the contact between the sandstones and underlying palaeosol is sharp and planar and likely represents a marine transgressive surface that eroded the upper part of the palaeosol, as indicated by the presence of carbonaceous matrix material in the basal part of the sandstone (Fig. 4b). The sheet-like sandstones formed in a shoreface to foreshore setting that was subjected to rapid deepening as indicated by overlying marine carbonaceous shales that, in turn, are overlain by shallow-marine carbonates of the Malmani Subgroup. The Lanseria palaeoregolith shows evidence for a reducing environment during chemical weathering. Iron was mobile and removed from the upper levels of the profile (Fig. 7a), suggesting anoxic atmospheric conditions and dissolved oxygen-free meteoric waters. Cobalt and Zn concentrations correlate positively with Fe (Fig. 9d–e, $R^2 = 0.79$ and 0.92 , respectively). Prior to soil formation they were probably hosted in biotite. During weathering, they became leached together with Fe and are now largely associated with chlorite. A reducing environment may also be supported by the immobility of V and Cr (Fig. 7b). Vanadium and Cr concentrations are positively correlated with Ti concentrations ($R^2 = 0.88$ and 0.34 , respectively), with Ti being hosted in micron-sized rutile and anatase crystals in the sericite matrix (Fig. 6). V and Cr were likely liberated from biotite, titanite and Fe-Ti-oxides present in the granodiorite, but retained as authigenic Ti-oxides in the soil profile, which commonly is the case in modern soils (Milnes and Fitzpatrick, 1989). A reducing environment favours Cr and V in their immobile state as Cr(III)

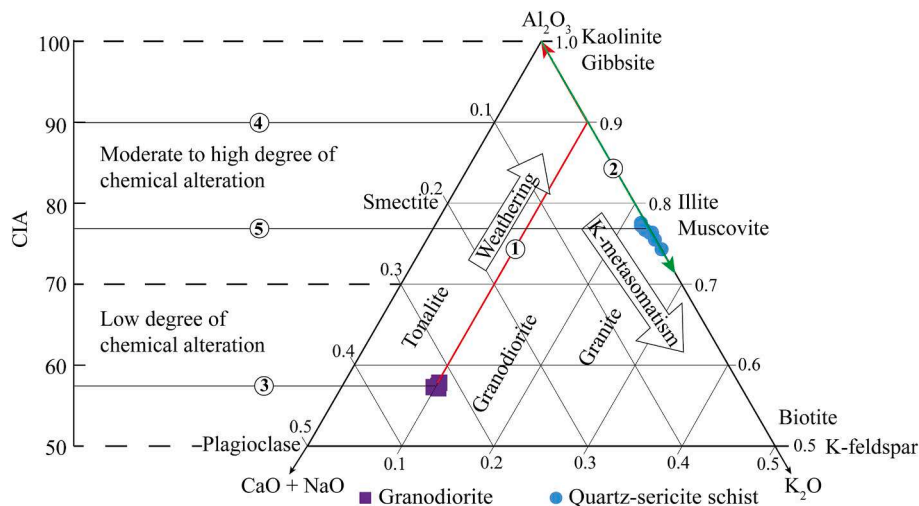


Fig. 12. A-CN-K plot for the Lanseria palaeosol. 1: The expected weathering path for the granodiorite parent. 2: The effect of K metasomatism of the palaeoreolith. 3: Initial average CIA value of relatively unweathered granodiorite samples. 4: Minimum CIA value for the pre-metasomatised palaeoreolith. 5: Average CIA value for the metasomatised palaeoreolith.

and V(III), respectively (Murakami et al., 2016) and both ions can substitute for Ti in Ti-oxides (Meinhold, 2010). Uranium was mostly hosted in zircon due to a moderate positive correlation of U and Zr ($R^2 = 0.41$) and lack of correlation with P. Its immobility in the Lanseria palaeoreolith may be due to zircon's refractory nature rather than reducing conditions. The degree of weathering giving rise to the palaeoreolith was high. The original CIA value of the weathering products would have been > 90 (Trend 1, Fig. 12), but was lowered to a maximum CIA of 76 (Trend 2) during diagenesis, suggestive of a mature palaeoreolith that formed under a warm and wet climate and/or during a prolonged time interval, as is also shown by the complete dissolution of feldspars in the upper levels of the palaeoreolith (e.g., Driese et al., 2011; Liivamägi et al., 2021). The Black Reef Formation is overlain by thick platform carbonates of the Chuniespoort Group, suggesting deposition in the tropics. The REE in the palaeoreolith profile are concentrated in P-bearing phases and zircon as shown by positive correlations between Σ REE and P ($R^2 = 0.74$) and Zr ($R^2 = 0.95$). The MREE depletion near the nonconformity (Figs. 8 and 10) is likely a result of apatite dissolution under intense weathering conditions, as apatite is frequently enriched in the MREE (Bea, 1996; Compton et al., 2003). The MREE may have also been derived from the breakdown of titanite, which may also show MREE enrichment (Gromet and Silver, 1983; Bea, 1996; Che et al., 2013), although maybe to a lesser extent as there is no clear correlation between Σ REE and Ti concentrations. We do note, however, that P is depleted throughout the palaeoreolith (Fig. 7b), and not only at its top.

6.4. Source of carbon

We propose two possible sources of CM, either from soil microbes during pedogenesis or via migration of hydrocarbons along the nonconformity much later. The Transvaal Supergroup sedimentary cover of the central part of the Kaapvaal Craton experienced regional hydrocarbon formation and migration in the Palaeoproterozoic. Fuchs et al. (2016) documented evidence of hydrocarbon migration in BRF conglomerates and argued that hydrothermal and hydrocarbon fluids sourced from the Witwatersrand Supergroup were transported through fault networks and infiltrated the BRF. If migration of hydrocarbons occurred, evidence of this percolation would be recorded in the presence of pyrobitumen: (1) along veins/fractures in the BRF quartzites and palaeosol, (2) in the pore space between quartz grains in the BRF quartzites, and (3) as bituminous nodules, as is commonly observed in carbon-rich conglomerate seams of the Witwatersrand Supergroup (Spangenberg and Frimmel, 2001; Drennan and Robb, 2006) and

conglomerate reefs of the BRF (Buick et al., 1998; Fuchs et al., 2016). No such features have been observed in the present study. Despite the stratigraphic proximity of the BRF slates to the nonconformity (~ 1.5 m), it is unlikely that they were the source of hydrocarbons in the palaeosol and Black Reef conglomerate, as hydrocarbons generated by the maturation of organic matter in the black shales (now slates) would be expected to be isotopically similar to the source (Schoell, 1984), which is not observed. Carbonaceous matter in the BRF slates is isotopically much lighter, and is likely fossilised remnants of marine methanogens, as suggested by such negative $\delta^{13}\text{C}$ values (e.g., Stüeken and Buick, 2018). It is therefore more likely that CM formed biologically and in-situ at ~ 2.6 Ga at the top of the soil profile. In this case, the carbon isotope values reflect the near-primary composition of this CM, assuming a maximum change of $+3$ ‰ towards more heavy values during the maturation of the CM to kerogen (e.g., Hayes et al., 1983; Schidlowski and Aharon, 1992). The $\delta^{13}\text{C}$ values (-27 to -23 ‰) of the CM from the basal BRF conglomerate and palaeosol suggest primary metabolic productivity involving terrestrial photoautotrophic organisms (e.g., Hayes et al., 1999). A terrestrial environment for the soil microbes is also favoured because the $\delta^{13}\text{C}$ values of the soil carbon are starkly different from those in the overlying marine slates of the BRF. CM in the Lanseria palaeosol was likely derived from cyanobacteria that colonised the uppermost part of the palaeosol and its surface, e.g., Homann et al. (2018). Samples from the Kalkkloof palaeosol share similar isotopic and TOC characteristics to the Lanseria palaeosol (Fig. 11). Less fractionated $\delta^{13}\text{C}$ values (average of -15 ‰) for CM from the Schagen palaeosol were explained by Watanabe et al. (2004) by soil biota consisting of an assemblage of cyanobacteria and heterotrophs in a strongly evaporating environment. That CM in the Schagen and Kalkkloof palaeosols is microbe-derived gives good grounds to compare CM in these palaeosols with CM in the Lanseria palaeosol, despite the palaeosols having different parent lithologies. This signifies a diverse adaptability of Archaean microbial life to substrates of different compositions. The presence of organic matter in the Lanseria, Schagen and Kalkkloof palaeosols suggests widespread colonisation of the Kaapvaal Craton by terrestrial life at 2.6 Ga. Partial reworking of soil clays and associated organic matter and its incorporation into basal conglomerate of the Black Reef Formation as muddy carbonaceous matrix may be part of the reason for the designation of the conglomerate as Black Reef.

6.5. Soil microbes and their significance for soil formation

The carbon-sericite zone of the Lanseria palaeoreolith and

immediately overlying Black Reef conglomerate have overlapping TOC contents, $\delta^{13}\text{C}_{\text{org}}$ isotopic compositions and similar modes of CM occurrence. We suggest that the CM was reworked from the palaeosol surface and incorporated into the sericite matrix of the conglomerate during sedimentation. The presence of carbonaceous fragments in the sericite matrix (Fig. 6a, f and h) of the palaeosol indicates that carbonaceous matter was associated with biological soil mats/crusts. These fragments are remarkably similar to those reported by Rye and Holland (2000b) from the 2.76 Ga Mount Roe #2 palaeosol in Western Australia and the 3.2 Ga fluvial conglomerates of Moodies Group, South Africa (Homann et al., 2018), both interpreted as fossilised remains of microbial mats. Shrinking-and-swelling of the soil material during wetting-and-drying cycles, reworking of the upper part of the palaeosol and/or low shear strains during deformation would have caused the disintegration of the mats into such fragments. Although clay derived from the weathering of feldspar would have had low extensibility on wetting (e.g., kaolinite), some expandable clay (e.g., smectite) would have been present initially, derived from the breakdown of biotite. In addition, or alternatively, microbes may have been dispersed in the upper parts of the soil matrix as a microbial earth, with the carbonaceous fragments

representing crack fills (Retallack, 2012). Further evidence of an in-situ origin for CM in the palaeosol is preserved in the behaviour of Cu, P and Al. Copper is depleted in the palaeoregolith (Fig. 7b), which may seem to contradict an anoxic environment of soil formation (Goyné et al., 2006; Murakami et al., 2016). However, the loss of Cu can be attributed to the presence of organic, microbe-derived acids, which are known to enhance Cu solubility regardless of oxygen levels (Goyné et al., 2006). Similarly, Al loss relative to Ti as observed in (Fig. 7a) may be attributed to organic acid-enhanced silicate weathering (Beaty and Planavsky, 2020). In addition, P was mobile in the palaeoregolith (Fig. 9f) and MREE are depleted in the upper part of the palaeoregolith and attributed to apatite dissolution (Figs. 8 and 10), a process generally only observed in records of palaeoweathering after the GOE (Bekker and Holland, 2012). Neaman et al. (2005) suggested that depletion in P may also indicate elevated levels of organic acids, consistent with our interpretation. The presence of organic acids could also explain some depletion of Al and the intensity of weathering as indicated by the thickness of the saprolite, since organic acids increase the rate of silicate weathering (Barman et al., 1992; Drever and Stillings, 1997). Terrestrial weathering aided by soil microbes was thus a process for the release and recycling of

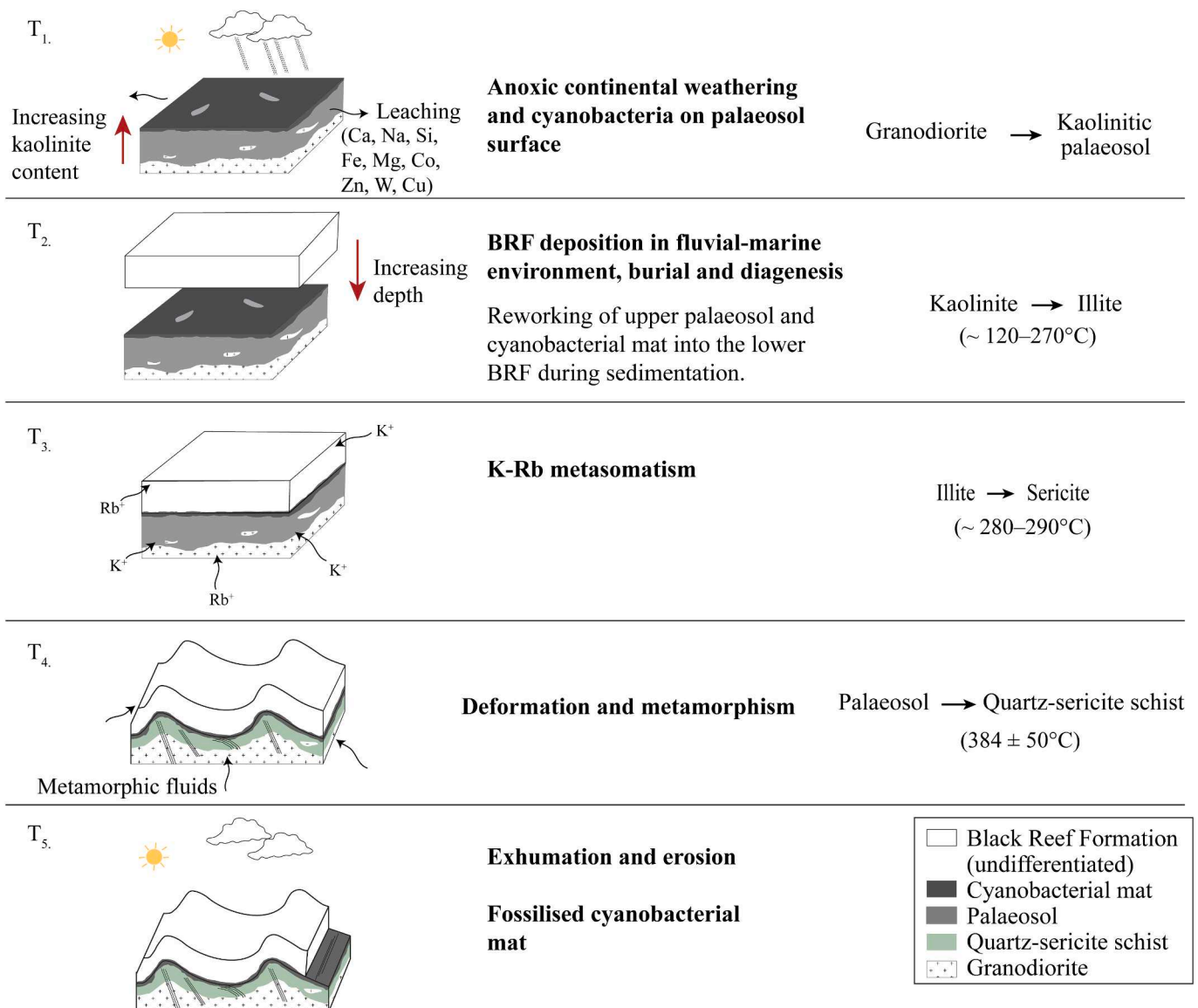


Fig. 13. Summary diagram showing the progression of events for the Lanseria palaeosol. The diagram is not to scale. See text for details. Conversion temperatures are from Novoselov and de Souza Filho (2015).

bioessential elements Cu and P to the surface environment, so these elements were thus not necessarily biolimiting. This is in line with high P contents recorded in Neoproterozoic marine carbonates (Ingalls et al., 2022).

7. Conclusion

Field observations, petrographic data and geochemical results show that the quartz-sericite schist exposed below the Black Reef Formation along the northern margin of the Johannesburg Dome is a deformed and metamorphosed palaeoregolith. The granodiorite-derived palaeoweathering profile lost major elements (Na, Ca, Fe, Mg, and Si) and some minor and trace elements (e.g., P, Cu, Zn, Co), resulting in distinct mineralogical and geochemical zoning with distance from the nonconformity, consistent with weathering under anoxic atmospheric conditions at the time of pedogenesis (Fig. 13). The results agree with reducing atmospheric conditions before the GOE, at least at ~2.6 Ga. Carbonaceous matter in the uppermost part of the soil profile was derived from photosynthetic microbes, as suggested by the range of depleted $\delta^{13}\text{C}$ values, that colonised the surface of the palaeosol, rather than via deposition of hydrocarbon fluids. A similar isotopic composition and occurrence of carbonaceous matter in the overlying basal conglomerate of the Black Reef Formation suggest that some carbonaceous matter was reworked into the conglomerate. The similarities between carbonaceous matter in the Lanseria, Schagen and Kalkkloof palaeosols suggest that the Kaapvaal Craton was extensively colonised by photosynthesizing cyanobacteria at 2.6 Ga and that soil horizons formed an important carbon sink by that time. Unlike most Precambrian palaeoweathering profiles, the Lanseria palaeosol is well exposed and represents a suitable and reliable reference for Archaean climatic reconstructions and early terrestrial life studies.

CRedit authorship contribution statement

Gobona L. Tau: Writing – original draft, Visualization, Project administration, Investigation, Funding acquisition, Data curation, Conceptualization. **Axel Hofmann:** Writing – review & editing, Supervision, Investigation, Conceptualization. **Jeremie Lehmann:** Writing – review & editing, Supervision, Funding acquisition. **Trishya Owen-Smith:** Writing – review & editing, Supervision. **Alice Pellerin:** Writing – review & editing, Investigation. **Christophe Thomazo:** Writing – review & editing. **Christian Reinke:** Investigation. **Allan H. Wilson:** Investigation.

Declaration of competing interest

The authors declare that they have no known competing financial interests or personal relationships that could have appeared to influence the work reported in this paper.

Data availability

All data have been made available and are included.

Acknowledgements

This research was part of the MSc project of GLT. Funding was provided through the Global Excellence and Stature (GES) scholarship from the University of Johannesburg. The Department of Tertiary Education and Financing (DTEF) under the Botswana Government is also acknowledged for funding the early stages of the research. AH acknowledges Chris Hatton, who enabled a visit to the Schagen and Kalkkloof localities, and the DSI-NRF Centre of Excellence for Integrated Mineral and Energy Resource Analysis (CIMERA) for support. Carl Anhaeusser is acknowledged for introducing the area to JL. GLT thanks Gina Forster, Lizzie and Alan Lawrence, Brian and Gerda Latellier, Dieter

Beier and Ilse Klemm for access to the field area. Gerhard Roodt is thanked for training in XRF sample preparation and Robyn MacRoberts, Samuel Nunoo and Jaganmoy Jodder for fruitful discussions and reviews of the MSc thesis. Finally, the authors thank the reviewers who immensely improved this manuscript.

Appendix A. Supplementary material

Supplementary data to this article can be found online at <https://doi.org/10.1016/j.precamres.2024.107352>.

References

- Albut, G., Babechuk, M.G., Kleinhans, I.C., Bengler, M., Beukes, N.J., Steinhilber, B., Smith, A.J., Kruger, S.J., Schoenberg, R., 2018. Modern rather than mesoarchaean oxidative weathering responsible for the heavy stable Cr isotopic signatures of the 2.95 Ga old Ijzermijn iron formation (South Africa). *Geochim. Cosmochim. Acta* 228, 157–189.
- Bangert, B., Stollhofen, H., Lorenz, V., Armstrong, R., 1999. The geochronology and significance of ash-fall tuffs in the glaciogenic Carboniferous-Permian Dwyka Group of Namibia and South Africa. *J. Afr. Sci.* 29 (1), 33–49.
- Barman, A.K., Varadachari, C., Ghosh, K., 1992. Weathering of silicate minerals by organic acids. I. Nature of cation solubilisation. *Geoderma* 53 (1–2), 45–63.
- Bea, F., 1996. Residence of REE, Y, Th and U in granites and crustal protoliths; implications for the chemistry of crustal melts. *J. Petrol.* 37 (3), 521–552.
- Beatty, B.J., Planavsky, N.J., 2020. A 3 b.y. record of a biotic influence on terrestrial weathering. *Geology* 49 (4), 407–411.
- Bekker, A., Holland, H.D., 2012. Oxygen overshoot and recovery during the early paleoproterozoic. *Earth Planet. Sci. Lett.* 317–318, 295–304.
- Beukes, N.J., Dorland, H., Gutzmer, J., Nedachi, M., Ohmoto, H., 2002. Tropical laterites, life on land, and the history of atmospheric oxygen in the paleoproterozoic. *Geology* 30 (6), 491–494.
- Beysac, O., Goffé, B., Chopin, C., Rouzaud, J.N., 2002. Raman spectra of carbonaceous material in metasediments: a new geothermometer. *J. Metam. Geol.* 20 (9), 859–871.
- Brimhall, G.H., Dietrich, W.E., 1987. Constitutive mass balance relations between chemical composition, volume, density, porosity, and strain in metasomatic hydrochemical systems: results on weathering and pedogenesis. *Geochim. Cosmochim. Acta* 51 (3), 567–587.
- Buick, R., Rasmussen, B., Krapez, B., 1998. Archean oil: Evidence for extensive hydrocarbon generation and migration 2.5–3.5 Ga. *AAPG Bull.* 82 (1), 50–69.
- Button, A., Tyler, N., 1981. The character and economic significance of Precambrian paleoweathering and erosion surfaces in southern Africa. *Econ. Geol.* 75, 686–709.
- Che, X.D., Linnen, R.L., Wang, R.C., Groat, L.A., Brand, A.A., 2013. Distribution of trace and rare earth elements in titanite from tungsten and molybdenum deposits in Yukon and British Columbia, Canada. *Can. Mineral.* 51 (3), 415–438.
- Colwyn, D.A., Sheldon, N.D., Maynard, J.B., Gaines, R., Hofmann, A., Wang, X., Gueguen, B., Asael, D., Reinhard, C.T., Planavsky, N.J., 2019. A palaeosol record of the evolution of Cr redox cycling and evidence for an increase in atmospheric oxygen during the Neoproterozoic. *Geobiology* 17, 579–593.
- Compton, J.S., White, R.A., Smith, M., 2003. Rare earth element behaviour in soils and salt pan sediments of a semi-arid granitic terrain in the Western Cape, South Africa. *Chem. Geol.* 201, 239–255.
- Delvigne, C., Opfergelt, S., Cardinal, D., Hofmann, A., André, L., 2016. Desilication in Archean weathering processes traced by silicon isotopes and Ge/Si ratios. *Chem. Geol.* 420, 139–147.
- Department of Mineral and Energy Affairs, Council for Geoscience, South Africa, 1986. 2527DD Broederstroom, 1:50 000 geological series.
- Department of Mineral and Energy Affairs, Council for Geoscience, South Africa, 2018. 1: 1 000 000 geological series.
- Drennan, G.R., Robb, L.J., 2006. The nature of hydrocarbons and related fluids in the Witwatersrand Basin, South Africa: Their role in metal redistribution.
- Drever, J.I., Stillings, L.L., 1997. The role of organic acids in mineral weathering. *Colloids Surf. A Physicochem. Eng. Asp.* 120 (1–3), 167–181.
- Driese, S.G., Jirsa, M.A., Renc, M., Brantley, S.L., Sheldon, N.D., Parker, D., Schmitz, M., 2011. Neoproterozoic paleoweathering of tonalite and metabasalt: implications for reconstructions of 2.69 Ga early terrestrial ecosystems and paleoatmospheric chemistry. *Precamb. Res.* 189 (1–2), 1–17.
- Eglington, B.M., Armstrong, R.A., 2004. The Kaapvaal Craton and adjacent Orogens, southern Africa: a geochronological database and overview of the geological development of the craton. *S. Afr. J. Geol.* 107 (1–2), 13–32.
- Eriksson, K.A., Truswell, J.F., 1974. Stratotypes from the Malmani subgroup north-west of Johannesburg, South Africa. *Trans. Geol. Soc. S. Afr.* 77, 211–222.
- Fedo, C.M., Nesbitt, H.W., Young, G.M., 1995. Unravelling the effects of potassium metasomatism in sedimentary rocks and palaeosols, with implications for paleoweathering conditions and provenance. *Geology* 23 (10), 921–924.
- Finke, N., Simister, R.L., O'Neil, A.H., Nomosatryo, S., Henny, C., MacLean, L.C., Canfield, D.E., Konhauser, K., Lalonde, S.V., Fowle, D.A., Crowe, S.A., 2019. Mesophilic microorganisms build terrestrial mats analogous to Precambrian microbial jungles. *Nat. Commun.* 10 (1), 4323.

- Fuchs, S., Williams-Jones, A.E., Przybyłowicz, W.J., 2016. The origin of the gold and uranium ores of the black reef formation, Transvaal supergroup, South Africa. *Oré Geol. Rev.* 72, 149–164.
- Goyne, K.W., Brantley, S.L., Chorover, J., 2006. Effects of organic acids and dissolved oxygen on apatite and chalcopyrite dissolution: implications for using elements as organomarkers and oxymarkers. *Chem. Geol.* 234, 28–45.
- Grandstaff, D.E., Edelman, M.J., Foster, R.W., Zbinden, E., Kimberley, M.M., 1986. Chemistry and mineralogy of Precambrian palaeosols at the base of the dominion and Pongola groups (Transvaal, South Africa). *Precamb. Res.* 32 (2–3), 97–131.
- Gromet, L.P., Silver, L.T., 1983. Rare earth element distributions among minerals in a granodiorite and their petrogenetic implications. *Geochim. Cosmochim. Acta* 47 (5), 925–939.
- Gumsley, A., Stamsnijder, J., Larsson, E., Söderlund, U., Naeraa, T., de Kock, M., Salacińska, A., Gawęda, A., Humbert, F., Ernst, R., 2020. Neoproterozoic large igneous provinces on the Kaapvaal Craton in Southern Africa re-define the formation of the Ventersdorp supergroup and its temporal equivalents. *GSA Bull.* 132 (9–10), 1829–1844.
- Harnois, L., 1988. The CIW index: a new chemical index of weathering. *Sediment. Geol.* 55, 319–322.
- Hayes, J.M., Kaplan, I.R., Wedeking, K.W., 1983. Precambrian organic geochemistry, preservation of the record. *The Earth's Earliest Biosphere: Its Origin and Evolution*. Princeton University Press.
- Hayes, J.M., Strauss, H., Kaufman, A.J., 1999. The abundance of ^{13}C in marine organic matter and isotopic fractionation in the global biogeochemical cycle of carbon during the past 800 Ma. *Chem. Geol.* 161, 103–125.
- Heard, A.W., Arons, S.M., Hofmann, A., He, X., Ireland, T., Bekker, A., Qin, L., Dauphas, N., 2021. Anoxic continental surface weathering recorded by the 2.95 Ga Denny Dalton Palaeosol (Pongola Supergroup, South Africa). *Geochim. Cosmochim. Acta* 295, 1–23.
- Holland, H.D., 1984. *The Chemical Evolution of the Atmosphere and Oceans*. Princeton University Press.
- Homann, M., Sansjöfö, P., Zuilien, van Zuilien, Heubeck, C., Gong, J., Killingsworth, B., Foster, L.S., Airo, A., van Kranendonk, Ader, M.J. and Lalonde, S.V. (2018). Microbial life and biogeochemical cycling on land 3,220 million years ago. *Nature Geoscience*, 11(9), 665–671.
- Ingalls, M., Grotzinger, J.P., Present, T., Rasmussen, B., Fischer, W.W., 2022. Carbonate-associated phosphate (CAP) indicates elevated phosphate availability in Neoproterozoic shallow marine environments. *Geophys. Res. Lett.* 46 (6), e2022GL098100.
- Kimberley, M.M., Grandstaff, D.E., 1986. Profiles of elemental concentrations in Precambrian palaeosols on basaltic and granitic parent materials. *Precamb. Res.* 32 (2–3), 133–154.
- Kositcin, N., Krapež, B., 2004. Relationship between detrital zircon age-spectra and the tectonic evolution of the Late Archaean Witwatersrand Basin, South Africa. *Precamb. Res.* 129 (1–2), 141–168.
- Lenhardt, N., Eriksson, P.G., Catuneanu, O., Bumby, A.J., 2012. Nature of and controls on volcanism in the ca. 2.32–2.06 Ga Pretoria group, Transvaal supergroup, kaapvaal craton, South Africa. *Precamb. Res.* 214–215, 106–123.
- Liivmägi, S., Srodoń, J., Bojanowski, M.J., Stanek, J.J., Roberts, N.M.W., 2021. Precambrian palaeosols on the great unconformity of the east European Craton: an 800-million-year record of Baltica's climatic conditions. *Precamb. Res.* 363, 106327.
- Martin, D.M., Clendenin, C.W., Krapež, B., McNaughton, N.J., 1998. Tectonic and geochronological constraints on late Archaean and palaeoproterozoic stratigraphic correlation within and between the Kaapvaal and Pilbara Cratons. *J. Geol. Soc. Lond.* 155, 311–322.
- Martini, J.E.J., 1994. A late Archaean-Palaeoproterozoic (2.6 Ga) palaeosol on ultramafics in the eastern Transvaal, South Africa. *Precamb. Res.* 67, 159–180.
- Maynard, J.B., 1992. Chemistry of modern soils as a guide to interpreting Precambrian palaeosols. *J. Geol.* 100, 279–289.
- Maynard, J.B., Sutton, S.J., Robb, L.J., Ferraz, M.F., Meyer, F.M., 1995. A palaeosol developed on hydrothermally altered granite from the hinterland of the Witwatersrand Basin: characteristics of a source of basin fill. *J. Geol.* 103, 357–377.
- McDonough, W.F., Sun, S.S., 1995. The composition of the Earth. *Chem. Geol.* 67 (5), 1050–1056.
- Meinhold, G., 2010. Rutile and its applications in earth sciences. *Earth Sci. Rev.* 102 (1–2), 1–28.
- Milnes, A.R., Fitzpatrick, R.W., 1989. Titanium and zirconium minerals. *Miner. Soil Environ.* 1, 1131–1205.
- Murakami, T., Sreenivas, B., Das, S.S., Sugimori, H., 2011. Quantification of atmospheric oxygen levels during the paleoproterozoic using paleosol compositions and iron oxidation kinetics. *Geochim. Cosmochim. Acta* 75, 3982–4004.
- Murakami, T., Matsuura, K., Kanzaki, Y., 2016. Behaviours of trace elements in neoproterozoic and paleoproterozoic palaeosols: Implications for atmospheric oxygen evolution and continental oxidative weathering. *Geochim. Cosmochim. Acta* 192, 203–219.
- Neaman, A., Chorover, J., Brantley, S.L., 2005. Implications of the evolution of organic acid moieties for basalt weathering over geological time. *Am. J. Sci.* 305 (2), 147–185.
- Nesbitt, H., 1992. Diagenesis and metasomatism of weathering profiles, with emphasis on Precambrian palaeosols. *Dev. Earth Surf. Process.* 2, 127–152.
- Nesbitt, H.W., Young, G.M., 1982. Early proterozoic climates and plate motions inferred from major element chemistry of lutites. *Nature* 299, 715–717.
- Novoselov, A.A., de Souza Filho, C.R., 2015. Potassium metasomatism of Precambrian palaeosols. *Precamb. Res.* 262, 67–83.
- Obbes, A.M., 2001. The structure, stratigraphy and sedimentology of the Black Reef-Malmani-Rooihooft succession of the Transvaal Supergroup southwest of Pretoria. *Bull. Council Geosci.* 127, 89p.
- Ormond, R.J., Lehmann, J., 2022. Polyphase Archean to paleoproterozoic deformation along the northwest margin of the Johannesburg Dome, Kaapvaal Craton. *J. Struct. Geol.* 157, 104554.
- Planavsky, N.J., Crowe, S.A., Fakrae, M., Beatty, B., Reinhard, C.T., Mills, B.J.W., Holstege, C., Konhauser, K.O., 2021. Evolution of the structure and impact of Earth's biosphere. *Nat. Rev. Earth Environ.* 2, 123–139.
- Poujol, M., Anhaeusser, C.R., 2001. The Johannesburg Dome, South Africa: new single zircon U-Pb isotopic evidence for early Archaean granite-greenstone development within the central Kaapvaal Craton. *Precamb. Res.* 108 (1–2), 139–157.
- Retallack, G.J., 2001. *Soils of the Past: An Introduction to Paleopedology*, second ed. John Wiley & Sons.
- Retallack, G.J. (2012). Criteria for distinguishing microbial mats and earths. In: Noffke, N., Chafetz, H. (Eds.), *Microbial mats in siliciclastic depositional systems through time*. *Soc. Econ. Paleont. Mineral. Spec. Pap.*, vol. 101, pp. 139–152.
- Robb, L.J., Meyer, F.M., 1995. The Witwatersrand Basin, South Africa: geological framework and mineralization processes. *Oré Geol. Rev.* 10 (2), 67–94.
- Rye, R., Holland, H.D., 1998. Palaeosols and the evolution of atmospheric oxygen: a critical review. *Am. J. Sci.* 298 (8), 621–672.
- Rye, R., Holland, H.D., 2000a. Geology and geochemistry of palaeosols developed on the Hekpoort basalt, Pretoria group, South Africa. *Am. J. Sci.* 300 (2), 85–141.
- Rye, R., Holland, H.D., 2000b. Life associated with a 2.76 Ga ephemeral pond?: Evidence from mount Roe# 2 palaeosol. *Geology* 28 (6), 483–486.
- Schidlowski, M., Aharon, P., 1992. Carbon cycle and carbon isotope record: Geochemical impact of life over 3.8 Ga of Earth history. *Early Organic Evolution*. Springer, Berlin.
- Schoell, M., 1984. Recent advances in petroleum isotopic geochemistry. *Org. Geochem.* 6, 645–666.
- Scott, K., Pain, C. (Eds.), 2009. *Regolith Science*. Csiro Publishing.
- Sheldon, N.D., Mitchell, R.L., Dzombak, R.M., 2021. Reconstructing Precambrian pCO₂ and pO₂ using Paleosols. Cambridge University Press.
- Siahi, M., Hofmann, A., Master, S., Wilson, A., Mayr, C., 2018. Trace element and stable (C, O) and radiogenic (Sr) isotope geochemistry of stromatolitic carbonate rocks of the Mesoarchaean Pongola Supergroup: Implications for seawater composition. *Chem. Geol.* 476, 389–406.
- Spangenberg, J.E., Frimmel, H.E., 2001. Basin-internal derivation of hydrocarbons in the Witwatersrand Basin, South Africa: evidence from bulk and molecular $\delta^{13}\text{C}$ data. *Chem. Geol.* 173 (4), 339–355.
- Strauss, H., Beukes, N.J., 1996. Carbon and sulfur isotopic compositions of organic carbon and pyrite in sediments from the Transvaal Supergroup, South Africa. *Precamb. Res.* 79, 57–71.
- Stüeken, E.E., Buick, R., 2018. Environmental control on microbial diversification and methane production in the Mesoproterozoic. *Precamb. Res.* 304, 64–72.
- Tabor, N.J., Myers, T.S., 2014. Palaeosols as indicators of paleoenvironment and paleoclimate. *Annu. Rev. Earth Planet. Sci.* 43, 11.1–11.29.
- Tyler, N., 1979. Depositional environments within the Black Reef Quartzite of the West Central Transvaal. *Infor. Circ. Econ. Geol. Res. Unit, University of Witwatersrand*, 132, 11.
- Watanabe, Y., Martini, E.J., Ohmoto, H., 2000. Geochemical evidence for terrestrial ecosystems 2.6 billion years ago. *Nature* 574–578.
- Watanabe, Y.H., Naraoka, D.J., Wronkiewicz, K.C., Condie, A., Ohmoto, H., 1997. Carbon, nitrogen, and sulfur geochemistry of Archean and proterozoic shales from the Kaapvaal Craton, South Africa. *Geochim. Cosmochim. Acta* 61 (16), 3441–3459.
- Watanabe, Y., Stewart, B.W., Ohmoto, H., 2004. Organic- and carbonate-rich soil formation ~ 2.6 billion years ago at Schagen, East Transvaal district, South Africa. *Geochim. Cosmochim. Acta* 68 (9), 2129–2151.
- White, A.F., Bullen, T.D., Schultz, M.S., Blum, A.E., Huntington, T.G., Peters, N.E., 2001. Differential rates of feldspar weathering in granitic regoliths. *Geochim. Cosmochim. Acta* 65 (6), 847–869.
- Yang, W., Holland, H.D., Rye, R., 2002. Evidence for low or no oxygen in the late Archean atmosphere from the ~2.76 Ga Mt. Roe #2 palaeosol, Western Australia: part 3. *Geochim. Cosmochim. Acta* 66 (21), 3707–3718.
- Zeh, A., Wilson, A.H., Gerdes, A., 2020. Zircon U-Pb-Hf isotope systematics of Transvaal supergroup – constraints for the geodynamic evolution of the Kaapvaal Craton and its hinterland between 2.65 and 2.06 Ga. *Precamb. Res.* 345, 105760.

A.2. Book Chapter “Interactions géosphère-biosphère”, Chapter 6 “L’importance du vivant dans les cycles du carbone et de l’azote ”

For this textbook on the interactions between the biosphere and the geosphere, written mainly for Bachelor and Master students, I co-wrote a chapter with Magali Ader on the importance of the biosphere in the C- and N-biogeochemical cycles. Initially written in French, this textbook should be published in 2024-2025 and later translated into English by the publisher.

L'importance du vivant dans les cycles du carbone et de l'azote

Alice Pellerin - Magali Ader

Université de Bourgogne - Institut de Physique du Globe de Paris

6.1. Cycles biogéochimiques : de quoi parle-t-on ?

Pour représenter le comportement d'un élément à l'échelle de la Terre et de son histoire, les géochimistes ont développé un outil conceptuel, celui du cycle géochimique de cet élément. Ce cycle est constitué de réservoirs qui sont les contenants de l'élément considéré, dont certains sont reliés entre eux par des flux qui représentent les processus par lesquels l'élément considéré est transféré d'un réservoir à l'autre (figure 1).

Les cycles biogéochimiques sont un sous-ensemble des cycles géochimiques, pour lesquels le vivant peut-être un réservoir de l'élément considéré mais aussi un opérateur pour certains des flux. Quand on commence à se pencher sur les cycles, on remarque assez vite que presque tous les cycles des éléments sont en fait des cycles biogéochimiques, ce qui signifie en d'autres termes que le vivant est, et a été, partie intégrante du fonctionnement de la Terre et que l'on ne peut pas réfléchir à l'environnement terrestre et à son évolution au cours du temps sans le prendre en

compte. Les cycles biogéochimiques du carbone et de l'azote sont des exemples emblématiques de cycles biogéochimiques, d'une part car le carbone et l'azote sont les constituants principaux du vivant et d'autre part car le vivant opère directement ou influe de manière indirecte mais significative sur de nombreux flux de carbone et d'azote.

6.2. Le cycle biogéochimique du carbone

6.2.1. Pourquoi s'intéresser au cycle biogéochimique du carbone ?

Le cycle biogéochimique du carbone est particulièrement important pour la compréhension du fonctionnement de la Terre. Non seulement les teneurs en CO_2 et CH_4 dans l'atmosphère (deux gaz à effets de serre) ont un rôle crucial sur la régulation du climat, du pH de l'océan et de l'altération des roches continentales (cf. chapitres 2 et 8), mais en plus le flux d'enfouissement de carbone sous forme de matière organique a largement contribué à réguler la concentration en dioxygène de l'atmosphère et des océans au cours des temps géologiques (Des Marais 1997 ; Kasting 2013 ; cf. chapitres 6 et 8). Dans ce chapitre, nous allons nous intéresser plus particulièrement à ce lien entre l'évolution du cycle du carbone et l'oxygénation de la surface terrestre.

6.2.2. Les principaux réservoirs et flux de carbone

Le carbone est, et a été par le passé, présent dans tous les compartiments terrestres. Dans l'atmosphère, il est majoritairement présent sous forme de CO_2 et CH_4 . Dans l'hydrosphère, il est sous forme de carbone inorganique dissous (CID), composé du $\text{CO}_2(\text{aqueux})$, H_2CO_3 , HCO_3^- et CO_3^{2-} dissous, HCO_3^- étant la forme majoritaire dans l'océan actuel dont le pH moyen est autour de 8. Enfin, dans les sols et les sédiments, il est présent sous forme de carbonates (C_{carb}) et de matière organique (C_{org}). Dans tous ces réservoirs de surface, il est aussi présent sous forme de carbone organique, principalement formé par les organismes vivants. Du fait du rôle essentiel et de l'efficacité de la biosphère à transférer du carbone d'un réservoir de surface à l'autre, on regroupe tous les organismes vivants dans un réservoir, souvent nommé « biomasse » afin de faciliter la conceptualisation et la représentation des échanges de carbone contrôlés par le vivant. A l'échelle de l'ensemble du cycle, on trouve l'essentiel du carbone dans les roches sédimentaires et plus largement crustales, principalement sous forme de C_{carb} et de C_{org} , et dans celles du manteau, sous des formes variées incluant le graphite, le diamant et les carbonates, et d'autres formes encore peu connues. Il est probable que le noyau terrestre contienne aussi du carbone, le carbone étant sidérophile, i.e. avec une forte affinité pour le fer, dans les conditions

physico-chimiques du noyau. Si on commence à bien connaître, pour les temps géologiques récents, les ordres de grandeur des quantités de carbone stockées dans ces réservoirs ainsi que celles échangées entre eux (Figure 6.1), il n'en est pas de même pour les temps anciens car en dehors de la modélisation (cf. chapitre 8), il existe très peu de moyens de tracer directement les modifications passées du cycle du carbone. Les principales archives de ces modifications sont :

- l'étude du contenu en carbone des roches magmatiques, mantelliques et sédimentaires précambriennes, qui donne des renseignements partiels sur l'évolution au cours du temps de la spéciation et des stocks de carbone dans la croûte et le manteau ;
- l'étude des compositions isotopiques des carbonates sédimentaires ($\delta^{13}\text{C}_{\text{carb}}$) qui donne des renseignements sur les flux de carbone entrants et sortants de l'océan ;
- l'étude des compositions isotopiques de la matière organique sédimentaire ($\delta^{13}\text{C}_{\text{org}}$) qui donne des renseignements sur les métabolismes à l'origine de la genèse de matière organique.

C'est à ces deux dernières archives que nous allons nous intéresser dans ce chapitre.

Généralités sur les isotopes stables

La composition isotopique et la notation δ

Les géochimistes mesurent les rapports isotopiques des échantillons naturels par rapport à un standard de référence international et les expriment par la notation δ (Craig 1961), développée dans les équations [6.1] et [6.2]. Les rapports isotopiques de l'échantillon et du standard sont notés $(^{13}\text{C}/^{12}\text{C})_{\text{ech}}$ et $(^{13}\text{C}/^{12}\text{C})_{\text{std}}$ pour le carbone, $(^{15}\text{N}/^{14}\text{N})_{\text{ech}}$ et $(^{15}\text{N}/^{14}\text{N})_{\text{std}}$ pour l'azote. Par convention, l'isotope lourd est au numérateur du rapport isotopique et l'isotope léger est au dénominateur.

Pour le carbone, la notation δ est écrite comme suit :

$$\delta^{13}\text{C} = ((^{13}\text{C}/^{12}\text{C})_{\text{ech}} / (^{13}\text{C}/^{12}\text{C})_{\text{std}} - 1) \times 1000 \quad [6.1]$$

Pour l'azote, la notation δ est écrite comme suit :

$$\delta^{15}\text{N} = ((^{15}\text{N}/^{14}\text{N})_{\text{ech}} / (^{15}\text{N}/^{14}\text{N})_{\text{std}} - 1) \times 1000 \quad [6.2]$$

La composition isotopique d'un échantillon est donc exprimée en ‰ sous forme d'une déviation du rapport isotopique de l'échantillon par rapport au standard. Pour le carbone, le standard international est le PDB (Pee Dee Belemnite) qui correspond aux bélemnites de la formation de Pee Dee du Crétacé, en Caroline du Sud. Plus un échantillon a une valeur de $\delta^{13}\text{C}$ supérieure à 0 plus il est enrichi en ^{13}C relativement au standard, et plus sa valeur est

inférieure à 0 plus il est appauvri en ^{13}C (ou enrichi en ^{12}C). Pour l'azote, le standard international est le diazote atmosphérique, qui par convention a donc une valeur de 0‰, et s'exprime ainsi : $\delta^{15}\text{N}_{\text{N}_2}=0\text{‰}$ (vs. air).

Le fractionnement isotopique et la notation Δ

L'inégalité de masse entre les deux isotopes ^{13}C et ^{12}C ou ^{15}N et ^{14}N entraîne l'existence de différences dans certaines propriétés thermodynamiques des molécules qui contiennent ces isotopes : volume molaire, température de fusion, viscosité, vitesse de réaction, constante d'équilibre. Ces différences de propriétés peuvent être à l'origine de différences de comportement et donc de répartitions des isotopes au cours des réactions chimiques. Ces différences conduisent à des fractionnements isotopiques. Autrement dit, le fractionnement isotopique est le fait qu'au cours du déroulement d'une réaction faisant intervenir un mélange d'isotopes d'un même élément, la réaction a lieu préférentiellement avec un type d'isotope.

Le fractionnement isotopique créé lors d'une réaction ($\text{A} \rightarrow \text{B}$), noté Δ ou ε , peut être approximé par l'écart de composition isotopique entre A et B.

Par exemple pour le carbone avec la notation Δ :

$$\Delta^{13}\text{C}_{\text{A-B}} = \delta^{13}\text{C}_{\text{A}} - \delta^{13}\text{C}_{\text{B}}$$

pour l'azote avec la notation ε :

$$\varepsilon \approx \delta^{15}\text{N}_{\text{A}} - \delta^{15}\text{N}_{\text{B}}$$

Il existe deux types de fractionnement isotopique, celui dit à l'équilibre thermodynamique et celui dit cinétique.

Le fractionnement isotopique à l'équilibre thermodynamique caractérise les réactions d'échange isotopique et est gouverné par les règles de la thermodynamique. Les réactions d'échange isotopiques accompagnent des réactions réversibles qui se font à l'équilibre thermodynamique chimique. Il y a alors partition des isotopes d'un même élément entre deux composés ou deux phases ayant des rapports isotopiques différents. C'est le cas de l'équilibre entre le CO_2 atmosphérique et le CO_2 dissous dans l'eau, des équilibres entre les espèces du CID et de celui de la précipitation/dissolution des carbonates.

Le fractionnement isotopique peut aussi être associé à une réaction unidirectionnelle irréversible, au cours de laquelle il n'y a pas de réaction d'échange isotopique possible. On parle alors de fractionnement isotopique cinétique. Dans ce cas les liaisons établies par l'isotope léger réagiront plus aisément et plus rapidement que celles faisant intervenir l'isotope lourd. Il y a ainsi un enrichissement en isotopes légers du produit par rapport au substrat de départ. Les fractionnements isotopiques cinétiques ne peuvent pas être prédits par les lois de la thermodynamique. Le plus souvent quand ils sont connus, c'est qu'ils ont

été déterminés empiriquement ou expérimentalement. C'est le cas lors de la réaction de photosynthèse.

6.2.3. La systématique isotopique du cycle du carbone

La composition isotopique des flux de CO₂ qui entrent dans l'atmosphère et/ou l'océan (i.e. les flux volcanique, métamorphique et ceux issus de l'altération) est voisine de -5‰. La valeur de $\delta^{13}\text{C}$ du CO₂ atmosphérique est actuellement de -8,5‰, celle du CID de l'océan voisine de +1‰, celle des carbonate sédimentaires (CaCO₃) de 0‰. L'écart entre les valeurs actuelles de $\delta^{13}\text{C}$ de -8,5‰ pour le CO₂ atmosphérique et de +1‰ pour le CID des océans résulte de l'ensemble des fractionnements à l'équilibre entre le CO₂ atmosphérique et les différentes espèces de carbone inorganique dissous dans l'océan.

La valeur du $\delta^{13}\text{C}_{\text{org}}$ des réservoirs contenant du carbone organique (biomasse, sols, et matière organique crustale) est voisine de -25‰. La composition isotopique des réservoirs contenant du carbone inorganique est donc très différente de celle des réservoirs contenant de la matière organique. Cette différence est due au fractionnement isotopique associé à la réaction de photosynthèse qui favorise l'incorporation du ¹²C lors de la fixation du CO₂ atmosphérique en carbone organique.

Pour ce qui est des autres flux entre réservoirs, ils ne fractionnent pas (ou presque pas) les isotopes stables du carbone. Les flux qui sortent de l'océan, c'est-à-dire ceux de la sédimentation des carbonates et de la matière organique conservent la composition isotopique des carbonates et de la matière organique au moment de leur genèse dans l'océan au cours de l'enfouissement. La similitude entre la valeur de $\delta^{13}\text{C}_{\text{org}}$ de la matière organique sédimentaire et celle de la biomasse indique que la respiration ne fractionne pas les isotopes du carbone. De même, le faible écart entre la valeur de $\delta^{13}\text{C}$ du CID et celle des carbonates crustaux indique que la précipitation des carbonates à partir du CID ne fractionne quasiment pas les isotopes du carbone.

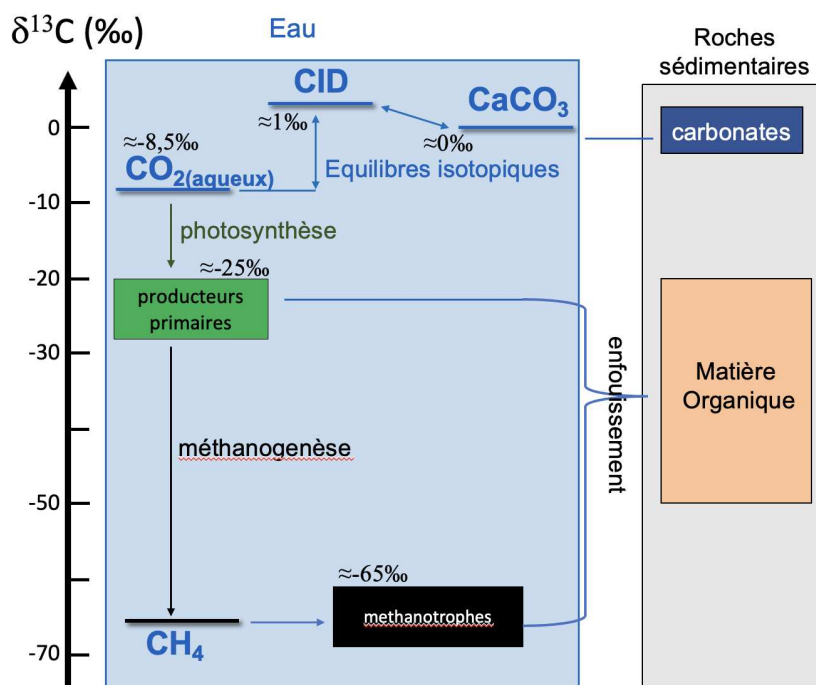


Figure 6.1. Schéma des relations isotopiques entre le CO_2 dissous, le CID, les producteurs primaires, les méthanotrophes, et les carbonates et la matière organique sédimentaires. Les flèches simples correspondent aux fractionnements liés aux métabolismes. Les flèches doubles aux fractionnements à l'équilibre isotopique et les trait sans flèche à l'enfouissement. Adaptée d'après Hayes et al. (1999) et Des Marais (1997).

6.2.4. Le $\delta^{13}\text{C}_{\text{carb}}$ des roches sédimentaires carbonatées : archive du $\delta^{13}\text{C}_{\text{CID}}$ de l'océan

Le $\delta^{13}\text{C}_{\text{carb}}$ reflète donc fidèlement la composition du carbone inorganique dissous de l'eau à partir de laquelle précipite le carbonate (figure 6.1). Ainsi, la mesure du $\delta^{13}\text{C}_{\text{carb}}$ de carbonates dits primaires, c'est-à-dire ayant précipité à partir de l'eau de l'environnement de dépôt (et non ultérieurement lors de processus de diagenèse à partir de l'eau de porosité des sédiments), donne directement accès au $\delta^{13}\text{C}_{\text{CID}}$ des océans, mers intérieures ou lacs dans lesquels les sédiments se sont déposés.

De très nombreuses mesures de $\delta^{13}\text{C}_{\text{carb}}$ ont été réalisées, surtout depuis quelques décennies (figure 6.2, d'après Krissansen-Totton *et al.* 2015). Elles montrent une

valeur moyenne constante et voisine de 0‰ depuis 3,8 Ga, mais une dispersion importante au cours du temps, avec deux périodes de variabilité maximale entre 2,3 et 2,0 Ga et entre 750 et 540 Ma.

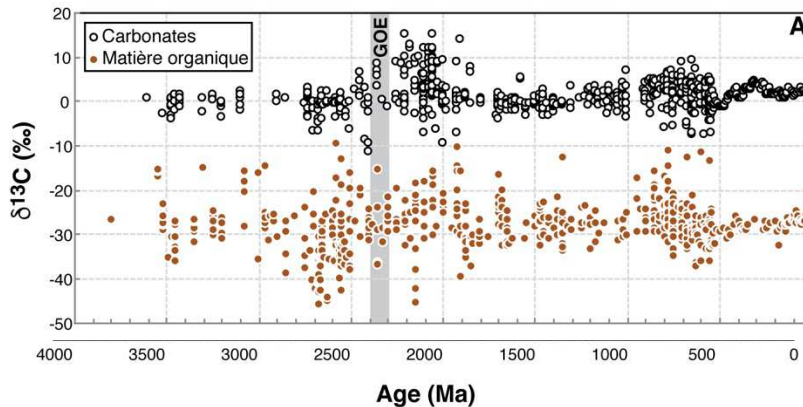


Figure 6.2. Compilation des données isotopiques du carbone des archives sédimentaires au cours des temps géologiques (compilation de Krissansen-Totton et al. 2015).

6.2.5. Signification de la relative stabilité du $\delta^{13}\text{C}_{\text{carb}}$ depuis 3,5 Ga

Aux très longues échelles de temps de plusieurs Ga, la constance de la valeur moyenne du $\delta^{13}\text{C}_{\text{carb}}$ des roches sédimentaires indique que le $\delta^{13}\text{C}_{\text{CID}}$ des océans n'a que peu varié au cours du temps (figure 6.2). Il est donc probable que les flux relatifs de carbone entrants et sortants de l'océan n'aient pas non plus changé drastiquement au cours des temps géologiques (Schidlowski 2001). Nous détaillons ci-dessous les implications.

6.2.5.1. Quantification des flux relatifs d'enfouissement de la matière organique par bilan massique et isotopique

On peut utiliser la valeur moyenne de $\delta^{13}\text{C}_{\text{carb}}$ au cours des temps géologiques pour obtenir des éléments de quantification des flux de carbone entrants et sortants de l'océan. Pour cela, il est nécessaire de simplifier le cycle du carbone au maximum (figure 6.3). On ignore ici le noyau terrestre qui n'échange probablement plus de carbone avec le reste des réservoirs terrestres depuis le début de l'Archéen et on regroupe l'océan, l'atmosphère et la biomasse dans un même réservoir (le système

océan-atmosphère), car à ces grandes échelles de temps, les flux entre ces réservoirs sont à l'équilibre.

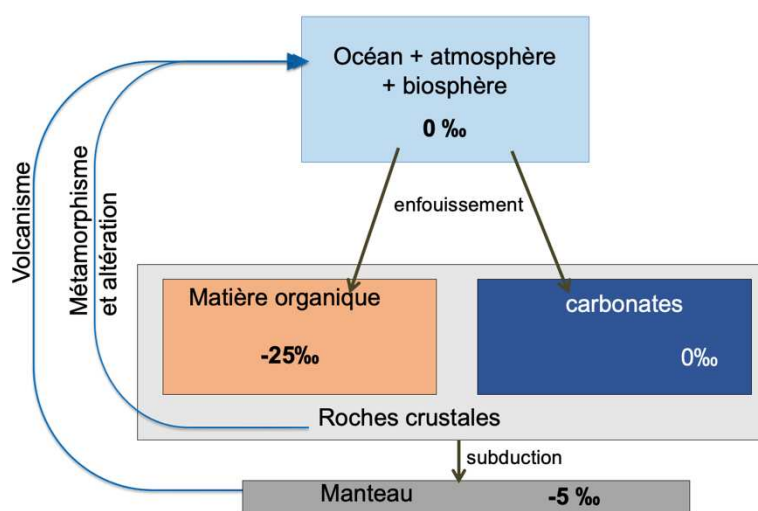


Figure 6.3. Représentation simplifiée en modèle de boîtes du cycle biogéochimique du carbone. Les flèches noires de l'enfouissement correspondent à des flux de carbone sortants du système océan-atmosphère, les flèches bleues à des flux entrants.

Pour continuer à simplifier le fonctionnement du système, on fait l'hypothèse de la conservation de la masse du carbone dans le réservoir océan-atmosphère-biosphère (la quantité de carbone dans ce réservoir est stationnaire, c'est-à-dire qu'elle n'a pas changé au cours du temps) et de celle de ses deux isotopes (la composition isotopique $\delta^{13}\text{C}$ n'a pas changé au cours du temps dans ce réservoir), hypothèse dite de l'état stationnaire, qui implique que les flux entrants dans ce réservoir sont équivalents aux flux sortants.

Cela permet d'écrire deux équations de conservation de masse :

- celle de la masse de l'élément carbone

$$\text{Flux}_{\text{C entrant}} = \text{Flux}_{\text{Corg enfoui}} + \text{Flux}_{\text{Ccarb enfoui}} \quad [6.3]$$

- celle de la conservation de sa composition isotopique :

$$\text{Flux}_{\text{C entrant}} \times \delta^{13}\text{C}_{\text{entrant}} = \text{Flux}_{\text{Corg enfoui}} \times \delta^{13}\text{C}_{\text{org}} + \text{Flux}_{\text{Ccarb enfoui}} \times \delta^{13}\text{C}_{\text{carb}} \quad [6.4]$$

Enfin pour réduire au maximum le nombre d'inconnues, on peut définir les proportions relatives des flux de matière organique et de carbonate par rapport au flux de carbone entrant :

$$f_{\text{org}} = \text{Flux}_{\text{Corg enfoui}} / \text{Flux}_{\text{C entrant}} \quad [6.5]$$

$$f_{\text{carb}} = 1 - f_{\text{org}} = \text{Flux}_{\text{Carb enfoui}} / \text{Flux}_{\text{C entrant}} \quad [6.6]$$

ce qui permet d'obtenir une équation à deux inconnues, le $\delta^{13}\text{C}_{\text{entrant}}$ et f_{org} , puisque les compositions isotopiques du carbone organique et des carbonates peuvent être mesurées.

$$\delta^{13}\text{C}_{\text{entrant}} = f_{\text{org}} \times \delta^{13}\text{C}_{\text{org}} + (1 - f_{\text{org}}) \times \delta^{13}\text{C}_{\text{carb}} \quad [6.7]$$

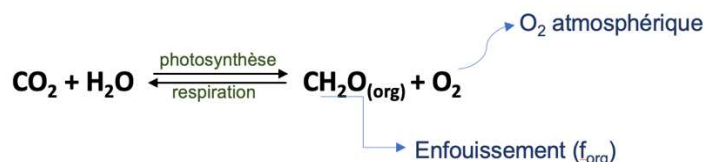
En remaniant l'équation 6.7, on peut écrire :

$$f_{\text{org}} = (\delta^{13}\text{C}_{\text{entrant}} - \delta^{13}\text{C}_{\text{carb}}) / (\delta^{13}\text{C}_{\text{org}} - \delta^{13}\text{C}_{\text{carb}}) \quad [6.8]$$

qui permet de calculer, à partir des valeurs de $\delta^{13}\text{C}_{\text{carb}}$ et $\delta^{13}\text{C}_{\text{org}}$ à chaque instant de l'histoire de la Terre, la proportion relative d'enfouissement de matière organique par rapport à l'enfouissement de carbonates. Pour faire ce calcul, on fait une dernière hypothèse en considérant le CO_2 volcanique comme le principal flux entrant et en fixant son $\delta^{13}\text{C}_{\text{entrant}}$ à la valeur de -5‰ (Cartigny et al. 1998). Pour la valeur moyenne du $\delta^{13}\text{C}_{\text{carb}}$ de 0‰ , on trouve $f_{\text{org}} = 0,2$ et $f_{\text{carb}} = 0,8$, c'est-à-dire que 20% du carbone entrant dans le système océan-atmosphère est enfoui sous forme de matière organique et 80% l'est sous forme de carbonates.

6.2.5.2. Corollaire à l'enfouissement de matière organique : l'oxydation de l'atmosphère et des océans

Le couplage de la photosynthèse, la respiration et l'enfouissement de matière organique relie étroitement les cycles du carbone et de l'oxygène. En effet, pour chaque mole de matière organique produite par photosynthèse, une mole de O_2 est produite, mais sera, la plupart du temps, reconsumée par la respiration. En l'absence de dioxygène, la respiration s'effectue à l'aide d'accepteurs d'électrons alternatifs, principalement les sulfates. Ainsi, pour chaque mole de matière organique soustraite à la respiration par enfouissement sédimentaire, une mole d'oxydant s'accumule à la surface de la Terre (Des Marais 1997 ; Kasting 2013). L'oxygénation de l'atmosphère terrestre (cf. chapitre 6) a donc impliqué un enfouissement de matière organique.



6.2.6. Origine de la variabilité du $\delta^{13}\text{C}_{\text{carb}}$ entre 2,3 et 2,0 Ga et entre 750 et 540 Ma

Les périodes de plus grande dispersion des valeurs de $\delta^{13}\text{C}_{\text{carb}}$ (entre 2,3 et 2,0 Ga et entre 750 et 540 Ma), indiquent :

- soit une altération des signatures originelles par des processus de diagenèse qui ont tendance à faire diminuer les valeurs de $\delta^{13}\text{C}_{\text{carb}}$. En effet, les carbonates secondaires peuvent incorporer du carbone provenant de la dégradation de la matière organique enrichie en ^{12}C . Ceci pourrait expliquer une bonne partie des valeurs négatives (Grotzinger *et al.* 2011 ; Swart et Kennedy 2012).

- Soit, pour les valeurs de $\delta^{13}\text{C}_{\text{carb}}$ les plus positives, des modifications importantes du cycle du carbone. A ce jour il existe deux hypothèses pour expliquer ces valeurs : (i) celle de variations régionales du $\delta^{13}\text{C}_{\text{carb}}$ de l'océan et (ii) celle de variations globales.

6.2.6.1. HYPOTHESE 1 : Des perturbations régionales du cycle du carbone

Les dernières études font apparaître que cette dispersion pourrait refléter des environnements sédimentaires qui n'étaient ni en équilibre avec l'atmosphère, ni bien mélangées avec le reste des océans à l'époque de leur dépôt (Prave *et al.* 2022). Selon cette hypothèse, les fortes dispersions entre 2,3 et 2,0 Ga et entre 750 et 540 Ma seraient dues à des perturbations régionales du cycle du carbone dans ces systèmes isolés de l'océan, soit complètement (*e.g.*, mers épicontinentales) ou bien partiellement (*e.g.*, lagunes). Les deux principaux mécanismes envisagés ayant la capacité de générer des valeurs plus positives de $\delta^{13}\text{C}_{\text{carb}}$ sont l'évaporation et la méthanogenèse (Cadeau *et al.* 2021 ; Prave *et al.* 2022 ; Frimmel 2010). Le mécanisme de la méthanogenèse serait compatible avec l'idée que les océans étaient alors largement anoxiques (c'est-à-dire dépourvus d'oxygène) et pauvres en sulfate, laissant la méthanogenèse comme principal mécanisme de dégradation de la matière organique. L'évaporation serait compatible avec l'hypothèse d'un climat plus chaud, qui pourrait être testée en s'intéressant à un autre isotope des carbonates : l'oxygène.

6.2.6.2. HYPOTHESE 2 : Des perturbations globales du cycle du carbone

Même si une part de la dispersion peut être liée à des effets régionaux, il reste possible que le $\delta^{13}\text{C}_{\text{CID}}$ de l'océan ouvert présente lui aussi des variations, c'est-à-dire que ces perturbations aient été globales. Pour le démontrer, il faudrait pouvoir identifier les données obtenues sur des roches déposées en milieu océanique ouvert et n'ayant pas été modifiées après leur dépôt par des processus diagénétiques. Cela est relativement facile à faire jusqu'au Jurassique, âge des plus vieux fonds océaniques actuels, car il n'y a aucun doute sur le fait que les sédiments qui y sont déposés enregistrent bien le $\delta^{13}\text{C}_{\text{CID}}$ de l'océan ouvert. Mais cet exercice d'identification est de plus en plus complexe en remontant dans le temps car les roches sédimentaires ont souvent été subductées, déplacées et déformées. Pour le Précambrien, un travail systématique de caractérisation des environnements de dépôt commence à émerger (Prave *et al.* 2022) mais nous ne sommes pas encore en mesure aujourd'hui de connaître la courbe des fluctuations temporelles globales, autour de la moyenne de 0‰, du $\delta^{13}\text{C}$ du système océan-atmosphère.

L'élaboration de cette courbe est fondamentale car elle permettra de documenter des variations au cours du temps du cycle global du carbone et permettra ainsi également de mieux comprendre les subtilités de l'histoire de l'oxygénation de l'atmosphère et des océans (cf. chapitre 6). Par exemple, si les périodes de forte dispersion des valeurs de $\delta^{13}\text{C}_{\text{carb}}$, avec des valeurs très positives sont associées à une augmentation globale du $\delta^{13}\text{C}_{\text{CID}}$ des océans, cette augmentation indiquerait une augmentation du taux d'enfouissement de matière organique elle-même responsable d'une oxygénation (Des Marais 1997 ; Schidlowski 2001 ; Karhu et Holland 1996 ; Kasting 2013). Au contraire, une diminution du $\delta^{13}\text{C}_{\text{CID}}$ du système océan-atmosphère vers des valeurs négatives, comme cela pourrait avoir été le cas lors de glaciations globales telles que les épisodes de Terre boule de neige (714 et 630 Ma) (Och et Shields-Zhou 2012 ; Halverson *et al.* 2005 ; Grotzinger *et al.* 2011), marquerait une chute brutale de la productivité primaire. Les flux d'enfouissement de matière organique chuteraient alors, laissant le système océan-atmosphère s'équilibrer autour de la valeur de $\delta^{13}\text{C}$ du flux de CO_2 entrant, soit autour de -5‰. La baisse correspondante de libération d'oxygène dans l'environnement pourrait aussi expliquer le retour des conditions anoxiques dans les océans lors de ces épisodes marqués de plus par la présence de formations riches en fer.

6.2.7. Le $\delta^{13}\text{C}_{\text{org}}$ des roches sédimentaires : archive des métabolismes autotrophes

La figure 9.2 montre une compilation des mesures de $\delta^{13}\text{C}_{\text{org}}$ réalisées depuis quelques décennies. On y voit que la valeur moyenne du $\delta^{13}\text{C}_{\text{org}}$ est restée voisine de

-25‰ depuis 3,8 Ga, avec pour le Précambrien une dispersion autour de cette valeur moyenne allant de -10 à -45‰, un peu plus importante que pour les valeurs de $\delta^{13}\text{C}_{\text{carb}}$.

On fait l'approximation raisonnable que le $\delta^{13}\text{C}_{\text{org}}$ des sédiments océaniques reflète le $\delta^{13}\text{C}$ du CO_2 qui est assimilé par les organismes autotrophes marins, fortement modifié par le fractionnement isotopique associé à la photosynthèse (Des Marais 1997 ; Hayes *et al.* 1999). Comme le CO_2 atmosphérique est à l'équilibre avec le CO_2 dissous dans l'eau de mer, qui est lui-même à l'équilibre isotopique avec les autres espèces du CID (figure 6.1), le $\delta^{13}\text{C}_{\text{org}}$ (comme le $\delta^{13}\text{C}_{\text{carb}}$) renseigne donc aussi indirectement sur le $\delta^{13}\text{C}_{\text{CID}}$ des océans. La constance de la valeur moyenne du $\delta^{13}\text{C}_{\text{org}}$ au cours des temps géologiques, comme celle du $\delta^{13}\text{C}_{\text{carb}}$, suggère que le $\delta^{13}\text{C}_{\text{CID}}$ des océans est resté stable et donc qu'au premier ordre, le fonctionnement du cycle du carbone n'a probablement pas changé significativement.

Le $\delta^{13}\text{C}_{\text{org}}$ donne, à partir de son écart avec le $\delta^{13}\text{C}_{\text{carb}}$, des informations sur le fractionnement isotopique associé à la production de matière organique (Des Marais 1997). On voit que, globalement, ce fractionnement n'a pas changé significativement au cours des temps géologiques, ce qui implique que la photosynthèse a été le mécanisme principal de production de matière organique au moins depuis 3,5 Ga (âge des plus vieilles roches sédimentaires peu métamorphisées) et que son fractionnement isotopique n'aurait par la suite pas ou peu évolué au cours de l'évolution biologique et géologique du système Terre. On remarque cependant un seuil net dans la dispersion des valeurs de $\delta^{13}\text{C}_{\text{org}}$ au passage de la transition Précambrien-Cambrien, avec une diminution de la dispersion due essentiellement à la disparition des valeurs de $\delta^{13}\text{C}_{\text{org}}$ les plus basses. Cette dispersion est à ce jour interprétée comme reflétant des modifications post-dépôt, liées au métamorphisme, ou de la variabilité spatiale et temporelle des processus de genèse de matière organique (Des Marais 1997).

Si les valeurs les plus hautes sont essentiellement interprétées comme une modification post-dépôt due au métamorphisme, les valeurs les plus basses observées dans les sédiments précambriens ne peuvent pas être expliquées, ni de cette manière, ni simplement par la photosynthèse telle qu'on la connaît aujourd'hui. Elles impliquent une activité importante, par endroits au moins, de métabolismes de synthèse de matière organique beaucoup plus rares au Phanérozoïque. Par exemple, les métabolismes de la méthanogenèse et de la méthanotrophie ont été proposés pour expliquer ces valeurs basses, par analogie isotopique avec ce que l'on connaît de la signature isotopique de ces métabolismes à l'heure actuelle (Des Marais 1997 ; Shidlowski 2001 ; figure 6.1). Cependant, on ne peut pas exclure qu'une autre forme de métabolisme, inconnue ou peu abondante dans les environnements actuels, ait été présente et active au Précambrien.

6.2.8. Conclusions à propos du cycle biogéochimique du carbone

En résumé, les archives isotopiques du carbone ($\delta^{13}\text{C}_{\text{carb}}$ et $\delta^{13}\text{C}_{\text{org}}$) indiquent un taux relatif d'enfouissement de carbone organique relativement stable autour de 20% depuis au moins 3,5 Ga. Cet enfouissement aurait contribué à l'oxydation progressive de la surface terrestre menant à l'oxygénation de l'atmosphère et des océans. D'autres mécanismes d'oxygénation auraient également contribué, comme l'enfouissement de pyrite sédimentaire, le passage d'une activité volcanique sous-marine à une activité aérienne (Gaillard *et al.* 2011), et/ou l'échappement atmosphérique d'hydrogène produit par photodissociation de méthane biologique (Catling *et al.* 2001). Il est aussi probable que des fluctuations du taux d'enfouissement du carbone organique aient été responsables d'épisodes d'oxygénation accrue ou au contraire de retour à des conditions plus anoxiques à certaines périodes de l'histoire de la Terre. Ce point devrait être précisé dans les prochaines années. Les dispersions vers des valeurs plus positives du $\delta^{13}\text{C}_{\text{carb}}$ et plus négatives du $\delta^{13}\text{C}_{\text{org}}$ indiquent probablement un fonctionnement de la biosphère différent au Précambrien par rapport au Phanérozoïque, avec une composante non négligeable de métabolismes anaérobies, possiblement associés au cycle du méthane.

6.3. Le cycle biogéochimique de l'azote

6.3.1. Pourquoi s'intéresser au cycle biogéochimique de l'azote ?

L'azote est un élément chimique présent dans tous les réservoirs géologiques de la planète (noyau, manteau, croûte), et le diazote (N_2) est le gaz dominant de l'atmosphère terrestre. L'évolution de la biogéochimie de l'azote est donc liée à celle des environnements terrestres. Plus particulièrement, l'azote est un élément fondamental de la vie au sein de ces environnements, puisqu'il fait partie intégrante des molécules majeures constituant les « briques » du vivant, comme les acides aminés ou les acides nucléiques, à la base des protéines et de l'ADN. Par ailleurs, les apports en azote aux organismes, s'ils sont trop faibles, peuvent limiter la productivité primaire, puisque la matière organique marine contient en moyenne 106 atomes de carbone pour 16 atomes d'azote et un atome de phosphore (rapport de Redfield). L'azote est donc un nutriment important qui, avec le phosphore et le fer, contrôle l'activité biologique.

Enfin, les différentes molécules azotées présentent chacune un état redox spécifique, et la plupart des voies du cycle biogéochimique de l'azote sont contrôlées par la présence ou non de dioxygène dans l'environnement. Cela fait de l'azote un excellent marqueur de l'état d'oxydoréduction des écosystèmes. Dans ce chapitre, nous explorerons plus en détail comment l'étude de l'évolution du cycle

biogéochimique de l'azote au cours des temps géologiques permet de tracer l'oxygénation des environnements passés, en particulier lors du Grand Évènement d'Oxygénation de l'atmosphère terrestre autour de la transition Archéen-Protérozoïque ($\approx 2,4$ Ga).

6.3.2. Les principaux réservoirs et flux d'azote actuels

Sur la Terre actuelle, et depuis au moins le début du Phanérozoïque, l'azote est présent dans le réservoir atmosphérique sous forme de diazote (N_2), gaz le plus abondant de l'atmosphère. Dans le réservoir océanique, il est présent sous la forme de diazote dissous et de molécules biodisponibles comme l'ammonium (NH_4^+), les nitrites (NO_2^-) et les nitrates (NO_3^-), ainsi que sous des formes organiques dissoutes et particulaires (DON et PON pour *dissolved organic nitrogen* et *particulate organic nitrogen*). Une fraction de l'azote de la colonne d'eau peut être transférée et préservée dans le sédiment, soit sous forme d'azote organique, soit sous forme d'ammonium au sein des argiles. Toutes ces formes sont interconnectées par des processus biogéochimiques (Figure 6.4).

Le cycle biogéochimique de l'azote a la particularité de mettre en jeu de grands réservoirs relativement inertes, comme l'atmosphère et la croûte terrestre, et des flux entre de petits réservoirs dynamiques et temporaires à l'échelle des temps géologiques, dont la quasi-totalité sont biologiques. Ainsi, l'assimilation biologique d'azote via la fixation de N_2 atmosphérique en ammonium NH_4^+ (Figure 6.4), suivie de la production de composés azotés organiques, soutient la production primaire biologique sur le long terme. Le cycle biogéochimique de l'azote dans l'océan moderne (Figures 6.4 et 6.5C) reflète donc principalement le devenir des produits azotés dans le réservoir océanique, et leur recyclage en interaction avec la biosphère, l'atmosphère et la géosphère.

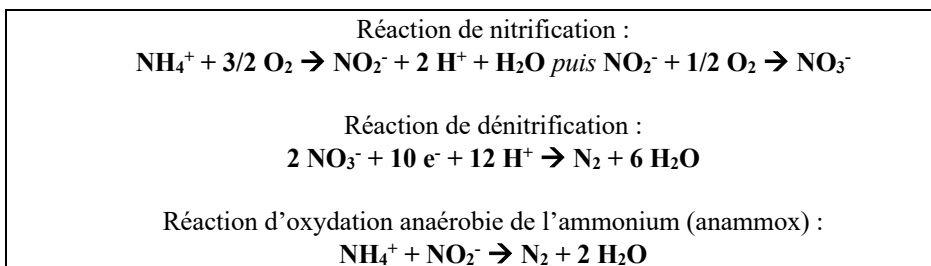
Le réservoir d'azote principal à la surface de la Terre est le réservoir de N_2 atmosphérique. La fixation biologique de N_2 (Figure 6.4) nécessite l'hydrolyse de la liaison covalente $N\equiv N$: cette réaction très endergonique (c'est-à-dire très défavorable thermodynamiquement) ne peut être réalisée que par certains procaryotes dits « diazotrophes », possédant le complexe enzymatique de la nitrogénase¹. La fixation biologique de N_2 est principalement limitée par la disponibilité en phosphate, dont les organismes eux-mêmes ont besoin pour se multiplier. D'autres éléments comme le fer

¹ La nitrogénase est un complexe enzymatique propre à certains organismes procaryotes, dits diazotrophes. Elle catalyse la réduction de N_2 en NH_3 , c'est-à-dire la fixation biologique. Le fer, le molybdène et/ou le vanadium en sont des cofacteurs métalliques. La nitrogénase étant inhibée par la présence de dioxygène, les diazotrophes ont développé des stratégies évolutives pour l'en protéger, tels que la compartimentation cellulaire.

ou le molybdène peuvent aussi être biolimitants en raison de leur utilisation comme cofacteurs enzymatiques de la nitrogénase. Du fait de son coût énergétique important pour les organismes diazotrophes (16 ATP nécessaires pour l'hydrolyse de chaque liaison $N\equiv N$), la fixation biologique de N_2 n'est avantageuse que lorsque la disponibilité en azote fixé (NH_4^+ , NO_3^-) dans l'environnement devient fortement limitante.

Une fois fixé, c'est-à-dire biodisponible, l'azote peut prendre part à différents processus biogéochimiques en fonction des teneurs en dioxygène dans le système. La minéralisation de l'azote organique suite à la décomposition de la biomasse phytoplanctonique relâche l'azote sous forme d'ammonium (NH_4^+), qui peut (i) être de nouveau assimilé dans la biomasse ; (ii) être oxydé lors de la nitrification en conditions aérobies par des bactéries nitrifiantes en nitrites (NO_2^-) puis en nitrates (NO_3^-). La nitrification constitue la source de nitrates de l'océan actuel, et fournit de l'azote à de nombreux organismes hétérotrophes. Enfin, l'azote organique océanique peut (iii) tomber sur le fond de la colonne d'eau et être préservé dans la matière organique sédimentaire ou éventuellement sous forme d'ammonium dans les argiles (Figure 9.4).

Le retour d'azote de l'océan à l'atmosphère se fait sous forme de N_2 . La conversion des nitrates et de l'ammonium en N_2 est permise par deux voies métaboliques, qui sont : (i) la dénitrification et (ii) l'oxydation anaérobie de l'ammonium (anammox). Ces deux réactions se produisent en conditions suboxiques ou anoxiques (Figure 6.4). L'ensemble de ces processus sont replacés dans un cycle biogéochimique de l'azote, représenté dans la figure 6.4, qui montre de plus la valeur des fractionnements isotopiques, notés avec le symbole ϵ .



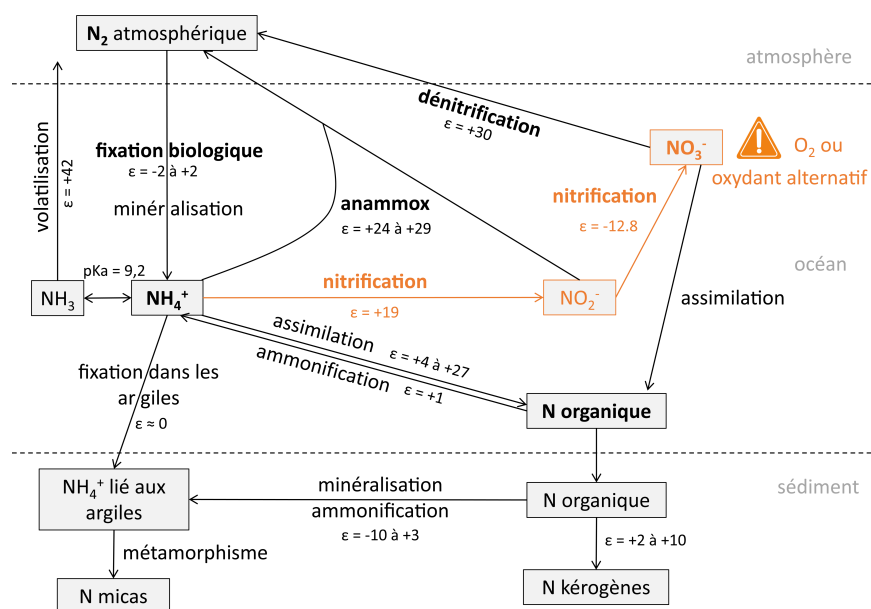


Figure 6.4. Modèle simplifié de cycle biogéochimique de l'azote dans les océans modernes (modifié d'après Thomazo et al. 2011). Les flèches pleines représentent les voies métaboliques. Les fractionnements isotopiques sont notés tels que $\epsilon = \delta^{15}\text{N}_{\text{réactif}} - \delta^{15}\text{N}_{\text{produit}}$.

6.3.3. La systématique isotopique du cycle de l'azote

La fixation biologique de N₂ atmosphérique ($\delta^{15}\text{N}_{\text{N}_2}=0\text{‰}$) par les diazotrophes (Figure 6.4), source quasiment exclusive d'azote pour la biosphère, ne cause pas de fractionnement isotopique significatif entre l'atmosphère et l'azote organique (le fractionnement étant compris entre -2 et +2‰, on le considère généralement égal à 0‰). De même, la libération d'ammonium lors de la minéralisation de la matière organique dans la colonne d'eau (ammonification, Figure 6.4), ne fractionne pas significativement les isotopes de l'azote ($\epsilon=+1\text{‰}$). L'ammonium ainsi libéré constitue un nutriment préférentiel pour les organismes ; il est donc rapidement assimilé dans la biomasse. Même si cette réaction incorpore préférentiellement du ¹⁴N, elle est généralement quantitative, c'est-à-dire que la totalité du réservoir d'ammonium est consommée. Il en résulte que le fractionnement n'est pas exprimé : en effet, la composition isotopique du produit est égale à celle du réactif puisqu'il s'est entièrement transformé. En conditions oxydées, l'ammonium peut être nitrifié en

nitrites puis en nitrates par deux réactions de nitrification successives (Figure 6.4). Les fractionnements de ces deux réactions se compensent ($\epsilon=+19\%$ et $-12,8\%$, respectivement). Par la suite, nitrites et nitrates peuvent être réassimilés par les organismes photosynthétiques ou réduits par dénitrification ou anammox en conditions dysoxiques et anoxiques (Figure 6.4). La dénitrification et l'anammox utilisent préférentiellement du ^{14}N , et, lorsqu'elles ne sont pas quantitatives, elles laissent respectivement les réservoirs de nitrates et d'ammonium fortement enrichis en ^{15}N . Le fractionnement induit par ces réactions peut aller jusqu'à $\epsilon=+30\%$.

Ainsi, la composition isotopique des producteurs primaires d'un écosystème dépend de la composition isotopique de la ou des sources d'azote assimilées (NH_4^+ , NO_3^- , N_2 et azote organique dissous DON), lesquelles dépendent du fractionnement isotopique associé à chaque voie métabolique les produisant ou consommant (fixation, ammonification, nitrification, dénitrification, anammox, etc.).

Dans les océans actuels, les valeurs de $\delta^{15}\text{N}$ sédimentaire autour de $+5\%$ résultent de la balance entre la fixation biologique (entrée) et la dénitrification/l'anammox (sortie) (Figure 6.5C).

6.3.4. Les archives de l'azote dans les temps géologiques anciens : préservation, réservoirs et flux

Dans les roches sédimentaires, l'azote est préservé principalement sous forme d'azote organique dans la matière organique fossile, mais aussi sous forme d'ammonium NH_4^+ qui, libéré de la matière organique en décomposition lors de la diagenèse, se substitue au potassium K^+ pour entrer dans le réseau cristallin des phyllosilicates (argiles) comme l'illite ou la smectite (Figure 6.4). Après métamorphisme, on pourra retrouver cet ammonium « minéral » dans les micas. Ces formes d'azote préservées dans les roches à l'échelle des temps géologiques sont, à l'exception de quelques inclusions fluides, les seuls outils disponibles pour tracer indirectement le cycle de l'azote sur la Terre primitive.

Néanmoins, il est nécessaire de garder à l'esprit que pour que la signature isotopique de l'azote organique préservé dans les roches sédimentaires puisse être utilisée comme un traceur de la composition isotopique des producteurs primaires dans la colonne d'eau à un moment donné de l'histoire de la Terre, un certain nombre de paramètres doivent être respectés. Tout d'abord, la signature isotopique ne doit pas avoir été modifiée par les processus post-dépôt comme le métamorphisme, la diagenèse de surface dans le sédiment, ou la diagenèse dans la colonne d'eau. De plus, l'azote doit être incorporé dans la matière organique à l'équilibre isotopique, c'est-à-dire sans fractionnement. Enfin, les voies métaboliques du cycle biogéochimique de

l'azote et leurs effets isotopiques doivent être conservés à l'échelle de l'évolution, ce qui permet d'appliquer le principe d'actualisme.

L'analyse de N₂ contenu dans des inclusions fluides datant de 3,5 Ga (Nishizawa et al. 2007 ; Marty et al. 2013) montre des valeurs isotopiques similaires aux valeurs actuelles ($\delta^{15}\text{N}_{\text{N}_2} \approx 0\%$, cf. encadré « Généralités sur les isotopes stables »). Cela suggère un cycle géologique de l'azote à l'état stationnaire depuis au moins 3,5 Ga. Si la composition isotopique du réservoir atmosphérique d'azote est effectivement restée stable depuis le Paléoarchéen (3,6 – 3,2 Ga), alors l'évolution des métabolismes peut être approchée par une analyse actualiste des fractionnements isotopiques (cf. 6.3.4.). Dans la mesure où les taux de dioxygène atmosphérique ont changé de façon importante depuis l'Archéen (Canfield 2005), et que les réactions biologiques du cycle de l'azote dépendent fortement de la spéciation redox dans la colonne d'eau, il est attendu que l'évolution du cycle biogéochimique de l'azote soit enregistrée dans les archives géologiques. Par conséquent, si l'on peut retracer l'évolution du cycle de l'azote à l'aide des restes azotés préservés dans les roches, on dispose alors d'un traceur indirect des changements d'oxydo-réduction des océans, comme nous le détaillons ci-dessous.

6.3.5. Le $\delta^{15}\text{N}$ des roches sédimentaires précambriennes : une archive de l'oxygénation des océans

Au-delà de l'identification de métabolismes passés (fixation, nitrification, dénitrification), la composition isotopique de l'azote est surtout largement utilisée comme un marqueur d'oxydation des paléoenvironnements. En effet, la composition isotopique en azote de la matière organique biologique est dépendante des conditions d'oxydo-réduction au sein de la colonne d'eau, puisque les réactions biogéochimiques du cycle de l'azote se font à des états redox différents. La nitrification nécessite des conditions localement oxydantes, tandis que la dénitrification et l'oxydation anaérobie de l'ammonium (anammox) se produisent en conditions suboxiques ou anoxiques (Figures 6.4 et 6.5). Si l'on observe un enrichissement en ¹⁵N dans l'azote de la matière organique sédimentaire, on en déduit que la biomasse phytoplanctonique a assimilé des nitrates fortement enrichis en ¹⁵N. Pour que cela soit le cas, il faut qu'un réservoir résiduel de nitrates soit préservé malgré la dénitrification ou l'anammox, et donc que le réservoir initial soit de taille suffisamment importante pour qu'il ne puisse pas être entièrement réduit. Cela ne se produit que lorsque la colonne d'eau des océans est suffisamment oxygénée (Figure 6.5). Par conséquent, une matière organique sédimentaire présentant des $\delta^{15}\text{N} > 5\%$ indique généralement des conditions océaniques oxygénées, au moins dans la partie supérieure de la colonne d'eau.

Attention toutefois, il convient de rester prudent et de mettre une telle interprétation en regard d'autres indicateurs d'oxydation (cf. chapitre 6).

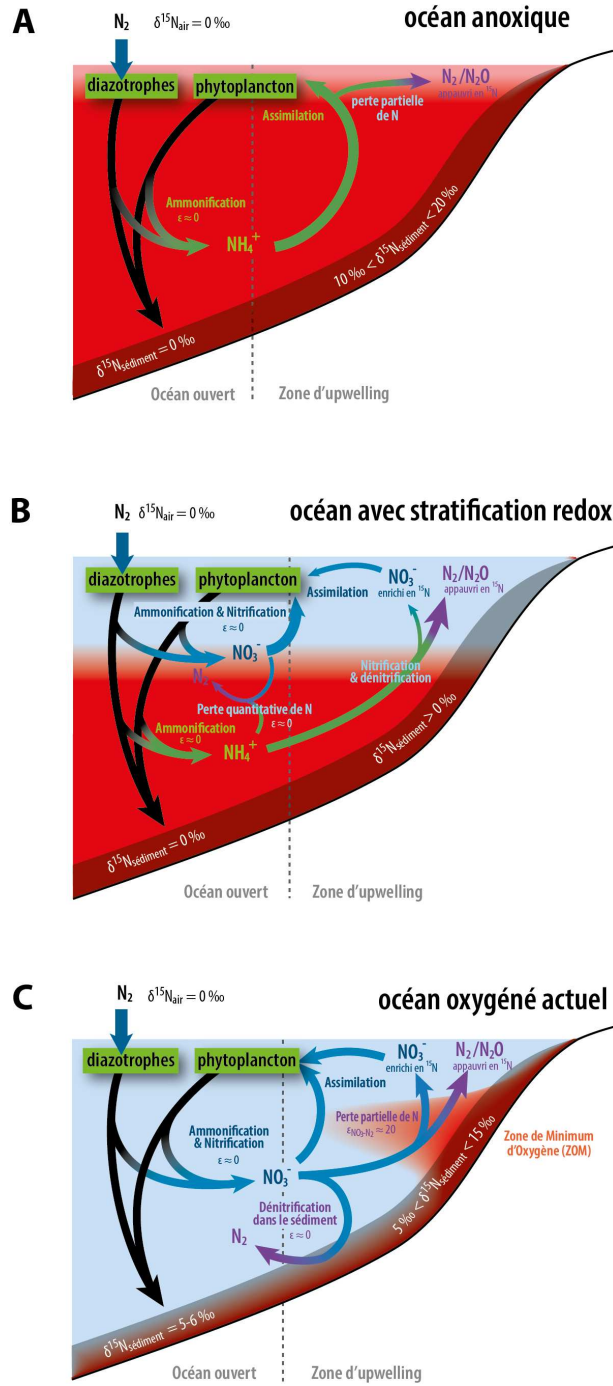


Figure 6.5. Représentation simplifiée de l'évolution redox du cycle biogéochimique de l'azote dans les océans du Précambrien à l'actuel (A puis B puis C) et de la signature isotopique de l'azote sédimentaire associée (modifié d'après Ader et al. 2016). Les zones anoxiques figurent en rouge, et les zones oxygénées en bleu. Les fractionnements isotopiques sont indiqués en notation ϵ .

Ainsi, avant l'accumulation de quantités significatives de dioxygène ou d'un oxydant alternatif dans l'océan précambrien, les valeurs de $\delta^{15}\text{N}$ des roches sédimentaires restent centrées autour de 0‰ (Figure 6.6), reflétant un cycle biogéochimique primitif de l'azote dominé par la fixation de N_2 , l'ammonification et l'assimilation de NH_4^+ . L'augmentation des teneurs en dioxygène permettant d'initier le couplage nitrification/dénitrification a probablement eu lieu au cours du Néoarchéen, où des valeurs positives du $\delta^{15}\text{N}$ ont été mesurées dans différentes formations géologiques (Figure 6.6 ; Garvin et al. 2009 ; Godfrey & Falkowski 2009 ; Thomazo et al. 2011 ; Stüeken et al. 2015).

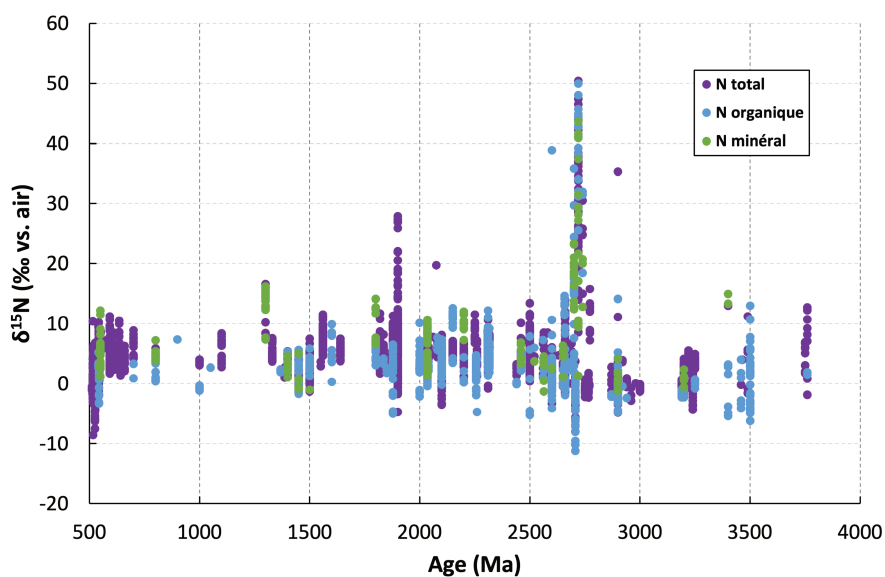


Figure 6.6. Compilation des données isotopiques de l'azote des archives sédimentaires au cours des temps géologiques (modifiée d'après Ader et al. 2016 et Stüeken et al. 2016).

A l'heure actuelle, le faible nombre de mesures d'isotopes de l'azote sur des roches archéennes ne permet pas de déterminer avec précision la temporalité de

l'accumulation d'oxygène dans les océans, ni de savoir si certaines localités ont joué un rôle clé en formant des « oasis d'oxygène », c'est-à-dire des zones spatialement limitées où les teneurs en dioxygène étaient plus élevées. L'augmentation du nombre de données isotopiques et le couplage avec d'autres traceurs redox devraient permettre d'approfondir notre compréhension de l'oxygénation des océans.

6.3.6. Démêler les effets locaux des changements globaux

Comme évoqué pour les isotopes du carbone, l'une des difficultés majeures d'interprétation des signaux géochimiques enregistrés dans les roches sédimentaires est de les transposer à l'échelle d'une colonne d'eau entière, d'un bassin sédimentaire voire d'un océan global. En d'autres termes, il est difficile de déterminer si les conditions environnementales déterminées à partir de l'étude des fractionnements isotopiques sont généralisables à grande échelle.

Par exemple, on peut se demander si des perturbations du cycle biogéochimique de l'azote ont eu lieu à une échelle globale il y a 2,7 Ga. En effet, au sein de la formation géologique de Tumbiana (2,72 Ga, craton de Pilbara, Australie), des roches sédimentaires présentant une forte anomalie positive en azote (valeurs de $\delta^{15}\text{N}$ jusqu'à +50‰) ont été mises en évidence (Thomazo et al. 2011 ; Stüeken et al. 2015). Cette anomalie isotopique extrême semble correspondre à une signature primaire, car les roches de la formation de Tumbiana sont peu métamorphisées. Deux hypothèses ont été formulées pour l'expliquer :

- Le début de la nitrification, qui correspondrait au début de l'accumulation d'oxygène dans les océans plusieurs centaines de millions d'années avant le GOE (Thomazo et al. 2011).
- Un enrichissement de l'ammonium en ^{15}N suite à la volatilisation d'ammoniac (NH_3) à pH élevé, en contexte particulier de lac alcalin (Fig. 1) (Stüeken et al. 2015).

La première hypothèse plaide en faveur d'un changement redox des océans autour de 2,7 Ga, donc à l'échelle globale, tandis que la deuxième plaide en faveur d'un lac alcalin, donc à une échelle régionale et non globale. Bien que ces deux scénarios ne soient pas incompatibles, cet exemple montre à quel point il est difficile de démêler les effets locaux par rapports aux changements globaux.

La meilleure stratégie reste de coupler un grand nombre d'indicateurs disponibles, par exemple des traceurs indépendants sensibles au degré redox (comme le fer, le manganèse, le molybdène...), sur une même série d'échantillons de roches, puis de

généraliser cette pratique à différents bassins sédimentaires de même âge dans des contextes géologiques variés.

6.4. Conclusions générales - D'un cycle géochimique à un cycle biogéochimique : comment détecter l'apparition des premiers flux biologiques d'azote et de carbone ?

Un certain nombre de sources et de flux abiotiques d'azote ont été mis en évidence. Les plus importants sont la réduction photochimique et la réduction hydrothermale, qui produisent respectivement de l'ammoniac (NH_3) et des ions ammonium (NH_4^+), les impacts météoritiques et la foudre qui produisent des oxydes d'azote (NO_x , x pouvant valoir 1, 2 ou 3), et le volcanisme qui produit de l'acide nitrique (HNO_3). Néanmoins, les modélisations tendent à montrer que ces flux abiotiques d'azote sur Terre sont extrêmement faibles. En effet, ils sont tous estimés inférieurs à 10^{12} moles N/an, alors que la fixation biologique est de 10^{13} moles N/an (Stüeken et al. 2016). Ces flux semblent donc incompatibles avec la quantité de biosphère estimée d'après les quantités de carbone organique (TOC pour *total organic carbon*) à partir du Paléoarchéen. De plus, le $\delta^{13}\text{C}_{\text{org}}$ de la matière organique montre des valeurs compatibles avec des métabolismes biologiques (photosynthèse, méthanogenèse, méthanotrophie), et ce depuis au moins 3,0 Ga (Schidlowski 2001). Néanmoins, il est important de souligner que les quantités d'azote minéral et organique préservées dans les roches sédimentaires ne sont pas toujours représentatives des quantités d'azote initialement présentes dans la colonne d'eau. En effet, une grande partie de l'azote de la colonne d'eau n'est pas nécessairement consommée ou préservée dans le sédiment, et peut de plus être perdue par dévolatilisation lors du métamorphisme.

La recherche de couplages avec d'autres systèmes isotopiques aux échelles locales et globales, comme le fer ou le soufre, est une piste à explorer pour préciser l'apparition des mécanismes biologiques et leur impact sur les cycles biogéochimiques au cours de l'histoire de la Terre.

6.5. Bibliographie

Ader, M., Thomazo, C., Sansjofre, P., Busigny, V., Papineau, D., Laffont, R., Cartigny, P., Halverson, G.P., 2016. Interpretation of the nitrogen isotopic composition of Precambrian sedimentary rocks: Assumptions and perspectives. *Chemical Geology* 429, 93–110.

- Cadeau, P., Jézéquel, D., Leboulanger, C., Fouilland, E., Floc'h, L., Chaduteau, C., ... & Ader, M. (2020). Carbon isotope evidence for large methane emissions to the Proterozoic atmosphere. *Scientific reports*, 10(1), 1-13.
- Canfield, D.E., 2005. The early history of atmospheric oxygen: Homage to Robert M. Garrels. *Annual Review of Earth and Planetary Sciences* 33, 1–36.
- Cartigny, P., Harris, J. W., & Javoy, M. (1998). Eclogitic diamond formation at Jwaneng: no room for a recycled component. *Science*, 280(5368), 1421-1424.
- Catling, D. C., Zahnle, K. J., & McKay, C. P. (2001). Biogenic methane, hydrogen escape, and the irreversible oxidation of early Earth. *Science*, 293(5531), 839-843.
- Craig, H. (1961). Standard for reporting concentrations of deuterium and oxygen-18 in natural waters. *Science*, 133(3467), 1833-1834.
- Des Marais, D. J. (1997). Isotopic evolution of the biogeochemical carbon cycle during the Proterozoic Eon. *Organic Geochemistry*, 27(5-6), 185-193.
- Frimmel, H. E. (2010). On the reliability of stable carbon isotopes for Neoproterozoic chemostratigraphic correlation. *Precambrian Research*, 182(4), 239-253.
- Gaillard, F., Scaillet, B., & Arndt, N. T. (2011). Atmospheric oxygenation caused by a change in volcanic degassing pressure. *Nature*, 478(7368), 229-232.
- Garvin, J., Buick, R., Anbar, A.D., Arnold, G.L., Kaufman, A.J., 2009. Isotopic Evidence for an Aerobic Nitrogen Cycle in the Latest Archean. *Science* 323, 1045–1048.
- Grotzinger, J. P., Fike, D. A., & Fischer, W. W. (2011). Enigmatic origin of the largest-known carbon isotope excursion in Earth's history. *Nature Geoscience*, 4(5), 285-292.
- Godfrey, L.V., Falkowski, P.G., 2009. The cycling and redox state of nitrogen in the Archaean ocean. *Nature Geoscience* 2, 725–729.
- Halverson, G. P., Hoffman, P. F., Schrag, D. P., Maloof, A. C., & Rice, A. H. N. (2005). Toward a Neoproterozoic composite carbon-isotope record. *GSA bulletin*, 117(9-10), 1181-1207.
- Hayes, J. M., Strauss, H., & Kaufman, A. J. (1999). The abundance of ¹³C in marine organic matter and isotopic fractionation in the global biogeochemical cycle of carbon during the past 800 Ma. *Chemical Geology*, 161(1-3), 103-125.
- Karhu, J. A., & Holland, H. D. (1996). Carbon isotopes and the rise of atmospheric oxygen. *Geology*, 24(10), 867-870.

- Kasting, J. F. (2013). What caused the rise of atmospheric O₂?. *Chemical Geology*, 362, 13-25.
- Krissansen-Totton, J., Buick, R., & Catling, D. C. (2015). A statistical analysis of the carbon isotope record from the Archean to Phanerozoic and implications for the rise of oxygen. *American Journal of Science*, 315(4), 275-316.
- Marty, B., Zimmermann, L., Pujol, M., Burgess, R., Philippot, P., 2013. Nitrogen Isotopic Composition and Density of the Archean Atmosphere. *Science* 342, 101–104.
- Nishizawa, M., Sano, Y., Ueno, Y., Maruyama, S., 2007. Speciation and isotope ratios of nitrogen in fluid inclusions from seafloor hydrothermal deposits at ~ 3.5 Ga. *Earth and Planetary Science Letters* 254, 332–344.
- Och, L. M., & Shields-Zhou, G. A. (2012). The Neoproterozoic oxygenation event: Environmental perturbations and biogeochemical cycling. *Earth-Science Reviews*, 110(1-4), 26-57.
- Prave, A. R., Kirsimäe, K., Lepland, A., Fallick, A. E., Kreitsmann, T., Deines, Y. E., ... & Hodgskiss, M. S. W. (2022). The grandest of them all: the Lomagundi–Jatuli Event and Earth's oxygenation. *Journal of the Geological Society*, 179(1).
- Schidlowski, M., 2001. Carbon isotopes as biogeochemical recorders of life over 3.8 Ga of Earth history: evolution of a concept. *Precambrian Research* 106, 117–134.
- Stüeken, E.E., Buick, R., Schauer, A.J., 2015. Nitrogen isotope evidence for alkaline lakes on late Archean continents. *Earth and Planetary Science Letters* 411, 1–10.
- Stüeken, E.E., Kipp, M.A., Koehler, M.C., Buick, R., 2016. The evolution of Earth's biogeochemical nitrogen cycle. *Earth-Science Reviews* 160, 220–239.
- Swart, P. K., & Kennedy, M. J. (2012). Does the global stratigraphic reproducibility of $\delta^{13}\text{C}$ in Neoproterozoic carbonates require a marine origin? A Pliocene–Pleistocene comparison. *Geology*, 40(1), 87-90.
- Thomazo, C., Ader, M., Philippot, P., 2011. Extreme ¹⁵N-enrichments in 2.72-Gyr-old sediments: evidence for a turning point in the nitrogen cycle. *Geobiology* 9, 107–120.

A.3. Conference abstracts

A.3.1. Goldschmidt (2021, online)

Nitrogen isotope variations across the 3.4 Gyr Buck Reef Chert, South Africa, question early nitrogen sources and pathways

Alice Pellerin¹, Christophe Thomazo¹, Magali Ader², Johanna Marin-Carbonne³, Julien Alleon³, Emmanuelle Vennin¹ and Axel Hofmann⁴

(1) Laboratoire Biogéosciences, UMR CNRS 6282, Université de Bourgogne Franche-Comté, France, (2) Institut de Physique du Globe de Paris, France, (3) Institut des Sciences de la Terre, University of Lausanne, Lausanne, Switzerland, (4) University of Johannesburg, South Africa.

Nitrogen is a key element of the biosphere, present in numerous macromolecules and involved in major metabolic pathways. Its isotopic composition is controlled by metabolic activity and redox speciation. Reconstructing the biogeochemical nitrogen cycle on the Early Earth is therefore valuable to our understanding of the evolution of the atmosphere, ocean and biosphere. The present study intends to fill in the sparse Paleoproterozoic record by providing N isotope data from the ICDP BARB3 drill core (Hofmann et al., 2013) through the Buck Reef Chert sedimentary unit (3416 Myr), Barberton Greenstone Belt, South Africa. The nitrogen concentration and isotopic composition of 33 samples have been analyzed by dual-inlet mass spectrometry after sealed tube Dumas combustion, extraction and purification. The exceptional preservation of organic matter (Alleon et al., 2021) underlined by high TOC contents (up to 6%), low TOC/TN ratios (<145) and reported occurrences of biofilms (Tice and Lowe, 2006), makes the Buck Reef Chert a perfect candidate to explore early biological cycle of nitrogen. $\delta^{15}\text{N}$ values range from -0.7‰ to +5.1‰, with marked positive values (mean $\delta^{15}\text{N} = +2.7‰$) in the lower silicified part of the core, interpreted as shallow platform facies (Tice and Lowe, 2006), followed by a clear stratigraphic decrease from +5.1‰ to -0.5‰ as we dive deeper towards the more basinal, siderite-rich, banded iron formation facies. Although various redox species of nitrogen associated with a complex cycle at a biofilm-scale cannot be excluded, the isotopic variations displayed by $\delta^{15}\text{N}$ values seem consistent with the range of fractionation associated with biological fixation of N_2 by diazotrophs using alternative nitrogenases. Indeed, lower $\delta^{15}\text{N}$ values might be consistent with an increasing contribution of (Fe)-nitrogenase in sideritic facies, where Fe is in excess compared to Mo. Alternatively, this stratigraphic $\delta^{15}\text{N}$

evolution could result from a mixing between a ^{15}N -enriched continental source (+2-3‰) of fixed nitrogen and hydrothermally ^{15}N -depleted ammonium (-5‰). Finally, this study suggests that different nitrogen sources or fixation pathways sustained a flourishing early Earth biomass as far back as 3.4 Gyr.

References

Alleon, J., Bernard, S., Olivier, N., Thomazo, C., Marin-Carbonne, J., 2021. Inherited geochemical diversity of 3.4 Ga organic films from the Buck Reef Chert, South Africa. *Communications Earth & Environment* 2, 1–7. <https://doi.org/10.1038/s43247-020-00066-7>

Hofmann, A., Karykowski, B., Mason, P., Chunnet, G., Arndt, N., 2013. Barberton drilling project - Buck Reef Chert core BARB3 15, EGU2013-12227.

Tice, M.M., Lowe, D.R., 2006. The origin of carbonaceous matter in pre-3.0 Ga greenstone terrains: A review and new evidence from the 3.42 Ga Buck Reef Chert. *Earth-Science Reviews* 76, 259–300. <https://doi.org/10.1016/j.earscirev.2006.03.003>

**Carbon isotope data from the Neoproterozoic Campbellrand-Malmani carbonate platform:
new insight into carbon fixation pathways at the eve of the Great Oxidation Event**

Alice Pellerin¹, Robin Havas¹, Pierre Sansjofre², Nicolas Olivier³, Kevin Lepot^{4, 5}, Julien Alleon⁶, Johanna Marin-Carbonne⁶, Pieter T. Visscher^{1, 7}, Magali Ader⁸, Christophe Thomazo^{1, 5}

(1) Laboratoire Biogéosciences, UMR CNRS 6282, Université de Bourgogne Franche-Comté, Dijon, France, (2) Laboratoire IMPMC, UMR CNRS 7590, Muséum National d'Histoire Naturelle, Paris, France, (3) Université Clermont Auvergne, CNRS, IRD, Laboratoire Magmas et Volcans, Clermont-Ferrand, France, (4) Univ. Lille, CNRS, Univ. Littoral Côte d'Opale, UMR 8187 - LOG – Laboratoire d'Océanologie et de Géosciences, F-59000 Lille, France, (5) Institut Universitaire de France (IUF), (6) Institut des Sciences de la Terre, Faculté des géosciences et de l'environnement, Université de Lausanne, Lausanne, Switzerland, (7) Departments of Marine Sciences and Geosciences, Univ. Connecticut, Groton, USA, (8) Institut de Physique du Globe de Paris, France.

The accumulation of biologically produced oxygen in the early oceans is widely seen as the driving factor leading to the Great Oxidation Event. This oxygen production is thus linked to the evolution of metabolic carbon fixation pathways, particularly the appearance of oxygenic photosynthesis. Shallow platform settings are often considered to be niches for early aerobic systems. Among these settings, Precambrian stromatolitic carbonate platforms have been the focus of many geochemical studies as they offer an ideal target for exploring the link between biological innovations and the protracted oxygenation of Earth's oceans and atmosphere. Notably, previous studies of the 2.58-2.50 Ga Campbellrand-Malmani platform (Transvaal Supergroup, South Africa) have shown a depth-dependent trend from lower $\delta^{13}\text{C}_{\text{org}}$ values around -40‰ in deeper depositional settings to higher $\delta^{13}\text{C}_{\text{org}}$ values close to -25‰ towards the platform shelf (Eroglu et al., 2017). This trend has been interpreted as a change from anaerobic (e.g., methanogenesis and methanotrophy) to aerobic ecosystems (e.g., oxygenic photosynthesis) suggesting that various carbon fixation pathways operated in the ocean at that time.

The present study analyses the paired carbon isotopes of a meter-scale drill core retrieved from an unexplored part of the Campbellrand-Malmani platform harboring very shallow stromatolitic dolostone deposits. In these sediments, organic carbon exhibits a distinctive isotopic signature compared to the anoxic and aerobic endmembers described above, with ^{13}C -enriched values ranging from -22 to -16‰. Meanwhile, the $\delta^{13}\text{C}_{\text{carb}}$ of the samples narrows

between -1.3 and -1.1‰, leading to $\Delta^{13}\text{C}_{\text{carb-org}}$ values of around -17.7‰. It suggests that even if diagenetic processes may have overprinted the TOC content and the $\delta^{13}\text{C}_{\text{carb}}$, the $\delta^{13}\text{C}_{\text{org}}$ records a new type of biomass that has not been described in the Campbellrand-Malmani platform in previous studies. Together with 2.94 Ga stromatolites from the Red Lake carbonate platform in Canada (Lalonde et al., 2019), these results suggest that shallow water microbial communities may record a large diversity of metabolic carbon fixation pathways, that are key to understand their evolutionary trajectory.

References

- Eroglu, S., van Zuilen, M.A., Taubald, H., Drost, K., Wille, M., Swanner, E.D., Beukes, N.J., Schoenberg, R., 2017. Depth-dependent $\delta^{13}\text{C}$ trends in platform and slope settings of the Campbellrand-Malmani carbonate platform and possible implications for Early Earth oxygenation. *Precambrian Research* 302, 122–139. <https://doi.org/10.1016/j.precamres.2017.09.018>
- Lalonde, S., Sansjofre, P., Homann, M., Fralick, P., 2019. Sedimentology and geochemistry of Earth's oldest carbonate platform (2.94 Ga Red Lake Greenstone Belt, Ontario, Canada) 18783.

A.3.3. Goldschmidt (2022, Honolulu, U.S.A.)

Extreme carbon and nitrogen isotopic signatures overlapping the Fortescue excursion preserved in the 2.7 Ga Carajás basin, Brazil

Alice Pellerin¹, Christophe Thomazo^{1,4}, Magali Ader², Pascal Philippot^{3,6}, Eric Siciliano Rego^{2,3,5}, Camille Rossignol^{3,6,7}

(1) Laboratoire Biogéosciences, UMR CNRS 6282, Université de Bourgogne Franche-Comté, France, (2) Institut de Physique du Globe de Paris, CNRS, Université de Paris, France, (3) Géosciences Montpellier, Université de Montpellier, CNRS, Université des Antilles, Montpellier, France, (4) Institut Universitaire de France (IUF), (5) Instituto de Geociências, Universidade de São Paulo, Cidade Universitária, São Paulo, Brazil, (6) Instituto de Astronomia, Geofísica e Ciências Atmosféricas, Universidade de São Paulo, Cidade Universitária, São Paulo, Brazil, (7) Dipartimento di Scienze Chimiche e Geologiche, Università degli studi di Cagliari, Italy.

The nitrogen isotopic composition of sedimentary rocks is controlled by metabolic activity and redox speciation in the water column. Therefore, changes in the dominating nitrogen biogeochemical cycle's pathways have frequently been used to uncover the joint evolution of the atmosphere, the ocean and the biosphere. The transition from anoxic to oxygenated environments leading to the Great Oxidation Event (GOE) deserves a particular focus, especially as its timing and mechanisms remain debated.

Here we report new data from the Carajás basin, Amazonian Craton, Brazil. Samples from three Neoproterozoic drill cores through the Serra Sul and Azul formations, aged between 2.72 and 2.68 Ga and representative of shallow to deep oceanic settings (Rossignol et al., 2020), have been analyzed for their carbon and nitrogen abundances and isotopic compositions. These sediments display extremely positive $\delta^{15}\text{N}$ values of up to +35.1‰ combined with extremely negative $\delta^{13}\text{C}_{\text{org}}$ values down to -51.7‰, similar to those observed in the 2.72 Ga Tumbiana formation in Australia (Stüeken et al., 2015; Thomazo et al., 2011). The drivers of this unique isotopic excursion occurring \approx 300 million years before the GOE and named the Fortescue excursion are controversial, and two hypotheses have been put forward: (i) partial oxidation of ammonium through nitrification followed by complete denitrification, thus indicating the onset of an aerobic nitrogen cycling (Thomazo et al., 2011) and (ii) ammonia volatilization in anoxic, highly alkaline conditions typical of restricted lacustrine environments (Stüeken et al., 2015).

The Carajás basin has uncovered a new occurrence of the 2.7 Ga extreme ^{15}N -enrichments and ^{13}C -depletions event from oceanic settings. Whether this event is related to widespread redox changes in marine chemistry or rather reflect a peculiar signal related to restricted alkaline conditions still needs to be discussed, but in any case it points towards environmental conditions specific to this particular Neoproterozoic interval.

References

Rosignol, C., Siciliano Rego, E., Narduzzi, F., Teixeira, L., Ávila, J.N., Silva, M.A.L., Lana, C., Philippot, P., 2020. Stratigraphy and geochronological constraints of the Serra Sul Formation (Carajás Basin, Amazonian Craton, Brazil). *Precambrian Research* 351, 105981. <https://doi.org/10.1016/j.precamres.2020.105981>

Stüeken, E.E., Buick, R., Schauer, A.J., 2015. Nitrogen isotope evidence for alkaline lakes on late Archean continents. *Earth and Planetary Science Letters* 411, 1–10. <https://doi.org/10.1016/j.epsl.2014.11.037>

Thomazo, C., Ader, M., Philippot, P., 2011. Extreme ^{15}N -enrichments in 2.72-Gyr-old sediments: evidence for a turning point in the nitrogen cycle. *Geobiology* 9, 107–120. <https://doi.org/10.1111/j.1472-4669.2011.00271.x>

Extreme carbon and nitrogen isotopic signatures preserved in 2.7 Ga sedimentary rocks: widespread redox changes or local environmental conditions? New insight from the Carajás basin, Brazil.

Alice Pellerin¹, Magali Ader², Christophe Thomazo^{1,4}, Pascal Philippot^{3,6}, Eric Siciliano Rego^{2,3,5}, Camille Rossignol^{3,6,7}

(1) Laboratoire Biogéosciences, UMR CNRS 6282, Université de Bourgogne Franche-Comté, France, (2) Institut de Physique du Globe de Paris, CNRS, Université de Paris, France, (3) Géosciences Montpellier, Université de Montpellier, CNRS, Université des Antilles, Montpellier, France, (4) Institut Universitaire de France (IUF), (5) Instituto de Geociências, Universidade de São Paulo, Cidade Universitária, São Paulo, Brazil, (6) Instituto de Astronomia, Geofísica e Ciências Atmosféricas, Universidade de São Paulo, Cidade Universitária, São Paulo, Brazil, (7) Dipartimento di Scienze Chimiche e Geologiche, Università degli studi di Cagliari, Italy.

Nitrogen is a key element of the biosphere, present in numerous macromolecules and involved in major metabolic pathways. As the nitrogen isotopic composition of sedimentary rocks is controlled by redox speciation in the water column together with biological activity, changes in the dominating nitrogen biogeochemical cycle's pathways have frequently been used to uncover the joint evolution of the atmosphere, the ocean and the biosphere. In particular, nitrogen isotopes can specify the timing and mechanisms of the transition from anoxic to oxygenated environments leading to the ≈ 2.4 Ga Great Oxidation Event (GOE), which remain debated. This study features new data from the Carajás basin, Amazonian Craton, Brazil. Samples from three Neoproterozoic drill cores through the Serra Sul and Azul formations, aged between 2.72 and 2.68 Ga and representative of shallow to deep oceanic settings (Rossignol et al., 2020), have been analyzed for their carbon and nitrogen abundances and isotopic compositions. These sediments display extremely positive $\delta^{15}\text{N}$ values of up to +35.1‰ combined with extremely negative $\delta^{13}\text{C}_{\text{org}}$ values down to -51.7‰, similar to those observed in the 2.72 Ga Tumbiana formation in Australia (Stüeken et al., 2015; Thomazo et al., 2011). The drivers of this unique isotopic excursion occurring ≈ 300 million years before the GOE and named the Fortescue excursion are controversial, and two hypotheses have been put forward: (i) the onset of an aerobic nitrogen cycling, with partial oxidation of ammonium through nitrification followed by complete denitrification (Thomazo et al., 2011) and (ii) ammonia volatilization in anoxic, highly alkaline conditions typical of restricted lacustrine environments (Stüeken et al., 2015). The Carajás basin uncovers a new occurrence of the 2.7 Ga extreme ^{15}N -enrichments and ^{13}C -depletions event

from oceanic settings. Therefore, it sheds new light on a previously isolated signal related to a restricted alkaline environment. Whether this event stands as evidence for widespread redox changes in marine chemistry or rather reflects local settings still needs to be discussed, but in any case it points towards environmental conditions specific to this Neoproterozoic interval.

References

Rosignol, C., Siciliano Rego, E., Narduzzi, F., Teixeira, L., Ávila, J.N., Silva, M.A.L., Lana, C., Philippot, P., 2020. Stratigraphy and geochronological constraints of the Serra Sul Formation (Carajás Basin, Amazonian Craton, Brazil). *Precambrian Research* 351, 105981. <https://doi.org/10.1016/j.precamres.2020.105981>

Stüeken, E.E., Buick, R., Schauer, A.J., 2015. Nitrogen isotope evidence for alkaline lakes on late Archean continents. *Earth and Planetary Science Letters* 411, 1–10. <https://doi.org/10.1016/j.epsl.2014.11.037>

Thomazo, C., Ader, M., Philippot, P., 2011. Extreme ^{15}N -enrichments in 2.72-Gyr-old sediments: evidence for a turning point in the nitrogen cycle. *Geobiology* 9, 107–120. <https://doi.org/10.1111/j.1472-4669.2011.00271.x>

A.3.5. Goldschmidt (2023, Lyon, France)

Upgrades in the framework of nitrogen isotopes interpretation in Archean sedimentary rocks

Alice Pellerin¹, Magali Ader² & Christophe Thomazo^{1,3}

(1) Laboratoire Biogéosciences, UMR CNRS 6282, Université de Bourgogne, Dijon, France, (2) Université Paris Cité, Institut de Physique du Globe de Paris, CNRS, Paris, France, (3) Institut Universitaire de France (IUF), Paris, France.

The nitrogen isotopic signature preserved in sedimentary rocks has become one of the standard tools for investigating redox changes in the ocean associated with the evolution of the biosphere. Indeed, nitrogen is both a nutrient directly limiting biological productivity and a redox tracer taking part in redox-dependent biological pathways. Specifically, it has largely been used to uncover the evolution of the biogeochemical nitrogen cycle and interpreted as showing a rise of oceanic oxidants in the Neoproterozoic, well before the Great Oxidation Event (GOE), followed by the progressive stabilization of a persistent nitrate reservoir. Yet, the Precambrian $\delta^{15}\text{N}$ record does not clearly show significant changes across the GOE (Fig. 1).

Confronting 3 chosen case studies spanning the Archean period (the 3.4 Ga Buck Reef Chert Formation, the 2.68 Ga Serra Sul Formation and the 2.55 Ga Malmani Formation), this communication will highlight the strengths and limits of using sedimentary $\delta^{15}\text{N}$ data as an oxygenation tracer, as well as the crucial need for context while interpreting them.

The 3.4 Ga Buck Reef Chert Formation, South Africa, draws attention to possible interactions between the iron and nitrogen cycles in anoxic and ferruginous conditions, which are relevant to most of the Paleoproterozoic. $\delta^{15}\text{N}$ results for this formation invite to carefully consider the meaning of positive nitrogen isotopic signatures in Paleoproterozoic sediments, which do not necessarily indicate the presence of nitrate.

The extremely positive $\delta^{15}\text{N}$ values from the 2.68 Ga Serra Sul Formation, Brazil, together with comparable data from the Pilbara Craton, Australia, may reveal a rise of oceanic oxidants 300 Ma before the GOE. Whether these oceanic redox changes were widespread or rather developed locally/regionally due to specific chemical conditions or depositional configuration will be discussed.

Finally, the $\delta^{15}\text{N}$ values close to 0‰ recorded in the 2.5 Ga stromatolitic dolostone of the Malmani Formation, South Africa, invite us to reflect on the reason why, despite the presence of undisputed photosynthetic microbial remains and a $\delta^{13}\text{C}_{\text{org}}$ signature compatible with the development of an aerobic biosphere, the oxidative part of the nitrogen cycle is not expressed in the sedimentary rock record.

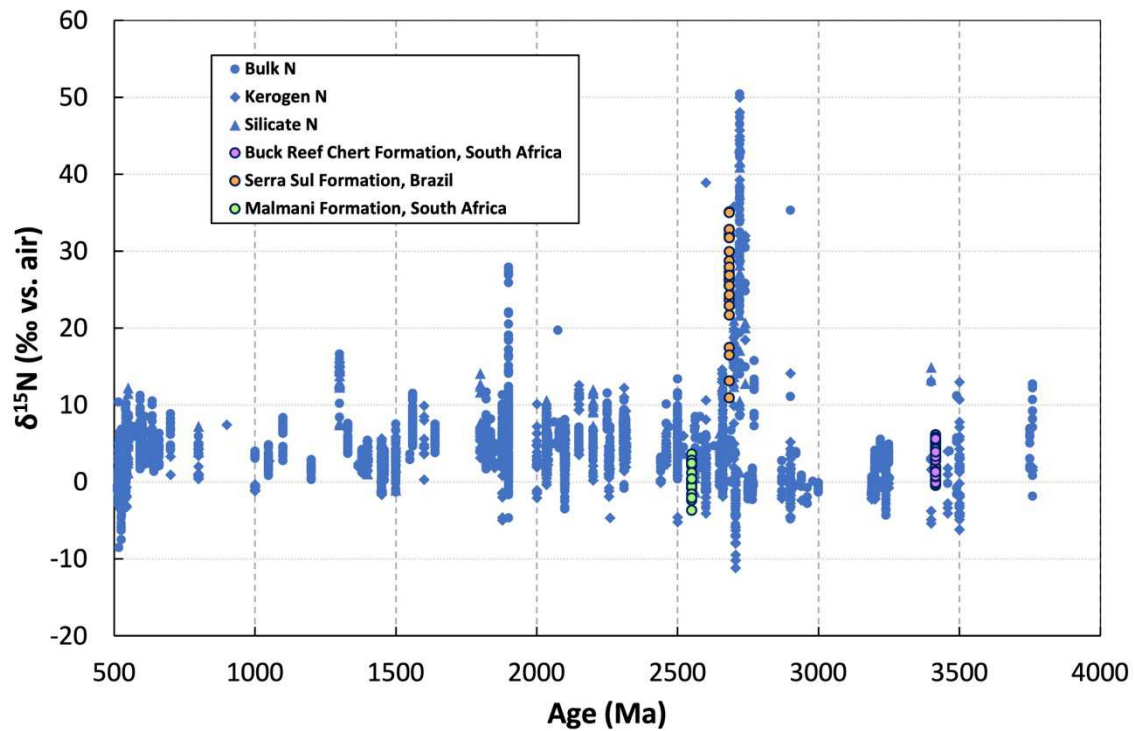


Fig. 1. Compilation of Precambrian sedimentary $\delta^{15}\text{N}$ data, including all lithologies and metamorphic facies.

A.3.6. M-FED Microbialites: Formation, Evolution, Diagenesis (2023, Leysin, Switzerland)

Theme: Microbialites through the geological record - “Microbialites as biological and environmental archives”

Are stromatolites ideal candidates to study the Archean N-biogeochemical cycle?

Alice Pellerin¹, Magali Ader², Robin Havas¹, Julien Alleon³, Nicolas Olivier⁴, Johanna Marin-Carbone⁵ & Christophe Thomazo^{1,6}

(1) Laboratoire Biogéosciences, UMR CNRS 6282, Université de Bourgogne, Dijon, France, (2) Université Paris Cité, Institut de Physique du Globe de Paris, CNRS, Paris, France, (3) LGL-TPE, Université de Lyon, Lyon, France, (4) Université Clermont Auvergne, CNRS, IRD, Laboratoire Magmas et Volcans, Clermont-Ferrand, France, (5) Institut des Sciences de la Terre, Université de Lausanne, Lausanne, Switzerland, (6) Institut Universitaire de France (IUF), Paris, France.

The nitrogen isotopic signature preserved in sedimentary rocks is one of the standard tools for investigating redox changes in the oceans associated with the evolution of the biosphere. Indeed, nitrogen is both a nutrient directly limiting biological productivity and a redox tracer taking part in redox-dependent biological pathways. Specifically, it has largely been used to uncover the evolution of the biogeochemical nitrogen cycle and interpreted as showing a rise of oceanic oxidants in Neoproterozoic oceans, followed by the progressive stabilization of a persistent nitrate reservoir.

Similarly, Precambrian stromatolitic carbonate platforms have been the focus of many geochemical studies targeting the link between biological innovations and Earth’s protracted oxygenation. Heavy nitrogen isotope signatures have been recorded in slope settings of the 2.58-2.50 Ga Campbellrand-Malmani platform (Transvaal Supergroup, South Africa), with $\delta^{15}\text{N}$ values centered around +5‰ and reaching up to +10‰ (Godfrey and Falkowski, 2009). They have been interpreted as the onset of oxic nitrogen cycling with a nitrate pool sufficiently stable to sustain denitrification overtime.

Meanwhile, we explored shallower settings of the Campbellrand-Malmani platform, that are often considered to be niches for early aerobic systems. We report $\delta^{15}\text{N}$ values centered around 0‰ from dolomitized stromatolites representative of proximal depositional environments, displaying a signature of diazotrophic N_2 -fixation. Such data invite us to rethink why, despite the presence of undisputed photosynthetic microbial remains and a $\delta^{13}\text{C}_{\text{org}}$ signature compatible with the development of an aerobic biosphere, the oxidative part of the nitrogen cycle is not

expressed in these microbialites. This communication will examine several hypotheses, including alternative metabolisms such as anoxygenic photosynthesis, the presence of a quantitatively consumed “cryptic” oxygen reservoir, and sampling bias, in an attempt to determine whether stromatolitic carbonates provide relevant archives to target Early Earth oxygenation.

References

Godfrey, L.V., Falkowski, P.G., 2009. The cycling and redox state of nitrogen in the Archaean ocean. *Nature Geoscience* 2, 725–729. <https://doi.org/10.1038/ngeo633>

Assessing biological innovation and trends in Earth's oxygenation using the nitrogen isotopic compositions of Precambrian organic matter

Christophe Thomazo^{1,2}, Alice Pellerin¹

(1) Laboratoire Biogéosciences, UMR CNRS 6282, Université de Bourgogne, Dijon, France, (2) Institut Universitaire de France (IUF), Paris, France.

Nitrogen is a chemical element present in all of Earth's geological reservoirs (core, mantle, crust), and dinitrogen (N₂) is the dominant gas in the Earth's atmosphere. Nitrogen is also a fundamental element of life since it is an integral part of the major molecules that make up the "building blocks" of life, such as amino acids and nucleic acids, the elementary unit of proteins and DNA. Moreover, insufficient nitrogen inputs restrict the growth of organisms, limiting primary productivity. Indeed, marine organic matter contains on average 106 atoms of carbon for 16 atoms of nitrogen and one atom of phosphorus (Redfield ratio). Nitrogen is therefore an essential nutrient which, along with phosphorus and iron, controls biological activity on Earth.

The nitrogen isotopic signature preserved in sedimentary rocks has become one of the standard tools for investigating the early evolution of the biosphere together with redox changes in the ocean. Because each fixed N species (NH₄⁺, NO₂⁻, NO₃⁻ and organic N) has a specific redox state and most pathways of the N-biogeochemical cycle are redox-controlled, nitrogen is an excellent marker of the redox state of ecosystems, indicating whether oxygen is present and stable in the environment.

Specifically, the nitrogen isotope composition of sedimentary organic matter has been used for more than two decades to uncover the evolution of the biogeochemical nitrogen cycle and has been interpreted as showing (Fig. 1): (i) an early rise of diazotrophy and iron-dependent anammox metabolisms during the Paleoproterozoic (Pellerin et al., 2023; Stüeken et al., 2015) and (ii) a Neoproterozoic rise of coupled nitrification-denitrification pathways associated with increasing oceanic oxidants budget several hundreds of millions of years before the Great Oxidation Event (GOE) (Ader et al., 2016; Stüeken et al., 2016; Thomazo et al., 2011). Yet, the Precambrian $\delta^{15}\text{N}$ record does not clearly show significant changes across the GOE (Fig. 1).

We present an extensive Precambrian $\delta^{15}\text{N}$ database spanning from the early Archean to the late Proterozoic (i.e. 3.8 Ga to 540 Ma). Using statistical methods applied to geochemical times

series on this compilation, we evaluate the impact of the $\delta^{15}\text{N}$ phase (kerogen N vs. bulk N, i.e. organic matter and ammonium within phyllosilicates), the lithology (shales, carbonates, cherts and Banded Iron Formations), and metamorphism.

Overall, the available Precambrian $\delta^{15}\text{N}_{\text{sed}}$ record shows a distribution roughly similar to that of the present ocean, but several “events” are suggested. Notably, we report a step change from +1 to +3‰ in the mode of the $\delta^{15}\text{N}_{\text{sed}}$ distributions at ca. 2.7 Ga and transient occurrences of extremely ^{15}N -enriched signatures at 2.7 and 1.9 Ga. These shifts in the N isotopic signal most probably reflect the evolution of nitrogen and carbon redox cycling in surface environments. They are in good agreement with independent geochemical tracer of Earth’s ocean (e.g. Mo and Cr isotopes) and atmosphere stepwise oxygenation through the Precambrian. This analysis reinforces the overlooked potential of deep time organic matter nitrogen isotopes to better understand Early Earth evolution.

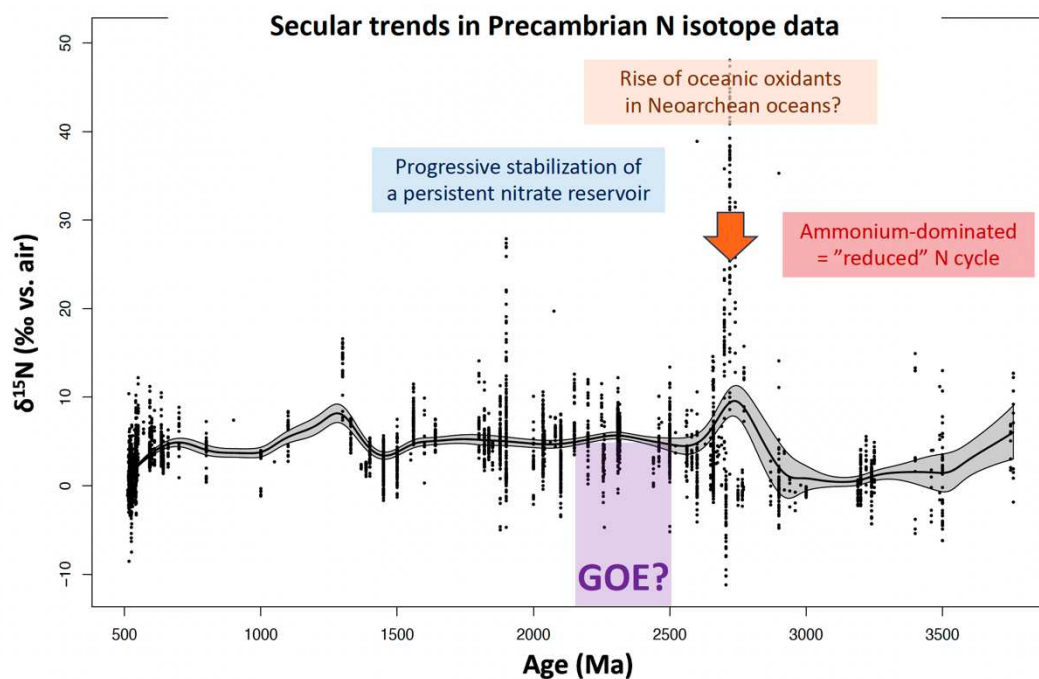


Fig. 1. Secular trends in Precambrian N isotope data with the inferred interpretations about the evolution of the marine N-biogeochemical cycle: an ammonium-dominated “reduced” N cycle in pre-GOE anoxic oceans, a rise of oceanic oxidants during the Neoproterozoic some time before the GOE, possibly around 2.7 Ga, followed by the progressive stabilization of a persistent nitrate reservoir in oxygenated surface waters. Smoothed curve and 95% confidence intervals are generated using kernel regressions with a bandwidth (h) of 100 Ma.

References

- Ader, M., Thomazo, C., Sansjofre, P., Busigny, V., Papineau, D., Laffont, R., Cartigny, P., Halverson, G.P., 2016. Interpretation of the nitrogen isotopic composition of Precambrian sedimentary rocks: Assumptions and perspectives. *Chemical Geology* 429, 93–110. <https://doi.org/10.1016/j.chemgeo.2016.02.010>
- Pellerin, A., Thomazo, C., Ader, M., Marin-Carbonne, J., Alleon, J., Vennin, E., Hofmann, A., 2023. Iron-mediated anaerobic ammonium oxidation recorded in the early Archean ferruginous ocean. *Geobiology* 21, 277–289. <https://doi.org/10.1111/gbi.12540>
- Stüeken, E.E., Buick, R., Guy, B.M., Koehler, M.C., 2015. Isotopic evidence for biological nitrogen fixation by molybdenum-nitrogenase from 3.2 Gyr. *Nature* 520, 666–669. <https://doi.org/10.1038/nature14180>
- Stüeken, E.E., Kipp, M.A., Koehler, M.C., Buick, R., 2016. The evolution of Earth's biogeochemical nitrogen cycle. *Earth-Science Reviews* 160, 220–239. <https://doi.org/10.1016/j.earscirev.2016.07.007>
- Thomazo, C., Ader, M., Philippot, P., 2011. Extreme ^{15}N -enrichments in 2.72-Gyr-old sediments: evidence for a turning point in the nitrogen cycle. *Geobiology* 9, 107–120. <https://doi.org/10.1111/j.1472-4669.2011.00271.x>

A.4. Reviewing activities

Geology, 2023: Uveges et al. An ammonium “nutrient capacitor” model for the $\delta^{15}\text{N}$ signatures associated with marine anoxic events.

Geophysical Research Letters, 2023: Du et al. Large Nitrogen Cycle Perturbations During the Early Triassic Hyperthermal Interval.

Geochimica et Cosmochimica Acta, 2023: Motomura et al. Marine redox state and nitrate bioavailability along the northern margin of the Superior Craton in the Late Paleoproterozoic.